Transactions of the ASME®

Transactions of the ASME, Journal of Turbomachinery (ISSN 0889-504X) is published quarterly (Jan., Apr., July, Oct.) by The American Society of Mechanical Engineers, Three Park Avenue, New York, NY 10016. Periodicals postage paid at New York, NY and additional mailing offices. POSTMASTER: Send address changes to Transactions of the ASME, Journal of Turbomachinery, c/o THE AMERICAN SOCIETY OF MECHANICAL ENGINEERS, 22 Law Drive, Box 2300, Fairfield, NJ 07007-2300.
CHANGES OF ADDRESS must be received at Society headquarters seven weeks before they are to be effective. Please send old label and new address.
STATEMENT from By-Laws. The Society shall not be responsible for statements or opinions advanced in papers or ... printed in its publications (B7.1, Par. 3).

INDEXED by Applied Mechanics Reviews and Engineering Information, Inc. Canadian Goods & Services Tax Registration #126148048

Journal of Turbomachinery

Published Quarterly by The American Society of Mechanical Engineers

VOLUME 123 • NUMBER 4 • OCTOBER 2001

TECHNICAL PAPERS

(Contents continued on inside back cover)

This journal is printed on acid-free paper, which exceeds the ANSI Z39.48-1992 specification for permanence of paper and library materials. ♾™
♻ 85% recycled content, including 10% post-consumer fibers.

Journal of Turbomachinery **Volume 123, Number 4** **OCTOBER 2001**

ANNOUNCEMENT

2001 International Gas Turbine Institute Gas Turbine Scholar Lecture

Convective Heat Transfer and Aerodynamics in Axial Flow Turbines

Michael G. Dunn
Gas Turbine Laboratory,
The Ohio State University,
Columbus, OH 43235

The primary focus of this paper is convective heat transfer in axial flow turbines. Research activity involving heat transfer generally separates into two related areas: predictions and measurements. The problems associated with predicting heat transfer are coupled with turbine aerodynamics because proper prediction of vane and blade surface-pressure distribution is essential for predicting the corresponding heat transfer distribution. The experimental community has advanced to the point where time-averaged and time-resolved three-dimensional heat transfer data for the vanes and blades are obtained routinely by those operating full-stage rotating turbines. However, there are relatively few CFD codes capable of generating three-dimensional predictions of the heat transfer distribution, and where these codes have been applied the results suggest that additional work is required. This paper outlines the progression of work done by the heat transfer community over the last several decades as both the measurements and the predictions have improved to current levels. To frame the problem properly, the paper reviews the influence of turbine aerodynamics on heat transfer predictions. This includes a discussion of time-resolved surface-pressure measurements with predictions and the data involved in forcing function measurements. The ability of existing two-dimensional and three-dimensional Navier–Stokes codes to predict the proper trends of the time-averaged and unsteady pressure field for full-stage rotating turbines is demonstrated. Most of the codes do a reasonably good job of predicting the surface-pressure data at vane and blade midspan, but not as well near the hub or the tip region for the blade. In addition, the ability of the codes to predict surface-pressure distribution is significantly better than the corresponding heat transfer distributions. Heat transfer codes are validated against measurements of one type or another. Sometimes the measurements are performed using full rotating rigs, and other times a much simpler geometry is used. In either case, it is important to review the measurement techniques currently used. Heat transfer predictions for engine turbines are very difficult because the boundary conditions are not well known. The conditions at the exit of the combustor are generally not well known and a section of this paper discusses that problem. The majority of the discussion is devoted to external heat transfer with and without cooling, turbulence effects, and internal cooling. As the design community increases the thrust-to-weight ratio and the turbine inlet temperature, there remain many turbine-related heat transfer issues. Included are film cooling modeling, definition of combustor exit conditions, understanding of blade tip distress, definition of hot streak migration, component fatigue, loss mechanisms in the low turbine, and many others. Several suggestions are given herein for research and development areas for which there is potentially high payoff to the industry with relatively small risk.
[DOI: 10.1115/1.1397776]

1 Introduction

This paper discusses the state of the art of turbomachinery heat transfer with an emphasis on propulsion, electric power generation, and marine gas turbines. Heat transfer is an important design consideration for all parts of a modern gas turbine, but especially the combustor, turbine, and exhaust nozzle. However, this paper focuses primarily on the turbine with limited discussion of the combustor and no discussion of the nozzle. In the propulsion gas turbine arena, modern high-pressure turbines are coming on line with significantly increased turbine inlet temperatures and stage pressure ratios. It is well known that the maximum allowable turbine inlet temperature strongly affects the efficiency of gas turbine engines and substantial performance increases can be achieved via this parameter. The current industry trend is to push the turbine inlet temperature closer to the fuel stoichiometric temperature, especially for military engines. This author sees no reason why the tendency to push for increasing turbine inlet temperatures will subside in the near future. There are numerous ongoing research activities designed to improve calculations of the hot-section heat loads, ranging from the basic to applied orientations. In discussing the state-of-the-art hot-section heat transfer research, it is important to keep in mind that the turbine designer, the ultimate customer of all of this research, is constantly under extreme pressures of time, affordability, durability, and reliability. The results of the research must not be so complicated and/or expensive that the designer elects to use the older, more familiar techniques and thus ignores the results of current research achievements.

Describing the dynamic condition of the gas exiting the combustor and entering the high-pressure turbine (HPT) nozzle is anything but simple. The flow field at the HPT inlet includes nonuniform radial and circumferential temperature profiles (hot streaks) and free-stream turbulence of some unknown intensity and scale. How these hot streaks progress through the high-pressure turbine

Contributed by the International Gas Turbine Institute and presented at the 46th International Gas Turbine and Aeroengine Congress and Exhibition, New Orleans, Louisiana, June 4–7, 2001. Manuscript received by the International Gas Turbine Institute February 2001. Paper No. 2001-GT-506. Review Chair: R. Natole.

(HPT) and on to the low-pressure turbine (LPT) is the subject of much current research activity. Several research efforts have attempted to measure turbulence intensity and scale of actual engine combustors at the combustor exit, but have had limited success. Because of difficulties with measurements associated with operating combustors, designers have speculated on what the appropriate turbulence intensity and scale might be, based on limited information. Techniques to incorporate combustor-generated turbulence into heat transfer design systems have been under development for many years, but with limited results. A significant portion of the experimental information used for this purpose has come from programs utilizing flat plates as the test article. The investigators assure the community that the turbulence intensity values generated for these measurements are representative of typical engine combustors. Seldom for these studies has there been an attempt to duplicate simultaneously the ''thought to be'' turbulence intensity and scale of the turbine free-stream inlet turbulence. In addition, a significant obstacle for the turbine heat transfer design community has been that flat-plate flows have not been demonstrated to be representative of the unsteady flow field environment associated with a turbine stage. There are many coupled phenomena associated with the unsteady turbine-stage flow field, and recent experimental results discussed later suggest that the influence of free-stream turbulence, wakes, fluid injection or ejection, and shock interaction may not be individually separable.

Experimental facilities and analysis tools in use at a particular time may not reflect the current understanding of the community. A time lag exists between the experimental facilities in use and the verified predictive codes, with the experimental facilities leading. The results used for CFD verification usually come from facilities that may be as much as a decade old. The early flat-plate and cascade research has been instrumental in the development of CFD prediction codes and the understanding of the underlying physics associated with turbine flows. Many of these flat-plate codes are still in use within the industry design systems. Further, these efforts have guided the development of the full-stage rotating facilities that can now be used to verify the underlying assumptions of earlier designs. However, use of flat-plate and cascade facilities as a tool for design code verification has been supplanted by the full-stage rotating rigs for obtaining data more closely representing the engine environment. These rotating rigs may be long run time facilities (with run times on the order of hours) or short-duration rigs (with run times on the order of fractions of seconds).

Because of advancements in experimental techniques and data acquisition, the roles of the different facilities have shifted. Full-scale rotating rigs can provide point measurements such as the early flat-plate experiments did. Modern flat-plate and cascade facilities have the promise of providing full-coverage surface measurements along with a detailed measurement of the incoming flow albeit in a more simple flow environment. Techniques developed in the flat-plate and cascade facilities often progress to the full-scale rotating rigs. Advances in the development of instrumentation techniques have led to the short-duration facilities becoming the primary source of internal flow data. The long run time facilities have become the source of macro-aerodynamic performance data where entire machines as opposed to components are used as the test article.

One of the more complicated flow environments associated with any practical machine occurs in the hot section of a turbine. The flow is always unsteady, it may be transonic, it is three dimensional, and it is subjected to strong body forces. In the pursuit of achieving higher efficiency, the turbine inlet temperature continues to be pushed to higher levels, requiring advances in cooling schemes and improved materials. Due to the ingenuity and intelligence of numerous dedicated design engineers, satisfactory designs have been achieved over the past fifty years. The past several years have seen a refinement in understanding of the underlying fluid and heat transfer mechanics that govern the basic physics occurring within the turbine. In addition, there have been several advances in materials and manufacturing processes over this same time. Most of this was accomplished due to refinements in approximations used by earlier designers. These approximations maintained a level of detail sufficient to reveal important physical effects while still allowing solutions using available analytical/numerical methods. The major milestones in the development of these early methods included many different assumptions and or methodologies. Among these are: (a) approximating the flow through each blade row to be steady in coordinates fixed to the blades, (b) assuming that three dimensionality can be handled by treating a series of two-dimensional flows in hub-to-shroud and blade-to-blade surfaces, (c) assuming that the effects of viscosity can be estimated by noninteracting boundary-layer calculations and by loss models to account for secondary flow, and (d) use of airfoil scaling to achieve periodicity and thus significantly reduce the computational time associated with a design phase calculation. Making simplifying assumptions can solve a current problem but create future ones. As recently shown by Clark et al. [1], designers should be cautious when using airfoil scaling since this methodology can lead to problems involving unsteady forcing function issues also of interest to the designer.

Many analyses and numerical codes are now available, refining the treatment of these flows past the levels of approximations discussed earlier. Because of the increased computational time required for the advanced codes they are generally used to provide refined estimates near a design point. Two areas where significant development has occurred over the past twelve to fifteen years that resulted in both increased understanding of the flow and better designs deal with three-dimensional and unsteady flow effects. The computational tools resulting from these efforts provide useful design information for the pressure loading, at least for the early stages of a multistage turbine.

Proper aerodynamic description of the flow field, which provides the boundary conditions for the heat transfer calculation, is essential if the predicted heat transfer distribution for the surface of a specific component is to be believed. Prediction of the stage aerodynamics is in itself a difficult problem that has received a significant amount of attention over the past decade or more. Many of the existing codes have been developed for two-dimensional flow, even though it was well known that for modern highly curved airfoils a three-dimensional calculation is necessary to account for the transverse pressure gradient and resulting secondary flows. Examples will be given in this paper where several of these two-dimensional codes have been used to predict the pressure loading and, in some cases, the heat transfer loading for vanes and blades in the absence of film cooling flows. However, because most modern high-pressure turbines are cooled, an important step in the advancement of these codes is incorporating film cooling for the vanes, outer air seal, and blades. Whether one has two-dimensional or three-dimensional aerodynamics as a starting point for the heat transfer calculation, it is still necessary to incorporate film cooling models into the codes. This aspect of the model development and subsequent incorporation into the prediction has been essentially ignored except for the work reported by Abhari [2]. The specific reference here is to the macro-model for film cooling as opposed to a micro-model that is associated with an isolated cooling hole. A wide variety of predictive techniques have been developed ranging from simple flat-plate correlations to large computer codes that are designed to solve the full three-dimensional Navier–Stokes equations. These flat-plate correlations lead to boundary layer calculations for which the boundary conditions can be taken from the aerodynamic codes just noted. Between these limits is a substantial body of analytical and numerical methods that account for most of the dominant physical phenomena while still being sufficiently convenient for use by a large fraction of turbine designers. A review of the state-of-the-art

heat transfer prediction techniques for the gas turbine engine prior to 1993 can be found in Simoneau and Simon [3].

This paper provides a discussion of several turbine aerodynamic CFD codes that are in use within the industry to predict the time-averaged and time-resolved surface-pressure distributions for single and multistage machines. The predictions of these codes are compared with experimental data at different times during the code development cycle as discussed in Section 2. It is critical to examine these aerodynamic codes because their output provides the input conditions for boundary-layer heat transfer calculations as discussed in Section 3. If the pressure field is not correct, it is unlikely that the corresponding heat transfer calculations will be correct. Section 3 also compares boundary layer correlation techniques, used for calculating component heat transfer distributions with experimental results. Included is a discussion of boundary layer transition as it relates to turbine heat transfer calculations, vane and blade film cooling and free-stream turbulence effects. Section 4 discusses internal heat transfer in nonrotating and rotating components, cavity flows, and predictive capabilities. The current state of the art is briefly summarized in Section 5. Section 6 provides suggestions for future turbine aerodynamic and heat transfer research and development needs.

Throughout the paper comparisons will be presented between CFD predictions and experimental results for both surface-pressure and heat transfer distributions on airfoils. The experimental data presented will often be those that were obtained by the authors and his colleagues since the results are readily available, but portions of data from other sources are also included. The predictions presented for comparison with experimental results were generally obtained directly from the developer of the specific CFD codes (or those who participated in development of the codes), instead of from third parties.

2 Current Technology: Turbine Aerodynamics

Many different CFD codes are in current use within the turbine design community. These vary between two-dimensional and three-dimensional, steady and time-accurate, Euler codes and Navier–Stokes codes. The following brief discussion of turbine aerodynamics is presented in this paper because of the importance to heat transfer predictions, and is not intended to be a review of CFD prediction techniques. The material described is limited to time-accurate unsteady solutions; time-mean values are the time average of the unsteady solutions. A convenient geometry to use for the purposes of this paper in comparing CFD predictions with experimental results is the Allison vane/blade interaction (VBI) turbine. Experimental results generated using the VBI turbine stage have been compared with the results of different CFD codes by many organizations over the past twelve years. The specific codes have evolved from time-accurate two-dimensional Euler to time-accurate three-dimensional Navier–Stokes over this time interval, all of which have been compared with this data set. Due to current interest in high-cycle fatigue, it is also important to couple the aerodynamic codes to structural damping as reviewed later in this section.

History shows that CFD codes progress through a natural evolution that may be conveniently grouped into three stages. In the initial stage, experimental results from a simplified geometry are used and ''knobs are twisted'' (such as changing the transition point on an airfoil) to get a reasonable match between the calculation and the data. In the second stage of the development, the code is used in the design of a particular experiment to perform predictions prior to performance of the measurement program. In this stage of the development, there may be a necessity to re-run the predictions in order to match the actual experimental input conditions but there should be limited ''knob turning.'' In the third stage, the CFD code is applied to a much more complicated geometry and a more realistic flow field environment. The geometry of interest might be a full-stage or vaneless counterrotating three-dimensional machine instead of a cascade airfoil and the flow field might be compressible and transonic instead of incompressible and subsonic. A code or algorithm that has progressed to stage three is often used as part of the design system, although those in earlier stages of development may be used under some circumstances. The reason for selecting the VBI geometry for code comparison in this section is that the codes described have progressed through the stages just noted. One limitation of the VBI geometry is that it was designed to be generally two-dimensional to aid with code development in the late 1980s. This makes comparing the output of the codes with three-dimensional machines more critical as is done later in this section.

2.1 Brief Review of CFD Capabilities. Designers often use boundary layer based codes to calculate HP turbine stage heat transfer loads in the absence of full Navier–Stokes solutions. Many techniques used for performing these calculations have their origin in boundary layer models that are based on flat-plate data and correlations. It is common practice to utilize the output of the more sophisticated aerodynamic calculations (along selected streamlines) to obtain local pressure distributions as the input conditions for the boundary-layer heat transfer calculations. This procedure is often used rather than integrating the heat transfer algorithms directly into the aerodynamic codes. One of the important reasons for this is that the heat transfer calculation requires a significantly different calculation grid than does the surface-pressure calculation and until recently, it was not possible to consider running these concurrently. This topic will be addressed in more depth in Section 3.

The ability to calculate the time-resolved pressure loading for a multistage turbine has advanced significantly over the past ten to fifteen years. Descriptions of techniques used for this purpose is beyond the scope of this paper but can be found in references [4–23]. Understandably, very few of these CFD codes are generally available in the public domain. This is true whether they were developed by government, university, or industry. In some cases, the rights to use an executable version of the code can be purchased from the developer along with a user manual, but seldom is the source code available (for understandable reasons). Codes are categorized by their general structure and that suffices for comparing their performance.

2.2 Comparison of Time-Resolved Surface-Pressure Measurements With CFD Prediction for Full-Stage Rotating Turbines. In this section, several of the CFD code types noted in Section 2.1 are compared with experimental data. Such comparisons demonstrate how the codes perform and help identify where more work is needed. It is important to briefly review sample cases of these calculated surface-pressure loadings, since they represent an important input parameter to the discussion of the heat transfer calculations to follow. The literature contains many examples of vane and/or blade surface-pressure measurements taken on full-stage rotating turbines of different geometries. Various CFD codes representing a wide range of types as noted above were used to compare the data with predictions. Among them are references [24–36]. Again, a discussion of the CFD codes beyond what is necessary for the discussion of heat transfer predictions and analysis is beyond the scope of this paper. Dring et al. [25] and Blair et al. [26] report time-averaged surface pressures on the blade, which were obtained using a large-scale, low-speed rotating rig with ambient inlet conditions. The surface-pressure results reported in the other papers just noted were obtained in short-duration facilities and the turbines were generally operated at design corrected conditions. Some of these studies report only steady surface-pressure results versus time-accurate results of other studies.

The three papers (Busby et al. [30], Venable et al. [31], and Barter et al. [32]) allow the opportunity to compare the predictions of several different CFD codes with the same data set. In addition, the data set for which the comparisons are made exercises the codes a bit, because data for vane/blade spacing of 20,

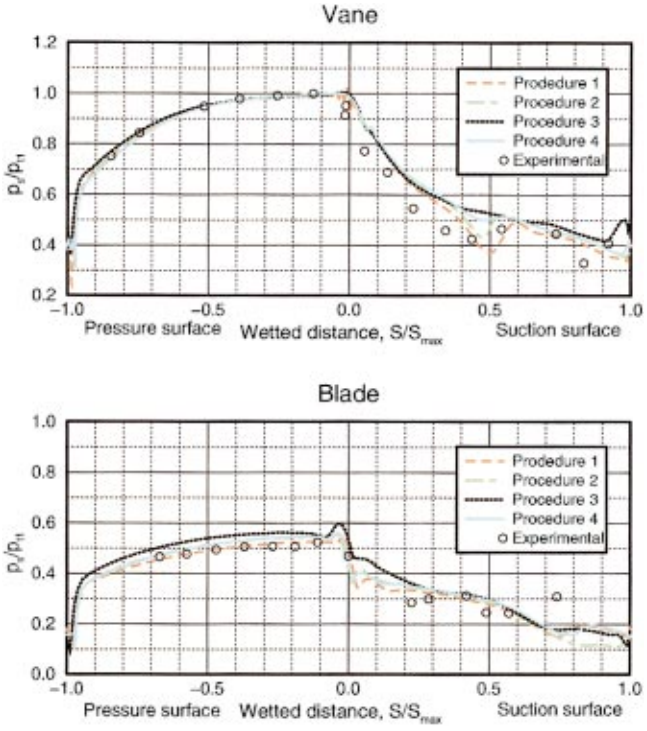

Fig. 1 Vane and blade time-mean pressure at 20 percent spacing [31]

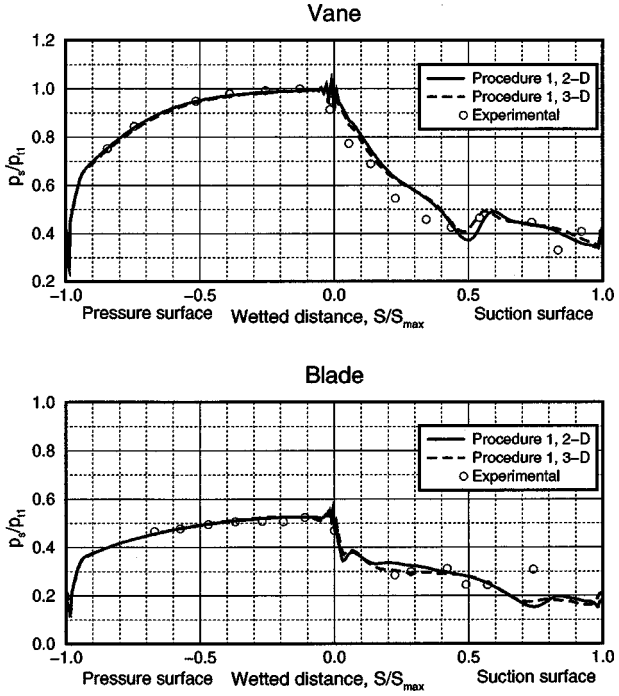

Fig. 3 Vane and blade time-mean pressure at 20 percent spacing, three-dimensional calculation [31]

40, and 60 percent of vane axial chord are included. The CFD code (UNSFLO 2-D) used to perform the calculations reported in Moss et al. [29] was one of the codes used in the work described in Busby et al. [30], Venable et al. [31], and Kielb et al. [37]. Barter et al. [32] used completely different CFD codes for their predictions. The experimental data used for the comparisons presented in these three papers were obtained in a short-duration facility described in Venable et al. [31]. Geometric and aerodynamic information for the turbine stage are given in [31]. For this case, the vane was set for a transonic exit condition, but both a subsonic and transonic condition is possible in this rig. Both the Kulite pressure transducers. These transducers are flush-mounted

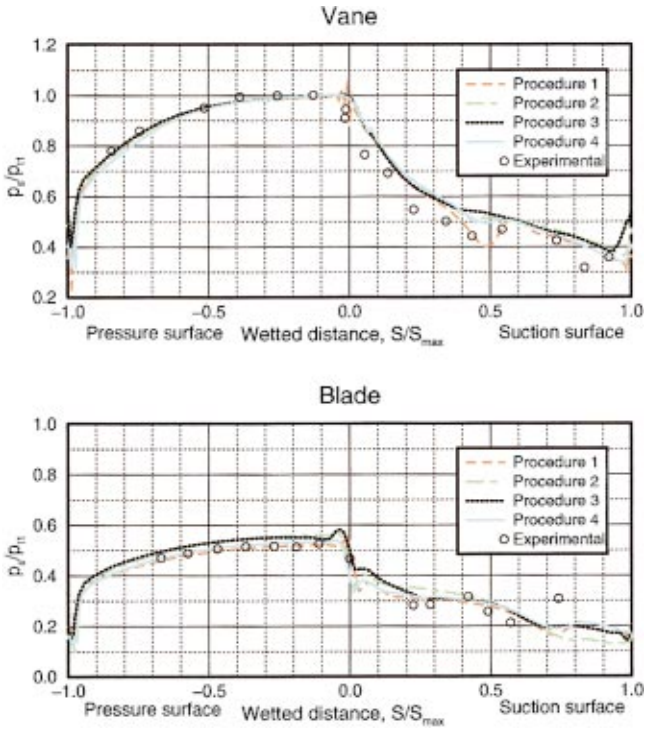

Fig. 2 Vane and blade time-mean pressure at 60 percent spacing [31]

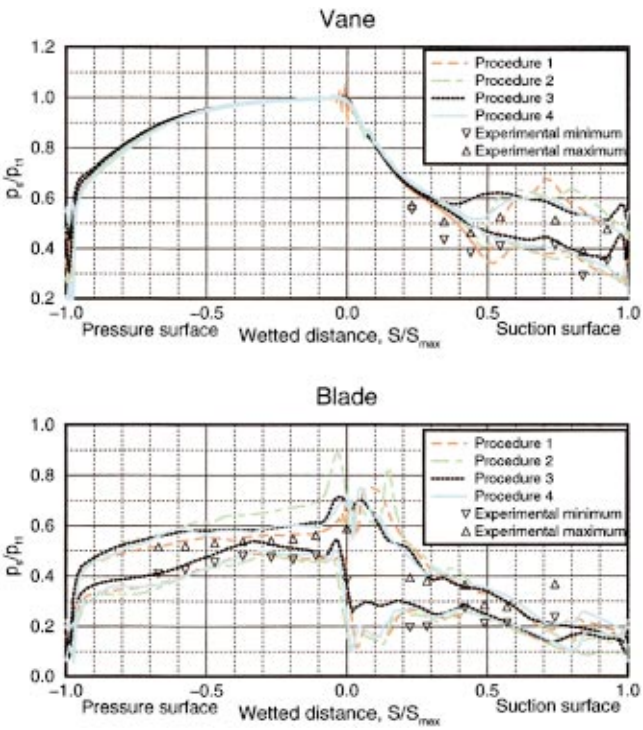

Fig. 4 Predicted versus measured unsteady pressure envelope at 20 percent vane/blade spacing [31]

to the surface and are built into the component. The natural frequency of the transducer is on the order of 400 kHz. A thin layer vanes and blades of the turbine were instrumented with miniature of silastic is placed over the transducer for thermal protection, resulting in a frequency response of the installed transducer of about 100 kHz. The locations of the transducers on the vanes and blades are also given in [31]. All of the pressure transducers are calibrated over the pressure range of applicability through the data recording system by pressurizing that portion of the facility containing the instrumented turbine stage on a daily basis.

Venable et al. [31] and Busby et al. [30] both used the same four CFD procedures to obtain the time-mean pressure distributions, the envelopes of the unsteady pressure, and the unsteady pressure histories at selected locations on the blade. Procedure 1 (Pratt and Whitney & UTRC) is a time-dependent, Reynolds-averaged Navier–Stokes solution, the details of which are described in references [12], [38], [39], and [19]. Both two-dimensional and three-dimensional solutions were obtained for Procedure 1 and the results are discussed in Venable et al. [31]. The two-dimensional solutions were obtained using three radial planes, with the first and third planes representing the boundary surfaces of the stream tube. The three-dimensional solutions incorporated the measured blade/shroud clearance. Procedure 2 (Rolls Royce/Allison) is a two-dimensional Vane–Blade Interaction (VBI) code that provides interactive solutions for a turbine stage flow by solving the Reynolds-averaged Navier–Stokes equations. More detail of this procedure can be found in references [40], [13], and [28]. Procedure 3 (Rolls Royce and MIT) is a two-dimensional Reynolds-averaged, unsteady multi-blade row code, UNSFLO 2-D, developed by Giles [8]. The numerical code UNSFLO 2-D is a coupled viscous/inviscid code. The thin shear layer Navier–Stokes equations are solved in a body-fitted boundary layer grid using an implicit algorithm, while the Euler equations are solved on an outer inviscid grid using an explicit algorithm. The interface between the two regions is handled in a conservative manner. Procedure 4 (Pratt and Whitney and UTRC) is an extension of an approach initially developed by Rai [7]. For this procedure, the thin-layer or full Navier–Stokes equations are solved on both the O- and H-type grids. Additional information regarding this procedure can be found in Dorney and Davis [41]. For all four procedures, the turbulent viscosity is modeled using the Baldwin–Lomax [42] algebraic turbulence model. Venable et al. [31] report the results of several grid refinement studies conducted for each of the four procedures illustrating grid independence of the four solutions presented. Figures 1 and 2 present comparisons between the experimental results and the results of a two-dimensional calculation using procedures 1–4 for the time-mean pressure distribution for the vane and blade at 20 percent and 60 percent axial chord spacing. Reference [31] also presents results for 40 percent spacing.

The largest difference among the predictions occurs on the vane suction surface near the throat location and on the uncovered portion of the blade suction surface. All of the procedures predict a weaker expansion along the suction surface of the vane than indicated by the data for unknown reasons. It is suggested in the paper that a possible reason for the problem is that the stream tube thickness used in the two-dimensional calculations may be in error. Calculations were performed to demonstrate that by changing the stream tube thickness the data could be matched. However, the three-dimensional calculations shown in Fig. 3 would suggest that the stream tube thickness is not the source of the problem as would be expected because of the two-dimensional design of the stage.

All of the codes do a reasonable job of predicting the choke point for the vane suction surface. With the exception of the uncovered portion of the blade suction surface, all of the codes did a good job of predicting the blade surface-pressure distribution. At all three spacings, at about 82 percent wetted distance (on the suction surface), the data fell above the predictions. It is argued in Venable et al. [31] that this disagreement is most likely due to a difference in back pressure between the CFD solutions and the experimental test conditions. A pressure increase is shown at about 75 percent wetted distance on the blade suction surface caused by an impinging vane trailing edge shock. The lower back-pressure used in the prediction causes the shock to be inclined at a shallower angle relative to the blade suction surface, resulting in the wave striking the blade closer to the trailing edge. Reference [31] presents a comparison of the measured and predicted surface pressure distribution for the three spacings. The influence of spacing on the time-mean surface-pressure distribution is very small. As will be demonstrated later such is not the case for the unsteady pressure on the trailing edge of the vane suction surface.

The same four prediction techniques were used to calculate the unsteady pressure envelopes for the same three spacings, but only the 20 percent, and the 60 percent spacing results are shown here in Figs. 4 and 5.

The important concept demonstrated by Figs. 4 and 5 is that the magnitude of the unsteadiness in pressure loading increases as the axial spacing decreases. The magnitude of the suction surface unsteadiness for the vane trailing edge is significantly larger at 20 percent spacing than for either 40 or 60 percent spacing. The magnitude of the unsteadiness is nearly constant over the entire pressure surface of the blade. The unsteadiness on the blade suction surface is not constant, but is largest at wetted distances between 0 percent and 30 percent and then falls off considerably with increasing wetted distance. The relative consistency of the unsteady pressure over the entire pressure surface is important from a film cooling perspective because this surface has the minimum back pressure margin and the largest number of film cooling holes. Figures 4 and 5 illustrate that procedures 1–4 all do a reasonably good job of predicting the unsteady pressure envelopes on both the vane and the blade.

Barter et al. [32] compared the results of APNASA and MSU TURBO with the same data set as used by Venable et al. [31] and Busby et al. [30]. Neither of these codes is presently used to perform heat transfer predictions, but it is important for this capability to be added. Mississippi State University (MSU) TURBO (Whitfield et al. [11]) is a three-dimensional, viscous, time-accurate code that solves the Reynolds-averaged Navier–Stokes equations in Cartesian coordinates. APNASA is an Average Passage (Adamczyk [23]) steady-state analysis that has been applied to turbomachinery problems (Turner et al. [43]). Two analytical techniques (TURBO Stage and TURBO Wake-Blade) implemented in MSU TURBO were used to obtain a comparison between the measured and predicted magnitude and phase of the unsteady pressure at vane passing frequency and at twice vane passing frequency. The difference between the two versions of the code is that Wake-Blade is a time-accurate analysis of a single blade row and unsteadiness is introduced via the boundary conditions. Stage is a technique for which the time-dependent solutions for both vane and blade are calculated simultaneously. Since this stage analysis does not use the exact blade count, phase-lag boundary conditions are used to help resolve wave interactions while limiting the computational domain to a single passage. The advantage to TURBO Wake-Blade is that the cost of running that code is about 25 percent the cost of running TURBO Stage. As demonstrated in this paragraph, MSU TURBO does a good job of predicting the time-averaged and unsteady pressure loading for a representative transonic turbine stage. It also has the ability to predict the three-dimensional flow field (demonstrated later in this section) whereas many of the other codes are two-dimensional or quasi-three-dimensional. However, presently this CFD capability is of limited use to the turbine designer because it does not provide the ability to calculate surface heat transfer distributions for the vanes and blades. The code does solve the energy equation, so in principle, it should be a straightforward development task to incorporate the heat transfer calculation. Additional information

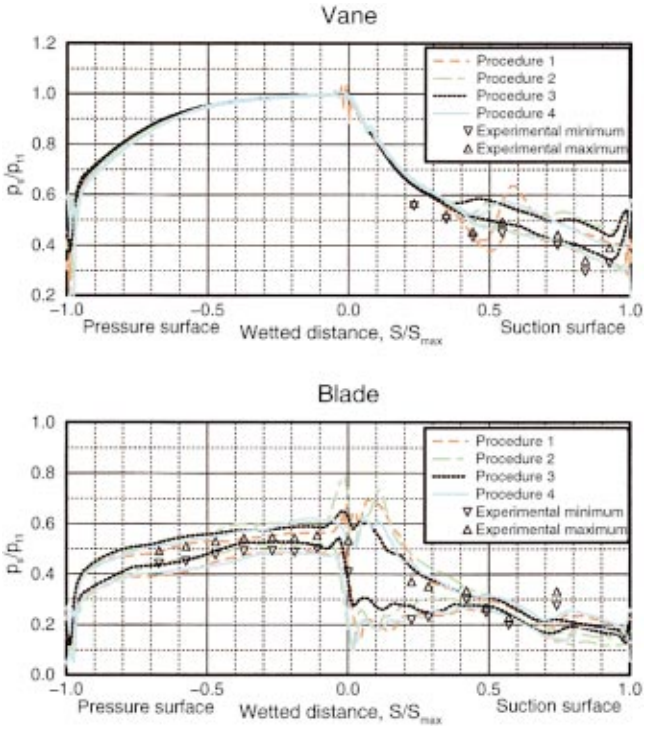

Fig. 5 Predicted versus measured unsteady pressure envelope at 60 percent vane/blade spacing [31]

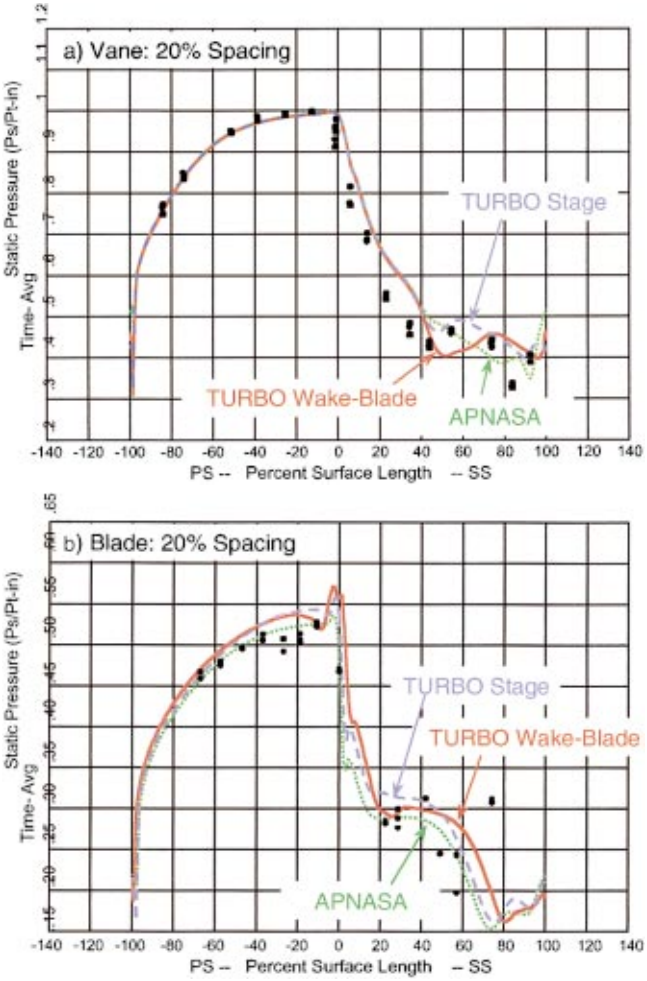

Fig. 6 Predicted versus measured time-averaged surface pressure for vane and blade at 20 percent vane/blade spacing [32]

concerning the MSU TURBO formulations and the numerical aspects of the solution can be found in Chen and Barter [44].

Modeling of the turbine stage for computational purposes can be done in several ways, as has been illustrated above, and each has advantages and disadvantages. The turbine could be designed to have three blades for every two vanes as was done for the Allison VBI measurement/analysis program (Dunn et al. [45] and Rao et al. [28]). For calculations performed for a more practical machine, one can use time tilting, as is done in UNSFLO 2-D, or phase-lag boundary conditions as done in TURBO. As will be demonstrated throughout this paper, UNSFLO 2-D does a reasonably good job of predicting both the surface-pressure distributions (both time-averaged and unsteady surface pressure and surface heat transfer) using reasonable computing assets. One disadvantage of the time-tilting technique is that when the pitch ratio exceeds 1.6 to 2.0, then more passages need to be included in the calculation. It is also demonstrated herein that TURBO, which uses phase-lag boundary conditions, produces satisfactory results for prediction of time-averaged and unsteady surface pressure using acceptable computer assets. One of the disadvantages of this

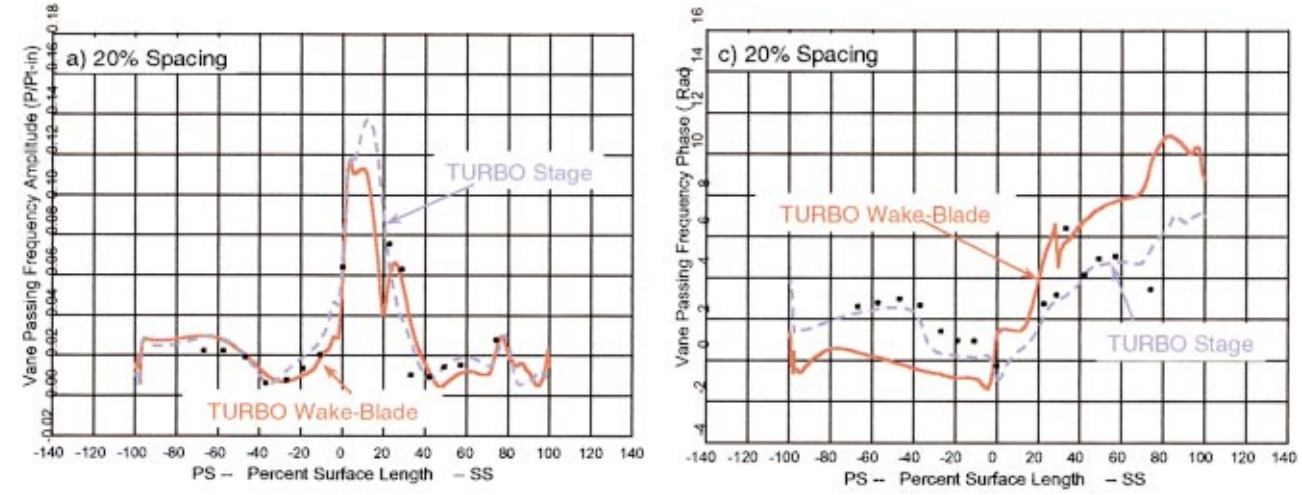

Fig. 7 Magnitude and phase of unsteady surface pressure on blade at vane passing frequency [32]

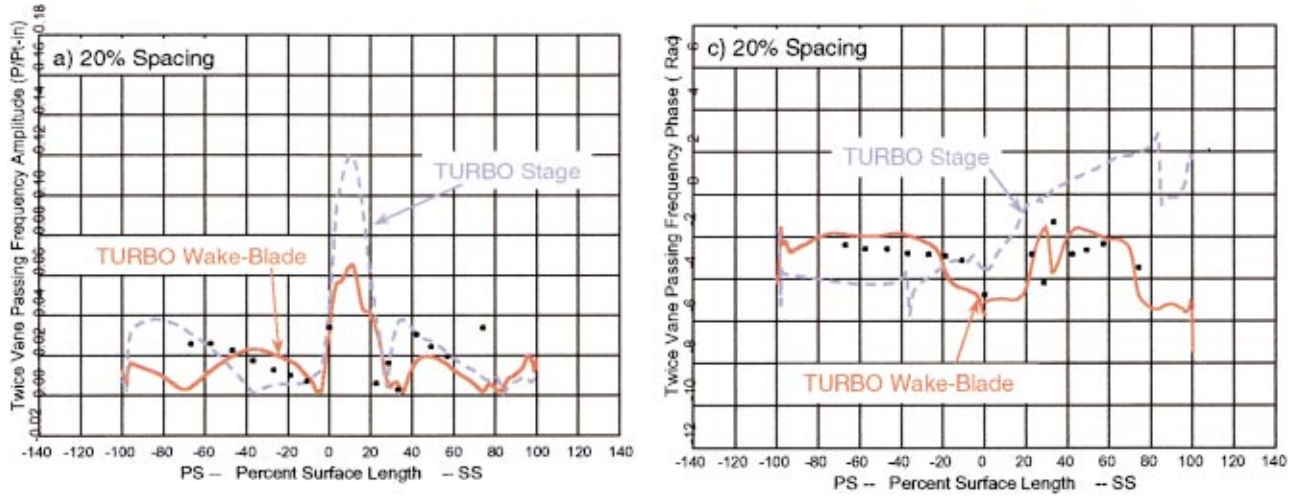

Fig. 8 Magnitude and phase of unsteady surface pressure on blade at 2× vane passing frequency [32]

technique is that it does require more iteration for convergence. In some cases, authors will resort to scaling the blade count in order to reduce the computational time and complexity. Clark et al. [1] investigated the consequences of scaling the blade count on the magnitude of the unsteadiness at twice vane passing frequency. In his work Clark achieved periodicity in the circumferential direction while modeling 1/18 of the annulus and compared these results with the results of a 1/4 wheel modeled without the use of airfoil scaling. Clark used experimental results obtained for a stage and 1/2 turbine. The experiments were performed in the same facility using the same experimental techniques as were used for the Allison VBI, Pratt/Whitney counterrotating turbine, GE counterrotating turbine, and TFE 731-2 measurement programs described at various locations in this paper. Clark found the time-averaged pressure distributions and the unsteady envelopes to be nearly the same for both types of modeling, but significant differences were observed in the results at twice vane passing frequency. This result signals a warning to designers to be careful when using the results from scaled calculations when attempting to reduce unsteadiness on a particular blade row.

A comparison between the predicted and measured vane and blade time-averaged surface-pressure distributions for the 20 percent spacing case (to be compared with Fig. 1) is given in Figs. 6(*a*) and 6(*b*). The comparisons presented in Barter et al. [32] are similar to the results of the four comparisons presented by Venable et al. [31]. For the three calculation techniques used by Barter et al. [32], TURBO Stage appears to do a better job of predicting the throat location on the vane suction surface than do either TURBO Wake-Blade or APNASA. Vane and blade pressure surface predictions obtained from the three calculations agree, but some differences are shown beyond the throat for the vane suction surface and for the blade suction surface. The largest differences occur at the 20 percent spacing.

The results reported by Barter et al. [32] for the amplitude and phase of the unsteady pressure at vane passing frequency and twice vane passing frequency for the 20 percent spacing are shown in Figs. 7 and 8, respectively. Similar results are also shown for 60 percent spacing in [32]. TURBO Stage does a good job of predicting both the amplitude and phase over the entire surface for the 20 percent spacing case at vane passing frequency as illustrated in Fig. 7. The phase distribution predicted by TURBO Wake-Blade is not in as good agreement with the data. However, both codes do an equally good job of predicting both the amplitude and phase at vane passing frequency at the 60 percent spacing. TURBO Wake-Blade predicts the phase at twice vane passing frequency for the 20 percent spacing case better than does TURBO Stage, but for the 60 percent spacing case both codes produce about the same result as shown in Fig. 8. The reasons for this are not presently clear.

Comparing the results of development CFD codes against multiple data sets can reduce design uncertainty. In the example given above, a comparison was presented for which eight CFD codes were compared to the same data set. There are two recent papers (Haldeman et al. [34] and Weaver et al. [36]) reporting time-averaged and unsteady surface pressure measurements versus prediction for two different transonic vaneless counterrotating turbines. These papers offer the opportunity to compare some of the same CFD codes to significantly different data sets. The two turbines used in the experiments were both vaneless counterrotating machines, but from different engine manufacturers. The experimental results used for both of these papers were performed in the same facility using the same experimental techniques to measure surface pressure on the vanes and blades.

Procedure 1 in Venable et al. [31] (Ni and Bogoian [12], Ni et al. [46], Sharma and Syed [47], and Sharma et al. [48]) was used in Haldeman et al. [34] to obtain vane/blade/blade surface-pressure predictions. It is important to note that the CFD results presented represent predictions obtained prior to the availability of the experimental results indicating the capabilities of the code as a design tool. Figure 9 presents a comparison of prediction versus data obtained for the midspan location of the high-pressure turbine (HPT) vane and blade.

The data for the blade suggest that the HPT is operating at slightly higher-pressure reaction than anticipated. This suggestion was confirmed by the stage static pressure measurements. For this turbine configuration, the impact of the HPT blade is to cause most of the unsteadiness to occur on the low-pressure turbine (LPT) blade. The driver of the unsteadiness is the shock emanating from the HPT blade trailing edge and impacting the LPT blade and to a lesser extent the HPT wake. Figure 10 presents comparisons between the predicted and measured unsteady pressure envelopes at 75 percent span on the LPT. Reference [34] presents a similar comparison for the 50 percent span location.

For both spanwise locations, the agreement between the measured and predicted unsteady envelopes is generally good from the stagnation region to about 70 percent-wetted distance. Beyond 70 percent wetted distance, the agreement at the lower bound is good, but the upper bound data is somewhat above the prediction. Figure 11 presents a comparison obtained at 21 percent wetted distance on the suction surface of the LPT blade between the predicted and measured time-resolved pressure history.

One can see from this comparison that there are differences

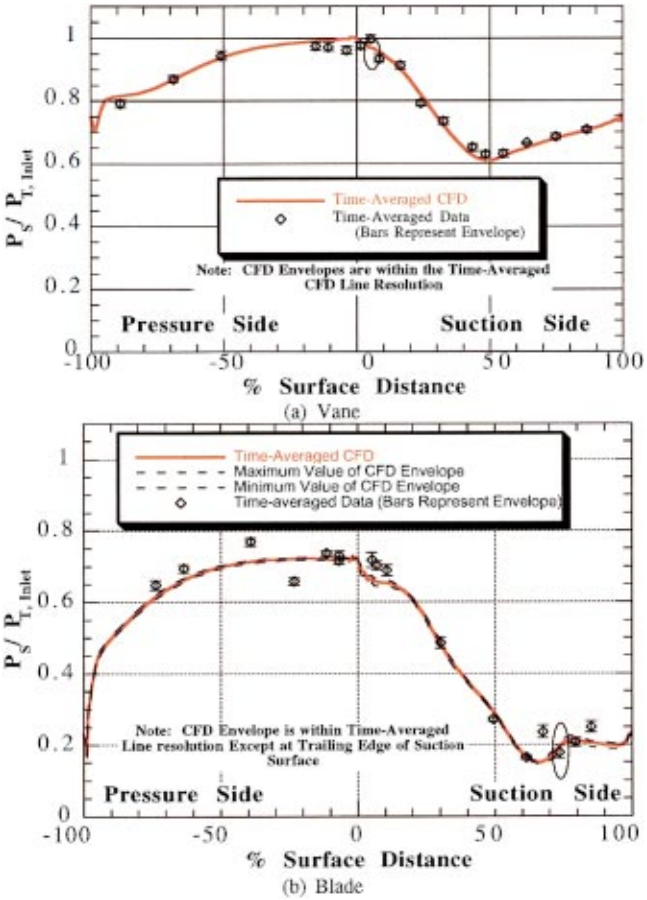

Fig. 9 Predicted versus measured time-averaged surface pressure for HPT vane and blade at midspan [34]

from passage to passage likely because of the physical construction of the hardware. However, the overall agreement between the time-resolved prediction and the data is very good. Figure 12 presents the same data in the frequency domain. At HPT blade passing frequency, the CFD code is conservative and somewhat overpredicts the magnitude of the unsteadiness. Clark has suggested that the modeling technique described in [1] may improve this comparison.

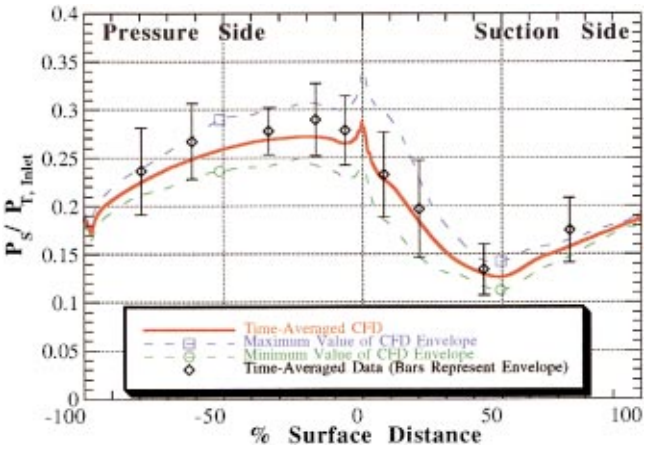

Fig. 10 Predicted versus measured unsteady surface pressure envelope at 75 percent span for LPT blade [34]

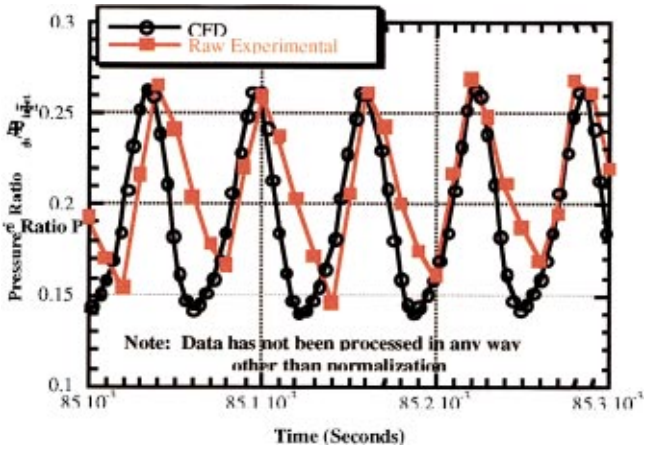

Fig. 11 Predicted versus measured unsteady surface pressure history at 50 percent span and 21 percent wetted distance on suction surface [34]

In the study reported by Weaver et al. [36] measurements were performed for three HPT blade exit Mach numbers, 1.05, 1.20, and 1.44, in order to ascertain the importance of the shock excitation of the LPT blade. Surface-pressure predictions were obtained using several different CFD codes for comparison with the measurements. Included were: (*a*) a nonlinear steady, linearized unsteady Euler solver (TACOMA, [21]), (*b*) MSU TURBO used in the previous study reported in [32] (see [16] for description of the code), (*c*) a three-dimensional Navier–Stokes solver, and (*d*) the VBI two-dimensional analysis (see procedure 2 of reference [31] described earlier). The measured and predicted time-averaged pressure distribution obtained using the four codes for the 20, 50, and 85 percent span on the LPT blade are given in [36]. Reasonable agreement between the predictions and the measurements is shown for all three locations. The authors also present a comparison of the results of the various predictions to the measured amplitude of the unsteady pressure at blade passing frequency. The predictions at midspan are in reasonably good agreement with the measurements, but at the 85 percent span location, the codes overpredict the amplitude of the unsteady pressure consistent with Haldeman et al. [34].

The results presented in Section 2.2 demonstrate that pressure distributions are predicted reasonably well by state-of-the-art CFD codes. The comparisons presented were for the vane and blade midspan region for subsonic high-pressure turbines, transonic

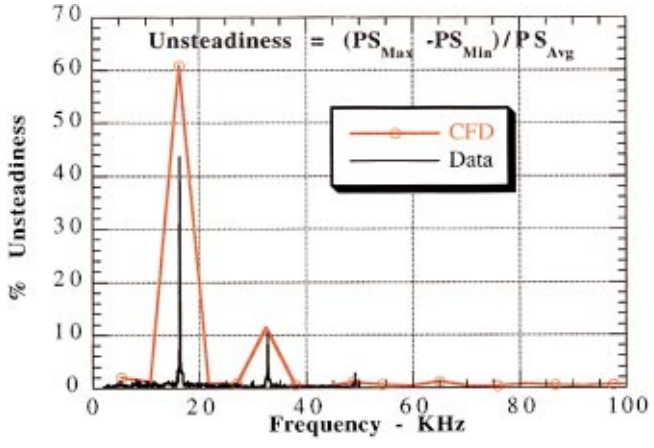

Fig. 12 Predicted versus measured unsteady surface pressure on LPT blade at 50 percent span and 21 percent wetted distance on suction surface [34]

high-pressure turbines, and vaneless counterrotating turbines currently of interest to the industry. However, near the hub and tip, the agreement between the predictions and the experimental results are not nearly as good, and the codes are in need of significant improvements. It is important to be able to predict the surface heat transfer as well as the surface pressure. Effort needs to proceed to initiate incorporation of the algorithms and modeling necessary to calculate heat transfer distributions for the vane and blade rows into the three-dimensional unsteady codes. It is well known that this step will require significantly denser grids near the surface of the components for which the heat transfer predictions are desired. The increased computing time and other difficulties associated with incorporating the ability to calculate heat transfer represent a challenge to the code developers, but much is to be gained by initiation of the effort.

2.3 Simultaneous Measurement of Forcing Function and Damping. At the elevated temperatures associated with the turbine blade, fluctuating loads may result in large resonant stresses eventually causing high-cycle fatigue of the component. Measurement programs described in [30,34], and [36] provided information helpful in understanding the source of the forcing function. Chiang and Kielb [49] give an approach for predicting the vibratory response of a blade for a given configuration. Kielb [50] presented a series of six lectures at the von Karman Institute for Fluid Dynamics on the subject of aeroelastic design of turbomachinery blades. One of these lectures also describes experimental techniques used to determine aeroelastic behavior for full-scale engines. However, predicting the component high-cycle fatigue life requires experimental data relevant to the forcing function (amplitude and phase of the unsteady pressure loading). These data calibrate the models being used for predicting the structural and aerodynamic damping of the system. Examples of forcing function measurements (a portion of the desired experimental information) for transonic turbines were cited earlier in this paper, and additional information for low-speed subsonic turbines can be found in [51] and [52]. Verdon and Casper [53] and Whitehead [54] have proposed linearized models for the numerical analyses of forced response and aerodamping. More recently, [55] and [56] described an Euler code formulation for this purpose and [57] described a Navier–Stokes code.

The obvious next step is to obtain simultaneously detailed surface-pressure and structural response and damping information within the same experimental program. This experimental effort must be accompanied by an analytical effort designed to couple the structural response with the aerodynamic forcing function information in order to be useful to the industry. Experimentally, it is a straightforward extension of the measurement technique described in [34] and [36] to place strain gages at predetermined locations on the component to obtain strain, damping, and pressure loading simultaneously. The short-duration facility used by these authors offers the opportunity, in the same experiment, to separate the aerodynamic damping from the mechanical damping. The supporting analytical portion of the task is underway at several institutions.

Aerodynamic damping measurements for transonic compressors using short-duration facilities were pioneered by Crawley [58] and Crawley and deLuis [59]. The data necessary to separate mechanical damping from aerodynamic damping is obtained by embedding piezoelectric crystals in selected blades (which have both strain gage and pressure instrumentation). Activating the piezoelectric crystals while the rotor is spinning (at the proper design corrected speed) in a vacuum immediately prior to initiation of airflow determines the mechanical damping. Many previous researchers have embedded piezoelectric crystals in airfoils and used them for various purposes, e.g., [60] and [61].

Abhari [62] was among the first to demonstrate successfully that piezoelectric actuators could be embedded in rotating blades and used to deduce structural damping for a rotating turbine blade. His experiments were performed in the same short-duration facility for which several of the aerodynamic and heat transfer measurement programs described herein were performed. In the work described by Abhari and his students, the rotor airfoils were instrumented with strain gages and pressure transducers in addition to the piezoelectric actuator. This initial work reported in Abhari [62] was followed by the work of Jeffers et al. [63], which described the technique reported by [62] in much more detail. Subsequently, Kielb [64], Kielb et al. [37] and Kielb and Abhari [65] demonstrated the application of this technique by obtaining a data set at turbine design corrected conditions for the HPT stage of a Garrett TFE-731-2 engine. The data set includes simultaneous measurement of the unsteady pressure and vibratory response. The turbine stage used by Kielb [64] has a subsonic vane exit Mach number (on the order of 0.8) so that the blade excitation is provided by vane wakes. The influence of aerodynamic loading on the airfoils is shown to provide a significant increase in total damping. Kielb used the CFD code UNSFLO 2-D (procedure 3 of Venable et al. [31] discussed earlier) to predict both the aerodynamic and structural response of the HPT blade for comparison to his experimental results. This code should not be expected to do a good job of predicting the pressure loading away from the midspan location if the airfoil flow field is three-dimensional. Figure 13 compares the measurement and prediction of blade surface-pressure distribution at midspan taken from Kielb [64]. This figure shows good agreement between experiment and the UNSFLO 2-D prediction for the midspan location. The author also presented data for the 85 percent span location, but the agreement was not as good.

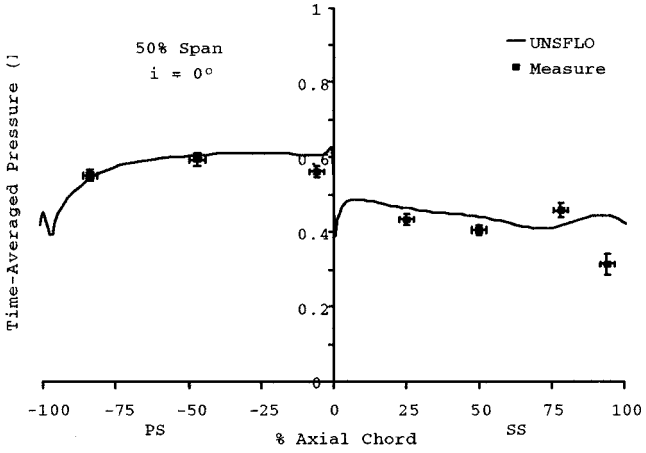

Fig. 13 Predicted versus measured surface pressure for blade at 50 percent span, TFE-731 [64]

Reference [64] also presented a comparison of the measured versus the predicted amplitude and phase of the first harmonic of the midspan time-averaged surface pressure. This comparison illustrates good agreement for the amplitude of the harmonic at blade passing frequency. The phase of the harmonic of the surface pressure appears to be a more difficult quantity to predict than the corresponding amplitude. The comparison between the predicted and measured phase of the unsteady pressure presented by Kielb [64] is similar to that presented by Barter et al. [32]. Barter et al. [32] utilized a different turbine operating under different aerodynamic conditions (the Allison VBI turbine) and they used different prediction techniques (TURBO Wake-Blade and TURBO Stage, see Fig. 7). The results of these works suggest that perhaps additional work is needed in this area to improve prediction capability for blade locations away from midspan. Prior to initiating the experimental phase of the program, a finite element analysis was undertaken to predict the mode shapes and the resonant frequencies anticipated for the target experimental conditions. The mode 4-second bending crossing predicted to occur at about 20,000 rpm (for 41 vanes this would be a frequency on the order of 14,000

Hz) is shown on the Campbell diagram presented in Kielb [64]. Reference [64] presents strain gage time histories for the blade strain gages. The data presented in the time domain illustrate a resonant bloom during the test period. The same data presented in the frequency domain illustrates the mode 4-second bending crossing at the blade passing frequency of about 14,000 Hz. The authors were able to separate aerodynamic damping from mechanical damping in this experiment by using piezoelectric crystals to excite the blades in a vacuum just prior to initiation of the airflow. Aerodynamic damping was a significant component of the total damping for this particular turbine. Data are reported for two values of vane/blade axial spacing, and it is shown that the smaller spacing results in large increases in the pressure harmonic amplitude, especially near the tip and on the suction surface. The results obtained by Kielb [64] provides a much needed data set that can be used to refine the models used in structural response CFD codes.

3 Description of the Heat Transfer Problem

Efforts focused on understanding turbine airfoil heat transfer have traditionally been overshadowed by the work done on the associated aerodynamics. This was not due to a lack of appreciation for heat transfer problems, but rather the difficulty of the problem that became more prominent as turbine inlet temperature increased. Early designers did not need a computer code to tell them that components had heat transfer problems. Partially melted, totally destroyed, or missing pieces provided all the evidence they needed.

Most conceptual models for heat transfer to a modern three-dimensional airfoil require significantly more information than is required for aerodynamic calculations. As for the aerodynamic calculation, defined inlet and exit flow field parameters must be prescribed. Also required are the free-stream turbulence and turbulence scale. A second boundary condition for the heat transfer problem is that the pressure distribution on the airfoil is known; which is the output of the CFD code development described in Section 2. Further, the computational grid required for the heat transfer calculation is much finer than required for the corresponding aerodynamic calculation. This is because the temperature gradient at the airfoil wall drives the heat-flux calculation and the grid resolution in the boundary layer must be significantly finer. The boundary layer approximation assumes a constant pressure through the boundary layer, but the temperature through the boundary layer is not constant. Thus heat transfer calculations were in difficulty until these airfoil surface-pressure predictions became, at least to a first-order approximation, relatively reliable. This was not really accomplished until recently (as discussed in section 2). Of course, the design problems were always present and the different techniques used to provide predictions given the limited knowledge available are discussed in this section. The codes progressed from boundary-layer codes that have their origin in correlations of early flat-plate data, through the two-dimensional or quasi-three-dimensional steady codes to the full three-dimensional unsteady Navier–Stokes codes.

Over the past twenty-five years, turbine heat transfer calculations and experimental data have been reported in the open literature by numerous industry, government, and university authors. The detail reported for a particular calculation technique generally depends upon the ''competition sensitive'' nature of the comparison. Government and university-authored papers usually provide a bit more detail about the calculation technique (but generally for a geometry that is relatively uninteresting to the industry) than provided in industrial based papers. Understandably, the company design codes distinguish the manufacturers and detail about these codes will be kept proprietary.

3.1 Heat Transfer Measurement Techniques. So much of the early heat transfer predictions were based on purely empirical relationships that it was common to report heat transfer results as Nusselt or Stanton numbers. Authors argue about which form of a nondimensional number is most appropriate for presenting their data. It is the opinion of the author that both are useful, with sometimes one taking the precedence over the other based on the calculations performed and/or data presented. It is important to realize that experimental and computational communities arrive at these numbers differently. This is because in the computational regime all the parameters are available (since they are all calculated), but in the experimental regime only a few parameters are measured. Thus, it is worthwhile to review these differences.

The Nusselt number (Nu_L) can be interpreted as the ratio of the convective to conductive heat transfer is a slab of fluid of thickness L, and is generally written in its most basic form as:

$$\mathrm{Nu}_L = \frac{hL}{k_f} \tag{1}$$

where h = heat transfer coefficient, L = a reference length, and k_f = thermal conductivity of fluid.

Computer codes often derive the Nusselt number from an internal calculation of the heat transfer coefficient. Standard experimental techniques do not measure the heat transfer coefficient directly, rather they derive q' (the local heat flux per unit area) as described below based on the time history of the surface temperature and some knowledge of the surface properties. For our purposes, q' then becomes the measured quantity and is related to h in the following manner.

$$q' = h(T_{\mathrm{ref}} - T_f) \tag{2}$$

where q' = heat flux/unit area, T_{ref} = reference temperature, and T_f = surface film temperature.

Equation (2) can be substituted into Eq. (1) to yield the relationship for Nusselt number most often used by experimentalists in presenting their results.

$$\mathrm{Nu}_L[t] = \frac{q'[t]L}{k_f[T_f[t]](T_{\mathrm{ref}} - T_f[t])} \tag{3}$$

The functional dependence on time and film temperature is shown in the square brackets for a time-accurate measurement.

A similar argument can be made for the Stanton number. More often the Stanton number, a normalized heat transfer coefficient, is either directly calculated or in older codes is the result of empirical relationships relating other nondimensional parameters. The base definition is usually given as one of two forms:

$$\mathrm{St} = \frac{h}{\rho u_\infty c_p} = \frac{\mathrm{Nu}_L}{\mathrm{Re}_L \mathrm{Pr}} \tag{4}$$

Re_L = Reynolds number based on L.

This contains many terms not directly measured in experiments. The mass flow usually is known and h is related to the Nusselt number as shown above, which results in a definition used by the experimentalists since it relates the Stanton number to measured quantities:

$$\mathrm{St}[t] = \frac{q'[t]}{\frac{\dot{m}}{A}(T_{\mathrm{ref}}[t]c_{p\mathrm{ref}} - T_f[t]c_{p\mathrm{film}})} = \frac{q'[t]}{\frac{\dot{m}}{A}(H_{\mathrm{ref}}[t] - H_f[t])} \tag{5}$$

$\dot{m}$ = mass flowrate; A = reference area. Prior to initiating a discussion of heat transfer measurements and comparison with prediction, it is appropriate to review briefly the techniques used by various groups to obtain these measurements.

There are many different techniques used to perform heat transfer measurements relevant to gas turbine engines, but space does not permit an exhaustive discussion of those techniques here. The work of Giel et al. [66] utilized a liquid crystal technique. Professor Terry Jones has pioneered [67,68,69] application of this technique to problems of interest to the gas turbine community at Oxford University and the interested reader is referred to his work for additional detail. The discussion herein will be confined to the

general type of heat-flux gage used by various groups that is, in one form or another, a metal thin-film gage. Thin-film heat-flux gage development work was initiated in the early 1950's to provide a heat-flux measuring capability for the emerging experimental devices used to create high Mach number flows. The post–World War II political environment focused on national defense interests involving vehicle velocities that were much greater than the speed of sound. Thus, the search for experimental facilities with the capability for producing representative fluid dynamic conditions was an active research area. Development of diagnostic instrumentation (of which the thin-film gage is but one element) proceeded along with facility development.

The thin-film gage is a device consisting of a thin metal element having a very small heat capacity bonded to the surface of an insulator. As will be demonstrated later in this discussion, the insulator may have a thin-film gage placed on one side or on both sides. When subjected to a change in the temperature field, a properly calibrated metal film can be used to determine the temperature history of the insulator surface. By employing existing theory for transient heat conduction in a nonhomogeneous body and making some assumptions about the physical properties of the insulator, the heat flux to the insulator surface can be calculated in a straightforward manner. The assumptions about the insulator properties and behavior range from simple one-dimensional heat conduction to more complicated transient conditions, depending upon the actual experiment. Early research relating to thin-film technology was performed at the California Institute of Technology [70], Lehigh University [71], Cornell Aeronautical Laboratory [72,73,74], and Avco Everett Research Laboratories [75]. The initial users of this device were interested in using it to measure surface temperature. Vidal [72] was among the first to develop the thin-film gage for measurement of heat flux in short-duration facilities. Schultz and Jones [76] provide a comprehensive review of the 1973 state of the art for measurement of heat transfer in short-duration facilities.

The specific type of thin-film gage used at the various research institutions varies because demands of the instrumentation are different. The available test times and the flow environments associated with the individual facilities differ and researchers are attacking different problems. The available test time determines the substrate thickness onto which the gage is painted. The substrate is designed to be sufficiently thick so that the thermal wave does not penetrate to the backside of the substrate during the test time, or that a second sensor is placed on the backside to monitor that temperature.

Test times on the order of 100 to 125 milliseconds are typical of short-duration facilities such as the shock-tube driven reflected-shock tunnel used at Calspan and now at The Ohio State University. Thus, the single-sided thin-film gage bonded to an insulating substrate is used unless the experiment involves film cooling measurements. Test times are on the order of 300 to 400 milliseconds for the intermediate short-duration facility (e.g., the free piston type facility used at Oxford University, [77]) and the small blowdown facility (e.g., MIT, [78]). Different types of gages have been developed for use in these facilities. The test time is on the order of 2 seconds for the large blowdown facility (e.g., the Turbine Research Facility (TRF) at Wright Laboratory). In this case, it is necessary to use thick single-sided gages, the MIT-type double-sided Kapton gage, or the Oxford vitreous enamel-coated metal gage.

For their earlier work, the research group at Oxford University has used a machinable ceramic (Macor) with platinum thin-film gages either painted or vacuum deposited at selected locations on the surface. If the component to be investigated is one for which the stress levels are relatively low, e.g., a vane, then the component shape can be machined from a Macor block and thermal penetration depth is not a problem. However, Macor does not have sufficient strength to be used for rotating components and it is difficult to construct a complex component that would allow film cooling. Thus, an alternate gage consisting of thin-film gages deposited on a vitreous enamel-coated metal was developed by Doorly and Oldfield [79,80] and Doorly [81].

The design, construction, calibration, and application of the MIT double-sided heat-flux gage that consists of a pair of metal thin-film gages on opposite sides of a polyamide (Kapton) insulating substrate is given in Epstein et al. [82]. This specific gage used a 25 μm (0.001 in.) thick polyamide insulator with electrolytic nickel deposition for the metal thin films on both surfaces. If one is doing film cooling research, this particular type of gage is a very attractive device for measuring heat transfer, since one is freed from the more restrictive assumption about one-dimensional semi-infinite behavior of the substrate.

Hager et al. [83] describe the initial design, construction, and calibration of a heat-flux microsensor consisting of a thin thermal resistance layer sandwiched between many thermocouple pairs forming a differential thermopile. The gages have a physical size of about 3 mm (0.12 in.) by 4 mm (0.16 in.) and are about 2 μm (0.00008 in.) thick. The gage can be placed on either glass or silicon substrates. Later Holmberg and Diller [84] report the results of a study conducted in a short-duration environment in order to characterize the response time and the calibration of the heat-flux sensor described in Hager et al. [83]. More recently Popp et al. [85], Smith et al. [86], and Popp et al. [87] have reported results of measurement programs that were performed in a transonic cascade wind tunnel utilizing these heat-flux sensors. The intent of the measurement programs was to determine the film effectiveness and heat transfer coefficient for the suction surface of a turbine blade.

Heat flux can be deduced from the measured voltage versus time history of the metal element for the different heat-flux gages described above. This is done using either an analytical or a numerical solution to the heat conduction equation with the appropriate boundary conditions. The data reduction process requires that specific calibration data (differing depending upon the specific gage) be available in order to proceed. A description of the solution for the different gage configurations can be found in Weaver et al. [88].

Heat-flux measurements have been in use since the 1950's and data using these techniques has been validated repeatedly against controlled experiments and flight tests. However, the care required in taking these measurements, the calibrations needed, and the complexity of making the sensors themselves has led to the search for other types of sensors. Many of these techniques do not have the frequency response to be used in rotating experiments, and it is unlikely that in the immediate future standard heat-flux gages will be replaced. Typical accuracy for these types of measurements is on the order of ± 5 percent of the reading (when all errors are accounted for). This has not been a problem since predictive techniques have not been near this level of accuracy. As the codes develop, there will be an effort to improve the accuracy of heat transfer instrumentation. This process also occurred with pressure instrumentation in the 1980's and 1990's that dramatically increased the accuracy of those measurements. We are not far from heat-flux measurements on the order of ± 1 percent accuracy.

3.2 Combustor Exit Flow. Heat transfer in turbines is the result of high-pressure, high-temperature gases leaving the combustor and entering the HPT, where extraction of the power necessary to operate the HPC is extracted from the flow. Upon leaving the HPT, the flow path gas is then directed into the LPT, where additional power is extracted to operate the fan stages of the machine. The combustor is the initial hot-section component and is responsible for all of the subsequent heat transfer difficulties experienced by the machine. In addition, as noted previously, it generates the inlet conditions that are needed in the computations. Thus, it is worthwhile to discuss how the combustor is normally treated, especially with respect to the turbulence intensity and scale of the gas leaving the combustor.

Many heat transfer–related papers begin by making the assertion that the flow leaving the combustor and entering the turbine has very high turbulence intensity with numbers cited ranging from 6 to 20 percent. Seldom do these publications cite an available reference with a measurement of turbulence intensity or turbulence length scale for an operating combustor (by operating it is meant at pressure and temperature). Within the confines of some engine companies, there may be results of measurement programs substantiating these numbers (such as Goebel et al. [89]). While this paper represents a thorough experimental study, the combustor configuration used was representative of that used for a stationary power plant gas turbine. While propulsion and power plant gas turbine combustors differ, the absence of other experimental results makes this paper valuable. The turbulence intensity and length-scale numbers used in a particular calculation are more likely selected based upon previous experience. That is, by how much the analysts had to ''turn the knobs on the local computer code'' in order to match predictions for sparse engine data. Often one of these ''knobs'' is the value for the free-stream turbulence, required by the code, but often unknown to the designers. Moss and Oldfield [90] performed pressure measurements (and then using the pressure spectrum deduced the velocity spectrum) using a room temperature combustor at atmospheric pressure. They then ran the combustor at atmospheric temperature and atmospheric pressure and concluded that the deduced velocity spectrum was similar in both cases and argued that the combustion didn't influence the turbulence spectrum. Missing from this argument is the influence of combustor geometry, significantly elevated pressure and further elevated temperature, combustion, plus the influence of the chemical kinetics, all of which may significantly influence the turbulence levels.

Goebel et al. [89] presents some of the most detailed measurements of turbulence intensity at the exit plane of the combustor found in the literature. These authors used a natural gas fired can combustor and report measurements made with the combustor operating at either 6.8 or 4.8 atm pressure and either room temperature (300 K, unfired) or at 1356 K (fired). Axial and swirl velocity and turbulence profiles are measured using a Laser-Doppler Velocimeter system. Temperature profiles in the exit plane were measured using thermocouples mounted on a traverse system. The authors independently measure the effect of combustor geometry, operating conditions (mass flow and pressure), and combustion on the measured turbulence intensity. They do not attempt to measure the associated turbulence scale. Swirl is demonstrated to have a major influence on the turbulence intensity distribution. The measured turbulence intensity in the center portion of the exit flow was on the order of 7 to 12 percent. The peak turbulence intensity was outboard of center and reached a maximum of about 20 percent depending upon the particular operational mode. The authors demonstrate that combustion has a significant influence on the magnitude of swirl and thus on the turbulence intensity. Figures 14(*a–c*) are taken from the results presented by Goebel et al. [89]. Figure 14(*a*) illustrates the effect of combustion on the exit-plane axial turbulence intensity for a low-swirl geometry. Figure 14(*b*) is a similar result for a high-swirl combustor. Figure 14(*c*) presents the influence of combuster geometry and temperature on the radial turbulence intensity for the same conditions as used for Figure 14(*b*).

Figure 14(*a*) shows that the main effects due to speed and temperature occur at radial distances greater than 0.4. In addition, the relative intensity is greater for the low-speed flows, but the absolute variation is greater for the high-speed flows. The low-swirl geometry has a significant variation of axial turbulence intensity as a function of radial position, values range from 7 to 20 percent. For the high-swirl geometry (Fig. 14(*b*)), the main result is that uniformity is preserved over a larger portion of the combustor exit. Figure 14(*c*) illustrates that the exit plane radial (swirl) turbulence intensity is similar to the axial turbulence intensity. It is not surprising that often the input ''knobs'' corresponding to free-

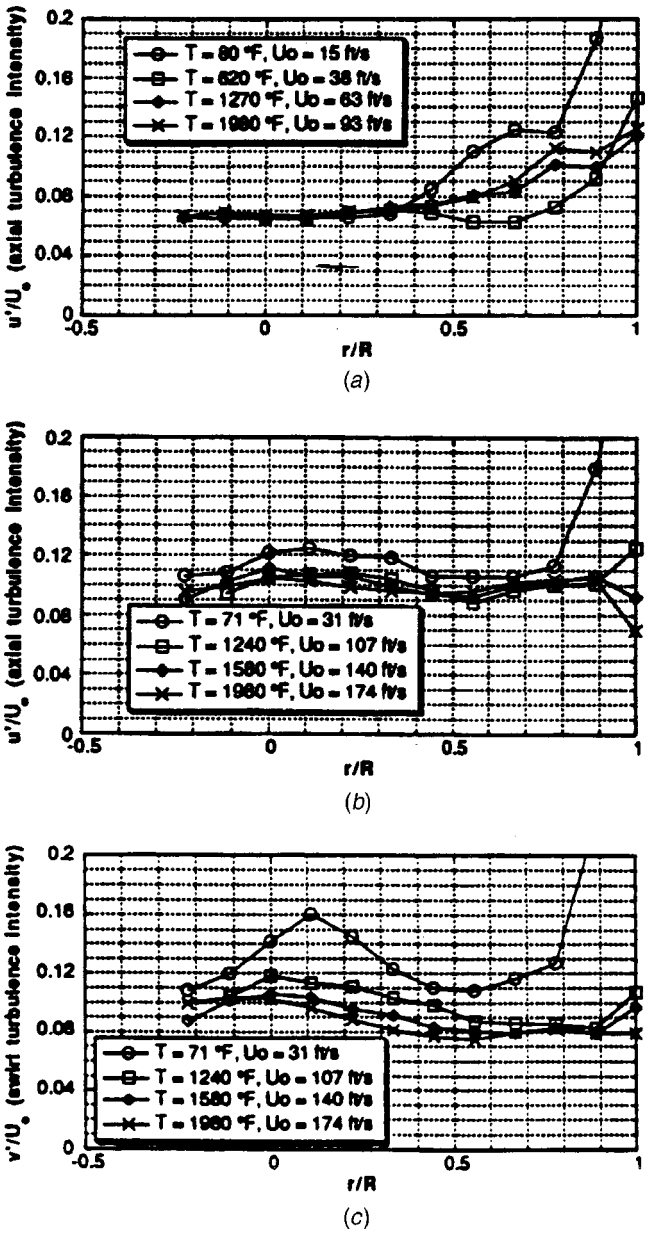

Fig. 14 (*a*) Influence of combustion on exit plane turbulence intensity for low-swirl geometry [89]; (*b*) Influence of combustion on exit plane turbulence intensity for high-swirl geometry [89]; (*c*) Exit plane radial turbulence intensity for high-swirl geometry [89]

stream turbulence on the codes are changed within the range of values just noted to make predictions align with data.

The most severe thermal conditions associated the gas turbine engine are experienced in the combustor. A requirement of satisfactory operation is that the liner walls of this component be cooled and temperature gradients within the material be controlled in order to maintain structural integrity. Cooling the combustor is accomplished by bleeding air from the HPC and injecting the bleed air into the combustor via cooling jets, louvers, air-blast nozzles, etc. This cooling process along with the combustion process contributes to the combustor exit plane turbulence intensity, length scale, and hot streaks. There is a significant body of literature describing various cooling design techniques for combustor liners. The work of Mularz and Schultz [91] provides combustor turbulence intensity information in the liner at a pressure of about six atmospheres, but does not address combustor exit plane turbu-

lence intensity and scale. Many years ago Marek and Tacina [92] were concerned with film cooling effectiveness for combustor liners. The turbulence intensity for this research was not produced by an engine combustor. Rather various blockage plates were used to produce turbulence intensity for a rectangular combustor operating at one atmosphere pressure and with air at an inlet temperature of 580 K to create four values of intensity ranging from 7 to 35 percent. The result of their studies was that film effectiveness on a flat plate placed downstream of the hot gas source was reduced by as much as 50 percent as the turbulence intensity was increased from 7 to 35 percent. The authors compared their data with the turbulent mixing correlation of Juhasz and Marek [93], but found very poor agreement. Juhasz and Marek [93] used a turbulent mixing equation to correlate film cooling effectiveness data that had been obtained in a sector combustor. They found little agreement between the mixing coefficient and the turbulence intensity (which were postulated to be equal) derived from combustor data resulting from low-turbulence wind tunnels. Their explanation was that the large differences were the result of the higher turbulence intensity associated with the combustor. However, Mularz and Schultz [91] used a full-scale annular gas turbine combustor operating at six atmospheres pressure with combustor inlet temperatures at approximately 900 K to make film cooling and turbulence measurements. They found that the turbulent mixing coefficient was only 10 percent of the turbulence intensity as opposed to being equal to the turbulence intensity. The combustor exit temperature for the measurements reported by Mularz and Schultz was on the order of 1400 K. Mularz and Schultz used a single hot wire probe to measure turbulence intensity (assumed to be isotropic) in the combustor liner region (not at the combustor exit plane) and then only under nonburning conditions. They concluded that near the wall the turbulence intensity was on the order of 35 percent. Marek and Tacina [92] argue that there are difficulties associated with making measurements in engine combustors because of the well-known pattern factor and thus question the results of Mularz and Schultz [91]. Marek and Tacina [92] note that testing their turbulent mixing correlation using an actual combustor is inaccurate because the associated large temperature and velocity gradients make it difficult to define a single value of hot gas velocity and temperature. It is true that these difficulties exist, but such are the facts of life when working with the real world of engine combustors. A great deal has been added to the combustor literature since the work of Mularz and Schultz [91], but measurements of the turbulence intensity and scale for an operational combustor are still missing. The more recent gas turbine literature includes a description of the design procedure for the cooling scheme (Kumar et al. [94]) and a description of a technique to calculate the radiative contribution (Kumar et al. [95]). Validation of the turbulence model is presented in Kumar and Mongia [96], and a discussion of film cooling effectiveness for a modern combustor liner is given in Kumar et al. [97].

Mayle et al. [98] conclude in their paper ''The Turbulence That Matters'' that the effects of turbulence can be explained when the full spectrum of turbulence is known. It is acknowledged, however, to be nearly impossible to obtain this information for the gas turbine application. In the absence of relevant experimental data, engineering approximations are made to permit predictions, and papers treating cooling jets and film effectiveness in combustor environments have appeared in the literature. As emphasized earlier in this paper, designers are able to make reasonable approximations as evidenced by the infrequency of in-flight engine shut down.

4 Turbine Airfoil Heat Transfer

Turbine airfoil heat transfer is a broad research area and spans several decades of work. Most research activities focus only on a small aspect of the problem at any one time, which makes reviewing the literature a complicated process. To help organize this task, this section is split into four areas that tend to follow the main research efforts in this field chronologically. Section 4.1 deals with external heat transfer (heat transfer to the metal surfaces exposed to the main core flow) in the absence of cooling. This is a large area, since it has seen the majority of the research effort, and is broken down further into a review of heat transfer to different parts of the turbine stage. Section 4.2 looks at the same physical process (external heat transfer) but with the addition of film cooling. Section 4.3 presents a discussion of the influence of free-stream turbulence and boundary layer transition on airfoil heat transfer. Finally, internal heat transfer with cooling (heat transfer inside passages) is discussed in Section 4.4. Internal prediction techniques are heavily dependent upon empirical lumped parameter models and a review of the data upon which the models are based is included. The information used to derive these models comes from both nonrotating and rotating measurement programs.

4.1 External Heat Transfer Without Film Cooling. The demand for operation of propulsion gas turbines at ever-increasing turbine inlet temperatures has put increasing emphasis on improving the calculation of heat loads for the machine. These increased temperatures can be tolerated because the combustor and turbine components are film cooled, but a discussion of film cooling will be deferred until Section 4.2. There is a wealth of experimental and computational information available for the uncooled turbine and it is appropriate to discuss this work because it represents the foundation upon which the current prediction techniques have been built and verified.

The geometry and flow field of specific interest to the designer has progressed from the midspan region of an uncooled two-dimensional flow airfoil to the hub, tip, and midspan regions of a three-dimensional airfoil with significant film cooling coverage. Progress in calculation techniques has made possible numerous two-dimensional Navier–Stokes codes and more recently, three-dimensional Navier–Stokes codes. The older method of using a two-dimensional calculation to obtain the surface-pressure loading along selected streamlines and then applying a modified flat-plate heat transfer code to estimate the local heat transfer coefficient is still used under some circumstances. However, as demonstrated in Section 2, the ability to calculate the surface-pressure distribution for three-dimensional airfoils has made some significant advances in the past ten years. The heat transfer community must now pick up the challenge and advance the state of the art to be able to perform heat transfer calculations for three-dimensional airfoils in a manner acceptable to the design community.

4.1.1 Development of Prediction Techniques. Common practice in the 1975 to late 1980's time period was to generate the local pressure or velocity field information for the airfoil using two-dimensional inviscid flow codes, MERIDL (Katsanis and McNally [99]) and TSONIC (Katsanis [100]). Then the user would employ either flat-plate correlations (Eckert and Drake [101]) or a two-dimensional parabolic boundary layer code, STAN5 (Crawford and Kays [102]), which uses the finite difference scheme of Patankar and Spalding [103] to generate the heat transfer predictions. Examples of this technique being used to compare prediction with experiment for a full-stage rotating turbine can be found in Dunn et al. [104] and Dunn and Chupp [105]. The heat transfer coefficients calculated using flat-plate correlations were obviously of limited use for gas turbine purposes (Graham [106]), but these flat-plate correlations are still used today to obtain ''sanity check'' estimates as will be demonstrated later. An example of the simple flat-plate prediction compared to full-stage rotating turbine data can be seen in Dunn et al. [107]. Improvements in the transonic flow field region were added by Wood [108] and the MERIDL and TSONIC codes were coupled and made more user friendly by Boyle et al. [109]. As an input condition, the boundary layer code STAN5 requires a description of the surface streamlines and the gas-stream velocity distribution. The code STAN5 was attractive to many users because of its general availability to those interested. The eddy-diffusivity turbulence model was included in the

early version of STAN5 that worked with success in rather simple flow environments. Significant changes were required of the STAN5 code to make it applicable to the turbine flow field. Since STAN5 was released in 1976 as a flat-plate prediction, a method for including free-stream turbulence, leading edge curvature, and pressure gradient was needed. The STAN5 code formed the basis of later codes, such as the KEP code still in use today by General Electric and described by Zerkle and Lounsbury [110]. The KEP code is based on a 1985 version of STAN5 that was modified by Rodi and Scheuerer [111], to include the Lam and Bremhorst [112], low-Reynolds-number version of the $k-\varepsilon$ turbulent flow model. This modification also included the capability of providing as an input parameter the desired value of free-stream turbulence. The way by which the free-stream turbulence influences boundary layer transition on the airfoil and a discussion of whether or not transition is an important consideration for a modern HPT stage is discussed later. Several modifications made by NASA Lewis Research Center to STAN5 (Crawford and Kays [102]) to make the computational code more applicable to gas turbine geometries are described in Gaugler [113]. These modifications included incorporation of a cylindrical leading edge calculation, incorporation of a boundary layer transition model, and incorporation of a more realistic gas properties model. Also included in the paper is a discussion of some of the NASA experiences realized by running the code. Goldman and Gaugler [114], describe their experiences using a more recent version of STAN5 (Crawford et al. [115,116]) that is used to model full-coverage airfoil film cooling. This version of STAN5 was verified by flat-plate cooling flow experiments.

Crawford has continued development of a boundary layer code used for prediction of heat transfer coefficients for gas turbine airfoils. He has made significant progress since the initial version of STAN5 was released. His more recent work is found in a version of the code known as TEXSTAN. Incorporated into this code are three levels of mean field closure, including mixing-length models, a one-equation turbulence kinetic energy (k) model, and a large variety of two-equation $k-\varepsilon$ models. Research versions of this code have extended closure to include full Reynolds stress models, turbulent heat-flux models, and multiple-time-scale $k-\varepsilon$ models. How large-scale free-stream turbulence affects transition is handled most successfully in TEXSTAN by the two-equation models. The start and end evolve from the $k-\varepsilon$ dynamics in either a natural way (no modifications to the models) or in a controlled way (Schmidt and Patankar [117]). The performance of these various models is described in Harasgama et al. [118] for a highly loaded transonic turbine guide vane (Arts et al. [119]). They discovered the models to be generally adequate for the laminar and fully turbulent portions of the vane surfaces over the various Mach and Reynolds numbers and free-stream turbulence levels of the experiments. However, the predictions indicate a somewhat inconsistent model performance for a given model in the start and end of transition region, especially at lower Reynolds numbers. In addition, film cooling and surface roughness have been incorporated into TEXSTAN (discussed later).

Researchers began to utilize more sophisticated (two- and three-dimensional Euler and Navier–Stokes) codes to calculate the pressure and velocity fields for gas turbine vanes and blades in the late 1980's. These results were then used in conjunction with an appropriate two-dimensional or three-dimensional boundary layer code to calculate heat transfer coefficients. An excellent example of this technique can be found in Sharma et al. [120]. State-of-the-art two-dimensional and three-dimensional codes were used to obtain estimates of the surface pressure distribution at midspan for the vane and blade of a highly loaded turbine stage. Sharma et al. [120] calculate the streamlines and pressure loading at the midspan locations of the vane and blade and on the endwall surfaces using the three-dimensional Euler code described by Ni [121] and the three-dimensional Navier–Stokes code described by Rhie [122]. The results of the calculation are compared with the experimentally determined surface pressure and heat transfer data reported in Dunn et al. [107]. The measurements were obtained for a Garrett Low Aspect Ratio Turbine (LART) stage. The results of both the three-dimensional Euler code and the three-dimensional Navier–Stokes code showed excellent agreement with the measured surface-pressure distribution for the vane midspan. Surface-pressure measurements were not available at airfoil locations other than vane midspan for this particular turbine stage, but the three-dimensional Euler calculation suggested significant three-dimensional effects. The three-dimensional Euler code and the three-dimensional Navier–Stokes code were used to calculate the blade midspan surface-pressure loading. Significant differences between the results of the two calculations are shown for the suction surface, but measurements were not available for comparison.

The predicted surface-pressure distributions obtained using the three-dimensional Euler code were then used to calculate the midspan Stanton number for the vane and the blade as well as the vane endwall. The calculated pressure loading was input to an extensively modified version of the STAN5 two-dimensional boundary layer code noted above to calculate the vane and blade midspan heat transfer loading. The heat transfer calculation obtained in this manner underestimated the measurements for both the pressure and suction surfaces of the vane, suggesting that the two-dimensional boundary layer calculation does not do well for three-dimensional airfoils. The three-dimensional boundary layer code developed by Vatsa [123] was also used to predict the vane midspan Stanton number history. This code was developed specifically for estimating heat loads to the endwall region of three-dimensional airfoils with application to cascade experiments. The comparison between the results of the three-dimensional boundary layer code and the data was about the same as described earlier for the two-dimensional boundary layer code comparison. The authors suggest that the disagreement between the prediction and the data for the vane indicate that some aspect of the airfoil geometry causes significant amplification of the heat transfer coefficient. By contrast to the vane, the midspan Stanton numbers for both surfaces of the blade were predicted reasonably well by the two-dimensional boundary layer code. The three-dimensional boundary layer code of Vatsa [123] was not used to obtain a prediction for the blade.

The vane endwall heat transfer loading was predicted using the above-noted three-dimensional boundary layer code developed by Vatsa [123]. The surface-pressure distribution obtained using the three-dimensional Euler code described in the preceding paragraphs provided the input condition for the boundary layer calculation. The predicted Stanton number history for the vane hub endwall near the suction surface was shown to be in good agreement with the measurements as was the prediction for the hub endwall at mid pitch. However, the prediction for the vane hub endwall near the pressure surface significantly under estimated the measurements. Similar comparisons are presented in Sharma et al. [120] for the tip endwall and the results are consistent with those described for the hub endwall. That is, the agreement between the prediction and the measurement is good for the endwall near the suction surface and at midpitch, but the prediction is below the data on the endwall near the pressure surface. The authors attribute the disagreement between prediction and measurement on the endwalls near the pressure surface to poor assumptions regarding initial conditions at the endwall intersection.

Dunn et al. [27] presents a comparison of heat transfer data for the vanes and blades of a full two-stage turbine with predictions obtained using the modified version of STAN5 (described in Gaugler [113]) and different Navier–Stokes codes. This study incorporated the transition model of Mayle [124] and the intermittency model of Mayle and Dullenkopf [125,126]. The results of this comparison will be described in more detail later in the paper.

Also in the 1980's and into the 1990's papers treating the subject of vane/blade interaction, transonic turbines with the associ-

ated shock waves, and the resulting unsteady heat transfer in turbine flows appeared in the literature. Among the early works that used subsonic turbines were Dring et al. [127], Dring and Joslyn [24], Dring et al. [25]. The studies reported by Dring and his co-workers were performed using a large scale (approximately five times engine scale), low-speed rotating rig operating at ambient temperature inlet conditions. Later, papers began to appear in the literature reporting blade heat transfer measurements for full-stage rotating turbines operating at design corrected conditions. Among these papers are references [128], [129], [130], [131], [132], [133], [134], and [28]. The paper of Guenette et al. [130] reports time-averaged heat transfer measurements (no surface pressure measurements for the rotating blade are reported) for the blade alone. The paper of Abhari et al. [134] reports time-averaged and time-resolved surface heat transfer measurements for the blade. Rao et al. [28] report both time-averaged and time-resolved surface-pressure and heat transfer measurements for both the vane and the blade. Kingcomb et al. [132] reported time-averaged heat transfer measurements on the vane (and comparison with prediction) and time-averaged surface-pressure measurements on the blade along with comparison with predictions. Also in the middle 1980's, Hodson [135,136,137] used several different rotating rigs to obtain measurements of wake-generated unsteadiness, boundary-layer transition, and flow separation in rotor passages. In Hodson [136], detailed measurements of the unsteadiness contained in the rotor inflow are presented that illustrate the change in incidence angle and turbulence associated with the vane wakes. Hodson does not present heat transfer data, but it is likely that both the change in incidence angle and the increased turbulence will influence the magnitude of local heat transfer. Binder et al. [138] investigated the influence of vane wakes on the unsteady rotor flow using a laser velocimeter system. They illustrate very high turbulence levels associated with the vane wakes. The authors do not address the potential influence of this high turbulence level on the local heat flux for the blade. The results of an interesting experiment designed to study the effects of shock waves and wakes shed by the vane row on the blade surface heat transfer are reported by Doorly et al. [139] and Doorly and Oldfield [140]. These experiments utilized a short-duration facility and a system of rotating bars. In Doorly and Oldfield [140], the authors present Schlieren photographs illustrating the structure of the bar wake and its subsequent passage through the cascade. This technique is an inexpensive way of providing an environment in which detailed understanding of the flow phenomena associated with wake interaction can be studied. An interesting outcome of the rotating bar technique is the description of the unsteady heat transfer experienced on the blade as a result of compression heating in the boundary layer because of the moving shock given by Rigby et al. [141]. In 1985, this study was of interest because of the detail that could be learned from the results. It remains to be demonstrated that the magnitude and phase of the pressure disturbance produced by the rotating bars is consistent with that experienced by a blade as it rotates through the vane wake and/or shock. The closest published attempt at doing this is the heat transfer study reported by Hilditch and Ainsworth [142]. Figure 25 of that paper compares the mean heat transfer rate measured on the surface of a rotating turbine blade with the corresponding values deduced from Doorly's results with bars and different grid-generated free-stream turbulence levels. There is little agreement between the turbine stage blade heat transfer data and the rotating bar heat transfer data suggesting that the flow fields may be very different. If one were to pursue use of the rotating bar technique for generating wakes and shocks for turbine applications, then it would be important to demonstrate experimentally that the generating system reproduces the flow field experienced by the rotating blade. For additional information on designing such an experiment, the reader is referred to Pfeil and Eifler [143], Schulte [144] and Banieghbal et al. [145].

Since some of the papers mentioned above began to incorporate more sophisticated time-averaged heat transfer calculations for comparison with the measurements, it is worthwhile to discuss some of them in a bit more detail. One of these papers is that of Guenette et al. [130], who report the results of a heat transfer measurement program for the blade of a single-stage uncooled transonic turbine. The authors demonstrate good comparison between the measured time-averaged and calculated (two-dimensional Navier–Stokes) blade Nusselt number distribution. In this work, the authors modeled the turbulence using an additional turbulence viscosity (Cebeci–Smith model, Cebeci [146]). Guenette et al. [130] do not present any measurements or predictions for the vane of the turbine stage. However, they do present an interesting comparison between cascade and full-stage data. One of the intentions of this paper was to demonstrate the influence (or lack thereof) of upstream vanes and rotation on the blade heat transfer results. This was accomplished by making a comparison between the measurements obtained in the MIT rotating rig and the same blade run in the Oxford cascade (Ashworth et al. [147]). The comparison between the cascade data obtained for the pressure surface of the blade with both a rotating bar and turbulence grid and rig results are reasonably good. However, if the turbulence grid was not used for the cascade, the agreement is not at all good. For the suction surface, the presence or absence of the turbulence grid made little difference in the cascade results. For the cases compared, the agreement between cascade and rotating rig data on the second half of the suction surface is not nearly as good as shown for the pressure surface.

Kingcombe et al. [132] reports the results of a rotating turbine measurement program conducted at RAE Pyestock for which the blade pressure distribution and the vane Nusselt Number distributions were measured. The local pressure distributions on the vane, vane endwall, and blade surfaces were calculated using Denton [148] and Dawes [149]. The vane heat transfer distribution was calculated using STAN5 (Crawford and Kays [102]). The heat transfer comparisons for the vane illustrated that the boundary layer code significantly overpredicted the experimental results.

Abhari et al. [134] presented a comparison between time-averaged and time-resolved blade heat transfer measurements and predictions for an uncooled turbine stage operating at transonic conditions. The calculation technique used for this comparison was the two-dimensional, multiblade row code UNSFLO 2-D developed by Giles [8] and Giles and Haimes [15]. UNSFLO 2-D is a coupled inviscid/viscous code in which an implicit algorithm is used to solve the thin shear layer Navier–Stokes equations on a body-fitted boundary layer grid. The Euler equations are solved on an outer inviscid grid using an explicit algorithm, and the interface between the two regions is treated in a conservative manner. The version of the predictive code used by Abhari et al. [134] used an algebraic Baldwin–Lomax turbulence model. The comparison presented for the time-averaged heat transfer shows the prediction to be below the data for the initial 30 percent of the suction surface, but in reasonable agreement from about 30 percent on to near the trailing edge. The prediction on the pressure surface was below the data to a lesser extent over the initial 30 percent and then in good agreement to near the trailing edge. The authors devote a significant portion of their paper to a comparison of the measured and calculated time-resolved heat transfer for selected positions on the blade. In performing this comparison, they do an excellent job of carefully examining the possible deficiencies in the flow modeling that may be causing the differences between the measurements and predictions for both the pressure and suction surfaces of the blade. The results of this analysis are excellent and suggest that the UNSFLO 2-D code capture the primary flow physics and shock wave structure. Possible multiple shock wave reflections and the way in which the turbulence from the wakes and the free stream are handled may be the source of disagreement between the predictions and the data.

Rao and Delaney [13] describe a two-dimensional Navier–Stokes code that uses an overlapping O–H grid system to include

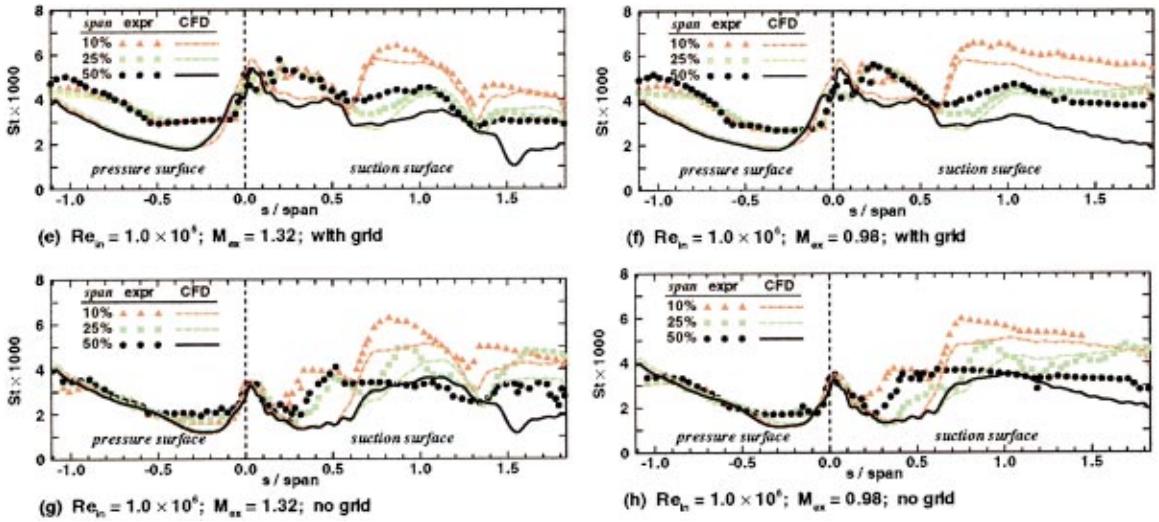

Fig. 15 Predicted versus measured Stanton number distribution for blade [66]

all of the viscous terms in the Navier–Stokes equations. Rao et al. [28] performed modifications to this code in order to obtain a comparison of predicted to measured midspan surface pressure for the vane and blade of a full-stage uncooled transonic turbine operating at design corrected conditions. The scheme used was second-order accurate in time and space. The Baldwin–Lomax model was employed to model turbulence. Rao et al. [150] describe the results obtained using this code to predict the time-averaged Stanton number distribution for the vane and for both the time-averaged and the time-resolved (unsteady) Stanton number distributions for the blade. Phase-resolved Stanton number histories for selected locations on the blade are also presented in the paper. More detail regarding the results presented in Rao et al. [150] will be presented later in the paper.

Although most of the investigations mentioned above utilized full-stage rotating turbine rigs as an essential ingredient of the experimental effort, there are many that have been performed using various kinds of cascade facilities. Lokay and Trushin [151], Scholz [152], and Sharma et al. [14] investigated the losses associated with specific rig environments (cascade versus rotating rig) as reflected by the unsteady flow associated with wakes and wake cutting and concluded that these losses are significant. Denton [153] presented a detailed discussion of loss mechanisms in turbomachines with emphasis on the understanding of the mechanisms, which may be more valuable than a quantitative prediction. Cascade measurements have been, and still are, an important ingredient in the understanding of turbine flows and thus are relevant to this discussion. Although space does not permit a complete review of the numerous cascade studies that have been reported in the literature, it is appropriate to discuss a select number of them that have direct relevance. Graziani et al. [154] report the results of an investigation that dealt with the endwall region as well as the midspan portion of the airfoil for a large-scale turbine blade cascade. In addition to the heat transfer measurements, the authors also report on simultaneously obtained flow visualization and surface-pressure measurements. The authors used STAN5 to calculate the airfoil midspan Stanton number distribution for comparison with the measurements. The calculation for the pressure surface was below the data, but in better agreement with the data than for the suction surface for which the calculation was well above the data. The prediction was dependent upon the incoming boundary layer thickness. The authors concluded that the passage secondary flows significantly influence not only the end wall heat transfer, but also the airfoil suction surface heat transfer at midspan.

Consigny and Richards [155] present the results of a transonic cascade program for which heat transfer measurements were performed at the midspan of a transonic airfoil and the influence of free-stream turbulence on the heat transfer distribution was measured. The experimental results were compared with predictions obtained using a two-equation closure model and the basic formulation presented by Jones and Launder [156]. Several different prediction techniques are described for predicting the influence of free-stream turbulence on the leading edge heat transfer, and the results of these predictions are compared with data.

The results of a recent full annular cascade measurement program are reported in Joe et al. [157] for which heat transfer and surface-pressure measurements were made at midspan using the vane of a modern high-pressure turbine. The measured vane pressure distribution was shown to compare favorably with a prediction obtained using the formulation of Ni and Bogoian [12]. The authors compare the results of their heat transfer measurements with predictions obtained using the STAN5 formulation as modi-

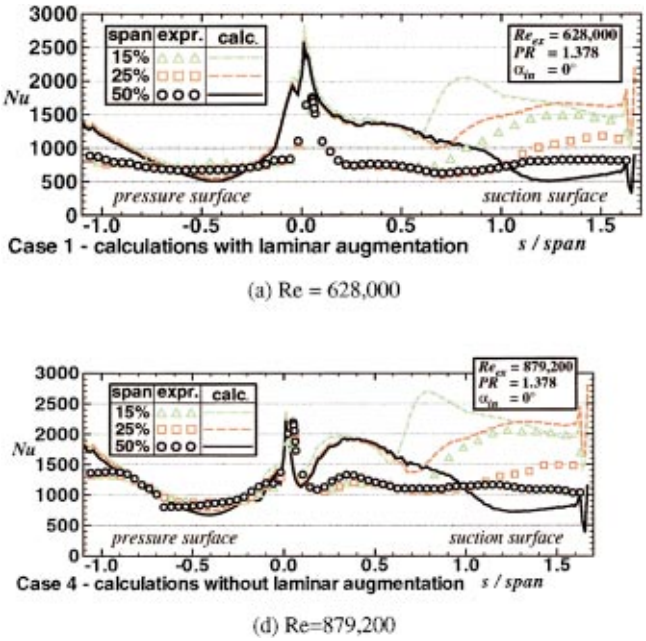

Fig. 16 Predicted versus measured Nusselt number distribution for blade, various Reynolds numbers [161]

fied by Sharma [158] and with classical flat-plate boundary layer correlations. The STAN5 prediction significantly underpredicts the data over the initial 60 percent of the suction surface and for the three locations on the pressure surface for which measurements were available. This result is qualitatively consistent with that reported by Sharma et al. [120] (discussed earlier in this section) using essentially the same STAN5 formulation, but applying it to a different turbine stage. The authors illustrate that the classical laminar and turbulent flat-plate boundary layer correlations bound the experimental results.

A more recent cascade experiment designed to obtain benchmark quality data for three-dimensional CFD code and model verification and to test the state-of-the-art CFD for heat transfer analysis is reported by Giel et al. [66]. This effort does not utilize STAN5 or a boundary layer analysis for heat transfer predictions. The paper is one of the more complete recent demonstrations of the capabilities of CFD to calculate vane heat transfer loading and thus is of interest here. The experimental rig used for this work was the NASA Glenn Research Center Transonic Turbine Blade Cascade, which is a large-scale linear cascade having a highly three-dimensional flow field resulting from thick inlet boundary layers. In order to quantify regions for which improvements in the CFD analysis are needed, the authors used as their baseline CFD analysis the NASA Glenn three-dimensional Navier–Stokes code RVC3D (see Chima and Yokota [159] and Chima [160]). The authors report measurements obtained with and without a turbulence grid for two Mach numbers, 0.98 and 1.32, at the exit and two Reynolds numbers 0.5×10^6 and 1×10^6. The heat transfer measurements are obtained using a liquid crystal technique so that they can achieve good spatial resolution of the measurements along the blade surface. The blade spanwise Stanton number comparisons given in Figs. 15(*a–d*) for the case of Reynolds number equal to 1×10^6 were obtained by Giel et al. [66] at 10, 25, and 50 percent span.

These results given in [66] for the low-Reynolds-number case, both with the grid in place and with the grid removed, illustrate that the midspan prediction generally underpredicts the data on the pressure surface. The midspan data are reasonably predicted from the stagnation region to about $s/\text{span}=0.6$ on the suction surface in the absence of the grid. Beyond 0.6 the shape of the predicted result and the measurement are quite different. For the low-Reynolds-number case with the grid, the midspan prediction for both exit Mach numbers is in reasonable agreement with the data from the stagnation point until $s/\text{span}=0.5$, but underpredicts the data beyond that location. The agreement between the 10 and 25 percent span predictions and data for the low-Reynolds-number case is good in some regions and not so good in others. Results for the higher Reynolds number case are shown in Figs. 15(*a–d*). With the grid in place, the calculation underpredicts the data significantly on both the suction and pressure surfaces, but is in better agreement with the pressure surface data when the grid is removed. With the grid removed, the agreement on the suction surface is good in some locations and not so good in others, depending upon specific location. The intent of the authors was achieved in this paper in that they demonstrate regions of the airfoil where improvements in prediction capability are needed.

Giel et al. [161] report the results of an investigation similar to the one described in the previous paragraph, but with a GE power generation turbine rotor blade. The same NASA Glenn Research Center transonic cascade facility noted above was used to perform the measurements. The experiments were performed for four exit Reynolds numbers, i.e., design point, ±20 percent, and $+40$ percent. Measurements were obtained for three exit pressure ratios corresponding to the design point and ±10 percent and at the design incidence angle and ±2 percent of design incidence. Predictions performed for the purpose of comparison with the experimental results were obtained using the same CFD codes as described in Giel et al. [66]. The results of the comparison between prediction and data at 15, 25, and 50 percent span for Reynolds numbers of 0.63×10^6 and 0.88×10^6 are illustrated in Figs. 16(*a, b*).

These results are reproduced from Figs. 5 and 8 of Giel et al. [161] for the design pressure ratio with the airfoil at 0 deg incidence and the design Reynolds number and $+40$ percent design. With the exception of the lowest Reynolds number case, the prediction overestimates the data in the pressure surface stagnation region, is in reasonable agreement between 0.3 and 0.7 blade span, and overpredicts the data beyond 0.7 blade span. The prediction falls well above the data (by about a factor of two from 0.1 to about 0.7 of the blade span for all three span locations on the suction surface at the design Reynolds number (Fig. 16(*a*)). The same holds true at $+20$ percent Reynolds number, and at $+40$ percent Reynolds number (Fig. 16(*b*)), but the 50 percent span prediction then falls below the data from 1.0 blade span to the end of the airfoil. The best agreement between prediction and experiment was achieved at -20 percent design Reynolds number. The results of this paper are similar to those shown in Giel et al. [66] and were successful in helping to define areas where additional effort is required with the CFD development.

Several methods for predicting turbine airfoil heat transfer distributions have been described above. Several of the examples cited have used one form or another of the two-dimensional boundary layer code STAN5 with mixed results. For those cases for which STAN5 was used to predict the vane and blade heat transfer for a full-stage rotating machine, better agreement between data and prediction was generally achieved for the blade. Two cascade airfoil heat transfer data sets were used to test the NASA Glenn three-dimensional Navier–Stokes code. The results of this comparison illustrated some cases of good agreement and other cases of not so good agreement. Heat transfer predictions obtained with the UNSFLO 2-D code and the VBI code were both compared with measurements and found to produce good results for both the vane and the blade.

Space does not permit a more in-depth discussion of the other numerous cascade and full-stage turbine studies relevant to the development of heat transfer prediction techniques. Among these are the work of Kirsten et al. [162], Bunker [163], Johnson et al. [164], and Sato and Takeishi [165]. However, additional cascade work will be described in Sections 4.2 and 4.3 during the discussion of external heat transfer with film cooling and the influence of boundary layer transition on airfoil heat transfer.

4.1.2 Vane Endwall Heat Transfer. Numerous studies have been reported in the literature dealing with heat transfer to the endwall region of the vane. Among these are references [120,154,166–174]. Sharma et al. [120] compare the results of a three-dimensional boundary-layer calculation with experimental results near the hub and tip endwalls for a low-aspect-ratio turbine vane. Good agreement is demonstrated with the measurements on both endwalls near the suction surface and at midpitch, but they underpredict the data near the pressure surface for both cases. However, the version of STAN5 modified by Gaugler [113], Kumar et al. [168] was able to demonstrate good correlation with the data on the vane endwall near the suction surface, at midpitch, and near the pressure surface. Ha [169] compares the results of his prediction with the data of Graziani [154] and demonstrates good comparison with the experimental results. In the same paper, Ha [169] presents a comparison of his predictions with the airfoil data of Blair [175], and demonstrates good agreement. Kumar et al. [168] describe a correlation derived from the endwall heat transfer data reported by York et al. [167]. Boyle and Jackson [172] compare the results of two different three-dimensional Navier–Stokes codes to experimental results for a vane endwall obtained in the Isentropic Light Piston Facility at Pyestock. The two codes used for the comparison were TRAF3D (Arnone et al. [176]) and RVC3D (Chima [160]). The most significant portion of the difference between the predictions of the two codes and the experimental results was attributable to the different turbulence models used

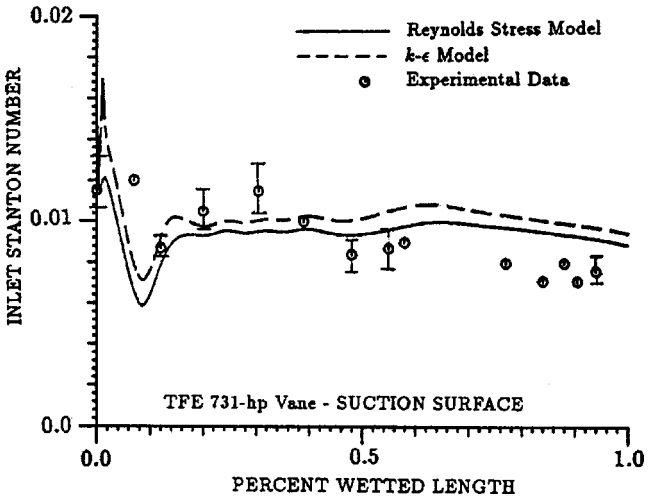

Fig. 17 Influence of stagnation point initial profiles on blade heat transfer distribution, TFE-731 [179]

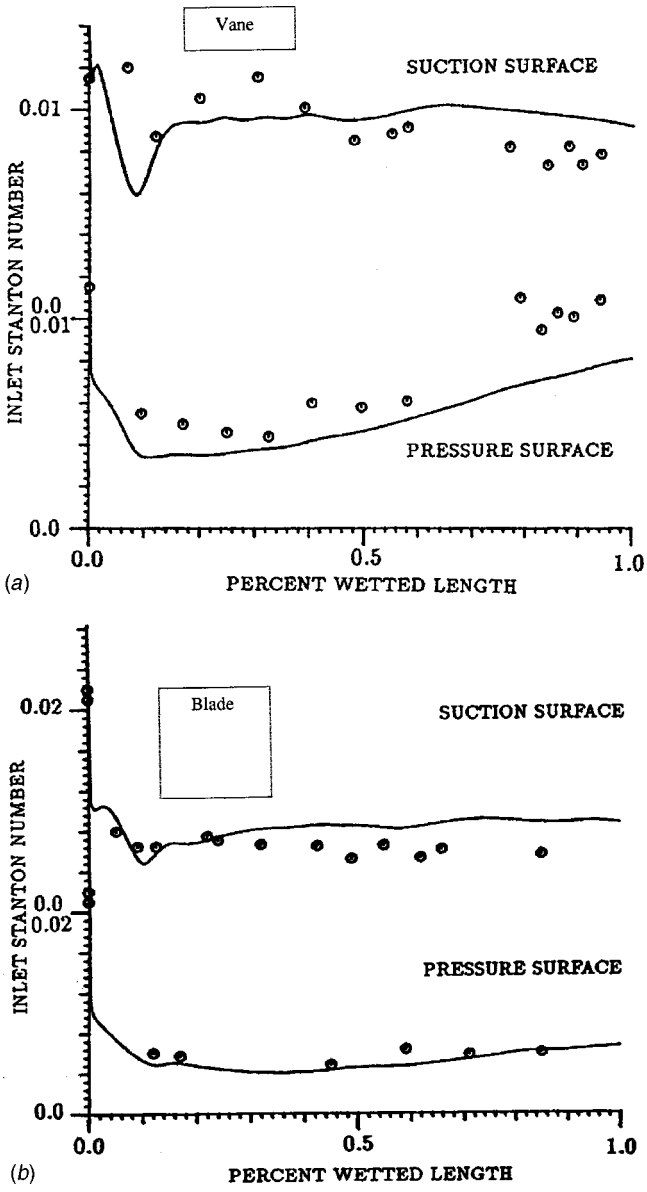

Fig. 18 Predicted versus measured Stanton number distribution for TFE 731-2 vane and blade, [179]

in the codes. In addition to the data sets noted above, many other endwall data sets that have appeared in the literature have not been adequately analyzed with current predictive codes.

4.1.3 Time-Averaged Vane and Blade Heat Transfer. The intent in this section is to review the current state-of-the art predictive capability by use of several examples that have appeared in the literature providing comparisons between experimental results and predictions for full-stage rotating turbines. By confining the discussion to rotating turbines, the facilities in which the measurements were performed are one form or another of a short-duration facility. The specific facilities of interest in much of the discussion that follows are the shock-tunnel (Calspan Corp. and Ohio State University), the blowdown (MIT and Wright Laboratories), and the light piston (Oxford University, Pyestock, and von Karman Institute). For the comparisons that will be presented (which cover a time span of approximately fifteen years), it is necessary to rely heavily, but not exclusively, on data obtained by the author, since those data are most readily available. In the majority of the cases cited for which the data of the author and associates have been used, the predictions were performed by others than the author. In the course of this comparison, some of the CFD codes discussed earlier are used for the prediction. This section includes a discussion of time-averaged heat transfer results for the vane and blade surfaces. Section 4.1.4 presents a discussion of time-resolved heat transfer results for the vane and blade surfaces. Both time-averaged and time-resolved results for the blade tip region are presented in Section 4.1.5.

The starting point for either a vane or a blade heat transfer calculation is the stagnation region requiring the calculation technique to have some method of handling this region. It was noted earlier in Section 4 that one of the major improvements incorporated into the flat-plate code STAN5 was to allow for a cylindrical leading edge. Although the leading edge of a vane or a blade is seldom a cylinder, it is often approximated using a cylinder. Several authors have investigated techniques for this starting condition, e.g., references [177–185]. Taulbee et al. [179] present a comparison of prediction with measurement for two different turbine stages, the Garrett TFE-731-2 and the Teledyne 702. They also present results obtained for the suction surface of the TFE-731-2 vane comparing predictions of the Reynolds stress model with those of the $k-\varepsilon$ model. Figure 17 illustrates the influence of turbulence model on the predicted suction surface Stanton-number distribution and compares the prediction with experimental results.

As shown in Fig. 17, the $k-\varepsilon$ model results in a high heat transfer prediction in the immediate stagnation-point region because of the excessively large amount of turbulent energy in the stagnation profile. This predicted high heat transfer rate decreases rapidly with increased distance along the surface such that the boundary layer prediction obtained from either turbulence model gives about the same predicted value.

The authors also present results for both the vane and the blade surfaces of these turbines. Reynolds stress modeling was used to calculate the variation of the turbulence quantities along the stagnation streamline, thus determining the stagnation-point heat transfer. The boundary-layer solution from which the surface heat transfer distribution on the vane and blade surfaces was determined was obtained using a two-equation $k-\varepsilon$ turbulence model. Figure 18 presents comparisons reported in Taulbee et al. [179] obtained for the midspan region of the vane and blade of the Garrett TFE-731-2 HPT stage.

This is the same turbine stage for which Kielb [64] reported surface-pressure measurements for the blade (Fig. 13 of this paper). This particular turbine has a modest stage pressure ratio (vane inlet total to blade exit static on the order of about 2) and

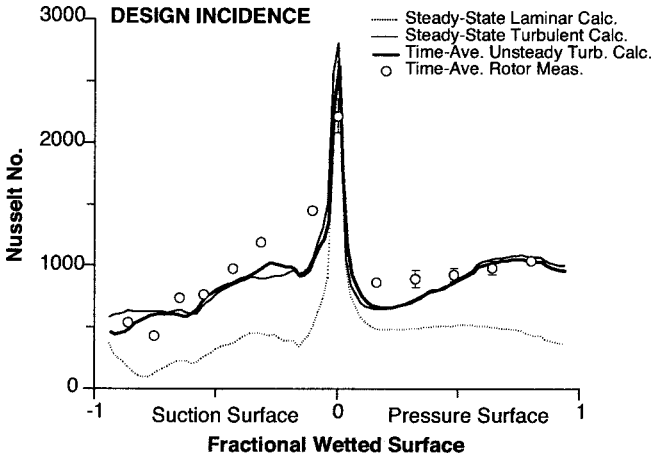

Fig. 19 Predicted versus measured Nusselt number distribution for Rolls-Royce ACE blade [134]

the vane and blade profiles are essentially two dimensional. The agreement between the prediction and measurements is in general reasonably good. The prediction underpredicts the data on the vane pressure surface, and overpredicts the data on the blade suction surface beyond about 25 percent wetted distance.

Taulbee et al. [179] also compare their prediction to data obtained for the Teledyne 702 HPT stage. This turbine has a significantly greater vane inlet total to blade exit static pressure ratio (on the order of about 4.2) and the vane and blade geometry is three-dimensional. Similar to the TFE 731-2 result, the vane pressure surface heat transfer is underpredicted and the blade suction surface heat transfer is overpredicted beyond 15 percent wetted distance. Rae et al. [186] present a comparison generated using a modified version of STAN5 with the same data as used by Taulbee. The results obtained by Taulbee were significantly better than those achieved with the flat-plate prediction technique.

Sharma et al. [120] present a comparison between a two-dimensional (vane and blade) and three-dimensional (vane only) boundary-layer predictions and measurement for yet a different turbine, the Garrett Low Aspect Ratio Turbine (LART). The vane and blade geometry of this particular turbine is three dimensional and the vane inlet total to blade exit total pressure ratio was about 3.2. The LART measurements were those reported in Dunn et al. [107]. Both the two-dimensional and the three-dimensional boundary-layer codes were found to underpredict the measurements on the vane, but the two-dimensional code did a reasonably good job of predicting the data on the blade.

The literature contains several references, e.g., Abhari et al. [134], Moss et al. [29], and Dunn et al. [187], for which the CFD code UNSFLO 2D (described in Section 2.2) has been used to predict heat transfer distributions. These predictions have been done for either the vane or the blade or both for turbine stages designed and manufactured by different companies. The measurements reported in Abhari et al. [134] were conducted in the MIT blowdown turbine facility and the test article was the full-stage Rolls Royce ACE high-pressure turbine. The authors present a comparison between prediction and measurement for the blade that is reproduced in Fig. 19.

On the early portion of the suction and pressure surfaces, they underpredict the measurement somewhat, but in general the prediction is good. Dunn et al. [187] used the same predictive code as part of a study to determine the influence of vane/blade spacing on the blade heat transfer distribution. The measurements reported in Dunn et al. [187] were performed in the Ohio State University short-duration facility and the test article was the full-stage Allison VBI high-pressure turbine. The conclusion of that study was that vane/blade spacing has a relatively small influence on blade heat transfer loading. The code UNSFLO 2-D was used to predict both the vane and blade heat transfer distributions. The results of the comparison with measurement at the 40 percent vane axial chord spacing case are shown in Figs. 20 and 21 for the vane and blade, respectively.

For the vane, the code does a good job of predicting the data, except for the data point at about 70 percent wetted distance on the suction surface. For the blade, the prediction is good on the pressure surface, but underpredicts the data early on the suction surface and then again beyond 70 percent wetted distance. However, overall the comparison is good between the data and the prediction. The nomenclature block on Figs. 20 and 21 contains an entry marked ''corrected.'' This note refers to a correction term (taken from Zilles and Abhari [188]) that has been applied to the data because of a potential heat-island effect, which is discussed in more detail in Dunn et al. [187].

For a much earlier experimental program using the same Allison high-pressure turbine stage, Rao et al. [150] reported a comparison of time-averaged and time-resolved heat transfer predictions obtained using the Allison two-dimensional VBI code (described in Section 2.2). The prediction presented by Rao et al. [150] was good except that they didn't do as good a job of predicting the data as Dunn et al. [187] for the vane suction surface and the blade suction surface. However, the result would be considered good considering the status of the code development at the time the calculation was performed.

The two-dimensional boundary-layer code KEP (discussed earlier in Section 4) was used by Bergholz et al. [189] for the midspan analysis of the vane and blade of a General Electric high-pressure turbine stage. The authors also present a comparison between measurement and predictions obtained using the three-dimensional code STAR CD for the blade hub and tip as well as at 20, 50, and 96 percent span. The measurements used for this comparison were obtained using the Ohio State University short-duration facility and the test article was a General Electric designed and constructed high-pressure turbine stage. The results of the comparison obtained using the two-dimensional boundary-layer code for the midspan region of the vane and blade are presented in Figs. 22 and 23, respectively.

The results of this comparison are considered generally good, with the prediction on the pressure surface of the vane being a bit below the data, but in good agreement with the data on the blade pressure and suction surfaces. A comparison between the STAR3D prediction and the experimental results obtained for the blade is presented in Fig. 24.

Measurements and predictions are compared for both the pressure and suction surfaces at 20, 50, and 96 percent span as well as for the blade platform. These color plots are typical of current CFD presentations. The numbers written on the lines are the experimental results. It is difficult from these types of plots to assess the quality of the prediction. However, the authors note that the comparison is reasonably good between the predictions and the data.

Narcus et al. [190] present the results of a study utilizing thermocouple instrumented vane airfoils of an operating engine to measure the vane heat load. The intent of the study was to determine the accuracy with which the external heat load to the vane can be determined using embedded thermocouple methods and to compare the results of the engine experiments with cascade results. The authors conclude that the engine measurement can be performed with an acceptable level of uncertainty. Their claim is to measure heat transfer coefficients in an engine environment to within ± 3.2 percent minimum absolute uncertainty, which is remarkable accuracy for using thermocouples in such a hostile environment as the engine presents. The authors favorably compare the operating-engine results obtained at one location on the vane suction surface with those obtained earlier by Soechting and Sharma [191] using an airfoil with identical midspan profiles in a cascade facility. Similar to the argument presented in Joe et al. [157], the authors show that the Nusselt number results for the

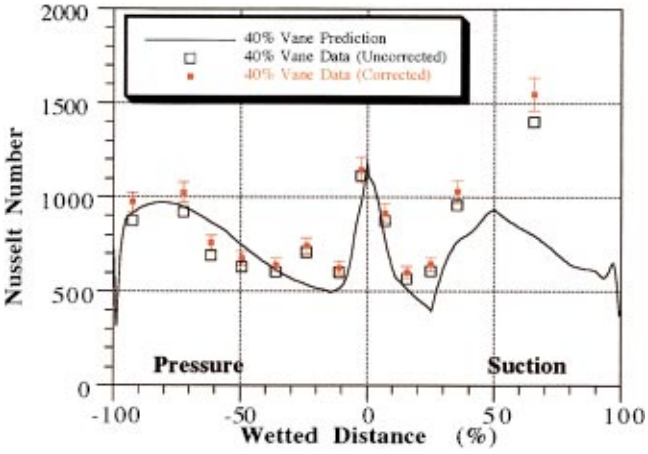

Fig. 20 Predicted versus measured Nusselt number distribution for Allison VBI [187]

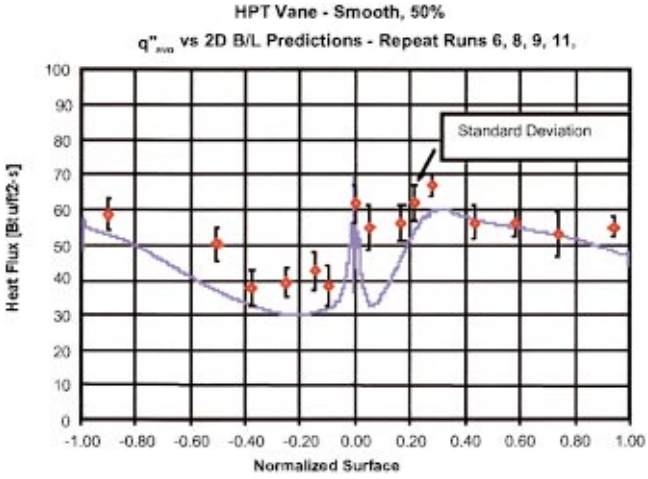

Fig. 22 Predicted versus measured heat flux distribution for GE vane [189]

engine experiment are bounded by the flat-plate turbulent and laminar boundary-layer predictions. The authors make special note to point out that the cascade experimental results did not duplicate heat transfer levels for all locations on the airfoil surface.

Several examples were given above for which predictions obtained using existing CFD codes were compared with experimental results. The UNSFLO 2-D code was used by two different groups to obtain comparisons between prediction and measurement for two different full-stage turbines with good success. The Allison VBI code was used to obtain a comparison between prediction and measurement for one of the same full-stage turbines used with UNSFLO 2-D with equally good success. Vane and blade midspan predictions obtained using the two-dimensional boundary layer codes generally demonstrated reasonable success for the blade, but not as good for the companion vane. Three-dimensional heat transfer predictions obtained with different CFD codes were compared with experimental results. For these comparisons, regions of the airfoil for which reasonable agreement between prediction and data was achieved were illustrated. Other regions were identified that require additional effort. Several of the three-dimensional codes described in Section 2 that demonstrated good ability for obtaining surface-pressure predictions are not currently being used to obtain heat transfer predictions. It is important for the heat transfer community to incorporate the proper gridding near the surface into these codes so that they can be used for heat transfer prediction.

All of the above having been said regarding the state of the art in the measurement and prediction of turbine heat transfer, one is still faced with the question: ''Who has the responsibility to predict component life, and how is it accomplished?'' With the increased demand for guarantees of engine operating time in excess of 20,000 hours, life prediction of turbine components can have an important financial impact. The replacement rates of hot-section components are among the highest in the engine, making the turbine a focus of the community. There is generally a separate group within the engine companies that is composed of persons with expertise in materials, heat transfer, structures, and aerodynamics, who have been associated in the design phase. Most of these people have years of engine experience and some have experienced higher than anticipated failure rates for turbine components with which they have been associated. Often mistakes made during the design phase couldn't be predicted by the then-current predictive capability, and the lessons learned were translated into ''rules of thumb'' for hot-section design. If the experience factor were to be discounted, then the tools that these individuals have to work with for predicting component life are no better than the design tools. Some of these design tools have been described

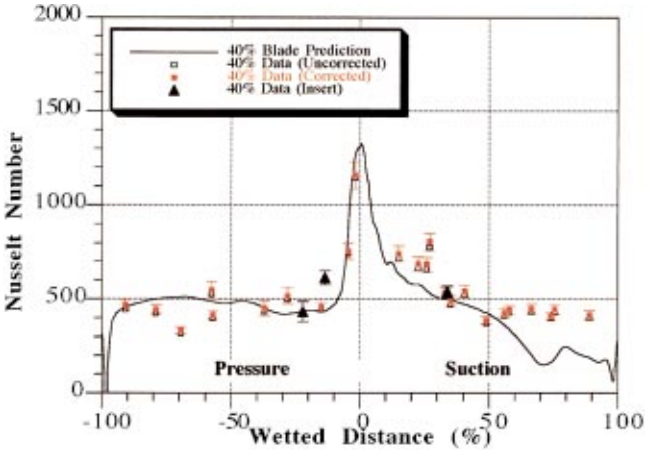

Fig. 21 Predicted versus measured Nusselt number distribution for Allison VBI blade, [187]

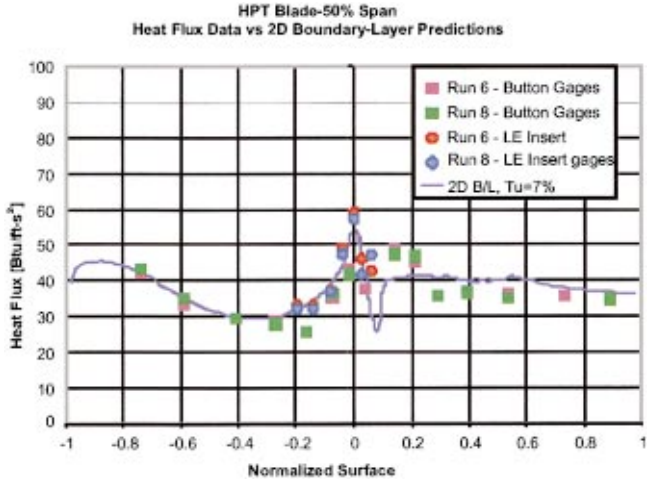

Fig. 23 Predicted versus measured heat flux distribution for GE blade [189]

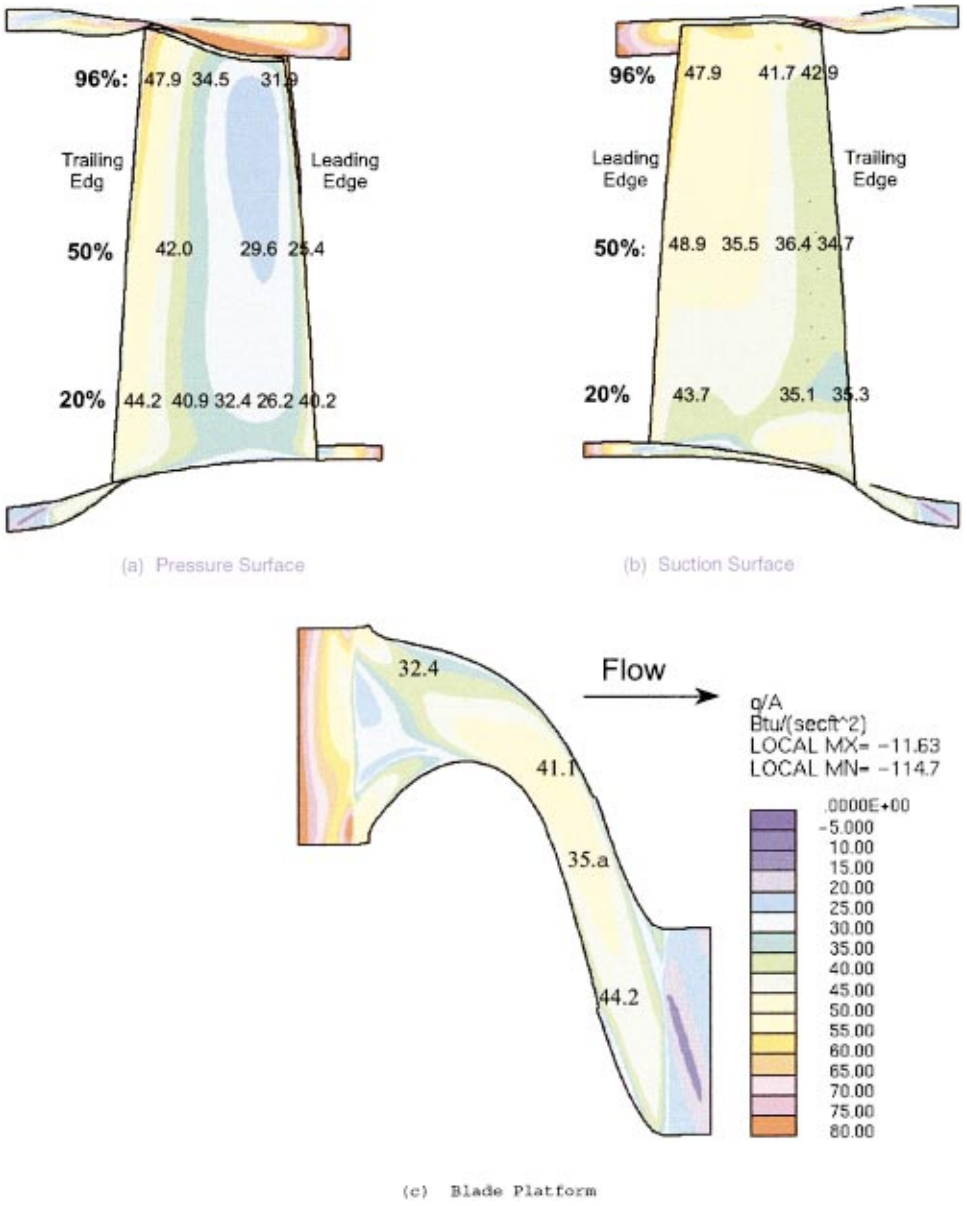

Fig. 24 Predicted versus measured heat flux distribution for GE blade, three-dimensional [189]

herein, so there are limitations to how well life can be predicted. Relevant measurements taken in the engine environment that could be used to refine a life analysis are scarce. Thus the foundation of the ''rule of thumb'' often used is based on engine tear down information from which the events that probably occurred in the engine to produce the failure mode observed are deduced. Unfortunately, it is difficult to generalize among engine configurations even within the same company so life prediction becomes more of an art than a science. It is anticipated that with improved predictive capability life predictions will become more representative of experience.

4.1.4 Time-Resolved and Phase-Resolved Rotating Blade Heat Transfer. Many authors have either measured or predicted the blade unsteady heat transfer loading for full-scale rotating turbines operating at design corrected conditions. Among these are references [128,107,130,131,142,134,192,193,150,187]. Space permits only selected of these to be described herein.

Abhari et al. [134] reported the results of a combined experimental and computational program that used the full-stage Rolls Royce ACE HPT stage operating at design corrected conditions. They did not measure surface pressure on the blade, but rather used the predicted blade unsteady pressure loading (obtained using UNSFLO 2-D) to calculate the local unsteady heat flux which was then compared with the measured heat flux. On the early portion of the pressure surface and for a good deal of the suction surface, Abhari et al. [134] found reasonably good agreement between the predicted and measured unsteady heat transfer. They did not find good agreement at the stagnation region of the blade. Dunn et al. [187] measured both the unsteady surface pressure and the unsteady heat flux at selected locations on the pressure and suction surface of the blade of the Allison VBI high-pressure turbine stage. Figures 25 and 26 present the comparisons between measured surface-pressure and heat-flux histories taken from Dunn et al. [187].

These comparisons illustrate that the results predicted by Abhari et al. [134] are consistent with the measurements of Dunn et al. [187]. The measured surface pressure and surface heat flux are in phase with each other on the early portion of the pressure surface, over most of the suction surface (see similar comparisons presented in [187]), but not in the stagnation region. Johnson et al.

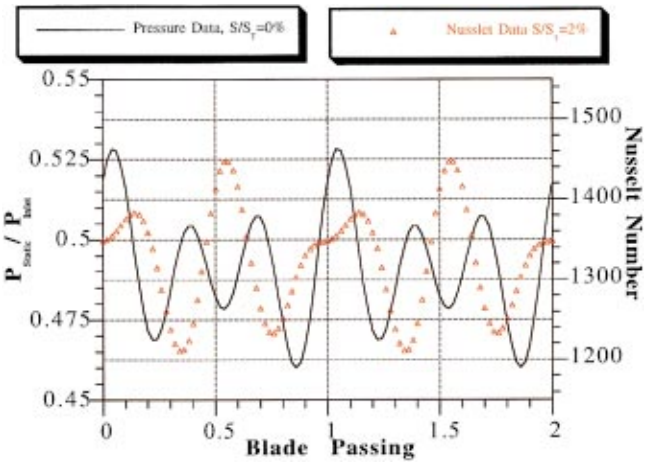

Fig. 25 Comparison of measured surface pressure with measured surface heat flux near blade stagnation point [187]

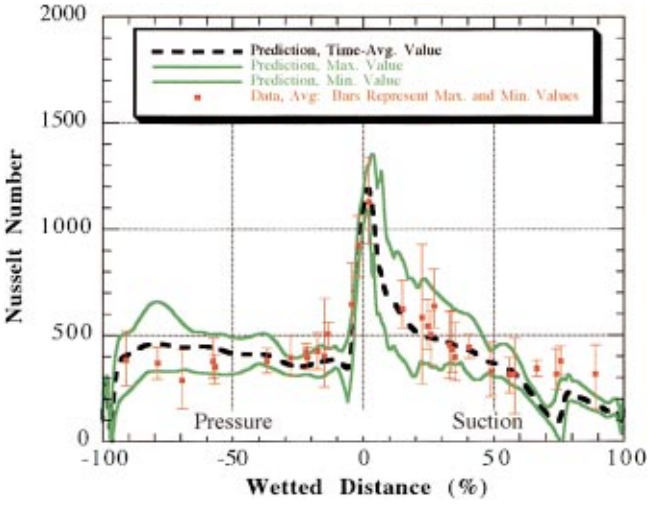

Fig. 27 Predicted versus measured unsteady Nusselt number for blade surface [187]

[164] and Rigby et al. [141] have both reported studies of the relationship between unsteady heat transfer and unsteady surface pressure. Rigby et al. [141] argue that it should be possible to determine the local heat transfer enhancement for a given unsteady pressure signal at various wall temperature ratios using temperature scaling. For this to be true there must be a linear relationship between the local heat-flux history and the local surface-pressure history. The surface pressure and heat transfer histories presented in Figs. 25 and 26 are both experimental results. Busby et al. [30] present comparisons of predicted to measured time histories of surface pressure (but not heat transfer) for several locations on the pressure and suction surface of the same blade. The predictions were done using four different predictive codes described in Section 2. It is demonstrated by Busby et al. [30] that two of the four codes did a reasonably good job of predicting the time history of the surface pressure on the suction surface. All of the codes did a good job at some wetted distance locations and not so good a job at other locations for the pressure surface.

The CFD code UNSFLO 2-D is used in Dunn et al. [187] to predict the unsteady envelope of heat flux on the blade surface. Figure 27 presents the predicted envelope compared with the measured envelope for the 60 percent vane/blade spacing case.

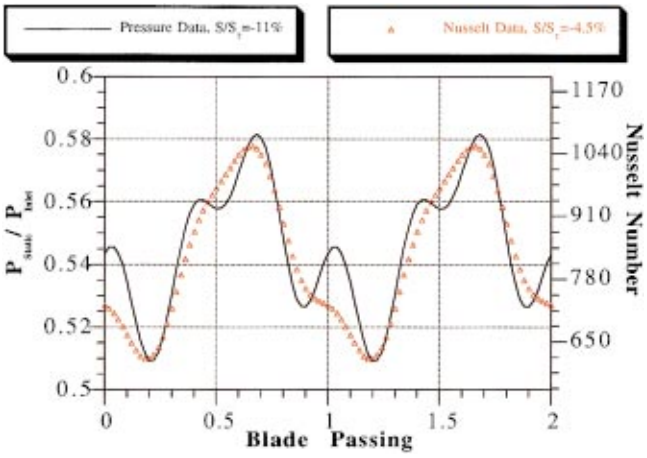

Fig. 26 Comparison of measured surface pressure with measured surface heat flux on blade pressure surface near stagnation point [187]

In general, the code does a good job of predicting the magnitude and distribution of the unsteady heat flux. Similar to the unsteady pressure envelope comparison, the prediction is in reasonably good agreement with the data over most of the blade surface. The most significant unsteadiness occurs on the suction surface from the stagnation region to about 40 percent wetted distance and the agreement between prediction and measurement over this region is good. The largest disagreement between the predicted envelope and the data occurs beyond 80 percent wetted distance on the suction surface, but even there, the agreement is acceptable. The unsteady envelope over the pressure surface is relatively constant from the leading edge to the trailing edge, and the agreement between prediction and data is good.

Rao et al. [28] also predicted the unsteady heat flux as a function of position on the blade as well as the unsteady envelope for the Allison VBI turbine, but for an earlier data set. The resulting comparison between predicted and measured unsteady heat-flux envelope obtained with the two-dimensional VBI CFD code is similar to that just illustrated for the UNSFLO 2-D calculation. UNSFLO 2-D and VBI 2-D are the only CFD codes that have been tested against unsteady heat transfer results for a transonic turbine stage. Both of these CFD codes are specifically applicable to a two-dimensional geometry. It is not clear how well either would predict the heat transfer data at the hub or tip for a three-dimensional blade configuration, but it is unlikely that they would do as well as demonstrated for the midspan region.

4.1.5 Blade Tip and Shroud Heat Transfer. The tips of axial HPT blades rotate in close proximity to a stationary outer seal or shroud. For performance reasons, the designer generally prefers to maintain the tip clearance as tight as feasible, but wants to avoid tip rubs. Some engine companies elect to utilize shrouded blades and eliminate the tip rub problem, while others use flat-tip or recessed-tip blades. For those aircraft engines using flat or recessed tips, significant variations in clearance occurs at different operating conditions such as takeoff and cruise. Differential thermal expansion between the rotating blades and the stationary outer shroud causes variations in the magnitude of the clearance gap depending upon engine operating point. Unfortunately, for some engine operating conditions, the shroud may cool more quickly than the disk, resulting in a significant reduction in tip gap to the point that rubbing occurs. Even with active clearance control, it is not always possible to eliminate tip rubs for all operating conditions. However, the use of recessed tips allows one to operate with tighter clearance gaps with a reduced probability of severe blade damage if a rub were to occur. Clearance gaps in mod-

ern axial gas turbines are typically less than one percent of the blade height for large engines, ranging up to 1.5 percent or more for smaller engines with low aspect ratio blading. Even with the tightest possible tolerances, the leakage flow can have significant effects on stage aerodynamic performance and on the structural durability of the blade. The surface area at the blade tip in contact with the working gas is an area for convection heat transfer and thermal loading on the blade. This heat must be removed by the blade internal cooling flows, along with heat transferred to the blade pressure and suction side-surface areas.

Bunker [194] presents an extensive review of public domain information regarding high-pressure turbine blade-tip region heat transfer covering the time from about 1955 to 2000. As demonstrated in Bunker's review, a significant portion of the literature relevant to tip gap flows has dealt with flat tip blades. In many cases, the measurements were performed for very low relative speed or the blades were not rotating at all relative to the outer shroud. The early work of Metzger and Rued, Parts I and II [195] were designed to obtain detailed information relevant to the source (pressure surface side) of the tip flow. Similar information for the sink (suction surface side) was also presented. These modeling experiments were conducted using a water tunnel facility. Several researchers have also investigated ways of reducing performance losses by controlling tip leakage flow ([196–199], and [200]). Others have concentrated on the heat transfer in the tip region ([201]). The work of Booth et al. [196] and Wadia and Booth [197] was also conducted using water tunnels as the test bed. Sjolander and Cao [198] used a single blade and shims were used to change the value of the gap in order to study the structure of the gap flow in the absence of relative motion. In a later study, Yaras et al. [199] used a cascade of three blades and added a moving outer belt to simulate the influence of rotation on tip leakage. The results of this study indicated that relative motion causes significant changes in the tip leakage vortex and passage vortex structures. It was concluded that the strength of the tip vortex was reduced considerably with the introduction of wall motion. In addition, the passage vortex was enhanced by the scraping effect of the blades. Both vortices were dragged toward the suction side of the passage and appeared to partially block the outlet flow from the tip gap. Heyes and Hodson [202] presented the results of an experimental study using linear cascades in the absence of a moving outer wall. They suggested a relative simple model that could be used in conjunction with a three-dimensional code to calculate the tip gap flow. One significant finding of their study was that the pressure gradients along the blade chord are a major factor influencing the tip leakage flow.

There are very few experimental data for the heat transfer distributions in the vicinity of recessed tips that have been obtained for full-scale rotating turbines operating at the design corrected conditions. It is well known that the pressure difference between the convex and concave sides of the blade drives flow through the clearance gap. However, because of the recessed cavity in the tip, the flow field associated with the recess is significantly more complicated than one would encounter on a flat tip blade. Near the leading edge of the blade, a strong vortex flow exiting the vane near the stationary shroud enters the tip region from head on or from the suction surface side of the blade. Ameri et al. [203] demonstrate in their calculation of the tip region flow for a recessed tip geometry that the flow field is very three dimensional with many vortices interacting. Their results suggest that there are at least two distinct vortices existing in the cavity region, and they persist throughout the length of the cavity. Their modeling of this flow suggests that one of the vortices is a result of separation off the pressure side of the lip and that this vortex hugs the cavity pressure sidewall. The second vortex is the result of a flow separation again at the lip on the blade suction side. There appears to be a dividing streamline after which the mainstream flow is turned into the gap from the pressure side of the blade. Flow separation occurs because of the lip. Strong secondary flows can be expected to be present in the gas path as a whole. This can have the effect of bringing very hot portions of the mainstream to the vicinity of the clearance gap, downstream of the blade leading edge lip. This lip acts like a rearward-facing step with resulting flow separation and attachment in the recessed cavity. As the flow emerges from the suction side of the gap, it is usually visualized as rolling into a vortex as it meets the oncoming shroud wall flow (Bindon [204] and Allen and Kofskey [205]). Thus near the tip on the aft portion of the suction surface the local heat transfer rates can become quite high causing trailing edge tip burn out.

Metzger published the results of several low speed outer wall studies applicable to the tip region heat transfer for recessed cavities ([206–208]). Ameri et al. [203] applied their calculation technique to the Metzger tip cavity data. They obtained reasonably good results for those configurations with depth to width ratios of 0.2 and 0.5 at a tip clearance to cavity width ratio of 0.1. Dunn and Haldeman [209] present the results of an experimental program designed to measure the heat transfer in the region of a recessed blade tip for a transonic turbine at different vane/blade spacing. The specific turbine used for this experiment was the Allison VBI transonic turbine discussed earlier. For reference purposes, the depth to width ratio of the cavity used in the study described in Dunn and Haldeman [209] range from 0 to 0.21 with a tip clearance to cavity width ratio of 0.14. The blade tip region was instrumented with thin-film heat-flux gages in the cavity floor, on the lip of the tip, and at 90 percent span on the suction side of the blade. The experimental data and the results of the Ameri et al. [203] calculation for the geometry closest to that used herein suggested that the peak Nusselt number occurred on the lip. The Nusselt numbers in the bottom of the cavity were about 42 percent of the lip values. In this same paper, Ameri et al. [203] have performed tip region calculations to simulate the fluid flow and heat transfer in the tip region for the GE-E^3 high pressure turbine. Their calculations were performed for a smooth tip, a 2 percent recess, and a 3 percent recess. The recessed tip used for the measurements reported by Dunn and Haldeman [209] was a 3 percent recess. Dunn and Haldeman [209] found that the peak heat flux (which was on the same order as the blade stagnation point value) occurred in the recessed cavity near the leading edge of the blade. This is at about the same location that a turbine designer would place the tip vent hole for the showerhead cooling tube of a film cooled blade. For the lip region of the blade, the peak values of heat flux occurred on the suction surface side of the cavity and were of the same order of magnitude as the blade stagnation point.

Bunker et al. [210] and Ameri and Bunker [211] report the results of a combined experimental and computational study designed to investigate the heat transfer to the first-stage blade tip of a power generation gas turbine. The experiment utilized a three blade linear cascade with no outer shroud motion. Using liquid crystals in the tip region, the authors were able to obtain a rather detailed distribution of heat transfer in the tip region. The computational phase of the effort used to support the experiments utilized the code reported in Rigby et al. [212] and Ameri et al. [203]. The authors showed good comparison between experiment and computation.

Three previous experimental/computational analyses of flow in the tip region for a flat tip blade were reported by Metzger et al. [213], Ameri and Steinthorsson [214], and Ameri and Steinthorsson [215]. For the Metzger et al. [207] paper, time-resolved heat transfer measurements obtained on the blade tip and simultaneously obtained time-resolved heat transfer and surface pressure measured on the adjoining stationary shroud was compared with the results of a CFD analysis. The turbine stage used for this work was Garrett TFE-731-2. Ameri and Steinthorsson [208] reported the results of time-averaged heat transfer calculations compared to the data of Dunn et al. [216] for the Garrett TFE-731 turbine. A similar comparison is presented by Ameri and Steinthorsson [215] for the data of Dunn et al. [217] obtained on the first blade of a

full two-stage Space Shuttle main engine hydrogen side turbopump. The predictions of Metzger et al. [213] and the predictions of Ameri and Steinthorsson [214,215] showed good agreement with the experimental results.

Heat transfer (and surface-pressure) measurements for the stationary shroud have been presented in the literature for several different full-scale rotating turbine stages. Dunn et al. [216] present results for the Garrett TFE731-2 turbine, and Epstein et al. [218] present similar results for the Rolls Royce ACE turbine. Other shroud results are described in Dunn et al. [107] for the Garrett Low Aspect Ratio Turbine (LART), and in Dunn and Kim [219] for the Space Shuttle Main Engine (SSME) two-stage turbine. The results for the TFE731-2 and the Rolls Royce turbines are similar. The shroud heat flux is shown to remain rather high (on the order of the blade stagnation region value) from the blade leading edge until about midchord. The magnitude of heat flux then falls rapidly from midchord to the trailing edge for both turbines. Both Epstein et al. [218] and Dunn [220] present the time-resolved heat-flux history on the stationary shroud. The tip and stationary shroud regions of these machines both have high heat-flux levels with similar shroud distributions. However, for other turbines, the heat-flux level on the stationary shroud was relatively constant along the blade chord and did not fall until after the blade trailing edge.

Missing from the tip region studies described above are surface-pressure data for the location on the moving tip corresponding to the heat transfer measurement. Surface pressure data are available for the stationary shroud that is in close proximity to the rotating blade, but this is not sufficient information to help with determination of the blade flow field. Also missing are experimental results obtained on a rotating blade configured to have a range of tip cavity configurations. None of the calculation techniques described above has the capability to calculate the unsteady heat transfer history in the blade tip region. Thus, comparison of the unsteady experimental results with prediction is not presently possible. Significant work remains to be done from both an experimental and computational perspective for the blade tip region flow.

4.1.6 Influence of Hot Streaks and Downstream Vane Clocking on Heat Transfer. Turbine inlet temperatures have been on the increase for a number of years. This temperature is limited only by the amount of cooling that can be supplied to strategic locations in the combustor or turbine, the melting temperature of the components, and the stoichiometric temperature of the fuel. As long as the gas turbine industry desires to maximize cycle performance and reduce fuel consumption, there will be pressure on the designer to find a way to increase hot-section temperatures. Flowpath temperatures used in modern machines are significantly greater (on the order of 500 K) than the maximum allowable operational temperatures of the component materials. Cold gas injection, internal cooling, or external film cooling methods are used to maintain structural integrity. However, there will be local areas where this hot gas will migrate to the blade surface (pressure surface and platform) resulting in a modest increase of local metal temperature, which may result in a major decrease in component life.

The hot-section design team has several important questions that they must answer. Important considerations include the number of fuel nozzles in the combustor and the number of vanes in the HPT vane row. They must also determine placement of the leading edges of the HPT vanes relative to the fuel nozzles (hot streaks) and placement of the vane leading edge of the second vane row relative to the first vane row. For very good reasons, seasoned designers have ''rules of thumb'' regarding fuel nozzle count relative to HPT vane count relative to HPT blade count, etc. These rules are based on years of experience that more often than not has involved a machine getting into serious trouble because of a particular configuration. However, continued demands to increase engine performance, increase thrust to weight, reduce part count, and to improve fuel consumption to mention but a few are causing some of these ''rules of thumb'' to be questioned and quantified.

It is well known that the flow exiting the combustor and entering the turbine has significant radial and circumferential temperature distortion or ''hot streaks.'' It is not surprising that the number of hot streaks at the exit of the combustor section frequently corresponds with the number of combustor fuel nozzles, and may be relatively in line with their physical position. The nonuniform temperature profile entering the HPT vane row has the potential when progressing on through to the rotating blade row to cause additional secondary flows (Hawthorne [221] and Lakshminarayana and Horlock [222]). Temperature segregation on the blade surface was initially described by Kerrebrock and Mikolajczak [223]. In the absence of major breakthroughs in new high-strength materials (and an accompanying decrease in the desire to increase turbine inlet temperature), it becomes important to model, as accurately as possible, hot streak migration through the turbine. Doing so allows one to maximize component life and to avoid excessive performance penalties because of cooling gas extraction from the compressor. Migration of multiple hot streaks through the turbine stage has been the subject of considerable computational attention in recent years. Among the papers describing this effort are references [224–231,235]. In the paper by Shang and Epstein [229] the authors utilize the three-dimensional unsteady Euler code described in Saxer [232] to explore in some depth the trends observed in the experiments performed by Shang [233] and reported in Shang et al. [234]. Secondary flow effects and tip clearance effects were ignored in this study, but the objective of the authors was to study trends and scaling as opposed to quantitative values. The work of Shang will be described in more detail in the following paragraph. Orkwis et al. [235] used a lumped deterministic source term technique to track a hot streak through the vane and blade of a typical HPT. They compare their results with those obtained using an inviscid unsteady solution (MSU TURBO, Chen et al. [16] and Chen and Barter [44], described earlier). Orkwis et al. [235] conclude that their deterministic source term technique offers the possibility of including unsteady effects in time-averaged calculations with minimal computer effort.

The experimental database available in the literature to guide the CFD code developers with modeling these flows is much more limited, e.g., Butler et al. [236], Roback and Dring [237], and Shang et al. [234]. The experimental database reported in the Roback and Dring [237] papers was obtained in a large-scale, low-speed, rotating rig. A single-stage turbine for which trace amounts of CO_2 were injected upstream of the vane inlet and subsequent tracking the seed gas through the turbine stage was the technique used to obtain the data. The measurements of Shang et al. [234] were performed using a transonic turbine stage. Radial and circumferential temperature distortions were introduced upstream of the vane inlet and the blade heat flux was measured at selected midspan locations. The results demonstrated that the spatial heat-flux distribution on the blade pressure surface was significantly altered by the presence of the hot streaks with local increases of 50 percent being measured. The experiment described in the paper by Shang et al. [234] was performed in the MIT blowdown turbine facility using the Rolls Royce designed ACE full-stage rotating turbine operating at design corrected conditions. Four hot streaks were introduced in one-third of the flow annulus upstream of the HPT vane row. The four injection sites were located at midpassage and were equally spaced circumferentially over one-third of the annulus. Heat transfer measurements were made on the blade at three spanwise locations on the pressure and suction surfaces at 79, 46, and 16 percent. Blade measurements obtained for uniform temperature conditions at the inlet demonstrated that the turbine has significant three-dimensional effects. There was as much as a 40 percent spanwise variation in measured heat transfer and the radial variation on the pressure surface was different than

on the suction surface. This measured radial profile is important when discussing the film cooling measurements and comparison with prediction (done for the same HPT) reported in Garg and Abhari [238] that will be described later. Measurements made on the blade in the presence of hot streaks suggest that the hot streaks have a significant influence on the time-averaged heat transfer level unless the additional energy added to the streak is accounted for in the comparison. However, when this extra energy is properly accounted for in the data analysis, then there is still an influence of the hot streak, but it is much less important. These authors also find that the hot gas migrates to the blade pressure surface and the cold gas migrates to the suction surface as found by previous investigators. Further, Shang et al. [234] also investigated the case of circumferentially uniform but radially varying temperature and found that this configuration results in significant changes in the blade heat transfer loading.

Dorney and Gundy-Burlet [239] present a calculation of hot streak migration through a one-and-a-half stage turbine. Results are presented for three cases: (1) the hot streak does not impinge on the HPT vane, (2) the hot streak has full impingement on the HPT vane, and (3) the hot streak impinges only on the suction surface of the HPT vane. The resulting temperature magnitudes and history on the HPT vane, the HPT blade, and the second vane are all very different depending upon where the hot streak happens to be located relative to the HPT vane. It is clear from the results of this study that one must take a careful look at how to place the hot streaks relative to the HPT vane and the second vane. Then the overall cooling gas penalty associated with the selection must be evaluated.

This discussion leads to the obvious question of how clocking may impact on turbine performance. Dorney and Sharma [240] have presented the results of a numerical study for a one-and-a-half stage turbine intended to provide insight into this question. The authors conclude that clocking the second vane relative to the first can result in performance increases in excess of 2 percent for their configuration. The maximum performance increase occurs when the first vane wake is aligned with the leading edge of the second vane. The minimum occurs when the first vane wake is located in midpassage of the second vane, and at the maximum efficiency clocking position, the second vane has significant increases in unsteadiness. Huber et al. [241] reports the results of a combined analytical and experimental study (see Griffin et al. [242] for the analytical portion). They used a full two-stage turbine with 54 first-stage vanes, 50 first-stage blades, 54 second-stage vanes, and 50 second-stage blades. Huber et al. [241] found that an efficiency gain of about 0.8 percent could be achieved by locating the second vane so that the first vane wake impinges on the second vane leading edge. The minimum efficiency occurred when the first vane wake occurred at second vane midpassage (consistent with the calculations of Dorney and Sharma [227]). The numerical analysis reported in Griffin et al. [242] for the Huber et al. [241] experiments predicted a potential efficiency gain due to vane clocking of 0.3 percent as compared to the measured 0.8 percent. However, the prediction suggested an average efficiency of 94.8 percent, but the experiments gave an average efficiency of 89.7 percent. The authors could not adequately explain the difference between predicted and measured average efficiency and further work is required.

Several other authors have also investigated the implications of vane clocking from either a heat transfer or performance viewpoint, e.g., Eulitz et al. [243], Gundy-Burlet and Dorney [244], Johnson and Fleeter [245], and Tiedemann and Kost [246]. As demonstrated by the calculations and experimental results presented in the previous paragraph, there are potential gains to be realized by clocking the upstream vane row relative to the fuel nozzles. Potential performance gains are also possible by clocking the downstream vane row relative to the upstream vane row, enough so that additional work is warranted. Although there are several different CFD codes that can be used to predict the influence of clocking on stage performance and on downstream heat transfer, there is relatively little experimental data with which to compare the predictions. It is not difficult to design experiments that would provide both the performance and the heat transfer data that are needed in order to improve the modeling inherent in the CFD codes. This subject is treated in a little more depth in Section 5.2.

4.2 External Heat Transfer With Film Cooling. As mentioned earlier, turbine inlet temperatures continue to increase, putting pressure on the design community to improve calculation of heat loads for the hot-section components. These increased temperatures can be tolerated because the combustor and turbine components are film cooled. The expected life of the component is critically dependent upon accurate knowledge of film cooling effectiveness and the resulting metal temperature prediction. A relatively small error in metal temperature may result in a significant loss of component life. The ability of the designer to predict heat transfer distributions for film cooled surfaces has not kept pace with the required temperature increases. Thus, the design response has been to bleed more cooling air from the compressor to compensate for these higher temperatures (and thus increased heat loads). Increased compressor bleed air leads to a performance penalty that the compressor designer resists. It is appropriate at this stage of gas turbine development for the turbine designer to cease the practice of increased bleeding and to improve prediction of film cooled heat loads if future performance goals are to be met.

The vane airfoils and endwalls, the blade airfoil, platform, tip, trailing edge, and the stationary shroud for a modern gas turbine engine all get very hot. The engine would have very short life expectancy if it weren't for the thermal protection afforded by film cooling. The quantity of papers appearing over the past 60 years pertaining to heat transfer in the presence of film cooling and the associated film effectiveness is staggering. With some effort, one can find in excess of 2500 references on the subject in the open literature dating back to 1940. There are two abbreviated bibliographies of film cooling research available in the literature that help to direct one to a significant portion of the available literature (Kercher [247,248]). These provide film cooling references from 1971 through 1996 and leading edge film cooling references from 1972 through 1998. The body of information includes experimental and analytical treatments of the problem from a wide sector of the heat transfer community. Large fractions of these publications have their origin in universities and corporate research laboratories with a much smaller number coming from industry. Thus, the primary focus of this literature is on the fundamental aspects of the associated flow physics, on training graduate students, and on developing specific information for a design system. Understanding the fundamental physics is the foundation upon which the design technology must be built so this has been an important undertaking. It is beyond the scope of this paper to review the extensive literature relevant to film cooling and film effectiveness. However, typical examples of some of the university research in this area are as follows: Aachen University, [249–251]; Cambridge University, [252,253]; Clemson University, [254–256]; ETHL, [257,258]; Karlsruhe University, [259–261]; Leeds University, [262,263]; University of Minnesota, [264–267]; MIT, [268,269,2]; Oxford University, [270–272]; Pennsylvania State University, [273–275]; University of Texas, [276,277]; Texas A & M, [278–280]; University of Utah, [281–283]; VPI, [285,284]. Numerous contributions to the literature associated with film cooling and film effectiveness have come from industry and government laboratories. Among these are: ABB, [285,286]; General Electric, [287–289]; MHI, [290]; NASA, [291,238,292]; Rolls Royce, [293]; UTRC and Pratt and Whitney, [294,166], and [127].

To a turbine designer one of the difficulties with the existing knowledge base is that a significant portion is specific to simple flow geometries at flow conditions far from those associated with turbine operating conditions. For example, numerous studies ap-

pear in the literature for isolated holes or a single row of holes (which may be circular or shaped and have various values of L/D). The holes used in these studies may have been inclined to the surface at various angles or have compound angles, be laser drilled or electric discharge machined. The configuration used was likely a flat plate for which the approach Mach number was very low. Using different gases instead of duplicating the respective temperature and pressures of the internal and external flow fields is a technique often used to simulate the density ratio between the external and injected flow. Elovic and Koffel [295] presented detailed discussion of the 1983 state of the art regarding the design of turbine airfoil cooling systems. The authors included in this discussion a summary of current practice for predicting both external and internal heat transfer. A significant portion of the methodology described as standard practice almost eighteen years ago is still in use today.

Earlier in Section 4 the University of Texas boundary layer code TEXSTAN was briefly described, and it was noted that this code has also been used for predictions in the presence of film cooling. The film cooling models of TEXSTAN have evolved since the early version described by Miller and Crawford [296]. The revised film cooling models are derived based on the early work of Tafti and Yavuzkurt [297] and the extensions to that work by Neelakantan and Crawford [298,299]. Those references show extensive validation of the models for flat-plate conditions. For film cooled airfoils, very little validation of the Crawford models has been carried out. Weigand et al. [300] evaluated TEXSTAN and a three-dimensional Navier–Stokes code for predicting heat transfer on a fully film cooled vane for both film cooling effectiveness and heat transfer. They found the boundary layer program provided good agreement with the data, providing the appropriate boundary conditions are used for the velocity loading.

For the past several years there has been an active research program at the Wright Research Laboratory, Aero Propulsion and Power Directorate, for which the structure of film cooling flows have been studied. The flow configuration for the majority of these studies has been a flat plate with a single row of cooling holes. The diagnostic tools have generally been two color, double-pulsed, Particle Image Velocimetry (PIV), and hot-wire anemometer. PIV has been used to characterize the behavior of the film cooling fluid for different values of the blowing ratio, Reynolds number, free-stream turbulence, and unsteady forcing function. Liquid crystals are used in these studies to help with determining the spread of the film coolant on the plate surface. Results of this work are reported in references [301–305].

The research activity described in the previous paragraphs is directed at coolant injection from holes in the stagnation region, on the pressure surface, or on the suction surface of the airfoil. However, the trailing edge is another important region of the airfoil from which coolant is frequently discharged for turbines in general, but especially for power turbines. For the case of a transonic vane, this coolant discharge may influence the shock structure and thus the resulting interaction between the vane and the downstream blade. Several papers have appeared in the literature describing the aerodynamic performance of high-pressure turbines with trailing edge coolant injection. These studies include optimization of trailing edge mixing losses, the flow field downstream of a vane with trailing edge coolant injection, the aerodynamics of trailing-edge cooled vanes, and the influence of trailing edge injection on downstream blade heat transfer. Many other authors have reported the results of studies designed to describe the vane wake-generated flow in the immediate vicinity of the rotating blade in the absence of trailing edge ejection. Among these are [136,306,307], and [308]. The interest in this portion of the paper is in the with-ejection case. For this case Pappu and Schobeiri [309] and Schobeiri [310] present the results of an experimental program and an analysis technique, respectively. These studies were intended to allow discharge of coolant gas from the trailing edge of the airfoil and to minimize downstream mixing losses. These authors show that if the ejection velocity ratio is maintained equal to one, then trailing edge ejection reduces the mixing losses downstream of the airfoil to a minimum. Deckers and Denton [311,312] describe the results of a combined experimental and theoretical and computational effort designed to investigate the aerodynamics associated with trailing edge coolant ejection for a transonic airfoil. As would be anticipated, the ejected coolant makes a significant change in the near wake flow field. Kapteijn et al. [313] reported the results of a study designed to determine the aerodynamic performance of a transonic turbine vane with trailing edge coolant ejection. The authors used two different airfoil configurations. In one case, the coolant was ejected through the trailing edge and in the second case, the coolant was ejected from the pressure surface near the trailing edge. They concluded that ejection from the pressure surface configuration caused higher turning but also greater losses than ejection through the trailing edge. For the case of subsonic external flow, wake mixing for the pressure surface ejection occurred much more quickly than for trailing edge ejection, whereas for supersonic external flow they found no significant difference in wake mixing time. Deckers and Denton [311] find that the ejected coolant causes a significant increase in base pressure and reduction in overall loss. The authors found the surface-pressure distribution to be influenced directly by the base pressure and indirectly because of a changed trailing edge shock system. Interestingly, the authors found that for a specified exit Mach number and coolant ejection pressure ratio, the influence of the coolant stagnation temperature ratio on the resulting base pressure and loss was insignificant. The authors suggest in Deckers and Denton [312] that the relatively thick trailing edge associated with the cooled airfoil with a wide slot can be more efficient than a thin airfoil with a solid trailing edge. The influence of vane trailing edge ejection on blade heat transfer has not been studied in the detail to which base pressure and loss implications have been studied. Dunn [314] reports the results of a study designed to determine the impact of vane trailing edge ejection on the heat transfer distribution of the downstream rotating blade. The particular machine utilized in this work was the full-stage Garrett TFE 731-2 high-pressure turbine with pressure-surface slot ejection. The resulting blade measurements suggested that ejection near the blade stagnation region influenced the measured heat transfer to about 20 percent wetted distance on the suction surface and to about 10 percent wetted distance on the pressure surface. Du et al. [315] performed a similar measurement program, but instead of a rotating turbine they used a rotating spoked wheel to create the vane wakes and coolant gas was ejected from the rotating spoked wheel. Du et al. [316] is a continuation of the studies reported in Du et al. [315]. Du et al. [315] also found that trailing edge ejection increased the heat transfer (on the order of about 20 percent) on both the suction and pressure surfaces of the downstream blade in the stagnation region.

The remainder of this section will be devoted to a brief review of a small fraction of the available film cooling information. Emphasis is placed on those few publications felt to be most aligned with the interest of persons charged with the task of building a turbine cooling design system. The discussion will be confined to the three existing rotating turbine measurement programs that have included cooling gas injection on the rotating blade. In all three cases discussed, the authors have made comparisons of the rotating data with cascade data or flat-plate data. In two of the three cases, the identical blade was run in a cascade experiment so that a one-to-one comparison of the influence of rotation on film effectiveness could be made.

4.2.1 Full-Stage Turbine Film Cooling Experiments. One of the earliest measurement programs conducted for a full-scale turbine with film cooling on the rotor blade is described in Dring et al. [127]. The authors used a large-scale, low-speed, rotating rig for their experiments. Cooling gas was discharged from an isolated single cooling hole at midspan and 10 percent axial chord on

the suction surface and another isolated cooling hole at midspan and 16 percent axial chord on the pressure surface. The coolant to free-stream mass flux ratio was varied from 0.5 to 1.5 and the density ratio was varied from 1.0 to 4.0. Flow visualization and film effectiveness measurements were made for the vicinity of the injection holes. The authors compared their film effectiveness results with data available in the literature that was obtained for flat plates and for airfoils located in cascade flows. They found good agreement between these previous data and the rotating rig data for the suction surface. However, for the rotating rig, they measured very low values of film effectiveness on the pressure surface and found that the agreement between their data and the flat-plate and cascade data for the pressure surface was poor. The authors argue that the reasons for such poor agreement are likely due to the compound orientation of the hole due to measured large radial component of flow on the pressure surface and the surface curvature effects. It was also concluded that for the range of parameters investigated, the trajectory of the coolant gas at each of the two sites was uninfluenced by the coolant-blowing rate or by the coolant to free-stream density ratio.

Takeishi et al. [290] report the results of a study for which the film cooling effectiveness was measured for the same scaled model blades mounted either in a two-dimensional, low-speed stationary cascade or in a high-speed air turbine rotating rig. The specific application was for a stationary power plant turbine. The turbine stage consisted of 32 vanes and 72 blades. Two of the blades were configured so that heated or cooled air or CO_2 could be injected through them. Film cooling effectiveness was determined based on surface temperature measurements and by using gas chromatography to analyze the relative amounts of CO_2 collected at selected locations along the blade surface. The authors used engine hardware, but were not able to reproduce the proper density ratio (density ratio is known to have an influence on film effectiveness) for the operating conditions. However, for the rotating measurements they did match the density ratio used for the cascade experiments. For their rotating experiments, the blowing parameter is varied, and it is demonstrated that film effectiveness decreases with increased blowing because of the coolant gas penetrating the mainstream flow. A comparison between rotating and cascade results is presented for film effectiveness in the leading edge region and on the suction surface. It is shown that in the leading edge region, the film effectiveness data for the rotating blade decay much more rapidly than do the corresponding data for the stationary blade (cascade). It is also shown that for the suction surface, the film effectiveness measured for the rotating blade is about 30 percent less than measured for the stationary blade from $x/d=0$ until $x/d=45$. At about $x/d=45$ lines drawn through the two sets of results intersect. Beyond $x/d=45$ the rotating blade film effectiveness decreases and plateaus out roughly parallel to the cascade data but at a value about 50 percent less than the cascade result. Takeishi et al. [290] were able to obtain only limited rotating blade data for the blade pressure surface because of experimental difficulties, but the results that they did obtain suggested a low level of film effectiveness. They did not obtain sufficient rotating data to make a comparison with the pressure-surface cascade results.

Abhari and Epstein [317] report the results of a film cooling study for which unsteady heat transfer was measured on the rotating blade of a full-scale, single-stage transonic turbine with a stage pressure ratio of about 4:1. The film cooling results obtained in the rotating stage are compared with uncooled results obtained in the same rig for the same turbine and with cooling results obtained using the same blade profile but in a linear cascade facility. Not all of the blades in the rotor were cooled; rather, the instrumented blade and one blade on each side of each instrumented blade was cooled. Each of the cooled blades (for a total of about 15 blades) was configured with three rows of cooling holes on the pressure surface and two rows of holes on the suction surface (total of 93 cooling holes). Heat transfer measurements are made at blade midspan, near the blade tip and near the blade hub so that migration of the coolant flow in both the spanwise and chordwise directions could be monitored. The ratio of coolant flow to main flow was about 6 percent with corresponding blowing ratios in the range of 1 to 1.5 depending upon specific location on the blade surface. Prior to performing the fully cooled experiments, Abhari and Epstein ran a series of measurements in order to be able to differentiate between the vane wakes and the stage cooling effects. For these experiments, the blades were uncooled, but cooling gas was injected from near the trailing edge of the vane row. Cooling gas injection causes the stagnation region heat transfer to decrease significantly, relatively little change was observed for the suction surface, and the pressure surface heat transfer was found to increase. The authors were not able to explain these observations. For the cooled blade measurements, the authors demonstrate that the influence of unsteadiness has a significant influence on the resulting heat transfer distribution. The driver of this unsteadiness is the surface pressure unsteadiness on the blade, which results from wake cutting and shock wave interactions as discussed in Section 2.2.1 (see also Figs. 4 and 5). The coolant flow is correspondingly modulated, especially on the pressure surface of the blade and near the leading edge on the suction side of the blade where the coolant pressure margin (coolant supply pressure/external pressure) is reduced. The model includes the coolant flow exiting the hole that is being acted upon by the external unsteady flow field. They then propose a simple model to obtain an estimate of the cooling effectiveness (based on the work of Goldstein and Haji-Sheik [318]). This model is used in conjunction with the uncooled rotor to obtain an estimate of the cooled rotor heat transfer distribution. When compared with the experimental results, the model shows good agreement. The authors also compare the rotating cooled blade measurements with cascade results obtained with the same blade geometry (see Rigby et al. [141]), but found poor agreement. On the blade suction surface, the rotating cooled blade heat transfer was about 60 percent less than measured in the cascade experiments. Blade data on the pressure surface for the cooled rotating case were not obtained. However, a comparison between uncooled blade pressure-surface data and cooled cascade data were in good agreement. This comparison would suggest that in the cascade experiment, cooling gas injection had no influence on the heat transfer distribution. The results obtained by Dring et al. [127] indicated poor agreement on the blade pressure surface when comparing results for a rotating cooled blade with results obtained for the same blade configuration in a cascade. Dring et al. [127] found reasonably good agreement for the corresponding suction surface.

The authors of all three of the cooling gas rotating rig measurement programs described above compared their rotating blade data with corresponding flat-plate and/or cascade airfoil data. The common theme from all three papers is that the stationary measurements do not represent the rotating fluid dynamics adequately. However, none of the experiments described was performed with vanes or blades using modern film cooling schemes. Thus, there remains a tremendous void of applicable data for such an important design problem as film cooling design. The current experimental capability is such that an experiment using film cooled engine hardware is within reach. However, how to model the experimental results to make them useful to the designer remains a difficult task that is yet to be completed. The subject of modeling of film cooling will be addressed in a little more detail in the following section in an attempt to clarify why this problem exists.

4.2.2 Film Cooling Modeling. It comes as no surprise that the flow field near a cooling hole of a vane or blade is three dimensional. It is also not surprising that the analysis methods designed for two-dimensional flow field calculations would have to be modified in order to account for mixing interactions. Several investigators have attempted to do so in the past, e.g., references [115], [116], [319], [297], [320], and [2]. In Part II of Crawford et al. [116], the authors describe modifications that were made to

STAN5 in order to incorporate into the two-dimensional boundary layer code routines to model injected coolant and turbulence augmentation. Three possible injection models were investigated as part of the study. For low-Mach-number flows, the authors had some success with the various injection models. However, they do caution that for application to the gas turbine blade-cooling environment, the effects of mainstream turbulence, rotation, and curvature are missing from the analysis.

Abhari [2] revisited the data initially reported in Abhari and Epstein [317] for a full-stage, transonic, rotating turbine. The primary intent of this additional effort was to incorporate a steady-state injection model of the film cooling process into the CFD code UNSFLO 2-D. The injection model accounts for the penetration and spreading of the coolant jet as well as entrainment of the boundary-layer fluid by the coolant. Abhari compared the steady-state predictions of his code to the film cooled linear cascade data of Camci [321]. He found that in the immediate vicinity of the hole, the code overpredicted the experimental result, while away from the hole, the agreement was much better. The reason for this overprediction is felt to be due to an improper modeling of boundary layer fluid entertainment by the coolant gas. The time average of the unsteady code calculations and the steady-state prediction with film cooling were compared with the data reported in Abhari and Epstein [317]. At the blade midspan, they had several data points on the suction surface but only a single data point on the pressure surface. On the blade near the hub, they had several data points on both the suction and pressure surfaces. Film cooling has a much more significant influence on the suction-surface heat transfer than it does on the pressure-surface heat transfer. The comparison between the prediction and the experimental result is demonstrated to be good at both blade locations for both the pressure and suction surfaces. Abhari goes on to illustrate quantitatively how the unsteady pressure field on the blade influences the film effectiveness and how the flow rate of the injected coolant is influenced by the local wave systems (either compression or expansions). Substantial reductions in pressure-surface film effectiveness are shown, resulting in the time-average of the unsteady heat transfer predictions being significantly greater (as much as 230 percent) than the steady-state prediction.

As was noted earlier, Abhari and Epstein [317] obtained data at several spanwise locations on the blade of the Rolls Royce ACE turbine in the presence of film cooling. Garg and Abhari [238] used portions of this data set to compare with the results of a three-dimensional steady Navier–Stokes code. The particular code used was a modified version (to incorporate film cooling effects, Garg and Gaugler [322]) of that reported in Arnone et al. [176], which is a steady-state code and does not include an unsteady capability. The CFD code used by Abhari [2] for comparison made for the midspan region with the same data was UNSFLO 2-D, which is capable of doing the unsteady calculation. The calculation performed for the uncooled blade midspan region has been reproduced in Fig. 28.

This figure demonstrates that the results achieved using the three-dimensional Navier–Stokes code were in good agreement with the experimental results for the suction surface. However, the calculation underpredicted the data for the pressure surface by about 30 percent. For comparison purposes, Fig. 19 is the corresponding comparison presented in Abhari et al. [134] that was obtained using UNSFLO 2-D, which shows good agreement between prediction and data for both the pressure and suction surfaces. Garg and Abhari present predictions for three cooled stage cases. The specific cases are as follows: (*a*) case #71, which is a near design point condition, (*b*) case #72, which has a positive incidence angle, and (*c*) case #73, which was run at a lower stage pressure ratio and speed. These three cases make up a good range over which to test the predictive capability of the CFD code. The results of the prediction versus the data for all three cases are

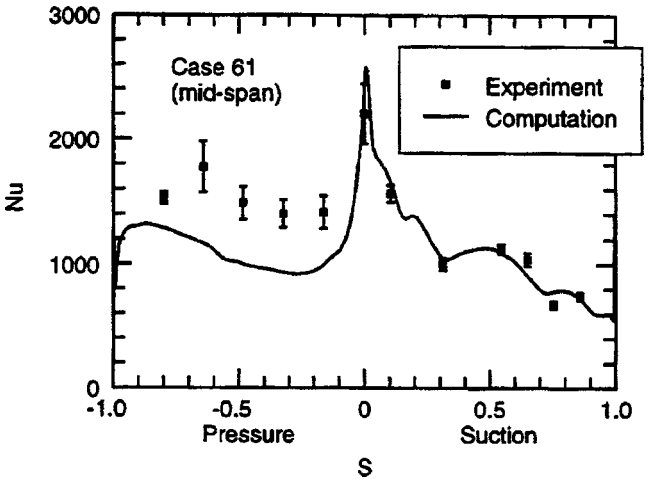

Fig. 28 Predicted versus measured Nusselt number distribution for an uncooled Rolls Royce ACE turbine blade [238]

given in [238]. The results for the design point case taken from [238] are reproduced in Fig. 29 for the blade locations noted as near hub, midspan, and near tip.

The location of the rows of cooling holes on the pressure and suction surfaces of the blade can be seen in Fig. 29. As can be observed by studying these figures and the companion ones presented in [238], the CFD analysis consistently underpredicted the pressure surface experimental results near the hub by a very large amount. However, near the hub on the suction surface, the agreement between the prediction and the data is good. For case #72, the agreement between data and prediction at the midspan suction surface location (there was only a single data point on the pressure surface, which was greatly underpredicted) was reasonably good. The exception to this comment is the data point immediately downstream of the injection holes. However, for cases #71 and #73, the midspan prediction on the suction surface underpredicted the data from 50 percent to more than 100 percent. There were no midspan pressure surface data for cases #71 and #73. For all three cases, their cooled prediction for the location near the tip on the suction surface was in reasonably good agreement with the experimental results. For cases #71 and #72 there was a single pressure surface data point (just downstream of the row of cooling holes) for the near tip location, and the prediction was about 30 percent below the data at that point. Shang et al. [234] note that the turbine used to obtain these measurements has significant three-dimensional effects and that the spanwise heat transfer for the uncooled case may vary by as much as 40 percent (see the discussion in Section 4.1.6). However, Garg and Abhari used a three-dimensional CFD code so these spanwise effects should have been properly accounted for. The authors suggest that the reason for this disagreement between prediction and experiment is most likely due to the neglect of unsteady effects in the Arnone et al. [176] code. This suggestion is supported by a figure presented in Garg and Abhari (reproduced in Fig. 30) for the blade midspan region.

This figure compares predictions versus data using Abhari's two-dimensional unsteady calculation and the results obtained using the three-dimensional steady code. Abhari [2] obtains significantly better agreement with the data than does Garg and Abhari. Later, Garg [323] revisited the same data set using a two-equation turbulence model instead of the Baldwin–Lomax turbulence model used in Garg and Abhari [238]. The choice of turbulence model made little difference in the resulting comparison with the experimental results from what was described earlier in this paragraph. It is important to note that the calculation presented by Garg and Abhari was a state-of-the-art attempt at calculating a

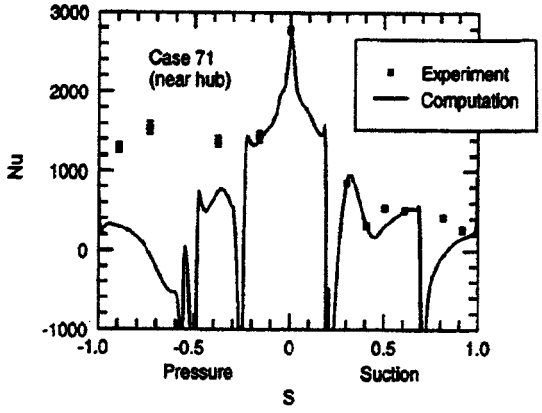

(*a*) Near Hub

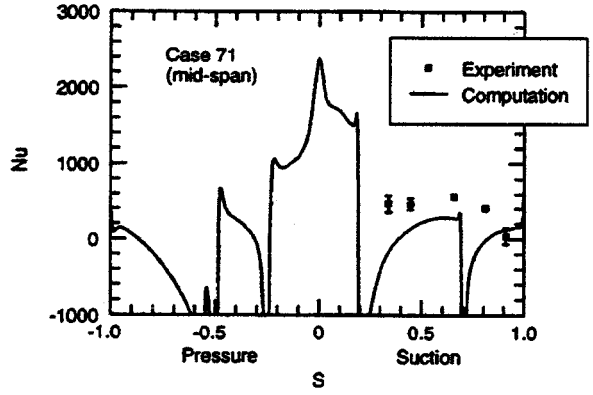

(*b*) Midspan

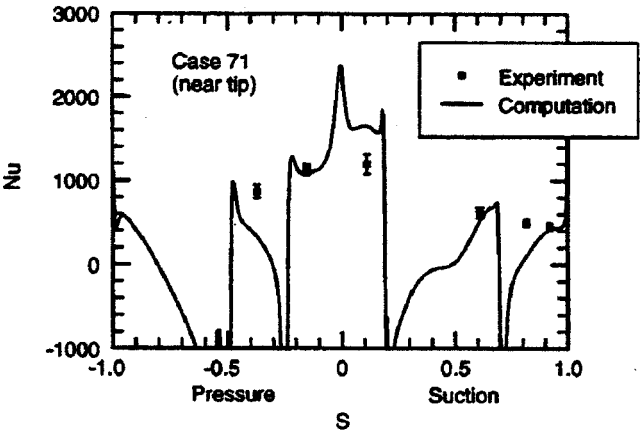

(*c*) Near tip

Fig. 29 Predicted versus measured Nusselt number distribution for a cooled Rolls Royce ACE turbine blade; case #71 [238]

very difficult flow environment. The results obtained are valuable in helping to direct future research efforts in this problem area that is very important to the gas turbine community.

Later, Garg and Gaugler [324] use the same code described in the previous paragraph to study the effect of coolant velocity and temperature distribution at the exit of the hole on the heat transfer coefficient. They compared their predictions to experimental results obtained on three film cooled blades: the C3X vane, the VKI rotor blade, and the ACE rotor blade. The primary difference between this comparison and the one described in the previous paragraph is that neither of the blades (the VKI rotor blade or the ACE rotor blade) was rotating. Further, the C3X vane was also stationary since all three (the C3X, VKI blade, and ACE blade) were in a stationary cascade. The comparison presented by the authors between their predictions and the experimental results were good as illustrated in Fig. 31 for the same rotor blade (but in a stationary rig) as used in the comparisons presented in Fig. 29.

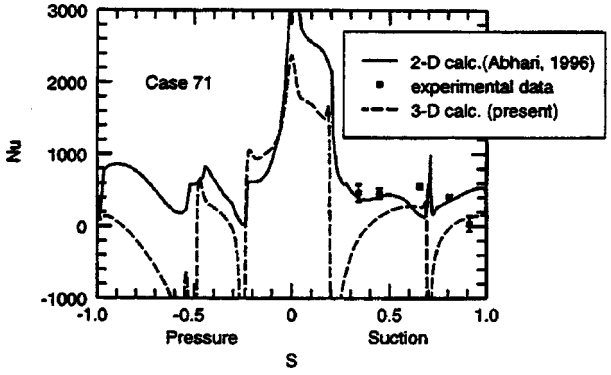

Fig. 30 Two-dimensional and three-dimensional predictions versus measured Nusselt number distribution for cooled blade of Rolls Royce ACE turbine, case #71 [238]

This comparison suggests that there may be a major difference between the fluid dynamics of film cooling in a rotating environment and film cooling in the stationary cascade and this difference may not be captured in the CFD code. It is important to clarify the source of the difficulty before one can be comfortable using the technique in an engine film cooling design system.

As part of an ongoing experimental measurement program at The Ohio State University Gas Turbine Laboratory (OSU GTL) that is being performed in cooperation with ETH Zurich, a Honeywell high-pressure turbine stage is being instrumented. As part of this research program, both the entire vane row and the entire blade row are film cooled. The vanes and blades are instrumented with surface-pressure transducers, thermocouples, and heat-flux gages. This instrumentation task is underway in preparation for a fully cooled measurement program. The measurements are to be conducted for an engine stage operating at design corrected conditions. More detail of this experiment will be provided in Section 5 of this paper. Garg [292] has presented a prediction of both the surface heat transfer and the surface pressure for the blade of the turbine for both the uncooled and the cooled upcoming OSU GTL experiments. The author is commended for publishing his predictions well in advance of the time that the experiments are to be performed. When the experimental results become available, his comparison with data truly will represent a prediction. In his cal-

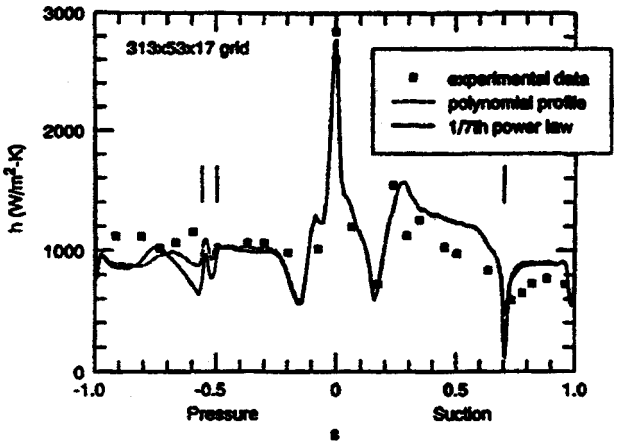

Fig. 31 Predicted versus measured heat transfer coefficient for cooled blade of Rolls Royce ACE turbine [324]

culation, Garg treats only the blade and not the vane. Thus, he has not included in his analysis the influence of the coolant flow from the upstream vane row on the downstream blade. Also not included is the cooling emanating from the coolant holes in the recessed tip of the blade or from the blade trailing edge. The CFD code used by Garg for this prediction is the NASA Glenn Research Center Multi-Block Navier–Stokes Convective Heat Transfer code, LeRC-HT (which was previously known as TRAF3D.MB; see Steinthorsson et al. [325,326]). This code is a steady state code and does not include the unsteady effects on the blade resulting from wake cutting or shock wave structure. Thus, neither the cooled upstream vane nor the unsteady effects are included in the prediction presented by Garg [292]. Abhari [2] argues the importance of considering the coolant flow coming from the upstream vane as well as the unsteady flow associated with wake cutting and shock wave structure for predicting the heat transfer distribution on the cooled blade. The reason given in Garg and Abhari [238] for having poor agreement between prediction and the experiments of Abhari was the absence of unsteady effects in the CFD code used for the analysis.

4.3 Influence of Free-Stream Turbulence and Boundary Layer Transition on Heat Transfer. Over the past twenty years, the subjects of free-stream turbulence, boundary layer transition, and film cooling have received an enormous amount of attention in the gas turbine heat transfer literature. A detailed review of this literature is far beyond the scope of this paper, but selected references containing ample direction to the relevant literature are noted for the interested reader. Free-stream turbulence has its origin in the combustor section of the engine. Two of the more important pieces of information still unknown about free-stream turbulence are the intensity and the scale. These are, unfortunately, two of the more important parameters needed when performing hot-section heat transfer predictions. The fact that definitive experimental data for the turbulence intensity, turbulent scale, etc., are not generally available for an engine combustor is not because researchers have stood idle, but rather because obtaining the relevant information is a very difficult task. In this regard, numerous authors have described the results of studies designed to determine the influence of free-stream turbulence on stagnation region heat transfer or heat transfer to uncooled turbine vanes. Among these are references [234,327–339]. Shang et al. [234] describe the results of a measurement program utilizing a full-stage uncooled rotating turbine for which the free-stream turbulence was varied over the range of 0.5 to 8 percent. The resulting heat transfer level and distribution on the rotating blade were uninfluenced by the magnitude of the free-stream turbulence. The authors do not present the corresponding uncooled vane data for these turbulence variations. It is very likely that the vane heat transfer would have been influenced by the level of turbulence if they were to measure the distribution (in the absence of leading-edge film cooling injection) without and with significant free-stream turbulence. In the presence of vane leading edge film cooling, the influence of free-stream turbulence would likely be significantly less. In the work reported by Ames, the influence of large-scale (energy scale on the order of 0.5 to 2 times the vane leading-edge diameter) high-intensity turbulence was investigated. Moss and Oldfield [340] and Dullenkopf and Mayle [341] were specifically interested in the question regarding the influence of turbulence length on heat transfer. Moss and Oldfield [340] found that for a given free-stream turbulence intensity, length scale has an important influence (enhancement factors of up to 40 percent) on the measured heat transfer. Burd and Simon [342] investigated the question of local turbulence addition near the vane cooling hole injection site because of injected coolant gas. The authors investigated hole L/D and coolant supply flow orientations, and concluded that length scale is relatively unaffected by the hole length, but dissipation appears to be greater for short holes.

The state of the boundary layer on the vane and blade of the turbine stage is important to the turbine designer because of heat transfer, aerodynamic loss, and component life considerations. From the first-stage vane on through the machine, other parameters influencing the boundary layer development are wake effects, shock waves, and coolant injection. Mayle and Dullenkopf [125,126] presented their turbulent-strip theory for transition from laminar to turbulent boundary layer for the turbomachinery case of unsteady, periodic turbulent wakes. In the 1991 IGTI Scholar Lecture, Mayle [124] presented a discussion of the role of laminar–turbulent transition in gas turbine engines from the viewpoint of the engine designer. This discussion included the different kinds of transition, e.g., natural transition (Tollmien–Schlichting), bypass transition (where creation and amplification of Tollmien–Schlichting waves is bypassed), separated-flow transition, periodic-unsteady transition, and reverse transition, and their respective importance in the gas turbine application. At the following IGTI meeting, Walker [343] revisited the topic and explained some differences of philosophy between his view and that of Mayle. Mayle [124] notes in his paper that in the case of turbomachinery applications, the boundary layer is often in a transitional state. Addison and Hodson [344] describe a model for transitional boundary layers that can be used to estimate profile loss in turbines. Ameri and Arnone [345] demonstrated the influence of transitional boundary layer modeling on predicted heat transfer distributions for a rotating blade. They compared their predictions to the data of Blair [346], which was obtained in the UTRC large, low-speed, rotating rig. Later, Halstead et al. [347] published a comprehensive four-part experimental and computational paper dealing with boundary layer development in axial compressors and low-pressure turbines. Boundary layer transition in the compressor and in the low-pressure turbine is similar in many ways. Much of the analytical work relating to boundary layer transition in the turbine has origin in the turbulent spot theory of Emmons [348]. The discussion presented here is intended to be of help to the turbine designer, so it is important to differentiate film cooled turbines from internally cooled turbines, high-pressure turbines from low-pressure turbines, and big turbines from little turbines. Transition in all of these machines is influenced by the unsteadiness of the flow, the magnitude and scale of the free-stream turbulence, and by the local Reynolds number. The Reynolds number (based on vane axial chord for example) for comparable components is obviously much greater in big engines than in small engines.

Tiedemann and Kost [349] present the results of a study conducted for the midspan region of a rotating blade using a full-stage turbine in the DLR Gottingen facilities. The authors demonstrate the simultaneous existence of two of the transition modes described by Mayle [124], bypass transition and separated-flow transition. The authors used a hot-film technique to deduce the local state of the boundary layer on the rotating blade. Volino and Simon [350] have combined several different data sets in an attempt to characterize the influence of free-stream turbulence, acceleration, and wall curvature on bypass transition. All of the data used in the Volino and Simon [350] study were taken from nonrotating configurations. Clark [351] demonstrated that the influence of Mach number on turbulent spot parameters is significant at much lower Mach numbers than previously thought. Boyle and Simon [352] incorporated the data of Clark [351] into the turbulent spot production models of Simon [353] and Solomon et al. [354] in order to investigate the effect of Mach number on transition length. However, in their study, Boyle and Simon [352] only compared their predicted results against isolated blade row experimental data. Thus, the periodic unsteadiness that is inevitably associated with gas turbines was not included in the analysis.

4.3.1 High-Pressure Turbine Stage. As noted in the previous paragraph, for the modern propulsion gas turbine engine, the flow entering the vane row of the high-pressure turbine has a high degree of free-stream turbulence along with embedded hot streaks (Section 4.1.6). The vane is normally configured with showerhead cooling in the leading edge region. Along the vane suction sur-

face, one will find two or three rows of spanwise cooling holes. The pressure surface will have three or four rows of film cooling holes, slot injection near the trailing edge, and distributed injection holes on both the inner and outer endwalls. The downstream blade will also have several spanwise rows of leading edge showerhead cooling holes. These blades will have one or two spanwise rows of cooling holes on the suction surface, three or four rows on the pressure surface, and trailing-edge slots across the span. The blade may also have distributed injection holes in the tip region, and injection holes on the platform. For this configuration, it is generally accepted (Mayle [124]) that transition is not a consideration. The high level of free-stream turbulence along with injected gas from the showerhead will trip the boundary layer in the immediate stagnation region of the vane. The combination of cold gas injection, wake cutting, and shock waves will trip the boundary layer close to the stagnation region on the blade. The tendency of the turbine designer is to be conservative and to assume the boundary layer to be turbulent over the airfoil. Two earlier studies of the influence of free-stream turbulence on boundary layer transition for the gas turbine application are those of Blair [175] and Hodson [137]. In contrast to the case of a propulsion gas turbine, the situation of a stationary power plant gas turbine may be somewhat different. The stationary power plant high-pressure turbine vane may have an incoming high free-stream turbulent flow with hot spots, but the vane and the blade of this turbine may be internally cooled, instead of having film cooling injection. It is often true that the combustor internal cooling configuration and exit temperature profile for a stationary gas turbine are significantly different from those for a propulsion engine, but hot streaks and turbulence still exist. With this scenario, the boundary layer transition question for the vane may be different from the situation just described for the propulsion turbine. The blade of this uncooled turbine is still subjected to the strong periodic-unsteady influences because of wake cutting and shocks so transition occurs near the leading edge of the airfoil. Some of the more recent power turbines do have film cooling and thus the same considerations described earlier for the propulsion turbines are applicable.

Figures 23–31 described earlier in Section 4.1.3 present vane and blade heat transfer data versus prediction for five different (Garrett TFE 731-2, Teledyne 702, Rolls Royce ACE, Allison VBI, and General Electric) uncooled high-pressure turbine stages. The TFE 731-2, the Teledyne 702, and the General Electric turbines all had subsonic vane exit Mach numbers while the Rolls Royce ACE and the Allison VBI turbines had transonic vane exit Mach numbers. Rivir et al. [355] used two separate techniques to measure the free-stream turbulence for the experiment noted above that utilized the Garrett TFE 731-2 turbine and found it to be on the order of 5.5 to 6 percent. Essentially the same experimental configuration was used for the Teledyne 702, Allison VBI, and General Electric turbines. Thus, one might anticipate that the free-stream turbulence intensity immediately upstream of the vane entrance was of the same order of magnitude as measured by Rivir et al. [355]. In all five cases reported in Figs. 23–31, the turbines are operating at the proper stage pressure ratio and at design corrected conditions. With the exception of the Rolls Royce ACE turbine, both vane and blade heat transfer data are presented. For the four vane comparisons and the five blade comparisons presented, the agreement between data and prediction is good. The vane predictions shown were performed assuming the boundary layer to be fully turbulent on the pressure surface, but forcing transition to occur on the suction surface at about 20 percent wetted distance. For the blade comparisons presented, the boundary layer was assumed fully turbulent on both the pressure and suction surfaces for all five turbines. Vane and blade calculations were performed assuming the boundary layer to be fully laminar, but the resulting predictions were so far below the experimental results that they are not shown on these figures.

Film cooling and the associated film effectiveness are very important considerations in the high-pressure turbine. The previously published studies for rotating turbines that included film cooling on the blade all had relatively low incoming free-stream turbulence at the high-pressure turbine vane. These include Dring et al. [127], Takeishi et al. [290], and Abhari and Epstein [317]. Of these, Takeishi et al. [290] had the highest free-stream turbulence level, 4 percent. None of the references noted in the discussion of free-stream turbulence in Section 4.3 considered the important question relating to the potential impact that free-stream turbulence might have on the film effectiveness. To do so requires that the turbulent free-stream be superimposed on the film cooled surface. Intuition (always dangerous in gas turbine flows) suggests that free-stream turbulence may be a hindrance or a help depending upon the relative magnitudes of some of the parameters involved. Some of these parameters are turbulence intensity, blowing ratio, coolant to free-stream gas density ratio, etc. Many years ago, Kadotani and Goldstein [356] looked at this problem for a low-speed, flat-plate flow, with a single row of inclined cooling holes. They conclude that the parameters most influencing the film effectiveness are the free-stream turbulence intensity, the length scale to boundary layer thickness at the injection site, the ratio of length scale to injection hole diameter, and the blowing ratio. More recently, Bons et al. [357] presented the results of an experimental investigation for flow conditions (low speed) and geometry (flat plate, single row of cooling holes) similar to those used by Kadotani and Goldstein [356]. However, Bons et al. [357] were not able to vary the turbulent length scale independently. The parameters that they could vary effectively were free-stream turbulence intensity and blowing ratio. The results demonstrate that the relative magnitudes of the free-stream turbulence and blowing ratio have a profound influence on the overall film cooling effectiveness (e.g., directly behind the hole, in between the holes, and far downstream of the hole). Increasing free-stream turbulence is shown to significantly reduce the effectiveness immediately downstream of the hole for low to moderate blowing ratios. By contrast, increasing free-stream turbulence intensity for higher blowing ratios results in improved effectiveness at locations downstream of the injection site. In another study, Bons et al. [358] investigated the influence of unsteadiness on film cooling effectiveness for a flat-plate configuration. Film cooling effectiveness was determined downstream of a single row of cooling holes. For these measurements, the film cooling flow was modulated as opposed to the external flow being modulated (which would be the normal environment for the blade leading edge). The results of this study suggested significant reduction in the film cooling effectiveness because of the unsteadiness. Drost and Bolcs [359] investigated cooling effectiveness for two different free-stream turbulence levels using a cooled turbine airfoil having eight rows of holes in the stagnation region, on the suction surface, and on the pressure surface. The airfoil was located in a cascade environment. From the cooling configuration sketched in the paper, it appears that the bulk of the cooling gas was directed toward the suction surface. The results suggested significant cooling effectiveness on the suction surface, but low cooling effectiveness on the pressure surface.

The high-pressure turbine vane endwalls are also regions that must be film cooled for modern turbines, and film effectiveness is of importance. One of the early works treating endwall film cooling is that of Blair [166]. Secondary flow effects were found to have a significant influence by decreasing film effectiveness on the early portion of the endwall. Others have also investigated the cooling effectiveness for injection on the vane endwall, e.g., Takeishi et al. [360], Granser and Schulenberg [361], and Friedrichs et al. [362].

Mehendale et al. [363], Funazaki et al. [364], Heidmann [291], and Du et al. [365] are among a large group of researchers who have investigated the influence of unsteady wakes on film effectiveness. All of these authors simulated the wakes via a series of rotating bars (described by Doorly and Oldfield [140]). They also all arrive at about the same conclusions, which are that film cool-

ing effectiveness is significantly reduced by the presence of the wakes, which should come as no surprise. They further conclude that increasing the blowing ratio increases film effectiveness until the blowing ratio gets so large as to allow entrainment of the hot external gas. Both Funazaki et al. [364] and Ekkad et al. [280] superimposed free-stream turbulence on the wake disturbance. In the case of Ekkad et al. [280], a medium (16.4 percent) to a strong (21 percent) free-stream turbulence superimposed on the unsteady wakes caused further degradation in film effectiveness beyond that observed for the wakes alone. By contrast, superimposing an unsteady wake on a strong free-stream turbulence (21 percent) caused little reduction in film effectiveness, which is probably not surprising.

Beyond what has been presented above, it is not productive to continue the discussion of film cooling and film effectiveness studies for high-pressure turbines. As indicated at the beginning of the previous paragraph, there are precious few applicable data sets with which to obtain insight. Further, for all three rotating turbine data sets that have been discussed, the comparisons made with cascade results suggested that rotational effects (secondary flows), wakes, and shock waves couldn't be neglected in either the experiments or the analysis. This point will be addressed in more detail in Section 5.

4.3.2 Low-Pressure Turbine Stage. There are increasing demands imposed upon a modern low-pressure turbine to generate as much power as possible to drive larger fans at lower speed without adding weight, cost, or complexity to the engine. This increase in power extraction being asked of a component that already operates with efficiency in excess of 90 percent puts great demands on the technology. The low-pressure turbine must operate efficiently over a large range of Reynolds numbers consistent with the take-off condition (on the order of 1,000,000) to the high-altitude cruise condition (on the order of 25,000). There have been several papers in the literature dealing with heat transfer in the low-pressure turbine section of the engine. Among these are [366,367], and [368]. Heat transfer is not the primary area of concern in this section of the machine. Much of the research effort has been concentrated in bodies of research that can broadly be described as transition studies. These studies are generally performed for relatively low values of inlet turbulence intensity for which transition to turbulent boundary layer can be helpful in preventing laminar separation (and thus loss in stage efficiency). Airfoil configuration studies are often designed to reduce the solidity of the LPT while not destroying the efficiency of the component, and controlling separation in the low-pressure turbine by use of passive or active vortex generators. Several groups have made major contributions to the research efforts associated with the low-pressure turbine. Among them, four account for a significant amount of the reported research results. These are groups led by Hodson at Cambridge University, Hourmouziadis at MTU, Wisler, Halstead, and Solomon at General Electric Aircraft Engines, and Rivir at Wright Laboratory.

One of the largest uncertainties associated with the LPT is the magnitude of the free-stream turbulence entering the individual blade rows. The magnitude of turbulence intensity and the way that the turbulence intensity changes as one progresses through the machine is a consideration in the low-pressure turbine. Related discussions are presented in [369,367,370], and [371]. Binder et al. [369] used hot films to measure the turbulence intensity in a low-pressure turbine. Significant spanwise variations in turbulence intensity were measured in the early stages of the five-stage machine varying from a high value of near 12 percent near the hub to near 6 percent at midspan to about 10 percent near the tip. At later stages of the turbine, the spanwise variation of turbulence intensity disappeared and the level across the airfoil was reduced to a value of about 5 percent or less. The 5 to 6 percent turbulence intensity number near midspan is consistent with the measurements of Halstead et al. [347]. In their study, Binder et al. [369] were able to determine within the various stages the presence or absence of profile separation. They concluded that separation is initiated when the upstream rotor wake enters the blade passage near the leading edge, preferably on the pressure surface. Separation occurred in only one of thee rotors, but the reasons for this observation are not clear. Most rig measurement programs will quote numbers in the 5 to 10 percent range, but the engine measurements reported by Sharma [372] indicated wake turbulence intensities in the range of 16 to 23 percent. The difference in the rig versus engine free-stream turbulence levels is large and potentially very important to the transfer of information from the laboratory to the design.

The experimental results described in numerous studies are related to the questions of boundary layer transition, reduction of solidity, losses, and boundary-layer separation control. Among these are references [347,373–382] helpful to the designer in answering the demands of the industry. There are several obvious advantages to being able to reduce separation on the airfoils and the resulting performance penalty just as there are advantages to reducing LPT solidity without reducing performance. If solidity can be reduced, then engine weight is reduced with an accompanying reduction in parts count, and thus increased thrust to weight of the engine. The question that remains to be answered is by how much can solidity be reduced without adverse effects. Wisler [383] notes that an experimental program was conducted using the GE Low-Speed Research Turbine in which the blade count of both the rotor and the nozzle were simultaneously reduced by 20 percent. At the increased levels of inlet turbulence intensity tested, the performance of this reduced solidity turbine was not measurably different from that of the baseline in either pressure coefficient or efficiency. The baseline turbine was designed using standard design practice. Howell et al. [384] and Rivir et al. [380] suggest that a solidity reduction more on the order of 34 percent is possible. It is important to note that with the reduced solidity, the blade loading and the potential mechanical problems increase and thus must be properly included in the design process.

Boundary layer transition and turbulence are both of importance in the low-pressure turbine. Two locations within a modern turbine engine where boundary layer transition is important are the compressor and the low-pressure turbine. The IGTI Scholar paper of Mayle [124] and the four-part paper of Halstead et al. [347] both treated the problem of transition in the low-pressure turbine and the compressor. Compressors utilize aerodynamic diffusion to achieve significant pressure increases, but along with this come adverse pressure gradients and the associated tendency for boundary layer separation. By contrast, the low-pressure turbine extracts work from the flow by expanding the gas stream. The designer takes advantage of this expansion and stable boundary layer on the blade suction surface for as long a distance along the airfoil as is possible. However, at some point there is a diffusion region and one has what Sharma et al. [385] refer to as the ''aft-loaded airfoil.'' Hourmouziadis [386] has pointed out that these airfoils operate very well at high-Reynolds-number conditions. However, when the Reynolds number falls, as it does at cruise altitude, then flow separation in the diffusing region can occur. Reattachment may not take place, resulting in increased loss and reduced aerodynamic performance, if the Reynolds number becomes too low or the pressure gradient too high.

The detailed experimental results presented in Halstead et al. [347] provide significant insight into the transition process on the low-pressure turbine vane and blade for Reynolds numbers consistent with both take off and cruise operation. The authors used a two-stage, low-speed, low-pressure turbine with the vanes and blades instrumented with hot films in order to deduce detailed boundary layer information. In Part 3 of their four-part paper, the authors demonstrate that the boundary layer over a significant portion of the airfoil suction surface is either laminar or transitional. The Reynolds number, the free-stream turbulence intensity, and the airfoil pressure loading determine the particular location of transition. Halstead et al. [347] properly duplicated the Rey-

nolds number and the airfoil pressure loading. However, they were concerned that because there is neither a combustor nor a high-pressure turbine upstream of the low-pressure turbine, they may not have the proper free-stream turbulence intensity and scale convected through to the low-pressure stage. The measured level of free-stream turbulence was 4.6 percent in the wake, and numbers ranging from 1.7 to 3.4 percent in between the wakes. Concerned about the level of free-stream turbulence, they removed a rotor airfoil and introduced a rod to generate high free-stream turbulence intensity (on the order of 16 percent) and found dramatic influences on their results. The authors cautioned that care must be taken when using rods to simulate airfoil wake turbulence intensity to assure oneself that the bar is producing a representative wake of a lifting airfoil. As part of their investigation, the authors also found that clocking of the turbine vanes has a significant influence on boundary layer development and loss at the midspan location. The measurements demonstrated that transition occurred near the leading edge (in the region of adverse pressure gradient) on the pressure surface of the airfoil when the blade was operating at design incidence angle. In the case of negative incidence angle, separated flow transition occurred at the leading edge, followed shortly by turbulent reattachment, while for positive incidence, wake-induced strips and regions of transitional and turbulent flow were found between wakes.

Solomon et al. [354] have proposed a model for estimating intermittence (a measure of the degree to which the flow is turbulent, being equal to zero for laminar flow and one for turbulent flow). This model can be used to predict the region of transitional flow for flow conditions similar to those experienced on the suction surface of low-pressure turbine airfoils. These authors have used their own experimental data along with that of many other authors in order to arrive at a generalized model that is demonstrated to be effective in predicting the transitional flow length for typical low-pressure turbine airfoils. More recently, Solomon [378] has investigated boundary layer development for two new blade configurations having identical design vector diagrams but substantially different loading levels. Earlier, Curtis et al. [387] and Cobley et al. [388] demonstrated use of a high lift blade, which could be used to take advantage of the effect of wake passing described by Schulte and Hodson [375]. Solomon [378] performed measurements for several combinations of blade profile and free-stream turbulence level. The primary goal of this research was to investigate ways in which the solidity could be reduced without decreasing performance. The results demonstrate that the large regions of laminar and transitional flow present on the blade suction surface at low inlet turbulence are also present when the inlet turbulence is increased to high levels. It was also found that the onset of transition for the high-lift profile is much less sensitive to inlet turbulence level than is the conventional profile. Solomon [378] clocked the second vane relative to the first and found that in certain orientations it was possible to nearly eliminate periodic transition effects, which results in more turbulent flow on the blade and increased loss.

Qiu and Simon [389] have investigated the influence of free-stream turbulence intensity and Reynolds number on boundary-layer transition and flow separation for low-pressure turbine blades using a cascade facility, but in the absence of unsteady wakes. The authors present detailed velocity profiles and intermittency distributions measured in the airfoil boundary layer for the different turbulent intensities and Reynolds numbers. Murawski et al. [377] reports the results of a low-Reynolds-number, linear cascade study of unsteady aerodynamics associated with a low-pressure turbine blade. This study is similar to that reported in Qiu and Simon in that there are no unsteady wakes present in the experimental configuration, but rather emphasis is placed on Reynolds number and free-stream turbulence intensity influences. Boundary-layer separation was experienced for all combinations of Reynolds number and turbulence intensity for which measurements were performed. Schulte and Hodson [375] performed a similar measurement program, but they used a series of upstream rotating bars to simulate the unsteady wakes. The authors make careful note of the experience of using rotating bars to generate free-stream turbulence that is described by Halstead et al., but argue that they have specifically designed their bar system to produce the desired turbulence intensity. The conclusion of the Schulte and Hodson work was that the suction surface boundary layer was dominated by the unsteady wakes. These authors also found that there is an optimum wake-passing frequency and that for this case the profile loss is nearly independent of Reynolds number. This result suggests the possibility of designing a highly loaded low-pressure turbine without having large profile losses at the low Reynolds numbers associated with the cruise operating condition.

The group at Wright Laboratory has been investigating the use of dimples, **V**-grooves, and passive and active air jets as means for reducing boundary-layer separation losses in the low-pressure turbine. Rivir et al. [380] and Lake et al. [382] describe the results of measurement programs for which dimples and steady and pulsed 90 deg skew injection are used as effective vortex generators. These techniques have been shown to reduce total losses significantly (by about 40 percent) for a low-pressure turbine airfoil operating at low Reynolds number. Most of the experiments described in this paragraph were conducted using a nine airfoil cascade housed in an open-loop induction wind tunnel and generally highly aft loaded airfoils were used. The authors demonstrate use of both steady jets and pulsed jets as vortex generators. The dimples and the jets were located on the airfoil near the natural separation point instead of near the leading edge that would be more common. However, the authors show that it is not necessary to know the separation point in order to achieve significant loss reduction with the proposed techniques. Additional work with use of passive jets and dimples to create steady vortex flow for control of boundary layer separation on the suction side of the low-pressure turbine blade noted earlier in the paragraph is discussed in [390]. Rivir et al. [380] reports the results of a similar study except that for these measurements both dimples active control (pulsed vortex generator jets) are used for control of boundary-layer separation. Bons et al. [381] describe the results of a similar measurement program, but use only active control in the absence of dimples. The results of all of these studies are consistent in that they report significant (on the order of 40 percent) reductions in total loss.

4.3.3 Influence of Surface Roughness on Aeroperformance and Heat Transfer. It is well known that propulsion, stationary power plant, and marine gas turbines experience corrosion, deposition, and pitting of the vanes and blades of the high-pressure turbine. This surface degradation results in decreased aerodynamic performance of the machine and increased heat transfer (and thus reduced life) for the component. For the film cooled vane, the surface degradation can have a significant influence on film cooling effectiveness because of the way in which deposited foreign material influences the geometry of the cooling hole. For the uncooled vane, surface roughness can have a significant influence of the location of boundary layer transition on the suction surface and thus on the heat transfer load to the surface. Deposition of foreign material on the blade is generally less of a problem than for the vane. Because of wake cutting and shock waves, the boundary layer is already mostly turbulent. However, corrosion and pitting can impact the leading-edge cooling holes, and thus the film cooling effectiveness.

The influence of blade surface roughness on aerodynamic performance and heat transfer has been investigated for the Rocketdyne Space Shuttle Main Engine (SSME) fuel side turbopump using the full-stage rotating turbine by several authors. Among them are references [391], [392], [393], [394], [27], [395], and [396]. This is a relatively good example to discuss because all of the papers just noted were attempting to deal with essentially the same hardware. However, the experiments were done using dif-

ferent facilities and experimental techniques while the analysis portions of the work ties the parts together. The first-stage turbine blade of the Rocketdyne two-stage machine was initially intended to have a thermal barrier coating (TBC) deposited on the surface. After the primer coat was deposited, a decision was made not to add the TBC and thus the way the turbine went into service was with a first-stage rough surface blade. Boynton et al. [395] measured the aeroperformance of the turbine with the rough first-stage blades, and then with those rough blades polished to a smooth condition, and found nearly a two percentage point difference in performance. For comparison purposes, the Reynolds number based on blade axial chord and rotor exit conditions for the aeroperformance experiments of Boynton was about $8.9\times10^{5.}$ This value of Reynolds number is about 2.3 times greater than the highest Reynolds number used by Dunn et al. [27] and about 1.5 times greater than the Reynolds number used in the experiments of Blair [394]. Boyle [396] used a Navier–Stokes analysis to investigate in depth the experimental results of Boynton et al. [395], which include both the influence of roughness and the influence of incidence angle on performance. The Navier–Stokes analysis was used because of the potential for separated flow to occur over the range of incidence angles used in the experiment. Boyle found that the predicted influence of incidence angle on performance was in reasonable agreement with other predictions and in agreement with the trend in the experimental results. The roughness model incorporated into the analysis of Boyle was that of Cebeci and Chang [397]. Boyle found that the estimate of the influence of roughness on performance was sensitive to the value selected for the damping parameter. The damping parameter that worked well for predicting performance didn't necessarily work as well for predicting heat transfer. Dunn et al. [27] used the same turbine configuration as Boynton et al. [395] and measured the heat transfer distribution to the first-stage vane, first-stage rough blade, and second-stage vane. The surface roughness for the first-stage blade was measured to be 15 μm rms for a blade with an axial chord of about 0.018 m. The experiments were run for two Reynolds numbers based on vane chord and vane inlet conditions, 1.4×10^5 and 2.5×10^5. For comparison with the results of Blair and Anderson [391] and Blair [394], the corresponding Reynolds numbers based on blade chord and rotor exit conditions are 2.1×10^5 and 3.8×10^5. The technique described by Boyle and Civinskas [392] was used to analyze the data for the rough blade. In their analysis, the authors concluded that the effect of the roughness on the heat transfer is a function of Reynolds number and the effective roughness height, which in turn is a strong function of the roughness and the density. For this particular blade, profilometer scans demonstrated that the peaks of roughness are not very close to each other. Although to the human eye the blade appeared to be very rough, the analysis suggested that it was not, and the experimental results confirmed this conclusion. Blair [394] performed an analogous experimental program for this same engine configuration, but in a large-scale 1-1/2 stage rotating rig. The blade used by Blair [394] was much larger than the engine hardware (which was used by Boynton et al. [395] and Dunn et al. [27]) so the roughness was scaled up accordingly from 15 to 660 μm. In addition, Blair [394] ran his measurements at higher Reynolds numbers based on blade axial chord and rotor exit conditions (4.2 to 5.8×10^5) than Dunn et al. [27]. The engine hardware rotor used in the experiments of Dunn et al. [27] was aft loaded and had a greater solidity than the rotor that Blair [394] used, which would tend to make that rotor less sensitive to roughness. Blair [394] found a significant increase in the heat transfer for the rough blade at the higher Reynolds number. Boyle and Civinskas [392] analyzed the data of both Blair and Anderson [391] and Dunn et al. [27]. They achieved good comparison between the experimental results and their predictions for both experimental data sets. The profilometer measurements taken (by Blair at United Technology Research Center) for the actual engine hardware blade used by Dunn et al. [27] gave an equivalent height ratio of 0.3. At the same Reynolds number, the roughness for the blade used by Blair and Anderson [391] would be about 15 times greater. It is believed that the reason for this significant difference in equivalent roughness height ratio is that Blair and Anderson [391] were attempting to match the k–plus value for the SSME engine Reynolds number condition. Boyle concluded that the much larger Reynolds number associated with the actual engine condition could explain the significantly increased heat transfer observed by Blair.

Numerous other authors have investigated the influence of surface roughness on vane heat transfer and or losses. These include references [163,398–409] Guo et al. [403] incorporated a roughness model into a CFD code commonly used at Rolls Royce in order to obtain comparisons with experimental results for hydraulically smooth and transitionally rough surfaces. The roughness modeling used by Guo et al. [403] is similar to that described by Boyle and Civinskas [392]. A comparison between prediction and data is presented in Fig. 7 of Guo et al. [403] for a roughened vane. This comparison illustrates that from the stagnation region to about 60 percent of the pressure surface the prediction underestimates the rough surface data by about 60 to 70 percent. However, at about 85 percent of the surface, the prediction and data are equal (mainly because the two results have very different slopes). For the suction surface from the stagnation region to about 30 percent of the surface distance, the prediction overestimates the data by about 30 percent, but beyond 40 percent of the surface distance, the data exceed the prediction by about 10 percent. To model stochastic surface roughness in the University of Texas code TEXSTAN, the discrete roughness model reported in Taylor et al. [410] and its modification for heat transfer by Tarada [411] have been incorporated into the research version of TEXSTAN. Tolpadi and Crawford [407] used this model to predict the suction and pressure side heat transfer data of airfoils (Abuaf et al. [406]) at four Reynolds numbers and high free-stream turbulence. The roughness elements were simulated using full-height right-circular cones, with parameters of the elements being matched to the airfoil's roughness statistical profile measurements. Both the heat transfer level and transition locations were in good agreement for all but the lowest of the Reynolds number cases.

References [398], [400], [404], and [412] are among the few to address the question of how surface roughness influences film cooling effectiveness. Of these four the two probably most relevant to turbine conditions is that of Schmidt et al. [404] and Weigand et al. [412]. Schmidt et al. [404] used a flat-plate configuration with two different values of roughness (differing by a factor of two) that the authors describe to be representative of an in-service airfoil. The authors conclude that surface roughness does not cause any significant loss in film cooling effectiveness, but it does result in significant loss in film cooling performance because of increased heat transfer rates due to the roughness. However, it appears that this conclusion would be dependent upon both the specific Reynolds number and the equivalent roughness–height ratio as discussed in the previous paragraph with respect to the roughness data for an operating turbine. Weigand et al. [412] evaluated TEXSTAN for the combined effects of its roughness and film cooling models using the flat-plate data included in Hoffs et al. [401]. The combined effects were successfully modeled for both the effectiveness and heat transfer.

4.4 Internal Heat Transfer With Cooling. Sections 4.2 was devoted to discussions of heat transfer in the presence of film cooling and film cooling modeling, but the discussion was confined to the coolant gas after being injected into the external flow. An equally important consideration has to do with the history of the coolant gas as it is directed from the compressor bleed region to the exit of the cooling holes on the vane, inner and outer bands, and the blade. There are many variations on the internal construction of these vane and blade cooling passages. These variations often include ribs, inclined ribs, roughened ribs, etc., which are designed to trip the internal boundary layer to turbulent in order to increase the internal cooling capacity above what it would be for

a laminar boundary layer. A significant database exists for the vane. Based upon engine experience, designers can often get by with using standard pipe flow correlations for estimating the internal heat transfer with an experience factor added to the correlations. However, in the case of the rotating hot turbine blade, Coriolis and buoyancy forces induce secondary flow vortices that result in different heat loads to the different internal walls depending upon their specific orientation. The fluid flow for the rotating blade has been characterized by several authors to describe their experimental results. It is common in this work to use a Buoyancy parameter (ratio of centrifugal to inertial forces), a Rotational parameter (ratio of Coriolis to inertial forces), and the Reynolds number. The inverse of the Rotational parameter is the Rossby number (ratio of inertial to Coriolis forces). These parameters can be expressed in several ways, but are often expressed as follows:

$$\mathrm{Re}_d = \frac{\rho d u_{\mathrm{in}}}{\mu} \tag{6}$$

where d = hydraulic diameter, ρ = gas density, u_{in} = inlet gas velocity, μ = gas viscosity;

$$\mathrm{Rot} = \frac{\Omega d}{u_{\mathrm{in}}} \tag{7}$$

where Ω = rotational frequency;

$$\mathrm{Ro} = \frac{1}{\mathrm{Rot}} \Rightarrow \frac{u_{\mathrm{in}}}{\Omega d} \tag{8}$$

$$\mathrm{Bo} = \left(\frac{T - T_{\mathrm{in}}}{T}\right) \mathrm{Rot}^2 \frac{R_m}{d} \tag{9}$$

where T = local static temperature, T_{in} = inlet gas temperature, R_{in} = mean radius of test section.

The combination of Coriolis forces, buoyancy forces, and forced convection determines the internal heat transfer. For this case, the common practice among designers is still to use the available database obtained for vanes and then to introduce enhancement factors to correct for the physics of the flow (rotation) missing from the data set being used. For the past eight to ten years, experiments have been designed to supplement the existing nonrotating data set and to provide insight into internal heat transfer for the turbine blade. However, it is not clear just how much of this recent information has migrated into the turbine designer's tools. It is generally agreed among the research community that the experiments designed to produce data applicable to the blade must be rotating to produce the proper Coriolis forces, and they must be heated to produce the proper buoyancy forces. Later in this section, both the nonrotating (vane) and the rotating (blade) literature will be briefly described.

For some applications the coolant gas (or liquid) remains confined to the internal passages of the vane and blade and does not exit cooling holes. In the case of stationary power plants, the cooling medium of choice is sometimes steam or water. The literature contains several proposals of this type of internal cooling for the vane of advanced propulsion gas turbine engines. The technique involves the use of heat pipes for which the potential coolants are alkali metals (sodium or sodium-potassium). The coolant material is in the solid phase at room temperature, but it is argued that the solid should liquefy quickly upon engine start up. The heat pipe technique is not confined to propulsion gas turbines, although many of the published studies are directed at this particular application. One of the advantages of the heat pipe technique is that it does not rely upon compressor bleed air, but rather uses a liquid, wick system, heat sink, and condenser to remove the heat load. A discussion of various research efforts involving heat pipes can be found in references [413–420]. Silverstein et al. [415] studied the application of heat pipe vane cooling for an advanced military turbofan engine and concluded that they could realize significant increase in thrust and a decrease in specific fuel consumption. Yamawaki et al. [418] discuss three alternative heat pipe configurations and cooling media applicable to propulsion gas turbine engines. Their heat pipe concept is similar to that proposed by Silverstein et al. [415] except that Yamawaki et al. [418] use cooling air to provide cooling for the vane leading edge and the thin trailing edge. In this paper, the authors devote attention to start up time for the heat pipe when being used in the propulsion engine application. They found that inclusion of a noncondensable gas in the cooling medium was an effective way to reduce start up time. The shortest startup time found for the heat pipes studied was on the order of six minutes.

4.4.1 Nonrotating Measurements. A significant database applicable to the nonrotating vane is available to the engine designer, e.g., references [421–425]. Included in this literature is a body of data dealing with the influence of ribs on internal heat transfer. Probably Taslim and his students have generated the most extensive data set. Taslim et al. [426] studied the influence of bleed holes on heat transfer and pressure drop in roughened trapezoidal passages with tapered turbulators. This configuration is representative of the trailing edge region of the airfoil. The authors concluded that the bleed holes provide a spanwise velocity component to the main flow and result in a more uniform spanwise heat transfer coefficient. Taslim and Wadsworth [427] demonstrated that the average heat transfer coefficient to the rib is significantly greater than the heat transfer coefficient for the floor, or the area between the ribs, which is a particularly important finding for small engines. Taslim et al. [428] investigated rib-roughened channels to simulate leading edge cavity heat transfer. Various shaped ribs consistent with engine application were used in this study. In a later paper, Taslim et al. [429] found that by roughening the walls of the ribs they could significantly increase the heat transfer coefficient of the ribs. Taslim et al. [430] investigated heat transfer coefficient enhancement in channels roughened with angled ribs, **V**-shaped and discrete ribs on opposite walls. The authors concluded that the resulting heat transfer coefficients were greater than corresponding 90 deg ribs, and reasoned that secondary flows generated by the angled ribs were responsible for the increased heat transfer coefficients. Wang et al. [431] have also investigated the use of angled ribs and found two major counterrotating vortices. However, Wang et al. [431] did not compare their results to the 90 deg rib data.

Several other authors have also investigated the influence of ribs (or turbulators) on the internal heat transfer. Among them are references [432–439]. Rivir et al. [438] describe an experiment for which hot-wire measurements were performed in a square channel roughened with ribs. The authors considered several rib configurations in their study. The turbulent intensity and scale in the immediate vicinity of the ribs were determined from hot-wire data. The interested reader is referred to these papers for a more detailed discussion of the additional results.

4.4.2 Moving the Coolant to the Disk and the Cavity Flow. One must move the coolant gas from the compressor bleed to the rotating blade in the gas turbine application. This must be accomplished without suffering significant losses, or contaminating the blade cooling air with hot disk cooling air or ingested flowpath gas in the process. Prakash and Zerkle [440] have shown that blade internal heat transfer is sensitive to the conditions of the incoming coolant flow. The flow in the disk cavity must also be understood so that proper cooling of the disk can be assured in order to prevent thermal distress. The rim seal between the rotor and the stationary vane will normally leak under the best of conditions, allowing hot gas from the flow path to move into the disk cavity thus presenting potential thermal stress for the disk. A significant portion of the database having application to these problem areas can be found in papers authored by Professor Owen and co-workers at the University of Bath and by Professor Bohn and co-workers at Aachen University of Technology. Examples of these papers are references [441–454]. Wilson et al. [448] used a

preswirl rotor–stator rig similar to that used by El-Oun and Owen [443] to perform detailed heat transfer, velocity, and temperature measurements for the surface of the disk, the stator, and the preswirl chamber. The authors had significantly less instrumentation in the preswirl chamber than for the stator and rotor. The blade cooling temperature was shown lowest when the swirl ratio was the highest. Predicted values of the measured parameters were obtained using an axisymmetric elliptic solver and a low-Reynolds-number $k-\varepsilon$ turbulence model. The trend of the predicted results was consistent with the measurements, but the magnitudes were significantly different. Karabay et al. [449] describes a combined theoretical, computational, and experimental research program treating the problems associated with the preswirl (inducer) system. In the process of preswirling the cooling air, the technique described also provides cooling to the disk to maintain the metal temperature within acceptable limits. It is demonstrated that the flow between the preswirl cover plate and the disk is similar to that in a rotating cavity with a radial outflow of air. Chen et al. [455] report the results of a combined experimental/computational study of heat transfer for the disk cavity, i.e., in a cavity bounded on one side by the rotating disk and on the other by a stationary wall. Measurements of local velocity and heat transfer in the cavity are reported. The authors show reasonably good agreement between measured and predicted heat transfer values in the cavity. Chen et al. [455] report the results of a similar experimental investigation for heat transfer in the cavity of contrarotating disks. Bohn et al. [454] investigated ingestion of hot gas into the disk area via the lip seal between the vane and the rotor. These measurements were performed for different values of the lip seal clearance, rotational Reynolds number, and Mach number of the gas path flow. The results of the study demonstrated that both the flow path Mach number and the rotational Reynolds number have a significant influence on the leakage flow. With increases in both of these parameters, the efficiency of the seal decreases. Bohn et al. [451] report the results of a combined experimental/computational study designed to study the convective heat transfer in a closed annuli cavity rotating about its horizontal axis. The steady-state results of the calculations and the experiment are shown to be consistent. However, the computed results inside the cavity appear to be influenced by an instability that could not be resolved from the experimental results. These internal cavity flows, which, when properly designed, are supposed to maintain the working temperature of the disk at an acceptable temperature to ensure reasonable life, are a very important consideration in the design of turbomachinery. Steltz [456] has presented the results of a generalized analysis that can be conveniently used to estimate thermal stress in the rotor disk during transient operation. The analysis was designed for specific application to stationary power plant machines, but the results are sufficiently general to be of use to many different applications. Several other papers dealing with disk cavity flows are also relevant to this discussion, e.g., Long et al. [457], Guo and Rhode [458], Chen et al. [455], and Roy et al. [459], but space does not permit further discussion.

4.4.3 Rotating Measurements. Measurements of internal turbine blade heating on rotating cooling passages have been ongoing for many years. Many of these studies have used square smooth ducts as the experimental vehicle. This configuration is acceptable for basic studies of the fluid mechanics associated with these flows. However, it may be difficult to build square ducts into a turbine blade and the industry generally doesn't run with smooth channels but rather builds turbulators into the airfoil in order to trip the boundary layer and enhance heat transfer. Han et al. [460] provide a review of the available literature relevant to heat transfer in ducts rotating perpendicular to the duct axis. It is noted in the paper that the difference in heat transfer between rotating and nonrotating flow conditions is very significant. The rotating trailing surface heat transfer coefficient increased up to 3.5 times the nonrotating value and the leading surface heat transfer coefficient was reduced to 40 percent of the nonrotating value. Thus, it is very important when designing a measurement program of this type to be sure to reproduce both the Coriolis and the buoyancy forces present in a heated turbine blade. Wagner et al. [461–463] and Johnson et al. [464] have studied the Coriolis effects on heat transfer in a serpentine square passage both with and without ribs at constant wall temperature. Dutta et al. [465] report the results of a rotating internal heat transfer experimental study obtained using the same experimental facility described in Han et al. [460] for which smooth-walled triangular ducts (instead of square or round ducts) were used. Their reason for doing so was that triangular ducts are a feasible configuration for internal passages of turbine blades. This configuration provides more restriction to secondary flows, thus avoiding symmetric vortex formation and reducing heat transfer disparities between the leading and trailing surfaces. Dutta et al. [465] considered three different wall heating conditions—constant wall temperature, constant wall heat flux, and engine condition—in order to impose both the Coriolis and buoyancy forces on the experimental condition. The results of the triangular duct are compared with the corresponding square duct results reported by Han et al. [466] and different heat transfer and vortex patterns are demonstrated. Bons and Kerrebrock [467] designed and conducted a unique experiment in which they obtained local velocity and surface temperature information in the heated rotating passage, which would then provide a data base to be used in code validation studies. They used a smooth-walled square duct in a large rotating rig, and heated the walls using indium tin oxide strips that operated as resistance heaters. The temperature of the wall was then measured using a mercury/cadmium/telluride infrared detector (frequency response typical of these detectors is on the order of 300 kHz). The internal flow was seeded with particles and the internal flow velocity was measured using Particle Image Velocimetry. In addition to providing a unique set of flow field velocity data for a heated rotating passage, this experiment also demonstrates the significant differences in wall heat transfer that occur when the buoyancy force is not duplicated in rotating measurements. The authors illustrate the importance of duplicating both the Coriolis and buoyancy forces simultaneously. They show a difference of a factor of two in Nusselt number from trailing to leading wall when both the Coriolis and buoyancy forces were present as compared to a ten-percent effect in the absence of buoyancy. Glezer et al. [468] describe the results of an experimental program designed to investigate the impact of a screw-shaped swirl cooling technique (described in Glezer et al. [469]) for cooling the turbine blade leading edge. It is argued that the jets induce a swirling motion in the leading edge passage, resulting in significant augmentation of the internal heat transfer along the leading edge with crossflow playing an insignificant role. Many years ago Kercher and Tabakoff [470] had demonstrated that jets impinging normal to the wall of the confining channel were inefficient for internal cooling because of the influence of crossflow. The rotating experiments described by Glezer et al. [469] were conducted using the same rotating rig as noted above in the discussion of the work reported by Bons and Kerrebrock [467]. Additional rotating measurements were performed using thermal sensitive paint (producing an irreversible color map) on a blade that utilized this same screw-shaped swirl cooling technique that was operated in an engine. Measurements for the same geometry were obtained using a hot cascade rig. The authors concluded that optimization of the internal passage geometry relative to the tangential slots is important to achieve the best results using the screw-shaped swirl for internal cooling.

4.4.4 Predictive Capability for Internal Cooling. The literature relevant to predicting heat transfer in blade coolant passages is not as extensive as that for measurement of the heat transfer for these passages. A significant portion of the available information has been done for cylindrical, square, or rectangular configurations rotating about an axis that is normal the axis of the duct. Among these references are [471,472,473], and [440]. Although

these studies did not consider the typical 180 deg bends commonly associated with a turbine blade internal cavity flow, they were quite successful in identifying the primary features of the flow field. The findings of these authors were in general agreement in that they identified strong rotational flow effects. They also noted that on the pressure side of the wall (trailing side) the turbulent mixing increases and the skin friction increases, resulting in thinner boundary layers and increased heat transfer. On the suction side of the wall (leading side), the heat transfer decreases near the inlet but increases further downstream. Prakash and Zerkle [440] treated the case of a rotating square duct and considered both Coriolis and buoyancy effects. These authors found that their predictions were quite sensitive to the inlet conditions, especially to the presence of rotation in the incoming flow. It was noted in Section 4.2 that getting the coolant flow into the blade cavity is not a trivial task and improperly doing so can have serious consequences.

Kumar and Deanna [474] describe a method for designing internal coolant passages for a radial flow turbine, which is based upon empirical lumped parameter models. Procedures similar to that described in Kumar and Deanna are today more widely used within the industry for doing internal designs than are three-dimensional Navier–Stokes solutions of the kind briefly noted in the remainder of this section. Later, Steinthorsson et al. [475,476] attempted to add computational rigor to the prediction scheme. They describe a CFD code that was developed for calculating the three-dimensional fluid flow within coolant passages of a radial turbine blade similar to that discussed by Kumar and Deanna. The calculation scheme solves the compressible Navier–Stokes equations for a turbulent rotating flow with the equations being formulated in the rotating frame of reference instead of the inertial frame. The numerical code is described in Steinthorsson et al. [475]. The grid generation technique, including provision for serpentine passages with pin fins, that was developed in order to obtain meaningful results from running the code is described in Steinthorsson et al. [476]. The specific problem treated in this paper is for the case of a coolant gas entering at the dovetail base of the rotating blade. The coolant then passes through a tortuous internal passage, which includes distributed pin fins, and exits at the blade trailing edge. The authors incorporated their formulation of the Navier–Stokes equations into an existing NASA code and performed calculations for a typical rotating blade configuration. They note in their discussion of results that caution was in order because some of the trends predicted were counter to intuition and in the absence of experimental results. They also note that improvement of the calculation technique additional work is required to reduce numerical diffusion without reducing robustness.

Dawes [477] used information available in the open literature to reconstruct the internal serpentine passages of an airfoil described in Snyder and Roelke [478]. Dawes [477] demonstrated application of an unstructured mesh, solution adaptive, three-dimensional Navier–Stokes solver to the geometry and flow conditions of a radial inflow turbine blade. For the case selected by Dawes, no experimental results were available. Therefore, he elected to compare the results of his calculation technique with calculations reported by Taylor et al. [479] for a multi-ribbed cylindrical duct for which there were limited experimental results available. However, the lumped parameter predictions of Kumar and Deanna [474] (noted in the previous paragraph) were available for the radial inflow turbine airfoil configuration and Dawes demonstrates favorable comparison between his predictions and those of Kumar and Deanna [474].

Rigby [480] describes heat transfer predictions in a ribbed coolant channel with a 180 deg bend. The full Reynolds-averaged Navier–Stokes equations are solved in obtaining these calculations. The calculation procedure utilizes the Wilcox $k-\omega$ turbulence model (Wilcox [481,482]). The intent of the paper was to concentrate on grid structure for internal cooling passages and on turbulence modeling. Rigby [480] shows reasonable agreement with the experimental results reported by Park et al. [483]. Rigby et al. [212] present the results of a numerical simulation of three-dimensional flow and heat transfer in a rectangular duct with a 180 deg bend. One of the intentions of this paper was to compare the results obtained with single-block versus multi-block grids. The calculated results were compared with the experimental data of Arts et al. [484] and shown to be in reasonable agreement. For the same number of cells, the multi-block grid produced more accurate results than did a single-block grid. The same turbulence modeling was used here as was used in the Rigby [480] work. This internal flow calculation effort continues in Rigby et al. [485]. This later paper describes the results of a numerical simulation designed to treat the case of flow in a straight channel with square cross section, but with three smooth walls and the fourth configured to contain ribs and bleed holes. For completeness, the authors performed calculations with the fourth wall as noted above or with holes only, with ribs only, or smooth. The calculations were performed in order to provide a prediction of the experimental results of Ekkad et al. [486]. The predictions presented capture the general trend of the experimental results. With the exception of the immediate vicinity of the ribs, the predictions are in good agreement with the measured heat transfer. The authors once again used the $k-\omega$ turbulence model proposed by Wilcox [481,482], and find that this model works well for them without requiring reference to the distance to a solid surface.

5 Summary Remarks and Suggestions for Future Turbine Aerodynamic and Heat Transfer Research and Development Needs

Brief reviews of current hot-section heat transfer measurements and predictions have been presented. The pressure and velocity fields in the immediate vicinity of the airfoil are essential for predicting local heat flux. Thus, the capability of the current CFD codes for predicting both the time-averaged surface-pressure distributions on the vanes and blades has been described. It was possible for some cases to compare the results of six different predictive codes run by five different groups to the same data set. Five of these CFD codes also predicted the unsteady pressure envelope on the blade for comparison with the experimental results. In addition, time-averaged and unsteady surface pressure predictions were compared with measurements for two different vaneless counterrotating turbine stages. In this case, the individual engine company responsible for design and construction of the machine using their internal codes performed the predictions, and a third group performed the experiments using both machines. The results of the comparison demonstrated regions of the stage where agreement between prediction and experiment was quite good and other locations where improvements are needed.

The state of the art with respect to high-pressure turbine heat transfer was reviewed for both external and internal heat transfer. The scarcity of definitive information regarding the turbulence intensity and scale of turbulence of the flow exiting the combustor presents a difficult hurdle in predicting the heat transfer for the high-pressure uncooled vane. It is of less importance if the vane is film cooled and most likely less important for the blade because of the disturbances caused by the vane wakes and shock waves interacting on the blade. Standard practice within the community is to assume values for turbulence intensity and scale and to proceed with predictions of heat transfer distribution for the vane and blade. It is then argued that if the proper values were selected then one would obtain the presented result.

Several examples comparing measurements with predictions of heat transfer distribution for both rotating rigs and cascades are discussed (both with and without film cooling). In general, the parameters being varied in these studies were the Reynolds number, the airfoil incidence angle, and the airfoil exit Mach number. It is demonstrated that even for the simple case of an uncooled airfoil in a cascade, there is still great room for improvement in the CFD predictive capability. Prediction of surface pressure dis-

tributions is much further advanced than the ability to predict the corresponding heat transfer distributions. Film cooling was treated in some depth because it is obviously a significant part of the high-pressure turbine design system. There is an abundance of film cooling information for simple low-Mach-number flat-plate flows using isolated cooling holes of different configurations. However, data for a film cooled stage with a fully cooled vane and a fully cooled rotating blade are nonexistent. There are three data sets described in this paper for which isolated blades of the rotating disk were cooled, but the upstream vane was not. For these specific cases, comparison of rotating blade results with the results obtained for the same airfoil run in a cascade facility gave poor agreement. Limited attempts have been made to predict surface heat transfer distributions for film cooled rotating blades. Based on these, it appears that in order to obtain reasonable agreement with measurements, one will need to use a CFD code capable of calculating the unsteady blade flow in the presence of wakes and shocks. Similarly, a review of existing results obtained for internal cooling of rotating blades demonstrated the importance of including both Coriolis and buoyancy effects in the experiments. The conclusion of these studies was that if one is interested in obtaining design system experimental results for the blade, then the blade must both be rotating and heated if one is to obtain the proper internal heat transfer loading. The discussion of internal cooling also addresses the effectiveness of ribs and internal roughness on the enhancement of convective heat transfer. Another important factor influencing high-pressure turbine heat transfer for which a discussion regarding the current state of the art is included is surface roughness. In this regard, it was possible to compare experimental results from three different groups designed to investigate the same turbine with the same rough blade, and a fourth group performed the analysis of the roughened blade.

A significant amount of research has been done with regard to the low-pressure turbine with respect to transition, losses, reduction of solidity, and flow control. It is apparent that several of the research groups working this problem have been communicating and results coming out of one group appear to supplement those coming from the others quite nicely. It appears that it will be possible for the industry to take advantage of vane clocking and airfoil design in order to reduce losses, parts count, and weight. The impact on mechanical requirements because of the higher blade loading appears to be a relatively straightforward problem to solve.

The earlier discussion related to unsteady pressure loading of the turbine demonstrated that the state of the art has advanced to the point where the short-duration facility can be effectively used to obtain forced response data relative to high cycle fatigue. The results of an experimental/numerical program, which produced a data set consisting of unsteady aerodynamics and structural response for a full-stage rotating Garrett TFE 731-2 turbine, are described which demonstrate the feasibility of the technique. The rotating blade of the turbine was instrumented with flush-mounted miniature pressure transducers, strain gages, and piezoelectric crystals. The turbine stage measurements were obtained with the turbine being operated at design corrected conditions. Both aerodynamic and piezoelectric excitation techniques were used to study the blade vibratory response with and without aerodynamic loading. In this way, it was possible to measure the total damping and to obtain estimates of the contributions from structural and aerodynamic sources. The results of this measurement/analysis program provide the coupled measurement of unsteady pressure and vibratory response of a high-pressure turbine blade due to vane/blade interaction that can be used to validate predictive CFD codes.

The state of the art regarding experimental and computational capabilities relative to heat transfer in gas turbine engines has made significant progress over the past thirty years. It is also clear that the experimental and computational capabilities available today are significantly greater than they were even a few years ago, and that equally large advancements are within the grasp of the community. The following discussion is not intended to be exhaustive of specific problem areas requiring further attention. Rather it is intended to be a brief description of several targets of opportunity with potentially high dividends for relatively little investment for the interested parties. The specific research areas are not given necessarily in order of importance since the individual user of the technology is responsible for determining importance.

For the purposes of this discussion, the list is confined to the turbine and the combustor sections of the machine. Within the confines of this portion of the machine, some problem areas stand out from the others because of their first level importance to the immediate needs of the community. It was noted early in the paper that the tendency of the design community to push the turbine inlet temperature closer and closer to fuel stoichiometric is not likely to diminish with time. Accordingly, potential solutions to heat transfer problems and design methods to diminish harmful effects of excessive heating while preserving performance are high on the priority list. Also high on the list is improving our understanding of the fluid flow in the low-pressure turbine stages and the potential weight savings and performance gains that may be realized by this information. The following list of research and development needs is intended as a list of that the author feels are of the highest priority and is not intended to be a shopping guide.

5.1 Fully Cooled Turbine Stage. Because of increasing turbine inlet temperatures, the ability to design efficient film cooling schemes is essential. However, the basic design information required to perform such a design is not available. A significant contribution to the gas turbine industry for the film cooling design system can be made if the experimentalist, code developers, and modelers can join forces to develop the necessary validated design tools. From the experimental perspective, a very important link for turbine heat transfer prediction is missing from the data bank. This missing link is a data set for a full-stage rotating turbine obtained using fully cooled engine hardware. Use of such hardware would provide current cooling hole technology and passages for both the vane and the blade (shroud band cooled also if that is how the particular engine operates). This data set should be composed of several components obtained for specific conditions of interest. Included in this subset of measurements would be: (a) the vanes are cooled but the blades are not, (b) the blades are cooled, but the vanes are not, and (c) the vanes and blades are simultaneously cooled. In addition, the free-stream turbulence should be varied over an acceptable range. The coolant blowing ratio, density ratio, momentum ratio, and coolant-to-wall temperature ratio should be varied over a range consistent with engine parameters. The adiabatic wall temperature is an important parameter in this study and must be measured. In order to measure that quantity; it will be necessary to be able to change the wall temperature, which will require heating the walls (which was previously demonstrated for a rotating blade in Bergholz et al. [189]). Many quantities must be measured and be included in the database. Among these are: (a) internal cavity temperatures and pressures, (b) cooling gas flow rates, (c) vane and blade surface temperature, (d) vane and blade heat flux, (e) vane and blade surface pressure, and (f) flowpath pressure and temperature.

Modeling of film cooling can be divided conveniently into micro and macro models. A significant amount of information has appeared in the literature describing micro models. The micro model represents those cases for which millions upon millions of grid points are utilized to grid the inside of one or two isolated holes and maybe a little of the internal and external airfoil surface. By contrast, the macro model represents a more encompassing description of the film hole-surface interaction, but with significantly less detail regarding individual holes since the entire external surface of the component must be included in the model description. Clearly, the micro model is too demanding of time and computer resources to be useful for describing film cooling for a section of engine hardware, but rather is useful when used in

conjunction with more fundamental laboratory studies. A generalized macro model that could be used to describe the interaction between the coolant flow and the external flow needs to be developed. Neither the macro model nor the missing experimental information may be as difficult to develop as some might think. Abhari [2] has outlined the structure of a potential macro model that could be for this purpose. In his work, the vane row was not cooled and only selected blades were cooled with fewer holes than an actual blade would have. However, he has demonstrated that the heat transfer model can be incorporated into an unsteady flow field code (UNSFLO 2-D) and that heat transfer predictions in the presence of film cooling can be obtained. As part of this work, the results of his predictions are compared with experimental results and good agreement is demonstrated. The modelers and the experimentalist have demonstrated in the past that they can find a way to work together effectively. Assuming that this cooperation can be repeated, then the detailed data coming from the fully three-dimensional experiment using actual engine hardware described in the preceding paragraph would provide the missing links in the development of this interaction model. Several groups have operational three-dimensional unsteady codes that are routinely used to predict the unsteady pressure field on the blade. Section 2.2 demonstrated the capability of some of these codes to predict the three-dimensional pressure field on a rotating blade. Modifying these codes so that they do an adequate job of incorporating the cooling flow model and the heat transfer calculation is far from a simple task, but with insight and dedication it is a feasible task.

5.2 Combustor Hot Streaks and Vane Clocking. Combustors are known to produce hot streaks that may impinge on the HPT vanes; a discussion related to this topic was presented earlier in Section 4.1.6. Many researchers have demonstrated potential advantages for clocking downstream vane rows relative to upstream vane rows for both the high-pressure turbine and the low-pressure turbine. There is certainly good reason for the design community to be interested in further investigation of these concepts. However, as demonstrated earlier in the paper, little is known about the hot streak migration through the machine. A demonstration of the existence of hot streaks can be seen in a photograph of a Rolls Royce RB211 HPT vane row presented in Chambers [487] and in Campbell [488]. There are many CFD calculations of hot streak migration, but very limited data with which to verify the calculation techniques. Tracking the hot streaks through the blade row is not a simple task, but it is possible to track them with existing technology. Heat-flux gages located at strategic locations on the blade can be used to measure the potential impact of the hot streak on the surface heat transfer. However, a high-frequency response device to measure temperature will be required to track the hot streak in the flow path. Tracking these hot streaks in the flow path will also require a traverse mechanism to move the temperature sensing device through the blade and/or vane wakes, which is also possible within the current state-of-the-art technology. Sieverding et al. [489] provide an excellent review of high-frequency measurement techniques and describe a device that has the required frequency response for this purpose.

It is within the experimental state of the art to design and perform a measurement program directed at providing a database for validating the hot streak migration CFD codes noted in the previous paragraph. In this regard, it is important to duplicate representative temperature profiles with respect to their circumferential and radial distribution consistent with the engine. Upstream vane clocking relative to the hot streak and downstream vane clocking relative to the upstream vane are important parameters in this study.

5.3 Blade Tip Heat Transfer. Burnout of high-pressure turbine blade tips is currently one of the more expensive problems facing the industry. In Section 4.1.5, a brief discussion of heat transfer to the blade tip was presented. It was demonstrated that the heat-flux values at local sites in the blade tip region could be in excess of the blade midspan stagnation value. One of the large expenses within the gas turbine industry is the necessity to replace or re-work HPT blades because of thermal distress in the tip region. The blade tip burn spot (spots) can sometimes be reworked and the blade returned to service, but in other cases structural cracks develop and the blade must be replaced. The industry has a great deal of field information for various blade-tip configurations, but this information comes as the result of engine tear down, and is of a nature that indicates either distress or unacceptable structure. Laboratory measurements for rotating turbines operating at realistic conditions of the type needed to supplement predictive techniques for blade distress are very limited. The available data and predictions of this type were described in Section 4.1.5 for flat and recessed blade tips. It is easy to arrive at the conclusion that much is left to be desired if one wishes to understand heat transfer in the blade tip region better. Similar to the case of film cooling, this is another area for which the state-of-the-art experimental and computational capability has advanced significantly. Assembling a combined experimental and computational research effort with both groups working very closely together has potentially high pay off for the gas turbine industry. The design of this effort needs to incorporate a machine capable of operating over a range of vane exit Mach number conditions, tip configurations, tip/shroud clearance values, and vane/blade spacing. In addition, measurements and predictions need to be obtained for situations having and not having hot streaks both with and without cooling gas.

5.4 Turbulence Intensity and Scale Measurements for Operating Gas Turbine Combustor. Gas turbine engine combustors are known to have associated with them varying degrees of turbulence intensity and scale. In Section 3.2, it was noted that the magnitude and scale of the turbulence entering the HPT vane isn't a well-known quantity. However, several groups of researchers are willing to state that the turbulence intensity ''must be a high value'' (where high is often quoted to mean 10 to 18 percent). Further, these same folks are willing to approximate the scale of the turbulence as on the order of 0.1, 1.0, or 10 times a characteristic dimension of the HPT vane. The fact that little is known about combustor turbulence intensity and scale is not because researchers over the years haven't tried to measure these quantities. Rather, it is because the environment in which the measurements are to be made is extremely hostile. It is very doubtful that within the near term anyone will produce more specific information about combustor turbulence than was noted in Section 3. However, the results reported by Goebel et al. [89] are a reasonable start for a measurement program utilizing an operating combustor and perhaps the effort could be extended to an annular configuration. In the absence of further combustor measurement programs, it would be instructive to create a turbulence of documented intensity and scale and then to subject a rotating turbine stage to the turbulent flow. Measurements on the vane and blade surfaces would include, but not be limited to, heat-flux and surface-pressure distributions. The obvious next step would be to remove the turbulence generator, determine the free-stream turbulence (and associated scale) in the absence of the turbulence generator, and then repeat the heat-flux measurements for the same turbine hardware. It would be important to perform the measurements for both an uncooled and a fully cooled turbine stage (see Section 5.1).

5.5 Blade Vibratory Response for Turbine. The modern turbine designs have associated with them large stage pressure ratios and reduced vane and blade count in an effort to extract more work from the flow and to reduce the weight of the machine. There have been some instances for these modern designs for which high-cycle-fatigue (HCF) has become a source of concern. The ability of the turbine designer to predict HCF may not be as good as the ability to predict surface-pressure distributions and

surface heat transfer distributions. It is generally agreed within the industry that the uncertainty associated with predicting vibratory response and blade damping is relatively large and data with which to compare the predictive codes are in scarce supply. However, the state of the art in experimental techniques has progressed to the point where useful information regarding HCF can now be obtained at an affordable price with sufficient accuracy to interest the design community.

The work of Kielb et al. [37,65] was performed using a machine that is more than forty years old that was designed to operate at a very modest pressure ratio with the vane at subsonic exit Mach number. Similar data sets for more modern turbine stages operating at transonic exit conditions and more aggressive pressure ratios are not available for comparison purposes.

Short-duration facilities have demonstrated sufficient test time to produce the modal response for many of the important excitations of interest. There is now the opportunity for the industry to extend the techniques developed in this earlier work to a significantly more modern turbine stage operating at much more aggressive stage pressure ratios. Several turbine stages of current interest to the industry could be used in conjunction with the experimental technique noted above to provide valuable design information. Among these are the vaneless counterrotating machines described in References [34] and [36] that both operate at transonic conditions. However, with little effort one could envision many other turbine configurations for which affordable experimental information could be generated that would prove useful to the industry.

5.6 Low-Pressure Turbine Measurements. All of the low-pressure turbine measurement programs described herein have been performed in the absence of an upstream high-pressure turbine. Thus, the disturbances generated by the HPT have been assumed to either be relatively small or have been simulated by bars, grids, or some other mechanism. Further, the addition of dimples and/or vortex generator jets to the low-pressure turbine blades in order to achieve passive or active control of boundary-layer separation still is in need of verification in a rotating rig environment. In a long run time rig, it is a difficult task to operate a HPT in conjunction with the LPT. The major advantage to a long run time is the availability of measurement techniques that have increased accuracy at the expense of significant integration time. However, short duration facilities can complement the more expensive long duration facilities. As described, measurement programs have been performed using short duration facilities for which the high-pressure turbine (with a significant stage pressure ratio) was followed by a second stage. These measurement programs demonstrated that there was sufficient second-stage exit pressure to install additional stages. Further, the capability existed to increase the first-stage inlet pressure so that the later stages would have sufficient pressure to allow for reasonable signal to noise ratio for the pressure transducers. The instrumentation suite available for the short duration facility is significantly different than for the long duration facility. Primary measurements are composed of surface heat transfer, surface pressure, strain gages mounted on the airfoils, and flowpath quantities such as static pressure and total temperature and pressure. The suggested measurements would provide a significant supplement the already existing knowledge base for low-pressure turbines. They are designed to fill the rather obvious gaps in the existing technology, but not to supercede the existing database or to replace existing experimental techniques.

5.7 Internal Cooling. Internal cooling measurements relevant to the high-pressure turbine blade obtained at conditions representative of the engine are difficult to find in the literature. Computational techniques are available that can be used to predict the blade internal heat transfer. A concerted effort designed to provide such experimental information would be beneficial to the heat transfer community. These measurements could be used to verify many of the lumped parameter correlations that are currently used to predict internal heat transfer and to provide anchor points for more advanced calculations. To be useful to the community, it is necessary that engine hardware blades and disk be used as the experimental vehicle. Instrumentation capable of measuring temperature, pressure, and heat transfer at selected locations internal to the blade and disk would be installed. As optical diagnostics improve and the associated frequency response increases, they would become a very useful addition to the instrumentation suite. Heaters would be installed in the blade skin so that the proper buoyancy can be duplicated and the disk would be rotated at the design engine speed to duplicate the rotational parameter. Performance of this measurement program is within the capability of the current state of the art.

6 Selected References

The reference section of this paper contains numerous citations relevant to the development of turbine aerodynamics and heat transfer, but this collection is likely more than the person with casual interest desires. Thus, this section lists approximately fifty references (grouped by topic) which provide a reasonable starting point for interested readers. The references have been selected to provide an overall historical view of the specific area. The list begins with papers that generally do not include comparisons between prediction and measurement. The middle portion includes papers showing comparison between prediction with measurement and concludes with a recent paper or two that represent the current level of technology in the field. An attempt has been made in compiling the list to cite the different organizations involved in the research activities discussed in the paper.

6.1 Turbine Aerodynamics

Rai, M. M., 1987, ''Unsteady Three-Dimensional Navier–Stokes Simulations of Turbine Rotor–Stator Interaction,'' AIAA Paper No. 87-2058.

Giles, M. B., 1988, ''Calculation of Unsteady Wake Rotor Interaction,'' AIAA J. of Propulsion and Power, **4**, No. 4, pp. 356–362.

Whitfield, D. L., Janus, J. M., and Simpson, L. B., 1988, ''Implicit Finite Volume High Resolution Wave-Split Scheme for Solving the Unsteady Three-Dimensional Euler and Navier–Stokes Equations on Stationary or Dynamic Grids,'' MSSU-EIRS-ASE-88-2.

Sharma, O. P., Pickett, G. F., and Ni, R. H., 1990, ''Assessment of Unsteady Flows in Turbines,'' ASME J. Turbomach., **114**, pp. 79–90.

Rao, K. V., Delaney, R. A., and Dunn, M. G., 1994, ''Vane–Blade Interaction in a Transonic Turbine, Part I—Aerodynamics,'' AIAA J. Propulsion and Power, **10**, No. 3, pp. 305–311.

Busby, J. A., Davis, R. L., Dorney, D. J., Dunn, M. G., Haldeman, C. W., Abhari, R. S., Venable, B. L., and Delaney, R. A., 1998, ''Influence of Vane–Blade Spacing on Transonic Turbine Stage Aerodynamics Part II: Time Resolved Data and Analysis,'' ASME Paper No. 98-GT-482.

Adamczyk, J. J., 2000, ''Aerodynamic Analysis of Multistage Turbomachinery Flows in Support of Aerodynamic Design,'' ASME J. Turbomach., **122**, No. 2, pp. 189–217.

Denos, R., Arts, T., Paniagua, G., Michelassi, V., and Martelli, F., 2000, ''Investigation of the Unsteady Rotor Aerodynamics in a Transonic Turbine Stage,'' ASME Paper No. 2000-GT-435.

Barter, J. W., Vitt, P. H., and Chen, J. P., 2000, ''Interaction Effects in a Transonic Stage,'' ASME Paper No. 2000-GT-0376.

6.2 Turbine Heat Transfer

Crawford, M. E., and Kays, W. M., 1976, ''STAN5—A Program for Numerical Computation of Two-Dimensional Internal and External Boundary Layer Flows,'' NASA CR-2742.

Gaugler, R. E., 1981, ''Some Modifications to, and Operation Experience With, the Two Dimensional, Finite-Difference, Boundary Layer Code, STAN 5,'' ASME Paper No. 81-GT-89.

Dring, R. P., Joslyn, H. D., Hardin, L. W., and Wagner, J. J., 1982, ''Turbine Rotor-Stator Interaction,'' ASME J. Eng. Power, **104**, pp. 729–742.

Dunn, M. G., Rae, W. J., and Holt, J. L., 1983, ''Measurement and Analysis of Heat Flux in a Turbine Stage: Part II—Discussion of Results and Comparison With Prediction,'' ASME J. Eng. Gas Turbines Power, **106**, pp. 234–240.

Guenette, G. R., Epstein, A. H., Giles, M. B., Haimes, R., and Norton, R. J. G., 1988, ''Fully Scaled Transonic Turbine Rotor heat Transfer Measurements,'' ASME Paper No. 88-GT-171.

Goebel, S. G., Abuaf, N., Lovett, J. A., and Lee, C.-P., 1993, ''Measurement of Combustor Velocity and Turbulence Profiles,'' ASME Paper No. 93-GT-228.

Owen, J. M., and Rogers, R. H., 1995, *Flow and Heat Transfer in Rotating-Disc Systems, Vol. 2: Rotor–Stator Systems*, Research Studies Press, Taunton, UK; Wiley, New York.

Hilditch, M. A., and Ainsworth, R. W., 1990, ''Unsteady Heat Transfer Measurements on a Rotating Gas Turbine Blade,'' ASME Paper No. 90-GT-175.

Abhari, R. S., Guenette, G. R., Epstein, A. H., and Giles, M. B., 1991, ''Comparison of Time-Resolved Turbine Rotor Blade Heat Transfer Measurements and Numerical Calculations,'' ASME Paper No. 91-GT-268.

Taslim, M. E., Li, T., and Spring, S. D., 1993, ''Experimental Study of the Effects of Bleed Holes on Heat Transfer and Pressure Drop in Trapezoidal Passages With Tapered Turbulators,'' ASME J. Turbomach., **117**, pp. 281–289.

Giel, P. W., VanFossen, G. J., Boyle, R. J., Thurman, D. R., and Civinskas, K. C., 1999, ''Blade Heat Transfer Measurements and Predictions in a Transonic Turbine Cascade,'' ASME Paper No. 99-GT-125.

Dunn, M. G., Haldeman, C. W., Abhari, R. S., and McMillan, M. L., 2000, ''Influence of Vane/Blade Spacing on the Heat Flux for a Transonic Turbine,'' ASME Paper No. 2000-GT-206.

Bergholz, R. F., Dunn, M. G., and Steuber, G. D., 2000, ''Rotor/Stator Heat Transfer Measurements and CFD Predictions for Short-Duration Turbine Rig Tests,'' ASME Paper No. 2000-GT-208.

6.3 Blade Tip Heat Transfer

Mayle, R. E., and Metzger, D. E., 1982, ''Heat Transfer at the Tip of an Unshrouded Turbine Blade,'' *Proc. 7th International Heat Transfer Conference*, Vol. 3, pp. 87–92.

Bindon, J. P., 1986, ''Pressure and Flowfield Measurements of Axial Turbine Tip Clearance Flow in a Linear Cascade,'' Cambridge University Engineering Department, TR 123.

Metzger, D. E., Bunker, R. S., and Chyu, M. K., 1989, ''Cavity Heat Transfer on a Transverse Grooved Wall in a Narrow Flow Channel,'' ASME J. Heat Transfer, 111, pp. 73–79.

Metzger, D. E., Dunn, M. G., and Hah, C., 1991, ''Turbine Tip and Shroud Heat Transfer,'' ASME J. Turbomach., **113**, pp. 502–507.

Ameri, A. A., Steinthorsson, E., and Rigby, D. L., 1997, ''Effect of Squealer Tip on Rotor Heat Transfer and Efficiency,'' ASME J. Turbomach., **120**, pp. 753–759.

Bunker, R. S., 2000, ''A Review of Turbine Blade Tip Heat Transfer,'' presented at Turbine 2000 International Symposium on Heat Transfer in Gas Turbine Systems, Izmir, Turkey.

6.4 Temperature Migration and Vane Clocking

Butler, T. L., Sharma, O. P., Joslyn, H. D., and Dring, R. P., 1989, ''Redistribution of an Inlet Temperature Distortion in an Axial Flow Turbine Stage,'' AIAA J. Propulsion, **5**, pp. 64–71.

Takahashi, R., and Ni, R. H., 1991, ''Unsteady Hot Streak Simulation Through 1-1/2 Stage Turbine,'' AIAA Paper No. 91-3382.

Shang, T., Guenette, G. R., Epstein, A. H., and Saxer, A. P., 1995, ''The Influence of Inlet Temperature Distortion on Rotor Heat Transfer in a Transonic Turbine,'' AIAA Paper No. AIAA-95-3042.

Dorney, D. J., and Sharma, O. P., 1996, ''A Study of Turbine Performance Increases Through Airfoil Clocking,'' AIAA Paper No. 96-2816.

Tiedemann, M., and Kost, F., 2000, ''Some Aspects of Wake–Wake Interactions Regarding Turbine Stator Clocking,'' ASME Paper No. 2000-GT-487.

6.5 Turbulence and Boundary Layer Transition

Blair, M. F., 1983, ''Influence of Free-Stream Turbulence on Turbulent Boundary Layer Heat Transfer and Mean Profile Development, Part I—Experimental Data, and Part II—Analysis of Results,'' ASME J. Heat Transfer, **105**, pp. 33–47.

Hodson, H. P., 1984, ''Boundary-Layer Transition and Separation Near the Leading Edge of a High-Speed Turbine Blade,'' ASME Paper No. 84-GT-179.

Mayle, R. E., 1991, ''The Role of Laminar-Turbulent Transition in Gas Turbine Engines,'' ASME J. Turbomach., **113**, pp. 509–537.

Addison, J. S., and Hodson, H. P., 1991, ''Modeling of Unsteady Transitional Boundary Layers,'' ASME Paper No. 91-GT-282.

Mayle, R. E., Dullenkopf, K., and Schultz, A., 1997, ''The Turbulence That Matters,'' ASME Paper No. 97-GT-274.

6.6 Turbine Cooling

Blair, M. F., 1974, ''An Experimental Study of Heat Transfer and Film Cooling on Large-Scale Turbine Endwalls,'' ASME J. Heat Transfer, **96**, pp. 524–529.

Dring, R. P., Blair, M. F., and Joslyn, H. D., 1980, ''An Experimental Investigation of Film Cooling on a Turbine Rotor Blade,'' ASME J. Eng. Power, **102**, pp. 81–87.

Yavuzkurt, S., 1985, ''Full-Coverage Film Cooling a One-Equation Model of Turbulence for the Calculation of the Full-Coverage and the Recovery-Region Hydrodynamics,'' ASME Paper No. 85-GT-119.

Takeishi, K., Aoki, S., Sato, T., and Tsukagoshi, K, 1991, ''Film Cooling on a Gas Turbine Rotor Blade,'' ASME Paper No. 91-GT-279.

Abhari, R. S., 1996, ''Impact of Rotor–Stator Interaction on Turbine Blade Film Cooling'' ASME J. Turbomach., **118**, pp. 123–133.

Kercher, D. M., 1998, ''A Film Cooling CFD Bibliography: 1971–1996,'' Int. J. Rotating Machinery, **4**, No. 1, pp. 61–72.

Kercher, D. M., 2000, ''Turbine Airfoil Leading Edge Film Cooling Bibliography: 1972-1998,'' Int. J. Rotating Machinery, **6**, No. 5, pp. 313–319.

6.7 Low-Pressure Turbine

Hourmouziadis, J., Buckl, F., and Bergmann, P., 1986, ''The Development of the Profile Boundary Layer in a Turbine Environment,'' ASME Paper No. 86-GT-244.

Binder, A., Schroeder, T., and Hourmouziadis, J., 1988, ''Turbulence Measurements in a Multistage Low-Pressure Turbine,'' ASME Paper No. 88-GT-79.

Hourmouziadis, J., 1989, ''Aerodynamic Design of Low Pressure Turbines,'' AGARD Lecture Series 167.

Denton, J. D., 1993, ''Loss Mechanisms in Turbomachines,'' ASME Paper No. 93-GT-435.

Schulte, V., and Hodson, H. P., 1996, ''Unsteady Wake-Induced Boundary Layer Transition in High Lift LP Turbines,'' ASME Paper No. 96-GT-486.

Halstead, D. E., Wisler, D. C., Okiishi, T. H., Walker, G. J., Hodson, H. P., and Shin, H.-W., 1997, ''Boundary Layer Development in Axial Compressors and Turbines: Part 1 of 4—Composite Picture,'' *ibid.*, 119, pp. 114–127. ''Part 2 of

4—Compressors,'' *ibid.*, 119, pp. 426–444. ''Part 3 of 4—LP Turbines,'' *ibid.*, 119, pp. 225–237. ''Part 4 of 4—Computations and Analyses,'' *ibid.*, **119**, pp. 128–139.

Hodson, H. P., 1998, ''Bladerow Interactions in Low Pressure Turbines,'' *Blade Row Interference Effects in Axial Turbomachinery Stages*, von Karman Institute for Fluid Dynamics, Lecture Series 1998-02.

Sharma, O., 1998, ''Impact of Reynolds Number on LP Turbine Performance,'' *Minnowbrook Workshop on Boundary Layer Transition in Turbomachines*, J. E. LaGraff and D. E. Ashpis, eds., pp. 65–69. (See also NASA/CP-1998-206958.)

Bons, J. P., Sondergaard, R., and Rivir, R. B., 2000, ''Turbine Separation Control Using Pulsed Vortex Generator Jets,'' ASME Paper No. 2000-GT-262.

Howell, R., Ramesh, O., and Hodson, H. P., 2000, ''High Lift and Aft Loaded Profiles for Low Pressure Turbines,'' ASME Paper No. 2000-GT-261.

Acknowledgments

The author expresses his appreciation to the IGTI Scholar Lecture committee for providing the opportunity and motivations to perform this review of turbine heat transfer state of the art. The author would also like to express appreciation to his friends and colleagues, as well as to the IGTI Scholar Lecture committee, for their dedicated effort in providing technical reviews and critical comments of the draft of the paper. Much of the material presented in this paper comes from research performed by the author and his colleagues at the Ohio State University Gas Turbine Laboratory. In this regard, the author would like to acknowledge the dedication of two talented individuals, Charles W. Haldeman and Jeffrey L. Barton. These individuals have collaborated with the author in performing numerous turbine aerodynamics and heat transfer studies for the past eleven and twenty years, respectively. Charlie Haldeman was extremely helpful in providing critical technical review comments regarding the manuscript. The author would also like to express his appreciation to many friends in academia, government, and industry who have graciously shared information for inclusion in this review. The author would further like to express his appreciation to ASME for granting permission to reproduce herein figures published in previous ASME publications. A more detailed version of this paper is available as an Ohio State University Gas Turbine Laboratory technical report.

References

[1] Clark, J. P., Stetson, G. M., Magge, S. S., Ni, R. H., Haldeman, C. W., and Dunn, M. G., 2000, ''The Effect of Airfoil Scaling on the Predicted Unsteady Loading on the Blade of a 1 and 1/2 Stage Transonic Turbine and a Comparison With Experimental Results,'' ASME Paper No. 2000-GT-0446.

[2] Abhari, R. S., 1996, ''Impact of Rotor–Stator Interaction on Turbine Blade Film Cooling,'' ASME J. Turbomach., **118**, pp. 123–133.

[3] Simoneau, R. J., and Simon, F. F., 1993, ''Progress Towards Understanding and Predicting Heat Transfer in the Turbine Gas Path,'' Int. J. Heat Fluid Flow, **14**, No. 2, pp. 106–127.

[4] Denton, J. D., and Singh, U. K., 1979, ''Time Marching Methods for Turbomachinery Flow Calculations. Part I—Basic Principles and 20 Applications and 11 Three Dimensional Flows,'' *Application of Numerical Methods to Flow Calculations in Turbomachinery*, VKI Lecture Series 1979-7.

[5] Denton, J. D., 1982, ''An Improved Time Marching Method for Turbomachinery Flow Calculations,'' ASME Paper No. 82-GT-239.

[6] Rai, M. M., 1987, ''Navier–Stokes Simulations of Rotor–Stator Interaction Using Patched and Overlaid Grids,'' J. Propul. Power, **3**, No. 5, pp. 387–396.

[7] Rai, M. M., 1987, ''Unsteady Three-Dimensional Navier-Stokes Simulations of Turbine Rotor–Stator Interaction,'' AIAA Paper No. 87–2058.

[8] Giles, M. B., 1988, ''UNSFLO: A Numerical Method for Unsteady Inviscid Flow in Turbomachinery,'' MIT Gas Turbine Laboratory Report No. 195.

[9] Giles, M. B., 1988, ''Calculation of Unsteady Wake Rotor Interaction,'' J. Propul. Power, **4**, No. 4, pp. 356–362.

[10] Sharma, O. P., Renaud, T. L., Butler, T. L., and Milsaps, K., 1988, ''Rotor–Stator Interaction in Multi-Stage Axial-Flow Turbines,'' AIAA Paper No. 88-3013.

[11] Whitfield, D. L., Janus, J. M., and Simpson, L. B., 1988, ''Implicit Finite Volume High Resolution Wave—Split Scheme for Solving the Unsteady Three-Dimensional Euler and Navier–Stokes Equations on Stationary or Dynamic Grids,'' MSSU-EIRS-ASE-88-2.

[12] Ni, R. H., and Bogoian, J. C., 1989, ''Prediction of Three-Dimensional Multistage Turbine Flow Field Using a Multiple-Grid Euler Solver,'' AIAA Paper No. 89-0203.

[13] Rao, K. V., and Delaney, R. A., 1990, ''Investigation of Unsteady Flow Through a Transonic Turbine Stage: Part I—Analysis,'' AIAA Paper No. 90–2408.

[14] Sharma, O. P., Pickett, G. F., and Ni, R. H., 1992, ''Assessment of Unsteady Flows in Turbines,'' ASME J. Turbomach., **114**, pp. 79–90.

[15] Giles, M. B., and Haimes, R., 1991, ''Validation of a Numerical Method for Unsteady Flow Calculations,'' ASME Paper No. 91-GT-271.

[16] Chen, J. P., Celestina, M. L., and Adamczyk, J. J., 1994, ''A New Procedure for Simulating Unsteady Flows Through Turbomachinery Blade Passages,'' ASME Paper No. 94-GT-151.

[17] Rangwalla, A. A., 1994, ''Unsteady Navier-Stokes Computations for Advanced Transonic Turbine Design,'' AIAA Paper No. 94-2835.

[18] Merz, R., Kruckels, J., Mayer, J. F., and Stetter, H., 1995, ''Computation of Three-Dimensional Viscous Transonic Turbine Stage Flow Including Tip Clearance Effects,'' ASME Paper No. 95-GT-76.

[19] Davis, R. L., Shang, T., Buteau, J., and Ni, R. H., 1996, ''Prediction of Three-Dimensional Unsteady Flow in Multi-Stage Turbomachinery Using an Implicit Dual Time-Step Approach,'' AIAA Paper No. 96-2565.

[20] Arnone, A., and Pacciani, R., 1996, ''Numerical Investigation on Wake Shedding in a Turbine Rotor Blade,'' Proc. 15th International Conference on Numerical Methods in Fluid Dynamics,, Monterey, CA, June 24–28.

[21] Holmes, D. G., Mitchell, B. E., and Lorence, C. B., 1997, ''Three Dimensional Linearized Navier-Stokes Calculations for Flutter and Forced Response,'' Proc. 8th International Symposium on Unsteady Aerodynamics and Aeroelasticity of Turbomachines, pp. 211–224.

[22] von Hoyningen-Huene, M., and Jung, A. R., 2000, ''Comparison of Different Acceleration Techniques and Methods for Periodic Boundary Treatment in Unsteady Turbine Stage Flow Simulations,'' ASME J. Turbomach., **122**, pp. 234–246.

[23] Adamczyk, J. J., 2000, ''Aerodynamic Analysis of Multistage Turbomachinery Flows in Support of Aerodynamic Design,'' ASME J. Turbomach., **122**, No. 2, pp. 189–217.

[24] Dring, R. P., and Joslyn, H. D., 1981, ''Measurement of Turbine Rotor Blade Flows,'' ASME J. Eng. Power, **103**, pp. 400–405.

[25] Dring, R. P., Joslyn, H. D., Hardin, L. W., and Wagner, J. J., 1982, ''Turbine Rotor–Stator Interaction,'' ASME J. Eng. Power, **104**, pp. 729–742.

[26] Blair, M. F., Dring, R. P., and Joslyn, H. D., 1988, ''The Effects of Turbulence and Stator/Rotor Interactions on Turbine Heat Transfer Part I: Design Operating Conditions,'' ASME Paper No. 88-GT-125.

[27] Dunn, M. G., Kim, J., Civinskas, K. C., and Boyle, R. J., 1994, ''Time-Averaged Heat Transfer and Pressure Measurements and Comparison With Prediction for a Two-Stage Turbine,'' ASME J. Turbomach., **116**, pp. 14–22.

[28] Rao, K. V., Delaney, R. A., and Dunn, M. G., 1994, ''Vane–Blade Interaction in a Transonic Turbine, Part I—Aerodynamics,'' J. Propul. Power, **10**, No. 3, pp. 305–311.

[29] Moss, R. W., Ainsworth, R. W., Sheldrake, C. D., and Miller, R., 1997, ''The Unsteady Pressure Field Over a Turbine Blade Surface: Visualization and Interpretation of Experimental Data,'' ASME Paper No. 97-GT-474.

[30] Busby, J. A., Davis, R. L., Dorney, D. J., Dunn, M. G., Haldeman, C. W., Abhari, R. S., Venable, B. L., and Delaney, R. A., 1999, ''Influence of Vane-Blade Spacing on Transonic Turbine Stage Aerodynamics. Part II: Time Resolved Data and Analysis,'' ASME J. Turbomach., **121**, pp. 673–682.

[31] Venable, B. L., Delaney, R. A., Busby, J. A., Davis, R. L., Dorney, D. J., Dunn, M. G., Haldeman, C. W., and Abhari, R. S., 1999, ''Influence of Vane-Blade Spacing on Transonic Turbine Stage Aerodynamics, Part I: Time-Averaged Data and Analysis,'' ASME J. Turbomach., **121**, pp. 663–672.

[32] Barter, J. W., Vitt, P. H., and Chen, J. P., 2000, ''Interaction Effects in a Transonic Stage,'' ASME Paper No. 2000-GT-0376.

[33] Denos, R., Arts, T., Paniagua, G., Michelassi, V., and Martelli, F., 2001, ''Investigation of the Unsteady Rotor Aerodynamics in a Transonic Turbine Stage,'' ASME J. Turbomach., **123**, pp. 81–89.

[34] Haldeman, C. W., Dunn, M. G., Abhari, R. S., Johnson, P. D., and Montesdeoca, X. A., 2000, ''Experimental and Computational Investigation of the Time-Averaged and Time-Resolved Pressure Loading on a Vaneless Counter-Rotating Turbine,'' ASME Paper No. 2000-GT-445.

[35] Laumert, B., Martensson, H., and Fransson, T., 2000, ''Investigation of the Flowfield in the Transonic VKI BRITE EURAM Turbine Stage With 3D Steady and Unsteady N–S Computations,'' ASME Paper No. 2000-GT-433.

[36] Weaver, M. M., Manwaring, S. R., Abhari, R. S., Dunn, M. G., Salay, M. J., Frey, K. K., and Heidegger, N., 2000, ''Forcing Function Measurements and Predictions of a Transonic Vaneless Counterrotating Turbine,'' ASME Paper No. 2000-GT-375.

[37] Kielb, J. J., Abhari, R. S., and Dunn, M. G., 2001, ''Experimental and Numerical Study of Forced Response in a Full-Scale Rotating Turbine,'' ASME Paper No. 2001-GT-263.

[38] Ni, R. H., and Sharma, O. P., 1990, ''Using Three-Dimensional Euler Flow Simulations to Assess Effects of Periodic Unsteady Flow Through Turbines,'' AIAA Paper No. 90–2357.

[39] Takahashi, R., and Ni, R. H., 1991, ''Unsteady Hot Streak Simulation Through 1-1/2 Stage Turbine,'' AIAA Paper No. 91-3382.

[40] Lewis, J. P., Delaney, R. A., and Hall, E. J., 1989, ''Numerical Prediction of Turbine Vane–Blade Aerodynamic Interaction,'' ASME J. Turbomach., **111**, pp. 387–393.

[41] Dorney, D. J., and Davis, R. L., 1992, ''Navier-Stokes Analysis of Turbine

Blade Heat Transfer and Performance,'' ASME J. Turbomach., **114**, pp. 795–806.
[42] Baldwin, B. S., and Lomax, H., 1978, ''Thin Layer Approximation and Algebraic Model for Separated Turbulent Flow,'' AIAA Paper No. 78-257.
[43] Turner, M. G., Vitt, P. H., Topp, D. A., Saeidi, S., Hunter, S. D., Dailey, L. D., and Beach, T. A., 1999, ''Multistage Simulations of the GE90 Turbine,'' ASME Paper No. 99-GT-98.
[44] Chen, J. P., and Barter, J. W., 1998, ''Comparison of Time-Accurate Calculations for the Unsteady Interaction in a Turbomachinery Stage,'' AIAA Paper No. 98-3292.
[45] Dunn, M. G., Bennett, W. A., Delaney, R. A., and Rao, K. V., 1992, ''Investigation of Unsteady Flow Through a Transonic Turbine Stage: Data/Prediction Comparison for Time-Averaged and Phase-Resolved Pressure Data,'' ASME J. Turbomach., **114**, pp. 91–99.
[46] Ni, R. H., Sharma, O. P., Takahashi, R. K., and Bogoian, J. C., 1989, ''Prediction of 3D Multi-Stage Turbine Flow Field Using a Multiple-Grid Euler Solver,'' AIAA Paper No. 89-0203.
[47] Sharma, O. P., and Syed, S. A., 1991, ''Turbulence Modeling in Gas Turbine Design and Analysis,'' AIAA Paper 91-0514.
[48] Sharma, O. P., Ni, R. H., and Tanrikut, S., 1994, ''Unsteady Flows in Turbines and Impact on Design Procedures,'' AGARD Lecture Series #195, *Turbomachinery Design Using CFD*.
[49] Chiang, H., and Kielb, R., 1993, ''An Analysis System for Blade Forced Response,'' ASME J. Eng. Gas Turbines Power, **115**, pp. 762–770.
[50] Kielb, R. E., 1999, ''Aeroelasticity in Axial Flow Turbomachines,'' von Karman Institute for Fluid Dynamics, Lecture Series Program 1998–1999, May 3–7.
[51] Manwaring, S. R., and Wisler, D. C., 1993, ''Unsteady Aerodynamics and Gust Response in Compressors and Turbines,'' ASME J. Turbomach., **115**, pp. 725–740.
[52] Weaver, M. M., and Fleeter, S., 1994, ''Turbine Rotor Generated Forcing Functions for Flow Induced Vibrations,'' ASME Paper No. 94-GT-328.
[53] Verdon, J. M., and Casper, J. R., 1982, ''Development of a Linear Unsteady Aerodynamic Analysis for Finite Deflection Subsonic Cascades,'' AIAA J., **20**, No. 9, pp. 1259–1267.
[54] Whitehead, D. S., 1982, ''The Calculations of Steady and Unsteady Transonic Flow in Cascades,'' Cambridge University Engineering Dept., Report CUED/A-Turbo/TR 118.
[55] He, L., 1990, ''An Euler Solution for Unsteady Flows Around Oscillating Blades,'' ASME J. Turbomach., **112**, pp. 714–722.
[56] Verdon, J. M., Montgomery, M. D., and Kousen, K. A., 1995, ''Development of a Linearized Unsteady Euler Analysis for Turbomachinery Blade Rows,'' NASA CR 4677.
[57] Abhari, R. S., and Giles, M. B., 1997, ''A Navier-Stokes Analysis of Airfoils in Oscillating Transonic Cascades for the Prediction of Aerodynamic Damping,'' ASME J. Turbomach., **119**, pp. 77–81.
[58] Crawley, E. F., 1981, ''Measurement of Aerodynamic Damping in the MIT Transonic Rotor,'' MIT Gas Turbine Laboratory Report No. 157.
[59] Crawley, E. F., and deLuis, J., 1987, ''Use of Piezoelectric Actuators as Elements of Intelligent Structures,'' AIAA J., **25**, No. 10, pp. 1373–1385.
[60] Bailey, T., and Hubbard, J. E., 1985, ''Distributed Piezoelectric-Polymer Active Vibration Control of a Cantilever Beam,'' J. Guid. Control, **8**, No. 5, pp. 605–611.
[61] Cross, C. J., and Fleeter, S., 1999, ''Shunted Piezoelectric Control of Airfoil Vibrations,'' ASME Paper No. 99-GT-385.
[62] Abhari, R. S., 1998, ''A Novel Technique for the Measurement of Aerodynamic and Structural Damping of a Rotating Turbine Blade,'' presented at the 3rd National Conference on High Cycle Fatigue, San Antonio, TX.
[63] Jeffers, T. R., Kielb, J. J., and Abhari, R. S., 2000, ''A Novel Technique for Measurement of Rotating Blade Damping,'' ASME Paper No. 2000-GT-359.
[64] Kielb, J. J., 1999, ''Experimental and Numerical Study of Blade Forced Response in a Full-Scale Rotating Turbine at Actual Engine Conditions,'' MS Thesis, Ohio State University, OSU GTL Doc. #1999_8_M6.
[65] Kielb, J. J., and Abhari, R. S., 2001, ''Experimental Study of Aerodynamic and Structural Damping in a Full-Scale Rotating Turbine,'' ASME Paper No. 2001-GT-262.
[66] Giel, P. W., VanFossen, G. J., Boyle, R. J., Thurman, D. R., and Civinskas, K. C., 1999, ''Blade Heat Transfer Measurements and Predictions in a Transonic Turbine Cascade,'' ASME Paper No. 99-GT-125.
[67] Jones, T. V., and Schultz, D. L., 1970, ''A Study of Film Cooling Related to Gas Turbines Using Transient Techniques,'' University of Oxford Report No. 1121/70.
[68] Jones, T. V., and Hippensteele, S. A., 1988, ''High-Resolution Heat Transfer-Coefficient Maps Applicable to Compound-Curve Surfaces Using Liquid Crystals in a Transient Wind Tunnel,'' NASA TM 89855.
[69] Wang, Z., Ireland, P. T., and Jones, T. V., 1993, ''An Advanced Method of Processing Liquid Crystal Video Signals From Transient Heat Transfer Experiments,'' ASME Paper No. 93-GT-282.
[70] Rabinowicz, J., Jessey, M. E., and Bartsch, C. A., 1955, ''Resistance Thermometer for Transient High Temperature Studies,'' J. Appl. Phys., **23**, p. 97.
[71] Chabai, A. J., and Emrich, R. J., 1955, ''Measurement of Wall Temperature and Heat Flow in a Shock Tube,'' J. Appl. Phys., **26**, pp. 779–780.
[72] Vidal, R. J., 1956, ''Model Instrumentation Techniques for Heat Transfer and Force Measurements in a Hypersonic Shock Tunnel,'' Cornell Aeronautical Laboratory Report AD-917-A-1.
[73] Vidal, R. J., 1962, ''Transient Surface Temperature Measurements,'' Cornell Aeronautical Laboratory Report No. 114.
[74] Squire, W., 1953, ''Thermocouple With Insulated Backing,'' Cornell Aeronautical Laboratory Inter-Office Memorandum, Nov. 3.
[75] Rose, P. H., and Stark, W. I., 1956, ''Stagnation Point Heat Transfer Measurements in Air at High Temperature,'' AVCO Research Laboratory, Research Note No. 24.
[76] Schultz, D. L., and Jones, T. V., 1973, ''Heat Transfer Measurements in Short-Duration Hypersonic Facilities,'' AGARD-AG-165.
[77] Jones, T. V., Schultz, D. L., and Hendley, A., 1973, ''On the Flow in an Isentropic Light Piston Tunnel,'' ARC R&M 3731.
[78] Epstein, A. H., Guenette, G. R., and Norton, R. J. G., 1984, ''The MIT Blowdown Turbine Facility,'' ASME Paper No. 84-GT-116.
[79] Doorly, J. E. and Oldfield, M. L. G., 1986, ''New Heat Transfer Gages for Use on Multilayered Substrates,'' ASME Paper No. 86-GT-96.
[80] Doorly, J. E., and Oldfield, M. L. G., 1987, ''The Theory of Advanced Multi-Layer Thin Film Heat Transfer Gages,'' Int. J. Heat Mass Transf., pp. 1159–1168.
[81] Doorly, J. E., 1987, ''Procedures for Determining Surface Heat Flux Using Thin Film Gages on a Coated Metal Model in a Transient Test Facility,'' ASME Paper No. 87-GT-85.
[82] Epstein, A. H., Guenette, G. R., Norton, R. J. G., and Yuzhang, C., 1986, ''High-Frequency Response Heat-Flux Gage,'' Rev. Sci. Instrum., **57**, No. 4, pp. 639–649 (see also AGARD-CPP-390, Bergen, Norway, May 1985).
[83] Hager, J. M., Simmons, S., Smith, D., Onishi, S., Langley, L. W., and Diller, T. E., 1991, ''Experimental Performance of a Heat Flux Microsensor,'' ASME J. Eng. Gas Turbines Power, **113**, pp. 246–250.
[84] Holmberg, D. G., and Diller, T. E., 1995, ''High-Frequency Heat Flux Sensor Calibration and Modeling,'' ASME J. Fluids Eng., **117**, pp. 659–664.
[85] Popp, O., Smith, D. E., Bubb, J. V., Grabowski, H. C., Diller, T. E., Schetz, J. A., and Ng, W., 1999, ''Steady and Unsteady Heat Transfer in a Transonic Film Cooled Turbine Cascade,'' ASME Paper No. 99-GT-259.
[86] Smith, D. E., Bubb, J. V., Popp, O., Grabowski, H., Diller, T. E., Schetz, J. A., and Ng, W. F., 2000, ''An Investigation of Heat Transfer in a Film Cooled Transonic Turbine Cascade, Part I: Steady Heat Transfer,'' ASME Paper No. 2000-GT-202.
[87] Popp, O., Smith, D. E., Bubb, J. V., Grabowski, H., Diller, T. E., Schetz, J. A., and Ng, W. F., 2000, ''An Investigation of Heat Transfer in a Film Cooled Transonic Turbine Cascade, Part I: Unsteady Heat Transfer,'' ASME Paper No. 2000-GT-203.
[88] Weaver, M. M., Moselle, J. R., Dunn, M. G., and Guenette, J. G., 1994, ''Reduction of Data From Heat-Flux Gages—A Documentation of the MIT ACQ Code and an Adaptation to Single-Sided Gages,'' Calspan Technical Report No. 7733-4.
[89] Goebel, S. G., Abuaf, N., Lovett, J. A., and Lee, C-P., 1993, ''Measurement of Combustor Velocity and Turbulence Profiles,'' ASME Paper No. 93-GT-228.
[90] Moss, R. W., and Oldfield, M. L. G., 1991, ''Measurement of Hot Combustor Turbulence Spectra,'' ASME Paper No. 91-GT-351.
[91] Mularz, E. J., and Schultz, D. F., 1974, ''Measurement of Liner Cooling Effectiveness Within a Full-Scale Double-Annular Ram-Induction Combustor,'' NASA TN D-7689.
[92] Marek, C. J., and Tacina, R. R., 1975, ''Effect of Free-Stream Turbulence on Film Cooling,'' NASA TN D-7958.
[93] Juhasz, A. J., and Marek, C. J., 1971, ''Combustor Liner Film Cooling in the Presence of High Free-Stream Turbulence,'' NASA TN D-6360.
[94] Kumar, G. N., Rettig, M. G., Mongia, H. C., and Chauvette, C. H., 1998, ''Automated Cooling Design Procedure for Combustor Walls,'' AIAA Paper No. 98–0836.
[95] Kumar, G. N., Moder, J. P., Mongia, H. C., and Prakash, C., 1998, ''Development of a Three Dimensional Radiative Heat Transfer Computational Methodology for Aircraft Engine Combustors,'' AIAA Paper No. 98–0855.
[96] Kumar, G. N., and Mongia, H. C., 2000, ''Validation of Near Wall Turbulence Models for Film Cooling Applications in Combustors,'' AIAA Paper No. 2000–0480.
[97] Kumar, G. N., Duncan, B. S., and Mongia, H. C., 2000, ''Assessment of Advanced Turbulence Models and Unstructured Code for Calculating the Film Effectiveness of a Modern Film Cooled Combustor,'' AIAA Paper No. 2000–0333.
[98] Mayle, R. E., Dullenkopf, K., and Schultz, A., 1998, ''The Turbulence That Matters,'' ASME J. Turbomach., **120**, pp. 402–409.
[99] Katsanis, T., and McNally, W. D., 1977, ''Revised FORTRAN Program for Calculating Velocities and Streamlines on the Hub-Shroud Mid-Channel Stream Surface of an Axial-, Radial-, or Mixed-Flow Turbomachine or Annular Duct,'' 1, User's Manual, Vol. II, Programmers Manual, NASA TN D-8430, 8431.
[100] Katsanis, T., 1969, ''FORTRAN Program for Calculating Transonic Velocities on a Blade-to-Blade Stream Surface of a Turbomachine,'' NASA TN D-5427.
[101] Eckert, E. R. G., and Drake, R. M., 1959, *Heat and Mass Transfer*, 2nd ed., McGraw-Hill, New York.
[102] Crawford, M. E., and Kays, W. M., 1976, ''STAN5—A Program for Numerical Computation of Two-Dimensional Internal and External Boundary Layer Flows,'' NASA CR-2742.
[103] Patankar, S.-V., and Spalding, D.-B., 1970, *Heat and Mass Transfer in Boundary Layers* ed., International Textbook Co., London.
[104] Dunn, M. G., Rae, W. J., and Holt, J. L., 1984, ''Measurement and Analysis of Heat Flux in a Turbine Stage: Part II—Discussion of Results and Comparison With Prediction,'' ASME J. Eng. Gas Turbines Power, **106**, pp. 234–240.
[105] Dunn, M. G., and Chupp, R. E., 1988, ''Time-Averaged Heat-Flux Distribu-

tions and Comparison With Prediction for the Teledyne 702 HP Turbine Stage,'' ASME J. Turbomach., **110**, pp. 51–56.
[106] Graham, R. W., 1979, ''Fundamental Mechanics That Influence the Estimate of Heat Transfer to Gas Turbine Blades,'' ASME Paper No. 79-HT-43.
[107] Dunn, M. G., Martin, H. L., and Stanek, M. J., 1986, ''Heat Flux and Pressure Measurements and Comparison With Prediction for a Low Aspect Ratio Turbine Stage,'' ASME J. Turbomach., **108**, pp. 108–115.
[108] Wood, J. R., 1981, ''Improved Methods for Calculating Transonic Velocities on Blade-to-Blade Stream Surfaces of a Turbomachine,'' NASA TP-1772.
[109] Boyle, R. J., Haas, J. E., and Katsanis, T., 1984, ''Comparison Between Measured Turbine Stage Performance and the Predicted Performance Using Quasi-3D Flow and Boundary Layer Analysis,'' NASA TM-83640.
[110] Zerkle, R. D., and Lounsbury, R. J., 1987, ''The Influence of Freestream Turbulence and Pressure Gradient on Heat Transfer to Gas Turbine Airfoils,'' AIAA Paper No. 87-1917.
[111] Rodi, W., and Scheuerer, G., 1985, ''Calculation of Heat Transfer to Convection-Cooled Gas Turbine Blades,'' ASME J. Eng. Gas Turbines Power, **107**, pp. 621–627.
[112] Lam, C. K. S., and Bremhorst, K., 1981, ''A Modified Form of the $k-\varepsilon$ Model for Predicting Wall Turbulence,'' ASME J. Fluids Eng., **103**, pp. 456–460.
[113] Gaugler, R. E., 1981, ''Some Modifications to, and Operation Experience With, the Two Dimensional, Finite-Difference, Boundary Layer Code, STAN 5,'' ASME Paper No. 81-GT-89.
[114] Goldman, L. J., and Gaugler, R. E., 1980, ''Prediction Method for Two-Dimensional Aerodynamic Losses of Cooled Vanes Using Integral Boundary-Layer Parameters,'' NASA TP-1623.
[115] Crawford, M. E., Kays, W. M., and Moffat, R. J., 1980, ''Full Coverage Film Cooling on Flat, Isothermal Surfaces: A Summary Report on Data and Predictions,'' NASA CR-3219 (see also ASME J. Eng. Power, 102, pp. 1006–1012).
[116] Crawford, M. E., Moffat, R. J., and Kays, W. M., 1980, ''Full-Coverage Film Cooling—Part I: Comparison of Heat Transfer Data for Three Injection Angles,'' ASME Paper No. 80-GT-37 and ''Part II: Heat Transfer Data and Numerical Simulation,'' ASME Paper No. 80-GT-43.
[117] Schmidt, R. C., and Patankar, S. V., 1991, ''Simulating Boundary Layer Transition With Low Reynolds Number $k-\varepsilon$ Models: Part 2: An Approach to Improving Predictions,'' ASME J. Turbomach., **113**, pp. 13–26.
[118] Harasgama, S. P., Tarada, F. H., Baumann, R., Crawford, M. E., and Neelakantan, S., 1993, ''Calculation of Heat Transfer to Turbine Blading Using Two-Dimensional Boundary Layer Methods,'' ASME Paper No. 93-GT-79.
[119] Arts, T., Lambert de Rouvroit, M., and Rutherford, A. W., 1990, ''Aero-Thermal Investigation of a Highly Loaded Transonic Linear Turbine Guide Vane Cascade,'' VKI Technical Note 174.
[120] Sharma, O. P., Nguyen, P., Ni, R. H., Rhie, C. M., White, J. A., and Finke, A. K., 1987, ''Aerodynamics and Heat Transfer Analysis of a Low Aspect Ratio Turbine,'' AIAA Paper No. 87–1916.
[121] Ni, R. H., 1982, ''A Multiple-Grid Scheme for Solving the Euler Equations,'' AIAA J., **20**, No. 11, pp. 1565–1571.
[122] Rhie, C. M., 1986, ''A Pressure Based Navier–Stokes Solver With the Multigrid Method,'' AIAA Paper No. 86–207.
[123] Vatsa, V. N., 1985, ''A Three-Dimensional Boundary Layer Analysis Including Heat Transfer and Blade Rotation Effects,'' presented at the 3rd Symposium on Numerical and Physical Aspects of Aerodynamic Flows, Long Beach, CA.
[124] Mayle, R. E., 1991, ''The Role of Laminar-Turbulent Transition in Gas Turbine Engines,'' ASME J. Turbomach., **113**, pp. 509–537.
[125] Mayle, R. E., and Dullenkopf, K., 1990, ''A Theory of Wake-Induced Transition,'' ASME J. Turbomach., **112**, pp. 188–195.
[126] Mayle, R. E., and Dullenkopf, K., 1991, ''More on the Turbulent-Strip Theory for Wake-Induced Transition,'' ASME J. Turbomach., **113**, pp. 428–432.
[127] Dring, R. P., Blair, M. F., and Joslyn, H. D., 1980, ''An Experimental Investigation of Film Cooling on a Turbine Rotor Blade,'' ASME J. Eng. Power, **102**, pp. 81–87.
[128] Dunn, M. G., 1984, ''Time-Resolved Heat-Flux Measurements for a Full-Stage Turbine,'' AFWAL-TR-84-2025.
[129] Dunn, M. G., George, W. K., Rae, W. J., Woodward, S. H., Moller, J. C., and Seymour, P. J., 1986, ''Heat-Flux Measurements for the Rotor of a Full-Stage Turbine: Part II—Description of Analysis Technique and Typical Time-Resolved Measurements,'' ASME J. Turbomach., **108**, pp. 98–107.
[130] Guenette, G. R., Epstein, A. H., Giles, M. B., Haimes, R., and Norton, R. J. G., 1988, ''Fully Scaled Transonic Turbine Rotor heat Transfer Measurements,'' ASME Paper No. 88-GT-171.
[131] Dunn, M. G., Seymour, P. J., Woodward, S. H., George, W. K., and Chupp, R. E., 1989, ''Phase-Resolved Heat-Flux Measurements on the Blade of a Full-Scale Rotating Turbine,'' ASME J. Turbomach., **111**, pp. 8–19.
[132] Kingcombe, R. C., Harasgama, S. P., Leversuch, N. P., and Wedlake, E. T., 1989, ''Aerodynamic and Heat Transfer Measurements on Blading for a High Rim-Speed Transonic Turbine,'' ASME Paper No. 89-GT-228.
[133] Dunn, M. G., 1990, ''Phase and Time-Resolved Measurements of Unsteady Heat Transfer and Pressure in a Full-Stage Rotating Turbine,'' ASME J. Turbomach., **112**, pp. 531–538.
[134] Abhari, R. S., Guenette, G. R., Epstein, A. H., and Giles, M. B., 1991, ''Comparison of Time-Resolved Turbine Rotor Blade Heat Transfer Measurements and Numerical Calculations,'' ASME Paper No. 91-GT-268.
[135] Hodson, H. P., 1983, ''Boundary Layer and Loss Measurements on the Rotor of an Axial-Flow Turbine,'' ASME Paper No. 83-GT-4.
[136] Hodson, H. P., 1984, ''Measurement of Wake Generated Unsteadiness in the Rotor Passages of Axial Flow Turbine,'' ASME Paper No. 84-GT-189.
[137] Hodson, H. P., 1984, ''Boundary-Layer Transition and Separation Near the Leading Edge of a High-Speed Turbine Blade,'' ASME Paper No. 84-GT-179.
[138] Binder, A., Forster, W., Kruse, H. and Rogge, H., 1984, ''An Experimental Investigation Into the Effect of Wakes on the Unsteady Turbine Rotor Flow,'' ASME Paper No. 84-GT-178.
[139] Doorly, D. J., Oldfield, M. L. G., and Scrivener, C. T. J., 1985, ''Wake Passing in a Turbine Rotor Cascade,'' AGARD Conference Preprint 390, Bergen, Norway.
[140] Doorly, D. J., and Oldfield, M. L. G., 1985, ''Simulation of the Effects of Shock Wave Passing on a Turbine Rotor Blade,'' ASME Paper No. 85-GT-112.
[141] Rigby, M. J., Johnson, A. B., Oldfield, M. L. G., and Jones, T. V., 1989, ''Temperature Scaling of Turbine Blade Heat Transfer With and Without Shock Wave Passing,'' *Proc. 9th International Symposium on Air Breathing Engines*, Athens, Greece.
[142] Hilditch, M. A., and Ainsworth, R. W., 1990, ''Unsteady Heat Transfer Measurements on a Rotating Gas Turbine Blade,'' ASME Paper No. 90-GT-175.
[143] Pfeil, H., and Eifler, J., 1976, ''Turbulenzverhaltnisse hinter rotierenden Zylindergittern,'' Forschung im Ingenieurwesen, **42**, pp. 27–32.
[144] Schulte, V., 1995, ''Unsteady Separated Boundary Layers in Axial-Flow Turbomachinery,'' Ph.D. Dissertation, Cambridge University, United Kingdom.
[145] Banieghbal, M. R., Curtis, E. M., Denton, J. D., Hodson, H. P., Huntsman, I., Schulte, V., Harvey, N. W., and Steele, A. B., 1995, ''Wake Passing in LP Turbine Blades,'' AGARD Conf. Proc., pp. 5–8 to 5–12.
[146] Cebeci, T., 1970, ''Calculation of Compressible Turbulent Boundary Layers With Heat and Mass Transfer,'' AIAA Paper No. 70–741.
[147] Ashworth, D. A., LaGraff, J. E., Schultz, D. L., and Grindrod, K. J., 1985, ''Unsteady Aerodynamic and heat Transfer Processes in a Transonic Turbine Stage,'' J. Eng. Mech., **107**, pp. 1022–1030.
[148] Denton, J. D., 1976, ''Extension of the Finite Area Time-Marching Method to Three Dimensions,'' von Karman Institute Lecture Series '84.
[149] Dawes, W. N., 1986, ''A Numerical Method for the Analysis of Three-Dimensional Viscous Compressible Flows in Turbine Cascades: Application to Secondary Flow Development in a Cascade With and Without Dihedral,'' ASME Paper No. 86-GT-145.
[150] Rao, K. V., Delaney, R. A., and Dunn, M. G., 1994, ''Vane–Blade Interaction in a Transonic Turbine, Part II—Heat Transfer,'' J. Propul. Power, **10**, No. 3, pp. 312–317.
[151] Lokay, V. I., and Trushin, V. A., 1970, ''Heat Transfer From the Gas and Flow-Passage Elements of a Rotating Gas Turbine,'' Heat Transfer—Sov. Res., **2**, No. 4, pp. 108–115.
[152] Scholz, N., 1978, ''Aerodynamics of Cascades,'' AGARD–AG–229.
[153] Denton, J. D., 1993, ''Loss Mechanisms in Turbomachines,'' ASME Paper No. 93-GT-435.
[154] Graziani, R. A., Blair, M. F., Taylor, J. R., and Mayle, R. E., 1980, ''An Experimental Study of Endwall and Airfoil Surface Heat Transfer in a Large Scale Turbine Blade Cascade,'' ASME J. Eng. Power, **102**, pp. 257–267.
[155] Consigny, H. and Richards, B. E., 1981, ''Short Duration Measurements of Heat Transfer Rate to a Gas Turbine Rotor Blade,'' ASME Paper No. 81-GT-146.
[156] Jones, W. P., and Launder, B. E., 1972, ''The Prediction of Laminarization With a Two-Equation Model of Turbulence,'' Int. J. Heat Mass Transf., **15**, pp. 301–314.
[157] Joe, C. R., Montesdeoca, X. A., Soechting, F. O., MacArthur, C. D., and Meininger, M., 1998, ''High Pressure Turbine Vane Annular Cascade Heat Flux and Aerodynamic Measurements With Comparisons to Prediction,'' ASME Paper No. 98-GT-430.
[158] Sharma, O. P., 1987, ''Momentum and Thermal Boundary Layer Development on Turbine Airfoil Suction Surfaces,'' AIAA Paper No. 87–1918.
[159] Chima, R. V., and Yokota, J. W., 1990, ''Numerical Analysis of Three-Dimensional Internal Flows,'' AIAA J., **28**, No. 5, pp. 798–806.
[160] Chima, R. V., 1991, ''Viscous Three-Dimensional Calculation of Transonic Fan Performance,'' presented at the AGARD Propulsion and Energetics Symposium on Computational Fluid Mechanics for Propulsion, San Antonio, TX.
[161] Giel, P. W., Bunker, R. S., Van Flossen, G. J., and Boyle, R. J., 2000, ''Heat Transfer Measurements and Predictions on a Power Generation Gas Turbine Blade,'' ASME Paper No. 2000-GT-209.
[162] Kirsten, T. J., Lippert, A. M., Snedden, G. C., and Smith, G. D. J., 1996, ''Experimental Measurement and CFD Prediction of Heat Transfer to a Nozzle Guide Vane,'' ASME Paper No. 96-GT-237.
[163] Bunker, R. S., 1997, ''Separate and Combined Effects of Surface Roughness and Turbulence Intensity on Vane Heat Transfer,'' ASME Paper No. 97-GT-135.
[164] Johnson, A. B., Oldfield, M. L. G., Rigby, M. J., and Giles, M. B., 1990, ''Nozzle Guide Vane Shock Wave Propagation and Bifurcation in a Transonic Turbine Rotor,'' ASME Paper No. 90-GT-310.
[165] Sato, T., and Takeishi, K., 1987, ''Investigation of the Heat Transfer in High Temperature Gas Turbine Vanes,'' ASME Paper No. 87-GT-137.
[166] Blair, M. F., 1974, ''An Experimental Study of Heat Transfer and Film Cooling on Large-Scale Turbine Endwalls,'' ASME J. Heat Transfer, **96**, pp. 524–529.
[167] York, R. E., Hylton, L. D., and Mihelc, M. S., 1983, ''An Experimental Investigation of Endwall Heat Transfer and Aerodynamics in a Linear Vane Cascade,'' ASME Paper No. 83-GT-52.
[168] Kumar, G. N., Jenkins, R. M., and Sahu, U., 1985, ''Regionally Averaged Endwall Heat Transfer Correlations for a Linear Vane Cascade,'' ASME Paper No. 85-GT-19.
[169] Ha, C., 1989, ''Numerical Study of Three-Dimensional Flow and Heat Transfer Near the Endwall of a Turbine Blade Row,'' AIAA Paper No. 89–1689.
[170] Arts, T., and Heider, R., 1994, ''Aerodynamic and Thermal Performance of a

Three Dimensional Annular Transonic Nozzle Guide Vane. Part I: Experimental Investigation,'' AIAA Paper No. 94-2929.
[171] Spencer, M. C., Lock, G. D., and Jones, T. V., 1995, ''Endwall Heat Transfer and Aerodynamic Measurements in an Annular Cascade of Nozzle Guide Vanes,'' ASME Paper No. 95-GT-356.
[172] Boyle, R. J., and Jackson, R., 1997, ''Heat Transfer Predictions for Two Turbine Nozzle Geometries at High Reynolds and Mach Numbers,'' ASME J. Turbomach., **119**, pp. 270–283.
[173] Giel, P. W., Thurman, D. R., Van Fossen, G. J., Hippensteele, S. A., and Boyle, R. J., 1998, ''Endwall Heat Transfer Measurements in a Transonic Turbine Cascade,'' ASME J. Turbomach., **120**, pp. 305–313.
[174] Kang, M. B., Kohli, A., and Thole, K. A., 1999, ''Heat Transfer and Flowfield Measurements in the Leading Edge Region of a Stator Vane Endwall,'' ASME J. Turbomach., **121**, pp. 558–568.
[175] Blair, M. F., 1982, ''Influence of Free-Stream Turbulence on Boundary-Layer Transition in Favorable Pressure Gradients,'' ASME J. Eng. Power, **104**, pp. 743–750.
[176] Arnone, A., Liou, M.-S., and Povinelli, L. A., 1992, ''Navier-Stokes Solution of Transonic Cascade Flows Using Non-periodic C-Type Grids,'' J. Propul. Power, **8**, No. 2, pp. 410–417.
[177] Bellows, W. J., and Mayle, R. E., 1986, ''Heat Transfer Downstream of a Leading Edge Separation Bubble,'' ASME Paper No. 86-GT-59.
[178] Gorla, R. S. R., 1986, ''Combined Influence of Unsteady Free Stream Velocity and Free Stream Turbulence on Stagnation Point Heat Transfer,'' Int. J. Turbo Jet Engines, **3**, pp. 117–123.
[179] Taulbee, D. B., Tran, L. T., and Dunn, M. G., 1988, ''Stagnation Point and Surface Heat Transfer for a Turbine Stage: Prediction and Comparison With Data,'' ASME Paper No. 88-GT-30.
[180] Hanford, A. J., and Wilson, D. E., 1994, ''The Effect of a Turbulent Wake on the Stagnation Point: Part II—Heat Transfer Results,'' ASME J. Turbomach., **116**, pp. 46–56.
[181] Funazaki, K., 1996, ''Studies on Wake-Affected Heat Transfer Around the Circular Leading Edge of Blunt Body,'' ASME J. Turbomach., **118**, pp. 452–460.
[182] Benner, M. W., Sjolander, S. A., and Moustapha, S. H., 1997, ''Influence of Leading-Edge Geometry on Profile Losses in Turbines at Off-Design Incidence: Experimental Results and an Improved Correlation,'' ASME J. Turbomach., **119**, pp. 193–200.
[183] Abuaf, N., Dorri, B., Lee, C. P., and Flodman, D. A., 1997, ''Stagnation Point Heat Transfer With a Thermal Barrier Coated Cylinder,'' ASME Paper No. 97-GT-385.
[184] Brenner, M. W., Sjolander, S. A., and Moustapha, S. H., 1997, ''Influence of Leading-Edge Geometry on Profile Losses in Turbines at Off-Design Incidence: Experimental Results and an Improved Correlation,'' ASME J. Turbomach., **119**, pp. 193–200.
[185] Maslov, V. P., Mineev, B. I., Pichkov, K. N., Secundov, A. N., Vorobiev, A. N., Strelets, M. Kh., and Travin, A. K., 1999, ''Turbulence Intensity, Length Scale, and Heat Transfer Around Stagnation Line of Cylinder and Model Blade,'' ASME Paper No. 99-GT-423.
[186] Rae, W. J., Taulbee, D. B., Civinskas, K. C., and Dunn, M. G., 1988, ''Turbine-Stage Heat Transfer: Comparison of Short-Duration Measurements With State-of-the-Art Predictions,'' J. Propul. Power, **4**, No. 6, pp. 541–548.
[187] Dunn, M. G., Haldeman, C. W., Abhari, R. S., and McMillan, M. L., 2000, ''Influence of Vane/Blade Spacing on the Heat Flux for a Transonic Turbine,'' ASME J. Turbomach., **122**, pp. 684–691.
[188] Zilles, D. A., and Abhari, R. S., 1999, ''Influence of Non-Isothermal Button Gage Surface Temperature in Heat Flux Measurement Applications,'' Proc. IMECE99, Nashville, TN.
[189] Bergholz, R. F., Dunn, M. G., and Steuber, G. D., 2000, ''Rotor/Stator Heat Transfer Measurements and CFD Predictions for Short-Duration Turbine Rig Tests,'' ASME Paper No. 2000-GT-208.
[190] Narcus, A. R., Przirembel, H. R., and Soechting, F. O., 1996, ''Evaluation of the External Heat Transfer Coefficient in the High-Pressure Turbine of a Full-Scale Core Engine,'' ASME Paper No. 96-GT-172.
[191] Soechting, F. O., and Sharma, O. P., 1988, ''Design Code Verification of External Heat Transfer Coefficients Around a Turbine Airfoil,'' AIAA Paper No. 88–3011.
[192] Tran, L. T., and Taulbee, D. B., 1991, ''Prediction of Unsteady Rotor-Surface Pressure and Heat Transfer From Wake Passings,'' ASME Paper No. 91-GT-267.
[193] Dunn, M. G., and Haldeman, C. W., 1995, ''Phase-Resolved Surface Pressure and Heat Transfer Measurements on the Blade of a Two-Stage Turbine,'' ASME J. Fluids Eng., **117**, pp. 653–658.
[194] Bunker, R. S., 2000, ''A Review of Turbine Blade Tip Heat Transfer,'' presented at Turbine 2000 International Symposium on Heat Transfer in Gas Turbine Systems, Izmir, Turkey.
[195] Metzger, D. E., and Rued, K., 1989, ''The influence of Turbine Clearance Gap Leakage on Passage Velocity and Heat Transfer Near Blade Tips: Part I—Sink Flow Effects on Blade Pressure Side,'' ASME J. Turbomach., **111**, pp. 284–292; ''Part II—Source Flow Effects on Blade Suction Sides,'' ASME J. Turbomach., **111**, pp. 293–300.
[196] Booth, T. C., Dodge, P. R., and Hepworth, H. K., 1982, ''Rotor-Tip Leakage: Part I—Basic Methodology,'' ASME J. Eng. Power, **104**, pp. 154–161.
[197] Wadia, A. R., and Booth, T. C., 1982, ''Rotor Tip Leakage: Part 2—Design Optimization Through Viscous Analysis and Experiment,'' ASME J. Eng. Power, **104**, pp. 162–169.
[198] Sjolander, S. A., and Cao, D., 1995, ''Measurements of the Flow in an Idealized Turbine Tip Gap,'' ASME J. Turbomach., **117**, pp. 578–584.
[199] Yaras, M. I., and Sjolander, S. A., 1991, ''Effects of Simulated Rotation on Tip Leakage in a Planar Cascade of Turbine Blades,'' ASME Paper No. 91-GT-127.
[200] Basson, A., and Lakshminarayana, B., 1995, ''Numerical Simulation of Tip Clearance Effects in Turbomachinery,'' ASME J. Turbomach., **117**, pp. 348–359.
[201] Mayle, R. E., and Metzger, D. E., 1982, ''Heat Transfer at the Tip of an Unshrouded Turbine Blade,'' *Proc. 7th International Heat Transfer Conference*, Vol. 3, pp. 87–92.
[202] Heyes, F. J. G., and Hodson, H. P., 1992, ''The Measurement and Prediction of the Tip Clearance Flow in Linear Turbine Cascades,'' ASME Paper No. 92-GT-214.
[203] Ameri, A. A., Steinthorsson, E., and Rigby, D. L., 1998, ''Effect of Squealer Tip on Rotor Heat Transfer and Efficiency,'' ASME J. Turbomach., **120**, pp. 753–759.
[204] Bindon, J. P., 1986, ''Pressure and Flowfield Measurements of Axial Turbine Tip Clearance Flow in a Linear Cascade,'' Cambridge University Engineering Department, TR 123.
[205] Allen, H. W., and Kofskey, M. G., 1955, ''Visualization Studies of Secondary Flows in Turbine Rotor Tip Regions,'' NACA TN 3519.
[206] Chyu, M. K., Metzger, D. E., and Hwan, C. L., 1987, ''Heat Transfer in Shrouded Rectangular Cavities,'' J. Thermophys. Heat Transfer, **1**, No. 3, pp. 247–252.
[207] Chyu, M. K., Moon, H. K., and Metzger, D. E., 1989, ''Heat Transfer in the Tip Region of Grooved Blades,'' ASME J. Turbomach., **111**, pp. 131–138.
[208] Metzger, D. E., Bunker, R. S., and Chyu, M. K., 1989, ''Cavity Heat Transfer on a Transverse Grooved Wall in a Narrow Flow Channel,'' ASME J. Heat Transfer, **111**, pp. 73–79.
[209] Dunn, M. G., and Haldeman, C. W., 2000, ''Time-Averaged Heat Flux for a Recessed Tip, Lip, and Platform of a Transonic Turbine Blade,'' ASME J. Turbomach., **122**, pp. 692–698.
[210] Bunker, R. S., Bailey, J. C., and Ameri, A., 1999, ''Heat Transfer and Flow on the First Stage Blade Tip of a Power Generation Gas Turbine, Part I: Experimental Results,'' NASA TM 1999-209152.
[211] Ameri, A. A., and Bunker, R. S., 2000, ''Heat Transfer and Flow on the First Stage Blade Tip of a Power Generation Gas Turbine. Part 2: Simulation Results,'' ASME J. Turbomach., **122**, pp. 272–277.
[212] Rigby, D. L., Ameri, A. A., and Steinthorsson, E., 1996, ''Internal Passage Heat Transfer Prediction Using Multiblock Grids and $k-\omega$ Turbulence Model,'' ASME Paper No. 96-GT-188.
[213] Metzger, D. E., Dunn, M. G., and Hah, C., 1991, ''Turbine Tip and Shroud Heat Transfer,'' ASME J. Turbomach., **113**, pp. 502–507.
[214] Ameri, A. A., and Steinthorsson, E., 1996, ''Analysis of Gas Turbine Rotor Blade Tip and Shroud Heat Transfer,'' ASME Paper No. 96-GT-189.
[215] Ameri, A. A., and Steinthorsson, E., 1995, ''Prediction of Unshrouded Rotor Blade Tip Heat Transfer,'' ASME Paper No. 95-GT-142.
[216] Dunn, M. G., Rae, W. J., and Holt, J. L., 1984, ''Measurement and Analysis of Heat Flux Data in a Turbine Stage: Part II—Discussion of Results and Comparison With Predictions,'' ASME J. Eng. Gas Turbines Power, **106**, pp. 234–240.
[217] Dunn, M. G., Kim, J., Civinskas, K. C., and Boyle, R. J., 1994, ''Time-Averaged Heat Transfer and Pressure Measurements and Comparison With Prediction for a Two-Stage Turbine,'' ASME J. Turbomach., **116**, pp. 14–22.
[218] Epstein, A. H., Guenette, G. R., and Norton, R. J. G., 1985, ''Time Resolved Measurements of a Turbine Rotor Stationary Tip Casing Pressure and Heat Transfer Field,'' AIAA Paper No. 85–1220.
[219] Dunn, M. G., and Kim, J., 1995, ''Turbine Blade Platform, Blade Tip and Shroud Heat Transfer,'' Proc. Int. Soc. Airbreathing Engines, Melbourne, Australia.
[220] Dunn, M. G., 1990, ''Phase and Time-Resolved Measurements of Unsteady Heat Transfer and Pressure in a Full-Stage Rotating Turbine,'' ASME J. Turbomach., **112**, pp. 531–538.
[221] Hawthorne, W. R., 1951, ''Secondary Circulation in Fluid Flow,'' Proc. R. Soc. London, Ser. A, **206**, pp. 374–387.
[222] Lakshminarayana, B., and Horlock, J. H., 1973, ''Generalized Expressions for Secondary Vorticity Using Intrinsic Co-Ordinates,'' J. Fluid Mech., **59**, pp. 97–115.
[223] Kerrebrock, J. L., and Mikolajczak, A. A., 1970, ''Intra-Stator Transport of Rotor Wakes and Its Effect on Compressor Performance,'' ASME J. Eng. Power, **92**, pp. 359–369.
[224] Saxer, A. P., and Giles, M. B., 1994, ''Predictions of Three-Dimensional Steady and Unsteady Inviscid Transonic Stator/Rotor Interaction With Inlet Radial Temperature Nonuniformity,'' ASME J. Turbomach., **116**, pp. 347–357.
[225] Dorney, D. J., and Schwab, J. R., 1995, ''Unsteady Numerical Simulations of Radial Temperature Profile Redistribution in a Single-Stage Turbine,'' ASME J. Turbomach., **118**, pp. 783–791.
[226] Saxer, A. P., and Felici, H. M., 1996, ''Numerical Analysis of Three-Dimensional Unsteady Hot Streak Migration and Shock Interaction in a Turbine Stage,'' ASME J. Turbomach., **118**, pp. 268–277.
[227] Dorney, D. J., and Sondak, D. L., 1996, ''Study of Hot Streak Phenomena in Subsonic and Transonic Flows,'' ASME Paper No. 96-GT-98.
[228] Gundy-Burlet, K. and Dorney, D. J., 1997, ''Influence of 3D Hot Streaks on Turbine Heat Transfer,'' ASME Paper No. 97-GT-422.
[229] Shang, T., and Epstein, A. H., 1996, ''Analysis of Hot Streak Effects on Turbine Rotor Load,'' ASME J. Turbomach., **119**, pp. 544–553.
[230] Bohn, D., Funke, H., and Gier, J., 1999, ''Numerical and Experimental Inves-

tigations on the Flow in a 4-Stage Turbine With Special Focus on the Development of a Radial Temperature Streak,'' ASME Paper No. 99-GT-27.
[231] Boyle, R. J., and Giel, P. W., 1997, ''Prediction of Nonuniform Inlet Temperature Effects on Vane and Rotor Heat Transfer,'' ASME Paper No. 97-GT-133.
[232] Saxer, A. P., 1992, ''A Numerical Analysis of Three-Dimensional Inviscid Stator Rotor Interactions Using Non-reflecting Boundary Conditions,'' Ph.D. Thesis, Dept. of Aeronautics and Astronautics, MIT, Cambridge, MA.
[233] Shang, T., 1995, ''Influence of Inlet Temperature Distortion on Turbine Heat Transfer,'' Ph.D. Thesis, Dept. of Aeronautics and Astronautics, MIT, Cambridge, MA.
[234] Shang, T., Guenette, G. R., Epstein, A. H., and Saxer, A. P., 1995, ''The Influence of Inlet Temperature Distortion on Rotor Heat Transfer in a Transonic Turbine,'' AIAA Paper No. 95-3042.
[235] Orkwis, P. D., Turner, M. G., and Barter, J. W., 2000, ''Linear Deterministic Source Terms for Hot Streak Simulations,'' ASME Paper No. 2000-GT-509.
[236] Butler, T. L., Sharma, O. P., Joslyn, H. D., and Dring, R. P., 1989, ''Redistribution of an Inlet Temperature Distortion in an Axial Flow Turbine Stage,'' J. Propul. Power, **5**, pp. 64–71.
[237] Roback, R. J., and Dring, R. P., 1992, ''Hot Streaks and Phantom Cooling in a Turbine Rotor Passage. Part I—Separate Effects,'' ASME Paper No. 92-GT-75; and ''Part II—Combined Effects and Analytical Modeling,'' ASME Paper No. 92-GT-76.
[238] Garg, V. K., and Abhari, R. S., 1996, ''Comparison of Predicted and Experimental Nusselt Number for a Film Cooled Rotating Blade,'' ASME Paper No. 96-GT-223 (see also ''Comparison of Predicted and Experimental Nusselt Number for a Film Cooled Rotating Blade,'' Int. J. Heat Fluid Flow, **18**, No. 5, pp. 452–460).
[239] Dorney, D. J., and Gundy-Burlet, K., 1995, ''Hot-Streak Clocking Effects in a 1-1/2 Stage Turbine,'' ASME Paper No. 95-GT-202.
[240] Dorney, D. J., and Sharma, O. P., 1996, ''A Study of Turbine Performance Increases Through Airfoil Clocking,'' AIAA Paper No. 96–2816.
[241] Huber, F. W., Johnson, P. D., Sharma, O. P., Staubach, J. B., and Gaddis, S. W., 1996, ''Performance Improvement Through Indexing of Turbine Airfoils: Part I—Experimental Investigation,'' ASME J. Turbomach., **118**, pp. 630–635.
[242] Griffin, L. W., Huber, F. W., and Sharma, O. P., 1996, ''Performance Improvement Through Indexing of Turbine Airfoils: Part 2—Numerical Simulation,'' ASME J. Turbomach., **118**, pp. 636–642.
[243] Eulitz, F., Engel, K., and Gebing, H., 1996, ''Numerical Investigation of the Clocking Effects in a Multistage Turbine,'' ASME Paper No. 96-GT-26.
[244] Gundy-Burlet, K., and Dorney, D. J., 1997, ''Physics of Airfoil Clocking in Axial Compressors,'' ASME Paper No. 97-GT-444.
[245] Johnson, D. A., and Fleeter, S., 1999, ''Turbine Blade Unsteady Heat Transfer Change Due to Stator Indexing,'' ASME Paper No. 99-GT-376.
[246] Tiedemann, M., and Kost, F., 2000, ''Some Aspects of Wake–Wake Interactions Regarding Turbine Stator Clocking,'' ASME J. Turbomach., **123**, pp. 526–533.
[247] Kercher, D. M., 1998, ''A Film Cooling CFD Bibliography: 1971-1996,'' Int. J. Rotating Mach., **4**, No. 1, pp. 61–72.
[248] Kercher, D. M., 2000, ''Turbine Airfoil Leading Edge Film Cooling Bibliography: 1972-1998,'' Int. J. Rotating Mach., **6**, No. 5, pp. 313–319.
[249] Bohn, D., Kusterer, K., and Schonenborn, H., 1996, ''Three-Dimensional Numerical Simulation of the Flow Through a Turbine Blade Cascade With Cooling Injection at the Leading Edge,'' ASME Paper No. 96-GT-150.
[250] Bohn, D. E., Becker, V. J., and Rungen, A. U., 1997, ''Experimental and Numerical Conjugate Flow and Heat Transfer Investigation of a Shower-Head Cooled Turbine Guide Vane,'' ASME Paper No. 97-GT-15.
[251] Bohn, D. E., and Kusterer, K. A., 1999, ''Aerothermal Investigations of Mixing Flow Phenomena in Case of Radially Inclined Ejection Holes at the Leading Edge,'' ASME J. Turbomach., **122**, pp. 334–339.
[252] Friedrichs, S., Hodson, H. P., and Dawes, W. N., 1996, ''Aerodynamic Aspects of Endwall Film Cooling,'' ASME J. Turbomach., **119**, pp. 786–793.
[253] Friedrichs, S., Hodson, H. P., and Dawes, W. N., 1999, ''The Design of an Improved Endwall Film Cooling Configuration,'' ASME J. Turbomach., **121**, pp. 772–780.
[254] Leylek, J. H, and Zerkle, R. D., 1994, ''Discrete-Jet Film Cooling: A Comparison of Computational Results With Experiments,'' ASME J. Turbomach., **116**, pp. 358–368.
[255] Hyams, D. G., McGovern, K. T., and Leylek, J. H., 1996, ''Effects of Geometry on Slot-Jet Film Cooling Performance,'' ASME Paper No. 96-GT-187.
[256] Brittingham, R. A., and Leylek, J. H., 2000, ''A Detailed Analysis of Film Cooling Physics: Part IV—Compound-Angle Injection With Shaped Holes,'' ASME J. Turbomach., **122**, pp. 133–145.
[257] Drost, U., Bolcs, A., and Hoffs, A., 1997, ''Utilization of the Transient Liquid Crystal Technique for Film Cooling Effectiveness and Heat Transfer Investigations on a Flat Plate and a Turbine Airfoil,'' ASME Paper No. 97-GT-26.
[258] Reiss, H., and Bolcs, A., 2000, ''Experimental Study of Showerhead Cooling on a Cylinder Comparing Several Configurations using Cylindrical and Shaped Holes,'' ASME J. Turbomach., **122**, pp. 162–170.
[259] Martiny, M., Schulz, A., Wittig, S., and Dilzer, M., 1997, ''Influence of a Mixing-Jet on Film Cooling,'' ASME Paper No. 97-GT-247.
[260] Thole, K., Gritsch, M., Schulz, A., and Wittig, S., 1998, ''Flowfield Measurements for Film Cooling Holes With Expanded Exits,'' ASME J. Turbomach., **120**, pp. 327–336.
[261] Wittig, S., Schulz, A., Gritsch, M., and Thole, K. A., 1996, ''Transonic Film Cooling Investigations: Effects of Hole Shapes and Orientations,'' ASME Paper No. 96-GT-222.
[262] Andrews, G. E., Asere, A. A., Mkpadi, M. C., and Tirmahi, A., 1986, ''Transpiration Cooling: Contribution of Film Cooling to the Overall Cooling Effectiveness,'' ASME Paper No. 86-GT-136.
[263] Bazdidi-Tehrani, F., and Andrews, G. E., 1997, ''Full Coverage Discrete Hole Film Cooling: Investigation of the Effect of Variable Density Ratio (Part II),'' ASME Paper No. 97-GT-341.
[264] Goldstein, R. J., and Yoshida, T., 1982, ''The Influence of a Laminar Boundary Layer and Laminar Injection on Film Cooling Performance,'' ASME J. Heat Transfer, **104**, pp. 355–362.
[265] Cho, H. H., and Goldstein, R. J., 1997, ''Total-Coverage Discrete Hole Wall Cooling,'' ASME J. Turbomach., **119**, pp. 320–329.
[266] Burd, S. W., Kaszeta, R. W., and Simon, T. W., 1998, ''Measurements in Film Cooling Flows: Hole L/D and Turbulence Intensity Effects,'' ASME J. Turbomach., **120**, pp. 791–798.
[267] Berhe, M. K., and Patankar, S. V., 1999, ''Investigation of Discrete-Hole Film Cooling Parameters Using Curved-Plate Models,'' ASME J. Turbomach., **121**, pp. 792–803.
[268] Louis, J. F., 1975, ''Shock Tunnel Studies of Heat Transfer and Film Cooling Effectiveness,'' Proc. Tenth International Shock Tube Symposium, Kyoto, Japan.
[269] Abhari, R. S., and Epstein, A. H., 1992, ''An Experimental Study of Film Cooling in a Rotating Transonic Turbine,'' ASME Paper No. 92-GT-201.
[270] Jones, T. V., and Schultz, D. L., 1971, ''Film Cooling Studies in Subsonic and Supersonic Flows Using a Shock Tunnel,'' Proc. Eighth International Shock Tube Symposium, London, U. K.
[271] Byerley, A. R., Ireland, P. T., Jones, T. V., and Ashton, S. A., 1988, ''Detailed Heat Transfer Measurements Near and Within the Entrance of a Film Cooling Hole,'' ASME Paper No. 88-GT-155.
[272] Day, C. R. B., Oldfield, M. L. G., and Lock, G. D., 1999, ''The Influence of Film Cooling on the Efficiency of an Annular Nozzle Guide Vane Cascade,'' ASME J. Turbomach., **121**, pp. 145–151.
[273] Yavuzkurt, S., 1985, ''Full-Coverage Film Cooling: A One-Equation Model of Turbulence for the Calculation of the Full-Coverage and the Recovery-Region Hydrodynamics,'' ASME Paper No. 85-GT-119.
[274] Chernobrovkin, A., and Lakshminarayana, B., 1999, ''Numerical Simulation and Aerothermal Physics of Leading Edge Film Cooling,'' Proc. Inst. Mech. Eng., **213**, Part A, pp. 103–118.
[275] Uzol, O., and Camci, C., 2001, ''Aerodynamic Loss Characteristics of a Turbine Blade With Trailing Edge Coolant Ejection. Part 2; External Aerodynamics, Total Pressure Losses and Predictions,'' ASME J. Turbomach., **123**, pp. 238–338.
[276] Sen, B., Schmidt, D. L., and Bogard, D. G., 1996, ''Film Cooling With Compound Angle Holes: Heat Transfer,'' ASME J. Turbomach., **118**, pp. 800–806.
[277] Koli, A., and Bogard, D. G., 1998, ''Effects of Very High Free-Stream Turbulence on the Jet-Mainstream Interaction in a Film Cooling Flow,'' ASME J. Turbomach., **120**, pp. 785–790.
[278] Mehendale, A. B., and Han, J. C., 1992, ''Influence of High Mainstream Turbulence Leading Edge Film Cooling Heat Transfer,'' ASME J. Turbomach., **114**, pp. 707–715.
[279] Ekkad, S. V., Han, J. C., and Du, H., 1988, ''Detailed Film Cooling Measurements on a Cylindrical Leading Edge Model: Effect of Free-Stream Turbulence and Coolant Density,'' ASME J. Turbomach., **120**, pp. 799–806.
[280] Ekkad, S. V., Mehendale, A. B., Han, J. C., and Lee, C. P., 1997, ''Combined Effect of Grid Turbulence and Unsteady Wake on Film Effectiveness and Heat Transfer Coefficient of a Gas Turbine Blade With Air and CO_2 Film Injection,'' ASME J. Turbomach., **119**, pp. 594–600.
[281] Ligrani, P. M., and Mitchell, S. W., 1994, ''Effects of Embedded Vortices on Injectant From Film Cooling Holes With Large Spanwise Spacing and Compound Angle Orientations in a Turbulent Boundary Layer,'' ASME J. Turbomach., **116**, pp. 709–720.
[282] Ligrani, P. M., and Ramsey, A. E., 1997, ''Film Cooling From Spanwise-Oriented Holes in Two Staggered Rows,'' ASME J. Turbomach., **119**, pp. 562–567.
[283] Ligrani, P. M., Gong, R., and Cuthrell, J. M., 1997, ''Bulk Flow Pulsations and Film Cooling: Flow Structure Just Downstream of the Holes,'' ASME J. Turbomach., **119**, pp. 568–573.
[284] Lemmon, C. A., Kohli, A., and Thole, K. A., 1999, ''Formation of Counterrotating Vortices in Film Cooling Flows,'' ASME Paper No. 99-GT-161.
[285] Wilfert, G., and Fottner, L., 1996, ''The Aerodynamic Mixing Effect of Discrete Cooling Jets With Mainstream Flow on a Highly Loaded Turbine Blade,'' ASME J. Turbomach., **118**, pp. 468–478.
[286] Hoecker, R., Johnson, B. V., and Hausladen, J., 1999, ''Impingement Cooling Experiments With Flat Plate and Pin Plate Target Surfaces,'' ASME Paper No. 99-GT-252.
[287] Abuaf, N., and Cohn, A., 1988, ''Gas Turbine Heat Transfer With Alternate Cooling Flows,'' ASME Paper No. 88-GT-16.
[288] Buck, F. A., and Prakash, C., 1995, ''Design and Evaluation of a Single Passage Test Model to Obtain Turbine Airfoil Film Cooling Effectiveness Data,'' ASME Paper No. 95-GT-19.
[289] Bunker, R. S., 2000, ''Effect of Partial Coating Blockage on Film Cooling Effectiveness,'' ASME Paper No. 2000-GT-244.
[290] Takeishi, K., Aoki, S., Sato, T., and Tsukagoshi, K, 1991, ''Film Cooling on a Gas Turbine Rotor Blade,'' ASME Paper No. 91-GT-279.
[291] Heidmann, J. D., 1995, ''A Numerical Study of the Effect of Wake Passing on Turbine Blade Film Cooling,'' AIAA Paper No. 95–3044.
[292] Garg, V. K., 1999, ''Heat Transfer on a Film Cooled Rotating Blade,'' ASME Paper No. 99-GT-44 (see also ''Heat Transfer on a Film Cooled Rotating Blade,'' Int. J. Heat Fluid Flow, 21, 2000, pp. 134–145).

[293] Rigby, M. J., Johnson, A. B., and Oldfield, M. L. G., 1990, ''Gas Turbine Rotor Blade Film Cooling With and Without Simulated NGV Shock Waves and Wakes,'' ASME Paper No. 90-GT-78.
[294] Lander, R. D., Fish, R. W., and Suo, M., 1972, ''External Heat Transfer Distribution on Film Cooled Turbine Vanes,'' J. Aircr., **9**, No. 10, pp. 707–714.
[295] Elovic, E., and Koffel, W. K., 1983, ''Some Considerations in the Thermal Design of Turbine Airfoil Cooling Systems,'' Int. J. Turbo Jet-Engines, **1**, pp. 45–65.
[296] Miller, K. L., and Crawford, M. E., 1984, ''Numerical Simulation of Single, Double, and Multiple Row Film Cooling Effectiveness and Heat Transfer,'' ASME Paper No. 84-GT-112.
[297] Tafti, D. K., and Yavuzkurt, S., 1987, ''Prediction of Heat Transfer Characteristics for Discrete Hole Film Cooling for Turbine Blade Applications,'' ASME J. Turbomach., **109**, pp. 504–511.
[298] Neelakantan, S., and Crawford, M. E., 1995, ''Prediction of Film Cooling Effectiveness and Heat Transfer Due to Streamwise and Compound Angle Injection on Flat Surfaces,'' ASME Paper No. 95-GT-151.
[299] Neelakantan, S., and Crawford, M. E., 1996, ''Prediction of Effectiveness and Heat Transfer Using a New Two-Dimensional Injection and Dispersion Model of the Film Cooling Process,'' ASME Paper No. 96-GT-224.
[300] Weigand, B., Bonhoff, B., and Ferguson, J. R., 1997, ''A Comparative Study Between 2D Boundary Layer Predictions and 3D Navier-Stokes Calculations for a Film Cooled Vane,'' ASME National Heat Transfer Conference, ASME HTD-Vol. 350, pp. 213–221.
[301] Rivir, R. B., Roqumore, W. M., and McCarthy, J. W., 1987, ''Visualization of Film Cooling Flows Using Laser Sheet Light,'' AIAA Paper No. 87-1914.
[302] Gogineni, S. P., Trump, D. D., Rivir, R. B., and Pestian, D. J., 1996, ''PIV Measurements of Periodically Forced Flat Plate Film Cooling Flows With High Free Stream Turbulence,'' ASME Paper No. 96-GT-236.
[303] Rivir, R. B., and Gogineni, S. P., 1996, ''Characteristics of Simulated Turbine Film Cooling Flows,'' Proc. Int. Congress on Fluid Dynamics and Propulsion, Cairo, Egypt, Vol. 1, pp. 95–107.
[304] Rivir, R. B., Gogineni, S. P., Goss, L. P., and Pestian, D. J., 1997, ''The Unsteady Structure of Simulated Turbine Film Cooling Flows From PIV,'' Paper No. 47, AGARD Propulsion and Energetics Panel, 90th Symp. Nonintrusive Measurement Techniques for Propulsion Engines, Brussels, Belgium.
[305] Ou, S., Rivir, R., and Meininger, M., 2000, ''Transient Liquid Crystal Measurement of Leading Edge Film Cooling Effectiveness and Heat Transfer With High Free Stream Turbulence,'' ASME Paper No. 2000-GT-245.
[306] Joslyn, H. D., Caspar, J. R., and Dring, R. P., 1985, ''Inviscid Modeling of Turbomachinery Wake Transport,'' AIAA Paper No. 85-1132.
[307] Cicatelli, G., and Sieverding, C. H., 1997, ''The Effect of Vortex Shedding on the Unsteady Pressure Distribution Around the Trailing Edge of a Turbine Blade,'' ASME J. Turbomach., **119**, pp. 810–819.
[308] Hodson, H. P., and Dawes, W. N., 1998, ''On the Interpretation of Measured Profile Losses in Unsteady Wake—Turbine Blade Interaction Studies,'' ASME J. Turbomach., **120**, pp. 276–284.
[309] Pappu, K. R., and Schobeiri, M. T., 1997, ''Optimization of Trailing Edge Ejection Mixing Losses: A Theoretical and Experimental Study,'' ASME Paper No. 97-GT-523.
[310] Schobeiri, T., 1989, ''Optimum Trailing Edge Ejection for Cooled Gas Turbine Blades,'' ASME J. Turbomach., **111**, pp. 510–514.
[311] Deckers, M., and Denton, J. D., 1997, ''The Aerodynamics of Trailing-Edge-Cooled Transonic Turbine Blades: Part 1—Experimental Approach,'' ASME Paper No. 97-GT-518.
[312] Deckers, M., and Denton, J. D., 1997, ''The Aerodynamics of Trailing-Edge-Cooled Transonic Turbine Blades: Part 2—Theoretical and Computational Approach,'' ASME Paper No. 97-GT-519.
[313] Kapteijn, C., Amecke, J., and Michelassi, V., 1996, ''Aerodynamic Performance of a Transonic Turbine Guide Vane With Trailing Edge Coolant Ejection: Part I—Experimental Approach,'' ASME J. Turbomach., **118**, pp. 519–528.
[314] Dunn, M. G., 1986, ''Heat Flux Measurements for the Rotor of a Full-Stage Turbine: Part I—Time-Averaged Results,'' ASME J. Turbomach., **108**, pp. 90–97.
[315] Du, H., Ekkad, S. V., and Han, J. C., 1997, ''Effect of Unsteady Wake With Trailing Edge Coolant Ejection on Detailed Heat Transfer Coefficient Distributions for a Gas Turbine Blade,'' ASME J. Heat Transfer, **119**, pp. 242–248.
[316] Du, H., Ekkad, S. V., and Han, J. C., 1999, ''Effect of Unsteady Wake With Trailing Edge Coolant Ejection on Film Cooling Performance for a Gas Turbine Blade,'' ASME J. Turbomach., **121**, pp. 448–455.
[317] Abhari, R. S., and Epstein, A. H., 1992, ''An Experimental Study of Film Cooling in a Rotating Transonic Turbine,'' ASME Paper No. 92-GT-201.
[318] Goldstein, R. J., and Haji-Sheik, A., 1967, ''Prediction of Film Cooling Effectiveness,'' *Proc. JSME 1967 Semi-International Symposium*, pp. 213–218.
[319] Schonung, B., and Rodi, W., 1987, ''Prediction of Film Cooling by a Row of Holes With a Two-Dimensional Boundary Layer Procedure,'' ASME J. Turbomach., **109**, pp. 579–587.
[320] Haas, W., Rodi, W., and Schonung, B., 1992, ''The Influence of Density Difference Between Hot and Cold Gas on Film Cooling by a Row of Holes: Predictions and Experiments,'' ASME J. Turbomach., **114**, pp. 747–755.
[321] Camci, C., 1989, ''An Experimental and Numerical Investigation of Near Cooling Hole Heat Fluxes on a Film Cooled Turbine Blade,'' ASME J. Turbomach., **111**, pp. 63–70.
[322] Garg, V. K., and Gaugler, R. E., 1994, ''Prediction of Film Cooling on Gas Turbine Airfoils,'' ASME Paper No. 94-GT-16.
[323] Garg, V. K., 1997, ''Comparison of Predicted and Experimental Heat Transfer on a Film Cooled Rotating Blade Using a Two-Equation Turbulence Model,'' ASME Paper No. 97-GT-220.
[324] Garg, V. K., and Gaugler, R. E., 1997, ''Effect of Velocity and Temperature Distribution at the Hole Exit on Film Cooling of Turbine Blades,'' ASME J. Turbomach., **119**, pp. 343–351.
[325] Steinthorsson, E., Liou, M. S., and Povinelli, L. A., 1993, ''Development of an Explicit Multiblock/Multigrid Flow Solver for Viscous Flows in Complex Geometries,'' AIAA Paper No. 93–2380.
[326] Steinthorsson, E., Ameri, A. A., and Rigby, D. L., 1997, ''TRAF3D.MB—A Multi-Block Flow Solver for Turbomachinery Flows,'' AIAA Paper No. 97–996.
[327] Traci, R. M., and Wilcox, D. C., 1975, ''Freestream Turbulence Effects on Stagnation Point Heat Transfer,'' AIAA J., **13**, No. 7, pp. 890–896.
[328] Bayley, F. J., and Priddy, W. J., 1980, ''Effects of Free-Stream Turbulence Intensity and Frequency on Heat Transfer to Turbine Blading,'' ASME Paper No. 80-GT-79.
[329] Blair, M. F., 1983, ''Influence of Free-Stream Turbulence on Turbulent Boundary Layer Heat Transfer and Mean Profile Development, Part I—Experimental Data, and Part II—Analysis of Results,'' ASME J. Heat Transfer, **105**, pp. 33–47.
[330] O'Brien, J. E., and VanFlossen, G. J., 1985, ''The Influence of Jet-Grid Turbulence on Heat Transfer From the Stagnation Region of a Cylinder in Crossflow,'' ASME Paper No. 85-GT-58.
[331] Ames, R. E., and Moffat, R. J., 1990, ''Heat Transfer With High Intensity Large Scale Turbulence: The Flat Plate Turbulent Boundary Layer and the Cylindrical Stagnation Point,'' Report No. HMT-44, Thermosciences Division of Mechanical Engineering, Stanford University.
[332] Dullenkopf, K., and Mayle, R. E., 1992, ''The Effects of Incident Turbulence and Moving Wakes on Laminar Heat Transfer in Gas Turbines,'' ASME Paper No. 92-GT-377.
[333] Thole, K. A., and Bogard, D. G., 1995, ''Enhanced Heat Transfer and Shear Stress Due to High Free-Stream Turbulence,'' ASME J. Turbomach., **117**, pp. 418–424.
[334] Ames, F. E., 1997, ''The Influence of Large-Scale High-Intensity Turbulence on Vane Heat Transfer,'' ASME J. Turbomach., **119**, pp. 23–30.
[335] Yavuzkurt, S., 1997, ''Effects of Free-Stream Turbulence on the Instantaneous Heat Transfer in a Wall Jet Flow,'' ASME J. Turbomach., **119**, pp. 359–417.
[336] Ames, F. E., Kwon, O., and Moffat, R. J., 1999, ''An Algebraic Model for High Intensity Large Scale Turbulence,'' ASME Paper No. 99-GT-160.
[337] Moore, J. G., and Moore, J., 1999, ''Realizability in Turbulence Modelling for Turbomachinery CFD,'' ASME Paper No. 99-GT-24.
[338] Volino, R. J., 1998, ''A New Model for Free-Stream Turbulence Effects on Boundary Layers,'' ASME J. Turbomach., **120**, pp. 613–620.
[339] Van Flossen, G. J., and Bunke, R. S., 2001, ''Augmentation of Stagnation Region Heat Transfer Due to Turbulence From a DLN Can Combustor,'' ASME J. Turbomach., **123**, pp. 140–146
[340] Moss, R. W., and Oldfield, M. L. G., 1992, ''Measurement of the Effect of Free-Stream Turbulence Length Scale on Heat Transfer,'' ASME Paper No. 92-GT-244.
[341] Dullenkopf, K., and Mayle, R. E., 1995, ''An Account of Free-Stream Turbulence Length Scale on Laminar Heat Transfer,'' ASME J. Turbomach., **117**, pp. 401–406.
[342] Burd, S. W., and Simon, T. W., 1999, ''Turbulence Spectra and Length Scales Measured in Film Coolant Flows Emerging From Discrete Holes,'' ASME J. Turbomach., **121**, pp. 551–557.
[343] Walker, G. J., 1992, ''The Role of Laminar-Turbulent Transition in Gas Turbine Engines: A Discussion,'' ASME Paper No. 92-GT-301.
[344] Addison, J. S., and Hodson, H. P., 1991, ''Modelling of Unsteady Transitional Boundary Layers,'' ASME Paper No. 91-GT-282.
[345] Ameri, A. A., and Arnone, A., 1996, ''Transition Modeling Effects on Turbine Rotor Blade Heat Transfer Predictions,'' ASME J. Turbomach., **118**, No. 4.
[346] Blair, M. F., 1991, ''The Effects of Reynolds Number, Rotor Incidence Angle, and Surface Roughness on the Heat Transfer Distribution in a Large Scale Turbine Rotor,'' UTRC Report No. R91-970057-3.
[347] Halstead, D. E., Wisler, D. C., Okiishi, T. H., Walker, G. J., Hodson, H. P., and Shin, H-W., 1997, ''Boundary Layer Development in Axial Compressors and Turbines: Part 1 of 4—Composite Picture, '' ASME J. Turbomach., **119**, pp. 114–127. ''Part 2 of 4—Compressors,'' *ibid.* **119**, pp. 426–444; ''Part 3 of 4—LP Turbines,'' *ibid.* **119**, pp. 225–237; ''Part 4 of 4—Computations and Analyses,'' *ibid.* **119**, pp. 128–139.
[348] Emmons, H. W., 1951, ''The Laminar–Turbulent Transition in a Boundary Layer—Part I,'' J. Aeronaut. Sci., **18**, No. 7, pp. 490–498.
[349] Tiedemann, M., and Kost, F., 1999, ''Unsteady Boundary Layer Transition on a High Pressure Turbine Rotor Blade,'' ASME Paper No. 99-GT-194.
[350] Volino, R. J., and Simon, T. W., 1995, ''Bypass Transition in Boundary Layers Including Curvature and Favorable Pressure Gradient Effects,'' ASME J. Turbomach., **117**, pp. 166–174.
[351] Clark, J. P., Jones, T. V., and LaGraff, J. E., 1994, ''On the Propagation of Naturally Occurring Turbulent Spots,'' J. Eng. Math., **38**, pp. 1–19.
[352] Boyle, R. J., and Simon, F. F., 1999, ''Mach Number Effects on Turbine Blade Transition Length Prediction,'' ASME J. Turbomach., **121**, pp. 694–702.
[353] Simon, F. F., 1995, ''The Use of Transition Region Characteristics to Improve the Numerical Simulation of Heat Transfer in Bypass Transitional Flows,'' Int. J. Rotating Mach., **2**, No. 2, pp. 93–102.
[354] Solomon, W. J., Walker, G. J., and Gostelow, J. P., 1995, ''Transition Length Prediction for Flows With Rapidly Changing Pressure Gradient,'' ASME Paper No. 95-GT-241.

[355] Rivir, R. B., Elrod, W. C., and Dunn, M. G., 1985, ''Two Spot Laser Velocimeter Measurements of Velocity and Turbulence Intensity in Shock Tube Driven Turbine Flows,'' AGARD Heat Transfer and Cooling in Gas Turbines, Conference Proc. No. 390, pp. 33-1 to 33-12, Bergen, Norway.
[356] Kadotani, K., and Goldstein, R. J., 1979, ''On the Nature of Jets Entering a Turbulent Flow: Part A. Jet-Mainstream Interaction and Part B. Film Cooling Performance,'' ASME J. Eng. Power, **101**, pp. 459–470.
[357] Bons, J. P., MacArthur, C. D., and Rivir, R. B., 1994, ''The Effect of High Free-Stream Turbulence on Film Cooling Effectiveness,'' ASME Paper No. 94-GT-51.
[358] Bons, J. P., Rivir, R. B., and MacArthur, C. D., 1995, ''The Effect of Unsteadiness on Film Cooling Effectiveness,'' AIAA Paper No. 95–306.
[359] Drost, U., and Bolcs, A., 1999, ''Performance of a Turbine Airfoil With Multiple Film Cooling Stations. Part I: Heat Transfer and Film Cooling Effectiveness,'' ASME Paper No. 99-GT-171.
[360] Takeishi, K., Matsuura, M., Aoki, S., and Sato, T., 1990, ''An Experimental Study of Heat Transfer and Film Cooling on Low Aspect Ratio Turbine Nozzles,'' ASME J. Turbomach., **112**, pp. 488–496.
[361] Granser, D., and Schulenberg, T., 1990, ''Prediction and Measurement of Film Cooling Effectiveness for a First-Stage Turbine Vane Shroud,'' ASME Paper No. 90-GT-95.
[362] Friedrichs, S., Hodson, H. P., and Dawes, W. N., 1995, ''Distribution of Film Cooling Effectiveness on a Turbine Endwall Measured Using the Ammonia and Diazo Technique,'' ASME Paper No. 95-GT-1.
[363] Mehendale, A. B., Han, J. C., Ou, S., and Lee, C. P., 1994, ''Unsteady Wake Over a Linear Turbine Blade Cascade With Air and CO2 Film Injection: Part II—Effect on Film Effectiveness and Heat Transfer Distributions,'' ASME J. Turbomach., **116**, pp 730–737.
[364] Funazaki, K., Yokota, M., and Yamawaki, S., 1995, ''Effect of Periodic Wake Passing on Film Effectiveness of Discrete Cooling Holes Around the Leading Edge of a Blunt Body,'' ASME Paper No. 95-GT-183.
[365] Du, H., Han, J. C., and Ekkad, S. V., 1998, ''Effect of Unsteady Wake on Detailed Heat Transfer Coefficient and Film Effectiveness Distributions for a Gas Turbine Blade,'' ASME J. Turbomach., **120**, pp. 808–817.
[366] Baughn, J. W., Butler, R. J., Byerley, A. R., and Rivir, R. B., 1995, ''An Experimental Investigation of Heat Transfer, Transition, and Separation on Turbine Blades at Low Reynolds Number and High Turbulence Intensity,'' ASME Paper No. 95-WA/HT-25.
[367] Maciejewski, P. K., and Rivir, R. B., 1994, ''Effects of Surface Riblets and Free-Stream Turbulence on Heat Transfer in a Linear Turbine Cascade,'' ASME Paper No. 94-GT-245.
[368] Welsh, S. T., Barlow, D. N., Butler, R. J., VanTreuren, K. W., Byerley, A. R., and Baughn, J. W., 1997, ''Effect of Passive and Active Air Jet Turbulence on Turbine Blade Heat Transfer,'' ASME Paper No. 97-GT-131.
[369] Binder, A., Schroeder, T., and Hourmouziadis, J., 1988, ''Turbulence Measurements in a Multistage Low-Pressure Turbine,'' ASME Paper No. 88-GT-79.
[370] Hodson, H. P., 1998, ''Bladerow Interactions in Low Pressure Turbines,'' *Blade Row Interference Effects in Axial Turbomachinery Stages*, von Karman Institute for Fluid Dynamics, Lecture Series 1998–02.
[371] Arndt, N., 1991, ''Blade Row Interaction in a Multistage Low-Pressure Turbine,'' ASME Paper No. 91-GT-283.
[372] Sharma, O., 1998, ''Impact of Reynolds Number on LP Turbine Performance,'' Minnowbrook Workshop on Boundary Layer Transition in Turbomachines, J. E. LaGraff and D. E. Ashpis, eds.; pp. 65–69 (see also NASA/CP-1998-206958).
[373] Hourmouziadis, J., Buckl, F., and Bergmann, P., 1986, ''The Development of the Profile Boundary Layer in a Turbine Environment,'' ASME Paper No. 86-GT-244.
[374] Hodson, H. P., Huntsman, I., and Steele, A. B., 1993, ''An Investigation of Boundary Layer Development in a Multistage LP Turbine,'' ASME Paper No. 93-GT-310.
[375] Schulte, V., and Hodson, H. P., 0 1998, ''Unsteady Wake-Induced Boundary Layer Transition in High Lift LP Turbines,'' ASME J. Turbomach., **120**, pp. 28–35.
[376] Rivir, R. B., 1996, ''Transition on Turbine Blades and Cascades at Low Reynolds Numbers,'' AIAA Paper No. 96–2079.
[377] Murawski, C. G., Sondergaard, R., Rivir, R. B., Vafi, K, Simon, T. W., and Volino, R. J., 1997, ''Experimental Study of the Unsteady Aerodynamics in a Linear Cascade With Low Reynolds Number Low Pressure Turbine Blades,'' ASME Paper No. 97-GT-95.
[378] Solomon, W. J., 2000, ''Effects of Turbulence and Solidity on the Boundary Layer Development in a Low Pressure Turbine,'' ASME Paper No. 2000-GT-0273.
[379] Rivir, R. B., Sondergaard, R., Bons, J. P., and Lake, J. P., 2000, ''Application of Longitudinal Vortices for Control of Separation in Turbine Boundary Layers,'' International Workshop Organized Vortical Motion as a Basis for Boundary-Layer Control, Kiev, Ukraine, Sept. 20–22.
[380] Rivir, R. B., Sondergaard, R., Bons, J. P., and Lake, J. P., 2000, ''Passive and Active Control of Separation in Gas Turbines,'' AIAA Paper No. 2000–2235.
[381] Bons, J. P., Sondergaard, R., and Rivir, R. B., 2001, ''Turbine Separation Control Using Pulsed Vortex Generator Jets,'' ASME J. Turbomach., **123**, pp. 198–206.
[382] Lake, J. P., King, P. I., and Rivir, R. B., 2000, ''Low Reynolds Number Loss Reduction on Turbine Blades With Dimples and **V**-Grooves,'' AIAA Paper No. 00–738.
[383] Wisler, D. C., 2000, private communication, 10 Oct.
[384] Howell, R., Ramesh, O., and Hodson, H. P., 2001, ''High Lift and Aft Loaded Profiles for Low Pressure Turbines,'' ASME J. Turbomach., **123**, pp. 181–188.
[385] Sharma, O. P., Wells, R. A., Schlinker, R. H., and Bailey, D. A., 1982, ''Boundary Layer Development on Turbine Airfoil Suction Surfaces,'' ASME J. Eng. Power, **104**, pp. 698–706.
[386] Hourmouziadis, J., 1989, ''Aerodynamic Design of Low Pressure Turbines,'' AGARD Lecture Series 167.
[387] Curtis, E. M., Hodson, H. P., Banieghbal, M. R., Denton, J. D., and Howell, R. J., 1997, ''Development of Blade Profiles for Low Pressure Turbine Applications,'' ASME J. Turbomach., **119**, pp. 531–538.
[388] Cobley, K., Coleman, N., Siden, G., and Arndt, N., 1997, ''Design of New Three Stage Low Pressure Turbine for the BMW Rolls Royce BR715 Turbofan Engine,'' ASME Paper No. 97-GT-419.
[389] Qiu, S., and Simon, T. W., 1997, ''An Experimental Investigation of Transition as Applied to Low Pressure Turbine Suction Surface Flows,'' ASME Paper No. 97-GT-455.
[390] Bons, J. P., Sondergaard, R., and Rivir, R. B., 1999, ''Control of Low-Pressure Turbine Separation Using Vortex Generator Jets,'' AIAA Paper No. 99-367.
[391] Blair, M. F., and Anderson, O. L., 1989, ''The Effect of Reynolds Number, Rotor Incidence Angle and Surface Roughness on the Heat Transfer Distribution in Large-Scale Turbine Rotor Passage,'' United Technologies Research Center, Report UTRC-R89-957852-24.
[392] Boyle, R. J., and Civinskas, K. C., 1991, ''Two-Dimensional Navier–Stokes Heat Transfer Analysis for Rough Turbine Blades,'' AIAA Paper No. 91-2129.
[393] Taylor, R. P., Taylor, J. K., Hosni, M. H., and Coleman, H. W., 1991, ''Heat Transfer in the Turbulent Boundary Layer With a Step Change in Surface Roughness,'' ASME Paper No. 91-GT-266.
[394] Blair, M. F., 1994, ''An Experimental Study of Heat Transfer in a Large-Scale Turbine Rotor Passage,'' ASME J. Turbomach., **116**, pp. 1–13.
[395] Boynton, J. L., Tabibzadeh, R., and Hudson, S. T., 1993, ''Investigation of Rotor Blade Roughness Effects on Turbine Performance,'' ASME J. Turbomach., **115**, pp. 614–620.
[396] Boyle, R. J., 1994, ''Prediction of Surface Roughness and Incidence Effects on Turbine Performance,'' ASME J. Turbomach., **116**, pp. 745–751.
[397] Cebeci, T., and Chang, X. X., 1978, ''Calculation of Incompressible Rough-Wall Boundary Layer Flows,'' AIAA J., **16**, No. 7, pp. 730–735.
[398] Goldstein, R. J., Eckert, E. R. G., Chiang, H. D., and Elovic, E., 1985, ''Effect of Surface Roughness on Film Cooling Performance,'' ASME J. Eng. Gas Turbines Power, **107**, pp. 111–116.
[399] Hippensteele, S. A., Russell, L. M., and Torres, F. J., 1987, ''Use of a Liquid-Crystal, Heater-Element Composite for Quantitative, High-Resolution Heat Transfer Coefficients on a Turbine Airfoil, Including Turbulence and Surface Roughness Effects,'' NASA TM-87355.
[400] Barlow, D. N., Kim, Y. W., and Florschuetz, L. W., 1994, ''Transient Liquid Crystal Technique for Convective Heat Transfer on Rough Surfaces,'' ASME J. Turbomach., **116**, pp. 14–22.
[401] Hoffs, A., Drost, U., and Bolcs, A., 1996, ''Heat Transfer Measurements on a Turbine Airfoil at Various Reynolds Numbers and Turbulence Intensities Including Effects of Surface Roughness,'' ASME Paper No. 96-GT-169.
[402] Bogard, D. G., Schmidt, D. L., and Tabbita, M., 1998, ''Characterization and Laboratory Simulation of Turbine Airfoil Surface Roughness and Associated Heat Transfer,'' ASME J. Turbomach., **120**, pp. 337–342.
[403] Guo, S. M., Jones, T. V., Lock, G. D., and Dancer, S. N., 1998, ''Computational Prediction of Heat Transfer to Gas Turbine Nozzle Guide Vanes With Roughened Surfaces,'' ASME J. Turbomach., **120**, pp. 343–350.
[404] Schmidt, D. L., Sen, B., and Bogard, D. G., 1996, ''Effects of Surface Roughness on Film Cooling,'' ASME Paper No. 96-GT-299.
[405] Kind, R. J., Serjak, P. J., and Abbott, M. W. P., 1998, ''Measurement and Prediction of the Effects of Surface Roughness on Profile Losses and Deviation in a Turbine Cascade,'' ASME J. Turbomach., **120**, pp. 20–27.
[406] Abuaf, N., Bunker, R. S., and Lee, C. P., 1997, ''Effects of Surface Roughness on Heat Transfer and Aerodynamic Performance of Turbine Airfoils,'' ASME J. Turbomach., **120**, pp. 522–529.
[407] Tolpadi, A. K., and Crawford, M. E., 1998, ''Predictions of the Effect of Roughness on Heat Transfer From Turbine Airfoils,'' ASME Paper No. 98-GT-87.
[408] Boyle, R. J., Lucci, B. L., Spuckler, C. M., and Camperchioli, W. P., 2001, ''Infrared Low Temperature Turbine Vane Rough Surface Heat Transfer Measurements,'' ASME J. Turbomach., **123**, pp. 168–177.
[409] Boyle, R. J., Lucci, B. L., and Spuckler, C. M., 2000, ''Comparison of Predicted and Measured Turbine Vane Rough Surface Heat Transfer,'' ASME Paper No. 2000-GT-0217.
[410] Taylor, R. P., Coleman, H. W., and Hodge, B. K., 1985, ''Predictions of Turbulent Rough-Wall Skin Friction Using a Discrete Element Approach,'' ASME J. Fluids Eng., **107**, pp. 251–257.
[411] Tarada, F., 1990, ''Prediction of Rough Wall Boundary Layers Using a Low Reynolds Number k-ε Turbulence Model,'' Int. J. Heat Fluid Flow, **11**, pp. 331–345.
[412] Weigand, B., Crawford, M. E., and Lutum, E., 1998, ''A Theoretical and Experimental Investigation of the Effect of Surface Roughness on Film Cooling,'' ISROMAC-7, Honolulu, HI.
[413] Richter, R., and Gottschlich, J. M., 1990, ''Thermodynamic Aspects of Heat Pipe Operation,'' AIAA Paper No. 90-1772.
[414] Anderson, W. G., Hoff, S., and Winstanley, D., 1993, ''Heat Pipe Cooling of Turboshaft Engines,'' ASME Paper No. 93-GT-220.
[415] Silverstein, C. C., Gottschlich, J. M., and Meininger, M., 1994, ''The Feasibility of Heat Pipe Turbine Vane Cooling,'' ASME Paper No. 94-GT-306.
[416] Zuo, Z. J., Faghri, A., and Langston, L., 1996, ''Numerical Analysis of Heat

Pipe Turbine Vane Cooling,'' Third Biennial ASME European Joint Conference on Engineering System Design and Analysis, ASME PD-Vol. 78, No. 6.
[417] Zuo, Z. J., Faghri, A., and Langston, L., 1997, ''A Parametric Study of Heat Pipe Turbine Vane Cooling,'' ASME Paper No. 97-GT-443.
[418] Yamawaki, S., Yoshidi, T., Taki, M., and Mimura, F., 1998, ''Fundamental Heat Transfer Experiments of Heat Pipes for Turbine Cooling,'' ASME J. Eng. Gas Turbines Power, **120**, pp. 580–587.
[419] Tagashira, T., and Yoshida, T., 1999, ''Consideration on Gas Turbine Performance Improvement by an Advanced Cooling System,'' presented at the 14th International Symposium on Air Breathing Engines, Florence, Italy.
[420] Yoshida, T., 2000, ''Cooling Systems for Ultra-High Temperature Turbines,'' Proc. Int. Center for Heat and Mass Transfer Turbine 2000, Keynote Lecture, Cesme, Izmir, Turkey.
[421] Han, J. C., 1984, ''Heat Transfer and Friction in Channels With Two Opposite Rib-Roughened Walls,'' ASME J. Heat Transfer, **106**, pp. 774–781.
[422] Han, J. C., 1988, ''Heat Transfer and Friction Characteristics in Rectangular Channels With Rib Turbulators,'' ASME J. Heat Transfer, **110**, pp. 321–328.
[423] Han, J. C., and Zhang, Y. M., 1991, ''Effect of Rib-Angle Orientation on Local Mass Transfer Distribution in a Three-Pass Rib-Roughened Channel,'' ASME J. Turbomach., **113**, pp. 123–130.
[424] Han, J. C., Zhang, Y. M., and Lee, C. P., 1992, ''Influence of Surface Heat Flux Ratio on Heat Transfer Augmentation in Square Channels With Parallel, Crossed, and V-Shaped Angled Ribs,'' ASME J. Turbomach., **114**, pp. 872–880.
[425] Hedlund, C. R., Ligrani, P. M., Moon, H.-K., and Glezer, B., 1998, ''Heat Transfer and Flow Phenomena in a Swirl Chamber Simulating Turbine Blade Internal Cooling,'' ASME J. Turbomach., **121**, pp. 804–813.
[426] Taslim, M. E., Li, T., and Spring, S. D., 1995, ''Experimental Study of the Effects of Bleed Holes on Heat Transfer and Pressure Drop in Trapezoidal Passages With Tapered Turbulators,'' ASME J. Turbomach., **117**, pp. 281–289.
[427] Taslim, M. E., and Wadsworth, C. M., 1997, ''An Experimental Investigation of the Rib Surface-Averaged Heat Transfer Coefficient in a Rib-Roughened Square Passage,'' ASME J. Turbomach., **119**, pp. 381–389.
[428] Taslim, M. E., Li, T., and Spring, S. D., 1998, ''Measurement of Heat Transfer Coefficients and Friction Factors in Rib-Roughened Channels Simulating Leading-Edge Cavities of a Modern Turbine Blade,'' ASME J. Turbomach., **120**, pp. 601–609.
[429] Taslim, M. E., Li, T., and Spring, S. D., 1998, ''Measurements of Heat Transfer Coefficients and Friction Factors in Passages Rib-Roughened on All Walls,'' ASME J. Turbomach., **120**, pp. 564–570.
[430] Taslim, M. E., Li, T., and Kercher, D. M., 1996, ''Experimental Heat Transfer and Friction in Channels Roughened With Angled, V-Shaped, and Discrete Ribs on Two Opposite Walls,'' ASME J. Turbomach., **118**, pp. 20–28.
[431] Wang, Z., Ireland, P. T., Kohler, S. T., and Chew, J. W., 1998, ''Heat Transfer Measurements to a Gas Turbine Cooling Passage With Inclined Ribs,'' ASME J. Turbomach., **120**, pp. 63–69.
[432] Becker, B. R., and Rivir, R. B., 1989, ''Computation of the Flow Field and Heat Transfer in a Rectangular Passage With a Turbulator,'' ASME Paper No. 89-GT-30.
[433] Abuaf, N., and Kercher, D. M., 1994, ''Heat Transfer and Turbulence in a Turbulated Blade Cooling Circuit,'' ASME J. Turbomach., **116**, pp. 169–177.
[434] Shen, J. R., Wang, Z., Ireland, P. T., Jones, T. V., and Byerley, A., 1996, ''Heat Transfer Enhancement Within a Turbine Blade Cooling Passage Using Ribs and Combinations of Ribs With Film Cooling Holes,'' ASME J. Turbomach., **118**, pp. 428–434.
[435] Hwang, J.-J., and Liou, T.-M., 1997, ''Heat Transfer Augmentation in a Rectangular Channel With Slit Rib-Turbulators on Two Opposite Walls,'' ASME J. Turbomach., **119**, pp. 617–623.
[436] Mochizuki, S., Murata, A., and Fukunaga, M., 1997, ''Effects of Rib Arrangements on Pressure Drop and Heat Transfer in a Rib-Roughened Channel With a Sharp 180 deg Turn,'' ASME J. Turbomach., **119**, pp. 610–616.
[437] Hibbs, R. G., Acharya, S., Chen, Y., Nikitopoulos, D. E., and Myrum, T. A., 1998, ''Heat Transfer in a Two-Pass Internally Ribbed Turbine Blade Coolant Channel With Cylindrical Vortex Generators,'' ASME J. Turbomach., **120**, pp. 589–600.
[438] Rivir, R. B., Chyu, M. K., and Maciejewski, P. K., 1996, ''Turbulence and Scale Measurements in a Square Channel With Transverse Square Ribs,'' Int. J. Rotating Mach., **2**, No. 3, pp. 209–218.
[439] Rigby, D. L., 1998, ''Prediction of Heat and Mass Transfer in a Rotating Ribbed Coolant Passage With a 180 Degree Turn,'' ASME Paper No. 98-GT-329.
[440] Prakash, C., and Zerkle, R., 1992, ''Prediction of Turbulent Flow and Heat Transfer in a Radially Rotating Duct,'' ASME J. Turbomach., **114**, pp. 835–844.
[441] Owen, J. M., Pincombe, J. R., and Rogers, R. H., 1985, ''Source-Sink Flow Inside a Rotating Cylindrical Cavity,'' J. Fluid Mech., **155**, pp. 233–265.
[442] Owen, J. M., and Rogers, R. H., 1989, *Flow and Heat Transfer in Rotating-Disc Systems, Vol. 1: Rotor–Stator Systems*, Research Studies Press, Taunton, UK; Wiley, New York.
[443] El-Oun, Z., and Owen, J. M., 1989, ''Pre-swirl Blade-Cooling Effectiveness in an Adiabatic Rotor–Stator System,'' ASME J. Turbomach., **111**, pp. 522–529.
[444] Ong, C. L., and Owen, J. M., 1991, ''Prediction of Heat Transfer in a Rotating Cavity With a Radial Outflow,'' ASME J. Turbomach., **113**, pp. 115–122.
[445] Gan, X., Kilic, M., and Owen, J. M., 1995, ''Flow Between Contrarotating Disks,'' ASME J. Turbomach., **117**, pp. 298–305.
[446] Chen, J.-X., Gan, X., and Owen, J. M., 1997, ''Heat Transfer From Air-Cooled Contrarotating Disks,'' ASME J. Turbomach., **119**, pp. 61–67.
[447] Owen, J. M., and Rogers, R. H., 1995, *Flow and Heat Transfer in Rotating-Disc Systems, Vol. 2: Rotor–Stator Systems*, Research Studies Press, Taunton, UK; Wiley, New York.
[448] Wilson, M., Pilbrow, R., and Owen, J. M., 1997, ''Flow and Heat Transfer in a Preswirl Rotor–Stator System,'' ASME J. Turbomach., **119**, pp. 364–373.
[449] Karabay, H., Chen, J.-X., Pibrow, R., Wilson, M., and Owen, J. M., 1999, ''Flow in a 'Cover-Plate' Preswirl Rotor–Stator System,'' ASME J. Turbomach., **121**, pp. 160–166.
[450] Mirzaee, I., Gan, X., Wilson, M., and Owen, J. M., 1998, ''Heat Transfer in a Rotating Cavity With a Peripheral Inflow and Outflow of Cooling Air,'' ASME J. Turbomach., **120**, pp. 818–823.
[451] Bohn, D., Deuker, E., Emunds, R., and Gorzelitz, V., 1995, ''Experimental and Theoretical Investigations of Heat Transfer in Closed Gas-Filled Annuli,'' ASME J. Turbomach., **117**, pp. 175–183.
[452] Bohn, D., Kruger, U., and Nitsche, K., 1995, ''Numerical Investigation of Flow Pattern and Heat Transfer in a Rotating Cavity Between Two Discs of the Compressor of a Siemens KWU V84.3 Gas Turbine,'' ASME Paper No. 95-GT-144.
[453] Bohn, D., and Gier, J., 1998, ''The Effect of Turbulence on the Heat Transfer in Closed Gas-Filled Rotating Annuli,'' ASME J. Turbomach., **120**, pp. 824–830.
[454] Bohn, D., Rudzinski, B., Surken, N., and Gartner, W., 1999, ''Influence of Rim Seal Geometry on Hot Gas Ingestion Into the Upstream Cavity of an Axial Turbine Stage,'' ASME Paper No. 99-GT-248.
[455] Chen, J.-X., Gan, X., and Owen, J. M., 1996, ''Heat Transfer in an Air-Cooled Rotor-Stator System,'' ASME J. Turbomach., **118**, pp. 444–451.
[456] Steltz, W. G., 1987, ''Generalized Transient Rotor Thermal Stress,'' *Heat Transfer and Fluid Flow in Rotating Machinery*, Hemisphere Publishing Co.
[457] Long, C. A., Morse, A. P., and Zafiropoulos, N., 1995, ''Buoyancy-Affected Flow and Heat Transfer in Asymmetrically Heated Rotating Cavities,'' ASME J. Turbomach., **117**, pp. 461–473.
[458] Guo, Z., and Rhode, D. L., 1996, ''Assessment of Two- and Three-Scale k-ε Models for Rotating Cavity Flows,'' ASME J. Turbomach., **118**, pp. 826–834.
[459] Roy, R. P., Devasenathipathy, S., Xu, G., and Zhao, Y., 1999, ''A Study of the Flow Field in a Model Rotor–Stator Disk Cavity,'' ASME Paper No. 99-GT-246.
[460] Han, J. C., Zang, Y. M., and Lee, C. P., 1994, ''Influence of Surface Heating Condition on Local Heat Transfer in a Rotating Square Channel With Smooth Walls and Radial Outward Flow,'' ASME J. Turbomach., **116**, pp. 149–158.
[461] Wagner, J. H., Johnson, B. V., and Hajek, T., 1991, ''Heat Transfer in Rotating Passages With Smooth Walls and Radial Outward Flow,'' ASME J. Turbomach., **113**, pp. 42–51.
[462] Wagner, J. H., Johnson, B. V., and Kopper, F. C., 1991, ''Heat Transfer in Rotating Serpentine Passages With Smooth Walls,'' ASME J. Turbomach., **113**, pp. 321–330.
[463] Wagner, J. H., Johnson, B. V., Graziani, R. A., and Yeh, F. C., 1992, ''Heat Transfer in Rotating Serpentine Passages With Trips Normal to the Flow,'' ASME J. Turbomach., **114**, pp. 847–857.
[464] Johnson, B. V., Wagner, J. H., Steuber, G. D., and Yeh, F. C., 1994, ''Heat Transfer in Rotating Serpentine Passages With Trips Skewed to the Flow,'' ASME J. Turbomach., **116**, pp. 113–123.
[465] Dutta, S., Han, J.-C., Zhang, Y., Lee, C. P., 1996, ''Local Heat Transfer in a Rotating Two-Pass Triangular Duct With Smooth Walls,'' ASME J. Turbomach., **118**, pp. 435–443.
[466] Han, J. C., Zang, Y. M., and Kalkuehler, K., 1993, ''Uneven Wall Temperature Effect on Local Heat Transfer in a Rotating Two-Pass Square Channel With Smooth Walls,'' ASME J. Heat Transfer, **115**, pp. 912–920.
[467] Bons, J. P., and Kerrebrock, J. L., 1999, ''Complementary Velocity and Heat Transfer Measurements in a Rotating Cooling Passage With Smooth Walls,'' ASME J. Turbomach., **121**, pp. 651–662.
[468] Glezer, B., Moon, H. K., Kerrebrock, J., Bons, J., and Guenette, G., 1998, ''Heat Transfer in a Rotating Radial Channel With Swirling Internal Flow,'' ASME Paper No. 98-GT-214.
[469] Glezer, B., Moon, H. K., and O'Connell, T., 1996, ''A Novel Technique for the Internal Blade Cooling,'' ASME Paper No. 96-GT-181.
[470] Kercher, D. M., and Tabakoff, W., 1970, ''Heat Transfer by a Square Array of Round Air Jets Impinging Perpendicular to a Flat Surface Including the Effect of Spent Air,'' ASME J. Eng. Power, **92**, No. 1, pp. 73–82.
[471] Moore, J., 1968, ''Effects of Coriolis on Turbulent Flow in Rotating Rectangular Channels,'' MIT Gas Turbine Laboratory Report No. 89.
[472] Mori, Y., and Nakayama, W., 1968, ''Convective Heat Transfer in Rotating Radial Circular Pipes,'' Int. J. Heat Fluid Flow, **21**, pp. 1027–1040.
[473] Ito, H., and Nanbu, K., 1971, ''Flow in Rotating Straight Pipes of Circular Cross Section,'' ASME J. Basic Eng., **93**, pp. 383–394.
[474] Kumar, G. N., and Deanna R. G., 1988, ''Development of a Thermal and Structural Analysis Procedure for Cooled Radial Turbines,'' ASME Paper No. 88-GT-18.
[475] Steinthorsson, E., Shih, T. I.-P., and Roelke, R. J., 1991, ''Computation of the Three-Dimensional Flow and Heat Transfer Within a Coolant Passage of a Radial Flow Turbine,'' AIAA Paper No. 91-2238.
[476] Steinthorsson, E., Shih, T. I.-P., and Roelke, R. J., 1991, ''Algebraic Grid Generation for Coolant Passages of Turbine Blades With Serpentine Channels and Pin Fins,'' AIAA Paper No. 91-2366.
[477] Dawes, W. N., 1994, ''The Solution-Adaptive Numerical Simulation of the Three-Dimensional Viscous Flow in the Serpentine Coolant Passage of a Radial Inflow Turbine Blade,'' ASME J. Turbomach., **116**, pp. 141–148.

[478] Snyder, P. H., and Roelke, R. J., 1988, ''The Design of an Air-Cooled Metallic High Temperature Radial Turbine,'' AIAA Paper No. 88-2872.
[479] Taylor, C., Xia, J. Y., Medwell, J. O., and Morris, W. D., 1991, ''Numerical Simulation of Three Dimensional Turbulent Flow and Heat Transfer Within a Multi-ribbed Cylindrical Duct,'' ASME Paper No. 91-GT-8.
[480] Rigby, D. L., 1988, ''Prediction of Heat and Mass Transfer in a Rotating Ribbed Coolant Passage With a 180 Degree Turn,'' ASME Paper No. 88-GT-328.
[481] Wilcox, D. C., 1994, ''Turbulence Modeling for CFD,'' DCW Industries, La Canada, CA.
[482] Wilcox, D. C., 1994, ''Simulation of Transition With a Two-Equation Turbulence Model,'' AIAA J., **32**, No. 2, pp. 247–255.
[483] Park, C. W., Lau, S. C., and Kukreja, R. T., 1997, ''Heat/Mass Transfer in a Rotating Two-Pass Square Channel With Transverse Ribs,'' J. Thermophys. Heat Transfer, **11**, pp. 8–16.
[484] Arts, T., Lambert de Rouvroit, M., Rau, G., and Acton, P., 1992, ''Aero-Thermal Investigation of the Flow Developing in a 180 Degree Turn Channel,'' VKI preprint No. 1992–10.
[485] Rigby, D. L., Steinthorsson, E., and Ameri, A., 1997, ''Numerical Prediction of Heat Transfer in a Channel With Ribs and Bleed,'' ASME Paper No. 97-GT-431.
[486] Ekkad, S. V., Huang, Y., and Han, J. C., 1996, ''Detailed Heat Transfer Distributions in Two-Pass Smooth and Turbulated Square Channels With Bleed Holes,'' *Fundamentals of Augmented Single-Phase Convection*, ASME HTD-Vol. 330, pp. 133–140.
[487] Chambers, J. C., 1985, ''The 1982 Encounter of British Airways 747 With the Mt. Galuggung Eruption Cloud,'' AIAA Paper No. 85-0097.
[488] Campbell, E. E., 1990, ''Volcanic Ash,'' Proc. 1990 Flight Operations Symposium, pp. 2.3.1–2.3.34.
[489] Sieverding, C. H., Arts, T., Denos, R., and Brouckaert, J.-F., 2000, ''Measurement Techniques for Unsteady Flows in Turbomachinery,'' Exp. Fluids, **28**, pp. 285–321.

Mainstream Aerodynamic Effects Due to Wheelspace Coolant Injection in a High-Pressure Turbine Stage: Part I—Aerodynamic Measurements in the Stationary Frame

Christopher McLean[1]
e-mail: cmclean@techkor.com

Cengiz Camci
Professor of Aerospace Engineering.
e-mail: cxc11@psu.edu

Turbomachinery Heat Transfer Laboratory,
The Pennsylvania State University,
University Park, PA 16802

Boris Glezer[2]
Optimized Turbine Solutions,
4140 Calle Isabelino,
San Diego, CA 92130
e-mail: bglezer@san.rr.com

The relative aerodynamic and performance effects associated with rotor–NGV gap coolant injections were investigated in the Axial Flow Turbine Research Facility (AFTRF) of the Pennsylvania State University. This study quantifies the effects of the coolant injection on the aerodynamic performance of the turbine for radial cooling, impingement cooling in the wheelspace cavity and root injection. Overall, it was found that even a small quantity (1 percent) of cooling air can have significant effects on the performance character and exit conditions of the high pressure stage. Parameters such as the total-to-total efficiency, total pressure loss coefficient, and three-dimensional velocity field show local changes in excess of 5, 2, and 15 percent, respectively. It is clear that the cooling air disturbs the inlet end-wall boundary layer to the rotor and modifies secondary flow development, thereby resulting in large changes in turbine exit conditions. [DOI: 10.1115/1.1401026]

Introduction

Gas turbine systems are rapidly becoming one of the primary sources for electrical power generation throughout the world. The United States Department of Energy estimates that over the next 20 years, as much as half of the new power generating capacity added in the United States will be from gas turbine systems [1]. Improvements to gas turbine technology can take many forms, including lower specific fuel consumption/improved efficiency, better specific power, increased durability and service life, and lower acoustic noise, smoke, and gaseous emissions [2]. A direct result of the desire to increase gas turbine efficiency and specific power output is an increase in the required turbine entry temperature (TET) and overall pressure ratio. Modern engines operate well below theoretical limits. The stoichiometric combustion limit for turbine inlet temperature is approximately 2000°C, while modern metallurgy only allows surface temperatures of approximately 1000°C [3]. Aggressive air-cooling of turbine blades, platforms, and wheelspaces allows turbine inlet temperatures of 1450°C. However, cooling penalties can easily offset the benefits of the increasing TET. Energy is required to compress and pump the cooling air to the turbine blades and wheelspace, and cooling air bled from the compressor bypasses the combustion chamber so the full work potential is never realized. Overall turbine cycle efficiency is lowered in the process. In addition, when mixing cooling air with the mainstream gas, significant turbulence is generated and the end-wall rotor boundary layers are disturbed affecting the secondary flow. Enthalpy and stagnation pressures are lost, lowering the turbine stage efficiency. An effective turbine design must account for all of these factors.

A major concern in modern gas turbine engines is the cooling of turbine wheelspace. The complexity of a modern high-pressure turbine wheelspace is depicted in Fig. 1 [4]. Many present day gas turbine engines operate with mainstream gas temperatures exceeding 1450°C in the high-pressure turbine stage. Turbine designers need to give special attention to the cooling of turbine wheelspaces. Turbine wheelspaces contain rotor bearings and are constructed from lower temperature metals than turbine blades. Allowing the high-temperature gas from the mainstream to be ingested would significantly reduce turbine life. In a gas turbine engine, the spinning rotor disk induces periodic outward flow on the rotor side of the wheelspace that is counteracted by flow ingestion on the stationary side of the wheelspace [5,6]. This circulation leads to the ingestion of hot mainstream gases, and acts to raise the internal temperature of the wheelspace materials significantly. To counter this effect, cooling air is pumped into the wheelspace cavity. This continuous supply of cool air keeps internal components within thermal limits. However, the pumping of the wheelspace coolant and its eventual mixing with the mainstream boundary layer flow causing performance degradation.

Much literature exists on the aerodynamics of rotating disks and the heat transfer effects of cooling within the wheelspace cavity. Theodore von Karman [7] first reported the theoretical flow field for an infinite rotating disk in an infinite medium. Early works on wheelspace aerodynamics and wheelspace cooling include Cobb and Saunders [8], Maroti [9], Daily and Nece [10] and Dorfman [11]. Cobb and Saunders obtained data on rotor-averaged heat transfer coefficients, while Maroti demonstrated that the outflow from a rotating disk is periodic in nature. Daily and Nece studied the effects of cavity spacing on disk torque. Metzger et al. [12] presented experimental data for impingement flow onto a rotating disk. Later works by Popiel and Boguslawski [13], and Qureshi [14] obtained radial section-averaged rotor heat transfer information. Pincombe [15] performed detailed flow visualization studies with rotational and stationary disk combinations to study the highly three-dimensional secondary flow present in the wheelspace cavity. More recent studies such as those per-

[1]Present address: Division Manager, Techkor Instrumentation, A Division of ACT, Inc., Harrisburg, PA.

[2]Former Head of ''Turbine Cooling Design and Analysis'' at Solar Turbines, Inc., San Diego, CA.

Contributed by the International Gas Turbine Institute and presented at the 46th International Gas Turbine and Aeroengine Congress and Exhibition, New Orleans, Louisiana, June 4–7, 2001. Manuscript received by the International Gas Turbine Institute February 2001. Paper No. 2001-GT-119. Review Chair: R. Natole.

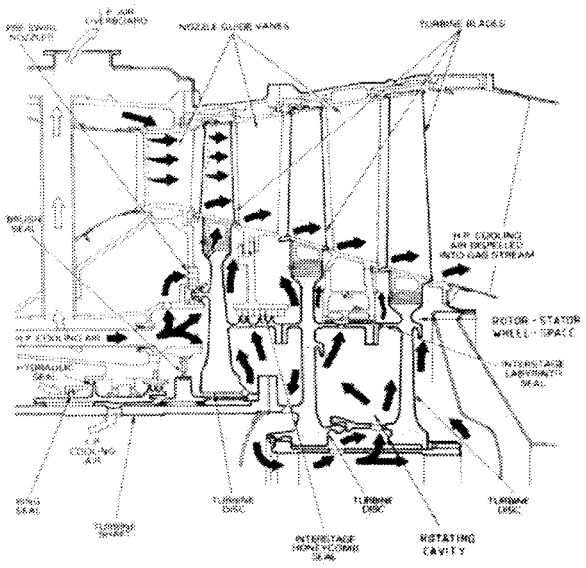

Fig. 1 Wheelspace coolant flow in a high-pressure turbine stage showing the complexity of the internal wheelspace and the mixing of the coolant flow with the mainstream flow, [4].

formed by Bunker [5,6] describe the detailed two-dimensional heat transfer patterns within turbine wheelspaces.

Published research neglects to study the secondary aerodynamic effects of wheelspace coolant mixing with the mainstream flow and its effects on platform heat transfer. Due to the fact that wheelspace coolant is injected upstream of the rotor blade throat, it will incur lower losses than film cooling injected after the throat. The wheelspace coolant has potential for endwall cooling given the proper geometry. The question remains as to the aerodynamic penalties of wheelspace coolant injected into the mainstream and its influence on turbine stage performance.

Endwall cooling studies can lend some understanding to the effect of wheelspace coolant injection. Both affect the rotor inlet boundary layer, pressure field, and the consequent vortex development. In film cooling, higher blowing ratios lead to higher losses due to increased shear and increased rotationality of the flow. Highly three-dimensional flow along the end wall interacts with the cooling flows. Passage vortices, boundary layers, shock waves, and horseshoe vortices all play a significant role.

Turbine designers require three important pieces of information in the design of cooled high-pressure turbines when active wheelspace cooling is required.

1 The cooling air should be injected in such a manner that the wheelspace is cooled below critical material temperatures. Much information exists in the form of empirical relationships.

2 The cooling air cannot cause excessive performance losses. If the losses due to the cooling are too high, they will negate any gains from increasing the turbine entry temperature. Overcooling causes windage losses due to rotational drag within the wheelspace and causes aerodynamic losses when mixed with the mainstream flow. The use of seals and jet preswirl greatly reduces the amount of cooling flow required and its associated losses. Little information exists on the mixing of the wheelspace cooling air with the mainstream flow and its associated losses.

3 The wheelspace cooling injected into the mainstream affects the rotor endwall heat transfer. Some information exists on platform cooling related to wheelspace cooling gap injection.

However, most of the research on platform cooling is focused on film cooling. Research has neglected the effects of the wheelspace cooling flow's interaction with the mainstream and the effects of modifying/disturbing the rotor end-wall boundary layer. This area is the subject of continued research.

Experimental Test Facility

The Axial Flow Turbine Research Facility (AFTRF) is a continuous flow open loop facility 0.916 m in diameter with an advanced axial turbine blading configuration (Fig. 2). The research facility is located at the Pennsylvania State University's Center for Gas Turbines and Power. The facility consists of a bellmouth inlet, a single high-pressure turbine stage with a nozzle guide vane assembly and rotor, and outlet guide vanes. The facility was used for the current research program with significant modifications to allow for wheelspace cooling. Table 1 lists the critical design and operating data for the AFTRF.

The AFTRF is powered by four stages of adjustable pitch axial flow fans. A detailed description of the AFTRF can be found in Lakshminarayana et al. [16]. An aerodynamically designed exit throttle is used to adjust the pressure rise across the stage. The

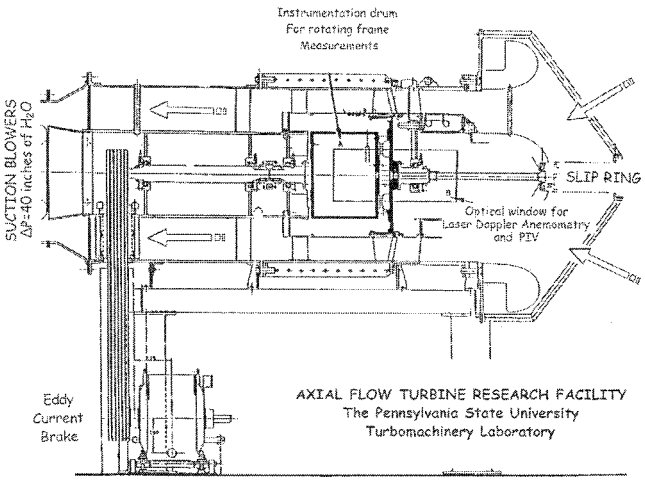

Fig. 2 Axial flow Turbine Research Facility of the Pennsylvania State University

Table 1 AFTRF critical data

AFTRF Parameter	Value	AFTRF Parameter	Value
Power	60.6 kW	Tip Radius	0.4582 m
Design RPM	1322	Tip Clearance	0.762 mm
Midspan Blade Speed (U_m)	54.89 m/s	Hub to Tip Ratio	0.7269
Design Mass Flow	11.05 kg/s	Rotor Chord Length	0.1287 m
Total-to-Total Efficiency	0.893	Rotor Spacing	0.1028 m
Nozzle Efficiency	0.994	Rotor Maximum Thickness	22.0 mm
Rotor Efficiency	0.882	Rotor Turning Angle	95° at Tip 126° at Hub
Pressure Ratio (P_{04}/P_{05})	1.078	Nozzle to Rotor Spacing	20%
Temperature Ratio (T_{05}/T_{04})	0.981	Number of Nozzle Vanes	23
Pressure Drop	56.04 mm Hg	Nozzle Turning Angle	70°
Inlet Re for Nozzle	3-4 x 10^5	Nozzle Chord Length	0.1768 m
Inlet Re for Rotor	3-5 x 10^5	Nozzle Spacing	0.1308 m
Number of Rotor Blades	29	Nozzle Maximum Thickness	38.8 mm
Hub Radius	0.3331m		

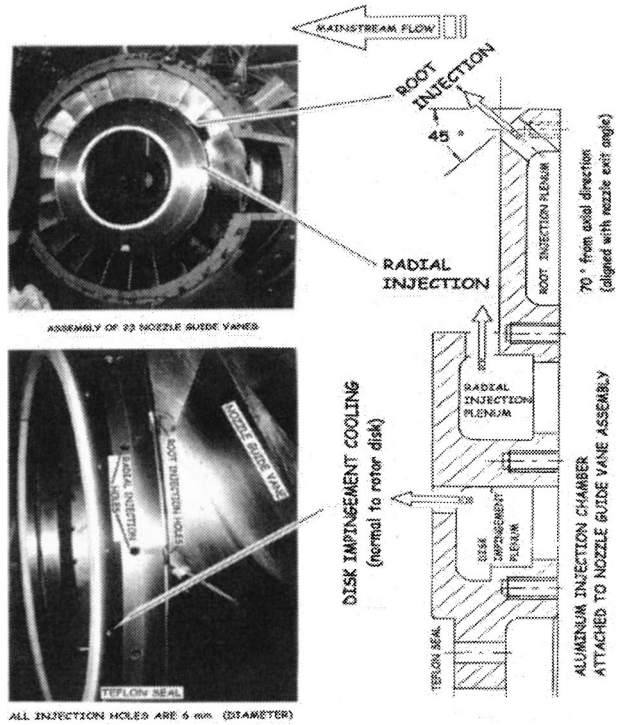

Fig. 3 Cooling flow injection chambers for radial cooling, impingement cooling, and root injection

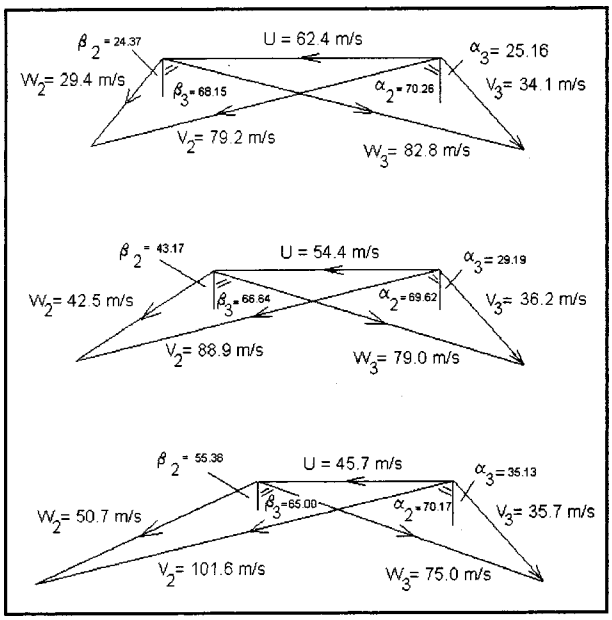

Fig. 4 Velocity triangles for the rotor at the hub (r = 0.3353 m), midspan (r = 0.3998 m), and tip (r = 0.4583 m)

four fans in series produce a pressure drop for the turbine test section of 74.7 mm Hg with a volumetric flow of 10.4 m^3/s (11.4 kg/s). A water-cooled eddy current brake dissipates the power generated by the turbine rotor. The speed of the rotor is fully adjustable from 175 to 1695 rpm and is stable to within ± 1 rpm. The operating point reference of 1322 rpm is at an ambient temperature and pressure of 25°C and 98.5 kPa, respectively. Operating the facility at corrected rotor speed minimizes effects of daily variations in inlet temperature conditions. The velocity triangles for the rotor at the hub, midspan and tip are shown in Fig. 4.

A major modification to the original AFTRF design was made to accommodate the injection of cooling air to the turbine wheelspace. Three independent sets of 23 cooling holes and plenums were added evenly spaced around the circumference. All cooling holes had a diameter of 6 mm.

Each set of 23 cooling holes is fed with a separate plenum and could be individually operated. All cooling holes are located around the circumference at the 23 nozzle trailing edge locations. Set I (radial cooling) injects cooling air radially along the nozzle wheelspace disk, Set II (impingement cooling) injects cooling air normal to the rotor disk, and Set III (root injection) injects cooling air at the nozzle guide vane root along the exit angle inclined 45 deg to the hub surface and aligned with the exit flow angle. The geometry of the three cooling hole sets is shown in Fig. 3. The cooling flow parameters are summarized in Table 2 where the mass flow ratio was defined as $\dot{m}_C/\dot{m}_P$, the mean discharge velocity was defined as $U_C = \dot{m}_C/n\rho A$, the mean discharge Mach number was defined as $M = U_C/\sqrt{\gamma RT_C}$, the blowing rate was defined as $\rho_C U_C/\rho_P U_P$ and the velocity ratio was defined as U_C/U_P.

Table 2 Coolant flow parameters for stationary frame measurements

Mass Flow Ratio $\dot{m}_C/\dot{m}_P$	Mean Discharge Velocity $U_C = \dot{m}_C/n\rho A$	Mean Discharge Mach Number $M = U_C/\sqrt{\gamma RT_C}$	Blowing Rate $\rho_C U_C/\rho_P U_P$	Velocity Ratio U_C/U_P
1.00%	158 m/s	0.46	1.56	3.95
1.25%	198 m/s	0.58	1.96	4.95
1.50%	237 m/s	0.70	2.35	5.93

The scaling of the various cooling flow parameters were established by considering the operational conditions of modern turbines. Blowing rates available in the AFTRF agree well with those in the literature.

Measurements

Exit flow surveys were taken in the AFTRF with and without cooling injection (1 percent) in the stationary frame. The flow field was measured using both five-hole and modified Kiel probes. The modified Kiel probe contained a miniature thermocouple in the stagnation tube. The probes were installed 1.5 axial chords downstream of the rotor. Probes were traversed in the radial and circumferential directions (stationary $r-\Theta$ traverse). Consequently, all rotor-induced variations in the circumferential direction were averaged out.

The cooled and noncooled data were taken in an interlaced manner. At each measurement point in the traverse grid, the probe readings were recorded with and without cooling flow. A set of high-speed solenoids controlled the coolant flow. This method ensured that the cooled and noncooled cases experienced the same mainstream flow conditions. Small variations in mainstream flow would otherwise be misreported as changes due to the cooling flow.

The pressures and temperatures sensed by the five-hole and Kiel probes were sampled via a personal computer with an analog to digital converter card. Cooled and noncooled data ($P_{05,1}, P_{05,2}, P_{05,3}, P_{05,4}, P_{05,5}$ for the five-hole probe and P_{05}, T_{05} for the Kiel probe) were sampled at 100 Hz for 15 seconds at each measurement point. The resulting data were time averaged at each measurement point and proper calibration equations were applied. The measured data at this sampling rate and duration were statistically stable. The result were data sets for cooled and noncooled cases containing T_0, P_0, P_S, u, v, w, U, a, and b at the rotor exit in (r, θ) plane.

Loading Coefficient. The loading coefficient gives insight into the total pressure drop across the turbine stage. The loading coefficient is defined as

Table 3 Percentage change in total pressure coefficient due to 1 percent cooling flow (passage-averaged)

$\Psi = \frac{P_{04} - P_{05}}{\frac{1}{2}\rho U_m^2}$	Radial Cooling Percentage Change	Impingement Cooling Percentage Change	Root Injection Percentage Change
Minimum	-1.50	-0.73	-2.57
Maximum	1.70	0.86	1.46
Average	-0.013	-0.067	-0.307

Table 4 Percentage change in static pressure coefficient due to 1 percent cooling flow (passage-averaged)

$\Psi_S = \frac{P_4 - P_5}{\frac{1}{2}\rho U_m^2}$	Radial Cooling Percentage Change	Impingement Cooling Percentage Change	Root Injection Percentage Change
Minimum	-0.18	0.00	-0.65
Maximum	0.31	0.30	0.29
Average	0.067	0.079	-0.126

$$\Psi = \frac{P_{04} - P_{05}}{1/2\rho U_m^2} \tag{1}$$

and the static pressure loss coefficient is defined as

$$\Psi_s = \frac{P_4 - P_5}{1/2\rho U_m^2} \tag{2}$$

where P_4 and P_{04} are the wall static pressure and midstream total pressure at location 4, respectively. Earlier measurements from Lakshminarayana et al. [17] showed these values to be representative of the inlet mass averaged values. The total and static pressure loss coefficients shown in Figs. 6 and 7 are simultaneously measured with a five-hole probe. The data with "no cooling" are displayed with the viewer looking upstream into the stage at location 5. Viewing direction is normal to the plane of data. The loss coefficients show significant radial and circumferential variations. Strong remnants of the nozzle wake and nozzle passage vortices are visible in the data shown in Figs. 6 and 7. Near the tip ($r = 0.44$) the loss coefficient is observed to be lower, showing the underturning due to leakage flow. Near the midspan ($r = 0.38$), a small region of overturning is visible.

The effect of the cooling injection can be seen qualitatively in the pressure coefficient data. The 1 percent cooling flow is able to cause significant local perturbations. Root injection shows the largest magnitude changes followed by radial cooling, and impingement cooling. In all cases the strongest effects are below midspan, but dwindling effects exist out to the tip regions. The magnitude changes in the total pressure coefficient were more significant that the static pressure coefficient.

All three cooling methods caused significant local changes and a general redistribution of the pressure coefficient data over the entire passage in both radial and tangential directions. Maximum effects ranged from 1.70, 0.86, and 2.57 percent for radial cooling, impingement cooling, and root injection, respectively.

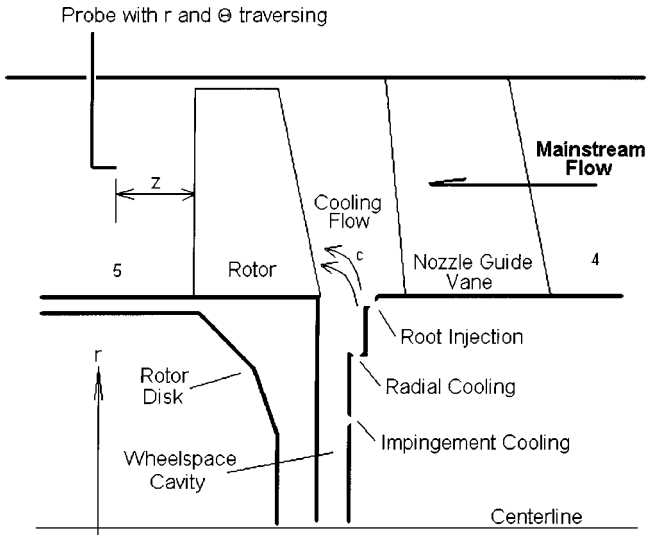

Fig. 5 Five-hole probe location in the stationary frame

Although the local perturbations were quite high, when passage average data were evaluated the changes were found to be significantly smaller. Radial and impingement cooling showed little overall effect on the pressure coefficient. The main result of radial and impingement cooling was a redistribution of pressure coefficient data. Root injection was able to affect the overall pressure coefficient as well as cause a redistribution of pressure coefficient data. The amount of change was almost five times that of impingement cooling and 30 times that of radial cooling. Passage averaged percentage changes in total pressure loss for radial cooling, impingement cooling, and root injection are -0.013, -0.067, and -0.307 percent, respectively. Summary data are presented in Table 3.

The decreases found in the pressure loss data are similar to that found by Friedrichs [18] in an endwall cooling study. He states that by neglecting the losses in the cooling lines, the change in overall loss is small for endwall cooling and can be positive or negative depending on the coolant supply pressure. Friedrichs further found that ejection of coolant ahead of the lift off lines could significantly change the secondary flow and reduce the associated losses.

Static pressure coefficients showed little effect from the cooling. Passage averaged percentage changes in static pressure loss for radial cooling, impingement cooling, and root injection are 0.067, 0.079, and -0.126 percent, respectively. Summary data are presented in Table 4.

Velocity Components and Exit Angles. The change in the individual velocity components due to wheelspace coolant injection can be observed best by examining the passage-averaged velocity components. Circumferentially averaged velocity components in radial, tangential, and axial directions are obtained from a

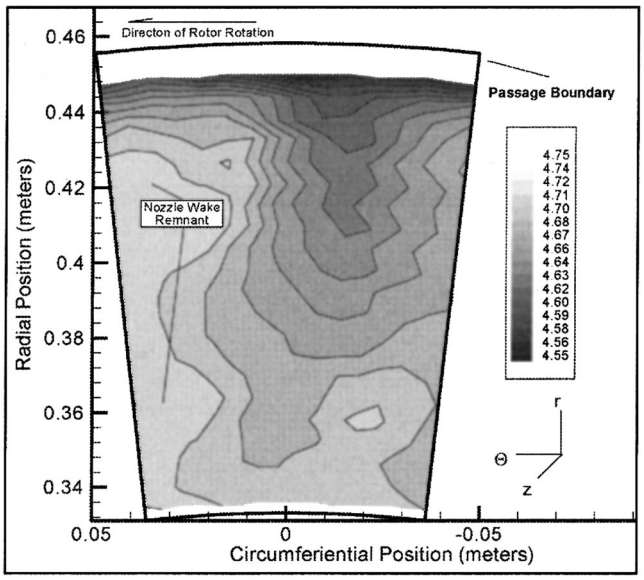

Fig. 6 Static pressure loss coefficient, 1.5 axial chords downstream of the rotor exit looking upstream from location 5

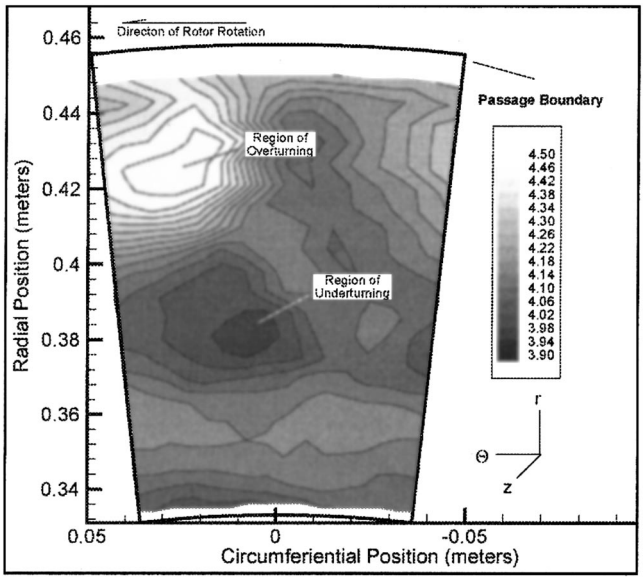

Fig. 7 Total pressure loss coefficient, 1.5 axial chords downstream of the rotor exit looking upstream from location 5

Table 5 Percentage change in total-to-total efficiency due to cooling flow (mass-averaged)

Mass Flow Ratio	Radial Cooling	Impingement Cooling	Root Injection
1.00%	+0.187	-0.777	+1.524
1.25%	-0.359	-0.248	+2.062
1.50%	+0.242	-0.149	+3.129

Table 6 Uncertainty in fundamental quantities

Parameter	Precision Error (S_x)	Bias Error (B_x)
u, v, w	0.4%	1.9%
Um	0.08%	0.4
Po, Ps	0.015%	0.2%
To	0.1 K	0.25 K
ρ	0.16%	2.0%

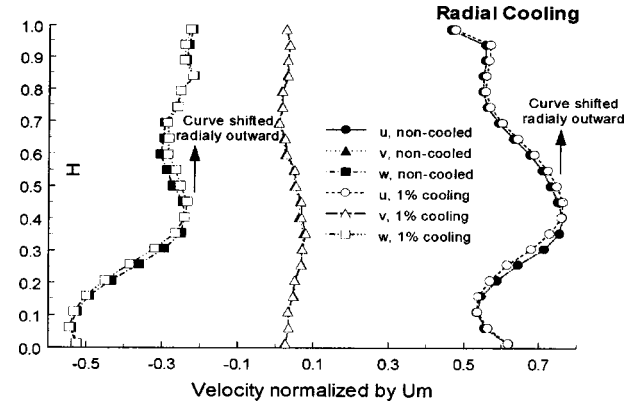

Fig. 8 Change in normalized, passage averaged, velocity components (u,v,w) due to 1 percent radial cooling. Stationary frame, 1.5 chords downstream.

subminiature five hole probe mounted 1.5 chord downstream of the rotor trailing edge plane, as shown in Fig. 5. Aerodynamic measurement details of this probe can be found in Wiedner [19]. The velocity data normalized by U_m and exit angles are displayed in Figs. 8–13. The radial velocity component (v) shows little

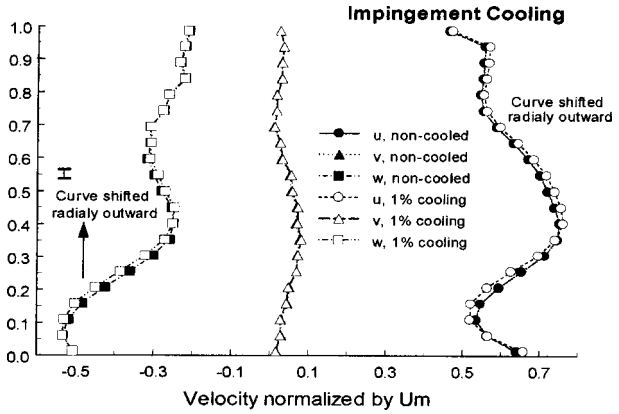

Fig. 9 Change in normalized, passage averaged, velocity components (u,v,w) due to 1 percent impingement cooling. Stationary frame, 1.5 chords downstream.

effect due to the coolant injection. In all three cases this velocity remains small and unperturbed. The effects of coolant inject are best observed in the axial (u) and tangential (w) components. The root injection shows the largest changes.

The baseline velocity distribution shows significant areas of overturning and underturning. Overturning and underturning refer to the deviation of the flow exit angle from invicid design. In a

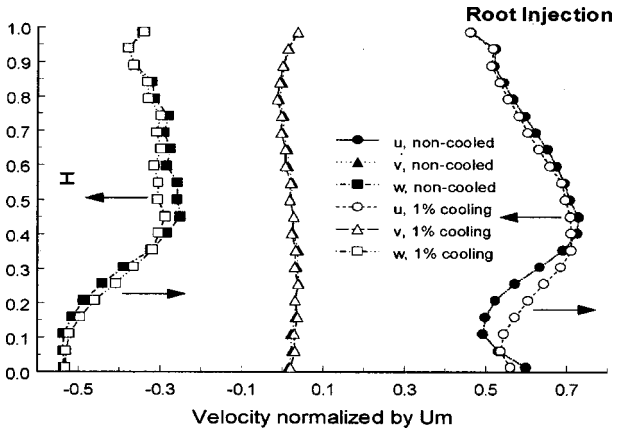

Fig. 10 Change in normalized, passage averaged, velocity components (u,v,w) due to 1 percent root injection. Stationary frame, 1.5 chords downstream.

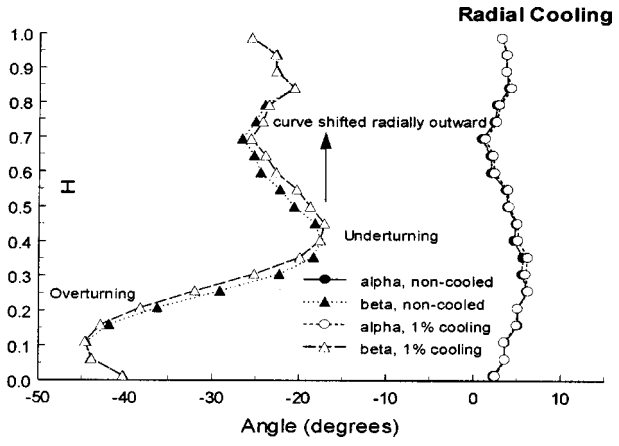

Fig. 11 Change in pitch (α) and yaw (β) angles due to 1 percent radial cooling. Stationary frame 1.5 chords downstream.

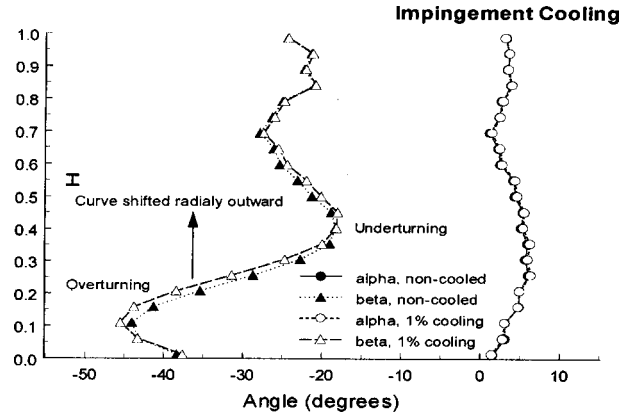

Fig. 12 Change in pitch (α) and yaw (β) angles due to 1 percent impingement cooling. Stationary frame, 1.5 chords downstream.

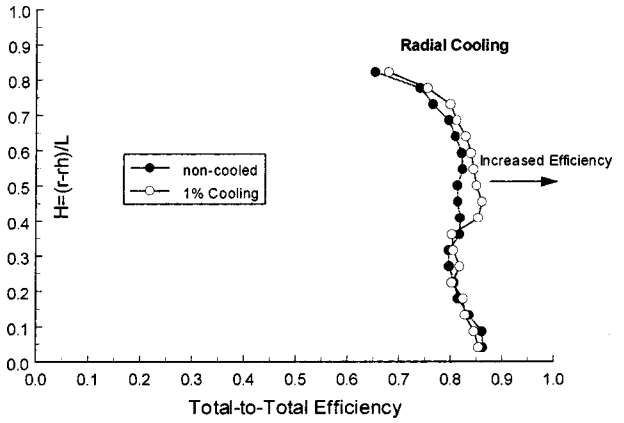

Fig. 14 Change in total-to-total efficiency (η) due to 1 percent radial cooling

real viscous fluid, the turbine passage has significant secondary flows in the form of vortices. These vortices will locally underturn or overturn the flow. An inviacid analysis of the AFTRF turbine stage yields an exit angle of approximately -30 deg. It can be seen that at an H of 0.1 a region of overturning exists and at an H of 0.4 a region of underturning exists. This flow profile is typical for the AFTRF and was first documented by Zaccaria [20].

Radial cooling shifts the velocity profiles radially outward. The overall magnitude of axial and tangential velocity is unchanged however, the point of maximum overturning is shifted radially by $H=0.10$. This can best be seen in the exit angle measurements (Fig. 17). This would seem to indicate that the vortex location is being modified but that the strength is not. Friedrichs [18] has also observed that endwall platform cooling could significantly shift the location of the passage vortex but that the strength was not significantly affected. The radial cooling is injected normal to the mainstream flow and would energize the rotor inlet boundary layer. This energizing would thicken the inlet rotor boundary layer. The thicker boundary layer would displace the core flow and the passage vortex slightly toward the tip region.

The impingement cooling shows similar effects to the radial cooling. Again, the overall magnitude of axial and tangential velocity is unchanged. The point of maximum overturning is shifted radially by $H=0.05$ smaller than with radial cooling. The impingement cooling enters the mainstream flow with minimal momentum having been stagnated on the rotor disk. The boundary layer would be thickened, but not to the degree found with radial cooling. The thicker boundary layer would displace the core flow and the passage vortex slightly toward the tip region.

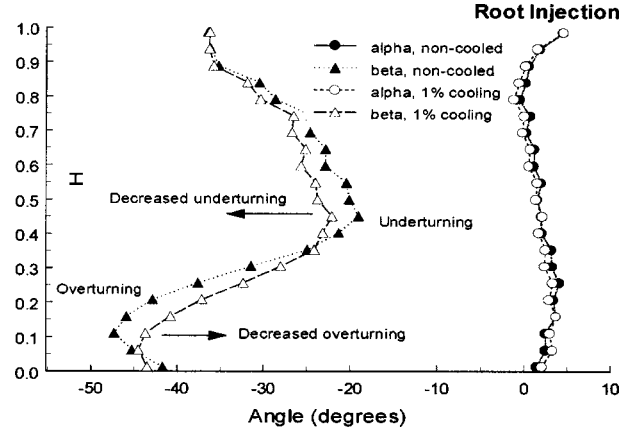

Fig. 13 Change in pitch (α) and yaw (β) angles due to 1 percent root injection. Stationary frame, 1.5 chords downstream.

The root injection shows the most significant effects due to the coolant injection and is fundamentally different from radial cooling and impingement cooling. Root injection has the ability to affect the magnitude of the overturning and underturning. The root injection energizes the nozzle wake and boundary layer near the hub wall. With an injection hole size on the order of the trailing edge thickness and with the injection inclined at 45 deg to the hub wall, the root injection can significantly energize the wake region. This has the effect of reducing the passage vortex and reducing the magnitude of overturning and underturning. Friedrichs et al. [18] also observed that significant cooling injection could delay the three-dimensional separation of the inlet boundary layer thereby reducing the strength of the passage vortex.

Total-to-Total Efficiency. Considering the primary flow (nozzle inlet to rotor exit) and one cooling stream (cooling inlet to rotor exit), the total-to-total efficiency can be written as:

$$\eta_{tt,c}=\frac{1+\left(\frac{\dot{m}_c}{\dot{m}_p}\right)\left(\frac{T_{oc}}{T_{04}}\right)-\left(\frac{\dot{m}_c}{\dot{m}_p}+1\right)\left(\frac{T_{05}}{T_{04}}\right)}{1+\left(\frac{\dot{m}_c}{\dot{m}_p}\right)\left(\frac{T_{oc}}{T_{04}}\right)-\left(\frac{\dot{m}_c}{\dot{m}_p}+1\right)\left(\frac{P_{05}}{P_{04}}\right)^{(\gamma-1)/\gamma}} \tag{3}$$

The specific efficiency equation suggested by McDonel and Eiswerth [21] is for total-to-total stage efficiency. Pumping work is not included in the stage efficiency equation. Pumping work losses are better handled in cycle analysis.

Measurements were taken at three blowing rates (1.00, 1.25, and 1.50 percent). Passage-averaged efficiency data are shown with their respective P_{05}/P_{04} and T_{05}/T_{04} in Figs. 21 and 22. Data are shown for 1 percent cooling only.

Cooling flows were able to modify the magnitude of the total pressure and total temperature ratios. As a result, the total-to-total efficiency was affected. Table 5 tabulates the mass-averaged changes in efficiency for 1.00, 1.25, and 1.50 percent relative cooling flow.

Radial cooling showed irregular changes in total-to-total efficiency. The changes in total-to-total efficiency due to radial cooling are shown in Figs. 14, 15, and 16. The passage-averaged efficiency change depended on the amount of coolant injection. For 1 percent coolant flow, the change was positive; at 1.25 percent the change was negative and at 1.5 percent the change was positive again. The mainstream pressure gradient turns the radial flow into the axial direction through a complex three-dimensional mix-

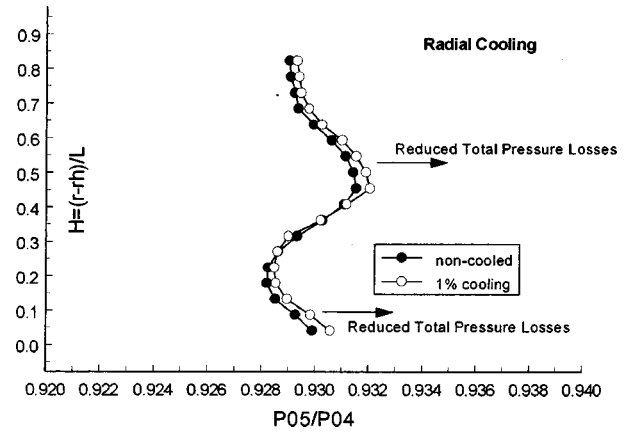

Fig. 15 Change in total pressure ratio (P_{05}/P_{04}) due to 1 percent radial cooling

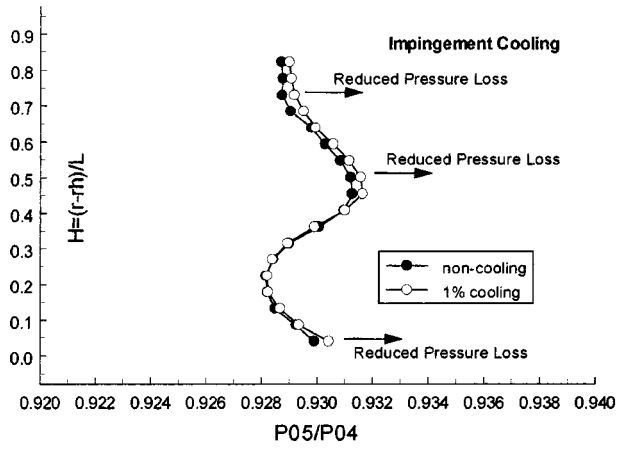

Fig. 18 Change in total pressure ratio (P_{05}/P_{04}) due to 1 percent impingement cooling

ing process. Different flow rates will cause possible separation of the mainstream flow and varying degrees of turbulent kinetic energy production and dissipation.

Impingement cooling caused the passage-averaged total-to-total efficiency to be lower. The results for the case of impingement cooling are given in Figs. 17, 18, and 19. The amount of change depended on the amount of cooling. The higher the flow rates, the less efficiency was lost. Over much of the passage the total pressure ratio was reduced, indicating lower pressure drop. In the midspan the total temperature ratio was increased leading to an increase in efficiency. However, the total temperature ratio was reduced over the hub and tip regions resulting in a lower efficiency. Very little useful energy is added to the flow through impingement cooling. Momentum is lost and the total temperature is increased when the fluid is stagnated on the rotor disk. The impingement cooling will tend to thicken the boundary layer with low-momentum fluid at a slightly elevated temperature. Increased total temperature, turbulent kinetic energy, and viscous dissipation in the boundary layer will lead to lower efficiency numbers.

Overall root injection results presented in Figs. 20, 21, and 22 showed the strongest changes in total-to-total efficiency. The passage-averaged efficiency increase was over 1.5 percent for 1 percent coolant injection. The total pressure ratio was significantly increased over $H=0.1$ to $H=0.5$. This in conjunction with a decrease in total temperature ratio over $H=0.2$ to $H=0.55$ cause the efficiency to rise significantly. The efficiency increase is localized to the midspan region of the blade. At both the hub and tip the efficiency is slightly lower. The root injection energizes the nozzle wake and boundary layer near the hub wall. With an injection hole size on the order of the trailing edge thickness and with the injection inclined at 45 deg to the hub wall, the root injection can significantly energize the wake region. The mean velocity gradients are reduced through midspan, thereby reducing turbulent

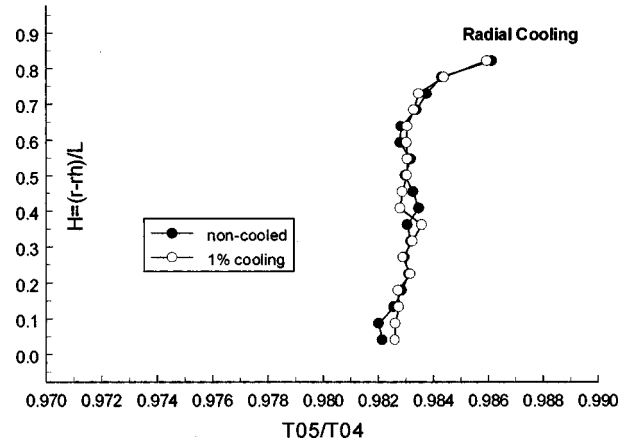

Fig. 16 Change in total temperature ratio (T_{05}/T_{04}) due to 1 percent radial cooling

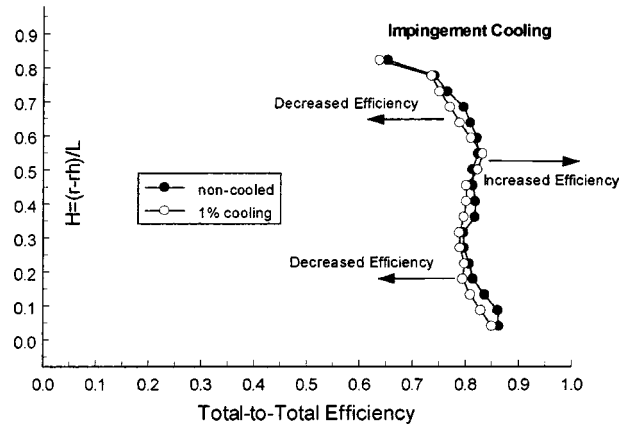

Fig. 17 Change in total-to-total efficiency (η) due to 1 percent impingement cooling

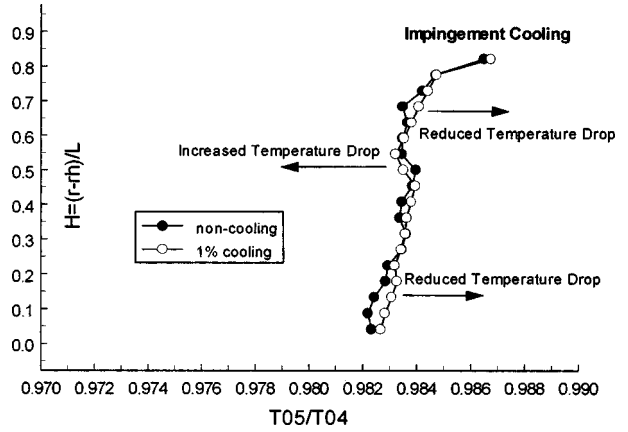

Fig. 19 Change in total temperature ratio (T_{05}/T_{04}) due to 1 percent impingement cooling

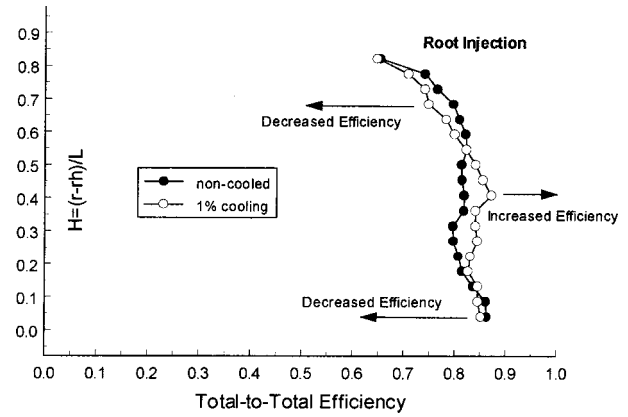

Fig. 20 Change in total-to-total efficiency (η) due to 1 percent root injection

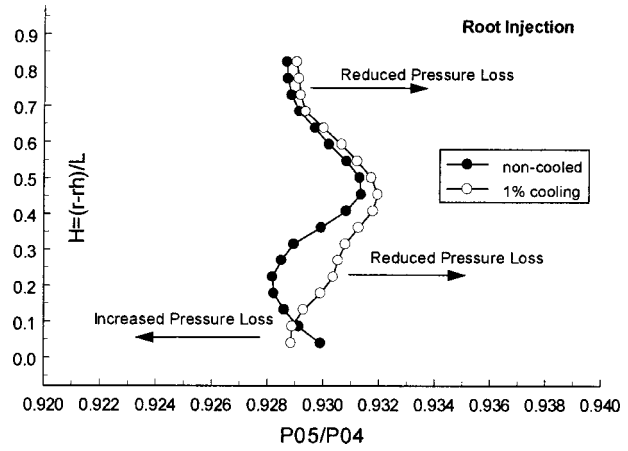

Fig. 21 Change in total pressure ratio (P_{05}/P_{04}) due to 1 percent root injection

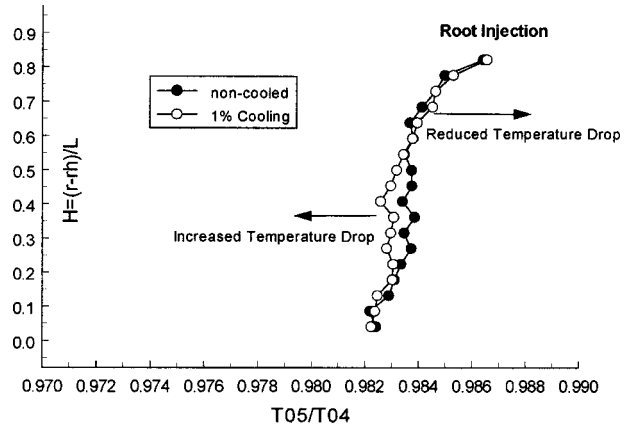

Fig. 22 Change in total temperature ratio (T_{05}/T_{04}) due to 1 percent root injection

mixing. Lower amount of turbulent mixing translates into less conversion of mean kinetic energy into internal energy via viscous dissipation.

Uncertainty Analysis

It was desired to both correct for quantifiable bias errors and to compute measurement uncertainties. The measurement philosophy of Wiedner [19] was adopted for the current research program. The philosophy is as follows:

Table 7 Absolute loading coefficient uncertainty

Parameter	Bias Error (B_x)	Effect on Loading Coefficient (ψ)
ρ	2.0%	1.96%
U_m	0.4%	0.80%
$P_{04} - P_{05}$	0.2%	0.2%

Table 8 Relative loading coefficient uncertainty

Parameter	Precision Error (S_x)	Effect on Loading Coefficient (ψ)
ρ	0.16%	0.16%
U_m	0.08%	0.15%
$P_{04} - P_{05}$	0.015%	0.015%

Table 9 Absolute efficiency uncertainty

Parameter	Bias Error (B_x)	Effect on Efficiency (η)
T_{04}	0.25 K	4.6%
T_{05}	0.25 K	4.7%
T_{0C}	0.25 K	0.005%
m_p	2.7%	0.005%
m_c	5.0%	0.01%
P_{04}	0.2%	0.21%
P_{05}	0.2%	0.21%

- When known sources of measurement error exist, avoid them.
- If known sources of error can not be avoided, and IF a repeatable bias error exists, correct for it.
- Avoid as many error sources as possible through calibration.
- If a source of error cannot be nulled thorough calibration or correction, provide an estimate of its magnitude.

Uncertainty in Fundamental Quantities. The five-hole and Kiel probe measurements were prone to various sources of error. They included turbulence effects, Reynolds number effects, Mach number effects, gradient effects, wall vicinity effects, probe blockage effects, recovery factor, misalignment errors, interpolation errors, calibration errors, data acquisition errors, and spatial location errors. Many of these error sources were quantifiable and were corrected for. The five-hole and Kiel probes were used to measure the fundamental quantities of u, v, w, P_o, P_s, and T_o. Following the methodology of Abernethy et al. [22], the uncorrectable uncertainty in velocity, pressure, and temperature and density are shown in Table 6.

It can be seen that there are significant differences between the precision (S_x) and bias errors (B_x). This is due to the interlaced manner in which the data sets were taken. In the present study it was desired to reduce the precision errors.

Following the error estimation of the five-hole probe and Kiel probe, the errors in the turbine performance parameters could be estimated. The ASME standard measurement uncertainty methodology [22] was used in conjunction with perturbation analysis to determine the measurement uncertainty.

Uncertainty in Loading Coefficient. The errors for the loading coefficient and change in loading coefficient are summarized in Tables 7 and 8. Combining the errors in Table 7 yields an uncertainty of 2.12 percent. The errors for the static pressure loss coefficient are identical to the loading coefficient. Combining the errors in Table 8 yields an uncertainty of 0.22 percent. The errors for the static pressure loss coefficient are identical to the loading coefficient.

Uncertainty in Total-to-Total Efficiency. The errors for the efficiency parameters are summarized in Tables 9 and 10. Combining the errors in Table 9 yields an efficiency error of 6.58

Table 10 Relative efficiency uncertainty

Parameter	Precision Error (S_x)	Effect on Efficiency (η)
T_{04}	0.1 K	1.8%
T_{05}	0.1 K	1.8%
T_{0C}	0.1 K	0.002%
m_p	0.44%	0.00087%
m_c	1.0%	0.002%
P_{04}	0.015%	0.02%
P_{05}	0.015%	0.02%

Table 11 Uncertainty summary

	Absolute Error (B_{xi})	Relative Error (S_{xi})	Relative with Circumferential Average (S_{xn}), n = 16	Relative with Passage Averaged (S_{xn}), n = 336
ι, v, w	1.9%	0.4%	0.3%	0.065%
'o, Ps	0.2%	0.015%	0.011%	0.0025%
To	0.25 K	0.1 K	0.075 K	0.016 K
ψ	2.12%	0.22%	0.17%	0.036%
η	6.58%	2.55%	1.91%	0.42%

percent. The errors for temperature measurement dominate. Combining the errors in Table 10 yields a relative efficiency error of 2.55 percent. The errors for temperature measurement dominate.

Uncertainty Summary. Table 11 summarizes the measured quantities and their respective uncertainties. The relationship in Eq. (4) was used to determine the uncertainty in an averaged quantity. It can be seen that the errors can be improved using circumferential and passage averaging on point quantities. This is useful, as most of the variations due to cooling are quite small and would be lost in the uncertainty variations otherwise.

$$S_{xn}=\frac{tS_{xi}}{\sqrt{n}} \tag{4}$$

Conclusions

The wheelspace coolant mixes with the mainstream flow and produces measurable changes in loss coefficient, velocity field, exit angle, and total-to-total efficiency. Local changes can be significant. The wheelspace coolant should not be neglected on the aerodynamic analysis of turbine blade stages. Overall, root injections showed the strongest effects although radial and impingement cooling showed measurable changes in loss coefficient, velocity, and efficiency.

The cooling flow caused significant local perturbations in the pressure coefficients. Root injection showed the largest changes, followed by radial cooling, and impingement cooling. In all cases, the strongest effects were below midspan but dwindling effects exist out to the tip regions. All three cooling methods caused significant local changes and a general redistribution of the data over the entire passage in both radial and tangential directions. Maximum effects ranged from 1.70, 0.86, and 2.57 percent for radial cooling, impingement cooling, and root injection, respectively. Although, the local perturbations were quite high, when passage-averaged data were evaluated, the changes were found to be small for radial cooling and impingement cooling. Root injection was able to affect the overall pressure coefficient as well as cause a redistribution of pressure coefficient data. The amount of change was almost five times that of impingement cooling and 30 times that of radial cooling.

The cooling flow was responsible for modifying the velocity profiles. Radial cooling and impingement cooling shifted the velocity profiles radially outward, while root injection was able to decrease the overturning and underturning. The point of maximum overturning was shifted radially by 10 percent for radial cooling and 5 percent for impingement cooling. The radial cooling is injected normal to the mainstream flow and would energize and thicken the rotor inlet boundary layer more than impingement cooling. The thicker boundary layer displaces the core flow and the passage vortex toward the tip region.

The root injection shows the most significant effects due to the coolant injection and is fundamentally different from radial cooling and impingement cooling. Root injection has the ability to affect the magnitude of the overturning and underturning. The amount of overturning and underturning is reduced.

Overall root injection showed the strongest changes in total-to-total efficiency. The passage-averaged efficiency increase was over 1.5 percent for root injection. The root injection efficiency increase was localized to the midspan region of the blade. With an injection hole size on the order of the trailing edge thickness and with the injection inclined at 45 deg to the hub wall, the root injection can significantly energize the nozzle wake region. Radial cooling showed irregular changes in total-to-total efficiency. For 1 percent coolant flow the change was positive, at 1.25 percent the change was negative and at 1.5 percent the change was positive again. Impingement cooling caused the passage-averaged total-to-total efficiency to drop.

Acknowledgments

This paper is based on university research funded by the U.S. Dept. of Energy, AGTSR program. The authors would like to acknowledge Drs. L. Golan, D. Fant, and R. Wenglarz as program monitors.

Nomenclature

A = exit area of single cooling hole
b = $\rho_C U_C / \rho_P U_P$
c_p = specific heat
H = normalized radial position $=(r-r_h)/L$
h = entropy
L = rotor blade height
R = gas constant
m = mass flow rate
M = Mach number $=U/\sqrt{\gamma RT}$
n = number of cooling holes (23)
P = pressure
r = radial position
T = temperature
u = axial velocity component
U, V, W = wheel speed, relative velocity, absolute velocity
U_d = discharge velocity $=m_C/n\rho A$
v = radial velocity component
w = tangential velocity component
α = pitch angle, exit flow angle inclined to the turbine axis
β = yaw angle, exit flow angle
γ = ratio of specific heats
η = efficiency
ρ = density
Θ = angle in circumferential direction

Subscripts

o = total condition
04 = entry of nozzle condition
05 = exit of rotor condition
1, 2, 3, 4, 5 = five-hole probe hole designation
c = cooling
h = hub
m = midspan condition
p = primary or mainstream
s = static condition
tt = total-to-total

References

[1] Karstensen, K., 1997, ''The Solar Turbines Project—Developing the 21st Century Gas Turbine,'' Department of Energy Office of Fossil Energy, Project Synopsis.

[2] Alwang, A., 1981, ''Measurement of Non-Steady Fluid Dynamic Quantitiés,'' von Karman Institute for Fluid Dynamics Lecture Series—Measurement Techniques in Turbomachines.

[3] Metzger, D., Kim, Y., and Yu, Y., 1993, ''Turbine Cooling: An Overview of Some Focus Topics,'' *Proc. 1993 International Symposium on Transport Phenomena in Thermal Engineering.*

[4] Owen, J. M., and Rogers, R. H., 1989, ''Flow and Heat Transfer in Rotating Disc Systems, Vol. 1: Rotor-Stator Systems,'' Research Studies Press ltd. and John Wiley.

[5] Bunker, R., Metzger, D., and Wittig, S., 1992, ''Local Heat Transfer in Turbine Disk Cavities: Part I—Rotor and Stator Cooling With Hub Injection of Coolant,'' ASME J. Turbomach., **114**.

[6] Bunker, R., Metzger, D., and Wittig, S., 1992, ''Local Heat Transfer in Turbine Disk Cavities: Part II—Rotor Cooling With Radial Location Injection of Coolant,'' ASME J. Turbomach., **114**.

[7] von Karman, T., 1921, ''Über Llaminare und Turbulente Reibung,'' Z. Angew. Math. Mech., **1**.

[8] Cobb, E., and Saunders, O., 1956, ''Heat Transfer From a Rotating Disk,'' Proc. R. Soc. London, Ser. A, **26A**, pp. 343–351.

[9] Maroti, L., Deak, G., and Kreith, F., 1960, ''Flow Phenomena of Partially Enclosed Rotating Disks,'' ASME J. Basic Eng., **82**.

[10] Daily, J., and Nece, R., 1960, ''Chamber Dimensional Effects on Induced Flow and Frictional Resistance of Enclosed Rotating Disks,'' ASME J. Basic Eng., **82**, pp. 217–232.

[11] Dorfman, L. A., 1963, *Hydrodynamic Resistance and the Heat Loss of Rotating Solids*, Oliver and Boyd, Edinburgh.

[12] Metzger, D., Mathis, W., and Grochowsky, L., 1979, ''Jet Cooling at the Rim of a Rotating Disk,'' ASME J. Eng. Power, **101**, pp. 68–72.

[13] Popiel, C., and Boguslawski, L., 1986, ''Local Heat Transfer From a Rotating Disk in an Impinging Round Jet,'' ASME J. Heat Transfer, **108**, pp. 357–364.

[14] Qureshi, G., Nguyen, M., Saad, N., and Tadros, R., 1989, ''Heat Transfer Measurements for Rotating Turbine Disks,'' ASME Paper No. 89-GT-26.

[15] Pincombe, J., 1989, ''Chapter 33, Gas Turbine Disk Cooling Flows,'' *Handbook of Flow Visualization*, Wen-Jei Yang, ed., Hemisphere Publishing Corp.

[16] Lakshminarayana, B., Camci, C., Halliwell, I., and Zaccaria, M., 1996, ''Design and Development of a Turbine Research Facility to Study Rotor–Stator Interaction,'' Int. J. Turbo Jet Engines, **13**, pp. 155–172.

[17] Laksminarayana, B., Camci, C., Halliwell, I., and Zaccaria, M., 1992, ''Investigation of Three Dimensional Flow Field in a Turbine Including Rotor/Stator Interaction,'' AIAA/SAE/ASME/ASEE 28th Joint Propulsion Conference and Exhibit, July 6–8, Nashville, TN.

[18] Friedrichs, S., Hodson, H. P., and Dawes, W. N., 1997, ''Aerodynamic Aspects of Endwall Film-Cooling,'' ASME J. Turbomach., **119**, pp. 786–795.

[19] Wiedner, G., 1994, ''Passage Flow Structure and Its Influence on Endwall Heat Transfer in a 90° Turning Duct,'' Ph.D. Thesis in Aerospace Engineering, The Pennsylvania State University.

[20] Zaccaria, M. A., 1994, ''Investigation of Three Dimensional Flow Field in a Turbine Including Rotor/Stator Interaction,'' Ph.D. Thesis in Aerospace Engineering, The Pennsylvania State University.

[21] McDonel, J. D., and Eiswerth, J. E., 1977, ''Effects of Film Injection on Performance of a Cooled Turbine,'' AGARD Conference Proceedings, CP-229.

[22] Abernathy, R. B., Benedict, R. P., and Dowdell, R. B., 1985, ''ASME Measurement Uncertainty,'' ASME J. Fluids Eng., **107**.

Mainstream Aerodynamic Effects Due to Wheelspace Coolant Injection in a High-Pressure Turbine Stage: Part II—Aerodynamic Measurements in the Rotational Frame

Christopher McLean[1]
e-mail: cmclean@techkor.com

Cengiz Camci
Professor of Aerospace Engineering
e-mail: cxc11@psu.edu

Turbomachinery Heat Transfer Laboratory,
The Pennsylvania State University,
University Park, PA 16802

Boris Glezer[2]
Optimized Turbine Solutions,
4140 Calle Isabelino,
San Diego, CA 92130
e-mail: bglezer@san.rr.com

The current paper deals with the aerodynamic measurements in the rotational frame of reference of the Axial Flow Turbine Research Facility (AFTRF) at the Pennsylvania State University. Stationary frame measurements of "Mainstream Aerodynamic Effects Due to Wheelspace Coolant Injection in a High Pressure Turbine Stage" were presented in Part I of this paper. The relative aerodynamic effects associated with rotor–nozzle guide vane (NGV) gap coolant injections were investigated in the rotating frame. Three-dimensional velocity vectors including exit flow angles were measured at the rotor exit. This study quantifies the secondary effects of the coolant injection on the aerodynamic and performance character of the stage main stream flow for root injection, radial cooling, and impingement cooling. Current measurements show that even a small quantity (1 percent) of cooling air can have significant effects on the performance and exit conditions of the high-pressure turbine stage. Parameters such as the total pressure coefficient, wake width, and three-dimensional velocity field show significant local changes. It is clear that the cooling air disturbs the inlet end-wall boundary layer to the rotor and modifies secondary flow development thereby resulting in large changes in turbine exit conditions. Effects are the strongest from the hub to midspan. Negligible effect of the cooling flow can be seen in the tip region. [DOI: 10.1115/1.1397303]

Introduction

This publication continues the documentation of the effects of wheelspace coolant on the mainstream flow in the AFTRF high-pressure gas turbine stage. Part I of this paper entitled ''Mainstream Aerodynamic Effects Due to Wheelspace Coolant Injection in a High-pressure Turbine Stage: Part I—Stationary Frame Measurements,'' documented the effects of the wheelspace cooling air in the stationary measurement frame. Following the measurements and analysis of the stationary frame data, it was desired to observe the effects in the rotational frame of reference. Data measured in the rotational frame would contain circumferential variations due to the rotor. In the stationary frame these variations were averaged out. Only in the rotational frame could the rotor wake and three-dimensional rotor exit velocity field be observed.

Most turbine cooling research has been limited to cascade facilities simulating nozzle blades. Little documented research exists with aerodynamic measurements from spinning rotors with cooling flows. Cascade studies similar to those of Eckert [1], Friedrichs [2]. Jabbari [3,4], Goldstein [5], Gaugler [6] and Graziani [7] demonstrate the complex nature of endwall cooling with stationary blades. However, the spinning rotor complicates the mixing of the cooling flow with the mainstream flow. Centrifugal forces and the periodic nature of turbine aerothermodynamics Abhari [8] necessitate that cooling research be performed in rotational environments when rotors are concerned. Periodic effects such as the circumferential variation in turbine entry temperature (TET) and the time-dependent variation in mainstream flow caused by the blade rotation cause a wide variation in cooling effectiveness. The cooling effectiveness fluctuation is driven by a change in the time averaged mass flux exiting from the cooling holes and by the interaction of the coolant with the unsteady external flow. Coolant jets are shown to pulsate due to the fluctuations of the instantaneous static pressure at the jet exit. Variations in the instantaneous film cooling effectiveness can be as high as 230 percent (Abhari [8]). A full understanding of turbine cooling flow effects can only be realized through rotational frame measurements.

Experimental Test Facility

The Axial Flow Turbine Research Facility (AFTRF) (Fig. 1) is a cold open-loop facility 0.916 m in diameter with a single-stage, high-pressure, axial turbine blading configuration. The facility consists of a bellmouth inlet, a single high-pressure turbine stage with a nozzle guide vane (NGV) and rotor, and outlet guide vanes. Detailed stage characteristics of this turbine facility can be found in Lakshminarayana, et al. [9,10] and Zaccaria [11]. The facility was used for the current research program with modifications to allow for the wheelspace cooling. Some of the facility details are also provided in Part I of this paper. The AFTRF is unique in its ability to operate continuously with a traversable sensor package in the rotational frame of reference. The AFTRF is able to traverse five-hole, thermocouple, and hot-wire probes in the rotational frame. A full two-dimensional traverse system is incorporated into the wheelspace allowing probe movements in the r and Q direc-

[1]Present address: Division Manager, Techkor Instrumentation, A Division of ACT, Inc., Harrisburg, PA.

[2]Former Head of ''Turbine Cooling Design and Analysis'' at Solar Turbines Inc., San Diego, CA.

Contributed by the International Gas Turbine Institute and presented at the 46th International Gas Turbine and Aeroengine Congress and Exhibition, New Orleans, Louisiana, June 4–7, 2001. Manuscript received by the International Gas Turbine Institute February 2001. Paper No. 2001-GT-120. Review Chair: R. Natole.

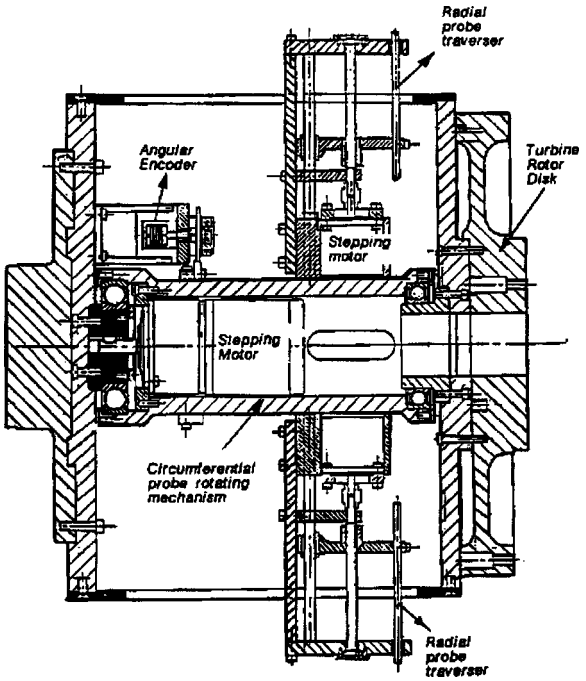

Fig. 1 Rotating instrument and traversing package contained within the rotor drum

Table 1 Coolant flow parameters for rotational frame measurements

Mass Flow Ratio	Mean Discharge Velocity	Mean Discharge Mach Number	Blowing Rate	Velocity Ratio
$\dot{m}_C/\dot{m}_P$	$U_C=\dot{m}_C/n\rho A$	$M=U_C/\sqrt{\gamma RT_C}$	$\rho_C U_C/\rho_P U_P$	U_C/U_P
1.00%	158 m/s	0.46	1.56	3.95

tions over one rotor blade passage in the mainstream. A 150-channel slip ring passes measurement data from the rotational to stationary frame. The rotational frame data were taken with the same three configurations for cooling air injection as the stationary frame measurements. The geometry of the three cooling hole sets is shown in Part I of this publication.

The cooling flow parameters are summarized in Table 1 where the mass flow ratio was defined as $\dot{m}_C/\dot{m}_P$, the mean discharge velocity was defined as $U_C=\dot{m}_C/n\rho A$, the mean discharge Mach number was defined as $M=U_C/\sqrt{\gamma RT_C}$, the blowing rate was defined as $\rho_C U_C/\rho_P U_P$ and the velocity ratio was defined as U_C/U_P.

The scaling of the various cooling flow parameters was established by considering the operational conditions of modern turbines. Blowing rates available in the AFTRF agree well with those in the literature. All rotational frame data were taken with a mass flow ratio of 1 percent.

Measurements

Five-hole probe surveys in the AFTRF were taken with and without cooling injection in the rotational frame. The subminiature five-hole probe was installed 1.5 axial chords downstream of the rotor trailing edge, as shown in Fig. 2. Data were taken with the five-hole probe mounted in the rotational frame and traversed in the radial and circumferential directions ($r-\Theta$ traverse). Aerodynamic measurement details of this probe can be found in Wiedner [12]. The velocity data were normalized by U_m. The rotational traverse had a circumferential sweep of 1.10 rotor blade passages.

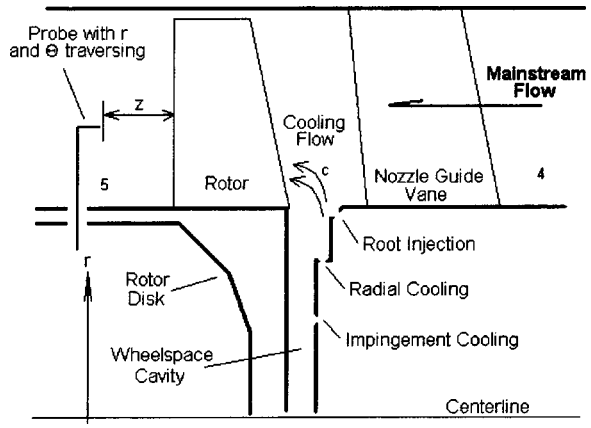

Fig. 2 Schematic diagram showing the placement of the five-hole probes for rotational frame data

The cooled and noncooled data were taken in an interlaced manner. At each measurement point in the traverse grid, the probe readings were recorded with and without cooling flow. A set of high-speed solenoids controlled the coolant flow. This method ensured that the cooled and noncooled cases experienced the same mainstream flow conditions. Small variations in mainstream flow would otherwise be misreported as changes due to the cooling flow.

The three-dimensional velocity field was measured with a subminiature five-hole probe. A data reduction method explained in Brophy et al. [13] was implemented. Measurement corrections due to the rotation of the probe mounted to the rotor exit were performed during the data reduction. The signals from the pressure transducers were internally amplified and passed through the slip ring to the stationary frame. The signals were then sampled via a personal computer with an analog to digital converter. Cooled and noncooled data ($P'_{05.1}, P'_{05.2}, P'_{05.3}, P'_{05.4}, P'_{05.5}$) were sampled at 100 Hz for 15 seconds at each measurement point. The measured data at this sampling rate and duration was statistically stable. The resulting data were statistically averaged and proper calibration equations were applied. The result were data sets for cooled and noncooled cases containing P_O, P_S, u, v, w, U, α, and β in the rotational frame. The legend for the data is given in Fig. 3.

Total Pressure Coefficient. The total pressure coefficient in the rotational frame was

$$\tilde{C}_p=\frac{\tilde{P}_{05}}{1/2\rho U_m^2} \tag{1}$$

computed from the following equation where the total pressure was measured with the rotating five-hole probe. The rotational total pressure was defined as:

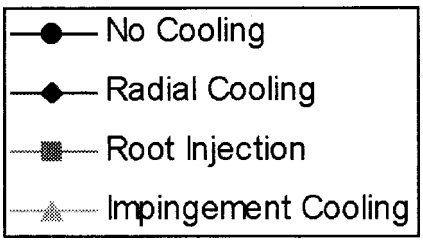

Fig. 3 Legend for data presentation of coolant flow measurements

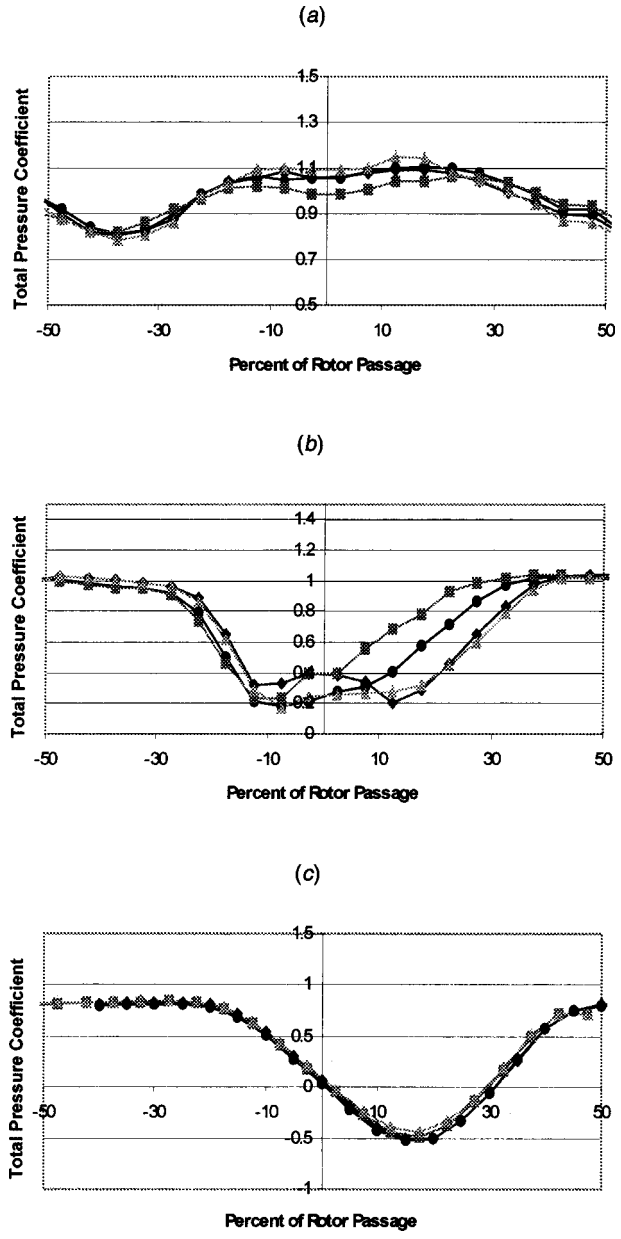

Fig. 4 Total pressure loss coefficient in rotational frame at *H* of 0.15 (*a*), 0.50 (*b*), and 0.90 (*c*). Probe 1.5 chords downstream of the rotor exit.

$$\tilde{P}_{05} = \tilde{P}_5 + \frac{1}{2}\rho\tilde{U}^2 \tag{2}$$

The total pressure coefficient, shown in Fig. 4, displays the rotor wake at three sections: hub ($H=0.15$), midspan ($H=0.50$), and tip ($H=0.90$).

At the hub section ($H=0.15$), the effects of the cooling injection are minimal. The radial and impingement cooling show relatively small changes of 3 percent. With the root injection, the magnitude of the wake is changed by up to 8 percent. It should be noted that the changes of root injection are opposite in direction to those of radial and impingement cooling.

The total pressure coefficient at the midspan ($H=0.50$) shows significant effects due to cooling injection. The 1 percent cooling injection has the ability to produce up to 88 percent local changes in total pressure coefficient (midspan, root injection, center of wake). The root injection reduces the width of the wake region while the radial, and impingement cooling causes the wake width to increase. The large changes in the rotor wake are due to a shift in the wake position and wake width rather than a change in the wake peak or trough magnitudes. For this reason the total pressure coefficient in the stationary frame (loss coefficient) shows relatively small changes (1 to 3 percent) due to cooling (see Fig. 7 in Part I of this publication). The changes observed in the stationary frame are due to a change in the rotor wake width in the rotational frame. The effect of the width change is smoothed out in the stationary frame measurements. To understand the physical mechanism, responsible for the loss coefficient changes it is necessary to look in the rotational frame.

At the tip section ($H=0.90$), the effects of the cooling injection are immeasurable. The cooling air does not mix with or effect the tip flow region. The variations found in the pressure loss data are similar to that found by Friedrichs [14] in an endwall cooling study. He states that the change in overall loss is small for endwall cooling and can be positive or negative depending on the coolant supply pressure. The direction of change would also depend on the cooling geometry.

Velocity Components. Axial, tangential, and radial velocity data are shown in Figs. 5, 6, and 7. All data have been normalized by the blade rotational velocity at midspan (U_m) as shown in Eqs. (3)–(5):

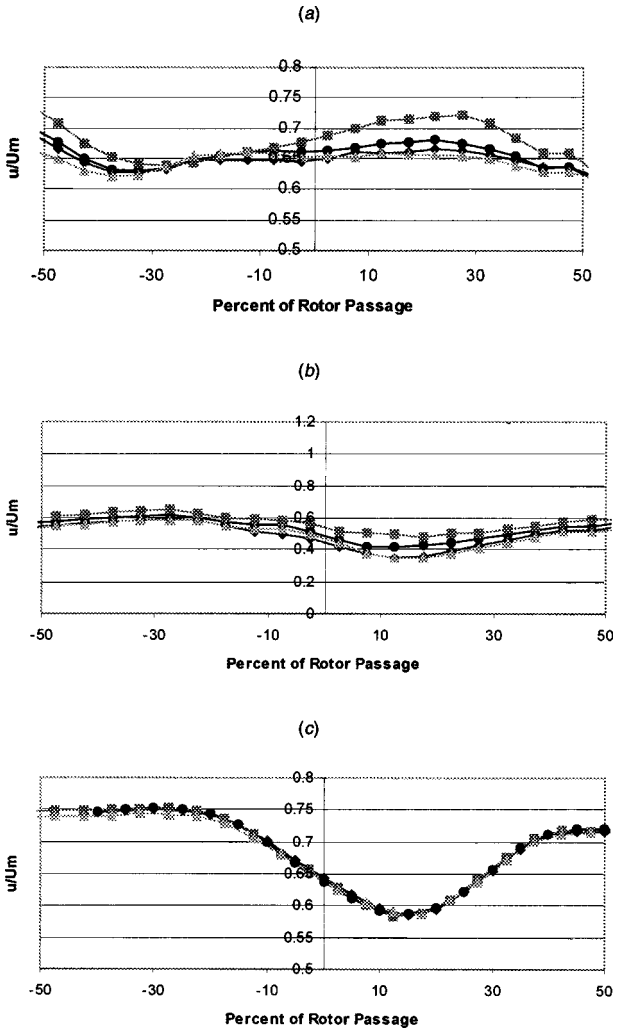

Fig. 5 Axial velocity in the rotational frame at *H* of 0.15 (*a*), 0.50 (*b*), and 0.90 (*c*). Probe 1.5 chords downstream of the rotor exit.

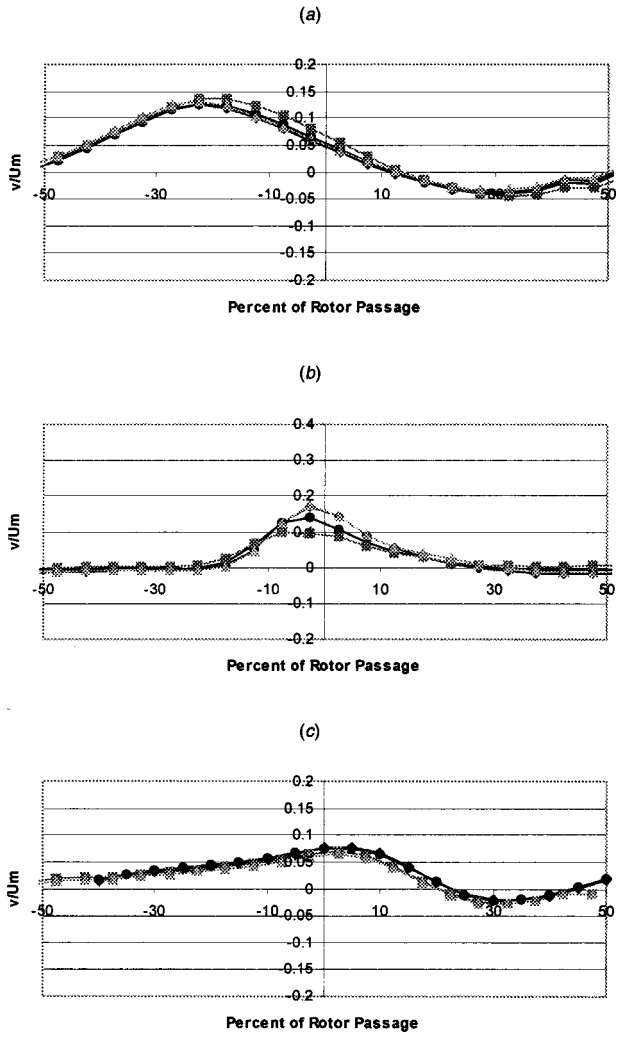

Fig. 6 Radial velocity in the rotational frame at *H* of 0.15 (*a*), 0.50 (*b*), and 0.90 (*c*). Probe 1.5 chords downstream of the rotor exit.

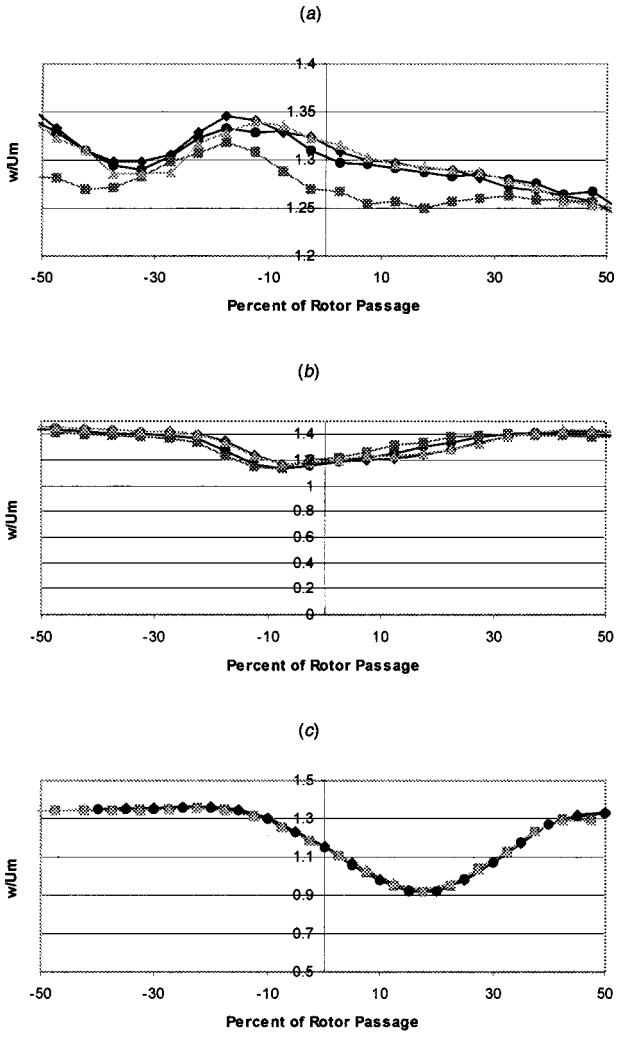

Fig. 7 Tangential velocity in the rotational frame at *H* of 0.15 (*a*), 0.50 (*b*), and 0.90 (*c*). Probe 1.5 chords downstream of the rotor exit.

$$\tilde{u}_{\text{normalized}} = \frac{u}{U_m} \tag{3}$$

$$\tilde{v}_{\text{normalized}} = \frac{\tilde{v}}{U_m} \tag{4}$$

$$\tilde{w}_{\text{normalized}} = \frac{\tilde{w}}{U_m} \tag{5}$$

The axial velocity (u) shows significant changes at the hub ($H = 0.15$) and midspan ($H = 0.50$) locations. At both the hub and midspan locations, the root injection tends to increase the axial velocity and the radial and impingement cooling tend to decrease the axial velocity. At the hub, the magnitudes of the root injection are twice those of the radial and impingement cooling. At the midspan, the magnitudes are comparable.

The axial velocity has immeasurable changes at the tip ($h/H = 0.90$). As was observed in the pressure coefficient data, the cooling flow does not mix with or affect the tip flow region. The tangential velocity (w) shows significant effects due to the cooling flow at the hub ($H = 0.15$) and midspan ($H = 0.50$) locations. The effect is reversed from that seen in the axial velocity. At both the hub and midspan locations, the root injection tends to decrease the axial velocity and the radial and impingement cooling tend to increase the axial velocity. At the hub, the magnitudes of the root injection changes (3.5 percent) are considerably higher than those of the radial and impingement cooling (0.5 percent). At the midspan, the magnitudes are comparable (4 percent). The tangential velocity has immeasurable changes at the tip ($H = 0.90$). As was observed in the pressure coefficient data, the cooling flow does not mix with or affect the tip flow region.

The radial velocities in the AFTRF tend to be small in magnitude, but large changes were observed in their magnitudes. The largest changes were observed at the midspan. Root injection was able to decrease the radial velocity by as much as 30 percent, while the radial and impingement cooling were able to decrease the axial velocity by up to 20 percent.

The radial velocity has immeasurable changes at the tip ($H = 0.90$). As was observed in the pressure coefficient data, the cooling flow does not mix with or affect the tip flow region.

Exit Angles. With the three-dimensional velocity field known, it was possible to compute the exit angles for the turbine stage. The exit angle in the axial-tangential plane (β) is shown in Fig. 8 and the exit angle in the axial-radial plane (α) is shown in Fig. 9. The axial–radial plane (α) exit angle shows significant variation at the hub ($H = 0.15$) and midspan ($H = 0.50$) sections. The change is driven by the large magnitude changes in the radial velocity. At the hub, the root injection increased the exit angle by up to 2 deg. At the midspan, the root injection decreases the exit

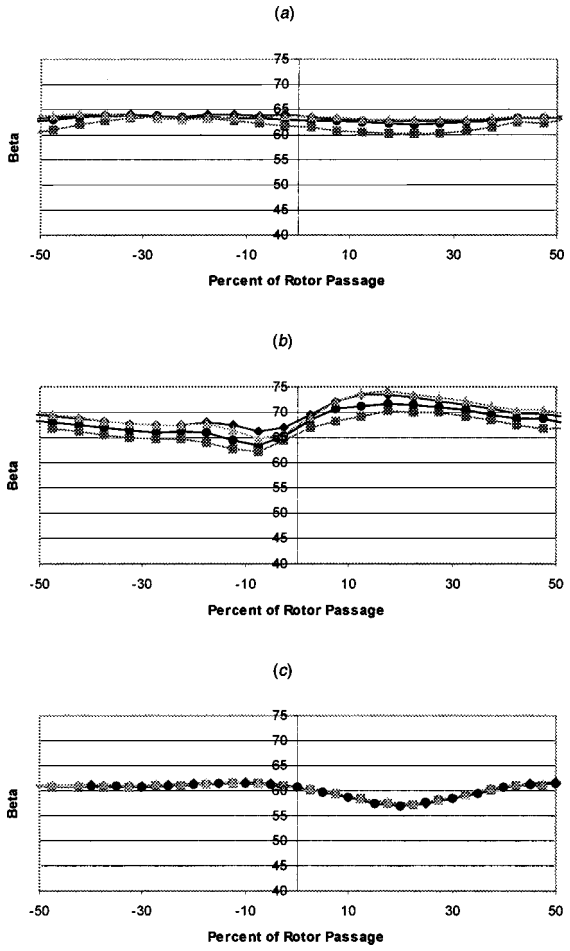

Fig. 8 Exit angle in the rotational axial-tangential plane (β) at H of 0.15 (*a*), 0.50 (*b*), and 0.90 (*c*). Probe 1.5 chords downstream of the rotor exit.

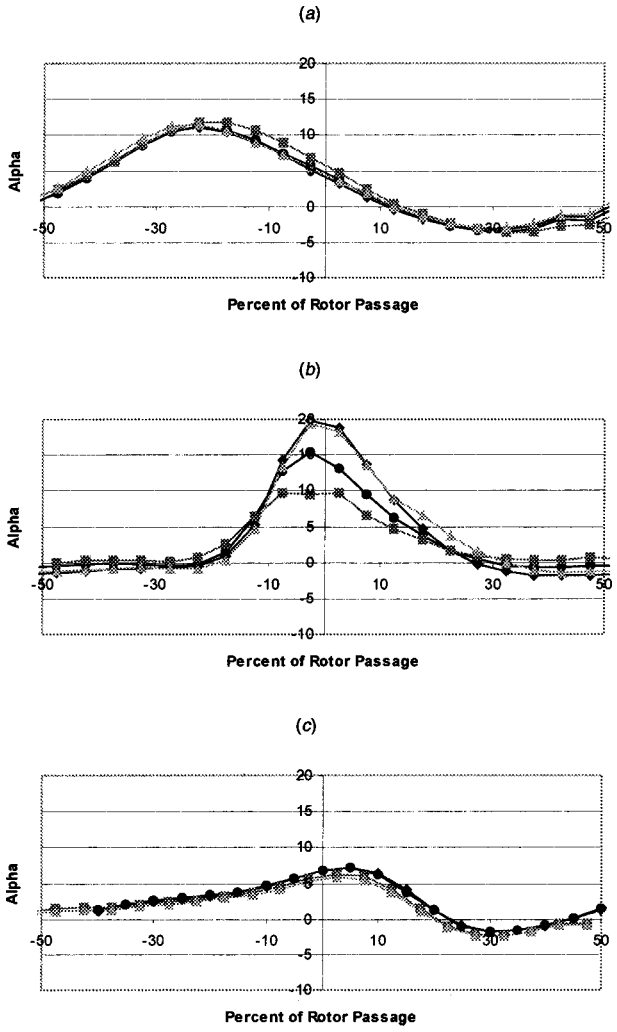

Fig. 9 Exit angle in the rotational axial-radial plane (α) at H of 0.15 (*a*), 0.50 (*b*), and 0.90 (*c*). Probe 1.5 chords downstream of the rotor exit.

angle by up to 5 deg, while the radial and impingement cooling increase the exit angle by up to 5 deg. At the tip region, root injection and impingement cooling were able to reduce the exit angle by 1 deg while radial cooling had no effect.

The axial–tangential plane (β) exit angle shows significant variation at the hub ($H=0.15$) and midspan ($H=0.50$) sections. The variations follow the changes in velocity in the axial and tangential directions. At the hub the root injection reduces the exit angle by up to 2.5 deg. The radial and impingement cooling show little effect. At the midspan location, the root injection reduces the exit angle by up to 2.5 deg while the radial and impingement cooling increase the exit angle by up to 2.5 deg. At the tip region none of the cooling flows show any measurable changes.

The opposite changes found in the rotational frame measurements are consistent with the exit angle changes seen in the stationary frame. However, in the stationary frame it was found that the radial and impingement exit angle changes were caused by a radial outward shift in the profiles, not a change in their overall magnitudes.

This would seem to indicate that the passage vortex location is being modified but that the strength is not. Friedrichs et al. [2] also observed that endwall platform cooling could significantly shift the location of the passage vortex but that the strength was not significantly affected.

Conversely, root injection in the stationary frame was found to be able to reduce the magnitude of the passage vortexes, thereby changing the overall magnitude of the exit angle. Friedrichs et al. [14] also observed that significant cooling injection could delay the three-dimensional separation of the inlet boundary layer thereby reducing the strength of the passage vortex.

Time Accurate Dynamic Pressure. Measurements of the surface pressure on the leading edge of the rotor were performed ($H=0.10$). The AFTRF contained embedded Kulite pressure transducers with a very high dynamic response. The Kulite transducers had thermal and long-term stability problems that prevented them from being calibrated for absolute pressure measurements. However, the Kulites were useful in measuring the relative changes in the nozzle wakes. The response time of the Kulites was fast enough to capture individual nozzle wakes as seen from the rotor tip.

A comparison of the three baseline measurements was performed to determine the level of repeatability in the Kulite data. Excellent repeatability was found between the three runs. Ensemble-averaged dynamic pressure data are shown in Fig. 10 for root injection. The 23 individual nozzle blade passings are visible in the measurement data. It should be noted that slight differences exist between the wakes. Each nozzle has a distinct wake profile. When taking data in the rotational frame only one specific wake profile is being analyzed, while when taking data in the stationary frame all wakes are being measured and averaged by the probe. As a result, comparisons between rotational frame data and stationary frame data must be made carefully.

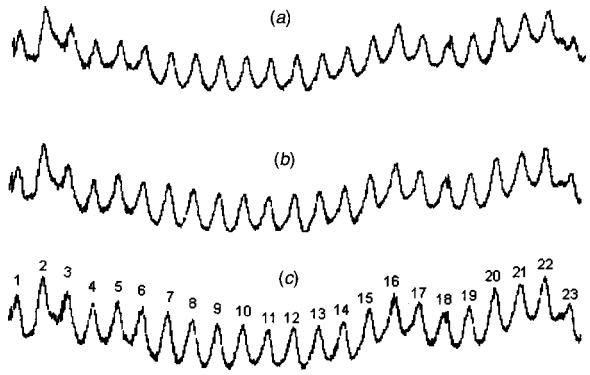

Fig. 10 Pressure measurements on the rotor leading edge for root injection blowing ratios of 1.00 percent (*a*), 1.25 percent (*b*), and 1.50 percent (*c*)

Fig. 11 Kulite data from the rotor platform. The root injection (jagged line) shows noticeable wake reduction from the non-cooled case. Four vane passages are shown.

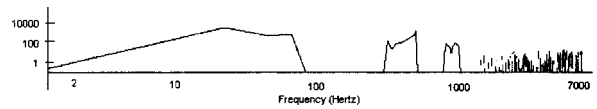

Fig. 12 Frequency domain processing of leading edge Kulite run data with fast Fourier transform

The frequency domain processed data are shown in Figs. 11 and 12. Several fundamental frequency components can be seen including the once-per-rev (22 Hz), nozzle blade passing (507 Hz), and twice nozzle blade passing (1014 Hz).

Conclusions

The effects of small (1 percent) coolant injection into the free stream of a high-pressure turbine stage can be very significant and should not be neglected on the aerodynamic analysis of turbine stages. The cooling air is affecting the structure of the three-dimensional secondary flow and inlet rotor boundary layer, which in turn has a large effect on the exit three-dimensional flow and stage performance.

The changes observed were large and three-dimensional in nature. Their neglect in stage blading design could lead to serious miscalculations. Parameters such as pressure coefficient, wake width, three-dimensional velocity field, and exit angles were observed to change significantly.

The cooling was able to produce significant changes in the total pressure coefficient. The large changes in pressure coefficient are due to a shift in the wake position and wake width rather than a change in the wake peak or trough magnitudes. In the rotational frame, root injection reduced the width of the wake while radial and impingement cooling increased the width. The effects of the rotational frame width changes are smoothed out in the stationary frame measurements. To understand the physical mechanism responsible for the loss coefficient changes (stationary frame), it is necessary to look in the rotational frame.

Root injection tended to have an opposite effect on the three-dimensional velocity field from radial and impingement cooling. This is consistent with the stationary frame data provided in Part I of this publication. Again, it is necessary to examine both the stationary and rotational frames to have a complete understanding of the physics controlling the velocity field.

The changes in rotor exit flow are highest at the midspan. The effects of the cooling are convected to the midspan by the action of the passage vortices. It is believed that the cooling air is energizing the boundary layer ahead of the rotor thereby effecting the development and effects of the secondary flows.

Additional research should be performed to detail the complex cooling-mainstream mixing process and its effects on the inlet rotor boundary layer and the resulting secondary flows.

Acknowledgments

This paper is based on university research funded by the U.S. Dept. of Energy, AGTSR program. The authors would like to acknowledge Drs. L. Golan, D. Fant, and R. Wenglarz as program monitors.

Nomenclature

A = exit area of single cooling hole
b = $\rho_C U_C / \rho_P U_P$
H = normalized radial position $= (r - r_h)/L$
h = entropy
L = rotor blade height
M = Mach number
$\dot{m}$ = mass flow rate
n = number of cooling holes (23)
P = pressure
R = gas constant
r = radial position
T = temperature
U, V, W = wheel speed, relative, velocity, absolute velocity
u = axial velocity component
v = radial velocity component
w = tangential velocity component
α = pitch angle, exit flow angle inclined to the turbine axis
β = yaw angle, exit flow angle
γ = ratio of specific heats
Θ = angle in circumferential direction
ρ = density

Subscripts

c = cooling
o = total condition
04 = entry of nozzle condition
05 = exit of rotor condition
h = hub
m = blade rotational velocity at midspan
p = primary
s = static condition
total = total condition

Superscripts

~ = rotational frame value

References

[1] Eckert, E., 1984, "Analysis of Film Cooling and Full Coverage Film Cooling of Gas Turbine Blades," ASME J. Eng. Gas Turbines Power, **106**.
[2] Friedrichs, S., Hodson, H., and Dawes, W., 1997, "Aerodynamic Aspects of Endwall Film-Cooling," ASME J. Turbomach., **119**, pp. 786–793.
[3] Jabbari, M., and Goldstein, R., 1993, "Film Cooling, Mass Transfer, and Flow at the Base of a Turbine Blade," J. Eng. Phys. Thermophys., **65**, No. 3.
[4] Jabbari, M., Marston, K., Eckert, E., and Goldstein, R., 1996, "Film Cooling of the Gas Turbine Endwall by Discrete-Hole Injection," ASME J. Turbomach., **118**, pp. 278–284.
[5] Goldstein, R., and Chen, H., 1985, "Film Cooling on a Gas Turbine Blade Near the End Wall," ASME J. Eng. Gas Turbines Power, **107**.
[6] Gaugler, R., and Russell, L., 1984, "Comparison of Visualized Turbine Sec-

ondary Flows and Measured Heat Transfer Patterns,'' ASME J. Eng. Gas Turbines Power, **106**.
[7] Graziani, R., Blair, M., Taylor, J., and Mayle, R., 1980, ''An Experimental Study of Endwall and Airfoil Surface Heat Transfer in a Large Scale Turbine Blade Cascade,'' ASME J. Eng. Power, **102**, pp. 257–267.
[8] Abhari, R., 1996, ''Impact or Rotor-Stator Interaction on Turbine Blade Film Cooling,'' ASME J. Turbomach., **118**.
[9] Lakshminarayana, B., Camci, C., Halliwell, I., and Zaccaria, M., 1992, ''Investigation of Three Dimensional Flow Field in a Turbine Including Rotor/Stator Interaction,'' presented at the AIAA/SAE/ASME/ASEE 28th Joint Propulsion Conference and Exhibit, July 6–8, Nashville, TN.
[10] Lakshminarayana, B., Camci, C., Halliwell, I., and Zaccaria, M., 1996, ''Design and Development of a Turbine Research Facility to Study Rotor-Stator Interaction,'' Int. J. Turbo and Jet Engines, **13**, pp. 155–172.
[11] Zaccaria, M. A., 1994, ''Investigation of Three Dimensional Flow Field in a Turbine Including Rotor/Stator Interaction,'' Ph.D. Thesis in Aerospace Engineering, The Pennsylvania State University.
[12] Wiedner, G., 1994, ''Passage Flow Structure and its Influence on Endwall Heat Transfer in a 90° Turning Duct,'' Ph.D. Thesis in Aerospace Engineering, The Pennsylvania State University.
[13] Brophy, M., Treaster, A., Stinebring, D., and Welz, J., 1984, ''Optimization of a Five-Hole Probe Wake Measurement System,'' Applied Research Laboratory, The Pennsylvania State University.
[14] Friedrichs, S., Hodson, H. P., and Dawes, W. N., 1995, ''Distribution of Film-Cooling Effectiveness on a Turbine Endwall Measured Using the Ammonia and Diazo Technique,'' ASME Paper No. 95-GT-1.

Heat Transfer and Flow on the Blade Tip of a Gas Turbine Equipped With a Mean-Camberline Strip

A. A. Ameri
AYT Corp.,
Brook Park, OH 44135-3109
e-mail: ameri@grc.nasa.gov

Experimental and computational studies have been performed to investigate the detailed distribution of convective heat transfer coefficients on the first-stage blade tip surface for a geometry typical of large power generation turbines (>100 MW). In a previous work the numerical heat transfer results for a sharp edge blade tip and a radiused blade tip were presented. More recently several other tip treatments have been considered for which the tip heat transfer has been measured and documented. This paper is concerned with the numerical prediction of the tip surface heat transfer for radiused blade tip equipped with mean-camberline strip (or "squealer" as it is often called). The heat transfer results are compared with the experimental results and discussed. The effectiveness of the mean-camberline strip in reducing the tip leakage and the tip heat transfer as compared to a radiused edge tip and sharp edge tip was studied. The calculations show that the sharp edge tip works best (among the cases considered) in reducing the tip leakage flow and the tip heat transfer. [DOI: 10.1115/1.1400114]

Introduction

Blade tips are susceptible to burnout and oxidation due to high thermal loading caused by the tip leakage flow. Efficient internal or film cooling schemes are necessary to protect turbine blades against damage. The design of such schemes requires detailed knowledge of heating patterns on and near the tips which could be gained by experimental and predictive methods. It was shown by Mayle and Metzger [1] that the heat transfer at a blade tip (and by extension total pressure loss) is not very much affected by rotation. This has spurred experimental work on measuring tip heat transfer for various blade tip treatments on stationary cascades and has provided data for numerical simulations. In a previous numerical study [2] the predicted tip heat transfer for a sharp edge tip and a radiused tip (blade tip with a rounded edge around the perimeter of the blade tip) was compared with the measured experimental data of Bunker et al. [3]. The data was, at the time, the only set of liquid crystal measurements of tip heat transfer. The results of simulations nicely agreed with the experimental data and showed that the tip heat transfer for radiused edge would be larger than that for a sharp edge tip due to the relatively higher velocity on the radiused edge tip. More recently, Bunker and Bailey [4] have made further measurements for various tip treatments including circumferential rub strip, 45-degree angled run strips, perimeter squealer rim, and mean-camberline strip.

The perimeter squealer tip case has already been computed by Ameri et al. [5] though for a different blade configuration. In this paper the mean-camberline strip (squealer) case has been computed. The computed tip heat transfer has been compared with experimental measurements. As the experiment was mainly concerned with the measurement of the rate of heat transfer, the numerical simulation attempts to construct the flow structure in order to help explain the phenomena observed in the experiments.

In the ensuing section, a brief description of the experiment simulated in this work is provided. The numerical method employed and the grid topology used to model the computational domain are described subsequently. The flow characteristics and tip leakage rate as well as the tip heat transfer are next presented and are followed by a summary and presentation of the conclusions of the work.

The Experimental Setup

The experimental setup and conditions are similar to those described in [3]. In that paper the pressure distribution and tip heat transfer for both a sharp edge tip and radiused edge tip of the present blade geometry were presented. The heat transfer measurement considered in this paper is for the same radiused edge blade in [3] but is equipped with a mean-camberline strip as given in Bunker and Bailey [4].

Figure 1 shows the definition of the airfoils and the shroud. The blade profiles are typical of a large power generation turbine. The cascade is linear and the span is 10.16 cm. As can be seen the shroud incorporates a recess ahead of the blades to model a similar feature found in an actual turbine shroud. The instrumented blade has a rounded edge of 2.54 mm radius. The tip clearance addressed in this paper is the nominal value of 2.03 mm measured from the top surface of the mean-camberline strip. The height of the mean-camberline strip was 1.27 mm. This places the blade tip surface at 3.30 mm from the shroud (in [3], this distance was 2.03 mm). The strip in the experiment and in the calculations has a square cross section and sharp edges. Figure 2 shows the design of the actual two passage blade cascade as reproduced from Bunker et al. [3]. The extent of the strip is from the leading edge to 85 percent axial chord. Table 1 lists the run conditions for the cascade and input to the numerical simulations.

The Computational Method

The simulations in this study were performed using a multiblock computer code called Glenn-HT [6] which is based on a single block code designed by Arnone et al. [7]. This code is a general purpose flow solver designed for simulations of flows in complicated geometries. The code solves the full compressible, Reynolds-averaged Navier-Stokes equations using a multi-stage Runge-Kutta based multigrid method. It uses the finite volume method to discretize the equations. The code uses central differ-

Contributed by the International Gas Turbine Institute and presented at the 46th International Gas Turbine and Aeroengine Congress and Exhibition, New Orleans, Louisiana, June 4–7, 2001. Manuscript received by the International Gas Turbine Institute February 2001. Paper No. 2001-GT-156. Review Chair: R. Natole.

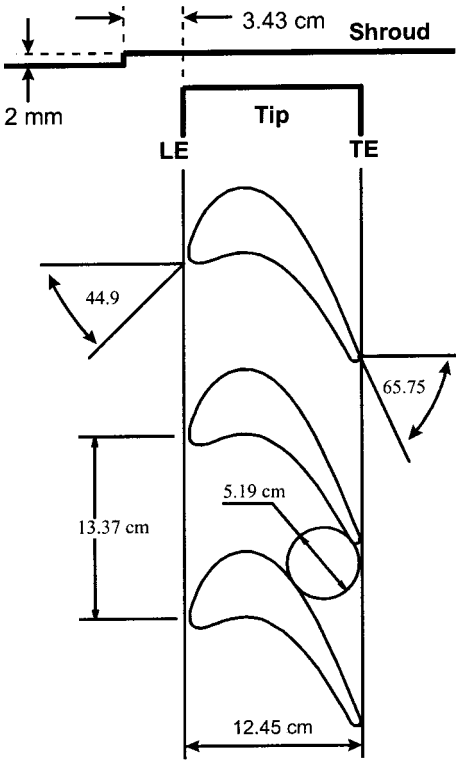

Fig. 1 Airfoil and shroud definition

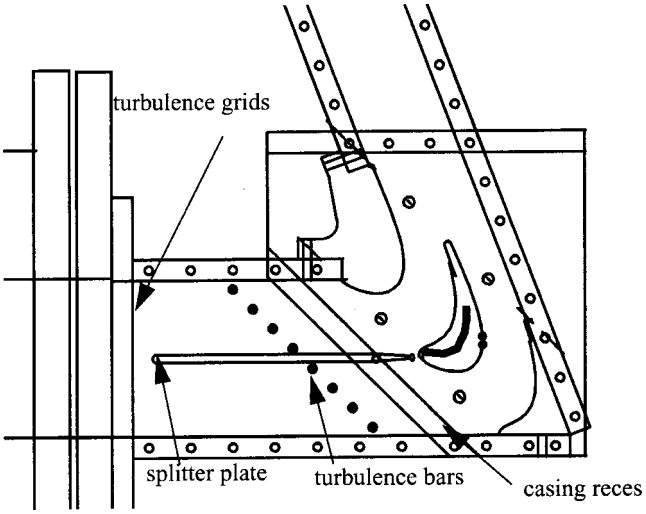

Fig. 2 Experimental rig

Table 1 Run conditions

Pressure ratio across the blade row	0.69
Exit Reynolds number	2.57E6
Inlet Mach number	0.30
Turbulence intensity	5%
Inlet angle	44.9 deg.

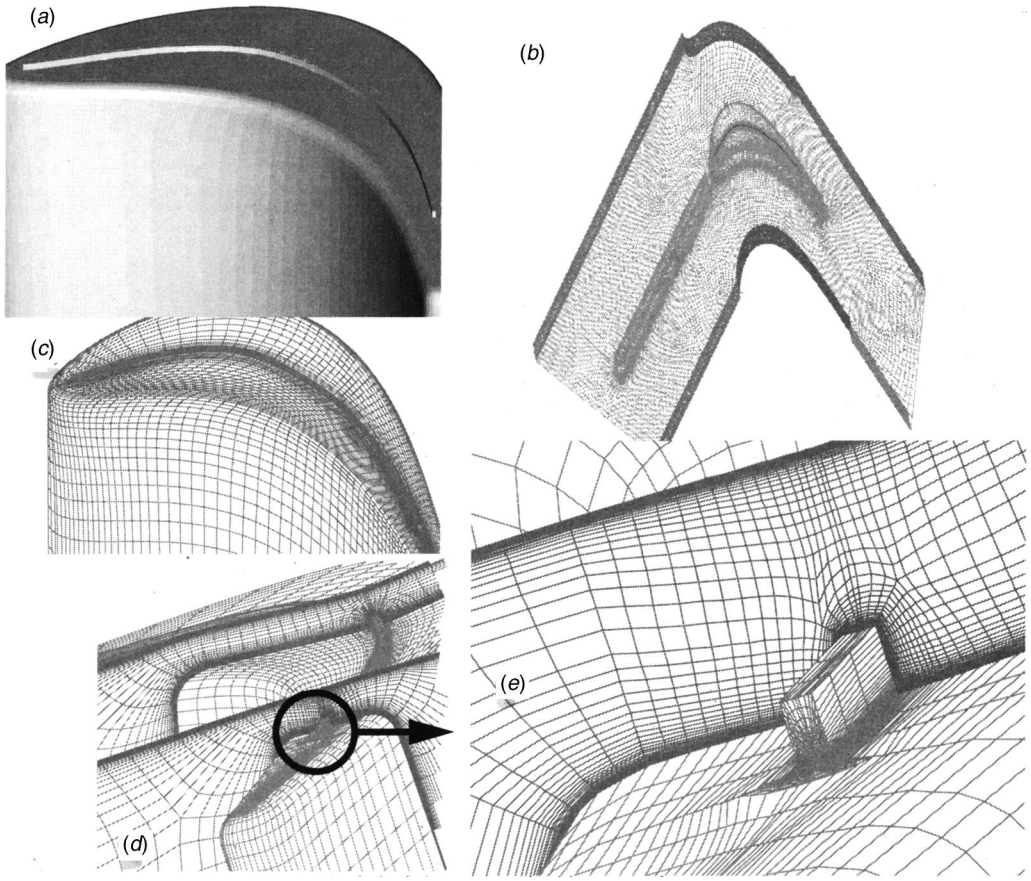

Fig. 3 Blade tip/passage and grid construction

encing together with artificial dissipation to discretize the convective terms. The overall accuracy of the code is second order. The present version of the code [5,8,9] employs the $k-\omega$ turbulence model developed by Wilcox [10,11] with modifications by Menter [12]. The model integrates to the walls and no wall functions are used. For heat transfer a constant value of 0.9 for turbulent Prandtl number, Pr_t and a value for Prandtl number (Pr) equal to 0.72 is used. Viscosity is a function of temperature through a 0.7 power law [13] and Cp is taken to be a constant.

Geometry Modeling and Grid System

As in [2] the complete two blade passage was modeled. This was done to achieve better agreement with the measured pressure distribution on the tip in the cited work. Figure 3(*a*) shows the blade surface and the modeled mean-camberline strip. Figure 3(*b*) (reproduced from [2]) shows the grid for the complete passage including the splitter plate. Figure 3(*c*) shows the surface grid on the blade tip with the radiused edge and the mean-camberline strip. The grid details on the tip including the mean-camberline strip is shown in Fig. 3(*d*). Figure 3(*e*) shows further the details of the grid around the strip. The topology is designed such that the viscous gridlines stay near the surfaces (including the strip) and do not spread in the ''inviscid'' regions of the flow. The main differences between the present simulation and the actual geometry are twofold: The mean-camberline in the experiment is made up of piecewise straight lines and starts right at the leading edge whereas in the CFD simulation the strip is placed as a continuous strip and starts at a location 5 percent of axial chord and not from the leading edge. This was done for practical grid generation reasons. The grid is generated using a commercially available computer program called *GridPro*™. The model of Fig. 3 consisted of 1.2 million cells when a sharp edge tip was used. The number of cells were 1.4 million for the geometry with the radiused edge smooth tip. For the present case of a blade with a mean-camberline strip 1.8 million cells were used. The viscous grid is generated by embedding grid lines where needed, including the grid around the splitter. The stretching ratio did not exceed 1.25 for the viscous grid away from the no-slip surfaces. The distance to the first cell center adjacent to solid wall is such that the distance in wall units, (y^+) is near or below unity. Specifically in the tip region the number of grid cells from the tip of the strip to the shroud was 50, and from the tip surface to the shroud was 58 cells. Further details about the grid may be found in [2].

Results and Discussion

Along with the conditions given in Table 1, a very thin boundary layer thickness of 0.1 percent of the passage height was imposed at the inlet to the computational domain upstream of the flow splitter (at the location of upstream turbulence grid in Fig. 2). The tunnel side walls were modeled using a slip boundary condition [2].

Figure 4 shows the streamline patterns of the flow in the tip clearance. Due to the rounded edge of the tip, the flow has little difficulty negotiating the turn into the clearance passage. In contrast on a sharp edge tip, a separation vortex forms along the pressure side edge of the blade tip thus narrowing the passage and thereby reducing the leakage [2]. Figure 4(*b*) shows the streamline pattern with the strip present. A separation vortex pattern behind the strip can be discerned from that figure. Figure 5 shows the pressure distribution over the blade tip. Note that the areas of low pressure are associated with high velocities. In Fig. 6, the velocity vectors over the blade tip for several axial cross sections (Fig. 6(*a*)) and a plane parallel to tip at the half height of the strip are plotted (Fig. 6(*b*)). The figures show that the flow behind the strip possesses a high velocity component parallel to the strip. It also shows that the velocity is reduced as the strip is approached. This flow pattern has implications for the blade tip heat transfer which will be discussed later in this paper.

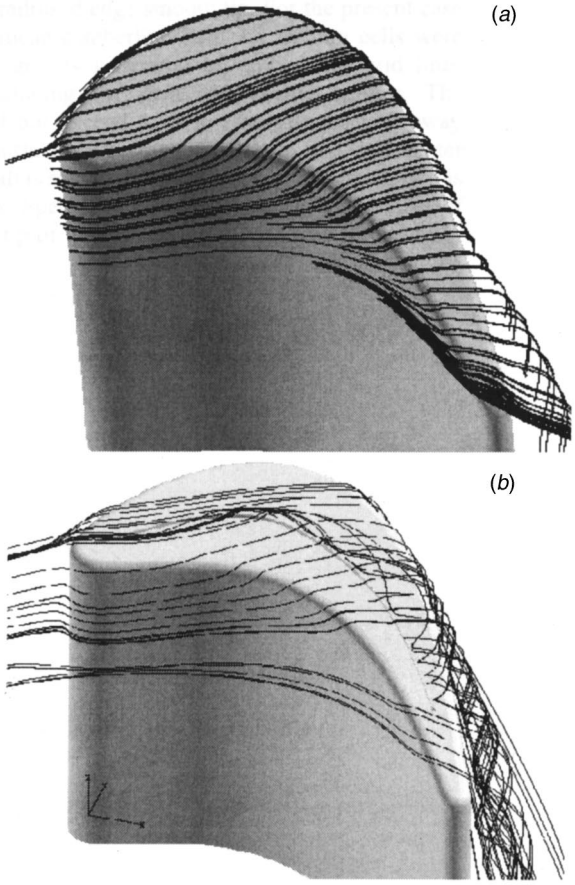

Fig. 4 Streamline patterns of the flow in the tip region for: (*a*) radius edged tip, (*b*) radius edged tip and mean camber line strip

Tip Leakage Rate and Efficiency Comparisons. Tip leakage flow rate is often a good indicator of tip losses and tip heat transfer in relation to different tip treatments. Usually the smaller the flow rate the lower the losses and smaller the tip heat transfer. Since it is difficult to measure the tip leakage flow rate, the computations can serve to provide such information as has been done

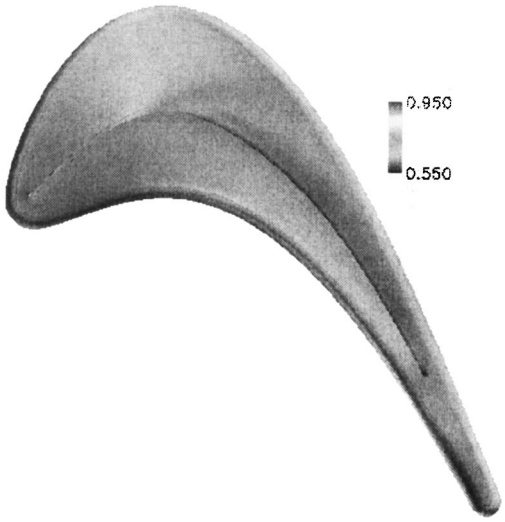

Fig. 5 Pressure distribution (P static/P_0) over the blade tip surface

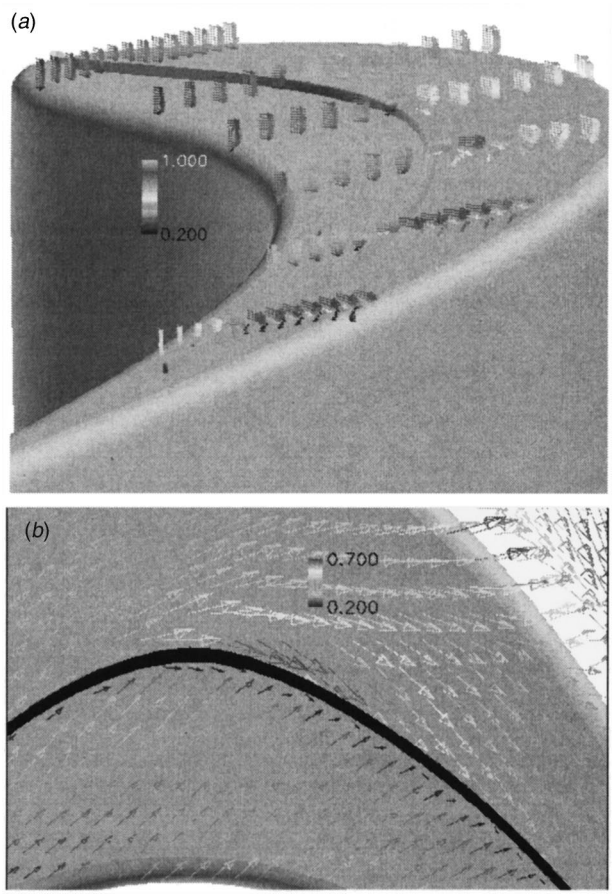

Fig. 6 Velocity vectors colored by the velocity magnitude $|V|$

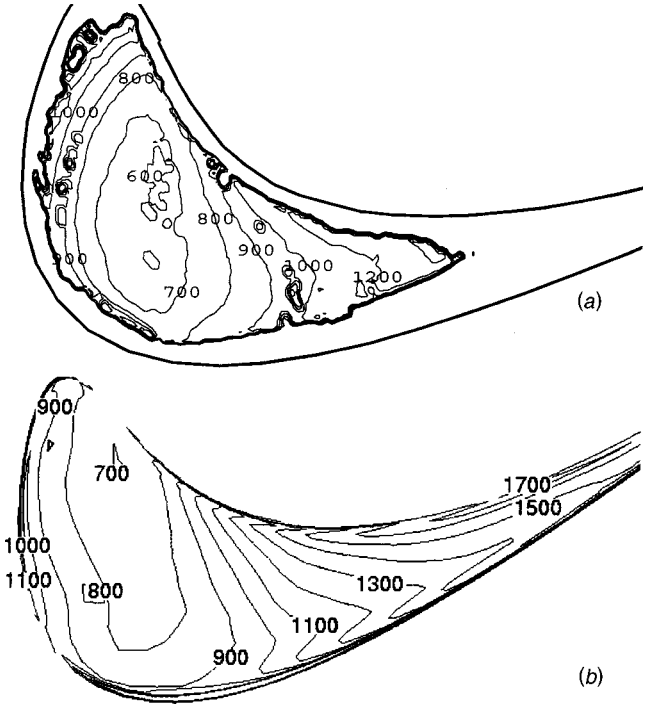

Fig. 7 Simple radiused edge blade tip. Heat transfer coefficient for 2.03 mm clearance and Tu=5 percent (W/m^2/K): (*a*) measured [3] and (*b*) calculated.

here. Table 2 below shows the tip leakage as a fraction of the total mass flow into the blade passage. Note that the total mass flow is for two passages.

Table 2 shows that the mean-camberline strip reduces the tip leakage by 20 percent as compared to the radiused edge blade tip without the strip. Interestingly for a sharp edge tip with the same clearance, as shown in that table, the reduction in the leakage mass flow rate is 28 percent. Also shown in Table 2 is the *Y* factor which is a measure of total pressure loss. The case with the mean-camberline strip, although with lower tip leakage than the rounded case, produces a larger loss. This also was the case with the squealer tip case of Ref. [5] where the reduction in leakage was not accompanied by a calculated improvement in efficiency.

Heat Transfer. The rate of heat transfer is presented in terms of heat transfer coefficient which is defined as:

$$h = \frac{Q_{wall}}{(T_{wall} - T_{inlet})} \tag{1}$$

T_{inlet} is the inlet total temperature and T_{wall} is the wall temperature. T_{wall} was determined from the experimental measurements to be 1.06 times the inlet total temperature. The heat transfer coefficient was calculated on the blade tip where a constant temperature boundary condition is imposed. An effectively adiabatic boundary condition was imposed on all the other surfaces.

Table 2 Tip leakage rates and total pressure losses

Tip treatment	Percent mass flow	Y
Radiused edge	2.5%	0.118
Radiused edge+MCL Strip	2.0%	0.125
Sharp edge	1.8%	0.114

In Fig. 7, the radiused edge blade tip heat transfer is reproduced from [2]. The agreement between the experiment and simulation for this case is consistently better than 15 percent over the entire tip. Figure 8 shows experimental and calculated tip heat transfer for the tip with the mean-camberline strip. The area of the largest heat transfer coefficient appears to be midehord near the suction side on the experiment and the simulation. Referring to Fig. 5, this area corresponds to the area of low surface pressure and thus high velocity over the blade tip. There are some discrepancies between the simulation and the experiment. They include the magnitude of the low island on the suction side near the strip and the apparent low value adjacent to the strip on the pressure side. These are likely caused by geometry differences between the model and the experiment discussed earlier or by the inadequacies of the turbulence model. The breakdown of the one-dimensional conduction assumption for the experimental data near the edges can also play a role in those differences. In the simulations the rate of heat transfer drops as the strip is approached on the pressure side of the strip and decreases away from the strip on the suction side. Figure 6 shows that the fluid velocity is diminished as it approaches the strip on the pressure side. This reduction in velocity reduces the heat convection to the blade. On the suction side of the strip there is a vortical zone within which the flow has a large velocity component parallel to the strip. This streamwise vortex continually feeds core temperature air to the blade tip, thus increasing the heat transfer. This accounts for the high heat transfer rate predicted by the numerical simulation.

It should be noted that without the mean-camberline strip, due to the increase in the clearance, the rate of heat transfer for the case of Fig. 8 would be larger than that of Fig. 7 for most of the blade tip surface except near the tail. The tail area in Fig. 6 does have a smaller rate of heat transfer. This has been reported in [14].

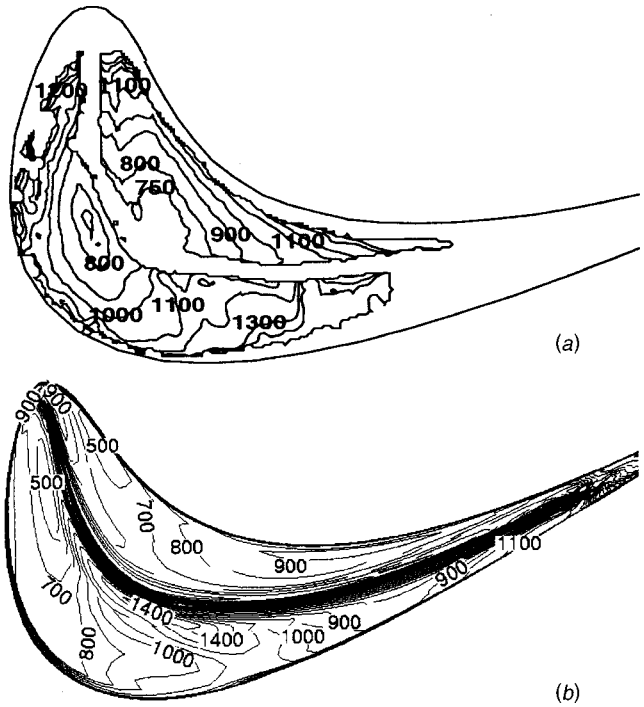

Fig. 8 Radiused edge blade tip with mean-camberline strip. Heat transfer coefficient for 2.03 mm clearance and Tu=5 percent (W/m^2/K): (*a*) measured [4] and (*b*) calculated.

Summary and Conclusions

In this paper, the numerical prediction of flow and heat transfer and comparison with the experimental heat transfer data of tip heat transfer for a blade equipped with a tip mean-camberline strip (squealer) was performed. The blade chosen represents a first stage blade of a large power generation turbine. The casing upstream of the blade tip was recessed. The effect of mean-camberline strip on the tip leakage flow was quantified and compared to plain tip surfaces with radiused edge and sharp edges. It was found that the sharp edge works better than the radiused edge in reducing the tip leakage flow. For the radiused edge case it was found that the mean-camberline strip reduces the tip leakage but the total pressure loss is not commensurately reduced. Reasonably good comparison with the experimental heat transfer was achieved. Areas of large heat transfer rate were identified and likely reasons for local heat transfer enhancement was given using flow patterns.

Acknowledgments

This work was sponsored by the Turbomachinery and Combustion Technology Project. The author wishes to express his gratitude to Dr. Raymond Gaugler, chief of the Turbine Branch, for his support and encouragement of this work and Dr. R. S. Bunker for sharing of the experimental data and figures. Thanks are also due to my colleague, Dr. Erlendur Steinthorsson, for his reading and criticism of the manuscript. Some of the computations were performed on the CRAY-C90 of NAS at NASA Ames Research Center.

Nomenclature

C_p = constant pressure specific heat
h = heat transfer coefficient
Pr = Prandtl number
R = gas constant
Re = Reynolds number
T = static temperature$=T_0$
Tu = turbulence intensity
V = magnitude of the velocity$=(R\,T_0)^{1/2}$
y^+ = dimensionless distance from a wall$=y\sqrt{\tau_w/\rho}/\nu$
γ = specific heat ratio
τ = shear stress
Y = total pressure loss$=P_{t_0}-P_{t_1}/P_{t_0}-P_1$

Subscripts

t = total conditions
w = wall value
0 = inlet condition
1 = exit conditions

References

[1] Mayle, R. E., and Metzger, D. E., 1982, "Heat Transfer at the Tip of an Unshrouded Turbine Blade," *Proc. Seventh Int. Heat Transfer Conf.*, Hemisphere Pub., pp. 87–92.
[2] Ameri, Ali A., and Bunker, R. S., 2000, "Heat Transfer and Flow on the First-Stage Blade Tip of a Power Generation Gas Turbine: Part 2—Simulation Results," ASME J. Turbomach., **122**, pp. 272–277.
[3] Bunker, R. S., Bailey, J. C., and Ameri, Ali A., 2000, "Heat Transfer and Flow on the First-Stage Blade Tip of a Power Generation Gas Turbine: Part 1—Experimental Results," ASME J. Turbomach., **122**, pp. 263–271.
[4] Bunker, R. S., and Bailey, J. C., 2000, "An Experimental Study of Heat Transfer and Flow on a Gas Turbine Blade Tip With Various Tip Leakage Sealing Methods," *Proc. of 4th ISHMT/ASME Heat and Mass Transfer Conf.*, Jan., India.
[5] Ameri, A. A., Steinthorsson, E., and Rigby, David L., 1998, "Effect of Squealer Tip on Rotor Heat Transfer and Efficiency," ASME J. Turbomach., **120**, pp. 753–759.
[6] Steinthorsson, E., Liou, M. S., and Povinelli, L. A., 1993, "Development of an Explicit Multiblock/Multigrid Flow Solver for Viscous Flows in Complex Geometries," Paper No. AIAA-93-2380.
[7] Arnone, A., Liou, M. S., and Povinelli, L. A., 1991, "Multigrid Calculation of Three Dimensional Viscous Cascade Flows," AIAA Paper No. 91-3238.
[8] Rigby, David L., Ameri A. A., and Steinthorrson E., 1996, "Internal Passage Heat Transfer Prediction Using Multiblock Grids and $k-\omega$ Turbulence Model," ASME Paper No. 96-GT-188.
[9] Rigby, D. L., Ameri A. A., and Steinthorrson E., 1997, "Numerical Prediction of Heat Transfer in a Channel With Ribs and Bleed," ASME Paper No. 97-GT-431.
[10] Wilcox, D. C., 1994, *Turbulence Modeling for CFD*, DCW Industries, Inc., La Canada, CA.
[11] Wilcox, D. C., 1994, "Simulation of Transition With a Two-Equation Turbulence Model," AIAA J., **32**, No. 2, pp. 247–255.
[12] Menter, F. R., 1993, "Zonal Two-Equation $k-\omega$ Turbulence Models for Aerodynamic Flows," Paper No. AIAA-93-2906.
[13] Schlichting, H., 1979, *Boundary Layer Theory*, McGraw-Hill, New York, Seventh Ed., pp. 312–313.
[14] Ameri, A. A., Steinthorsson, E., and Rigby, D. L., 1999, "Effects of Tip Clearance and Casing Recess on Heat Transfer and Stage Efficiency in Axial Turbines," ASME J. Turbomach., **121**, pp. 683–693.

Film-Cooled Turbine Endwall in a Transonic Flow Field: Part I—Aerodynamic Measurements

Friedrich Kost

Martin Nicklas

Institute of Propulsion Technology,
German Aerospace Center (DLR),
37073 Göttingen, Germany

Thermodynamic and aerodynamic measurements were carried out in a linear turbine cascade with transonic flow field. Heat transfer and adiabatic film-cooling effectiveness resulting from the interaction of the flow field and the ejected coolant at the endwall were measured and will be discussed in two parts. The investigations were performed in the Windtunnel for Straight Cascades (EGG) at DLR, Göttingen. The film-cooled NGV endwall was operated at representative dimensionless engine conditions of Mach and Reynolds number $Ma_{2is}=1.0$ and $Re_2=850{,}000$ respectively. Part I of the investigation discusses the aerodynamic measurements. Detailed aerodynamic measurements were carried out in the vicinity of a turbine stator endwall using conventional pressure measurements and a Laser-2-Focus (L2F) device. The L2F served as a velocimeter measuring 2D-velocity vectors and turbulence quantities and as a tool to determine the concentration of coolant ejected through a slot and through holes at the endwall. Pressure distribution measurements provided information on the endwall pressure field and its variation with coolant flow rate. Pressure probe measurements delivered cascade performance data. Oil flow visualization and laser velocimetry gave a picture of the near endwall flow field and its interference with the coolant. A strikingly strong interaction of coolant air and secondary flow field could be identified. The measurement of coolant concentration downstream of the ejection locations provided a detailed picture of the coolant flow convection and its mixing with the main flow. The relative coolant concentration in the flow field is directly comparable to the adiabatic film-cooling effectiveness measured by thermal methods at the wall. [DOI: 10.1115/1.1400112]

1 Introduction

High pressure turbine stages have to withstand increasingly high thermal and aerodynamic loads. Therefore, thorough information on the turbine aerodynamics and heat transfer is needed to enable the design of an efficient stage and particularly the design of efficient cooling systems. The endwall region is typically cooled by film cooling and as the endwall flow patterns are rather uncertain, coolant flows are often excessive and injection locations unfavorably distributed. At the endwall, the interaction of coolant air and secondary flow field plays a crucial role, and therefore, aerodynamic and thermal measurement methods have to be combined; only a complete picture of the complex three-dimensional flow field enables further improvements.

The term secondary flow is used for flows with transverse components appearing at the endwalls of turbine flow passages. Main features of the secondary flow are a saddle point at the endwall in front of the blade nose, 3D-separation lines connected with vortices like the horseshoe vortex at the blade leading edge, the passage vortex which is induced by the endwall crossflow from pressure to suction side, and finally counter or corner vortices caused by the main vortices. Sieverding [1] provided an extensive review of secondary flow behavior in turbine blade passages. In Fig. 1 many secondary flow features occuring in a turbine blade passage are sketched.

Injecting coolant into the secondary flow field will cause a massive interaction of the fluid flows [2,3]. Many authors of film cooling studies have noted that endwall air ejection can weaken secondary flows, notably the endwall crossflow and consequently the passage vortex are diminished in strength [5–8]. Coolant flow momentum re-energizes the boundary layer, enabling the endwall flow to better withstand the circumferential pressure gradient. The horseshoe vortex at the blade leading edge may be weakened or strengthened by upstream air injection [9].

2 Experimental Apparatus

2.1 The "Windtunnel for Straight Cascades" (EGG). The experiments reported in this paper were performed in the Windtunnel for Straight Cascades at the DLR Göttingen. The facility is of the blowdown type with atmospheric inlet. The ambient air first passes a silica-gel dryer and enters the cascade after a contraction. Downstream of the cascade, the flow passes an adjustable diffusor and the main butterfly valve and enters, finally, a large vacuum vessel (10,000 m^3). This vessel is evacuated by two sets of sliding-vane vacuum pumps (2×250 kW), enabling continuous measurements with a measurement time between 15 to 17 minutes in a transonic flow case. The inlet total pressure of the cascade is equal to the ambient pressure. The Reynolds number cannot be varied independently, but is a function of the Mach number. The downstream static pressure of the cascade is adjusted by the setting of an annular diffusor.

The cascade is mounted between two circular disks establishing the side walls of the flow channel. The inlet angle is adjusted by turning this assembly. The test section dimensions are 380×125 mm^2, which allows the special cascade of these tests to consist of 13 blades, i.e., 12 blade channels with flow. For more details, see Nicklas [10].

Coolant air is provided by the central compressed air supply. By passing a heat exchanger the coolant air could be adjusted to a preset temperature level (−5°C to 90°C) being lower or higher than the main flow temperature level (ambient). For the aerodynamic measurements, always isoenergetic conditions, i.e., a coolant temperature equal to the main flow temperature was chosen. The air passes standard measuring orifices and remotely con-

Contributed by the International Gas Turbine Institute and presented at the 46th International Gas Turbine and Aeroengine Congress and Exhibition, New Orleans, Louisiana, June 4–7, 2001. Manuscript received by the International Gas Turbine Institute February 2001. Paper No. 2001-GT-145. Review Chair: R. Natole.

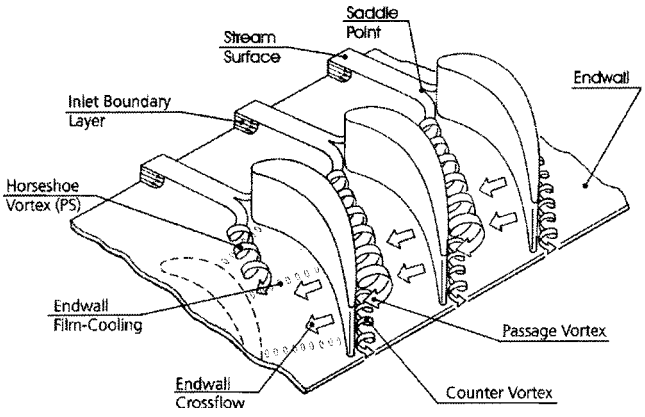

Fig. 1 Sketch of secondary flow features in a turbine passage according to Langston [4]

trolled valves to adjust the desired mass flow rates. Finally, the air is fed to two cavities in the blade platform from where it is ejected into the main flow.

2.2 The Turbine Stator and Film-Cooling Geometry. The investigated stator is a nozzle guide vane of an HPT and was designed by DaimlerChrysler MTU (Munich) in the course of the AG TURBO project. Some data on stator geometry are given in Table 1.

The experimental arrangement comprises a state-of-the-art stator including a platform film-cooling set-up. At the cascade sidewall near the center line of the tunnel where normally mineral glass panes enable the observation of the cascade flow, one sidewall was exchanged with an instrumented plate simulating the endwall platform of a cooled turbine. Two types of instrumented platforms were manufactured, one for the aerodynamic measurements, the other one for the thermal measurements (see Part II: Heat Transfer and Film Cooling Effectiveness). The platform for the aerodynamic measurements was made from metal equipped with the coolant ejection configuration and 144 pressure tappings distributed in two blade passages.

A cooling slot of width 1.2 mm was positioned with its downstream edge 7.2 mm ($x/l_{ax}=-0.20$) upstream of the cascade and extended over nearly 5 pitches. In two blade passages cooling holes are distributed according to Fig. 2. There are 19 holes per passage arranged in three rows in the forward part of the nozzle platform. The hole diameter is 0.6 mm. Figure 3 shows a section through the platform. The coolant air for the ejection through the slot and the ejection through the holes could be controlled independently.

2.3 The Laser-2-Focus Measurement Technique. The measurement principle of L2F is rather simple. The L2F-measuring device generates two highly focused light beams in the probe volume which act as a 'light gate' for tiny particles in the flow. The scattered light from the particles provides two successive pulses and from the time interval between the pulses the velocity perpendicular to the laser beams can be derived (Schodl [11]). The two foci of our special L2F device had diameters of 8 μm and their separation was 210.8 μm. The necessary particles are oil droplets of 0.3 μm diameter, which are produced by a special seeding generator and injected in the settling chamber into the flow. These particles are small enough to follow the flow even in supersonic regions where shocks occur [11].

Table 1 Geometric parameters of the nozzle guide vane T6.2

chord	axial chord	pitch	throat	trailing edge	span
l [mm]	l_{ax} [mm]	t [mm]	o [mm]	diameter[mm]	h [mm]
60	35.82	40.80	11.3	1.12	125

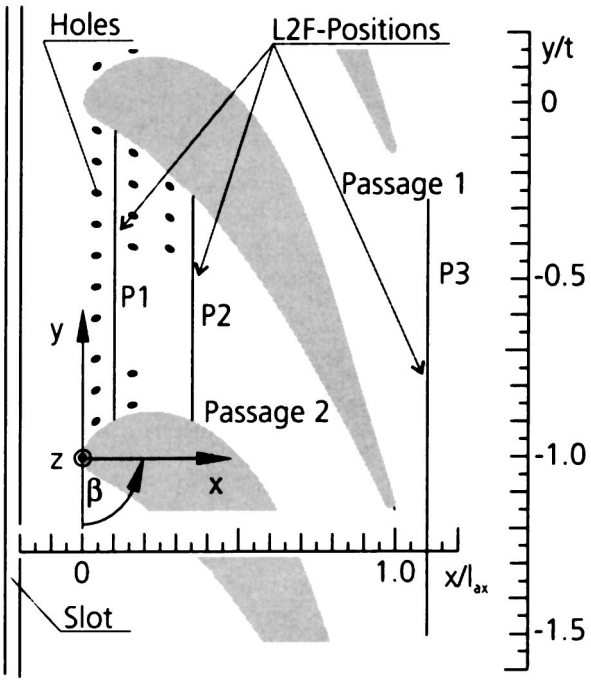

Fig. 2 Geometry of the stator and the cooling configuration

At DLR-Göttingen the Laser-Two-Focus Technique (L2F) is routinely applied to acquire flow field information for cascade and turbomachine flows [12]. The system measures 2D-vectors of the fluid velocity. An advantage of the 2D-system is the slender light cone of 7.5 deg enclosed angle, which provides excellent access to narrow blade channels. A statistical evaluation procedure is necessary to extract the desired mean flow values u, v, and the mean fluctuating values $\overline{u'^2}$, $\overline{v'^2}$, and $\overline{u'v'}$ from the stored velocity distributions. Using the measured total temperature, the velocity can be converted to a Mach number. In order to have a value for the turbulence intensity which is comparable at different locations in the flow, the turbulence level, Tu, was normalized either with the cascade upstream velocity u_1 in the case of measurements inside the cascade or with the cascade downstream velocity u_2 in the case of measurements downstream.

$$Tu=\frac{\sqrt{(\overline{u'^2}+\overline{v'^2})/2}}{u_{1,2}} \tag{1}$$

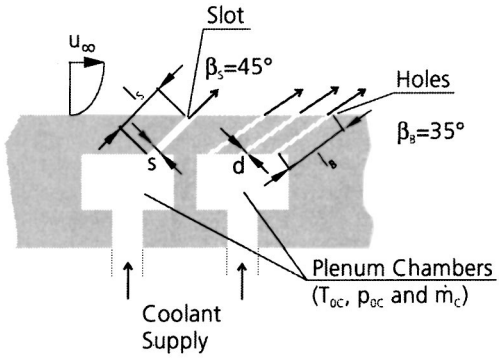

Fig. 3 Section through cooling geometry (schematic)

The error for the Mach number is equivalent to the velocity error, as the error of total temperature doesn't play a role according to sensitivity analysis. Errors for velocity and angle include a statistical part due to the number of events which are averaged during a measurement. This part is the main reason for different error bars inside and outside of wakes. Bias errors are due to errors in the determination of focus distance and particle flight time. All these errors were discussed by Kost [13], the present laser measurements were accordingly analyzed and the experimental uncertainties (on a 95 percent confidence level) have been determined: The error bar for the Mach number was 0.003 outside the wakes and 0.006 inside. The error bar for the angle was 0.2 deg outside the wake and 0.4 deg inside.

2.4 The Coolant Concentration Measurements. The development of coolant concentration downstream of the slot and the ejection holes could be investigated by seeding only the coolant flow and counting locally the number of particles per second which pass one of the laser foci. As seeding particles, the same submicron oil particles were used as in the L2F velocity measurements (see previous section), so we are certain that the particles follow the gas flow and as the seeding particles are added to the coolant well ahead of the coolant plenum chambers, the oil droplets are evenly distributed throughout the coolant. During the 5 s of measurement time up to 30,000 particles passed the focus thus ensuring a small statistical counting error. The counting rate of oil particles is equivalent to the measurement of the local coolant flow rate. Kapteijn [14] determined the development of the coolant from a turbine stator trailing edge slot with the same measurement procedure and received convincing results.

In order to distinguish stray light from the metal surfaces from stray light originating at the seeding particles, two measurements were always performed: First a measurement without seeding the flow, followed by a measurement where the ejected coolant was seeded. The two resulting particle flow rates were subtracted from each other to obtain the real relative coolant flow rate.

By summing up the particle flow rate (counting rate) $j(y,z)$ in a measurement plane of constant x extending itself from the suction to the pressure side of the blade channel and from the sidewall to a certain distance from the sidewall where not any more particles could be detected, the relative coolant flow rate can be converted to an absolute flow rate. The sum of the measured particle flow rate is in proportion to the known total coolant mass flow traversing the measurement plane:

$$\dot{m}_c = k \cdot \int_{z=0}^{z_e} \int_{y_a}^{y_e} j(y,z) \cdot \sin \beta(y,z) dy dz \tag{2}$$

The proportionality factor is named k. The local flow angle β is taken from the L2F-velocity measurement.

Besides, the following formula is valid: $\dot{m} = \rho u \cdot F$, and

$$F = \text{Area} = \int_{z=0}^{z_e} \int_{y_a}^{y_e} \sin \beta(y,z) dy dz \tag{3}$$

Comparing with Eq. (2), it follows:

$$\rho_c u_c(y,z) = k \cdot j(y,z) \tag{4}$$

Factor k can be determined from Eq. (2), consequently the quantitative local coolant flow rate $\rho_c u_c$ is known at every measurement location. Further, let us assume that the concentration measurements are taken so far from a coolant opening that the velocity vectors of coolant and main flow can no longer be distinguished, i.e., $u_c = u_{loc}$ and $\beta_c = \beta_{loc}$, where u_{loc}, β_{loc} are velocity vectors measured by L2F. Then the relative concentration of coolant, i.e. the ratio of coolant density to main flow density is determined in the following way:

$$con_{rel} = \frac{\rho_c}{\rho_{loc}} = \frac{\rho_c u_c}{\rho_{loc} u_{loc}} = \frac{k \cdot j(y,z)}{\rho_{loc} u_{loc}} = \frac{T_{0loc} - T_{01}}{T_{0c} - T_{01}} \tag{5}$$

Table 2 Flow parameters of the stator cascade at midsection

	inlet	exit
Isentropic Mach number Ma_{2is}	0.175	1.00
velocity u	59.0 m/s	311.6 m/s
Reynolds number Re	$0.24 \cdot 10^6$	$0.85 \cdot 10^6$
Design mass flow (per blade channel) $\dot{m}$		340 g/s

The right side of the last equation is a quantity called adiabatic film cooling effectiveness when taken at an impermeable wall (at $z=0$: subscript '0loc'→subscript 'recovery loc') as under certain assumptions, e.g. ignoring effects of compressibility,[10,15,16] the relative coolant concentration con_{rel} can be set equal to adiabatic effectiveness.

In Eq. (5), the density ρ_{loc} is still unknown. It can be approximately determined from the measured Mach number, the total temperature, and the total pressure at inlet. By determining ρ_{loc} in this way only total pressure may be incorrect, but when ignoring compressibility the difference between this ρ_{loc} and the exact one is negligible. Outside of boundary layers and wakes this ρ_{loc} equals the exact one, also for compressible flows. Sources of errors in the concentration values were of different origin: Statistical counting errors were negligible as normally thousands of particles were counted at one measurement location. Stray light only played a role near surfaces, especially at pressure and suction side and a minor role at the minimum distance of $z=0.5$ mm to the endwall. In the evaluation procedure the determination of main flow density ρ_{loc} produces an error, especially in the downstream plane. Accordingly, the uncertainty of the absolute concentration value con_{rel} is estimated to be normally 8 percent, related to a maximum value of 1. In the downstream plane the uncertainty has to be doubled, mainly because of an optical interference of the laser beam with the shock, discussed at the end of Section 4.4.

2.5 Pressure Measurements. The static pressures at the sidewall could be measured at 144 locations. In order to determine the performance of the cascade, wake flow measurements were made by traversing a pyramid probe (pyramid-like probe head with a hole on the top and holes on each of the four sides) far behind and a simple Pitot probe in front of and shortly behind the cascade. The Pitot probe head had a diameter of 1 mm and the pyramid probe head size was 3 mm. In the case of L2F- and Pitot-pressure measurements in the same plane, the L2F results (local Mach number and angle) and the Pitot pressure could be combined to obtain local flow data (with the exception of spanwise angle) in the same way as from the pyramid probe. But, whereas due to the probe size, reliable pyramid probe measurements could be performed only further downstream, the combination of L2F- and Pitot-pressure measurements allowed investigations in a plane shortly behind the cascade.

3 Test Conditions

Different main flow and coolant parameters were investigated in the AG TURBO platform cooling project. This presentation of the aerodynamics concentrates on the transonic test case with one coolant flow rate for slot ejection and one for ejection from holes. Preliminary experiments determined the flow at mid section (see Table 2; Reynolds number Re is based on stator true chord length L). Inlet total pressure and temperature are ambient. The Schlieren photo Fig. 4 visualizes the transonic flow field. Mainly shocks and wakes arising at the trailing edges can be seen.

The coolant parameter c_m of Table 3 is the ratio of coolant to design mass flow per blade channel. Pressures in the coolant plenum chambers p_{0c} are related to the inlet total pressure of the main flow. The blowing ratio $M = (\rho u)_c / (\rho u)_{loc}$ for the holes is varying considerably across the pitch as local velocity u_{loc} is much lower at the pressure side than at the suction side. Accordingly, high values of M occur near the pressure side.

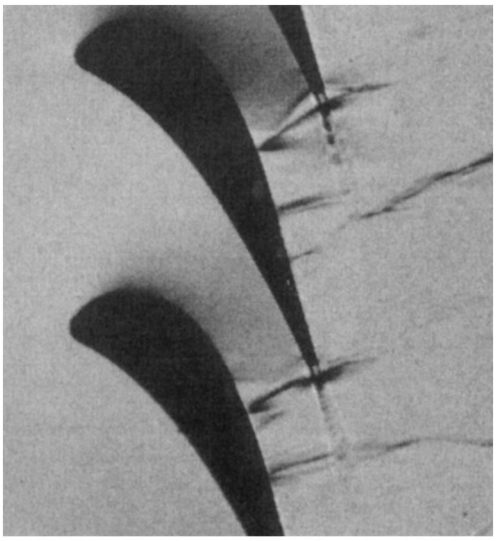

Fig. 4 Schlieren picture of flow field in the stator at $Ma_{2is}=1.00$

The boundary layer at the sidewall upstream of the cascade was measured with a Pitot probe and with L2F. The results are shown in Fig. 5 and summarized in Table 4. The turbulence at mid section was not so high to be representative for a real turbine, but because of the rather thick boundary layer, turbulence is increasing already relatively far from the endwall. The upstream boundary layer is very similar to a flat plate turbulent boundary layer and the thickness of the boundary layer may not be far from a real inlet flow to an HP turbine vane.

4 Results and Discussion

4.1 The Flow Field Without Coolant Ejection. The Isentropic Mach number distribution shown in Fig. 6 has been derived from the measured sidewall pressure distribution. At the suction side a maximum isentropic Mach number of 1.17 is attained, indicating the transonic nature of the flow field—compare it with the Schlieren photo, Fig. 4!

Table 3 Coolant flow parameters

	$\dot{m}_c$	c_m	p_{0c}/p_{01}	M_{mean}	M_{min}	M_{max}
slot	4.3 g/s	1.3 %	1.03	1.3		
holes	1.1 g/s	0.32%	1.30	3.0	1.4	3.7

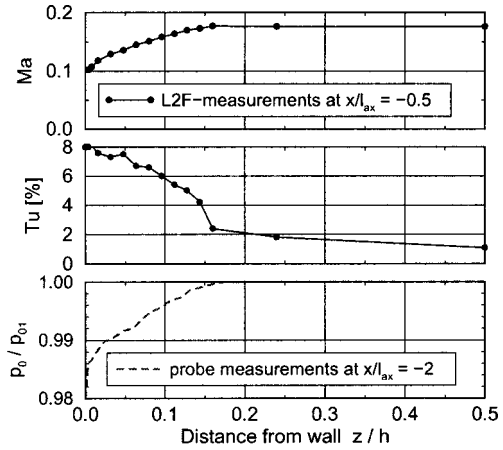

Fig. 5 Sidewall boundary layer upstream of cascade

Table 4 Parameters of the upstream sidewall boundary layer

	[mm]	[1/h]
Boundary layer thickness δ	20	0.160
Displacement thickness	3.3	0.026
Momentum thickness	2.3	0.018
Shape factors	$H_{12}=1.42$	$H_{32}=1.76$

Figure 7 presents an oil flow picture of the platform without coolant ejection. By the oil flow traces, the direction of wall shear stress is visualized. The oil flow traces are combined with velocity vectors measured by L2F at a wall distance of 0.5 mm. The two methods correspond rather well with a small divergence near the suction side at $x/l_{ax}=0.35$ where the flow angle even at the small wall distance of 0.5 mm seems to differ from the angle at the wall itself. Some dominant flow features of secondary flow are visible in the picture: the crossflow driven by the pressure difference between pressure and suction side, the stagnation region (saddle point) in front of the blade leading edge, the influence of the first trailing edge shock, leading to a locally considerably increased turning of the flow toward the suction side.

In this context, the saddle point, indicated by the accumulation of white color diagonally below the blade leading edge, plays an important role: the slot, drawn into the picture, though not existent during the real oil flow measurement without coolant ejection, traverses the saddle point. Therefore it may be expected that the coolant ejection from the slot is interacting strongly with the secondary flow.

From the laser velocimetry in the axial measurement planes quantitative information on the secondary flow field is obtained. The complete survey is documented by Kost and Nicklas [17]. Figures 8 and 9 present some interesting details. First of all, the Mach number diagram makes it clear that the thick upstream endwall boundary layer has been removed by the interaction with the bladerow. The Mach number at a wall distance of 0.5 mm ($z/h=0.004$) is still near the Mach number far away from the wall in contrast to the velocity decrease in the upstream boundary layer (Fig. 5).

The angle diagrams show the typical behavior of secondary flow (please note that according to our angle definition lower val-

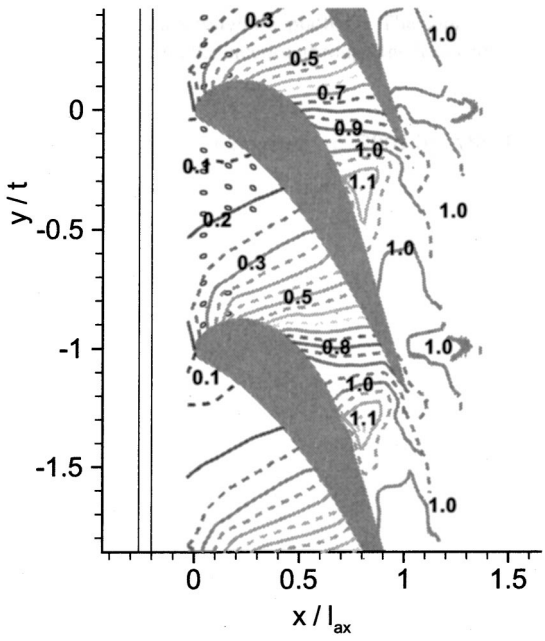

Fig. 6 Isentropic Mach number distribution at the sidewall without coolant ejection ($Ma_{2is}=1.00$)

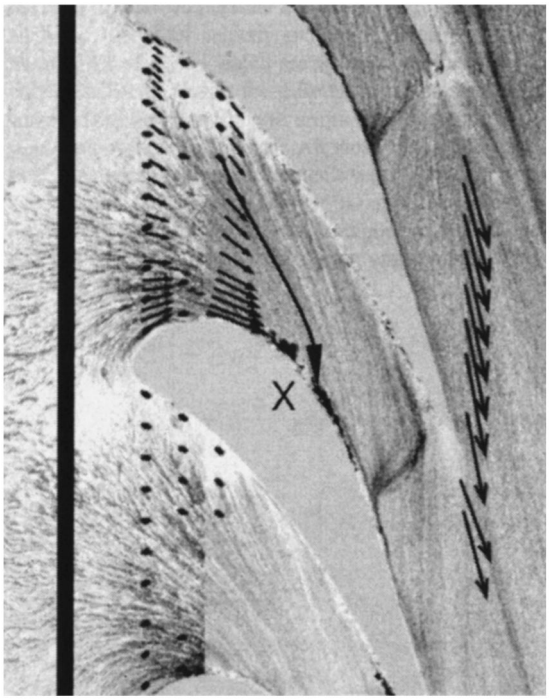

Fig. 7 Oil flow picture of sidewall together with velocity vectors measured by L2F at a wall distance of 0.5 mm, without coolant ejection

ues indicate more turning toward the blade suction side). Near the suction side the flow direction at 0.5 mm wall distance is pointing away from the profile contour indicating the suction side leg of the horseshoe vortex. This leg of the horseshoe vortex produces less turning at the wall compared to midsection up to a position of $y/t=-0.72$ at $x/l_{ax}=0.10$ and $y/t=-0.79$ at $x/l_{ax}=0.35$ which proves that the 3D-separation line associated with the horseshoe vortex is moving toward the suction side which it finally hits (see Fig. 7).

The pressure side leg of the horseshoe vortex is not as easy to detect as the leg of the horseshoe vortex that is circulating in the same direction as the endwall crossflow. Its effect is visible in the increased near wall flow turning near the pressure side but no 3D-separation line can be seen.

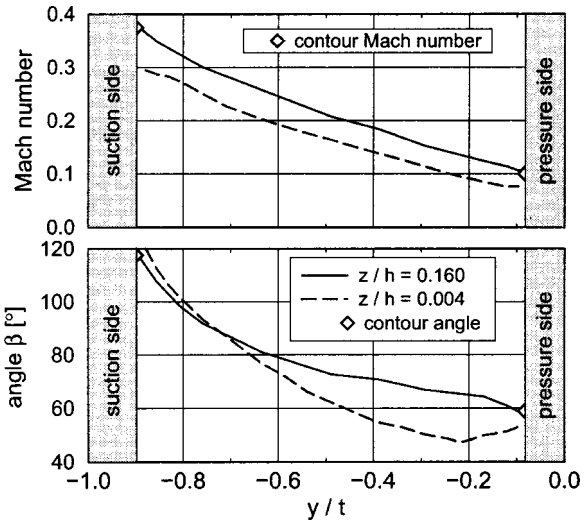

Fig. 8 L2F measurements at $x/l_{ax}=0.10$ and at two wall distances ($z=0.5$ and 20 mm), without coolant ejection; contour Mach number from a profile pressure distribution measurement at $z=20$ mm

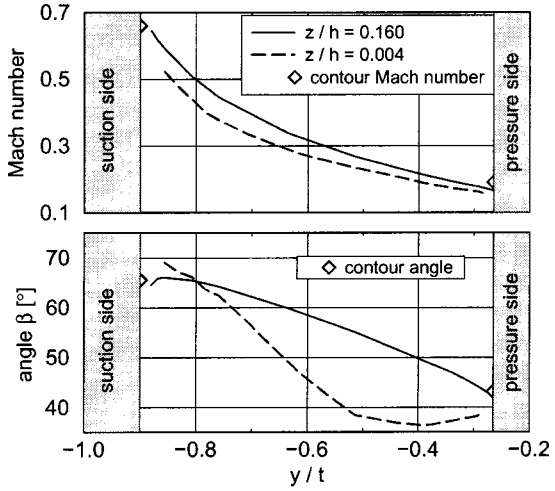

Fig. 9 L2F measurements at $x/l_{ax}=0.35$ and at two wall distances ($z=0.5$ and 20 mm), without coolant ejection

4.2 Coolant Ejection Solely From the Holes. There are 19 holes per passage arranged in three rows in the forward part of the nozzle platform (see Fig. 2). The first L2F-measuring-plane was placed at $x/l_{ax}=0.10$ just downstream of the first row of 10 coolant ejection holes and Fig. 10 presents results from the laser measurements.

The turbulence intensity, and still more pronounced, the coolant concentration, make the distinct coolant jets from the 10 holes visible. The coolant jets near the pressure side are clearly separated from the wall, toward the suction side the jets are more and more approaching the wall. The four coolant jets near the suction side seem to be well attached to the endwall. The reason for this different behavior of the coolant jets is the varying blowing ratio of the coolant, which is strongly increasing from values of 1.6 at the suction side to values of 3.7 at the pressure side (see Table 3). The higher kinetic energy of the suction side main flow is able to bend the coolant jets toward the endwall, whereas the low energy main flow near the pressure side is penetrated by the coolant jets.

The second L2F-measuring-plane was placed at $x/l_{ax}=0.35$ downstream of the last row of 3 coolant ejection holes near the pressure side. Figure 11 presents results from that measurement plane.

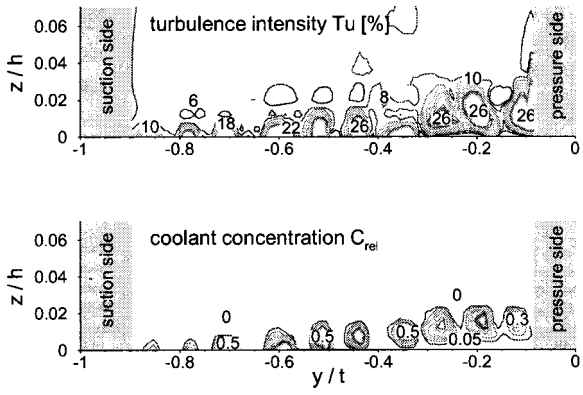

Fig. 10 L2F measurements at $x/l_{ax}=0.10$ with coolant ejection from the holes only

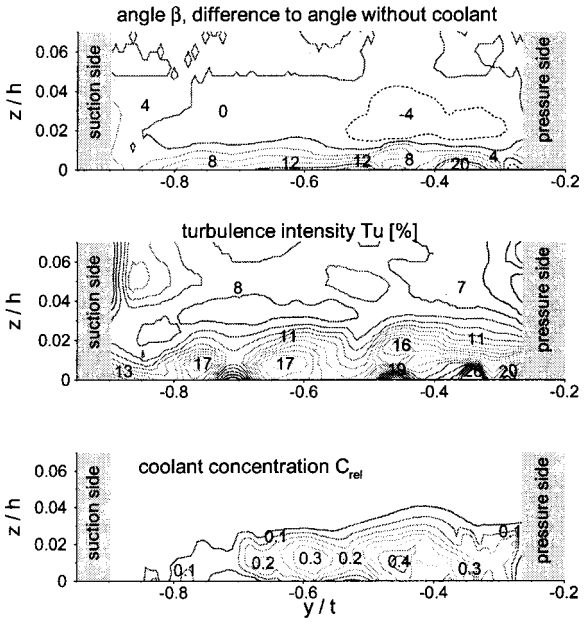

Fig. 11 L2F measurements at $x/l_{ax}=0.35$ with coolant ejection from the holes only

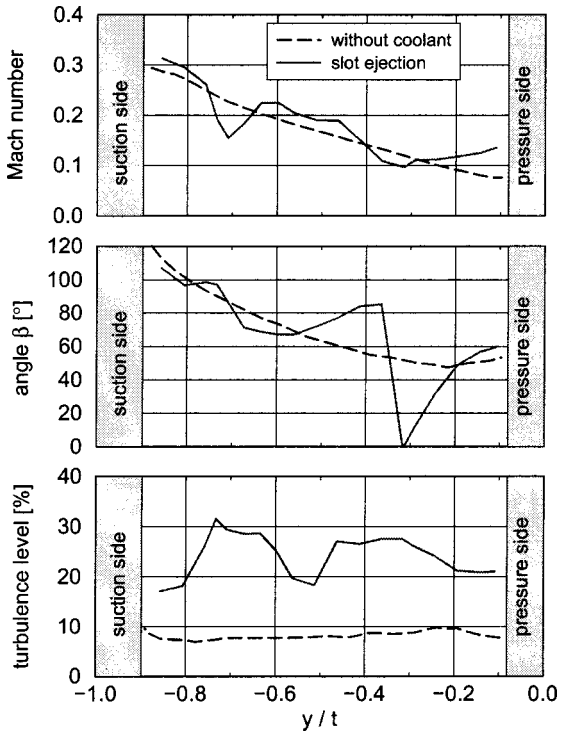

Fig. 12 L2F measurements at $x/l_{ax}=0.10$ and at the wall distance $z=0.5$ mm ($z/h=0.004$); without coolant ejection and with coolant ejection from the slot only

In this plane, distinct jets are not easily visible. In the turbulence diagram, high turbulence levels are observed near the endwall. This is mainly caused by coolant ejection as without coolant turbulence had a maximum level of 11 percent (see Fig. 14). The three highest turbulence peaks with values of 19 percent and more indicate the coolant from the last row of three holes near the pressure side. The peak nearest to the pressure side is not visible in the concentration plot, a fact we attribute to the effect of stray light from the pressure side spoiling the concentration measurements locally. Coolant concentration is generally higher near the pressure side which is caused by the larger number of ejection holes near the pressure side compared to the suction side of the blade channel. There may be some coolant near the suction side remaining attached to the wall and possibly not detected by the concentration measurement which had a nearest measurement distance of 0.5 mm to the wall. Additionally, the suction side leg of the horseshoe vortex washes the coolant away from the suction side. The combined action of the pressure side leg of the horseshoe vortex and the endwall crossflow have moved part of the coolant away from the pressure side, too. Therefore coolant concentration has its maximum around $y/t=0.45$.

In the diagram of the pitchwise angle the difference to the flow angle without coolant was plotted. It can be seen that positive angles in excess of 12 deg occur near the wall. This shows a decrease of the endwall crossflow as positive angles indicate less turning towards the suction side of the blade channel. The coolant from the holes is obviously strengthening the endwall boundary layer enabling it to better withstand the pressure gradient from pressure to suction side.

4.3 Coolant Ejection Solely From the Slot. The slot is placed upstream of the bladerow entrance at $x/l_{ax}=-0.20$. Figures 13 and 15 present the resulting coolant concentrations in the measuring planes of $x/l_{ax}=0.10$ and 0.35. The coolant mass flow from the slot is fourfold compared to the mass flow from the holes (see Table 3). Therefore, it is not astonishing that mean coolant concentration in the measuring planes is higher with slot ejection than with ejection from the holes, in spite of the larger downstream distance from the slot to the measuring plane. The coolant in the measuring planes has spread considerably away from the endwall; the spread has two maxima which are associated with flow movements away from the wall.

An explanation for the flow movements in the z direction may be found by looking at Figs. 12 and 14. In these figures the results of L2F-measurements at a wall distance of 0.5 mm are presented. The coolant ejection from the slot produces radical changes in the near wall flow field. These changes have their origin in a considerable intensification of the horseshoe vortices observable in the flow angle diagrams.

In the measurement plane at $x/l_{ax}=0.10$ an angle minimum of 0 deg (i.e., flow direction circumferentially towards the suction side) is observed at $y/t=-0.31$ followed by an increase of the angle of more than 80 deg in a distance of only 2 mm in the y-direction. This means that at this location neighboring fluid crashes against each other and has to move upwards. This is indicating the 3D-separation line connected with the pressure side leg of the horseshoe vortex at $y/t=-0.35$.

The suction side leg of the horseshoe vortex is intensified, too. Its footprint can be seen at $y/t=-0.71$ where the flow angle is increasing in a rather narrow region, indicating a 3D-separation line. Accordingly the concentration plot in Fig. 13 is showing a movement of coolant away from the endwall around the locations of the 3D-separation lines. The Mach number is locally decreased and turbulence increases in the vicinity of the 3D-separation lines.

In the measurement plane at $x/l_{ax}=0.35$, similar features as at

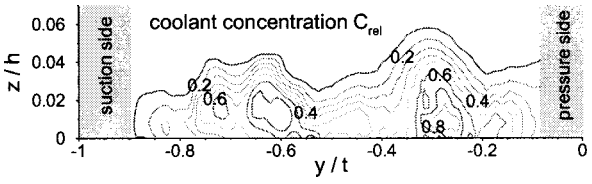

Fig. 13 Coolant concentration from slot ejection at $x/l_{ax}=0.10$

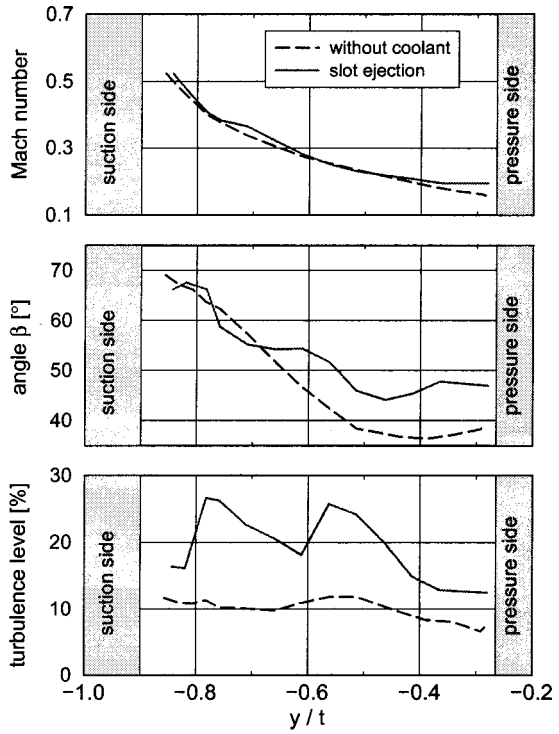

Fig. 14 L2F measurements at $x/l_{ax}=0.35$ and at the wall distance $z=0.5$ mm ($z/h=0.004$); without coolant ejection and with coolant ejection from the slot only

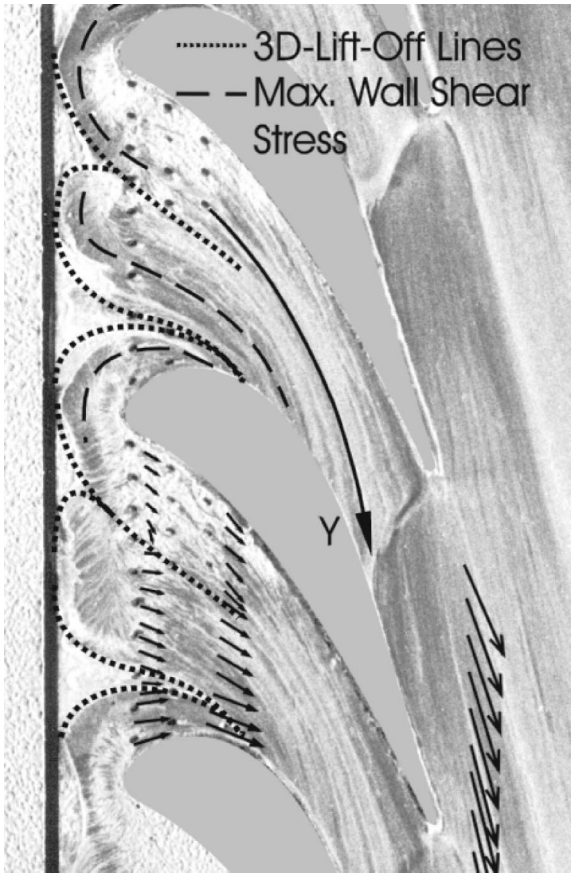

Fig. 16 Oil flow picture of the endwall together with velocity vectors measured by L2F at a wall distance of 0.5 mm, with coolant ejection from slot and holes

$x/l_{ax}=0.10$ can be observed (see Figs. 14 and 15) but they are less distinct. Both 3D-separation lines have moved nearer to the suction side.

The intensification of the horseshoe vortices is strongly connected with coolant ejection from the slot and the question arises as to what kind of mechanism may cause that intensification. The slot traverses the saddle point region of the endwall flow in front of the blade leading edge as already mentioned when discussing Fig. 7. In the saddle point region the approaching endwall boundary layer flow is moving upwards as it is not able to overcome the pressure rise in the stagnation region at the blade nose. This is happening already without coolant ejection and leads to the well-known horseshoe vortex. If additionally coolant is ejected at the saddle point with a momentum-component normal to the wall, it is likely that the horseshoe vortex is amplified. In our opinion this explanation is the most probable one.

If the slot would be moved much closer to the blade leading edge it has to be expected that an adverse effect could be achieved: The horseshoe vortex system could be decreased in strength because the coolant ejection would reduce the reverse endwall flow in front of the blade nose. But then a stronger pitchwise pressure variation at the slot exit would endanger the penetration of (hot) main flow gas into the slot.

Therefore, in order to prevent such an intensification of the horseshoe vortices as observed with the present configuration, it would be best to move the slot upstream. From the oilflow picture a 50 percent increased distance between slot and blade leading edge seems to be sufficient to prevent the intensification.

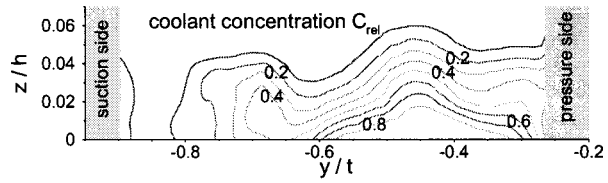

Fig. 15 Coolant concentration from slot ejection at $x/l_{ax}=0.35$

4.4 Coolant Ejection From Slot and Holes. In Fig. 16 the wall shear lines with coolant ejection are visualized. In the lower blade passage velocity vectors measured by L2F at a wall distance of 0.5 mm are added. As in the case without coolant (Fig. 7) the vectors show good correspondence with the oil flow traces with a small divergence near the suction side at $x/l_{ax}=0.35$. The oil flow picture with coolant ejection from slot and holes differs from the oil flow picture without coolant in great detail. A general effect of coolant ejection already discussed above is made visible by the oil flow trace (Y) in Fig. 16 when compared to trace (X) in Fig. 7. It can be clearly seen that, without coolant, trace (X) is hitting the suction side around $x/l_{ax}=0.5$ whereas, with coolant, trace (Y) approaches the suction side much more downstream, thus demonstrating the weakening of endwall crossflow by coolant ejection.

The slot ejection intensifies the horseshoe vortices. The 3D-separation lines connected with the horseshoe vortices are drawn into the oil flow picture, too. Especially the 3D-lift-off line of the pressure side leg can be identified by the measured velocity vectors: they are pointing towards the lift-off line forcing the fluid to escape in the z-direction. The bifurcation of the 3D-lift-off lines upstream of first row of coolant holes is caused by a separation bubble behind the slot.

In Fig. 17, results from the concentration measurements in plane $x/l_{ax}=0.10$ with coolant ejection from slot and holes are presented. The upper picture shows the coolant concentration in the case of seeding only the coolant from the holes. This picture should be compared to Fig. 10 where coolant was ejected solely from the holes. It can be seen that the coolant from the slot influ-

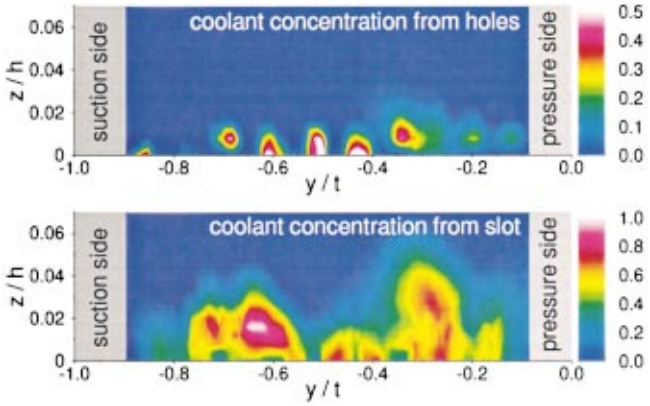

Fig. 17 Coolant concentration in plane $x/l_{ax}=0.10$ with coolant ejection from slot and holes

ences the flow in such a way that some of the coolant jets from the ten holes in the first row are lifted further away from the wall, others are moved nearer to the endwall, the biggest influences are obviously near the locations of the horseshoe vortices.

The lower picture in Fig. 17 shows the coolant concentration in the case of seeding only the coolant from the slot. This picture

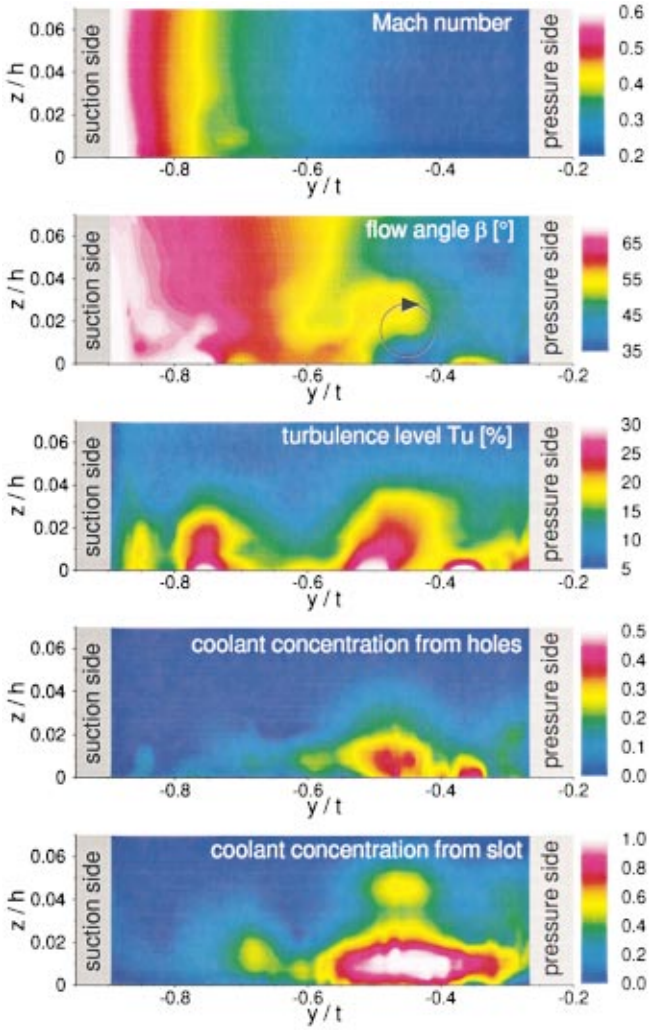

Fig. 18 Overview of flow values in plane $x/l_{ax}=0.35$ with coolant ejection from slot and holes

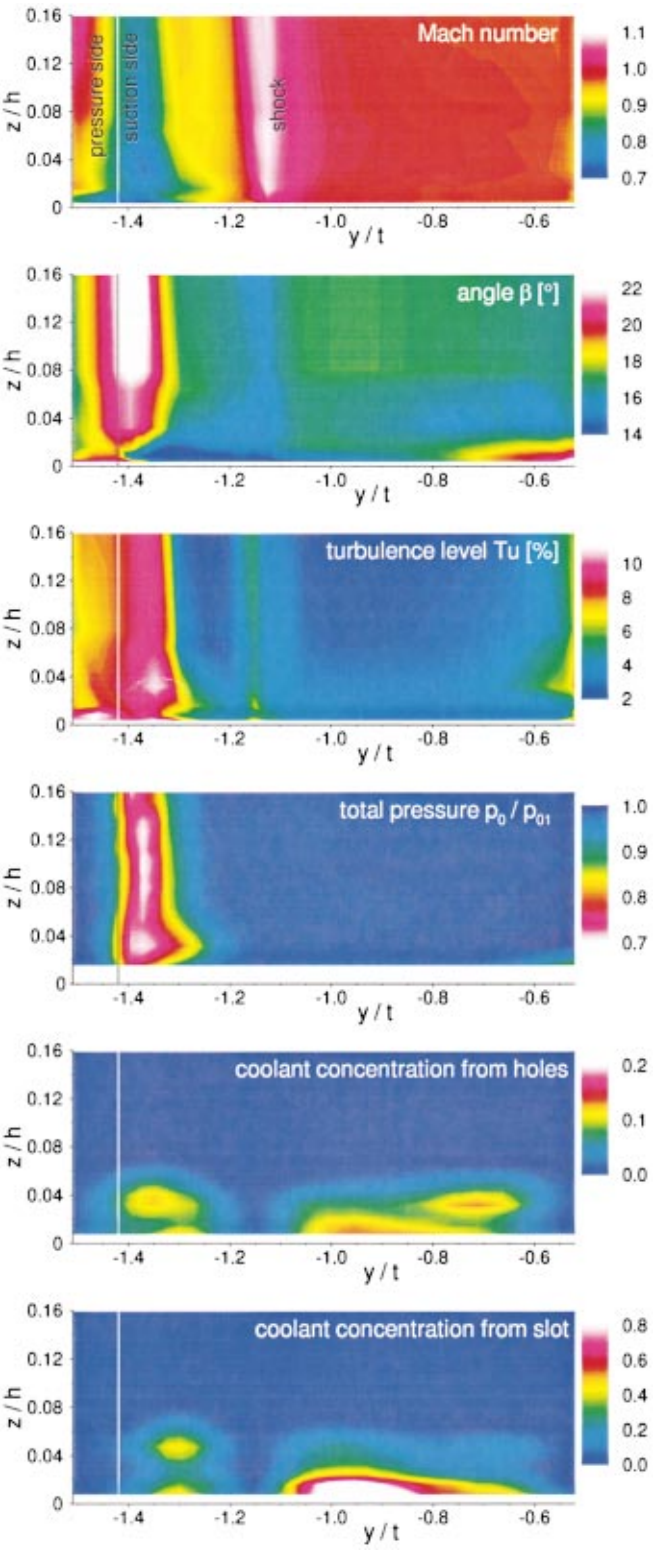

Fig. 19 Overview of flow values in downstream plane $x/l_{ax}=1.10$ with coolant ejection from slot and holes

should be compared to Fig. 13 where the coolant from the slot is made visible, but no coolant was ejected from the holes. The coolant concentration from the slot in Fig. 17 can be well compared to that from Fig. 13, if one bears in mind that the unseeded coolant jets from the holes disrupt the plane. In the case of coolant ejection from slot and holes, the total coolant concentration in this

plane is acquired by adding the concentrations from the upper and the lower picture. It can be stated that the coolant concentration field in the plane $x/l_{ax}=0.10$ is dominated by the coolant from the slot. In the case of slot ejection, the additional ejection from the first row of holes seems to be of not much use with the exception of the hole nearest to the suction side.

In Fig. 18, results from the L2F measurements in plane $x/l_{ax}=0.35$ with coolant ejection from slot and holes are presented. In the Mach number diagram, the velocity increase from pressure to suction side is the dominant feature. In the flow angle diagram the pressure side leg of the horseshoe vortex strengthened by the slot ejection can be distinguished remarkably well. A near wall flow movement toward the suction side at $y/t=-0.45$, as already mentioned when discussing Fig. 14, is connected with a flow movement toward the pressure side at the same y-position but further away from the endwall. The location of this vortex is indicated by a circle drawn into the plot.

The indicated strong vortex is not the only one which may be recognized in the flow angle plot of Fig. 18. At both sides of the pressure side leg of the horseshoe vortex, two more vortices can be deduced from the flow angle field—vortices which rotate in opposite direction to the horseshoe vortex and which obviously have their origin in the rotational movement of the strong horseshoe vortex leg. In combined action with the vortex left of it, the pressure side leg of the horseshoe vortex produces a 3D-separation line in between them where fluid is moved away from the endwall. Together with the vortex right of it, the pressure side leg of the horseshoe vortex produces a 3D-attachment line in between them where fluid is moved to the endwall and where consequently a maximum of wall shear stress and heat transfer can be expected.

The plot of turbulence intensity in Fig. 18 shows first the upwards movement of turbulent fluid at the locations of the 3D-separation lines connected with the horseshoe vortex (see discussion of Figs. 12 to 15) and secondly some turbulent spots caused by the ejection from the holes. Turbulence levels of 30 percent are easily exceeded whereas a turbulence level of roughly 10 percent was attained without coolant.

The lowest picture in Figure 18 displays the coolant concentration in the case of seeding only the coolant from the slot. This picture is globally very similar to Fig. 15 where the coolant from the slot is made visible, too, but no coolant was ejected from the holes. The coolant from the slot is concentrated in a mid passage region and has its maximum a short distance away from the endwall which is partly due to the displacement effect caused by the ejection from the holes.

The second picture from below in Fig. 18 shows the coolant concentration in the case of seeding only the coolant from the holes. This picture should be compared to Fig. 11 where the coolant from the holes is made visible, too, but no coolant was ejected from the slot. As the effective coolant concentration in the plane $x/l_{ax}=0.35$ is obtained by adding the concentrations from the slot and the holes, it can be seen that the ejection from the holes adds some coolant to the coolant fluid from the slot near the pressure side and at two spots near the suction side, but mainly stays in the region where already the coolant from the slot has its maximum concentration.

The cascade downstream plane where velocity measurements by L2F and concentration measurements were carried out, was located at $x/l_{ax}=1.10$. A certain distance away from the endwall the dominant flow features in this plane are shocks and wakes (see Schlieren photo Fig. 4 and oil flow picture Fig. 16).

In Fig. 19 results from the measurements in that plane with coolant ejection from slot and holes are presented. In the topmost picture of this figure the measured Mach number is plotted. The shock location is indicated and especially the extension of the trailing edge in direction of the mean downstream flow angle is marked as a thin line. From left to right Mach number and total pressure (see below) decrease steeply when entering the wake at that side of the wake which arises from the pressure side and increase at a slower rate when leaving the wake at the side coming from the blade suction side. The Mach number is additionally increased when traversing the shock from below. In the wakes turbulence is increased, too. A further peak of turbulence occurs at the shock location which is caused by slight shock oscillations leading to an apparent elevated flow turbulence in the L2F measurement result.

Typical features of secondary flow can be seen looking at the flow angle plot. At the endwall and near the suction side of the wake the flow turning rises (blue color), indicating the remnants of the endwall crossflow from pressure to suction side which proceeds to roll up to the passage vortex. At the right, near the pressure of the wake, a countervortex is visible, transporting fluid at the endwall to the pressure side of the wake (red color) and above the endwall into the opposite direction (light blue color). This countervortex occurs at the pressure side of the wake in contrast to the sketch in Fig. 1, but our measurement location is already 10 percent downstream of the blade trailing edge, therefore it is not clear wether the countervortex has its origin at the blade pressure side or has moved circumferentially from the suction to the pressure side of the wake.

Around $y/t=-1.35$ and $z/h=0.04$ the wake is deepest when looking at Mach number and total pressure; turbulence level, Reynolds shear stress (not shown here) and coolant concentration exhibit a local maximum. This spot probably marks the remnants of the pressure side leg of the horseshoe vortex, closely neighboured to the passage vortex; in any case it marks the location of fluid from the endwall boundary layer which has been transported onto the suction surface by the passage vortex and has been shed into the wake at the trailing edge.

Coolant concentration in the plane at $x/l_{ax}=1.10$ has its maximum in the mid passage, as already visible at $x/l_{ax}=0.35$. Concentration near the wake pressure side is diminished by the endwall crossflow transporting fluid from the pressure to the suction side of the blade passage. In contrast, the endwall crossflow is supplying coolant to the suction side of the wake, as mentioned above.

There is a peculiar minimum of coolant concentration near the shock location. We suspect that this may be due to the measurement method: The laser beam of the L2F is transmitted radially into the blade passage. When measuring near the shock the beam is traversing parallel to the density gradient caused by the shock and it may happen that the beam is slightly deflected by the density gradient—an effect which is exploited when making Schlieren pictures, but which may lead to a slight defocussing in our case. Velocity measurements are hardly affected, but a strict condition for the concentration measurements is a spatially and temporally constant visibility of the tracer particles, a condition which may be hurt by the deflection of the laser beam.

4.5 Cascade Performance. At $x/l_{ax}=1.10$, downstream of the cascade exit, L2F- and Pitot-pressure measurements by probe could be combined to obtain all the flow values in the traverse plane which are necessary to determine the performance of the cascade. The smallest distance to the endwall which could be achieved with the probe was 2 mm, whereas the L2F could take measurements down to 0.5 mm distance to the endwall. Pitchwise averaged quantities could be derived by integrating the inhomogeneous values at a constant distance z from the endwall over one pitch. Area-averaged values were determined by integrating over an area that covered a pitch in circumferential direction and a spanwise distance from $z=2$ mm ($z/h=0.016$) to an optional distance from the endwall. After this data reduction, by applying the equations of conservation of mass, momentum, and energy [18,13,10], the homogeneous (mixed out) flow Mach number Ma_2, the flow angle β_2 and the cascade losses are known. As a loss parameter, the energy loss derived from enthalpy h is used [19].

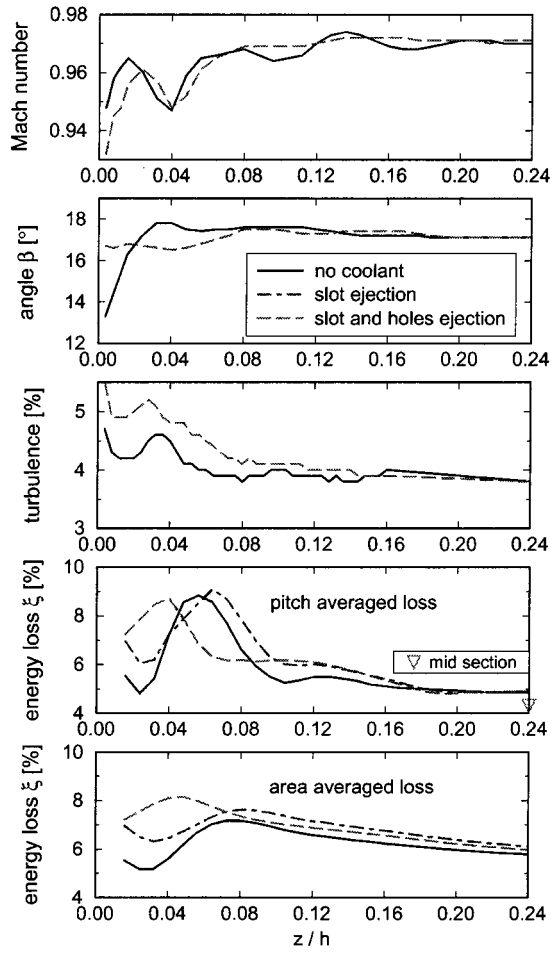

Fig. 20 Pitch-averaged flow values at $x/l_{ax}=1.10$, $Ma_{2is}=1.0$

$$\xi = 1 - \frac{h_{02}-h_2}{h_{01}-h_{2is}} = 1 - \frac{u_2^2}{u_{2is}^2} = 1 - \frac{1-\left(\frac{p_2}{p_{02}}\right)^{1-1/\kappa}}{1-\left(\frac{p_2}{p_{01}}\right)^{1-1/\kappa}} \qquad (6)$$

In Fig. 20, some averaged flow values from the downstream plane are displayed as functions of the wall distance *z*. The effect of coolant ejection on the near wall flow angle has been already discussed; also the comparison of the pitch-averaged flow angle without and with coolant ejection exhibits less turning near the wall and more flow turning from a wall distance of $z/h=0.02$ to 0.08, resulting in a more uniform exit flow angle with coolant ejection.

The pitch-averaged turbulence level with coolant ejection is exceeding the turbulence level without coolant at all spanwise locations up to $z/h=0.15$. This behavior is in accordance with the results of the L2F measurements inside the passage where coolant ejection from the slot or the holes always led to a considerable increase of the turbulence level (see Figs. 10 to 14). A dip in the pitch-averaged Mach number at $z/h=0.04$ is connected with a turbulence peak roughly in the same region, whereas pitch-averaged losses display more scatter in their peak location. Loss is mainly determined by the probe measurement and as the probe location could not be so precisely defined as the L2F measurement volume, it may be that the scatter of the loss peak locations is partly due to errors in the probe location.

When ejecting coolant through slot and holes, the loss and turbulence peaks, as well as the location of the Mach number dip all

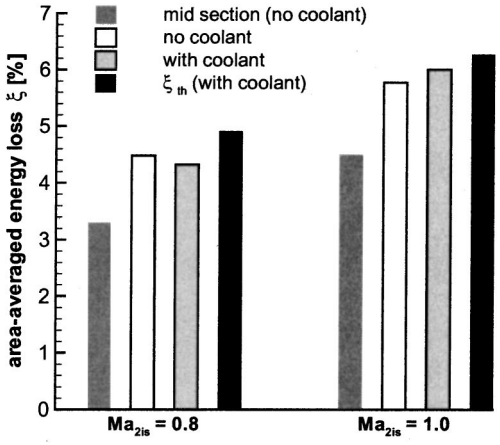

Fig. 21 Area-averaged energy loss values with the area extending from $z=2$ mm to 30 mm ($z/h=0.016$ to 0.24); coolant ejection from slot and holes

coincide well at $z/h=0.04$ and this can be compared to Fig. 19 where this location was suspected to be the location of a vortex core (see discussion there).

The magnitude of the area-averaged loss depends of course on the size of the area chosen. The values at $z/h=0.24$ from Figure 20 are separately plotted into Fig. 21. Included into Fig. 21 are additionally the losses at mid section and the thermodynamic energy loss ξ_{th}, and this is done for the Mach numbers $Ma_{2is}=0.8$ and 1.0.

The loss coefficient ξ does not take the energy of the coolant flow into account. The thermodynamic energy loss ξ_{th} is just an extension of the loss definition above but it includes the energy of the coolant flow. Therefore ξ_{th} is an adequate loss parameter in the case of coolant ejection [20].

$$\xi_{th} = 1 - \frac{(1+\Sigma\, c_{m,j})u_2^2}{u_{2,is}^2 + \Sigma\, c_{m,j} u_{c,is,j}^2}$$

$$= 1 - \frac{\left[1-\left(\frac{p_2}{p_{02}}\right)^{1-1/\kappa}\right]\left(1+\Sigma\, c_{m,j}\cdot\frac{T_{0c,j}}{T_{01}}\right)}{1-\left(\frac{p_2}{p_{01}}\right)^{\kappa-1/\kappa} + \Sigma\, c_{m,j}\frac{T_{0c,j}}{T_{01}}\left[1-\left(\frac{p_2}{p_{0c,j}}\right)^{1-1/\kappa}\right]} \qquad (7)$$

where the summation is carried out over all coolant openings (index *j*).

The difference of the area-averaged loss and mid section loss is approximately the net secondary flow loss, as the contribution of inlet flow boundary layer was checked to be negligible in the present case. Some error has to be taken into account, because the probe measurements could not be extended to the wall and therefore the endwall flow between $z=0$ and 2 mm had to be excluded from the considered area.

At $Ma_{2is}=0.8$ the area-averaged loss ξ is reduced by coolant injection from slot and holes, whereas at $Ma_{2is}=1.0$ this is not the case. This behavior depends on the balance between the production of losses by the coolant and the beneficial effect of coolant energy being higher than the local energy of the main flow. At both Mach numbers the thermodynamic energy loss ξ_{th} which correctly takes the coolant energy into account is exceeding the loss level without coolant.

5 Conclusions

The film-cooled endwall of a high pressure turbine nozzle guide vane, equipped with a cooling slot in front of the vane and cooling holes inside the blade passage, was explored by experimental techniques like laser velocimetry, coolant concentration measure-

ments, surface pressure distribution, and probe measurements. Additionally, thermal measurements were performed; their results are reported in Part II: Heat Transfer and Film Cooling Effectiveness. The flow field upstream, inside, and downstream of the blade row was investigated in detail with and without coolant injection. The interaction of the ejected coolant with the main flow turned out to be rather strong. The main results are:

- Endwall cross flow, and consequently the passage vortex, is reduced by coolant ejection, both by ejection from the holes and the slot.
- The horseshoe vortex was dramatically strengthened by the ejection from the slot. This was traced back to the location of the slot, being positioned just in the region of the saddle point in front of the blade nose. To prevent such an intensification of the horseshoe vortex as observed with the present configuration, it would be best to place the slot at a larger distance from the blade leading edge.
- Ejection from the holes or the slot considerably increases the turbulence level. Accordingly a rise in heat transfer is expected.
- The blowing ratio of the coolant ejected from the holes was partly too high, especially near the pressure side, that is why many of the coolant jets separated from the platform surface.
- The intensified horseshoe vortices are an important cause for the transport of coolant from the endwall into the main flow.
- The coolant concentration field was dominated by the coolant ejected at the slot, the coolant holes were of minor importance, only locally near the suction and the pressure side of the blade passage a beneficial effect of the holes was noticeable.
- The net secondary losses increase with coolant ejection, if thermodynamic energy losses are compared.

Acknowledgments

The authors are grateful to the German Ministry of Education and Research (Bundesministerium für Bildung und Forschung) for support of this investigation in the framework of the AG TURBO research program under the grant number 032 7040 H.

Nomenclature

l = chord
Ma = Mach number
T = temperature
u = streamwise velocity
t = blade pitch
p = pressure
Tu = turbulence level
v = transverse velocity
x = axial coordinate
z = distance from endwall
M = blowing ratio = $(\rho u)_c/(\rho u)_{\mathrm{loc}}$
c_m = coolant mass flow ratio
β = angle (zero in circumferential direction)
y = pitchwise coordinate
h = blade height
$\dot{m}$ = mass flow
ρ = density

Subscripts

0 = total condition
ax = axial
loc = local main flow
1,2 = stator inlet, stator exit
is = isentropic
c = coolant

References

[1] Sieverding, C. H., 1985, ''Recent Progress in the Understanding of Basic Aspects of Secondary Flows in Turbine Blade Passages,'' ASME J. Eng. Gas Turbines Power, **107**, pp. 248–257.
[2] Sieverding, C. H., and Wilputte, P., 1981, ''Influence of Mach Number and Endwall Cooling on Secondary Flows in a Straight Nozzle Cascade,'' ASME J. Eng. Power, **103**, pp. 257–264.
[3] Friedrichs, S., Hodson, H. P., and Dawes, W. N., 1997, ''Aerodynamic Aspects of Endwall Film-Cooling,'' ASME J. Turbomach., **119**, pp. 786–793.
[4] Langston, S., 1980, ''Crossflow in a Turbine Cascade Passage,'' ASME J. Eng. Power, **102**, pp. 866–874.
[5] Blair, M. F., 1974, ''An Experimental Study of Heat Transfer and Film Cooling on Large-Scale Turbine Endwalls,'' ASME J. Heat Transfer, **96**, pp. 524–529.
[6] Bourguignon, A. E., 1985, ''Etudes des Transferts Thermiques sur les Plates-Formes de Distributeur de Turbine avec et sans Film de Refroidissement,'' AGARD-CP-390, pp. 12-1–12-9.
[7] Granser, D., and Schulenburg, T., 1990, ''Prediction and Measurement of Film Cooling Effectiveness for a First-Stage Turbine Vane Shroud,'' ASME Paper No. 90-GT-95.
[8] Burd, S. W., and Simon, T. W., 2000, ''Effects of Slot Bleed Injection Over a Contoured Endwall on Nozzle Guide Vane Cooling Performance: Part I—Flow Field Measurements,'' ASME Paper No. 2000-GT-199.
[9] Georgiou, D. P., Papavasilopoulos, V. A., and Alevisos, M., 1996, ''Experimental Contribution on the Significance and the Control by Transverse Injection of the Horseshoe Vortex,'' ASME Paper No. 96-GT-255.
[10] Nicklas, M., 2000, ''Filmgekühlte Turbinenplattform in transsonischem Strömungsfeld,'' Dissertation, Rheinisch-Westfälische Technische Hochschule Aachen; additionally published as DLR-FB 2000-10, Cologne.
[11] Schodl, R., 1980, ''A Laser-Two-Focus (L2F) Velocimeter for Automatic Flow Vector Measurements in the Rotating Components of Turbomachines,'' ASME J. Fluids Eng., **102**, pp. 412–419.
[12] Kost, F., and Kapteijn, C., 1997, ''Application of Laser-Two-Focus Velocimetry to Transonic Turbine Flows,'' *Proc. 7th Int. Conf. on Laser Anemometry—Advances and Applications*, University of Karlsruhe, Germany.
[13] Kost, F., 1993, ''Längswirbelentstehung in einem Turbinenlaufrad mit konischen Seitenwänden,'' Dissertation, University of Göttingen; DLR-FB 93-13 (ISSN 0939-2963).
[14] Kapteijn, C., 1995, ''Wake Development Downstream of a Transonic Turbine Inlet Guide Vane With Trailing Edge Ejection,'' AGARD-CP-571, Paper No. 14.
[15] Friedrichs, S., and Hodson, H. P., 1994, ''The Ammonia and Diazo Surface Coating Technique for Measuring Adiabatic Film Cooling Effectiveness,'' *12th Symp. on Measuring Techniques for Transonic and Supersonic Flows in Cascades and Turbomachines*, Prague, Czech Republic.
[16] Haslinger, W., and Hennecke, D. K., 1996, ''The Ammonia and Diazo Technique With CO_2-Calibration for Highly Resolving and Accurate Measurement of Adiabatic Film Cooling Effectiveness With Application to a Row of Holes,'' ASME Paper No. 96-GT-438.
[17] Kost, F., and Nicklas, M., 2000, ''Der aerodynamische Einfluss von Plattformkühlung auf das wandnahe Strömungsfeld des Turbinenstators T6.2,'' DLR Internal Report IB 223-2000 A 03, Göttingen.
[18] Amecke, J., and Safařík, P., 1995, ''Data Reduction of Wake Flow Measurements With Injection of Another Gas,'' Forschungsbericht DLR-FB 95-32, Cologne.
[19] Horlock, J. H., 1966, *Axial Flow Turbines*, Robert E. Krieger Publishing Company, Malabar, USA.
[20] Lawaczeck, O., 1977, ''The Influence of Jets of Cooling Air Exhausted From the Trailing Edges of a Supercritical Turbine Cascade on the Aerodynamic Data,'' AGARD-CP-229, Paper No. 30.

Film-Cooled Turbine Endwall in a Transonic Flow Field: Part II—Heat Transfer and Film-Cooling Effectiveness

Martin Nicklas[1]
Institute of Propulsion Technology,
German Aerospace Center (DLR),
37073 Göttingen, Germany

Thermodynamic and aerodynamic measurements were carried out in a linear turbine cascade with transonic flow field. Heat transfer and adiabatic film-cooling effectiveness resulting from the interaction of the flow field and the ejected coolant at the endwall were measured and will be discussed in two parts. The investigations were performed in the Windtunnel for Straight Cascades (EGG) at the DLR, Goettingen. The film-cooled NGV endwall was operated at representative dimensionless engine conditions of Mach and Reynolds number $Ma_{2is}=1.0$ and $Re_2=850{,}000$ respectively. Part II of the paper discusses the thermodynamic measurements. Detailed temperature measurements were carried out on a turbine stator endwall. In order to determine the surface heat transfer and adiabatic film-cooling effectiveness, an infrared camera system in a rectilinear wind tunnel measured the endwall temperatures in the transonic flow field. The adiabatic film-cooling effectiveness was determined using the superposition method. Measurements were carried out to first, validate the assumptions of theory and second, analyze the error associated with the measurements. Effects of coolant ejection from a slot and three rows of holes were investigated and compared with each other. The influence of Mach number and blowing ratio on the heat transfer were further aspects of the investigation. Strong variations in heat transfer and film-cooling effectiveness due to the interaction of the coolant air and the secondary flow field were found. Based on the results of this investigation an improved cooling design will be investigated in a follow-up project.
[DOI: 10.1115/1.1397308]

1 Introduction

The accurate prediction of heat transfer, film-cooling effectiveness, and the aerodynamics of high-pressure turbine stages plays a crucial role in the design of efficient turbomachines. Designs for new high-pressure turbine stages require resistance to increasingly high thermal and aerodynamic loads. Therefore, thorough information on the turbine's aerodynamics and heat transfer is needed to enable the design of efficient cooling systems by decreasing the amount of coolant air needed. One of the most efficient cooling methods is film-cooling, where coolant air is extracted from the compressor and discharged through slots and holes in the blades and endwalls in HPT stages. In the ideal case, after leaving the orifices, the coolant air forms a stable and smooth protective layer between the hot mainstream and the surface of the component. Due to the increase in turbine inlet temperatures, intensive cooling of the endwalls is of crucial importance. In the endwall region, strongly three-dimensional effects from the main flow interact with the ejected coolant. These three-dimensional flows significantly influence loss and heat transfer in the turbine. Prediction of the coolant location is very difficult. The first published work on endwall film-cooling (Blair [1]) is unusual in investigating heat transfer and film-cooling together.

Heat transfer measurements have shown that at the endwall, next to the leading edge, the heat transfer is increased by the horseshoe vortex (Blair [1], Gaugler and Russell [2], Takeishi [3], Wedlake et al. [4], Boyle and Russell [5], York et al. [6]). This is the result of a thin boundary layer, which is formed from the effect of the secondary flows. Additionally this process is connected with a rise in turbulence level. Graziani et al. [7] and Harvey et al. [8] observed a rise in heat transfer due to the three-dimensional separation line from the pressure side branch of the horseshoe vortex. This effect though, was not observed by Gaugler and Russell [2]. A strong increase in heat transfer occurs due to the strong secondary flow fields at the suction side corner (Blair [1], Graziani et al. [7]). In the throat, the heat transfer in the suction side corner is dominated by the passage vortex (Graziani et al. [7]). Downstream of the cascade, the wake region at the endwall is particularly endangered by high heat transfers rates (Graziani et al. [7], Goldstein and Spores [9], Harvey et al. [8]).

The horseshoe vortex within the area of the leading edge causes a decrease of the film-cooling effectiveness (Takeishi et al. [3]). Coolant ejected upstream of the three-dimensional-separation lines does not cool downstream of these lines (Friedrichs et al. [10]). The passage vortex leads to a fast decrease of film-cooling effectiveness in the pressure side corner (Blair [1], Burd et al. [11]). Granser and Schulenberg [12] improved film-cooling effectiveness by increasing the blowing ratio. Investigations by Jabbari et al. [13] showed that the correlation between film-cooling and the main parameters like cooling ratio at the flat plate is similar to that of a turbine endwall.

2 Superposition Method

The quantities of interest in film-cooling experiments are the heat transfer coefficient h and the adiabatic film-cooling effectiveness η_f. The parameter h is a scalar that describes the relationship between the local heat flux and the defined temperature difference for one-dimensional heat transfer. A film-cooling situation is typically described by three temperatures. To reduce this problem to two temperatures, the heat transfer is described in the form:

[1]Present address: Department of Engineering Science, University of Oxford, Parks Road, Oxford OX1 3PJ, United Kingdom.

Contributed by the International Gas Turbine Institute and presented at the 46th International Gas Turbine and Aeroengine Congress and Exhibition, New Orleans, Louisiana, June 4–7, 2001. Manuscript received by the International Gas Turbine Institute February 2001. Paper No. 2001-GT-146. Review Chair: R. Natole.

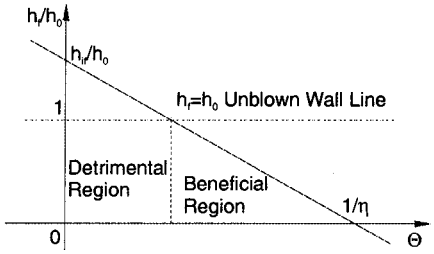

Fig. 1 Linear dependence of heat flux on coolant temperature (Metzger [20])

$$q_f = h_{if}(T_w - T_{aw}) \tag{1}$$

By choosing the adiabatic wall temperature, the heat transfer can be expressed by a coefficient h_{if}, which is a function of the aerodynamic flow field and independent of the temperature boundary layer conditions. The convective and conductive influence on heat transfer will be decoupled. Another definition describes convective heat transfer with the equation:

$$q_f = h_f(T_w - T_{r,\mathrm{loc}}) \tag{2}$$

This equation will be used here. The coefficient h_f is related to the temperature of the injected fluid. In the following the fluid is air. These two definitions are connected by the linear dependence of the heat transfer coefficient on temperature:

$$\frac{h_f}{h_0} = \frac{h_{if}}{h_0}(1 - \eta\Theta) \tag{3}$$

The wall temperature is often expressed by the dimensionless temperature:

$$\Theta = \frac{T_{0C} - T_{0\infty}}{T_w - T_{r,\mathrm{loc}}} \tag{4}$$

The adiabatic film-cooling effectiveness,

$$\eta = \frac{T_{aw} - T_{r,\mathrm{loc}}}{T_{0C} - T_{0\infty}} \tag{5}$$

denotes the change of temperature on a adiabatic wall at the point of interest due to the temperature difference between the injected fluid and the main flow, and the shift of the boundary layer caused by the coolant jet (Teekaram et al. [14]). In an incompressible flow field, the effectiveness η_f is equivalent to the coolant concentration (Eckert [15], Teekaram [14]). To apply the superposition method, the general equation of heat transfer is simplified by several assumptions. The following coordinates are in reference to the flow field (Fig. 1).

The velocity u in the x direction dominates the steady-state flow field. The properties a and ε_H of the ideal gas are not dependent on the temperature and therefore dependent on the aerodynamic properties alone. Terms in z are negligible and the characteristics of the boundary layer are simplified. As such, the time-averaged Navier–Stokes equations will apply. The energy equation is then described by the formula:

$$u\frac{\partial t}{\partial x} + v\frac{\partial t}{\partial y} - (a + \varepsilon_H)\frac{\partial^2 t}{\partial y^2} = \frac{u}{\rho c_p}\left(\frac{\partial p}{\partial x}\right) + \frac{v + \varepsilon_M}{c_p}\left(\frac{\partial u}{\partial y}\right)^2 \tag{6}$$

The difference in temperature t is related to the local recovery temperature $T_{r,\mathrm{loc}}$. The following boundary conditions should apply:

$$t = T - T_{r,\mathrm{loc}}$$

$$x = 0, \quad y = 0 : t = t_C, \quad t_C = T_{0C} - T_{r,\mathrm{loc}} \cong T_{0C} - T_{0\infty}$$

$$y = 0 \quad : \quad q = q_w$$

$$y = \infty \quad : \quad t = 0 \tag{7}$$

Reformulating, we have three solutions

(*a*) $q = q_w$, $t_C \neq 0 \rightarrow t_w = T_w - T_{r,\mathrm{loc}}$ (general)
(*b*) $q = q_w$, $t_C = 0 \rightarrow t_{iw} = T_{iw} - T_{r,\mathrm{loc}}$ (isoenergetic)
(*c*) $q = 0$, $t_C \neq 0 \rightarrow t_{aw} = T_{aw} - T_{r,\mathrm{loc}}$ (adiabatic wall).

Assuming a linear function, the general solution of the heat transfer equation (*a*) is obtained through summing the solutions of the isoenergetic (*b*) and the adiabatic (*c*) boundary conditions. Reformulating, the adiabatic wall temperature is given by $t_{aw} = t_w - t_{iw}$. In both cases (*a*) and (*b*), due to the specific heat flux q_w, a higher temperature level is attained than when observing a film-cooling situation on an adiabatic (unheated) wall. The temperature difference t_{aw} remains constant, independent of the absolute wall temperature, because of the energy equation's linear dependency on the temperature. This signifies that the two measurements, whose results are subtracted, are carried out on the sidewall with identical film-cooling proportions and heating power. In the following the assumption that $t_C = T_{0C} - T_{r,\mathrm{loc}} \cong T_{0C} - T_{0\infty}$ should apply. The cooling effectiveness is therefore described by the relationship:

$$\eta_f = \frac{T_{aw} - T_{r,\mathrm{loc}}}{T_{0C} - T_{0\infty}} \cong \frac{t_w - t_{iw}}{t_C}. \tag{8}$$

3 Experimental Apparatus

The experiments reported in this paper were performed in the Wind-tunnel for Straight Cascades at the DLR Goettingen, and are described in Part I—Aerodynamic Measurements.

3.1 The Turbine Stator and Film-Cooling Geometry. The investigated stator is an HPT nozzle guide vane and was designed by DaimlerChrysler MTU (Munich) in the course of the AG Turbo project. The experimental arrangement comprises a state-of-the-art stator including a film-cooling setup. The film-cooling configuration consists of a slot in front of the cascade inlet and three rows of holes in the front third of the endwall (Fig. 2). The slot represents a split between combustion chamber and the first stage of the turbine in the real machine. Slot and holes possess an independent air supply. The air passes through a plenum chamber before it enters the cascade. In the plenum chamber, total pressure p_{0C}, total temperature T_{0C}, and coolant mass flow $\dot{m}_C$ are measured. Some data on stator and cooling geometry are given in Fig. 2. The slot injects the coolant into the cascade in the direction of the main flow at an angle of $\beta_S = 45$ deg to the endwall at a depth to width ratio of $l_S/s = 6.0$. In two of the passages, on the respective endwalls, there are 19 holes. These are arranged in three rows in the front third of the endwall. The holes have a depth to diam-

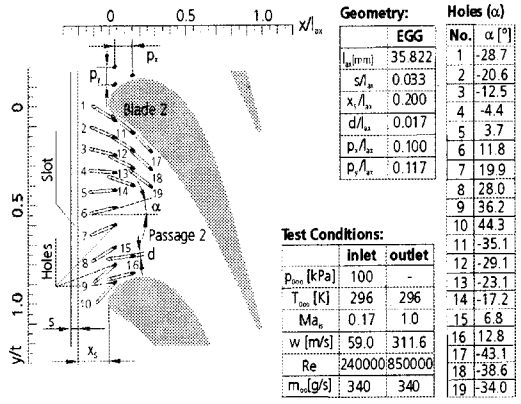

Fig. 2 Endwall film-cooling arrangement and test conditions

eter ratio of $l_B/d=14.5$. This ratio was selected because the endwall for the heat transfer measurements is made of plastic and therefore had to possess sufficient solidity and high insulation. The holes are drilled at an angle of $\beta_B=35$ deg to the endwall. In addition, each hole possesses a compound angle α to the inlet flow (Fig. 2).

3.2 IR Measurement Setup. The endwall used for measuring heat transfer and adiabatic film-cooling effectiveness consists of a high-temperature plastic material (TECATRON) with a thermal conductivity of 0.2 W/mK and a maximum operating temperature of about 500 K (Fig. 3). In order to create a constant specific heat flux, heating foils were appended on the wetted surface of the passage. The heating foils were composed of manganin-meander. This material's resistance changes at only 10^{-5}/K caused by temperature. Conduction losses at the endwall were measured by twelve heat flux sensors (RdF 20453-3), which were integrated into the endwall. Surface temperatures were measured by an NEC 6T62 infrared-camera system (IR-system) and thermocouples. The image of the test plate surface was digitized by an array of 256×207 pixels. All signals from the IR-system, thermocouples, heating foils, heat flux sensors and pressure systems were measured in a time-synchronized manner. To accomplish an optical access to the test section at the IR-wavelengths, a ZnS-window was substituted for one of the endwalls. The window was fitted with holes for mounting the blades (Fig. 4).

3.3 Test Conditions. A variety of test cases with different main flow and coolant parameters were investigated in the course of the AG Turbo project. The measurements of heat transfer and film-cooling effectiveness presented here focus on the transonic test case, and primarily on one coolant flow rate. This results in one blowing ratio for slot and hole coolant ejection. The main parameters of the wind tunnel are presented in Fig. 2 while the cooling parameters are described in Table 1. Further details are provided in Part I—Aerodynamic Measurements.

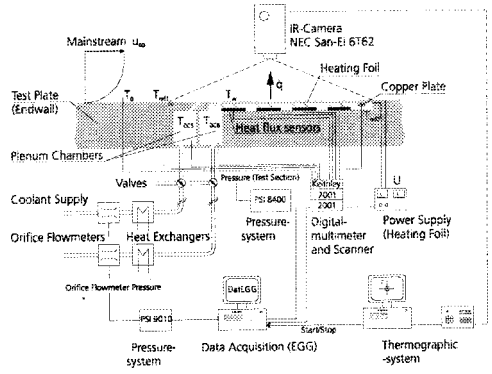

Fig. 3 Basic arrangement of the test setup for IR-measurements at the EGG

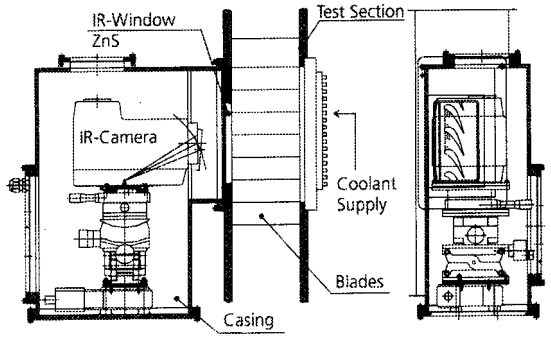

Fig. 4 Practical arrangement of the test setup for IR-measurements at the EGG

Table 1 Film cooling parameters

	$\dot{m}_C$	$c_m=\dot{m}_C/\dot{m}_\infty$	M (mean)	M_{min}	M_{max}
slot	4.3g/s	1.3%	1.3	-	-
holes	1.1g/s	0.32%	3.0	1.4	3.7

3.4 Data Evaluation and Procedure. A temperature field on the endwall was created with the heating foils. The IR-camera constantly measures the stationary temperature distribution on the endwall. This distribution settles in with the flow approximately two minutes after starting the wind tunnel. At each point of the endwall, a temperature, higher than the total temperature of the main flow, is reached. In 10 minutes, approximately 250 IR measurements are taken, to capture the smallest changes in the temperature field. The results of the IR-measurements consists of 20 pictures at the end of the IR-film. The temperature data of these pictures are arithmetically averaged and the obtained temperature field is calibrated and standardized using a temperature reference from the thermocouples (Nicklas [16]). Because all measurements were done at slightly differing temperatures of the main flow, the IR-data of a test series required for a result of the superposition method is related to one temperature: the average total temperature of the test series (e.g., $T_{0\infty}=296$ K), while the temperature of the main flow differs, e.g., $\Delta T_{0\infty}=0.7$ K. At the same time, all relevant data of the wind tunnel (temperatures, pressures, mass flows, heating power and power losses) are recorded. The specific heat flux q (Eq. (2)) is calculated through the total heating power generated in the passages by the heating foils. This power is calculated with the potential difference of the electrically driven heating foils, and their resistance ($R=8.75\,\Omega$). Due to the distribution of the meander on the heating foil (Fig. 5), a uniform distribution of the power on the heating foil ($A_F=1800$ mm^2, including kapton-framing) cannot be expected. The heat transfer coefficient at a specific point on the endwall is calculated through the average specific gross heating power q_F of an imagined surface around the point. The heat flux q_F is obtained through the proportion of heating coil e.g., $A_{RH}=3$ mm^2 present in the imagined area around the point, e.g., $A_R=4$ mm^2 in comparison to the total power of the surface of the heating coil ($A_{FH}=633$ mm^2).

Due to heat conduction and radiation from the endwall, losses occur that are taken into consideration when determining the net heat flux from foil to flow field. The equation for net heat flux is then

$$q=q_F-q_{\rm rad}-q_\lambda \tag{9}$$

where $q_{\rm rad}$ and q_λ are discussed below. The heat flux q_F represents the determined partial heat flux of the foil in the observed grid surface. The surface specific heat radiation $q_{\rm rad}=\sigma\varepsilon(T_w^4-T_{0\infty}^4)$ is taken as the radiation term of the equation. When calculating radiation losses, the specially coated surface has $\varepsilon=0.95$ (Nicklas [16]) and σ denotes the Stefan–Boltzmann constant. The losses resulting from heat conduction at the rear part of the platform are taken into account by q_λ measured by sensors. Typically values of the losses are $q_{\rm rad}=0.3-1.8$ percent and $q_\lambda=7-9$ percent related to the total heating power of the foil and dependent on the surface temperature. The net heating power was kept constant during all heat transfer and cooling effectiveness measurements. The average net heat flux in the grid surface was $q=35$ kW/m^2.

4 Validation of the Superposition Method

The use of the superposition method is based on the linear properties of the energy equation during temperature variations. The results used for the superposition must have equal parameters of main mass flow $\dot{m}_\infty$ and coolant mass flow $\dot{m}_C$. If the coolant mass flow is held constant for two measurements, then the blow-

ing ratio M remains unchanged. The advantage of this method is that the cooling effectiveness from two measurements with different coolant air temperatures can be directly superpositioned. Each result of endwall film-cooling effectiveness is then the direct subtraction (superposition) of two temperature pictures of the IR-camera (Eq. (8)). If, as in the present experiment, the coolant air temperature is varied for the two measurements, the result is a change in coolant fluid density. Through this, the variables I and $T_{0C}/T_{0\infty}$ are changed. The result of the change in temperature on the linearity of the energy equation is therefore investigated. This is achieved by comparing the results of film-cooling effectiveness, which can be obtained from two different derivations of the superposition method: Results obtained from the subtraction of two measurements are described as η_f, and results from the derivation of the linear dependency of the heat transfer coefficient h_f and the nondimensional coolant temperature Θ are described in the following as η_g (Eq. (3)).

The adiabatic film-cooling effectiveness results indirectly from the intersections of the straight lines and the abscissas. Theoretically, from a test series, a linear correlation $h_f = f(\Theta)$ is made at each point of the flow field from which the adiabatic film-cooling effectiveness results indirectly. The obtained cooling effectiveness at the observed point could then be compared with the result of the direct subtraction. To validate the theory, sections of the endwall where strong three-dimensional effects and high velocity gradients prevail are chosen. The linear dependency $h_f = f(\Theta)$ is observed at three points of the endwall (Fig. 5). Apart from the linear dependency of the results of each measurement, the precision of the cooling effectiveness measurements are estimated. The Fig. 6 is the result of a test series with coolant ejection from the slot ($M_S = 1.3$). The y axis is the ratio of the heat transfer coefficients h_f/h_0 with and without coolant ejection, and is represented as function of the temperature Θ. In Fig. 6, positive values of the temperature Θ mean that the coolant temperature is higher than the main flow temperature.

The intersection of the straight line and y axis defines the ratio of the heat transfer coefficients with the isoenergetic film-cooling. When the coolant flow reaches the total temperature of the main flow, the heat transfer coefficient at the observed position is 2.1 times higher than without coolant ejection. This results from the influence of the suction side horseshoe vortex stimulated by the coolant ejection. The linearity of different measurements, with equal coolant mass flow but distinct coolant temperatures, is clearly seen at individual points. The linear fit through the measurement points is extrapolated to the abscissa. The intersection of the straight line and abscissa represents the special case of no heat transfer and therefore the case of the adiabatic wall. In this case, the value of the dimensionless coolant temperature Θ is equal to the reciprocal value of the adiabatic film-cooling effectiveness at the point of interest. The film-cooling effectiveness that is deduced in this way is given as $\eta_g = 0.801$ in Fig. 6.

The results by superposition of the individual measurements are also represented in Fig. 6 and lie directly on the abscissa. As reciprocal values of the film-cooling effectiveness at the observed grid surface, they are clustered. The results should theoretically lie on a point and coincide with the intersection of the line and abscissa. The statistical values of the cooling effectiveness, obtained using the direct method, are indicated as arithmetic average value $\eta_f = 0.7832$ (standard deviation $s = 2.76$ percent and confidence interval $m = 1.74$ percent) of the test series. The absolute error $\Delta\eta_f = \pm 5.51$ percent describes the precision of the individual results at position 1 of Fig. 5 with a 95 percent confidence interval.

Figure 7 shows the results at positions 2 and 3, resulting from the test series with coolant ejection from the slot. Further downstream of position 1, the cooling effectiveness is lower due to mixing with the main flow. At position 2 (Fig. 7(a)), values of $\eta_f = 0.4215$ and $\eta_g = 0.4382$ are obtained for the cooling effectiveness. In the trailing edge wake region (position 3), these values are $\eta_f = 0.4125$ and $\eta_g = 0.4098$. Because of the lower values of cooling effectiveness, the intersection of the abscissa is at much higher values of the dimensionless temperature Θ. With a ratio of heat transfer coefficient $h_f/h_0 = 1.1$ at position 2, the change in heat transfer is very low. The absolute error of the individual measurements amounts to $\Delta\eta_f = \pm 5.02$ percent. The results in the downstream region are more precise in reference to the absolute value with errors smaller than $\Delta\eta_f = \pm 3.13$ percent.

Figure 8(a) shows the relationship $h_f = f(\Theta)$ at position 2 for slot and all holes blowing simultaneously. The linear dependency shows high correspondence with the results from the slot coolant ejection alone (Fig. 7(a)). The corresponding values are $\eta_f = 0.4176$ and $\eta_g = 0.4306$. The absolute error of the individual measurements is of a similar magnitude as when there is separate coolant ejection from the slot, with $\Delta\eta_f = \pm 5.38$ percent.

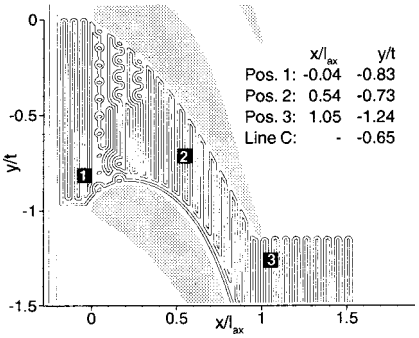

Fig. 5 Positions on the endwall for data validation of $h = f(\Theta)$

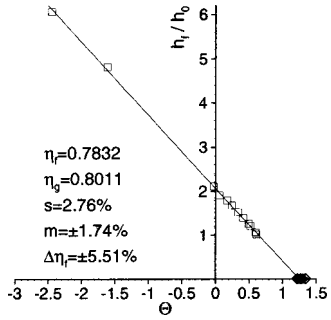

Fig. 6 Linear dependency between heat transfer ratio and nondimensional temperature at position 1 for slot coolant ejection

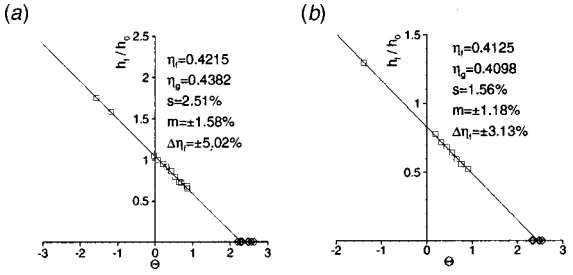

Fig. 7 Linear dependency $hf/h_0 = f(\Theta)$ at position 2 of Fig. 5 (7*a*) and position 3 of Fig. 5 (7*b*) for slot coolant ejection

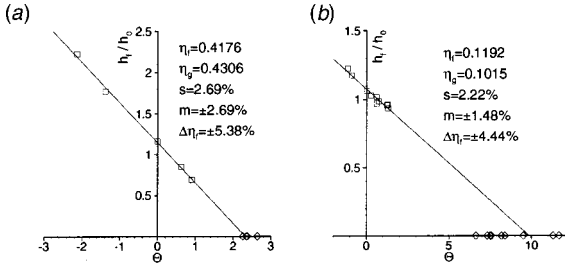

Fig. 8 Linear dependency $h_f/h_0 = f(\Theta)$ at Position 2: coolant ejection through (*a*) slot and all holes (*b*) all holes alone

Figure 8(*b*) shows the effect of coolant ejection from the holes on heat transfer, with a variation of Θ at position 2 of Fig. 5. The absolute level of film cooling effectiveness (with an average value of $\eta_f = 0.1192$ and a ''straight-line-value'' of $\eta_g = 0.1015$) is low in comparison to the measurements with slot coolant ejection. Because of this, the dimensionless temperature at the abscissa intersection is $\Theta = 9.85$. The absolute error of the measurement, $\Delta\eta_f = \pm 4.44$ percent, is the same as for slot coolant ejection. The results of the validation show that the superposition method remains valid with temperature differences of coolant air of around 30 K. The pressure gradients in the flow field do not influence the linear dependency of heat transfer coefficient and temperature. These results are confirmed by Teekaram et al. [14]. The present results show that an average absolute error of $\Delta\eta_f = \pm 5.00$ percent is obtained independently of the measuring point on the endwall and the film-cooling configuration.

The uncertainty values of the heat transfer measurements were calculated from the measurement errors in the absolute electrical power of the heating foils, the losses by radiation and thermal conduction, and the areas of the foil needed for calculation of the specific heat flux. An error of $\Delta h = \pm 5.8$ percent was calculated by the method of Sachs [17]. This value error may seem to be optimistic, even though the ordinate values of Figs. 6–8 show an optimal reproducibility and comparability with the theory, but these values are ratios of the heat flux and therefore sources of errors like lateral heat conduction in the foil are compensated for. A maximum deviation of $\Delta h = \pm 11$ percent is estimated for the heat transfer measurements. The direct boundary region of the foils show larger errors and cannot be included for the interpretation because of the strong lateral heat conduction. These areas of larger errors possess a width of 1 mm at the surrounding of the foils.

5 Heat Transfer: Results and Discussion

Based on the measurements, the influence of coolant ejection on the heat transfer coefficient was analyzed. The effect of different cooling configurations, as well as different blowing ratios is considered with the Mach number held constant at $Ma_{2is} = 1.0$. Furthermore, the effect of different downstream Mach numbers on the heat transfer coefficient during operation without film-cooling was analyzed.

The temperature difference used to analyze the heat transfer coefficients in the front part is that between the heated endwall temperature and the main flow total temperature. It can be experimentally proven with the IR-camera that the recovery temperature in this area corresponds to the total temperature of the main flow. At the rear part of the platform, the heat transfer coefficients are formed with the average recovery temperature, measured by the IR-camera. The average value of the recovery temperature amounts to 99.05 percent of the mainstream total temperature. To clarify the results with film-cooling, they are presented in relation to reference measurements without film-cooling. The measurements analyze the aerodynamic effect of film-cooling on the heat transfer coefficient, and therefore the cooling air is blown out with an isoenergetic temperature.

5.1 Measurements Without Film-Cooling. The heat transfer measurements in the front part of the passage, without film-cooling, show a relatively constant level of the heat transfer coefficients on the platform (Fig. 9). A heat transfer coefficient of $h_0 = 800-1200\ \mathrm{W/m^2K}$ is achieved over the majority of the surface. At the same axial position the heat transfer is higher at the blade-wall junction than in the center of the passage. This is caused by the secondary flow field, because the horseshoe vortex leads to high turbulence levels next to the blades.

Downstream, the velocity of the main flow increases and the heat transfer rises. At the pressure side corner a strong increase in heat transfer occurs, from an axial position of $x/l_{ax} > 0.4$, due to the passage vortex and the connected secondary flow effects (corner vortex). The large gradients in direct proximity to the slot are an artifact caused by the border of the foil.

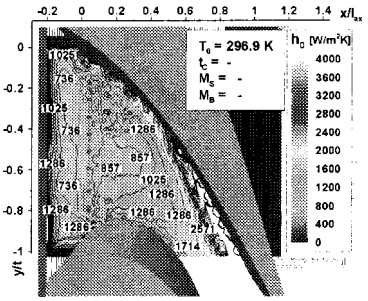

Fig. 9 Heat transfer coefficient h_0: unblown wall

In the downstream flow, the absolute values of the heat transfer coefficients (Fig. 13) are primarily characterized by a strong increase due to the acceleration of the flow field. Downstream of the cascade outlet, a maximum heat transfer of $h_0 = 3714\ \mathrm{W/m^2K}$ is caused by the wake. Farther downstream, the heat transfer continues to be three times as high as in the front part of the passage and reaches $h_0 = 2800\ \mathrm{W/m^2K}$. On the foil, the effect of the wake of the adjacent blade is detected at position $x/l_{ax} = 1.3$ and $y/t = -1.15$. Between the wakes, the heat transfer coefficients on the endwall are substantially smaller. At the same axial position, 55 to 75 percent of the values in the wake region are achieved. The effect of the wake can be explained by the increased turbulence level, which is five times as high in the wake as it is in the free stream (part I, Figs. 19 and 20) and the effect of the secondary flows, which is discussed below. At circumferential positions $y/t = -1.15$ and $y/t = -2.15$, strong gradients in heat transfer occur. These are caused by the splits between the foils.

The local temperature of the fluid at the endwall is a substantial parameter for the local heat transfer. If there is a strong exchange between the fluid in the boundary layer and the cooler air in the free stream, temperature decreases as heat transfer coefficient rises. The secondary flows are the exchange mechanism here. An additional effect, only in the rear part of the passage, is caused by the inactive boundary layer of the vanes. This is a unwanted effect, but the mass flow in the vane boundary layer is very small in relation to the mass transport due to the secondary flows from the midsection to the endwall and therefore for the discussed phenomena this effect is neglectable. The dependency between intensive secondary flows and the local rise of the heat transfer coefficient can be transferred to the turbine, because the radial temperature distribution downstream of the combustion chamber possess a strong dependency in the radial direction. The highest temperatures occur in the mid section. At the hub and the casing the temperature can decrease to 80 percent of the maximum value (Colantuoni [18]). The secondary flows lead hot fluid toward the endwall, and the temperature gradient and the heat transfer increases.

The results of the heat transfer measurements without film-cooling provide reference levels for measurements with film-cooling in the next section.

5.2 Influence of Film-Cooling Configuration Geometry. The following results show the change in heat transfer coefficient through film-cooling with the blowing ratio *M* described in Table 1. In Fig. 10 a comparison of film-cooled to unblown endwall is made for slot and all holes blowing simultaneously. The results clearly show that the increase in heat transfer is predominantly the result of coolant ejection. The heat transfer coefficient rises next to the leading edge and downstream of the holes. The maximum increase occurs at the pressure and suction sides of the vane leading edge ($x/l_{ax} = -0.1$ with $y/t = -0.2$ and $y/t = -0.95$). Normalized to the reference value without film cooling, the heat trans-

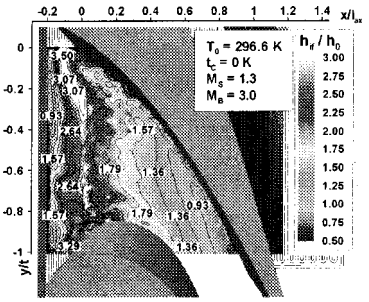

Fig. 10 Heat transfer ratio h_{if}/h_0: comparison of film-cooled to unblown endwall; slot and all holes blowing

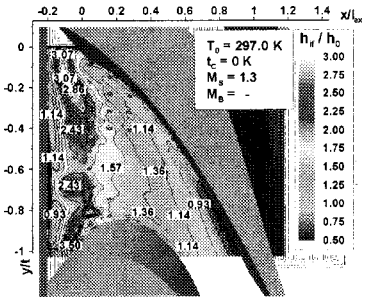

Fig. 11 Heat transfer ratio h_{if}/h_0: comparison of film-cooled to unblown endwall; slot coolant ejection

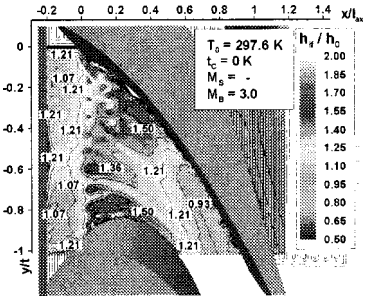

Fig. 12 Heat transfer ratio h_{if}/h_0: comparison of film-cooled to unblown endwall; all holes blowing simultaneously

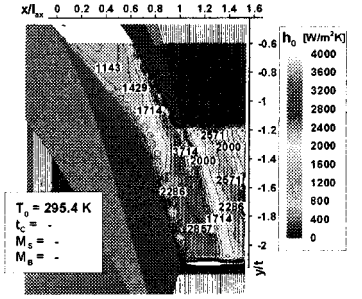

Fig. 13 Heat transfer coefficient h_0: unblown wall

fer increase in these regions is over 300 percent. This is caused by the horseshoe vortex, which is amplified by the cooling air from the slot (part I, Figs. 12 to 14).

Directly downstream of the slot, only a small increase in heat transfer occurs. This is explained by the results of the oil and dye surface flow visualization with coolant ejection (part I, Fig. 16), which in this section show a separation of the flow. In front of the cascade inlet, at the positions $x/l_{ax}=-0.15$ to $x/l_{ax}=0.0$, the heat transfer coefficient ratio increases up to values of $h_{if}/h_0=2.64$. At this position, the oil and dye surface flow visualization show the strong effect of coolant ejection on the secondary flow field. The horseshoe vortex system near the leading edge is strengthened by slot coolant ejection. This effect causes an increase in heat transfer over a large area in front of the cascade inlet. If the results of the heat transfer measurements with film cooling are compared with the oil and dye surface flow visualization, the heat transfer can easily be deduced from the course of the wall stream lines. In general, the lines of maximum shear stress also represent areas of high heat transfer.

The heat transfer coefficient increases likewise in the region of the holes. However, in comparison to the leading edge region, the ratio is smaller with values of $h_{if}/h_0=1.5-2.5$. This results from the sixfold increase in turbulence directly downstream of the holes (part I, Fig. 10), due to hole coolant ejection and from the superposition of the horseshoe vortex's reinforcement and the increase in turbulence level. A decrease in heat transfer occurs on the pressure side from $x/l_{ax}>0.5$. This decrease continues far downstream and occurs in all investigated configurations. The decrease can be explained by the decrease in intensity of the passage vortex when there is coolant ejection.

Further conclusions on the influence of film-cooling on the heat transfer can be gained from a comparison of the single operation of the slot or the holes. Simultaneous coolant ejection (slot and all holes) (Fig. 10) and single coolant ejection from the slot (Fig. 11) are compared. The dominant influence of slot coolant ejection on the heat transfer in the front part of the passage ($x/l_{ax}=-0.2$) is obvious. The results with single slot coolant ejection likewise clearly show the substantial increase of the horseshoe vortex due to the film cooling. In the proximity of the leading edge, the heat transfer coefficient is increased by 300 percent analogous to the configuration when slot and holes are operated together ($x/l_{ax}=-0.1$ and $y/t=-0.65$). An important result of the investigations is that at the pressure side corner the heat transfer coefficient is reduced. This effect is shown most clearly when coolant is ejected only through the slot. At $x/l_{ax}=0.6$ on the pressure side, the heat transfer coefficient is only 75 percent of the value in the unblown wall case. In comparison to the coolant ejection from slot and holes, this is a decrease of 18 percent because, if all holes are in operation, the turbulence level is much higher (part I, Figs. 10 and 11). With coolant ejection only from the holes (Fig. 12), an increase of the heat transfer coefficient ratio occurs downstream of the cooling drillings ($h_{if}/h_0=1.5$). This is caused by a rise in turbulence level in the observed area (part I). The results of coolant ejection separately from the slot and the holes show that there is no additive overlay of the effects taking place when they are operating together.

The results of the heat transfer measurements in the rear part and the downstream region of the passage are represented in Figs. 13–16. The results also show the ratio of the heat transfer coefficients of the measurements with film-cooling to the measurements without coolant ejection. In the front part of the endwall the Figs. 10–12 illustrate a decrease in heat transfer at the pressure side corner due to coolant ejection, in the present figures, it is obvious that the area with reduced heat transfer extends further downstream (Figs. 14, 15, and 16). This effect is qualitatively independent of the cooling configuration.

If the wake region is approached from the extension of the

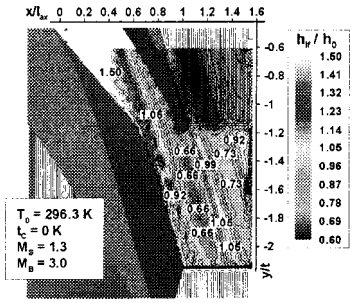

Fig. 14 Heat transfer ratio h_{if}/h_0: comparison of film-cooled to unblown endwall; slot and all holes blowing

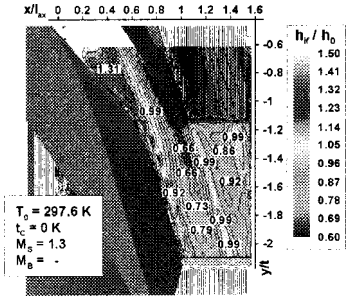

Fig. 15 Heat transfer ratio h_{if}/h_0: comparison of film-cooled to unblown endwall; slot coolant ejection

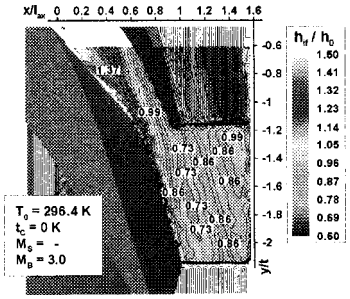

Fig. 16 Heat transfer ratio h_{if}/h_0: comparison of film-cooled to unblown endwall; all holes blowing simultaneously

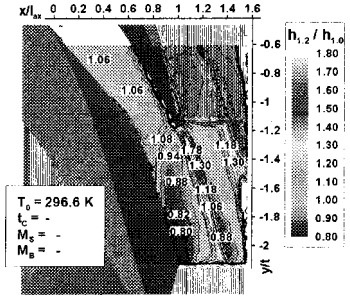

Fig. 17 Comparison of different Mach numbers $Ma_{2is}=1.2$ and $Ma_{2is_{ref}}=1.0$ (without coolant ejection)

pressure side, the maximum heat transfer coefficient substantially decreases due to film-cooling to 66 percent of the reference values of the unblown wall case (Fig. 14). The maximum heat transfer coefficient (hot spot) on the endwall directly downstream of the trailing edge though, is still approximately $h_{if}=2500\ \mathrm{W/m^2K}$ and therefore high values of heat transfer are achieved. In Fig. 14, the decrease of heat transfer coefficients can also be observed downstream of the adjacent blade at the position $x/l_{ax}=1.2$ and $y/t=-1.15$. However, due to the larger range of the adjacent wake, the effect is smaller.

In the extension of the suction side area of the wake region, starting at $x/l_{ax}=1.1$ and $y/t=-1.15$, little or no influence on heat transfer coefficient through film-cooling is detected. The decrease in heat transfer is in contradiction to the boost in wake turbulence level caused by coolant ejection. With the Laser-2-Focus-measurements (L2F, for more detail see part I and Nicklas [16]), a local increase of the turbulence level could be determined to be caused by the coolant (part I, Fig. 20) and therefore an increase of the heat transfer coefficient is expected. The decrease in heat transfer can be attributed to the influence to the passage vortex, which is influenced by the coolant ejection. The decrease in heat transfer is linked to a flow mechanical effect and thus to the modification of the secondary flow field by the coolant ejection.

An explicit argument is given by the L2F-measurements that show a decrease of the turning angle next to the endwall caused by film cooling. In addition, the comparison of the oil and dye pictures with and without film-cooling makes this effect obvious (part I, Figs. 7 and 16). The smaller intensity of the passage vortex at the endwall and the connected secondary flow systems (e.g., trailing edge vortex) causes the heat transfer coefficient decrease (compare section 5.1).

If the effect of single operation of slot and holes is compared to the combined operation of slot and holes, then qualitatively a very similar result is achieved downstream in all three possible configurations. Although the slot and the holes strongly differ in geometry and blowing parameters, the passage vortex in the rear part of the passage dominates the heat transfer. Effects, like the local film-cooling concentration fall aside.

5.3 Influence of the Mach Number. The influence of main flow velocity on heat transfer coefficient in the rear part of the passage is examined by varying the downstream isentropic Mach number. The results are represented in relation to the reference Mach number $Ma_{2is}=1.0$ (unblown wall case) and are measured without coolant ejection. The largest effect on the heat transfer by a variation of the Mach number is to be found in the wake region downstream of the cascade. If there is an increase of the isentropic Mach number from $Ma_{2is}=1.0$ to $Ma_{2is}=1.2$ then the heat transfer coefficient at the hot spot downstream of the trailing edge shows increases of 178 percent (Fig. 17). Upstream of the throat, the changes in heat transfer are small. Since in both cases the cascade is choked and the flow field in the throat is critical, the acceleration upstream is similar. In particular, in the throat the modification of the heat transfer coefficients can be neglected. It is striking that downstream of the throat an extended area between the wakes shows a lower ratio in heat transfer coefficients. The values drop to 80 percent of the reference level and therefore contradict the increase in the contour Mach number (Rehder [19]). This could be the effect of the shock in the throat to the endwall boundary layer. The impact of the shock causes a fast increase in the thickness of the endwall boundary layer or leads to separation. The consequence of this would be a reduction in heat transfer.

5.4 Influence of the Blowing Ratio. The effect of the blowing ratio on heat transfer coefficient in the rear part of the passage is examined by varying the coolant mass flow. The isentropic Mach number is held constant at $Ma_{2is}=1.0$ for the coolant ejection from the slot and all holes. For clearer interpretation, the results are represented normalized to the results with the blowing configuration in Table 1 ($M_S=1.3$, $M_B=3.0$). If the coolant mass flow and the blowing ratio are reduced to 50 percent of these values, a reduction in heat transfer occurs upstream. In contradiction to that, the heat transfer increases at the pressure side corner and in the wake region (Fig. 18). This means that, due to the reduced coolant mass flow, the passage vortex is influenced less and is therefore formed more strongly and leads to an increase in heat transfer. The results clearly show that the reduction of the heat transfer coefficient in the wake region is coupled with the interaction of the wake with the reduced secondary flow systems (passage vortex, trailing edge vortex).

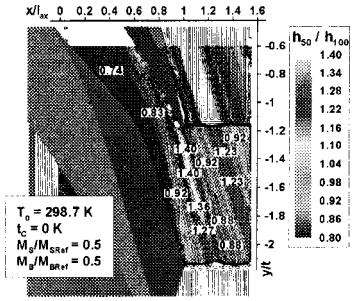

Fig. 18 Comparison of different blowing ratios M=50 percent and M_{ref}=100 percent

6 Adiabatic Film-Cooling Effectiveness: Results and Discussion

The adiabatic film-cooling effectiveness was also measured operating at the cooling configuration described in Table 1 ($M_S = 1.3$, $M_B = 3.0$). The downstream isentropic Mach number was held constant at $Ma_{2is} = 1.0$. To analyze the effect of slot and holes in detail they were operated singly and in common.

6.1 Results at the Front Part of the Passage. The front part of the passage extends from the slot to approximately the half axial length downstream (Figs. 19–21). If both, slot and holes were used, then directly downstream of the slot the film-cooling effectiveness amounts to $\eta_f \cong 90$ percent. If the flow field is considered on a virtual centerline through the passage, then downstream the effect of the bled air becomes continually smaller. This is caused by the mixture of the coolant with the main flow. The decrease in film-cooling effectiveness is particularly strong on the pressure side corner of the passage. Due to the passage vortex, the cooling air is diverted towards the suction side and therefore coolant at the pressure side is removed rapidly.

If results from dual operation (Fig. 19) are compared with the result from operation of the slot only (Fig. 20), it is obvious that the substantial effect of the film-cooling effectiveness in the front part is caused by the slot. If the slot is in operation alone, a film-cooling effectiveness close to $\eta_f = 100$ percent is achieved directly downstream of the slot. The results in Figs. 19 and 20 show very similar results both qualitatively and quantitatively. By the progression of the film-cooling effectiveness the effect of the horseshoe vortex can be detected very clearly in both figures. In the result with slot coolant ejection, as in the result with slot and holes, an effectiveness maximum in the center of the passage is noticeable and can be detected clearly by the iso-lines of film-cooling effectiveness. Due to the two branches of the horseshoe vortex, the film-cooling effectiveness is reduced next to the blade wall junction by the strong mixture with the main flow. Results were compared at the axial section $x/l_{ax} = 0.1-0.4$. In this area (downstream of the holes), single coolant ejection from the slot is $\Delta\eta_f \cong 7$ percent more efficient than with the additional operation of the holes. At first this effect seems contradictory, but can be explained by the jet trajectories of the coolant ejected from the holes. At the first row of holes, the trajectories in proximity to the pressure side are away from the endwall (compare L2F-measurements, part I). Additional coolant ejection from the holes leads to an increase of the turbulence level by a factor of up to six. As a result, the coolant from the holes contributes to a stronger mixing of the cooling air with the main flow, but within this area, it does not lead to an increase of the film-cooling effectiveness. If the coolant is only ejected from the holes, a film-cooling effectiveness of $\eta_f = 20$ percent is achieved slightly downstream (Fig. 21).

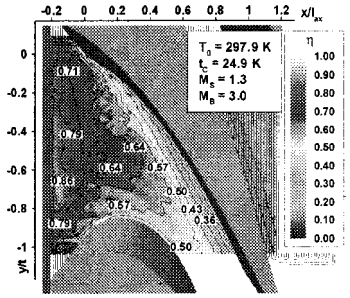

Fig. 19 Film-cooling effectiveness η_f: slot and all holes blowing simultaneously

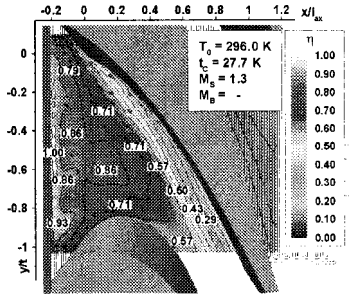

Fig. 20 Film-cooling effectiveness η_f: slot coolant ejection

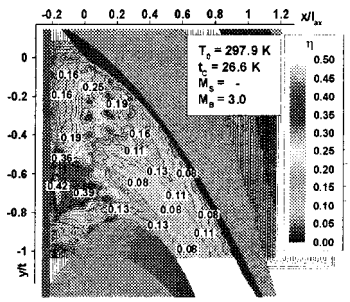

Fig. 21 Film-cooling effectiveness η_f: all holes blowing simultaneously

The main benefits of coolant ejection from the holes are on two sections downstream of them at $y/t = -0.3$ and $y/t = -0.7$. This results from the large number of holes at these positions. Between both sections a local minimum of the film-cooling effectiveness develops and indicates values around $\eta_f = 8$ percent. The coolant from one of these sections at the position $y/t = -0.7$, is pushed to the suction side corner and does not contribute to the film-cooling efficiency at the platform. The coolant, which is ejected in the section next to the pressure side ($y/t = -0.3$) also succumbs to the influence of the passage vortex and is deflected towards the suction side. Therefore in the pressure side corner a local minimum of $\eta_f = 5$ percent occurs. In spite of the influence of the passage vortex, the coolant from $y/t = -0.3$ remains in proximity to the pressure side. This is caused by the compound angle of the holes near the pressure side and especially by the high blowing ratio of the coolant ejected from them. Due to these blowing parameters the coolant trajectories possess a large inertia in relation to the influence of the secondary flow field. As a result, the coolant from this section contributes to film-cooling effectiveness further downstream of the passage.

Particularly conspicuous in Fig. 21 is the maximum of film-cooling effectiveness at the position $x/l_{ax} = -0.1$ and $y/t = -0.65$. This effect was observed during all series of measurements with single coolant ejection from the holes and is caused by the position of the slot, since the slot passes the saddle point on the endwall. During the investigations into the effect of the holes, no coolant was ejected from the slot. Thus air of the main flow enters the plenum chamber of the slot in the area of the saddle point (pressure maximum). Due to the position of the two plenum chambers, the ingested air of the main flow takes on the temperature of the adjacent plenum chamber, partly supplying the holes. Within the area of the pressure minimum of the slot ($y/t = -0.65$) the ingested air is discharged again: an apparent film-cooling effectiveness is obtained. If the slot between the combustion chamber and the first stage of the HPT passes the saddle point on the endwall, it might be possible that the hot gas from the main flow penetrates into the slot, this would entail a high thermal loading for the platform and the disk. This phenomenon could be caused by modifications from cooling design parameters, like changing operating conditions (e.g., starting) or by briefly occurring phenomena, e.g., the so-called ''hot-streaks,'' which are caused by the combustion chamber.

At the observed front part of the passage, the benefit of the slot prevails over the effect of the holes. This is due to the higher

coolant mass flow from the slot, which is quadruple to that of the holes, and accentuated by the different configurations of slot and holes and the associated blowing parameters. Thus the coolant from the slot is ejected with a moderate blowing ratio ($M_S = 1.3$) and the blowing ratio of the coolant ejected from the holes ($M_B = 3.0$) is obviously too high.

6.2 Results at the Rear Part of the Passage. In Figs. 22–24, the results of the adiabatic film-cooling effectiveness in the rear part of the passage ($x/l_{ax} = 0.6-1.55$) are shown. Figure 22 shows the result of the film-cooling effectiveness for dual operation of the slot and the holes. Within this downstream area, substantially smaller values of film-cooling effectiveness are measured than in the front part of the passage. Due to the distance covered by the coolant, mixing of coolant with main flow takes place, so that the benefits of film-cooling decrease strongly. The endwall pressure distribution shows a clear effect of ejected coolant on the shock in the throat conversely the film-cooling effectiveness shows no effect of injected coolant on the shock (Nicklas [16]).

Downstream of the cascade ($x/l_{ax} > 1.0$) a decrease of the film-cooling effectiveness occurs within the wake region of $\Delta\eta_f \cong 10$ percent. This results primarily from only small amounts of coolant entering into the boundary layer of the blades. If the boundary layer of the blades increases, this indicates a velocity component, which is perpendicular to the blade surface. The penetration of coolant into the boundary layer is then prevented.

In the unblown wall case, the results of the L2F-measurements show that close to the endwall, the turbulence levels increase fivefold in comparison with the free stream and that due to the coolant ejection, the turbulence level in the wake is locally doubled. Beyond that, the coolant ejection causes a widening of the turbulence-rich wake region. In the cascade exit plane, the passage vortex causes a deflection of the suction and the pressure-side branches of the horseshoe vortex toward the suction-side corner next to the trailing edge. These and possibly different secondary flow systems (corner vortex) lead to an expansion and intensification of the highly turbulent region next to the endwall and thus cause a strong mixture of the endwall fluid with the main flow. Therefore, coolant is mixed into the wake and this effect leads to a decrease in film-cooling effectiveness downstream of the cascade.

If the results of common operation of slot and holes (Fig. 22) are compared with those of single coolant ejection from the slot (Fig. 23), the coolant ejection from the holes causes an increase in film-cooling effectiveness η_f downstream of the cascade, next to the pressure side ($x/l_{ax} = 1.1$; $y/t = -1.3$) and in the area next to the suction side ($x/l_{ax} = 1.2$ and $y/t = -1.9$) as far as $\Delta\eta_f = 8$ percent. At these positions this can also be detected if the results of coolant ejection solely from the holes are analyzed since the gains in the film-cooling effectiveness are the highest (Fig. 24). In particular, single coolant ejection from the holes leads to an increase of up to $\eta_f = 14$ percent downstream of the cascade. The beneficial effect of the holes is also displayed by the L2F-measurements of the coolant concentration during common operation (part I, Fig. 19).

These results show that the amount of coolant from the holes at the positions $x/l_{ax} = 1.1$ and $y/t = -1.3$ is approximately 25 percent of slot coolant and therefore corresponds to the slot/holes ejected coolant ratio (Table 1). However, after achieving values of $\eta_f = 20$ percent directly downstream of the drillings, the film-cooling effectiveness decreases to $\eta_f = 11$ percent at the position $x/l_{ax} = 0.7$. At first, it is surprising that in the rear part of the passage some regions, especially at $x/l_{ax} = 1.1$ and $y/t = -1.3$, exhibit similar values, despite the strong mixture of the coolant with the main flow. This effect results from the clustered holes at the circumferential position $y/t = -0.3$. The results of the L2F-concentration measurements at the axial position $x/l_{ax} = 0.35$ show that a large part of the coolant ejected from the holes is distant from the endwall (part I, Fig. 18). Due to the acceleration of the flow field, the coolant is diverted to the endwall again and therefore contributes to film-cooling effectiveness downstream of the passage.

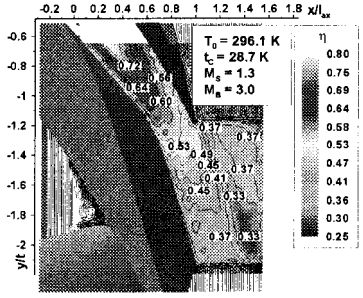

Fig. 22 Film-cooling effectiveness η_f: slot and all holes blowing simultaneously

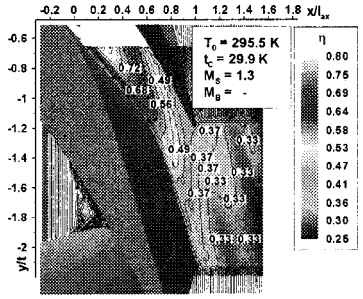

Fig. 23 Film-cooling effectiveness η_f: slot coolant ejection

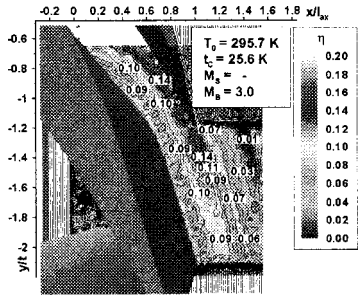

Fig. 24 Film-cooling effectiveness η_f: all holes blowing simultaneously

7 Conclusions

Measurements of heat transfer and adiabatic film-cooling effectiveness at the endwall of a turbine nozzle guide vane were carried out. These investigations are the first known where the complete extension at the endwall in transonic flow field is analyzed. In combination with the aerodynamic measurements (part I), the relevant points are:

- The higher intensity of the horseshoe vortex due to the coolant ejection from the slot causes a strong increase of the heat transfer coefficients at the endwall, in proximity of the leading edge.
- Due to the decrease of the passage vortex intensity near the endwall (caused by the coolant ejection) there is a decrease in heat transfer at the pressure side corner and downstream, next to the wake region.
- Heat transfer downstream of the cascade is mainly affected by the passage vortex.
- Coolant ejected from the holes causes a local sixfold increase of the turbulence level directly downstream and boosts the heat transfer coefficients in that area.

• Due to a rise in the downstream Mach number from transonic to supersonic speed range, there is a strong increase of the heat transfer coefficients in the wake-region downstream of the trailing edge.

The results of the adiabatic film-cooling effectiveness measurements provide further information for design improvement.

• In the front part of the passage high film-cooling effectiveness is obtained due to the coolant ejection from the slot. This results from the higher coolant mass flow from the slot and from the more optimal blowing parameters compared with those of the holes.
• Due to the passage vortex, the film-cooling effectiveness strongly decreases towards the pressure side corner, this effect strengthens downstream of the passage.
• Directly downstream of the exit plane, the wake region at the endwall is a region where cooling is extremely difficult without trailing edge cooling.

On the basis of these results, the following improvements in cooling-design at the platform are suggested:

- To prevent a reinforcement of the horseshoe vortex, the slot should be shifted upstream to avoid passing the saddle points.
- Film-cooling effectiveness can be increased by the holes at the rear part of the passage.

The implemented IR-camera system has proved itself an extremely flexible measuring technique, obtaining high accuracy. The results of the heat transfer measurements show that the heat transfer represents an indispensable tool for the evaluation of platform film-cooling design.

These investigations have provided further insight into the methods of controlling the heat transfer in a film-cooled turbine. A methodology for accurate analysis of heat transfer and film-cooling effectiveness in a complex transonic flow field has been presented. Design improvements for a film-cooling system have resulted from this investigations.

Acknowledgments

The main parts of this research were carried out during the course of the project ''Film Cooled Turbine Endwalls'' (grant number 032 7040 H), a part of the national AG Turbo program, funded by the Federal Ministry of Education and Research (BMBF). The author would also like to thank Andreas Uhl for his technical support.

Nomenclature

a = thermal diffusivity
c_p = specific heat
l = chord
M = $(\rho u)_C/(\rho u)_{\mathrm{loc}}$
Ma = Mach number
c_m = coolant mass flow ratio
h = heat transfer coefficient
$\dot{m}$ = mass flow blowing ratio
p = pressure
q = specific heat flux
T, t = temperature, blade pitch
u = streamwise velocity
η = film-cooling effectiveness
ε_M = eddy viscosity
σ = Stefan–Boltzmann constant
Θ = nondimensional temperature
Re = Reynolds number (depending on context)
v = transverse velocity
ε_H = eddy diffusivity
ε = emissivity
ρ = density
L2F = Laser-2-Focus

Subscripts

aw = adiabatic wall
C = coolant
g = straight-line-value (context)
is = isentropic
loc = local (but at the wall)
rad = radiation
λ = conduction
0 = total condition, unblown wall
ax = axial
f = film-cooled
if = isoenergetic
iw = isoenergetic wall
r = recovery
w = wall
∞ = free stream
1, 2 = stator inlet, stator exit

References

[1] Blair, M. F., 1974, ''An Experimental Study of Heat Transfer and Film Cooling on Large-Scale Turbine Endwalls,'' ASME J. Heat Transfer, **96**, pp. 524–529.
[2] Gaugler, R. E., and Russell, L. M., 1984, ''Comparison of Visualized Turbine Endwall Secondary Flows and Measured Heat Transfer Patterns,'' ASME J. Eng. Gas Turbines Power, **106**, pp. 168–172.
[3] Takeishi, K., Matsuura, M., Aoki, S., and Sato, T., 1990, ''An Experimental Study of Heat Transfer and Film Cooling on Low Aspect Ratio Turbine,'' ASME J. Turbomach., **112**, pp. 488–496.
[4] Wedlake, E. T., Brooks, A. J., and Harasgama, S. P., 1988, ''Aerodynamic and Heat Transfer Measurements on a Transonic Nozzle Guide Vane,'' *ASME Paper No. 88-GT-10*.
[5] Boyle, R. J., and Russell, L. M., 1990, ''Experimental Determination of Stator Endwall Heat Transfer,'' ASME J. Turbomach., **112**, pp. 547–558.
[6] York, R. E., Hylton, L. D., and Mihelc, M. S., 1984, ''An Experimental Investigation of Endwall Heat Transfer and Aerodynamics in a Linear Vane Cascade,'' ASME J. Eng. Gas Turbines Power, **106**, pp. 159–167.
[7] Graziani, R. A., Blair, M. F., Taylor, J. R., and Mayle, R. E., 1980, ''An Experimental Study of Endwall and Airfoil Surface Heat Transfer in a Large-Scale Turbine Blade Cascade,'' ASME J. Eng. Gas Turbines Power, **102**, pp. 257–267.
[8] Harvey, N. W., Wang, Z., and Jones, T. V., 1990, ''Detailed Heat Transfer Measurements in Nozzle Guide Vane Passages in Linear and Annular Cascades in the Presence of Secondary Flows,'' AGARD CP-469, pp. 24/1–24/13.
[9] Goldstein, R. J., and Spores, R. A., 1988, ''Turbulent Transport on the Endwall in the Region Between Adjacent Turbine Blades,'' ASME J. Heat Transfer, **110**, pp. 862–869.
[10] Friedrichs, S., Hodson, H. P., and Dawes, W. N., 1996, ''Distribution of Film-Cooling Effectiveness on a Turbine Endwall Measured Using the Ammonia and Diazo Technique,'' ASME J. Turbomach., **118**, pp. 613–621.
[11] Burd, S. W., Satterness, C. J., and Simon, T. W., 2000, ''Effects of Slot Bleed Injection over a Contoured End Wall on Nozzle Guide Vane Cooling Performance: Part II—Thermal Measurements,'' ASME Paper No. 2000-GT-200.
[12] Granser, D., and Schulenberg, T., 1990, ''Prediction and Measurement of Film Cooling Effectiveness for a First-Stage Turbine Vane Shroud,'' ASME Paper No. 90-GT-95.
[13] Jabbari, M. Y., Marston, K. C., and Eckert, E. R. G., 1996, ''Film Cooling of the Gas Turbine Endwall by Discrete-Hole Injection,'' ASME J. Turbomach., **118**, pp. 278–284.
[14] Teekaram, A. J. H., Forth, C. J. P., and Jones, T. V., 1991, ''Film Cooling in the Presence of Mainstream Pressure Gradients,'' ASME J. Turbomach., **113**, pp. 484–492.
[15] Eckert, E. R. G., 1992, ''Similarity Analysis of Model Experiments for Film Cooling in Gas Turbines,'' Waerme- Stoffuebertrag., **27**, pp. 217–223.
[16] Nicklas, M., 2000, ''Filmgekühlte Turbinenplattform in transsonischem Strömungsfeld,'' PhD thesis, Rheinisch-Westfälische Technische Hochschule Aachen; additionally published as DLR-FB 2000-10, Cologne.
[17] Sachs, L., 1972, *Statistische Auswerteverfahren*, 3rd ed., Springer-Verlag.
[18] Colantuoni, S., Colella, A., Di Nola, L. Carbone, D., and Marotta, D., 1993, ''Aero-Thermal Design of a Cooled Transonic NGV and Comparison With Experimental Results,'' AGARD Paper CP-527/33.
[19] Rehder, H.-J., 1990, ''Vergleich der gemessenen aerodynamischen Kenndaten von drei Gasturbinen-Hochdruck-Leitradgittern mit den Profilen MTU-T6.1/.2/.3,'' DLR Internal Report IB 222-92 C 35 Göttingen.
[20] Metzger, D. E., Carper, H. J., and Swank, L. R., 1968, ''Heat Transfer With Film Cooling Near Nontangential Injection Slots,'' ASME J. Eng. Gas Turbines Power, **90**, pp. 157–163.

Turbine Nozzle Endwall Film Cooling Study Using Pressure-Sensitive Paint

Luzeng J. Zhang
Aero/Thermal and Performance,
Solar Turbines, Inc.,
San Diego, CA 92101

Ruchira Sharma Jaiswal
Development Test,
Solar Turbines, Inc.,
San Diego, CA 92101

Endwall surface film cooling effectiveness was measured on a turbine vane endwall surface using the pressure-sensitive paint (PSP) technique. A double staggered row of holes and a single row of discrete slots were used to supply film cooling in front of the nozzle cascade leading edges. Nitrogen gas was used to simulate film cooling flow as well as a tracer gas to indicate oxygen concentration such that film effectiveness by the mass transfer analogy could be obtained. Cooling mass flow was controlled to be 0.5 to 3.0 percent of the mainstream mass flow. The free-stream Reynolds number was about 283,000 and Mach number was about 0.11. The free-stream turbulence intensity was kept at 6.0 percent for all the tests, measured by a thermal anemometer. The PSP was calibrated at various temperatures and pressures to obtain better accuracy before being applied to the endwall surface. Film effectiveness distributions were measured on a flat endwall surface for five different mass flow rates. The film effectiveness increased nonlinearly with mass flow rate, indicating a strong interference between the cooling jets and the endwall secondary flows. At lower mass flow ratios, the secondary flow dominated the near wall flow field, resulting in a low film effectiveness. At higher mass flow ratios, the cooling jet momentum dominated the near wall flow field, resulting in a higher film effectiveness. The comparison between hole injection and slot injection was also made.
[DOI: 10.1115/1.1400113]

Introduction

Turbine nozzle endwall cooling is complicated by secondary flows, mainly the passage vortex and endwall cross flows. The pressure gradient from the endwall surface near the pressure side to the suction surface is the potential of the endwall crossflow, and it joins and enhances the pressure side leg of the horseshoe vortices, developing into the so-called passage vortex. Traditional endwall cooling design usually employs an impingement cooling combined with local film cooling, often discharged downstream from the throat. Although the endwall can be effectively cooled, there are considerable aerodynamic penalties associated with the discharging of the spent film downstream from the throat. To eliminate those penalties and to improve turbine efficiency, film injection in front of the nozzle leading edge on the endwall is considered lately by a number of gas turbine companies.

The tendency that the cooling film can be blown away and dissipated by the secondary flows is reasonably understood by turbine cooling designers. To study the film jet behavior, thermal and aerodynamic effects of the endwall film cooling have been studied extensively. Among them, Takeishi et al. [1], Granser and Schulenberg [2], Harasgama and Burton [3,4], and Friedrichs et al. [5,6], studied endwall film cooling at various locations experimentally and numerically. Their results indicated the negative effect of the endwall secondary flow on endwall film cooling, particularly in the front half of the endwall surface, where the crossflow was the strongest and where the passage vortex started to form. Coping with this damaging effect, film cooling configuration was improved or optimized to obtain better film coverage. Experimental works by Friedrichs et al. [7] and Jabbari et al. [8] have indicated that the film effectiveness distribution can be improved to some degree, but the effect of secondary flow still exists. Recently, experimental and numerical works have been conducted to actively control secondary flow by considerably large mass flow ratio and large momentum film injection on the endwall in front of the nozzle leading edge. Theses works include Georgiou et al. [9], Burd and Simon [10], Liu et al. [11], Lapworth et al. [12], Burd et al. [13], and Oke et al. [14]. The results have indicated that high-momentum cooling jets can reduce the secondary flow to provide a better thermal protection and at the same time improve the aerodynamic performance of the nozzle passage. Although these results are encouraging, there are insufficient data available in the open literature for surface adiabatic effectiveness distribution for film injection in front of the nozzle leading edge.

In this paper, film effectiveness for a double-row cylindrical hole injection and for a single-row discrete slot injection was studied on a flat turbine nozzle endwall, while the other endwall was contoured. The cooling fluid was introduced from slots or holes located 0.2 axial chord length upstream from the cascade leading edge with an injection angle of 45 deg. Film effectiveness was measured using the heat transfer and mass transfer analogy. Nitrogen gas was used as the film cooling fluid and as a tracer gas. The pressure sensitive paint (PSP) was used to indicate the oxygen concentration of the mixture downstream from the injection to obtain film effectiveness (Zhang and Fox [15]; Zhang et al. [16]; Zhang and Pudupatty [17,18]). The tests were performed in a high-speed four-passage linear turbine nozzle cascade. Engine operating conditions such as free-stream Reynolds number, Mach number, and turbulence intensity were closely simulated. Measurements for film effectiveness distributions were presented, viewing from upstream and downstream of the cascade. A direct viewing was not possible due to the rig configuration. The effects of the mass flow rate ratio were discussed and a comparison between slot and hole injections was presented. The main objectives of this study are summarized below:

1 To measure the film cooling effectiveness on turbine nozzle endwall for a two-row staggered hole injection and a single row of discrete slot injection at simulated engine operating conditions.

2 To study the effect of mass flow ratio (MFR) on film effectiveness distribution.

Contributed by the International Gas Turbine Institute and presented at the 46th International Gas Turbine and Aeroengine Congress and Exhibition, New Orleans, Louisiana, June 4–7, 2001. Manuscript received by the International Gas Turbine Institute February 2001. Paper No. 2001-GT-147. Review Chair: R. Natole.

3 To study the relation of endwall inlet injection and the nozzle secondary flow.

Test Facility and Instrumentation

The tests were performed in the high-speed wind tunnel facility as shown in Fig. 1. The high-speed warm cascade test facility was discussed in more detail by Zhang et al. [16] and Zhang and Pudupatty [17,18]. The mainstream air is filtered and pressurized by a four-stage centrifugal compressor, which is mounted on the roof. The air was compressed and filtered by a four-stage compressor mounted on the roof. After flowing through the diverting valve, the flow passes through a control valve, a venturi meter, a flow straightener, a converging nozzle, and a rectangular duct before it enters the linear cascade test section. A turbulence grid was installed between the converging nozzle and the rectangular duct, which resulted in a turbulence intensity of about 6.0 percent at the nozzle cascade inlet, measured by a hot-film anemometer. The cascade test section is made of stainless steel, with transparent windows located on the sidewall and on the bottom upstream and downstream of the cascade to view the endwall surface. The airfoils in the cascade resemble those of a newly developed industrial gas turbine first-stage turbine nozzle. The linear cascade consists of three airfoils and two curved endwalls, a total of four flow passages. The top endwall is flat and the bottom endwall is contoured, resembling the actual engine geometry. The current study was performed on the top endwall. The cooling fluid was supplied to a flange upstream of the endwall and was ejected from holes or slots on the side surface of the flange. Downstream of the cascade, the flow passes through a diffuser and a control valve, and discharges through an exhaust. The mainstream mass flow rate can be as high as 4 kg/s and pressure can be as high as 0.16 MPa. With the downstream diffuser, an exit Mach number of two in the cascade can be attained. The temperature of mainstream air is about 350 K, heated by compression. The free-stream flow conditions are listed in Table 1. The test rig was validated by extensive flow measurements that included inlet/exit flow conditions, airfoil surface pressure/Mach number measurements, periodicity, and turbulence intensity and length scale measurements.

There are two flanges instrumented with film cooling holes or slots. Figure 2 shows a top view of the double row hole film cooling configuration. The film holes are divided into five sub-

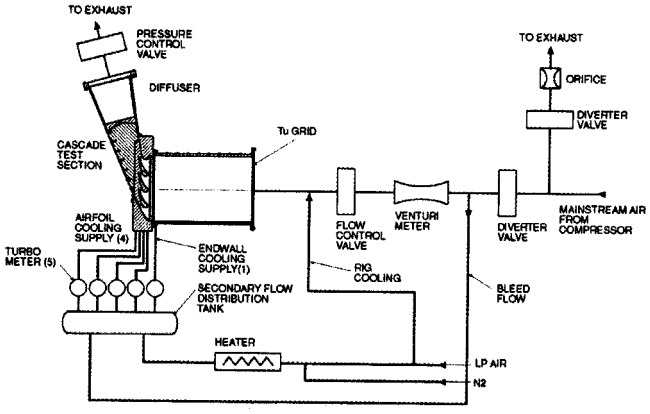

Fig. 1 Schematic of scaled cascade test rig

Table 1 Free-stream flow conditions

Condition	V_1, m/sec.	$Mach_1$	$Mach_2$	Re_1	Re_2
Reference	38.6	0.11	0.72	283,000	1,280,000

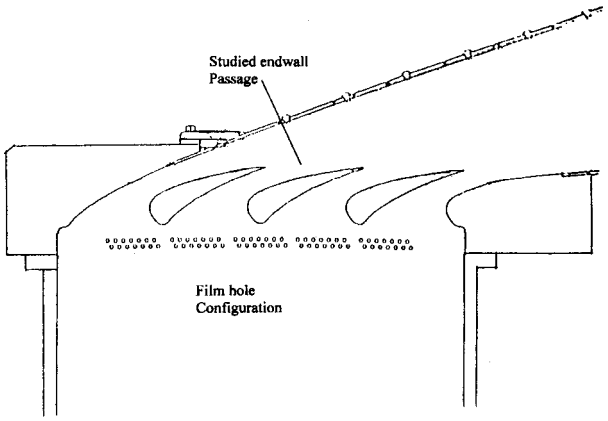

Fig. 2 Double row of hole injection geometry

Table 2 Film cooling geometry

Configuration	D or S, mm	L/D	P/D	VR*
Hole	3.05	2.946	2.083	1.025
Slot	2.54	3.546	-	0.843

* for MFR = 2.0 %.

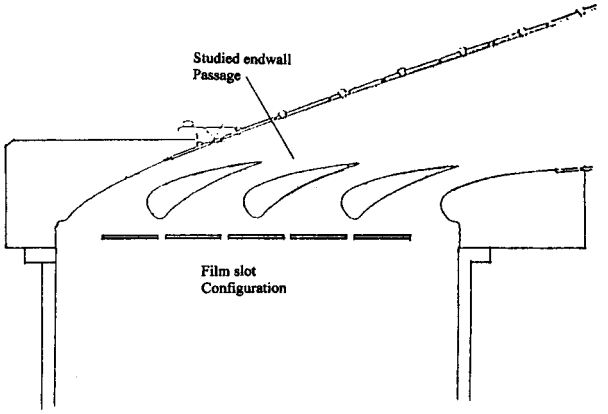

Fig. 3 Slot injection geometry

groups of film holes, limited by the rig configuration. Each group contains staggered double rows of 16 holes with a diameter of 3.05 mm. The distance between the center of the first row and the vane leading edge is 28.5 mm, representative of a design where the film cooling holes are located right in front of the nozzle piece. The spanwise and streamwise distances between the holes are the same, resulting in a P/D of 2.083. Table 2 shows the geometry and velocity ratios for both hole and slot configurations. Figure 3 shows the geometry of the slot configuration. The distance between the centerline of the slot and the vane leading edge is 28.5 mm, the same as the first row in the hole configuration. The slot is 2.54 mm wide and 55.8 mm long. The length to diameter (width) ratio of the hole is 2.946 and of the slot is 3.546. The injection angle for both configurations is 45 deg. Because the bottom of the test section is made of solid stainless steel, the camera was located either upstream or downstream of the endwall passage. As a result, the images are distorted due to the viewing angle and positions. Figures 4 and 5 show the typical views looking from the upstream and downstream location with square grids to indicate the view distortion.

Nitrogen gas and compressed air were used for the film cooling fluid and were supplied by pipelines into the test cell. They were introduced into the distribution plenums through a pressure regulator, a heater, and a turbine flow meter. The plenums are con-

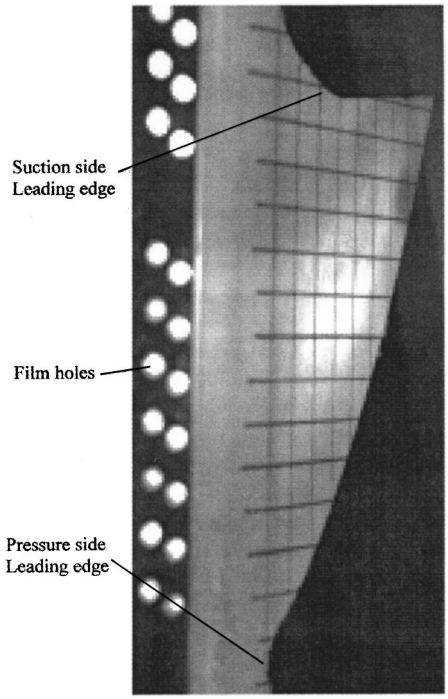

Fig. 4 Endwall flow passage, viewing from leading edge direction

trolled and monitored by an Allen Bradley PLC-5 programmable controller. Pressure taps and thermocouples were mounted in the plenums to measure and control the cooling air/nitrogen supply temperatures and pressures. To reduce the heat losses through the plumbing, rubber heater tape was used to maintain the temperature of the pipes and flow meters. The temperature difference between the mainflow and the secondary flow could be kept below 0.5 K.

Experimental Technique and Data Reduction of Pressure-Sensitive Paint (PSP)

PSP techniques are based on oxygen-quenched photoluminescence. Photoluminescence is a property of some compounds (active component of PSP) to emit light after being illuminated by a suitable light source. The emitted light intensity is related to the pressure of the test medium containing oxygen. In this study, the blue wavelength (450 nm) was used to excise the active molecules with the return signal in the yellow wavelength (600 nm). To detect and record the emitted light, which contains both pressure and concentration information, a filter and a CCD (Charge-Coupled Device) camera were used. In addition to measuring the static pressure distribution in the test plate, the oxygen sensitivity is used to indicate oxygen concentration in the gas mixture. Nitrogen gas was heated to the temperature of the free stream to eliminate any temperature effects. It was then ejected through the film cooling holes into the main flow. The mass concentration of the nitrogen/air mixture downstream from the point of injection was measured to obtain film effectiveness by using the mass transfer analogy.

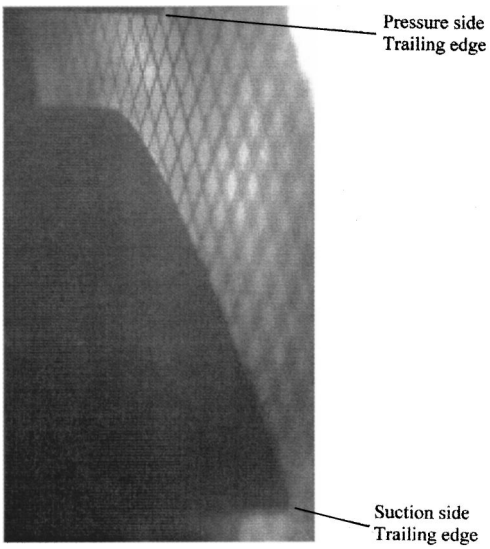

Fig. 5 Endwall flow passage, viewing from trailing edge direction

The mass fraction of the tracer gas in the mixture near the wall surface is related to the adiabatic wall temperature for the analogous heat transfer situation. In the current study, the mainstream contains approximately 79 percent nitrogen and the cooling flow contains approximately 100 percent nitrogen. The film effectiveness can be expressed by oxygen concentrations that can be measured by the PSP:

$$\eta = \frac{C_\infty - C_{\text{mix}}}{C_\infty}$$

where C_∞ is the oxygen concentration of the main stream (about 21 percent) and C_{mix} is the oxygen concentration of the air/nitrogen mixture (between 0 and 21 percent). Hence, the film effectiveness is between 0 percent (far downstream) and 100 percent (inside the hole).

The test setup of the PSP application to obtain film effectiveness includes the endwall surface, a CCD camera, and light sources. The endwall surface, flat and coated with PSP, was mounted at the top of the cascade. Transparent windows were located immediately upstream and downstream of the cascade. The CCD camera was mounted in front of these windows to view the endwall surfaces from upstream and downstream positions. Three halogen lamps, located around the camera, provided the light source for each of the camera positions. The images of luminescence intensity distribution from the endwall surfaces, recorded by the CCD camera, are originally gray scaled. These images are saved as TIF files and then calculated by a data reduction program, which compares the recorded intensity values with the calibration data to obtain surface pressure and film effectiveness distributions. For the PSP film cooling test, four images are required: a dark image (light off, airflow off); a reference image (airflow off, light on); an air injection image (airflow on, light on, hot air injection); and a nitrogen injection image (airflow on, light on, hot nitrogen injection). Hot refers to the temperature of the mainstream, about 350 K and cold means the reference temperature, controlled at 294 K. The air injection image contains information of surface static pressure only, while the nitrogen injection image contains both the surface static pressure and the oxygen concentration information. By ratios of intensities of these four images, the oxygen concentration on the airfoil surface downstream from the injection can be separated from the pressure distribution. The PSP is also sensitive to the surface temperature. The endwall surfaces were immersed long enough in the mainstream flow, so that the free-stream temperature could be assumed to be the same as the surface temperature. Ensuring that the temperature of the injected air/nitrogen was the same as that of the mainstream minimized possible temperature contamination. The difference between the free stream and the injection air or nitrogen was controlled below 0.5 K. In addition, the data reduction program uses different calibration curves for each of the mainstream (surface) temperatures (measured in each of the film cooling tests) when calculating the effectiveness.

Since the cascade rig operates at approximately 136 kPa and at 350 K at the cascade inlet, the PSP was calibrated between 344 and 356 K and pressures between vacuum and 150 kPa. Atmospheric pressure was used as a reference pressure for each of the calibrated temperatures. The results are presented as the reverse intensity ratio to the pressure ratio and were curve fitted and stored in the data reduction program, which can automatically select a correct curve at the corresponding calibration temperature if the test temperature varied from the reference temperature.

Flow Measurement

In order to meet the critical flow condition requirements and to guarantee a correct simulation of the engine operating parameters in the linear cascade, extensive flow measurements were performed prior to the current film cooling study. At the inlet of the cascade, mean velocity, turbulence intensity, and turbulence length scales were measured horizontally and vertically across the rectangular duct using the hot film anemometer and surface pressure taps. Flow uniformity and periodicity were achieved at the inlet. At the exit of the cascade, although a great effort was made, flow uniformity and periodicity were not attained due to the uneven diffusion effect of downstream side walls. Surface Mach number measurements were made for various freestream conditions on the airfoils of the linear cascade. Without a tailboard, a correct simulation of surface Mach number is achieved only in the mid-left flow passage, which is a combination of the suction surface of the middle airfoil and the pressure surface of the mid-left airfoil (viewing forward from the cascade inlet). The flow measurement results were published by Zhang et al. [16] and Zhang and Pudupatty [17].

Film Effectiveness Measurement Results

An uncertainty analysis was performed on the film effectiveness measurement using the PSP tests based on the method by Kline and McClintock [19]. The uncertainty of the pressure distribution, an intermediate result in this study, was 5.8 percent and that of film effectiveness at the nominal condition was 12.0 percent. The net film effectiveness variation ($\Delta\eta$) was 0.06 for the worst case.

Double-Staggered Row Injection. Film effectiveness measurements from the double staggered row of holes are presented in this section. Only the film effectiveness distribution for mid-left endwall flow passage was measured on the top (flat) endwall surface. Out of the five injection groups (Fig. 3), all the film jets from the second sub-group and approximately half from the third subgroup went through mid-left flow passage. As a result, the film cooling did not cover an area between the pressure side and the second injection sub-group and an area between the second subgroup and third sub-group. Although these gaps were not intentionally placed, they actually provided a means to indicate the interference of the cooling film with the endwall cross flow. Figure 6 shows the film effectiveness distributions for five mass flow ratios (MFR), viewing from upstream of the leading edge. Although the film effectiveness distributions are distorted, by qualitatively examining the results, they provided clear information on the interaction between the cooling jets and secondary flows. Therefore, no effort is made to reconstruct them to a flat view.

By examining the injection region on the leading edge views, at a lower mass flow ratio of 0.5 percent, the jets mixed quickly in the spanwise direction immediately downstream from the injection, an indication of the dominant endwall crossflow. The film effectiveness downstream from the film hole centerline is not noticeably higher than the remaining part of surface due to the endwall crossflow. The film jets are attached to the surface and no lift-off is suggested by the results. At higher mass flow ratios, the effectiveness downstream from the hole centerline appears to be higher than the remaining surface and the difference increases with the mass flow ratio. At higher mass flow ratios of 2.0 and 3.0

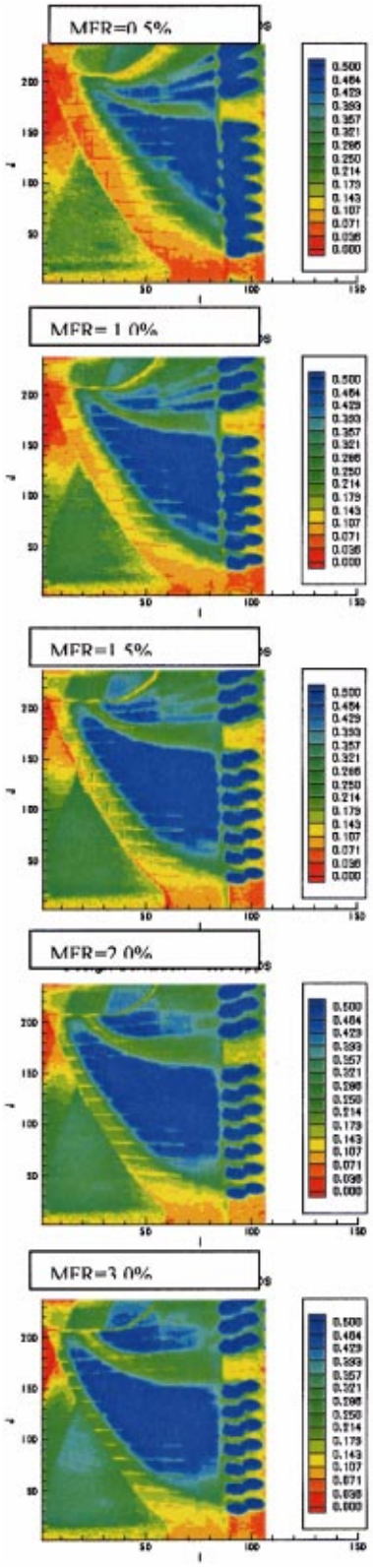

Fig. 6 Film effectiveness distribution on endwall surface, viewed from upstream hole injection

percent, a slightly lower effectiveness value immediately downstream from the injection suggests the occurrence of jet lift-off. Examining the area around the suction side leading edge, where the boundary layer usually rolls up to form horseshoe vortices, the current result shows a strong interaction between the cooling jets

and the boundary layer. The effectiveness distribution acts like a means of flow visualization to indicate the saddle point, separation and reattachment. At mass flow ratio of 0.5 percent, there is an area in front of the leading edge that is not covered by the cooling film, indicating a separation of the boundary layer, which swept away the film jets due to its small momentum ratio (less than 0.1). It is believed that this roll-over of the boundary layer divides into two by the airfoil leading edge to form the two legs of the horseshoe vortex. With the increase in the mass flow ratio (and therefore the momentum ratio), the uncovered region shrinks back to the airfoil leading edge. At mass flow ratios of 2.0 and 2.5 percent (momentum ratios one and above one), the film covers the entire area surrounding the leading edge, suggesting that the boundary layer separation is suppressed by the cooling jets. Downstream from the leading edge, the pitchwise migration of the cooling jets can be indicated by the gaps between the injection groups. At mass flow ratio of 0.5 percent, for the area downstream from the gap between the second and third injection sub-groups, the film effectiveness is close to the value downstream from the injections. With the increase in the mass flow ratio, film effectiveness in this area decreases significantly and the low effectiveness area becomes wider pitchwise. This can be explained by the fact that at a higher mass flow ratio, the film jets have a higher streamwise momentum and tend to carry themselves farther downstream, rather than being disturbed and dissipated quickly. On the other hand, high-momentum jets might suppress the endwall horseshoe vortex and reduces the crossflow effect. The effectiveness distribution on the area downstream from the gap between pressure side and the second injection sub-group is different, mainly due to the rigid pressure side wall (as compared to the soft stream line on the endwall surface). Downstream from the gap, the effectiveness is almost zero at mass ratio of 0.5 percent. There is no injection upstream of the pressure side airfoil leading edge; as a result, there is no film coming from pressure side direction. The pitchwise dissipation of the cooling film toward the pressure side direction is prohibited by the endwall crossflow, which is in the opposite direction. With the increase in the mass flow ratio and momentum ratio, the film jets are dissipated and shifted toward the pressure side and the width of the uncovered area becomes narrower. At a mass flow ratio of 2.5 percent, although there is no injection upstream of the near pressure side area, the high effectiveness area moved close to the pressure side. This tendency of carrying the film towards the pressure side trailing edge at a higher mass flow matches the findings by Burd et al. [13]. Generally speaking, the film coverage on the leading edge view improves with the mass flow ratio, both on the effectiveness value and the size of the area covered. It would be a reasonable assumption that the whole nozzle flow passage would have been better covered by the cooling film if there had been no gap in the injection region.

The relation between the film jets and the secondary flows discussed above are supported by the results of the trailing edge views, as shown in Fig. 7. At the mass flow ratio of 0.5 percent, the film effectiveness is below 0.1 away from the area near the suction side. The film covered area spreads from near the suction surface toward both the pressure side and downstream directions and the effectiveness value increases when the mass flow ratio increases. There is no trace of the reduction of the film effectiveness due to the gap between second and third sub-groups to be seen until mass flow ratio of 1.5 percent, where a thin line separates the effectiveness distribution into two. The line turns into an area as mass flow ratio reaches 2.0 and 2.5 percent. While the film is pushed to the suction side at lower mass ratios, the effectiveness is higher at the area near the pressure side trailing edge than the area near the suction side trailing edge for mass ratios 2.0 and 2.5 percent. Outside the trailing edges, the film effectiveness reaches 0.25 for MFR 2.0 percent and 0.3 for MFR 3.0 percent.

Single-Row Discrete Slot Injection. In this section, film effectiveness measurements from a single row of discrete slots are presented. Out of the five slots (Fig. 3), all the film from the second slot and approximately half from the third slot went through the mid-left endwall flow passage, leaving the area near the pressure side and an area between the second and third slots uncovered by the cooling film. For the same mass flow ratio, the

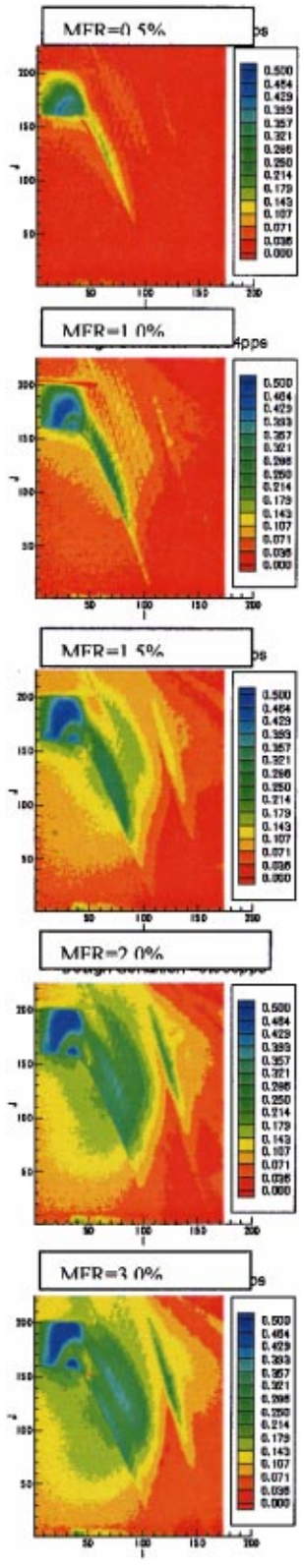

Fig. 7 Film effectiveness distribution on endwall surface, viewed from downstream hole injection

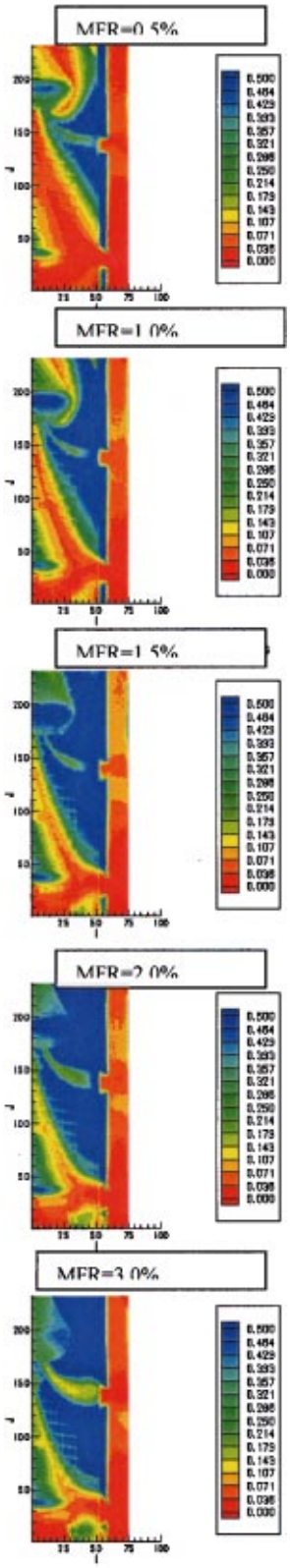

Fig. 8 Film effectiveness distribution on endwall surface, viewed from upstream slot injection

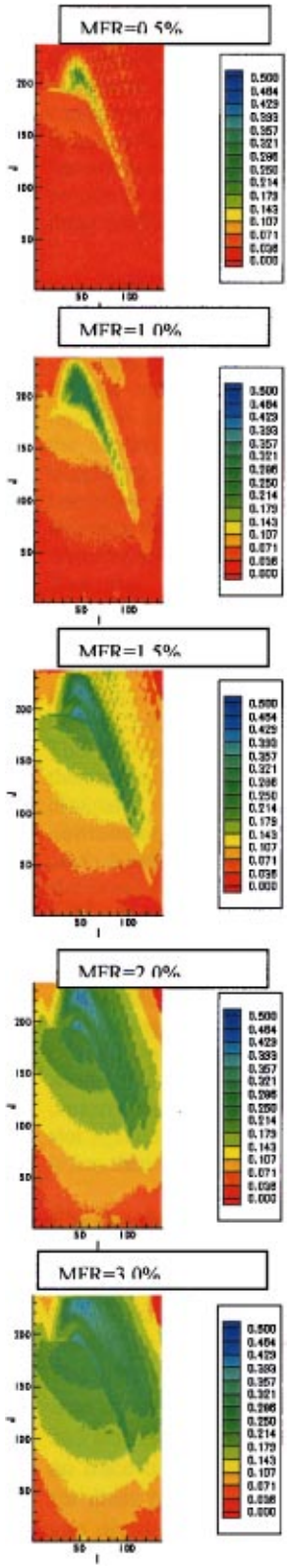

Fig. 9 Film effectiveness distribution on endwall surface, viewed from downstream slot injection

coolant-to-mainstream velocity ratio for the slot injection is smaller than that for the double-hole injection (for mass flow ratio of two, VR for slot injection is 0.843 and 1.025 for the hole injection). This may be one of the reasons that the slot injection results are different from those for double-row hole injection.

Figures 8 and 9 show the film effectiveness distributions for slot injection for five mass flow ratios studied, viewing from the upstream (leading edge) and from downstream (trailing edge) directions. Generally speaking, all the observations for the hole injection are true for slot injections. Examining the region just

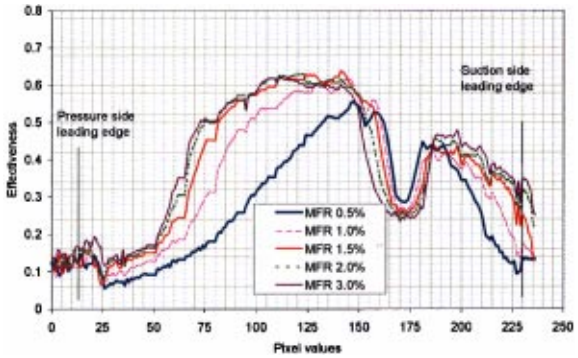

Fig. 10 Circumferential film effectiveness distribution, $X/C_{ax}=0$, leading edge hole injection

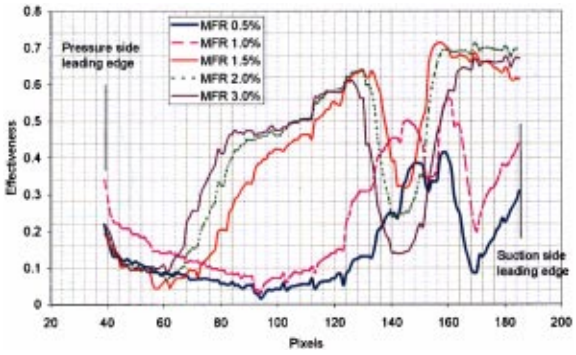

Fig. 11 Circumferential film effectiveness distribution, $X/C_{ax}=0$, leading edge slot injection

downstream from the injection, at a lower mass ratio of 0.5 percent there is an area not covered by the cooling film in front of the suction side airfoil leading edge, suggesting a separation of the boundary layer and the formation of the horseshoe vortices. The pattern of the effectiveness distribution indicates the locations of the separation and reattachment. The lower effectiveness region becomes smaller with the increase in the mass flow ratio. At mass flow ratios above 1.5 percent, the film covers the entire area around the leading edge. At mass ratios from 0.5 to 1.5 percent, the effectiveness at the area downstream from the gap between the second and third slots is close to the level of that downstream from the injection. It decreases significantly at the mass ratio of 2.0 percent. At mass ratio of 3.0 percent, the effectiveness between the injections is almost zero. This indicates that at a higher mass ratio, the film jets tend to carry themselves farther downstream rather than being disturbed, mixed and dissipated quickly. Unlike the film effectiveness for the area downstream from the gap between second and third slots, the area downstream from the gap between the pressure side and the second slot is not covered by the cooling film at mass flow ratios of 0.5 and 1.0 percent. The endwall crossflow prevents the cooling film from reaching the pressure side, pushing the film to the suction side direction, resulting in the low effectiveness downstream from the second slot close to the pressure side. At a higher mass flow ratio, the increase in the cooling flow momentum begins to dominate, compressing the endwall crossflow. The cooling film reaches the pressure side and the width of the lower effectiveness area becomes narrower. While a uniform distribution downstream from the injection is observed for slot injection at a higher mass flow ratio, the dominance of the film jet is less than that for double-row hole injection.

The results obtained from the trailing edge views (Fig. 9) support this discussion. For slot injection, the film effectiveness for the trailing edge view is generally lower compared to that for double-row hole injection. At a lower mass flow ratio, it is limited to the area near the suction side. The film effectiveness increases with the mass flow ratio. The area covered by cooling film spreads toward the pressure side and downstream directions at higher mass flow ratios. There is no trace of the gap between the second and third slot injection for mass ratio of 0.5 percent. At higher mass ratios, the trace of the gap divides the high effectiveness region into two. While the film is pushed to the suction side at lower mass ratios, the effectiveness is higher at the area near the pressure side trailing edge than the area near the suction side for mass ratios 1.5 percent and above. The effectiveness is more uniformly distributed compared to those for double-row hole injection near the trailing edge and beyond. Outside the trailing edges, the film effectiveness is slightly lower but is extended to a larger area for higher mass flow ratios.

Comparison Between Slot and Hole Injections. Figures 10 and 11 show circumferential film effectiveness distributions at the endwall leading edge location ($X/C_{ax}=0$) for hole and slot injections. Examining the effectiveness between the suction side leading edge and the gap between the second and third injection groups, both the trends and values are different for the hole and slot injections. For hole injection, the effectiveness near the leading edge increases for all the mass flow ratios until the area downstream from the gap between the second and third injection subgroups. The distribution moves higher with the mass flow ratio. For the area downstream from the gap, the effectiveness value decreases and the low effectiveness region becomes wider as the mass flow ratio increases. The lowest effectiveness in the gap for a mass flow ratio 3.0 percent is about 0.22. For slot injection, there is a low effectiveness valley away from the stagnation point (circumferential direction) for mass flow ratios 0.5 and 1.0 percent, suggesting the formation of the passage vortex. For mass flow ratios of 1.5 percent and above, the valley disappears and the effectiveness is above 0.6. It is reasonable to assume the formation of the passage vortex is prevented by the cooling film, resulting in a uniform film effectiveness distribution around the airfoil leading edge. Burd and Simon [10] and Burd et al. [13] proved this in their studies. The low effectiveness region downstream from the gap between the second and third slots becomes lower and moves toward the pressure side direction with the increase in the mass flow ratio. The lowest effectiveness value for mass flow ratio 3.0 percent is about 0.15. Examining the rest of the distribution, it can be observed that the effectiveness distribution downstream from the second group hole injection consistently moves toward the pressure side direction with the increase in mass flow ratio counteracting the endwall crossflow. For slot injection, the effectiveness downstream from the second slot for mass flow ratios 0.5 and 1.0 percent is low and is pushed to the suction side direction by the endwall cross flow. For higher mass flow ratios 1.5 to 3.0 percent the effectiveness is higher than 0.4 and moves toward the pressure side direction.

Figures 12 and 13 show circumferential film effectiveness distributions at the endwall trailing edge location ($X/C_{ax}=1.0$) for hole and slot injections. The film effectiveness increases significantly with the mass flow ratio and the distribution shifts to the pressure side direction for both configurations. At mass flow ratios 2.0 and 3.0 percent, the peak effectiveness for slot injection moves closer to the pressure side trailing edge compared to that for hole injection.

Figure 14 compares circumferential averaged film effectiveness distributions at both the endwall leading and trailing edge locations. For the leading edge results, the effectiveness for hole injection increases with the mass flow ratio until MFR 2.0 percent, where the curve becomes flat. The effectiveness for slot injection increases quickly from MFR 0.5 percent to about 1.7 percent, where it starts to decrease. The sharp increase in effectiveness suggests a strong interaction between the cooling jets and the endwall secondary flows as the cooling momentum increases. The effectiveness for slot configuration lies higher for mass flow ratio

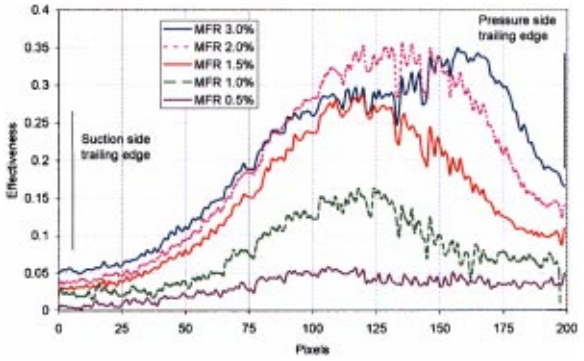

Fig. 12 Circumferential film effectiveness distribution, X/C_{ax} =1.0, trailing edge hole injection

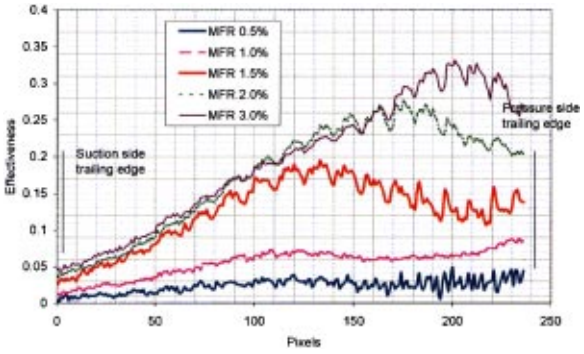

Fig. 13 Circumferential film effectiveness distribution, X/C_{ax} =1.0, trailing edge slot injection

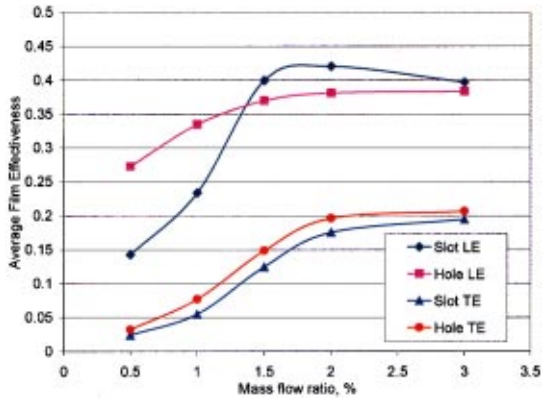

Fig. 14 Circumferential averaged film effectiveness, X/C_{ax}=0 and 1.0, slot and hole injections

above 1.5 percent. For trailing edge results, the distributions for both configurations are similar. The significant increase in film effectiveness supports the assumption of the secondary flow compression function of the higher momentum film jets. Comparing the effectiveness value, the effectiveness for hole injection lies slightly higher than that for slot injection.

Conclusions

Film effectiveness distributions were measured on the flat endwall surface in a warm cascade for both a double-row hole injection and a single-row discrete slot injection. The main conclusions are summarized below:

1 For both hole and slot injections, the endwall secondary flow dominates the near endwall flow field at a lower mass flow ratio where the cooling film is pushed to the suction side and decays quickly. At a higher mass flow ratio (above 2.0 percent), with a higher film jet momentum, the cooling film tends to dominate the near wall flow field and the secondary flow is suppressed. The film moves to the pressure side and acceptable film effectiveness can be obtained near the trailing edge.

2 Uniform effectiveness distribution can be achieved by discrete slot injection for higher mass flow ratios, while higher effectiveness near the trailing edge can be obtained by double staggered rows of hole injection.

3 Due to the geometry dependence, continued study is required to measure film effectiveness on shaped endwall or different injection configurations.

Acknowledgments

The authors of this paper wish to thank Solar Turbines Incorporated for permission to publish this paper.

Nomenclature

C = chord length, cm
CCD = Charge Coupled Device
D = film hole diameter, cm
I = light intensity
L = length of film hole, cm
LE = leading edge
MFR = mass flow ratio
Ma = Mach number
p = pressure, kPa
P = pitch value between film holes, cm
PSP = pressure sensitive paint
Re = Reynolds number=$\rho VC/12\text{-}\mu$
T = temperature, K
TE = trailing edge
Tu = turbulence intensity
V = velocity, m/s
VR = velocity ratio
X = streamwise distance, cm
Y = spanwise distance, cm
η = film effectiveness
μ = dynamic viscosity, Ns/M^2
ρ = density, kg/m^3

Subscripts

1 = cascade inlet
2 = cascade exit
ax = axial
c = coolant condition
o = reference condition
∞ = free stream condition
mix = mixture condition

References

[1] Takeishi, K., Matsuura, M., Aoki, T., and Sato, T., 1990, ''An Experimental Study of Heat Transfer and Film Cooling on Low Aspect Ratio Turbine Nozzles,'' ASME J. Turbomach., **112**, pp. 488–496.
[2] Granser, D., and Schulenberg, T., 1990, ''Prediction and Measurement of Film Cooling Effectiveness for a First-Stage Turbine Vane Shroud,'' ASME Paper No. 90-GT-95.
[3] Harasgama, S. P., and Burton, C. D., 1991, ''Film Cooling Research on the Endwall of a Turbine Nozzle Guide Vane in a Short Duration Cascade Part 1: Experimental Technique and Results,'' ASME Paper No. 91-GT-252.
[4] Harasgama, S. P., and Burton, C. D., 1991, ''Film Cooling Research on the Endwall of a Turbine Nozzle Guide Vane in a Short Duration Cascade Part 2: Analysis and Correlation of Results,'' ASME Paper No. 91-GT-253.
[5] Friedrichs, S., Hodson, H. P., and Dawes, W. N., 1996, ''Distribution of Film Cooling Effectiveness on a Turbine Endwall Measured Using the Ammonia and Diazo Technique,'' ASME J. Turbomach., **118**, pp. 613–621.
[6] Friedrichs, S., Hodson, H. P., and Dawes, W. N., 1997, ''Aerodynamic Aspect of Endwall Film cooling,'' ASME J. Turbomach., **119**, pp. 786–793.
[7] Friedrichs, S., Hodson, H. P., and Dawes, W. N., 1999, ''The Design of an Improved Endwall Film Cooling Configuration,'' ASME J. Turbomach., **121**, pp. 772–780.

[8] Jabbari, M. Y., Marston, K. C., Eckert, E. R. G., and Goldstein, R. J., 1996, ''Film Cooling of the Gas Turbine Endwall by Discrete-Hole Injection,'' ASME J. Turbomach., **118**, No. 2.
[9] Georgiou, D. P., Papavasilopoulos, V. A., and Alevisos, M., 1996, ''Experimental Contribution on the Significance and the Control by Transverse Injection of the Horseshoe Vortex,'' ASME Paper No. 96-GT-255.
[10] Burd, S. W., and Simon, T. W., 2000, ''Effects of Slot Bleed Injection over a Contoured Endwall on Nozzle Guide Vane Cooling Performance: Part I—Flow Field Measurements,'' ASME Paper No. 2000-GT-199.
[11] Liu, S., Liu, G., Xu, D., Lapworth, B. L., and Forest, A. E., 1999, ''Aerodynamic Investigation of Endwall Film-Cooling in an Axial Turbine Cascade Part I: Experimental Investigation,'' AIAA ISABE (Symposium on Air Breathing Engines), Paper No. 99-7080.
[12] Lapworth, B. L., Forest, A. E., and Liu, S., 1999, ''Aerodynamic Investigation of Endwall Film-Cooling in an Axial Turbine Cascade. Part II: Numerical Investigation,'' AIAA ISABE (Symposium on Air Breathing Engines), Paper No. 99-7193.
[13] Burd, S. W., Satterness, C. J., and Simon, T. W., 2000, ''Effects of Slot Bleed Injection over a Contoured Endwall on Nozzle Guide Vane Cooling Performance: Part II—Thermal Measurements,'' ASME Paper No. 2000-GT-200.
[14] Oke, R. A., Burd, S. W., Simon, T. W., and Vahlberg, R., 2000, ''Measurements in a Turbine Cascade Over a Contoured Endwall: Discrete Hole Injection of Bleed Flow,'' ASME Paper No. 2000-GT-214.
[15] Zhang, L. J., and Fox, M., 1999, ''Flat Plate Film Cooling Measurement Using PSP and Gas Chromatography Techniques,'' *Proc. Fifth ASME/JSME Joint Thermal Engineering Conference*, San Diego, CA.
[16] Zhang, L. J., Baltz, M., Pudupatty, R., and Fox, M., 1999, ''Turbine Nozzle Film Cooling Study Using the Pressure Sensitive Paint (PSP) Technique,'' ASME Paper No. 99-GT-196.
[17] Zhang, L. J., and Pudupatty, R., 1999, ''Turbine Nozzle Leading Edge Film Cooling Study in a High Speed Wind Tunnel,'' *Proc. 33rd National Heat Transfer Conference*, Albuquerque, NM.
[18] Zhang, L. J., and Pudupatty, R., 2000, ''The Effect of Injection Angle and Hole Exit Shape on Turbine Nozzle Pressure Side Film Cooling,'' ASME Paper No. 2000-GT-247.
[19] Kline, S. J., and McClintock, F. A., 1953, ''Describing Uncertainties in Single Sample Experiments,'' Mech. Eng. (Am. Soc. Mech. Eng.), **75**, Jan., pp. 3–8.

The Many Faces of Turbine Surface Roughness

Jeffrey P. Bons
Air Force Institute of Technology,
Wright-Patterson AFB, OH 45433

Robert P. Taylor
Mississippi State University,
Mississippi State, MS 39762

Stephen T. McClain
Mississippi State University,
Mississippi State, MS 39762

Richard B. Rivir
Air Force Research Laboratory,
Wright-Patterson AFB, OH 45433

Results are presented for contact stylus measurements of surface roughness on in-service turbine blades and vanes. Nearly 100 turbine components were assembled from four land-based turbine manufacturers. Both coated and uncoated, cooled and uncooled components were measured, with part sizes varying from 2 to 20 cm. Spanwise and chordwise two-dimensional roughness profiles were taken on both pressure and suction surfaces. Statistical computations were performed on each trace to determine centerline averaged roughness, rms roughness, and peak to-valley height. In addition, skewness and kurtosis were calculated; as well as the autocorrelation length and dominant harmonics in each trace. Extensive three-dimensional surface maps made of deposits, pitting, erosion, and coating spallation expose unique features for each roughness type. Significant spatial variations are evidenced and transitions from rough to smooth surface conditions are shown to be remarkably abrupt in some cases. Film cooling sites are shown to be particularly prone to surface degradation. [DOI: 10.1115/1.1400115]

Keywords: Roughness, Spallation, Turbine

Introduction and Background

Modern land-based turbine airfoils operate in severe environments with high temperatures and near critical stresses. Highly turbulent combustor exit flows, with significant thermal gradients, spew hot combustion products and other airborne particulates at the turbine surfaces for in excess of 20,000 hours before regularly scheduled maintenance. Due to this harsh operating environment, turbine surfaces experience significant degradation with service. Measurements reported by Acharya et al. [1], Taylor [2], and Tarada and Suzuki [3], among others, indicate an order of magnitude or greater increase in rms roughness is typical.

These elevated levels of surface roughness have a significant effect on the skin friction and heat transfer of turbine engine blades. Experimental studies with modeled rough blades have been conducted since the early 1980's in an attempt to quantify this effect. Bammert and Sandstede [4] initially showed that increases in sandgrain roughness in a low-speed turbine cascade caused earlier boundary layer transition and higher c_f. Turner et al. [5] corroborated this finding using a single-blade cascade and also showed that roughness increased the blade mean heat transfer by over 60 percent. Both research teams employed various sizes of sand grains to simulate roughness on the turbine blades. Comparable increases in heat transfer have subsequently been reported on simulated rough turbine blades by Blair [6], Hoffs et al. [7], Bogard et al. [8], and Abuaf et al. [9]. At a system level, Boynton et al. [10] demonstrated a 2.5 percent increase in the SSME high pressure fuel turbopump efficiency with an order of magnitude decrease in centerline-averaged roughness (*Ra*). Of course, none of these findings were particularly surprising given the long history of rough-walled wind tunnel and pipe flow experiments reported in the literature beginning with Nikuradse's work in 1933 [11].

With such a significant and experimentally well-documented influence on gas turbine performance, surface roughness has naturally been the focus of considerable attention. The point of departure for much of the analytical work in this area has been the equivalent sandgrain roughness (k_s) concept pioneered by Schlichting [12], with liberal use of the Reynolds analogy for heat transfer augmentation. Cebeci and Chang [13] were the first to incorporate this parameter into a two-dimensional turbulent boundary layer code to predict boundary layer development over a rough wall. Since that time, Boyle [14] and Guo et al. [15] have each employed a roughness adjustment based on k_s to the Van Driest damping function in turbine flow simulations.

An alternate discrete element model for roughness, alluded to by Schlichting [12] and first demonstrated in a two-dimensional boundary layer code by Finson and Wu [16], has also been investigated, with mixed results. This model predicts the increased losses of a rough surface by accounting for the pressure drag losses (or heat transfer) of isolated elements (cones or hemispheres), which in turn represent the actual surface roughness. Although it can be well-tuned to match data from regular roughness arrays (Taylor et al. [17] and Scaggs et al. [18]), attempts to use this model to represent real turbine roughness in boundary layer $k-e$ models (Tarada and Suzuki [3] and Tolpadi and Crawford [19]) have not been as promising.

Much of the frustration in modeling rough surfaces stems from the fact that sand grains and regular arrays of discrete elements bear little resemblance to real rough surfaces. As shown in measurements by Taylor [2] and Bogard et al. [8], turbine surface roughness is not uniform over the blade surface. Thus, using a single roughness representation for the entire blade is inappropriate. In addition, different degradation mechanisms (erosion, corrosion, and foreign deposits) have different roughness signatures, each with unique features. Finally, the situation is even more complicated with the rising use of thermal barrier coatings (TBCs), which are subject to surface debond or spallation. TBC spallation occurs nonuniformly around blade surfaces and results in yet another unique surface characterization. There has been very little reported in the open literature about these ''real'' turbine surfaces, although it is reasonable to assume that they each affect the heat transfer and aerodynamics in different ways. Without better documentation of the attributes of real turbine roughness, the increased accuracy of design tools such as computational fluid dynamics (CFD) will have limited relevance after the engine has seen significant service.

The objective of this paper is to provide relevant data on actual turbine roughness for use in experimental and computational modeling. To this end, a wide variety of representative land-based turbine hardware were assembled for detailed surface measurements. All of the degradation mechanisms cited above were evaluated and documented in order to provide the community with an accurate depiction of real surfaces. In the process, detailed three-

Contributed by the International Gas Turbine Institute and presented at the 46th International Gas Turbine and Aeroengine Congress and Exhibition, New Orleans, Louisiana, June 4–7, 2001. Manuscript received by the International Gas Turbine Institute February 2001. Paper No. 2001-GT-163. Review Chair: R. Natole.

dimensional maps of nearly 50 different surfaces have been generated and are available for general use in modeling. This work also serves as the point of departure for further turbine roughness characterization as part of a multi-year effort by the authors.

Measurement Techniques

Nearly 100 turbine components were provided by four manufacturers: General Electric, Solar Turbines, Siemens-Westinghouse, and Honeywell. The articles were selected by each manufacturer to be representative of surface conditions generally found in the land-based gas turbine inventory. Of the total inventory, over one third of the items were vanes or vane sets, while the remainder were turbine blades. Approximately one quarter had some film cooling and 15 percent were coated with a thermal barrier coating (TBC). Component dimensions ranged from large 20 cm chord blades used in MW power units down to 2 cm chord blades from smaller auxiliary power units. In order to respect proprietary concerns of the manufacturers, strict source anonymity has been maintained for all data presented in this publication.

Two-dimensional surface measurements were taken of each part using a Taylor-Hobson Form Talysurf Series 2 contact stylus measurement system. This device uses a diamond-tipped conical stylus (1.5 μm radius tip) to follow the surface features for a given part. The instrument has a maximum stroke of 50 mm and can measure a total vertical range of 2 mm with a precision of 32 nm.

The use of a contact measurement system presents several inherent sources of data uncertainty. First, surface features with a slope greater than the 60 deg conical stylus tip are mechanically smoothed. For example, a 70 deg sawtooth wave with a peak-to-peak amplitude of 20 μm is measured as a 60 deg sawtooth with an amplitude of only 12.6 μm. If the surface feature is an isolated 70 deg peak, the amplitude is accurately measured, but the peak's base diameter is exaggerated by a factor of 1.6. Although these errors are considerable, fortunately confocal microscope surface images taken as part of this study indicated that turbine component surfaces are not characterized by sawtooth-type, high-angled formations. Rather, they are a random combination of canyons, peaks, and plateaus interspersed over a rugged landscape (Fig. 1). Electron micrographs presented in Bogard et al. [8] and Abuaf et al. [9] corroborate this finding.

For turbine blading, this mechanical smoothing limitation is exacerbated by the natural curvature of the surface. As the contact stylus follows this curvature, it is not always normal to the contact surface over the entire extent of a measurement. Thus, if a measurement is made of a sawtooth pattern inscribed around the circumference of a cylinder wall, peaks at either end of the trace would be skewed rather than symmetric. The severity of this effect is alleviated somewhat by mechanical constraints of the stylus itself. The maximum range of the stylus vertical motion is 2 mm, compared to the maximum horizontal stroke of 50 mm, a 25:1 ratio. Hence, for a typical measurement the ratio of curvature related elevation change to horizontal stroke length was 15:1 or greater. The result is only a small-angle error to the roughness signature after mean-line form removal (see below).

The use of an optical surface measurement system would, of course, avoid the first of these two contact system limitations. Accordingly, a laser-based system (CyberOptics Cyberscan Cobra DRS-500) was employed for measurement comparison. Measurements of the same surfaces using the two devices produced images that were qualitatively similar and had comparable statistics (within 15 percent). Thus, the uncertainties introduced by the use of the contact stylus system were considered to be within acceptable limits. Of course the optical measurement spot was finite (16–23 μm diameter) and features smaller than the spot size were naturally smoothed or averaged.

One final limitation of the contact system relates to the measurement of surfaces with loose deposits. Upon inspection, many of the turbine components provided for the study were coated with a layer of grit or dirt that could be removed with normal handling. Despite the contact stylus' miniscule contact force of less than 1 mN, it noticeably dislodged some of these surface contaminants, thus altering the surface from its operational condition. The optical measurement system obviously did not suffer from this limitation. Due to its three-dimensional capability and the ease of data retrieval, the contact instrument was used for all the data presented in this report.

A typical two-dimensional surface trace is shown in Fig. 2 (the vertical axis has been magnified to reveal the micron-level roughness over the 15 mm long trace). As mentioned earlier, the stylus picks up both the surface roughness and the form of the part. For flow that is not separated, the flow streamlines near the surface generally follow the local surface curvature. Since the long-term goal of this study is to assess the effect of roughness on flow-related parameters such as St and c_f, only surface features that depart from the natural form (and thus the local flow streamlines) were considered to be of interest. Thus, the relevant data were extracted from the raw data trace by performing a mean-line fit to the natural curvature of the part. This was done using a spline-fit to the raw data (also indicated in Fig. 2). The roughness data after removal of the mean line spline fit are shown above the raw data. With the form removed, the relevant statistics could be extracted from the roughness data. Evaluations were conducted to compute the centerline averaged roughness, *Ra*, the rms roughness, *Rq*, the maximum peak-to-valley roughness, *Rt*, the skewness, *Sk*, and the kurtosis, *Ku*, as defined below:

$$Ra = \frac{1}{N}\sum_{i=1}^{N} |y_i|, \tag{1}$$

$$Rq = \sqrt{\frac{1}{N}\sum_{i=1}^{N} y_i^2}, \tag{2}$$

$$Rt = y_{\max} - y_{\min} \tag{3}$$

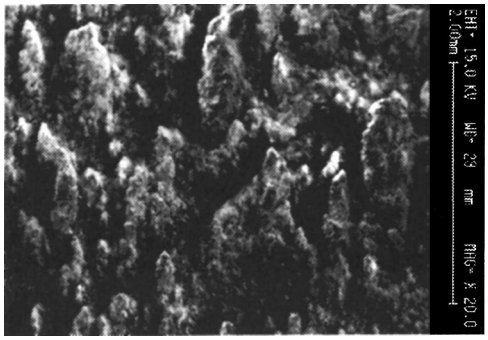

Fig. 1 Confocal microscopic image of PS/TE fuel deposits

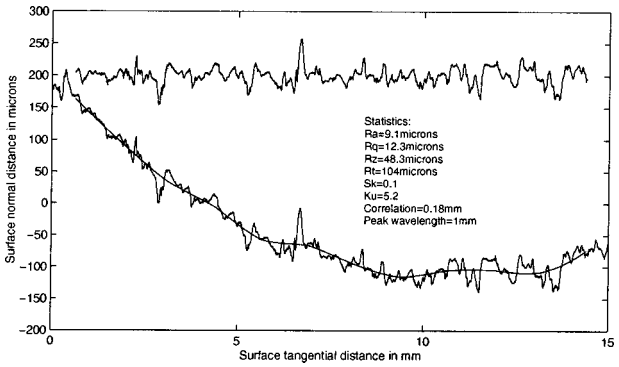

Fig. 2 PS/MC/Hub chordwise trace: raw data, meanline, and data with meanline removed

$$Sk = \left\{ \frac{1}{N} \sum_{i=1}^{N} y_i^3 \right\} \frac{1}{Rq^3}, \tag{4}$$

$$Ku = \left\{ \frac{1}{N} \sum_{i=1}^{N} y_i^4 \right\} \frac{1}{Rq^4} \tag{5}$$

Each trace was also evaluated in 1 mm subsets (or cutoffs) to determine localized values for *Ra*, *Rq*, and *Rt*. This allowed the assessment of spanwise and chordwise gradients in roughness character. It also permitted the estimation of *Rz*, the average of the local *Rt* values over the entire trace. *Rz* is commonly used as an estimate of the average roughness height, *k*, which in turn can be related to k_s, the equivalent sandgrain roughness. As mentioned, k_s is used in most empirical estimations of increased c_f and St due to surface roughness.

In addition, each two-dimensional trace was evaluated in the frequency domain. A Fourier decomposition provided the dominant wavelengths (λ) and the correlation length, λ_c, was calculated as the distance at which the autocorrelation function falls to a value of 0.1.

Two-dimensional traces were taken in both the spanwise and chordwise directions (where possible) at various locations around each article. For the smaller hardware, single traces could often be made across the entire span of the part showing the surface roughness variation with span. With the largest blades, complete spanwise coverage was prohibitive and instead spot measurements were taken in regions of particular interest. From 3 to 15 individual two-dimensional measurements were made of each part.

After the two-dimensional traces had been evaluated, specific regions of interest were measured using the three-dimensional mapping capability of the Taylor-Hobson unit. The three-dimensional map is made by indexing the part by specified increments in the direction perpendicular to the stroke of the contact stylus. Increments from 5 to 40 μm were used to map out regions from 1×1 mm square to 40×40 mm square for various components. Once a three-dimensional map was taken, the Talymap™ software was used to remove the part's form with a polynomial least-squares surface fit. The resultant roughness could then be analyzed in the same manner as the two-dimensional traces. Two additional parameters were calculated for the three-dimensional data: the rms deviation of surface slope angles, α_{rms}, and the roughness shape/density parameter, Λ_s. The former was shown by Acharya et al. [1] to be an important roughness parameter, while the latter was developed by Sigal and Danberg [20] in an attempt to correlate the k_s estimation process to both the spacing and shape of roughness elements. The parameter was derived for use with two and three-dimensional roughness elements mounted to a smooth surface. It is defined as

$$\Lambda_s = \frac{S}{S_f} \left(\frac{A_f}{A_s} \right)^{-1.6} \tag{6}$$

where S is the reference area of the sample surface (without roughness), S_f is the total frontal surface area of the roughness elements on the sample, A_s is the windward wetted surface area of a roughness element, and A_f is the frontal surface area of a roughness element. Since the surfaces being evaluated in this study are real roughness surfaces rather than ordered cones or hemispheres, the calculation of A_f, S_f, and A_s had to be adapted accordingly. To do so, each cell of the surface height matrix was evaluated independently to determine its windward frontal area and windward wetted area. These were then summed to obtain A_f and A_s for the entire surface. Since there are no discrete elements, $A_f = S_f$ following this procedure. Performing the calculation cell by cell in this manner removed any subjectivity that might have been introduced by selecting only conically shaped peaks above some critical height in the surface height matrix. Values of Λ_s can be correlated directly to k_s/k using data assembled by Sigal and Danberg and repeated in Bogard et al. [8]. Since the three-dimensional maps were extremely time consuming, not every part was mapped in this manner. Overall, nearly 50 three-dimensional maps were made of various surface features.

Experimental Results and Discussion

A summary of the two-dimensional statistical measurements is presented first as a function of spatial location and service history. A table of representative three-dimensional measurement statistics is included at the end of this discussion. Following this, documentation is provided of various forms of surface deposits, pitting, and erosion. Measurements of surface coatings and spallation are treated separately. Finally, the effects of film cooling on surface condition are presented.

Spatial Variations. As mentioned above, the hardware inventory included over 30 unique configurations, split about equally between vanes and blades. With such a wide variety of parts from four manufacturers, the authors considered that it would be useful to present the aggregate roughness data before enumerating specific findings about roughness characteristics. These summary data from all two-dimensional traces are presented in Figs. 3 and 4. From the numerous statistical characterizations available, those of *Ra* and *Rt* seemed to be of the most general utility: *Ra* since it is by far the most commonly used industry standard and *Rt* because it gives a measure of the maximum amplitude of observed surface variations to which the turbine flowfield may be exposed. As noted above, *Ra* can be related to k_s if desired by employing an empirical correlation for k/Ra and k_s/k or k_s/Ra directly. For the two-dimensional data acquired in this study, $Rz(\approx k)$ values ranged from 4 to 8 times *Ra*. This compares with a value of $k/Ra \approx 5$ for both Taylor's [2] and Bogard et al.'s [8] turbine roughness data. The figures present the *Ra* and *Rt* data for each of nine regions on both the suction and pressure surface of all the airfoils studied. The data is divided into regions in order to underscore the dramatic spatial variations discovered in this study.

To assemble these data, roughness measurements were taken on each article as described in the previous section. For the smaller blades, a single spanwise or chordwise trace may include two or three of the regions indicated. In such cases, the data trace was divided into regions prior to statistical evaluation. So as not to skew the statistical averages toward multiple measurements on any one blade, if multiple measurements were made in the same region of the same blade, the *Ra* and *Rt* were first averaged before adding the data from that region to the aggregate pool. Also, for those cases where identical parts with the same service history were evaluated, the measurements from all parts were averaged to obtain a single set of regional statistics for that configuration before adding the data to the aggregate pool. As such, the data in Figs. 3 and 4 represent the average statistics from the 30+ unique configurations used in the study. The regions are labeled using the

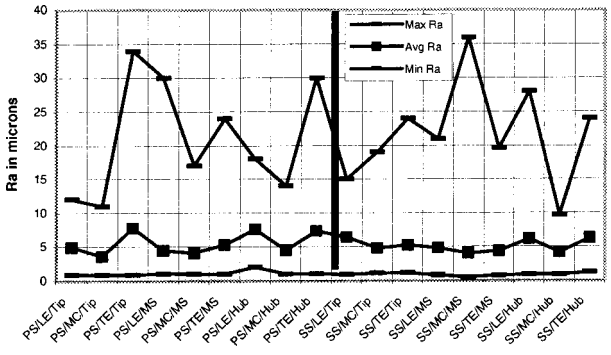

Fig. 3 Regional values of Ra (min, avg, and max) from aggregate data

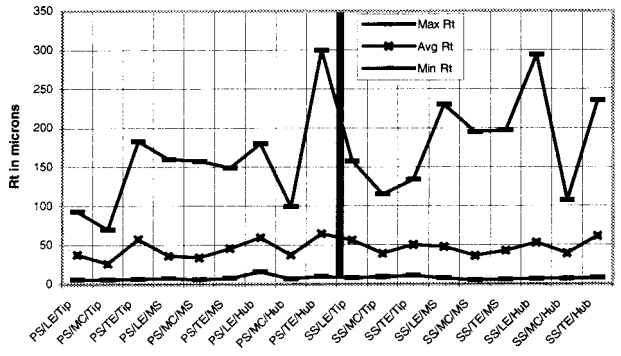

Fig. 4 Regional values of Rt (min, avg, and max) from aggregate data

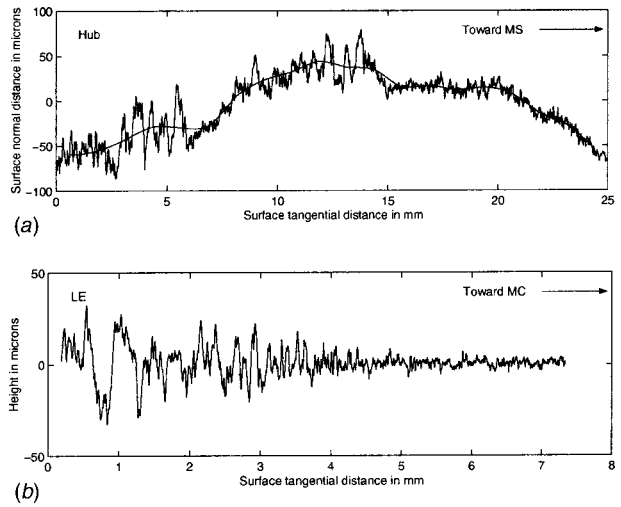

Fig. 5 (*a, b*) Traces showing variations in roughness from region to region on PS and SS

abbreviated nomenclature listed at the end of this report. Represented in each figure are the minimum, average, and maximum values found in the region indicated.

The first (and perhaps most obvious) conclusion that can be drawn from the data is that no single region of modern turbine blading can be considered off-limits to roughness (limited measurements on hub and tip endwalls are consistent with this conclusion). In addition to this general conclusion, several spatial trends can be extracted from the data in this aggregate format. Although the mean of all the regional *Ra* values is similar for the *PS* and *SS* (mean average $Ra=5.5$ μm for *PS* and 5.1 μm for *SS*, mean maximum $Ra=21.1$ μm for *PS* and 21.8 μm for *SS*), the pressure surface has larger spatial variations in average *Ra* and *Rt*. On the pressure surface there is a dip in both parameters at midchord, with the trailing edge generally higher than the leading edge. At the hub and tip, this variation can be greater than a factor of 2 from midchord to *TE* aggregate values (on an individual blade, variations of greater than a factor of 10 were not uncommon). Regions with consistently high roughness include the *TE*/Tip and the *LE* and *TE* Hub. All three regions show heightened levels of corrosive deposits and erosion as well as spallation for the coated articles. The spanwise trace in Fig. 5(*a*) illustrates an abrupt drop in deposit and erosion-induced roughness levels along the *PS*/*LE* from Hub to *MS*.

On the suction surface, again the midchord region is at reduced roughness levels on average. However, over much of this surface, roughness appears to decrease monotonically from the leading edge. It was not uncommon to find a test article with substantial *SS*/*LE* deposits or erosion followed by a nearly pristine ($Ra<1$ μm) surface from mid-chord on (Fig. 5(*b*)). Noteworthy also on the suction surface is that the *LE* is, on average, rougher than the trailing edge, opposite from the pressure surface trend.

Taken in the aggregate, the two-dimensional statistical data in Figs. 3 and 4 mask the magnitude of spatial variations found on individual articles. Indeed, the aggregate plots lend credibility to the common CFD practice of using a single average *Ra* or k_s value for both *PS* and *SS* without regard to regional variations. This is an erroneous conclusion, however, as will be shown. Taking, for instance, the side mean maximum *Ra* statistic quoted earlier (mean maximum $Ra=21.1$ μm for *PS* and 21.8 μm for *SS*), if these same data are computed for coated and noncoated hardware separately, an interesting observation is made. For noncoated parts, the mean maximum *Ra* on the *PS* was 19.7 μm while that on the *SS* was 12.5 μm. For coated parts, the mean maximum *Ra* was 13.1 μm on the *PS* versus 19.4 μm on the *SS*. This view of the data clearly illustrates an important qualitative finding of this study: Corrosive deposits and erosion (the dominant sources of roughness on noncoated articles) are more prevalent on the *PS* Hub and Tip regions, while spallation (the dominant roughness source for coated articles) is more pronounced on the *SS* near the leading edge.

Observed spatial variations increase even more dramatically when each article is assessed on an individual basis. For example, taking each article's surface data individually rather than in the aggregate, *Ra* measurements over the 18 regions identified earlier were found to have maximum region to minimum region *Ra* ratios from 2:1 to 68:1 (with an average of 8:1). This means that for a typical part, if the minimum *Ra* region was 1 μm, on average there would be a maximum *Ra* region of 8 μm somewhere else on the part. Considering the well-documented influence of roughness on surface heat transfer, spatial roughness variations of this magnitude would make it extremely difficult for a CFD code that only uses a constant *Ra* value to match Stanton number data from real experimental hardware. Comparable spatial roughness variations have been reported by Taylor [2] and Bogard et al. [8]. Taylor reported *Ra* values from the leading edge suction surface of 30 first-stage *F*-100 turbine blades that exceeded 4 to 5 times the *Ra* values measured elsewhere on the blades. Interestingly, Taylor reported a rise in roughness at midchord on the pressure surface compared to the aggregate finding in this study of lower *Ra* there. On the suction surface, Taylor reported decreasing *Ra* with chord to the trailing edge, similar to this study. It is worth noting that Taylor's measurements were all made at mid-span, thus excluding regions (Hub and Tip) found to be of considerable interest in this review. Bogard et al. reported spatial variations from pressure surface measurements on two first-stage aero-engine vanes. Here, roughness levels were found to be approximately constant with chord with a 2 to 3-fold increase at the trailing edge.

The actual transitions from rough to smooth regions of the turbine surfaces were as varied as the surfaces themselves. Transitions usually occurred gradually as in traces 5(*b*) and 6(a). Often though, abrupt transitions in surface character were recorded, as in traces 5(*a*) and 6(*b*). These transitions are even more pronounced over coated surfaces with spallation (trace 6(*c*)). These data bring to mind the recent work of Pinson and Wang [21] with coarse and fine grit sandpaper in a transitional boundary layer. They found that abrupt rough-to-smooth surface transitions actually induced earlier boundary layer transition (laminar to turbulent) compared to rough to moderately rough surface transitions at the same Re_x. Their explanation of this phenomenon was that vortices shed from the large coarse grit were rapidly amplified into destabilizing instabilities over a succeeding smooth surface; whereas, if the following surface was even moderately rough, these shed vortices were broken up by the succeeding smaller grit, thus reducing their effectiveness as a catalyst for boundary layer transition. Taylor and Chakroun [22] also reported curious variations in St and cf following finite strips of roughness in a turbulent boundary layer. Their experimental work showed that the local value of St (and

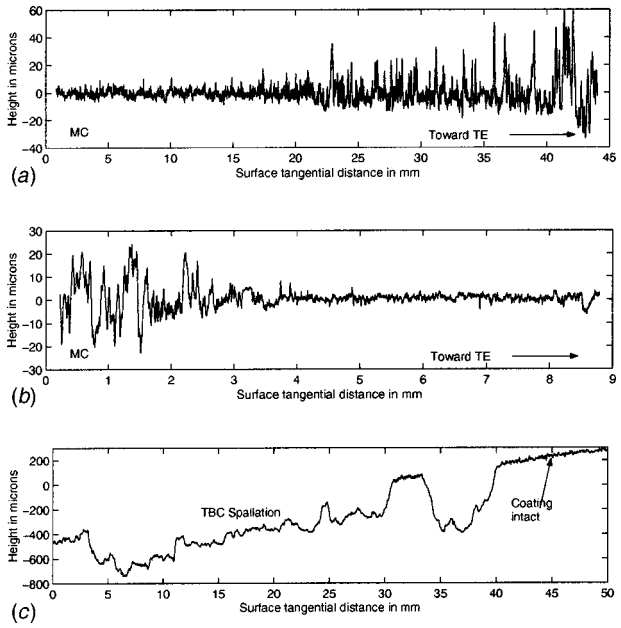

Fig. 6 Various transitions from region to region: (*a*) gradual, (*b*) abrupt, and (*c*) spallation related

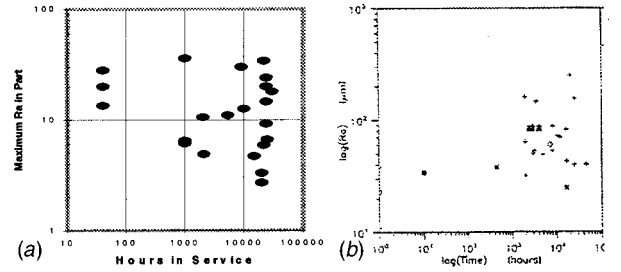

Fig. 7 (*a*) Maximum Ra versus service hours for present study; (*b*) similar data reproduced from Tarada and Suzuki [3], Fig. 2

c_f) temporarily undershot the turbulent smooth-wall value (for the same Re_x) immediately following an abrupt rough to smooth surface transition. Considering these experimental findings, it could be that roughness transitions are as important to model as the roughness itself. Accurate computational models of rough surfaces may require not only the discrete regional roughness data but also the transition information from region to region, or better still, a complete three-dimensional surface roughness map.

One final observation from the aggregate data set is the magnitude of the maximum roughness (Rt) for these turbine specimens. Though the mean average Rt, for all regions is approximately 46 μm, roughness as large as 300 μm was measured for some turbine components. For the smaller airfoils in the study ($C_x \approx 2$ cm) with boundary layer thicknesses of 1 to 2 mm, these levels of roughness exceed 10 percent of δ and would certainly be considered ''completely rough'' (or roughness-dominated) following the generally accepted classification of Nikuradse [11]. For the larger blades ($C_x \sim 20$ cm) the roughness is correspondingly less important, and surfaces could be transitionally rough or even aerodynamically smooth in some regions. These roughness magnitudes (Ra and Rt) are comparable to those reported by Taylor [2] ($1.5 < Ra < 11$) for aero-engine blades, but considerably less than values reported by Bogard et al. [8] ($8 < Ra < 46\ \mu$m) and Tarada and Suzuki [3] ($25 < Ra < 220\ \mu$m). The latter study was conducted at ABB using over 50 blades from aero, industrial, and marine applications. This disparity in magnitude may be partially explained by the different analysis techniques employed. While all four studies used a contact stylus for measurement, Bogard et al. and Tarada and Suzuki did not perform an independent mean-line fit to remove surface curvature as was done by Taylor and in the present study. As mentioned in the previous section, this form removal was deemed necessary to extract the roughness as ''seen'' by the flow streamlines. Retaining this surface curvature in the statistical procedure can result in considerable differences in Ra and Rt depending on the ''cut-off'' or filtering parameter employed by the measurement device. Also, coating spallation sites identified in this study were typically bordered with steep vertical transitions of 100 to 400 μm. Rather than allow these steep transitions to skew the two-dimensional statistical analysis, data from the un-spalled coating adjacent to the site and data from the spallation floor were processed separately. This filtering was performed only when the length of the spalled region exceeded the height of the spall edge by a factor of 2 to 3. By not including the steep drop or rise at the spallation edge in the statistical analysis, lower roughness statistics are obtained. The spall edge transitions were not removed for the three-dimensional statistical analyses.

Service History. An expected determinant of surface condition is service history. Figure 7(*a*) shows the maximum Ra data versus operating hours (since last service overhaul) for the parts surveyed. (Unfortunately, service history information was only available on less than one quarter of the articles measured.) Here, the Ra plotted is the maximum value found on the part regardless of region. Although the data appear to indicate a lack of correlation between surface roughness and service hours, this conclusion is premature. In order to obtain a true correlation between operating hours and surface roughness, measurements must be taken at successive operating intervals for the same hardware in a constant operating environment. Since the data in Fig. 7(*a*) are from numerous unique configurations taken at a single point in their operational life, they cannot provide the desired roughness-to-use correlation. The same can be said for Tarada and Suzuki's [3] data reproduced in Fig. 7(*b*). Although their report states that ''this figure shows a clear trend of increased roughness level with number of service hours,'' their data (taken using the same ''single point in time'' method) appear to be equally uncorrelated with operating hours.

In the same report, Tarada and Suzuki go on to site operating environment as the key contributor to surface condition; civilian aero-engine blades operated over North America had a mean Ra of 85 μm while military aero-engine blades exhibited salt or sand deposits and had nearly double the Ra with an order of magnitude less service hours.

In an effort to highlight similar process-related roughness correlations for the present data, a representative sample of the individual three-dimensional surface statistical data are presented in Table 1. The surfaces in the table are grouped by roughness-generating process and have been numbered so that they can be referenced in the following discussion of specific roughness-generating processes.

Specific Roughness-Generating Processes. Foreign deposits:

The two sources for deposition-related roughness are the combustion ingredients, fuel, and air (including airborne contaminants). Fuel deposits are more prevalent in land-based turbines than in aero-engines due to the wide range of relatively impure fuels used by operators. Figures 8(*a*) and (*b*) show three-dimensional maps of two distinct forms of fuel deposits (surfaces #1 and #3 from two different blades). The first is a highly anisotropic deposit with an elliptic, streamwise-oriented characteristic shape. This deposit is layered in thicknesses from 50 to 200 μm, especially in the TE region of the pressure surface (no fuel deposits were detected on the suction surface of this blade). In contrast

Table 1 Representative three-dimensional surface statistical data grouped by roughness-generating process

Surf #	Region	Process	Size(mm)	Ra (μm)	Rq (μm)	Rt (μm)	Sk	Ku	λ_c (μm)	α_{rms} (deg)	Λ_s
1	PS/MS/TE	Fuel deposits	4x4	33.2	39.4	226	0.22	2.23	380	19.9	42
2	PS/Hub/MC	Fuel deposits	2x2	4.2	5.2	38.4	0.52	3.04	39.6	21.3	42
3	SS/MS/MC	Fuel deposits	2x2	7	8.8	55	-0.08	2.91	340	14.2	175
4	PS/MS/MC	Deposits	4x4	2.6	3.4	48	0.17	4.5	169	8.2	834
5	SS/MS/LE	Deposits	2x2	2.7	4.9	90	1.43	24.2	131	11.4	276
6	SS/Tip/TE	Deposits	4x4	7	8.9	80	0.33	3.3	60	24	30
7	PS/MS/LE	Deposits	6x6	7.1	10.5	127	2.18	11	140	20.4	53
8	SS/MS/LE	Deposits	4x4	14.1	19	168	0.5	4.4	314	21.2	45
9	SS/MS/MC	Deposits	10x10	3.7	4.8	49	0.72	4.15	408	12.1	240
10	SS/MS/LE	LE erosion and deposits	2x4	6.5	8.2	76	-0.11	2.96	242	15	114
11	SS/Hub/LE	LE erosion and deposits	5x5	4.4	5.5	47	-0.3	3.08	114	12.5	212
12	PS/Hub/TE	Erosion and deposits	1x1	9	11.2	73.2	0.03	2.98	69	25.3	22
13	PS/Tip/TE	Erosion and deposits	10x10	16.6	21	220	0.37	4.65	3000	14.4	134
14	PS/Tip/TE	Deposits and erosion	9x9	15.1	19.7	201	0.03	4	208	21.4	40
15	Endwall	Hot corrosion and erosion	6x6	28	36	258	.19	3.2	530	13.8	219
16	SS/MS/TE	Pitting and erosion	4x4	7.5	10.7	130	-1.4	9.7	650	14.5	164
17	PS/MS/TE	Pitting	4x4	4.2	7.1	79.5	-3.1	17.5	209	7.4	1130
18	PS/MS/MC	Erosion	2x2	1.9	2.4	23	-0.11	3.1	372	10.6	345
19	SS/Tip/LE	Tip Erosion	3x3	4.4	5.9	57	0.02	4.4	307	11.9	235
20	PS/MS/TE	Rough TBC, no visible spall	30x30	11.7	14.7	250	-0.11	3.41	418	12.8	217
21	SS/MS/LE	Mild Spallation	15x7.5	4.1	7	156	-4.1	36	495	10.1	505
22	SS/Hub/LE	Large spallation	15x15	19.3	26.3	394	-1.08	6	954	17.7	77
23	SS/Hub/LE	Large spall near FC row	21x21	41.3	52.5	446	-0.25	3.5	2236	13.4	200
24	SS/Tip/LE	Islands of residual TBC	15x15	17.5	25.9	333	-0.33	8.4	1020	15.2	132
25	PS/Tip/MC	Coating erosion/spallation	2x2	13.7	17.5	126	-0.1	3.16	119	26.4	21
26	SS/MS/TE	Clean surface	3x4	1.1	1.3	10	-0.4	3	170	4.1	5000

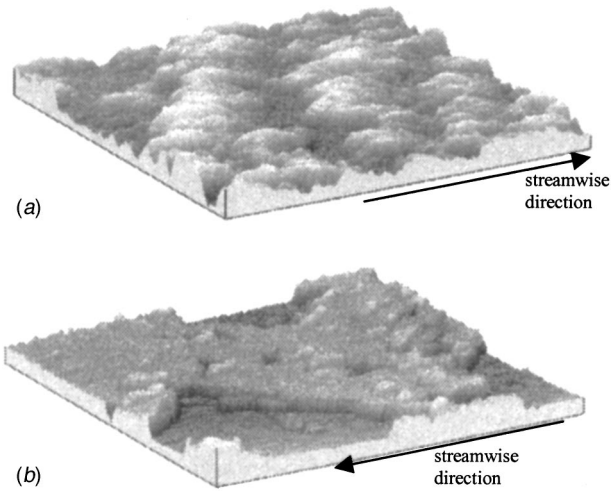

Fig. 8 Two distinct forms of fuel deposits

to this, the Fig. 8(*b*) deposit is a more uniform 20–40 μm thick layer, which coats nearly the entire blade. There is no directional preference for this deposit and its surface is of comparable roughness to the underlying metal (Ra$\approx$4 μm). Full-coverage deposits of this type may actually perform the same function as thermal barrier coatings; though in the 8(*a*) case, the ''coating'' is very rough (Ra$>$30 μm) and would substantially alter the blade performance.

Figures 9(*a*) and (*b*) (surfaces #7 and #5) show various sizes of discrete contaminants embedded in the leading edge region. This type of isolated roughness might be well modeled with the discrete element roughness model of Taylor et al. [17]. The drag-inducing elements in this model are usually cones or hemispheres, a good approximation to the contaminants shown in Fig. 9. Isolated deposits were also observed on unspalled thermal barrier coatings and may play a role in creating sites for subsequent spallation. In regions of advanced coating spallation, where the underlying metal is completely exposed, stubborn islands of coating (Fig. 10(*a*) surface #24) have a signature similar to that of isolated contaminants and probably result in similar aero-thermal penalties. Turbines operated in marine environments suffer from corrosive scale due to salt and sand. This buildup results in a wide range of roughness scales similar to erosion, as shown in the suction surface *TE*/Tip trace in Fig. 10(*b*).

Regions with deposits generally exhibit a positive statistical skewness and a wide range of α_{rms} and Λ_s values, depending on the number and shape of the deposit. A positive skewness indicates that heights above the mean tend to be larger than heights below the mean. That is, the profile tends to have more high peaks than deep valleys. This is important because it is expected that

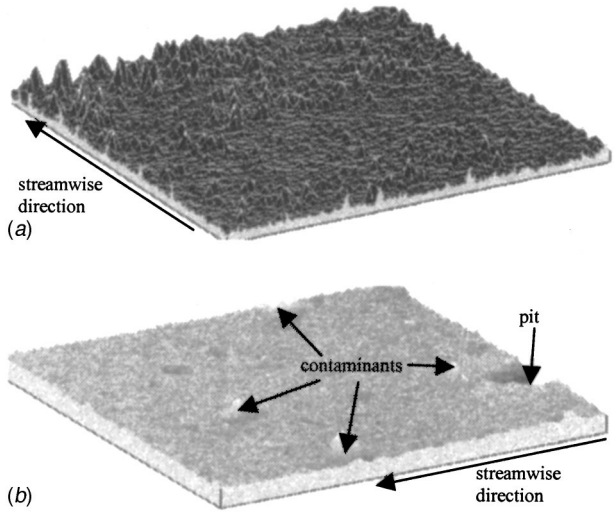

Fig. 9 Leading edge deposits/contaminants

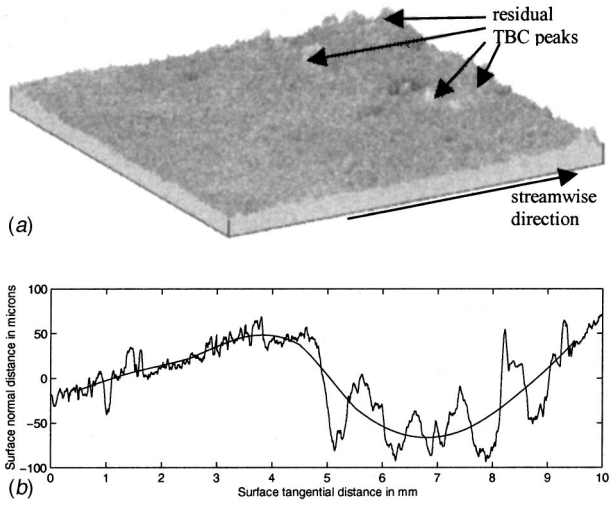

Fig. 10 Other forms of contaminants: (*a*) TBC residue islands and (*b*) scale from salt and sand

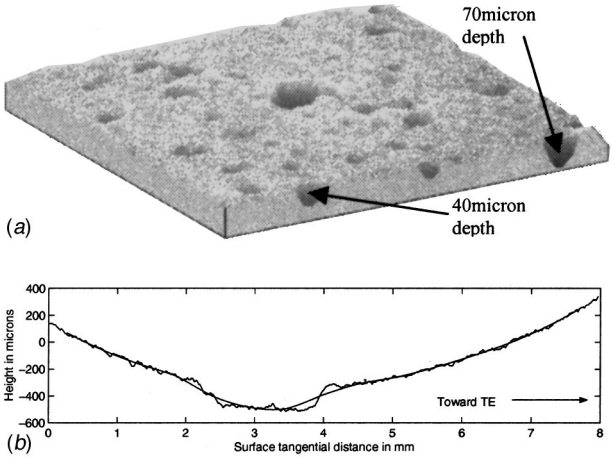

Fig. 11 Examples of surface pitting and erosion

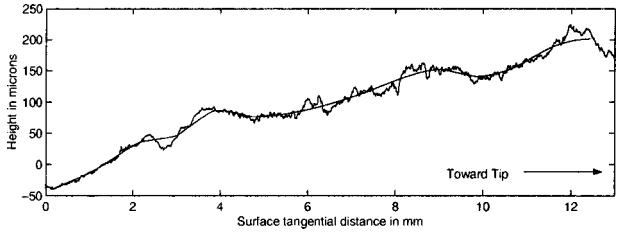

Fig. 12 Spanwise LE waviness pattern due to erosion/deposits ($\lambda = 5$ mm, raw data with meanline)

peaks have a more significant impact on heat transfer and skin friction than valleys. Taylor [2] reported an average positive skewness in his blade measurements, signaling the probable presence of foreign deposits.

Pitting/erosion: Pitting due to hot corrosion was observed on the suction surface of a handful of vanes near the trailing edge (Fig. 11(*a*), surface #17). Although these pits were sometimes over 50 μm deep, their impact on c_f and St is probably minimal due to their negligible flow blockage. Larger pits (craters; Fig. 11(*b*)) resulting from particulate impact and/or erosion could be expected to have a more significant impact on performance. Erosion was most prevalent in the leading edge region (Fig. 5(*a*)) where the heat load is greatest. Leading edge surface degradation

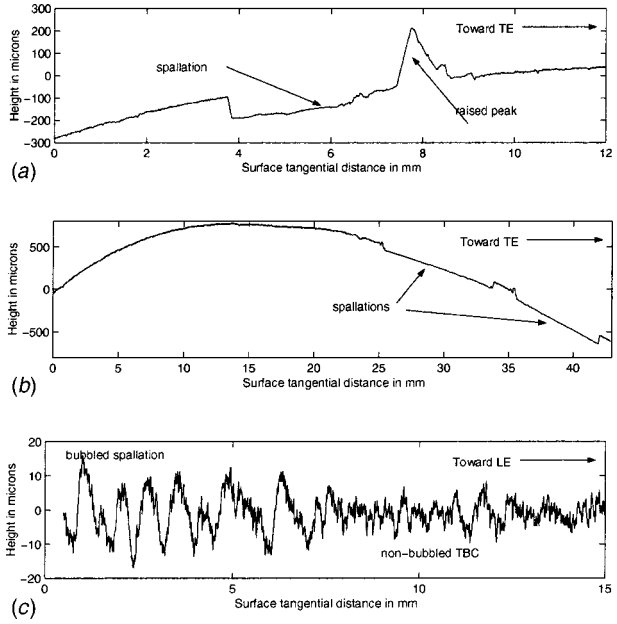

Fig. 13 Examples of TBC spallation

is liable to have the greatest detrimental effect on blade performance since it is also the region of highest heat load, where the roughness element size to boundary layer thickness ratio is largest. The eroded blade *LE* in Fig. 12 shows a distinct spanwise waviness ($\lambda \approx 5$ mm) from Hub to Tip. Spanwise erosion patterns were also measured across film cooling discharge paths, as will be shown later. Since these waves are spanwise, they may generate streamwise vortices in the boundary layer or prevent radial migration of the flow or coolant.

Pitting and erosion both typically have signatures with a negative skewness due to the removal of metal substrate. The larger Λ_s and lower $\alpha_{\rm rms}$ values also indicate a reduced roughness compared to deposits. The combination of these three observations leads to the expectation that pitting and erosion should have less of an impact on the blade's aerothermal performance than deposits. While this may indeed be true, deposits may actually pose a reduced threat to blade life (compared to erosion/pitting) since they also add an insulating layer to effectively shield the underlying metal from high thermal loads.

Spallation: This was the most significant form of surface roughness measured, with height variations on the order of the coating thickness (100 to 400 μm). It occurred primarily on the suction surface leading edge and pressure surface trailing edge, as well as in the immediate vicinity of any film cooling holes. In fact, if a coated blade exhibited spallation anywhere on its surface, the region near the cooling holes was sure to be spalled. This is probably due to a combination of two factors: The heat loads are most severe there (thus the application of film cooling) and the holes present an obvious stress concentration for a debond to occur.

Spallation occurred differently with different coatings and in different use environments. Figure 13 shows two-dimensional traces of three spallation sites. A fourth was already presented in Fig. 6(*c*). It showed a large region of removed coating directly adjacent to areas of unaffected coating. The spalled region measured an Ra value nearly 5 times that of the surrounding coating. Figure 13(*a*) is a coating which exhibited small (2–3 mm) debonds from the metal substrate, with raised peaks of coating material (or foreign contaminants) at the border of the debond site. Figure 13(*b*) shows a spallation site where the underlying metal is fairly smooth and the coating appears to have experienced a clean debond. The final trace (Fig. 13(*c*)) is not a spallation site in the traditional sense that the coating has been removed. Rather the

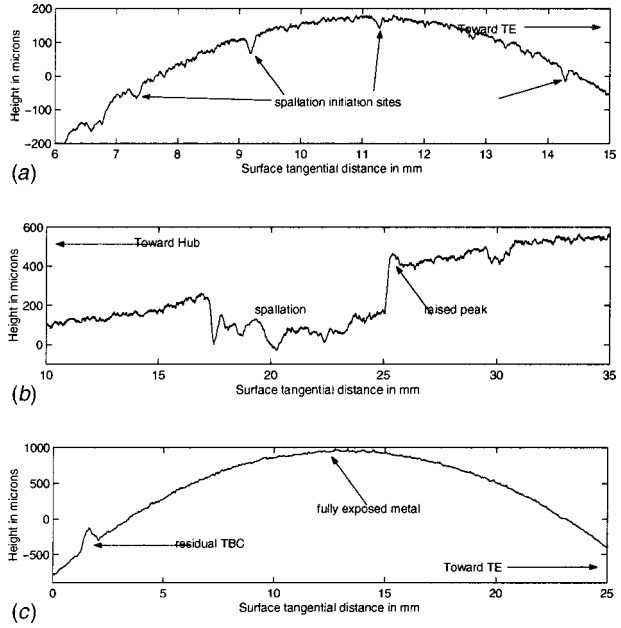

Fig. 14 Examples of TBC spallation life-cycle evolution

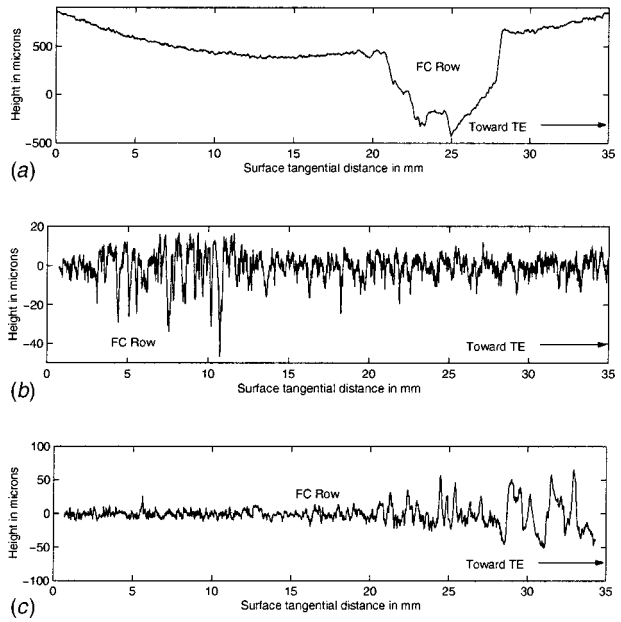

Fig. 15 Chordwise roughness variation across FC rows

coating on this blade had bubbled up from the surface forming a bumpy region ($\lambda \approx 0.8$ mm) over much of the pressure surface *MC* & *TE*. This trace was taken in the chordwise direction from midchord forward and shows the transition from the bubbled region to the unaffected coating.

Although different coatings exhibited different spallation signatures, there appeared to be a common evolution of spallation sites. Initially, spallation sites had a similar appearance to pitting and formed either due to flow contaminants or a localized failure of the coating itself (Fig. 14(*a*)). As the number of sites increased, the statistical skew of the roughness registered more and more negative values. In fact, the average skewness of all of the two-dimensional measurements on coated (but unspalled) surfaces was -0.3, compared to an average over the noncoated surfaces of $+0.2$. Accordingly, the spallation sites at this initial stage (like the pitting shown earlier) probably have little impact on the flow. Gradually, these initiation sites grow down to the base metal and broaden to form craters with significant roughness signature (Fig. 14(*b*)). Many of these spallation sites show a raised edge at the side of the crater. The rise may be an embedded contaminant from the flow, suggesting that the coating spallation might have been initiated by foreign particle impact. These craters then eventually grow to expose large sections of metal which can at times have lower roughness than the original coated surface (Fig. 13(*b*)). Finally, the metal is fully exposed (Fig. 14(*c*)) and becomes subject to all of the roughness inducing mechanisms discussed earlier. Note the deposit-like island of coating still intact on this leading edge suction surface trace.

This life cycle of surface degradation is unique from that of an uncoated metal part which would be expected to have a monotonic increase in roughness with use. Following this proposed spallation life cycle, a coated part could experience a peak in roughness when the craters are large (Fig. 14(*b*)) followed by a period of constant or decreasing roughness as the metal becomes completely exposed. Then as the metal surface degradation ensues, roughness levels would again rise with use.

Film cooling: Film cooling sites were typically regions of dramatic spatial variations in surface roughness. Figure 15 contains three chordwise traces across film cooling rows (not over the holes themselves). The location of the row is indicated in each trace, though it is probably unnecessary. The first is a veritable canyon of TBC spallation evidenced all along this pressure surface trailing edge film cooling row. The second trace shows a subtle rise in surface erosion at the cooling site with a return to ambient levels thereafter (the most common signature). The third trace shows a rise in deposits at and beyond the cooling row. Goldstein et al. [23] and Barlow and Kim [24] have both looked at the effect of roughness on film cooling effectiveness. Goldstein et al. modeled roughness using cylinders with dimensions on the order of the boundary layer thickness mounted before and after the film cooling site. They reported increased film effectiveness at high blowing rates due to reduced coolant blow-off. Barlow and Kim etched small pedestals into the stainless steel panel which contained the film cooling row in their study. The pedestal dimensions were selected so that the panel's Ra value was approximately equal to the boundary layer momentum thickness at the injection site. Barlow and Kim also reported increased effectiveness with roughness at higher blowing rates and showed better lateral coolant coverage as well. Whether the results with these regular roughness arrays would approximate that of the real roughness traces shown in Fig. 15 is unclear. Certainly, for the case of spallation (Fig. 15(*a*)) coolant blowoff may actually be worsened due to roughness.

One surface feature due to film cooling that has not been treated in the open literature is the spanwise pattern downstream of the film cooling row. Several, though not all, of the film cooled blades evaluated in this study showed a periodic distribution of furrows downstream of each film cooling hole. The three-dimensional map in Fig. 16(*a*) (surface #13) and associated trailing edge spanwise trace (16(*d*)) show that these furrows have elevated levels of roughness compared to the regions between the holes. The depth of the furrows can range from 80 μm (for trace 16(*b*)) taken approximately $5d$ downstream of the holes) up to 500 μm (trace 16(*c*) taken on a vane endwall about $15d$ from the hole location. The mechanism(s) responsible for these furrows is unknown, although they have been observed by others (Soechting [25]), who have suggested that they may be due to a suppression of deposits in the path of the film cooling flow. Molten combustion matter would tend to cool and harden in the film cooling path thus reducing its ability to adhere to the blade surface. This is a plausible explanation for the large furrows in Fig. 16(*c*), since the vane in question did exhibit extensive deposits. The vane in Fig. 16(*a, b*) however, shows elevated roughness levels in the furrow, suggesting the possibility of enhanced erosion from the film cooling jet.

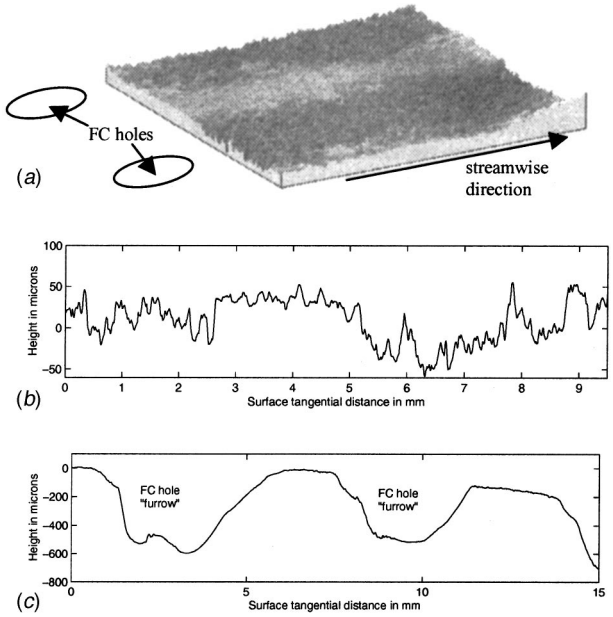

Fig. 16 Spanwise roughness variations downstream of film cooling rows

Whatever the cause, these larger trenches would certainly curtail spanwise diffusion of the coolant and may inhibit jet blow-off altogether.

Summary and Conclusions

Surface roughness measurements have been presented for a wide range of in-service land-based turbine hardware provided from four manufacturers. A summary of findings follows:

Based on the aggregate data from all roughness measurements taken, it is clear that no region of turbine hardware is ''off-limits'' to roughness. Although some regions on both the pressure and suction surface are traditionally more prone to specific roughness mechanisms, on average all regions showed roughness levels 4 to 8 times greater than the levels for production line hardware (Ra $<1\ \mu$m).

Taken individually, blades exhibited spatial variations from 2:1 to 68:1 in the maximum to minimum Ra ratio. Transitions between rough and smooth regions were usually gradual, but could be very abrupt.

A thermal barrier coating spallation appears to follow an evolutionary life-cycle from pits to craters to completely exposed metal, which can at times see reductions in local roughness with use.

Film cooling sites are regions of dramatic spatial variations in surface roughness with roughness increasing at the injection site and downstream. Erosion furrows detected behind some of the film cooling holes could have a significant influence on the coolant effectiveness.

Finally, the various roughness mechanisms had very distinct signatures. Air-borne contaminants were typically observed as surface spikes while hot corrosion resulted in surface pitting. The surface statistical skewness is a natural delineator between these two roughness forms and may be an important parameter for roughness modeling. Erosion due to the combination of airborne contaminants and corrosion resulted in much more irregular surfaces. Spallation was the most significant form of surface roughness measured, with huge variations in surface character. Given these findings, the authors are lead to conclude that no one characterization (cones, pedestals, hemispheres, cylinders, etc., ...) can accurately capture the range of features exhibited by the various forms of surface roughness.

Acknowledgments

The authors are indebted to numerous personnel at the four industrial partners for their timely response to our request for hardware. Primary among these are: Dr. Boris Glezer at Solar Turbines, Dr. Ron Bunker and Mr. Paul Suttmann at General Electric, Mr. Mohan Hebbar at Siemens-Westinghouse, and Dr. William Troha and Mr. Shawn Pollock at Honeywell. The authors would also like to acknowledge those who assisted in the collection of this data: Mr. Jay Anderson and Capt. Jess Drab at the Air Force Institute of Technology. In addition, collaborations with Dr. Keith Hodge at Mississippi State University and Dr. Rolf Sondergaard of the Air Force Research Lab are appreciated. This work was sponsored by the US Department of Energy—National Energy Technology Laboratory through a cooperative agreement with the South Carolina Institute for Energy Studies at Clemson University. The views expressed in this paper are those of the authors and do not reflect the official policy or position of the United States Air Force, Department of Defense, or U.S. Government.

Nomenclature

A_f = windward frontal surface area of roughness
A_s = windward wetted surface area of roughness
c_f = skin friction coefficient
C_x = blade axial chord
d = film cooling hole diameter
FC = film cooling
Hub = blade hub or vane inner radius
k = average roughness height $\approx Rz$
k_s = equivalent sandgrain roughness
Ku = kurtosis of height distribution
LE = leading edge
MC = midchord
MS = midspan
N = number of points in profile record
PS = pressure surface
Ra = centerline average roughness
Re_x = Reynolds number based on streamwise direction, x
Rq = rms roughness
Rt = maximum peak to valley distance
Rz = average peak to valley distance
S = surface area of sample without roughness
S_f = total frontal surface area of sample
Sk = skewness of height distribution
St = Stanton number
SS = suction surface
TE = trailing edge
Tip = blade tip or vane outer radius
y = surface height coordinate after removal of meanline fit
$y_{\max}$ = maximum height in profile record
$y_{\min}$ = minimum height in profile record
α_{rms} = rms deviation of surface slope angles
δ = boundary layer thickness
Λ_s = roughness shape/density parameter
λ = wavelength
λ_c = correlation length

References

[1] Acharya, M., Bornstein, J., and Escudier, M., 1986, ''Turbulent Boundary Layers on Rough Surfaces,'' Exp. Fluids, **4**, pp. 33–47.
[2] Taylor, R. P., 1990, ''Surface Roughness Measurements on Gas Turbine Blades,'' ASME J. Turbomach., **112**, pp. 175–180.
[3] Tarada, F., and Suzuki, M., 1993, ''External Heat Transfer Enhancement to Turbine Blading Due to Surface Roughness,'' ASME Paper No. 93-GT-74.
[4] Bammert, K., and Sandstede, H., 1980, ''Measurements of the Boundary Layer Development Along a Turbine Blade With Rough Surfaces,'' ASME J. Eng. Power, **102**, pp. 978–983.
[5] Turner, A., Tarada, F., and Bayley, F., 1985, ''Effects of Surface Roughness on Heat Transfer to Gas Turbine Blades,'' AGARD-CP-390, pp 9–1 to 9–9.

[6] Blair, M. F., 1994, ''An Experimental Study of Heat Transfer in a Large-Scale Turbine Rotor Passage,'' ASME J. Turbomach., **116**, pp. 1–13.
[7] Hoffs, A., Drost, U., and Bolcs, A., 1996, ''Heat Transfer Measurements on a Turbine Airfoil at Various Reynolds Numbers and Turbulence Intensities Including Effects of Surface Roughness,'' ASME Paper No. 96-GT-169.
[8] Bogard, D. G., Schmidt, D. L., and Tabbita, M., 1998, ''Characterization and Laboratory Simulation of Turbine Airfoil Surface Roughness and Associated Heat Transfer,'' ASME J. Turbomach., **120**, pp. 337–342.
[9] Abuaf, N., Bunker, R. S., and Lee, C. P., 1998, ''Effects of Surface Roughness on Heat Transfer and Aerodynamic Performance of Turbine Airfoils,'' ASME J. Turbomach., **120**, pp. 522–529.
[10] Boynton, J. L., Tabibzadeh, R., and Hudson, S. T., 1993, ''Investigation of Rotor Blade Roughness Effects on Turbine Performance,'' ASME J. Turbomach., **115**, pp. 614–620.
[11] Nikuradse, J., 1933, ''Laws for Flows in Rough Pipes,'' VDI-Forchungsheft 361, Series B, Vol. 4 (English Trans NACA TM 1292, 1950).
[12] Schlichting, H., 1936, ''Experimentelle Untersuchungen zum Rauhigkeits-Problem,'' Ingenieur-Archiv., VII, No. 1, pp. 1–34. (Also ''Experimental Investigation of the Problem of Surface Roughness,'' NACA TM 823).
[13] Cebeci, T., and Chang, K., 1978, ''Calculation of Incompressible Rough-Wall Boundary-Layer Flows,'' AIAA J., **16**, pp. 730–735.
[14] Boyle, R. J., 1994, ''Prediction of Surface Roughness and Incidence Effects on Turbine Performance,'' ASME J. Turbomach., **116**, pp. 745–751.
[15] Guo, S. M., Jones, T. V., Lock, G. D., and Dancer, S. N., 1998, ''Computational Prediction of Heat Transfer to Gas Turbine Nozzle Guide Vanes With Roughened Surfaces,'' ASME J. Turbomach., **120**, pp. 343–350.
[16] Finson, M. L., and Wu, P. K. S., 1979 ''Analysis of Rough Wall Turbulent Heating with Applications to Blunted Flight Vehicles,'' AIAA Paper No. 79-008.
[17] Taylor, R. P., Coleman, H. W., and Hodge, B. K., 1985, ''Prediction of Turbulent Rough-Wall Skin Friction Using a Discrete Element Approach,'' ASME J. Fluids Eng., **107**, pp. 251–257.
[18] Scaggs, W. F., Taylor, R. P., and Coleman, H. W., 1988, ''Measurement and Prediction of Rough Wall Effects on Friction Factor—Uniform Roughness Results,'' ASME J. Fluids Eng., **110**, pp. 385–391.
[19] Tolpadi, A. K., and Crawford, M. E., 1998, ''Predictions of the Effect of Roughness on Heat Transfer From Turbine Airfoils,'' ASME Paper No. 98-GT-087.
[20] Sigal, A., and Danberg, J., 1990, ''New Correlation of Roughness Density Effect on the Turbulent Boundary Layer,'' AIAA J., **28**, pp. 554–556.
[21] Pinson, M. W., and Wang, T., 2000, ''Effect of Two-Scale Roughness on Boundary Layer Transition over a Heated Flat Plate: Part I—Surface Heat Transfer,'' ASME J. Turbomach., **122**, pp. 301–307.
[22] Taylor, R. P., and Chakroun, W. M., 1992, ''Heat Transfer in the Turbulent Boundary Layer With a Short Strip of Surface Roughness,'' Paper No. AIAA 92-0249.
[23] Goldstein, R., Eckert, E., Chiang, H., and Elovic, E., 1985, ''Effect of Surface Roughness on Film Cooling Performance,'' ASME J. Eng. Gas Turbines Power, **107**, pp. 111–116.
[24] Barlow, D. N., and Kim, Y. W., 1995, ''Effect of Surface Roughness on Local Heat Transfer and Film Cooling Effectiveness,'' ASME Paper No. 95-GT-14.
[25] Soechting, F., 2000, private communication.

High-Resolution Measurements of Local Heat Transfer Coefficients From Discrete Hole Film Cooling

S. Baldauf[1]

A. Schulz

S. Wittig

Lehrstuhl und Institut für Thermische Strömungsmaschinen, Universität Karlsruhe (TH), 76128 Karlsruhe, Germany

Local heat transfer coefficients on a flat plate surface downstream a row of cylindrical ejection holes were investigated. The parameters blowing angle, hole pitch, blowing rate, and density ratio were varied over a wide range, emphasizing engine relevant conditions. A high-resolution IR-thermography technique was used for measuring surface temperature fields. Local heat transfer coefficients were obtained from a Finite Element analysis. IR-determined surface temperatures and backside temperatures of the cooled test plate measured with thermocouples were applied as boundary conditions in this heat flux computation. The superposition approach was employed to obtain the heat transfer coefficient h_f based on the difference between actual wall temperatures and adiabatic wall temperatures in the presence of film cooling. The h_f data are given for an engine relevant density ratio of 1.8. Therefore, heat transfer results with different wall temperature conditions and adiabatic film cooling effectiveness results for identical flow situations (i.e., constant density ratios) were combined. Characteristic surface patterns of the locally resolved heat transfer coefficients h_f are recognized and quantified as the different ejection parameters are changed. The detailed results are used to discuss the specific local heat transfer behavior in the presence of film cooling. They also provide a base of surface data essential for the validation of the heat transfer capabilities of CFD codes in discrete hole film cooling. [DOI: 10.1115/1.1387245]

Introduction

Film cooling, in combination with internal convective cooling, is the common method for preventing turbine blades from excessive material temperatures. The great majority of investigations in the literature concentrate only on the temperature problem of film cooling, that is, the determination of the adiabatic film cooling effectiveness

$$\eta = \frac{T_G - T_{aw}}{T_G - T_C} \tag{1}$$

In fact, the prediction of the material temperatures is a heat flux problem. Heat transfer from the hot gas into the wall, conduction within the wall, and heat transfer from the wall to the internal cooling air flow have to be considered. Furthermore, with the internal cooling air temperature being dependent on the transferred heat flux, an iterative solution for the wall temperature has to be employed.

The prediction of the heat transfer on the hot gas side in the presence of film cooling is especially difficult. With respect to structural and manufacturing constraints, cooling air ejection on turbine blades is restricted to discrete holes. The ejected cooling air jets induce a highly complex turbulent mixing situation, affecting the boundary layer temperature patterns as well as the local velocity profiles and, therefore, the local heat transfer coefficients. General effects of the jet and hot gas flow interaction for typical cases of inclined jets in crossflow observed by highly resolved flowfield measurements were documented by Lee et al. [1]. Detailed flowfield measurements and additional data on the production of heat transfer enhancing turbulence by the jet ejection are provided by Pietrzyk et al. [2,3], Burd et al. [4], and Thole et al. [5] for similar ejection situations. Highly resolved experimental data on the temperature fields responsible for the driving temperature gradients of the heat flux are given by Rydholm [6] and Kohli and Bogard [7]. Other recent studies, including also compound angle ejection, are given by Sen et al. [8], Schmidt et al. [9], and Bell et al. [10]. Computational studies with highly refined grids were carried out by Sgarzi and Leboeuf [11] for a normal ejection baseline case and by other authors, e.g., Walters and Leylek [12], for the inclined coolant ejection. From these and other authors' investigations, the basic large and small-scale flowfield phenomena of inclined jets in crossflow, like jet lift-off and entrainment of hot gas under the coolant jet and the resulting vortex structures, are known.

The present paper focuses on the local heat transfer coefficient, while a companion paper (Baldauf et al. [13]) treats details of the local adiabatic film cooling effectiveness. For the determination of the heat flux from the hot gas to the wall, two different approaches are common. The first employs the temperature of an adiabatic wall

$$q_w = h_f (T_{AW} - T_W) \tag{2}$$

Herein the heat transfer coefficient h_f particularizes the heat flux process from the cooling film to the wall. The second utilizes the known hot gas temperature to give

$$q_w = h(\theta)(T_G - T_W) \tag{3}$$

The heat transfer coefficient $h(\theta)$ describes the whole heat transport behavior form the outer hot gas flow to the wall. Therefore, the influence of the actual cooling film temperature on the heat transfer in this formulation necessitates the dependence of the heat transfer coefficient on the dimensionless temperature ratio

[1]Present address: Siemens Power Generation, 45473 Mülheim an der Ruhr, Germany.

Contributed by the International Gas Turbine Institute and presented at the 44th International Gas Turbine and Aeroengine Congress and Exhibition, Indianapolis, Indiana, June 7–10, 1999. Manuscript received by the International Gas Turbine Institute February 1999. Paper No. 99-GT-43. Review Chair: D. C. Wisler.

$$\theta = \frac{T_G - T_C}{T_G - T_W} \tag{4}$$

An analysis of the simplified boundary layer equations of the convective heat transfer problem reveals a differential energy equation of a linear form for constant flow properties. Thus, a general solution can be derived from the linear superposition of two special solutions (Metzger and Fletcher [14], Choe et al. [15], Jones [16]). A very detailed examination of the practical relevance of the superposition approach by Gritsch et al. [17] shows that the linear approach is still appropriate for the range of typical temperature ratios and property variations of film cooling applications employed in operating engines. However, use of a constant density ratio to conserve an identical flow situation, for measurements with a variation of θ is imperative. Linearity of the problem implies both the wall temperature independence of h_f and the linearity of $h(\theta)$. For large ratios of wall to flow temperature where the flow properties (i.e., viscosity, thermal conductivity, specific heat) within the thermal sublayer are affected, a correction of the heat transfer coefficient depending on a -0.25 power law of this temperature ratio is used (e.g., Kays and Crawford [18]). As confirmed by other authors (considerations and results of Loftus and Jones [19], Forth et al. [20,21], Teekaram et al. [22]), for all practical purposes linearity is not greatly affected by this effect, since this temperature ratio at the film-cooled wall is usually still close to that of the referenced unblown case. If a correction is not considered, deviations of up to 5 percent were stated by Teekaram et al. [22]. With the correction this deviation should disappear. Therefore, the property effects on the heat transfer coefficients are dominated by the local temperatures of the cooling film near the wall, and the linearity of the $h(\theta)$ data is not affected significantly. Since either of the two Eqs. (2) and (3) designate the same heat flux, the relation of the two types of heat transfer coefficient is given by

$$h(\theta) = h_f(1 - \eta\theta) \tag{5}$$

In the present study, h_f are presented for an engine relevant density ratio of 1.8. Under such experimental conditions with realistic temperature ratios, θ is always non-zero and the wall temperature independent h_f cannot be measured directly. The only way to determine h_f is to carry out two or more experiments at different θ (where one may be an adiabatic wall experiment) and extrapolate $h_f = h(\theta = 0)$ by use of Eq. (5). This is done using measurements at the same density ratio as θ is varied. The result is the heat transfer coefficient h_f of the actual high-density-ratio flow field for use in Eq. (2). Thus, note that these heat transfer coefficients are different from those measured with the same coolant and main flow temperatures (i.e., iso-energetic conditions used by Choe et al. [15] and others).

Investigations of the local heat transfer coefficients were performed in the vicinity of ejection holes by Kumada et al. [23], Goldstein and Taylor [24], and Cho and Goldstein [25] using the mass transfer analogy at unity density ratio. They provide insight into the near ejection mixing phenomena and can be related very closely to the flowfield structures described by the authors quoted earlier. Investigations extending downstream into the film region have been undertaken by Ammari et al. [26], Ekkad et al. [27], and Goldstein et al. [28]. The great majority of the published investigations concentrate on ejection angles of 30–35 deg so that detailed data for other geometries are sparse. Only few experiments were conducted at turbine like density ratios with high local resolution (e.g., Gritsch et al. [29]). Such local experimental data are needed for the development and validation of refined wall and heat flux models for CFD predictions. Highly resolved local surface data are necessary for a better understanding of the physics of the turbulent jets in hot gas flow interactions and their impact on the heat transfer coefficients.

The present study addresses these issues. Thus, the objective of the present study is the determination and analysis of local heat transfer coefficient distributions in the presence of high-density-ratio film cooling on a flat plate downstream of a row of cylindrical ejection holes. The optimization of film cooling depends on the ability to eject an adequate amount of coolant without significant augmentation of the heat transfer coefficient. Therefore, high-resolution surface data are acquired beginning close to the ejection and extending over a sufficient downstream distance. A systematic alteration of the parameters of primary influence provides information on conditions for optimal film cooling behavior. The data are additionally valuable for the validation of the heat transfer capability of CFD codes in film cooling predictions and for the development of refined wall and turbulence models.

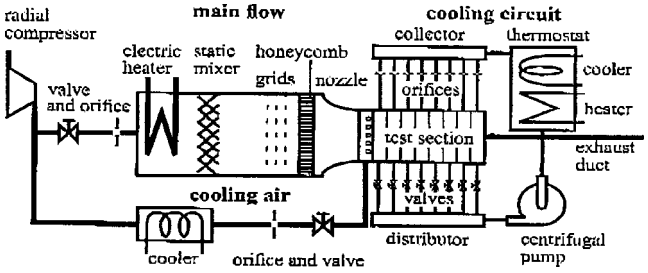

Fig. 1 Extended hot wind tunnel scheme with cooling circuit

Experimental Facilities

The experimental method of the present investigation is based on stationary experiments in a scaled-up geometry realizing engine-like flow conditions. Proper temperature ratios of hot gas to cooling air are applied to obtain realistic density gradients and heat flux directions. The use of foreign gas and the mass transfer analogy was avoided to exclude effects from foreign media properties.

The heat transfer measurements were carried out in an open-circuit hot wind tunnel at the Institute of Thermal Turbomachinery, University of Karlsruhe. A schematic of the installation is shown in Fig. 1. For a detailed description of its basic features, see [13]. For the heat transfer measurements, an additional cooling circuit was installed to generate a heat sink, resulting in a heat flux from the hot gas into the test surface. To allow a variation of the wall temperature of the test surface, the cooling fluid temperature can be adjusted in the range of 280 K to 470 K. The cooling fluid used is silicon oil.

A scheme of the test section is shown in Fig. 2. The cooling air enters the test section from a plenum through cylindrical ejection holes of $D = 5$ mm diameter. The cross-sectional area of the test duct is $21 \times 44D$. Different ejection geometries are realized as modules that fit into the coolant plenum duct. The ejection modules are made from the semi-crystalline thermoplast TECAPEK, which combines high thermoresistance and low thermal conductivity. They approximate an adiabatic surface at the ejection loca-

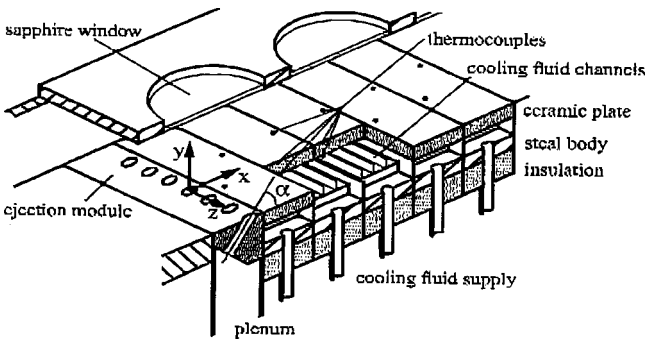

Fig. 2 Test section for heat transfer measurements

tion. Effects of a coolant temperature rise in the hole passage were correlated based on the thermocouple measured plenum temperature, the blowing rate, and the hot gas temperature. Coolant temperatures thus represent values at the exits of the holes. The test plate connected to the ejection module extends from $2D$ to $82D$ downstream of the ejection location. It consists of eight plates of a machinable ceramic material (Corning Macor) with a downstream length of $10D$ and a thickness of $2D$, respectively, having a thermal conductivity of 2.0 W/mK. The plates are supported by a steel body of the same thermal expansion coefficient as the ceramic material, also bearing the connections for the cooling fluid supply. Channels are embedded below the plates to allow the direct contact of cooling fluid and ceramic. The coolant fluid was applied at high flow rates, resulting in very high heat transfer coefficients and a homogeneous temperature on the backside of the test plate. The temperature rise of the coolant fluid crossflow was very small.

The local surface temperature measurements are performed with a high resolution IR-camera system. Ejection modules and test surface are coated with a constant emissivity dye to assure uniform radiation conditions. Two 0.25 mm thermocouples are mounted flush to the test surface on every segment at varying lateral positions of $2.6D$ to $6.1D$ from the channel centerline for surface temperature control and *in situ* calibration of the IR camera images. A total of five to eight thermocouple measurement points were used to fit the temperature processing parameters of the IR camera images, accounting for all effects of reflection of the surrounding channel temperature from the test surface as well as transmission and emission from the sapphire windows (Martiny et al. [30]). A second set of thermocouples is mounted on the cold side of the segmented test plate opposite to the surface measuring points. They allow an estimation of the heat flux at the measuring locations and were found to be sufficient to control the backside temperature boundary of the test plate. A minimum test plate thickness is needed to enable a precise distance of opposite thermocouples and the measurement of real surface temperatures. Thus, plate material and thickness were selected to realize a Biot number near unity of the regarded heat transfer process from the hot gas through the wall, to minimize the error of heat transfer coefficient determination (Jacobsen [31]).

In a test run operating point, IR images, and thermocouple temperatures were recorded simultaneously. The accuracy of the thermocouple measured temperatures was ± 0.2 K. Local surface temperatures on the calibrated IR images deviated less than 1 percent of the actual cooling air to hot gas temperature difference. The operating conditions and examined geometries of the heat transfer measurements were the same as those of the adiabatic film cooling effectiveness measurements presented in the companion paper [13]. Hot gas velocity was kept constant at $u=60$ m/s to ensure uniform velocity profile conditions at the ejection location. The cooling air temperature was kept at about $T_C=300$ K and density ratio was adjusted by a variation of the hot gas temperature. The flow cases of the present study are specified by the dimensionless geometry and flow parameters. For every geometry and combination of blowing rate

$$M=\frac{(\rho u)_C}{(\rho u)_G} \tag{6}$$

and density ratio

$$P=\frac{\rho_C}{\rho_G} \tag{7}$$

i.e., identical flow conditions, a set of measurements with different θ was attained by a variation of the cooling circuit temperature. In this setup, the parameter θ becomes a dimensionless wall temperature and is the result of the measurement in every point of the regarded surface. Both flow parameters blowing rate and density ratio can be combined to form the momentum ratio

Table 1 Operating parameters

Geometry	$a=30$, 60, 90 deg $s/D=2,3,5$ $L/D=6$
Hot gas flow	$\mathrm{Re}_D=6800-14{,}000$ $\delta_1/D=0.1$ $\mathrm{Tu}=1.5$ percent
Coolant flow	$M=0.2-2.5$ $P=1.2,1.8$ $\theta=1.6-4$

$$I=\frac{(\rho u^2)_C}{(\rho u^2)_G} \tag{8}$$

The experiments were carried out in an environment of low channel background turbulence with typical large length scales to ensure that the development of important vortex phenomena of the ejection is not impeded by increased turbulent viscosity. A compilation of the dimensionless operating parameters is given in Table 1.

Data Processing

Surface temperature data were acquired thermographically over a range of several hole pitches in the middle of the channel. The full information of a periodically uniform row of holes is contained in a stripe of 1/2 hole pitch, extending between z-normal symmetry planes in the hole centerline and in the midspan. Subsequently, IR information over several hole pitches was condensed to one-half pitch stripe by averaging the temperature from the surface points of an even number of half pitches with the same streamwise coordinate and identical distance from the according centerline.

To calculate the local heat transfer coefficient using Eq. (2), the local surface heat flux is required. It was obtained by an FE analysis of the three-dimensional internal heat flux within the test plate and ejection module, considering their different properties. The test plate was modeled as a monolithic block; interfaces between the single segments were not considered. The computational model and a typical result of this analysis are shown in Fig. 3. IR data were applied as a temperature boundary condition on the test surface; the streamwise interpolation of the thermocouple data from the discrete measuring points on the backside of the test plate was applied to the backside of the FE model as laterally constant temperatures. The heat transfer coefficients on the backside of the ejection module and in the ejection hole were correlated using empirical equations of Gnielinski [32] for tube inlet flow and developing flow over a flat plate, depending on tube length and downstream distance on the surface, respectively. The complex heat transfer situation was approximated by applying the

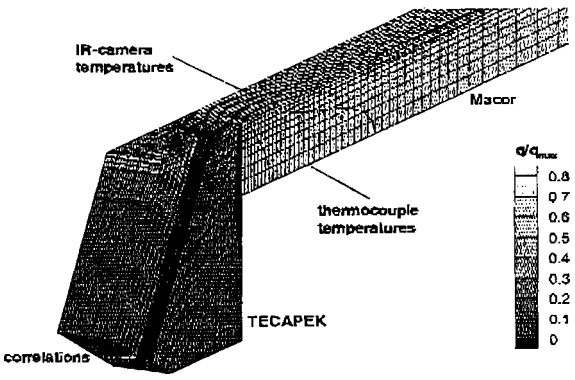

Fig. 3 FE model of the test plate, $a=60$ deg, $s/D=3$

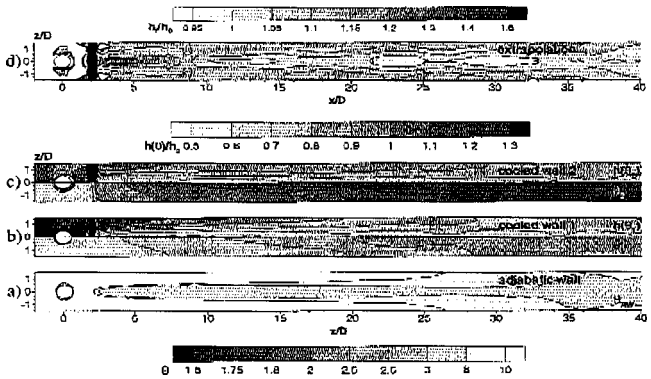

Fig. 4 Local h_f resulting from a set of surface heat transfer measurements at varying dimensionless wall temperature conditions

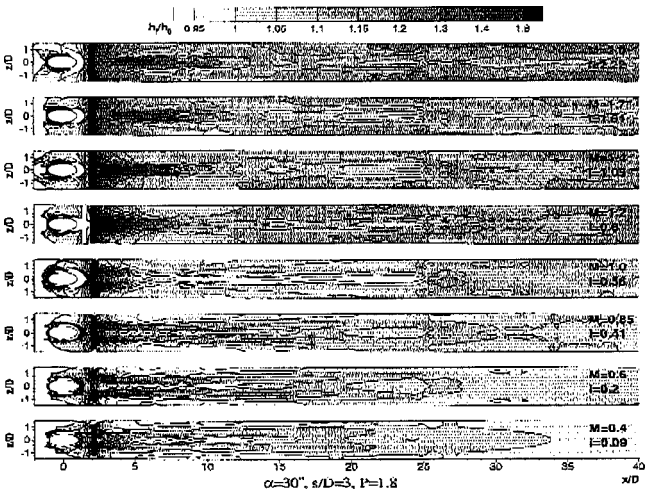

Fig. 5 Local heat transfer coefficient distributions for typical application conditions

averaged heat transfer coefficients based on the mean flow velocities as a constant on the regarded surfaces, with the coolant temperature as a reference. For all other surfaces of the model adiabatic conditions were assumed.

The computation yields a precise result for the local surface heat flux q_W into the test plate as an excerpt from the three-dimensional solution. On the surface of the ejection module, qualitative observations are possible and reasonable heat exchange conditions at the front end of the test plate are provided. The local surface heat flux on the test plate balances the sum of local convective heat flux and local radiative heat flux

$$q_W = q_{\text{conv}} + q_{\text{rad}} \tag{9}$$

The radiative heat transfer from the surrounding channel walls was approximated by an enclosed body approach

$$q_{\text{rad}} = \sigma \varepsilon_W (T_a^4 - T_W^4) \tag{10}$$

where an effective local temperature T_a was applied on basis of a measured channel wall temperature. Local heat transfer coefficients $h(\theta)$ were calculated from the remaining convective heat flux for every surface data point. The surface heat transfer coefficient was normalized with the heat transfer coefficient of the unblown case, that could be well described with the empirical equation of Kays and Crawford [18] considering an uncooled starting length x_s of the boundary layer and the temperature ratio at the wall

$$h_0 = (\rho u c_p) 0.03\, \text{Re}^{-0.2}\, \text{Pr}^{-0.67} \left[1 - \left(\frac{x_s}{x + x_s} \right)^{0.9} \right]^{-1/9} \left(\frac{T_W}{T_G} \right)^{-0.25} \tag{11}$$

The procedure of extrapolating h_f follows the linear superposition scheme described in detail by Gritsch et al. [17] and was applied as follows:

Displayed in Figs. 4(*a–c*) are the surface distributions of the dimensionless temperatures from several runs at identical flow conditions, where those of the cooled surface (Fig. 4(*b*), 4(*c*)) are processed to $h(\theta)/h_0$ data. A further local datum was taken from the adiabatic effectiveness measurement at $h(1/h = \theta_{AW}) = 0$ ([13], Fig. 4(*a*)). Note that at the adiabatic condition only θ_{AW} values are given in Fig. 4. In this way a minimum of three and a maximum of six single measurements at varying wall temperature conditions for every flow case were used to find the functional relation of $h(\theta)$. At every surface location, a linear regression of the points $h(1/h = \theta_{AW})$, $h(\theta_1), h(\theta_2), \ldots$, results in the appropriate values of h_f/h_0 (Fig. 4(*d*)) and h referring to Eq. (5). This regression is thus implemented as the ratio of coolant to hot gas density ratio is held constant. Gritsch et al. [17] provide additional details.

It can be seen than the junction of the ejection module and the test plate at $x/D = 2$ introduces significant perturbations to the FE analysis results, since the contact of ejection module and test plate could not be modeled perfectly. Furthermore, the single test plate segments can be detected in the result of h_f/h_0 by regular deviations of the heat transfer coefficient in streamwise direction. On the cooled test plate the accuracy of the surface heat flux computation mainly depends on the surface temperature measurement: The error of the surface heat flux is about 1 percent. The determination of the radiation reference temperature T_a has an error of 2 percent. At typical conditions, the error of the resulting heat transfer coefficient $h(\theta)$ is 3.5 percent. The error of the extrapolated wall temperature independent normalized heat transfer coefficient h_f/h_0 is about 7 percent, including the described effects of surface contour perturbations.

Results

The results of the heat transfer measurements are displayed as surface contour plots of the normalized heat transfer coefficient h_f/h_0. For reasons of clarity, the actual results available for one-half pitch are mirrored at the hole centerline to result in a full pitch picture. The results are presented with respect to the blowing rate as the important design parameter, and the according values of the momentum ratio are also stated.

Figure 5 shows a set of heat transfer results for a shallow ejection angle, typical hole spacing, and high density ratio at the low turbulence level of 1.5 percent. At lower blowing rates ($M = 0.4–0.85$ and $I = 0.09–0.41$, respectively), typical flow conditions of a fully attached coolant jet are present. The counter rotating vortices of the coolant jet flow are lying on the surface and cause significant traces of enhanced heat transfer. These are extending from the lateral rims of the ejection hole up to about $25D$ downstream the ejection. By mixing and spreading of the coolant into the hot gas flow, the vortices fade and the strong surface interaction diminishes. A low heat transfer region is present in the wake between and under the vortices in the centerline, where relatively low velocities are acting on the surface.

In the midspan between two ejection holes, a slight decrease of the heat transfer is seen. Since the coolant jet at the given conditions is significantly slower than the hot gas flow, it is accelerated by a turboviscous transfer of momentum from the hot regions of high velocity close to the jet. Especially in the midspan between the coolant jets, this causes a deceleration of the hot gas flow near the wall and, subsequently, a reduction of the heat transfer below

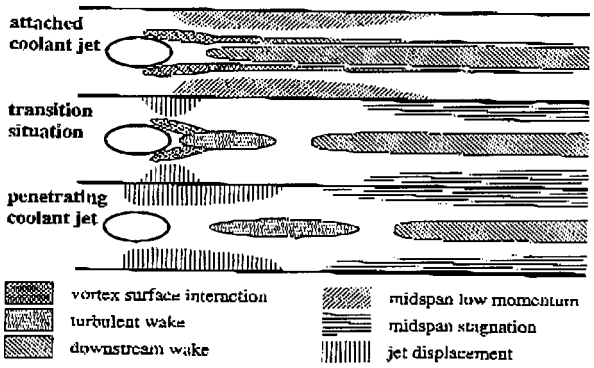

Fig. 6 Characteristic heat transfer patterns for typical application conditions at high density ratios

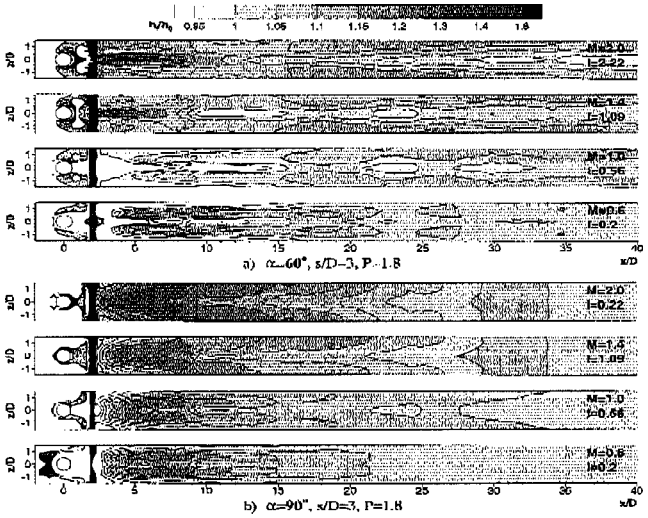

Fig. 7 Effect of the blowing angle on local heat transfer coefficient distributions

the level of the unblown case. The downstream heat transfer of the very low blowing rate is slightly below the unblown case approaching unity at $M=0.6$ ($I=0.2$).

Up to $M=0.85$ ($I=0.41$) only minor changes in the vortex behavior are visible. The vortex traces are slightly bent toward the centerline around $x/D=6$. The vortex surface interaction is intensified very near to the ejection, but the low-momentum surface patterns are still present. The vortex traces tend toward midspan farther downstream where heat transfer is slightly augmented. The traces of adjacent jets vortices get into contact at around $x/D=22$ creating a stagnation line of fluid downwashed on the surface in the midspan by the vortex flow motion.

At a blowing rate of $M=1.0$ ($I=0.56$), a significant change in the flow situation can be observed. The vortex surface interaction is lost at around $7D$ downstream of the ejection, where the vortex traces are expected to be nearest to the centerline. Coolant flow and vortices are driven apart from the surface by the increased coolant momentum normal to the surface. Very close to the ejection hole, where the vortices have intense surface contact before they lift off, heat transfer is still intensified. The low midspan heat transfer region is filled up as expected from the increasing displacement effect of the ejected coolant jets (Goldstein and Taylor [24]). As a result of the increasing jet to hot gas interaction, flow turbulence is enhanced (Pietrzyk et al. [2]) and downstream heat transfer is rising. With a further augmentation of the blowing rate to $M=1.4$ ($I=1.09$), the high heat transfer spots near the ejection hole move toward the centerline and merge. They form an area of combined vortex and turbulent wake heat transfer augmentation in the centerline, followed by the low heat transfer wake region. Midspan heat transfer is rising near the ejection because of the displacement effect of the coolant jets. Beginning at locations of about $x/D=12$, the midspan stagnation region is shifting upstream and overall heat transfer is increasing.

For blowing rates of $M=1.7$ ($I=1.61$) and beyond, a second significant change in the flow pattern takes place. Vortex interaction with the surface is suspended as the coolant jet completely detaches from the surface and penetrates into the hot gas flow. The high heat transfer area near the ejection hole reduces to a turbulent wake region in the centerline, extending $12D$ downstream. It is now separated from the ejection hole and followed by the low heat transfer wake region. The midspan stagnation region is even more pronounced and extending upstream while the midspan displacement region extends farther downstream. This situation is stable up to high blowing rates, accompanied by a further increase of the overall heat transfer coefficient ratios to around 1.2 within $50D$ downstream of the ejection.

The heat transfer distributions shown in Fig. 5 very precisely indicate characteristic flow situations. The observed footprints of the mixing and lift-off effects allow the allocation of specific flow behavior and resulting coolant film development. Therefore, these typical heat transfer patterns are schematized in Fig. 6 for the application relevant high density ratios and shallow angle ejection. They serve as a reference for the effects of alterations of these typical conditions.

Coinciding with the results of the adiabatic effectiveness measurements [13], an attached coolant jet is present for typical conditions and blowing rates below $M=1.0$ or momentum ratios of $I=0.5$. In this range an increase of the effectiveness with increasing blowing rates or momentum ratios is found. The surface patterns are those of a flow situation governed by the single jet in crossflow mixing. The coolant jet vortices cause traces of high heat transfer separating low heat transfer areas in the midspan and in the wake region in the centerline.

At moderate to elevated blowing rates, the coolant jet begins to lift off the surface. The coolant flow separation near the hole exit becomes obvious as the vortices of the jet lose surface contact. The lifting jet opens space beneath to the formation of a turbulent wake region that emerges from the trailing edge of the ejection hole. Only spots of intense surface interaction at both sides of the trailing edge of the ejection hole can be found. These spots are oriented toward the centerline and merge with the turbulent wake region. The surface patterns indicate a flow situation that is dominated by the jet in crossflow mixing in the vicinity of the ejection and by the interaction of adjacent jets downstream. The counterrotating vortices generate laterally alternating regions of low heat transfer in the wake on the centerline and high heat transfer on the stagnation line between the vortices of adjacent jets in the midspan. To the sides of the ejection holes enhanced heat transfer due to displacement effects of the ejected coolant jet can be found.

At high blowing rates of $M=1.7$ ($I=1.61$) and above, the jet is completely detached and penetrates into the hot gas flow. The vortex surface interaction at the ejection is lost. The turbulent wake region moves downstream and separates from the ejection hole. Near the ejection location the displacement effect of the coolant jet is amplified by the joined effect of the adjacent jets, resulting in further heat transfer augmentation. The situation is dominated by the interaction of adjacent coolant jets. The interacting jets cause significant displacement and stagnation regions in the midspan and a wake region in the centerline. In the following, the experimental results will be discussed according to these typical heat transfer patterns.

In Fig. 7 the effect of steeper ejection angles on the local heat transfer is demonstrated. At steep angle ejection (Fig. 7(a)) and low blowing rates, the vortex traces show about the same downstream extension as for shallow angle ejection. Higher turbulence production from the more intense coolant jet in hot gas crossflow

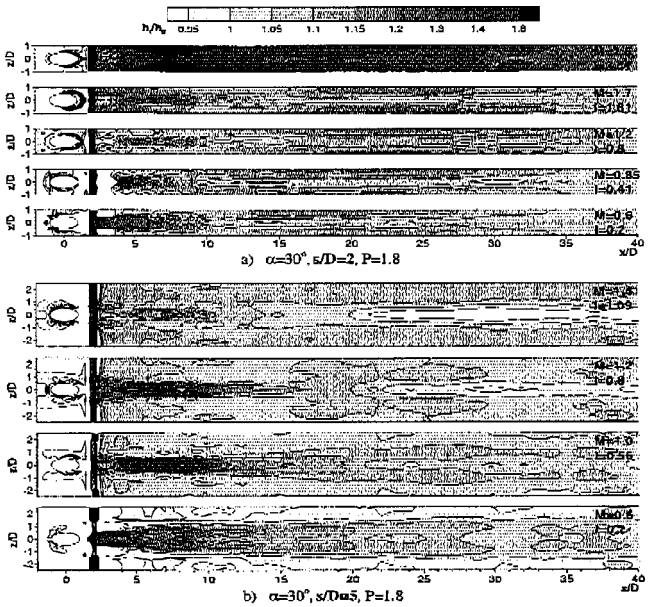

Fig. 8 Effect of the hole spacing on local heat transfer coefficient distributions

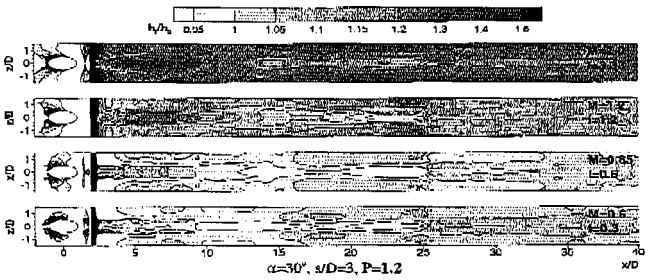

Fig. 9 Effect of the density ratio on the local heat transfer coefficient distributions

mixing can be expected at the steep angle ejection, resulting in higher heat transfer coefficients. The jets seem to be mostly detached at the hole trailing edges as indicated by a region of very low heat transfer upstream at $x/D=4$. Obviously, the jets do not rise to high trajectories, since intense vortex traces can be seen downstream of $x/D=4$. Increasing the blowing rate to $M=1.0$ ($I=0.56$), the traces are gradually fading and moving toward midspan where they merge and transform to a midspan stagnation region. Starting at $M=1.4$ ($I=1.09$) typical patterns of the penetrating jet flow are present as a separated high heat transfer turbulent wake region occurs in the centerline, spreading to midspan at $x/D=8$. The vortex traces have moved completely to the midspan, integrating into the midspan stagnation regions at about $15D$. In the midspan near the ejection, the heat transfer is enhanced by the jet displacement and increases with the blowing rate. Overall heat transfer at moderate and high blowing rates is somewhat lower than for shallow angle ejection, caused by a reduced surface interaction of the coolant jets as expected from a higher jet trajectory.

At normal injection (Fig. 7(*b*)) an even more intense interaction of the hot gas flow with the coolant jets should take place, causing a augmented production of jet mixing turbulence. The resulting vortex traces show higher heat transfer but the surface flow also settles earlier at lower downstream distances. In contrast to inclined ejection, this pattern intensifies until blowing rates of $M=1.0$ ($I=0.56$) are reached without indication of a significant jet lift-off. With increasing blowing rate ($M=1.4$, $I=1.09$ and above), the vortex traces grow together, smoothly transforming into a separated turbulent wake region that stretches over the whole span at $x/D=8$. The midspan stagnation region is wider than for the inclined ejection cases and the flowfield is homogenized early around $x/D=25$. At high blowing rates, normal ejection produces spanwise-oriented patterns rather than the streamwise-oriented patterns that are expected from a vortex-structured coolant flow. In addition to a significant wake in the centerline very high and spanwise uniform heat transfer is found within a distance of $20D$ downstream of the ejection. Pronounced jet displacement effects can not be observed. In contrast to Figs. 5 and 7(*a*), it can be seen from Fig. 7(*b*) that the areas of highest heat transfer coefficients are confined to downstream distances of $3D$ to $10D$. Farther downstream, the values decay quickly across the whole span for the normal ejection. This differs significantly from the inclined ejection, where explicit traces of locally augmented heat transfer can be observed beyond $40D$.

Figure 8 shows the influence of the hole spacing on the local heat transfer. At small pitch ejection (Fig. 8(*a*)) and low blowing rates, vortex traces start near the ejection hole very close to the centerline. They are soon directed toward midspan, where a pronounced stagnation region is present. Low heat transfer is found downstream in the centerline wake and at the ejection location in the midspan. At $M=0.85$ ($I=0.41$) the midspan stagnation region moves upstream, suppressing the development of the vortex traces. Close to the ejection, the interaction of the narrowly spaced adjacent jets is expected to be very intense. Here the early contact of the vortices with the surface seems to be obstructed, resulting in a low heat transfer area upstream of $x/D=3.5$. Typically of the steep angle ejection, no typical transition to the penetrating jet flow situation can be found. Beyond $M=1.0$ ($I=0.56$) the vortex traces merge in the centerline upstream of $x/D=10$ and transform into a turbulent wake region. Compact midspan stagnation regions reach from about $x/D=12$ to about $x/D=35$.

The established pattern is stable and remains unchanged up to high blowing rates of $M=2.0$ ($I=2.22$) with rising overall heat transfer. Adjacent jet interaction is, therefore, dominant within the whole range of examined blowing rates. Compared to a hole spacing of $s/D=3$, higher overall heat transfer is induced even at low blowing rates. At very high blowing rates of $M=2.5$ ($I=3.47$), the midspan stagnation regions become so intense, that they are blinding out the turbulent wake region in the centerline. The heat transfer coefficient ratios are rising beyond 1.5 within the first $15D$ and to about 1.4 within $30D$ downstream of the ejection. The flowfield is homogenized early at a downstream distance of about $x/D=25$.

A completely different situation can be found for large pitch ejection (Fig. 8(*b*)). The typical vortex traces of the attached jet are present up to blowing rates of $M=1.0$ ($I=0.56$). They are closer to the centerline and more intense than for a hole spacing of $s/D=3$. In contrast to the situation at smaller pitch, the traces are not interrupted at lift-off or obstructed by adjacent jet interaction. They are smoothly growing together in the centerline upstream of $x/D=20$ while being still fully present far downstream. A stretched vortex and turbulent wake region is formed in the centerline ($M=1.0$, 1.2; $I=0.56$, 0.8) followed downstream by the low heat transfer wake. Advancing to a blowing rate of $M=1.4$ ($I=1.09$), the spots of intense vortex surface interaction close to the ejection location move back to the ejection hole. This indicates that the coolant jets are gradually losing surface contact. A separated turbulent wake region of the penetrating jet flow is left. The situation remains stable with a further augmentation of the blowing rate. The midspan region near the ejection shows gradually increasing heat transfer ratios, emerging from the ejection holes and caused by moderate jet displacement effects. Midspan heat transfer is not affected by stagnation effects for low blowing rates, and at higher blowing rates only a slight increase of the midspan heat transfer can be found.

Figure 9 shows the effect of a reduced density ratio of P

$=1.2$, which is close to the iso-energetic ejection case, on the local heat transfer. Compared to Fig. 5, it displays the difference in the results of a typical, low-density-ratio experimental setup to real engine conditions. For low density ratio and blowing rates up to $M=0.6$ ($I=0.3$) vortex surface traces can be detected, being less pronounced than for a high density ratio. Therefore, heat transfer is lower than for the high density ratio case close to the ejection, indicating the reduced surface contact of the coolant. Since coolant velocity is closer to the hot gas velocity at these conditions, jet into hot gas crossflow mixing and momentum transfer to the coolant is expected to be less intense. This permits a higher trajectory of the still-attached jet. A significant decrease of the heat transfer at midspan as found for the high density ratio cannot be observed. Farther downstream stagnation regions are present at midspan even for low blowing rates, starting at around $x/D=15$.

At $M=0.85$ ($I=0.6$) the vortex traces have merged in the centerline, transforming into a turbulent wake region similar to large pitch ejection. The vortex traces end at $x/D=13$ framed by midspan stagnation regions, indicating the beginning of jet lift-off. Overall heat transfer is still lower than for the high density ratio because of the higher coolant jet trajectory caused by the higher ejection momentum. A separated turbulent wake region can be seen at $M=1.2$, as the jets penetrate into the hot gas flow. This occurs at considerably lower blowing rate than for the high density ratio and suggests a momentum ratio of $I=1.2$ for jet penetration with this typical configuration. The situation is stable up to high blowing rates with rising overall heat transfer. The heat transfer is now significantly higher than for the high density ratio, as expected from an intensified turbulent mixing at the high coolant velocity of these blowing rates with respect to the high density ratio case.

Discussion

In contrast to adiabatic effectiveness distributions [13], characteristic heat transfer surface patterns precisely denote characteristic flow structures. Changes in these flow structures, displayed in Fig. 6 for typical application-relevant configurations, clearly specify transition from the attached to the penetrating coolant jet flow. They also display the mechanisms of jet in crossflow mixing and adjacent jet interaction. The described patterns are confirmed by observations of several authors in the near-hole region (Kumada et al. [23], Goldstein and Taylor [24], Cho and Goldstein [25], Gritsch et al. [29]) who provide surface heat transfer data with high local resolution. Typical downstream heat transfer distributions for shallow angle ejection, especially at low density ratios, are provided by Ammari et al. [26], Ekkad et al. [27], and Goldstein et al. [28]. The patterns of their surface heat transfer results coincide in shape and local heat transfer augmentation with the present results. Their data also exhibit the double vortex traces close to the centerline at lower blowing rates and a single turbulent wake region in the centerline at higher blowing rates. At high blowing rates, the midspan displacement and stagnation regions compare well.

To obtain a quantitative validation of the heat transfer results at high density ratios, spatially averaged magnitudes of the net heat flux reduction are compared to those of other authors. The present effectiveness data (from [13]) and heat transfer coefficient data were averaged over the downstream region from $x/D=3$ to 15. They were processed using a constant value of $\theta=1.75$ and the equation of Sen et al. [8] given by

$$\mathrm{NHFR}=1-\frac{h_f}{h_0}(1-\eta\theta) \tag{12}$$

Displayed in Fig. 10 are the results for cylindrical hole ejections with a hole spacing of $s/D=3$ of Sen et al. [8] and Bell et al. [10], compared to the results of the present study as displayed in Fig. 5. The data are plotted with respect to the momentum ratio. The present data are situated well in between the data points given

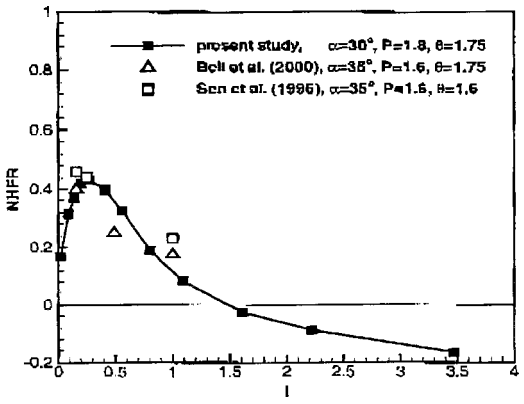

Fig. 10 Spatially averaged net heat flux reduction

by the other authors. For lower momentum ratio, where density ratio effects are weak, an excellent match of all data is evident. At higher momentum ratios, the trends are still consistent, while slight deviations of the absolute values occur. These deviations are due to different experimental boundary conditions as different density ratios for the determination of h and h_f values, as well as slightly different ways of spatial averaging.

For such typical configurations, an attached coolant jet with only minor heat transfer augmentation can be expected up to a momentum ratio of $I=0.5$. Complete jet lift-off and penetration into the hot gas flow, producing severe heat transfer augmentation, is present beyond $I=1.2$. At momentum ratios between these limits, a transition pattern with both vortex traces and turbulent wake components can be found, causing a moderate heat transfer augmentation. Important variations from the patterns for typical conditions displayed in Fig. 6 could be observed for specific combinations of the ejection parameters.

With an ascending ejection angle and successively diminishing downstream momentum of the ejected coolant, the vortex structures on the surface become shorter. The development of the vortex systems and subsequent coolant mixing processes have to take place within this shorter downstream length. At the extreme of a normal ejection, all heat transfer enhancing flow effects are confined to within $20D$ downstream of the ejection location. Then, caused by the zero downstream momentum of the coolant, large velocity gradients in the flowfield are present and the flow situation then is governed by the violent turbulent jet into hot gas mixing. From the heat transfer patterns it can be derived that the development of compact streamwise vortices that could lift from the surface is spoiled at moderate and prevented at high blowing rates, while the settling of the flow is enhanced.

The downstream heat transfer patterns indicate that the hole pitch is scaling the streamwise vortex structures of the jet flow farther downstream of the ejection location. The surface patterns of small pitch ejection document a domination of the flow situation by intense interaction of the adjacent coolant jets, even at low blowing rates. The development of the single jet in crossflow mixing at the ejection location appears impeded. At moderate blowing rates surface structures from the jet in crossflow mixing are missing; thus, the single jet vortices may not contact the surface. Downstream, the heat transfer patterns indicate the formation of a dense and stable layer of small-scaled, high-vorticity streamwise swirls. At large pitch ejection, adjacent jet interaction seems to be merely present. Flow perturbations causing heat transfer augmentation are restricted to a relatively small band in the centerline. According to their surface effects, the unaffected single jets very smoothly lift off the surface as the single jet in hot gas crossflow mixing is freely developing. Penetration of the jet into the hot gas flow occurs somewhat earlier. This was expected from the weak adjacent jet interaction reducing the hot gas crossflow impact on the coolant jets. Lower density ratios evoke moderate velocity

ratios at lower blowing rates, causing less intense jet in crossflow mixing close to the ejection. Surface structures similar to the large pitch ejection suggest that the development of the vortices is taking place farther from the surface. Downstream, the effect of the interaction of the adjacent high-momentum jets is more pronounced throughout all blowing rates of the low-density-ratio case. At high blowing rates the larger normal momentum of the coolant jet seems not to be transposed into a higher jet trajectory. The high velocity ratio enhances the adjacent jet vortex interaction and vortex motion. Subsequently, the rising crossflow impact keeps the jets near to the surface while the surface heat transfer is enhanced by the intensified vorticity.

In general, the observations indicate a major dependence of the single row ejection surface patterns on the two governing factors that are mixing of the coolant jet in the hot gas crossflow and adjacent jet interaction. The jet in crossflow mixing governs the flow situation at lower blowing rates and near the ejection location. The adjacent jet interaction is dominant farther downstream and grows more important upstream at high blowing rates and low pitch. The transition patterns as displayed in Fig. 6 are only present at typical shallow angle ejections. They occur as the adjacent jet interaction effects near the ejection grow to the same order as the mixing effects without one of the mechanisms getting dominant. Since this situation is present for typical applications, the interplay of both effects has to be considered for the prediction of the cooling potential of a specific configuration.

The effects of turbulence variations on the heat transfer coefficient augmentation were not examined in this investigation. However, since hot gas turbulence is expected to impact mainly on the mixing of coolant jet and hot gas flow, the results imply how elevated turbulence levels should affect certain configurations. In situations where the flow is dominated by adjacent jet interaction effects, as in the case of small pitch ejection, no significant turbulence dependence is expected. This applies also for very intense mixing situations creating excessive turbulence themselves, i.e., normal ejection. Increased turbulence is believed to have an adverse effect on the formation of compact vortex structures and to promote spreading and settling of the coolant flow, especially at low blowing rates. These assumptions are supported by a study of the turbulence effects on the flowfield by Burd et al. [4]. With respect to the unblown high-turbulence case, less significant heat transfer augmentations are expected.

Conclusions

The local heat transfer coefficients downstream of a row of cylindrical holes were investigated, emphasizing application-typical high-density ratio conditions. A high-resolution thermography system provided detailed two-dimensional surface temperature data for the processing of local heat flux by a Finite Element analysis. Correction of radiation effects ensured accurate surface heat transfer coefficient data. The superposition approach was applied to sets of measurements with identical flow parameters, i.e., identical coolant to hot gas density ratio. They were used to extrapolate the wall temperature independent local heat transfer coefficients h_f of the high density ratio flow, accounting for all effects of variable properties within the cooling film.

The local heat transfer coefficients were far from the situation without coolant ejection and highly dependent on the specific blowing situation. Especially at elevated blowing rates in typical configurations, a pronounced increase of the heat transfer coefficients up to 120 percent of the unblown reference over large downstream distances was found. This is confirmed by results of other previous studies. Specific ejection parameter combinations of application relevant configurations produced an increase of more than 150 percent within 20 hole diameters from the ejection.

Besides general effects of heat transfer augmentation, characteristic patterns of the heat transfer coefficient distribution could be identified. Excellent observations of the jet lift-off effects and mixing phenomena on the heat transfer coefficient from the present results confirm previous models and observations for typical applications. From the systematic study of these heat transfer patterns for a wide range of parameters and based on the known primary flow structures, the underlying flow behavior of specific configurations could be traced. The presented data document significant and systematic changes in the flow behavior with the change from a shallow ejection angle to normal ejection as well as at low pitch ejection. Deviations from the typical behavior encountered in film cooling effectiveness examinations at these conditions could be explained.

The observed heat transfer patterns coincide with those of other authors (e.g., Ammari et al. [26], Ekkad et al. [27], Goldstein et al. [28]). Further quantitative analysis of the data is to be undertaken to enable the prediction of the heat transfer effect of discrete hole ejection on the base of laterally averaged data for design purposes. The high-resolution local heat transfer data are suited to be compared with computational results of heat flux and heat transfer coefficients in the presence of film cooling. They can thus be used for the validation of CFD codes for the prediction of the heat transfer to film-cooled gas turbine components, as well as for the development of refined turbulence and wall models.

Acknowledgments

This study was partly funded by the Ministry of Research and Technology of the Federal Republic of Germany through the German joint research program AG Turbo and Siemens AG/KWU, Mülheim a. d. Ruhr, Germany. Very special thanks are due to Professor P. M. Ligrani of the University of Utah for his discussions and advice on high-density-ratio ejection effectiveness and heat transfer.

Nomenclature

D = ejection hole diameter, m
h = heat transfer coefficient, W/m^2K
I = momentum ratio, Eq. (8)
L = ejection hole length, m
M = blowing rate, defined in Eq. (6)
q = heat flux, W/m^2
R = coolant to hot gas density ratio, Eq. (7)
Re = Reynolds number
s = ejection hole spacing, m
T = temperature, K
Tu = turbulence intensity
u = velocity, m/s
x = streamwise coordinate, m
y = wall normal coordinate, m
z = lateral coordinate, m
α = blowing angle
δ_1 = displacement thickness of the boundary layer, m
ε = radiative emissivity
η = film cooling effectiveness, Eq. (1)
θ = dimensionless temperature ratio, Eq. (4)
ρ = density, kg/m^3
σ = Stefan–Boltzmann constant $= 5.67 \times 10^{-8}$ W/m^2K^4

Subscripts

AW = adiabatic wall
C = coolant
conv = convective transferred
D = hole diameter based
f = cooling film
G = hot gas
max = maximum
rad = radiative transferred
s = starting length
a = ambient
W = wall

References

[1] Lee, S. W., Lee, J. S., and Ro, S. T., 1994, ''Experimental Study on the Flow Characteristic of Streamwise Inclined Jets in Crossflow on Flat Plate,'' ASME J. Turbomach., **116**, pp. 97–116.

[2] Pietrzyk, J. R., Bogard, D. G., and Crawford, M. E., 1989, ''Hydrodynamic Measurements of Jet in Crossflow for Gas Turbine Film Cooling Applications,'' ASME J. Turbomach., **111**, pp. 139–145.

[3] Pietrzyk, J. R., Bogard, D. G., and Crawford, M. E., 1990, ''Effect of Density Ratio on the Hydrodynamics of Film Cooling,'' ASME J. Turbomach., **112**, pp. 437–443.

[4] Burd, S. W., Kaszeta, R. W., and Simon, T. W., 1998, ''Measurements in Film Cooling Flows: Hole L/D and Turbulence Intensity Effects,'' ASME J. Turbomach., **120**, pp. 791–798.

[5] Thole, K., Gritsch, M., Schulz, A., and Wittig, S., 1998, ''Flow Field Measurements for Film-Cooling Holes With Expanded Exits,'' ASME J. Turbomach., **120**, pp. 327–336.

[6] Rydholm, H. A., 1998, ''An Experimental Investigation of the Velocity and Temperature Fields of Cold Jets Injected Into a Hot Crossflow,'' ASME J. Turbomach., **120**, pp. 320–326.

[7] Kohli, A., and Bogard, D. G., 1997, ''Adiabatic Effectiveness, Thermal Fields, and Velocity Fields for Film Cooling With Large Angle Ejection,'' ASME J. Turbomach., **119**, pp. 352–358.

[8] Sen, B., Schmidt, D. L., and Bogard, D. G., 1996, ''Film Cooling With Compound Angle Holes: Heat Transfer,'' ASME J. Turbomach., **118**, pp. 800–806.

[9] Schmidt, D. L., Sen, B., and Bogard, D. G., 1996, ''Film Cooling With Compound Angle Holes: Adiabatic Effectiveness,'' ASME J. Turbomach., **118**, pp. 807–813.

[10] Bell, C. M., Hamakawa, H., and Ligrani, P. M., 2000, ''Film Cooling From Shaped Holes,'' ASME J. Heat Transfer, **122**, pp. 224–232.

[11] Sgarzi, O., and Leboeuf, F., 1997, ''Analysis of Vortices in Three-Dimensional Jets Introduced in a Cross-Flow Boundary Layer,'' ASME Paper No. 97-GT-517.

[12] Walters, D. K., and Leylek, J. H., 2000, ''A Detailed Analysis of Film Cooling Physics Part I: Streamwise Ejection With Cylindrical Holes,'' ASME J. Turbomach., **122**, pp. 102–112.

[13] Baldauf, S., Schulz, A., and Wittig, S., 2001, ''High-Resolution Measurements of Local Effectiveness by Discrete Hole Film Cooling,'' ASME J. Turbomach., **123**, No. 4.

[14] Metzger, D. E., and Fletcher, D. D., 1971, ''Evaluation of Heat Transfer for Film-Cooled Turbine Components,'' ASME J. Eng. Power, **8**, pp. 181–184.

[15] Choe, H., Kays, W. M., and Moffat, R. J., 1974, ''The Superposition Approach to Film-Cooling,'' ASME Paper 74-WA/HT-27.

[16] Jones, T. V., 1991, ''Definition of Heat Transfer Coefficients in the Turbine Situation,'' in: *Turbomachinery: Latest Developments in a Changing Scene*, Paper C423/046, Proc. IMechE, pp. 201–206.

[17] Gritsch, M., Baldauf, S., Martiny, M., Schulz, A., and Wittig, S., 1999, ''The Superposition Approach to Local Heat Transfer Coefficients in High Density Ratio Film Cooling Flows,'' ASME Paper No. 99-GT-168.

[18] Kays, W. M., and Crawford, M. E., 1980, *Convective Heat and Mass Transfer*, McGraw-Hill, New York.

[19] Loftus, P. J., and Jones, T. V., 1983, ''The Effect of Temperature Ratios on the Film Cooling Process,'' ASME J. Eng. Power, **105**, pp. 615–620.

[20] Forth, C. J. P, Loftus, P. J., and Jones, T. V., 1985, ''The Effect of Density Ratio on the Film Cooling of a Flat Plate,'' *Heat Transfer and Cooling in Gas Turbines*, AGARD-CP-390, Paper 10.

[21] Forth, C. J. P., and Jones, T. V., 1986, ''Scaling Parameters in Film Cooling,'' *Proc. 8th Int. Heat Transfer Conf.*, Vol. 3, pp. 1271–1276.

[22] Teekaram, A. J. H., Forth, C. J. P., and Jones, T. V., 1989, ''The Use of Foreign Gas to Simulate the Effects of Density Ratios in Film Cooling,'' ASME J. Turbomach., **111**, pp. 57–62.

[23] Kumada, M., Hirata, M., and Kasagi, N., 1981, ''Studies of a Full-Coverage Film Cooling. Part 2: Measurement of Local Heat Transfer Coefficient,'' ASME Paper No. 81-GT-38.

[24] Goldstein, R. J., and Taylor, J. R., 1982, ''Mass Transfer in the Neighborhood of Jets Entering a Crossflow,'' ASME J. Heat Transfer, **104**, pp. 715–721.

[25] Cho, H. H., and Goldstein, R. J., 1995, ''Heat (Mass) Transfer and Film Cooling Effectiveness With Injection Through Discrete Holes: Part II—On the Exposed Surface,'' ASME J. Turbomach., **117**, pp. 451–460.

[26] Ammari, H., Hay, N., and Lampard, D., 1990, ''The Effect of Density Ratio on the Heat Transfer Coefficient From a Film-Cooled Flat Plate,'' ASME J. Turbomach., **112**, pp. 444–450.

[27] Ekkad, S. V., Zapata, D., and Han, J. C., 1997, ''Heat Transfer Coefficients Over a Flat Surface With Air and CO_2 Injection Through Compound Angle Holes Using a Transient Liquid Crystal Image Method,'' ASME J. Turbomach., **119**, pp. 580–586.

[28] Goldstein, R. J., Jin, P., and Olson, R. L., 1999, ''Film Cooling Effectiveness and Mass/Heat Transfer Downstream of One Row of Discrete Holes,'' ASME J. Turbomach., **121**, pp. 225–232.

[29] Gritsch, M., Schulz, A., and Wittig, S., 1998, ''Heat Transfer Coefficient Measurements of Film-Cooling Holes With Expanded Exits,'' ASME Paper No. 98-GT-28.

[30] Martiny, M., Schiele, R., Gritsch, M., Schulz, A., and Wittig, S., 1996, ''In Situ Calibration for Quantitative Infrared Thermography,'' Quirtë96 Eurotherm Seminar No. 50, Stuttgart, Germany, Sept. 2–5.

[31] Jacobsen, K., 1987, ''Experimentelle Untersuchungen zum Durchflufl und Wärmeübergang in Durchblick- und Stufenlabyrinthen,'' Dissertation, Institut für Thermische Strömungsmaschinen, Universität Karlsruhe.

[32] Gnielinski, V., 1975, Forschung im Ingenieurswesen 41, No. 1.

High-Resolution Measurements of Local Effectiveness From Discrete Hole Film Cooling

S. Baldauf

A. Schulz

S. Wittig

Lehrstuhl und Institut für Thermische Strömungsmaschinen, Universität Karlsruhe (TH), 76128 Karlsruhe, Germany

Local adiabatic film cooling effectiveness on a flat plate surface downstream a row of cylindrical holes was investigated. Geometric parameters such as blowing angle and hole pitch, as well as the flow parameters blowing rate and density ratio, were varied in a wide range emphasizing engine relevant conditions. IR thermography was used to perform local measurements of the surface temperature field. A spatial resolution of up to seven data points per hole diameter extending to 80 hole diameters downstream of the ejection location was achieved. Since all technical wall materials have a finite thermoconductivity, a procedure for correcting the measured surface temperature data based on a Finite Element analysis was developed. Heat loss over the back and remnant heat flux within the test plate in lateral and streamwise directions were taken into account. The local effectiveness patterns obtained are systematically analyzed to quantify the influence of the various parameters. As a result, a detailed description of the characteristics of local adiabatic film cooling effectiveness is given. Furthermore, the locally resolved experimental results can serve as a data base for the validation of CFD codes predicting discrete hole film cooling. [DOI: 10.1115/1.1371778]

Introduction

Film cooling of thermally highly loaded components represents losses to the gas turbine process. To improve the thermal efficiency of modern gas turbines, it is necessary to reduce the amount of cooling air used while aiming at higher turbine inlet temperatures. The idea of film cooling is to establish a closed film of cooling air on a surface to prevent it from direct hot gas exposure. Because of restrictions arising from structural integrity and manufacturing economy of turbine blades, film cooling is usually realized by ejecting the cooling air from discrete holes. The flow patterns induced by the turbulent mixing process of the cooling air jets in the hot gas crossflow are very complex. Highly resolved flowfield measurements for typical cases of inclined jets in crossflow were performed by Lee et al. [1], illustrating the jet and main flow interaction. Detailed flowfield measurements and additional data on turbulence development of the jet ejection are provided by Pietrzyk et al. [2,3], Burd et al. [4], and Thole et al. [5] for similar ejection situations. Highly resolved experimental data on the temperature fields of this type of flows are given by Ryndholm [6] and Kohli and Bogard [7]. A computational study of Sgarzi and Leboeuf [8], using a highly refined grid, provides important information on the small-scale vortex structures of a normal ejection baseline case. Other authors, e.g., Walters and Leylek [9], show the transformation of such structures and the resulting flowfield effects with computations of inclined jet ejection cases. From these and other authors' investigations, the basic large and small-scale flowfield phenomena of inclined jets in crossflow, like jet liftoff and entrainment of hot gas under the coolant jet and their mechanisms, are known.

In the present paper, the local surface temperature effect of film cooling is discussed. It is quantified by the adiabatic effectiveness

$$\eta = \frac{T_G - T_{AW}}{T_G - T_C} \tag{1}$$

Since cooling effectiveness represents only half of the information necessary for fully describing film cooling heat transfer, a companion paper focuses on the local heat transfer coefficients caused by the film cooling situation considered [10]. Most of the research work on film cooling from discrete holes concentrates on overall or laterally averaged effectiveness. However, to get an in-depth understanding of the physical phenomena of film cooling from discrete holes, precise local data from the ejection down to the film region are required. Measurements of local surface values are provided, for example, by Sen et al. [11], Schmidt et al. [12], Ekkad et al. [13], Goldstein et al. [14], Lutum and Johnson [15], Drost and Bölcs [16], and Bell et al. [17]. Effectiveness data of sufficiently high resolution to retrieve the measured and calculated temperature field effects on the surface, e.g., Gritsch et al. [18] in the near vicinity of a single ejection hole, are rare. Usually only a few flow cases are examined, and the majority of the published investigations concentrate on the ejection angles of 30–35 deg. The computation of film cooling configurations still suffers from problems of inadequate turbulence modeling and limited computational resources. Local experimental data are needed for the development and validation of improved models. Furthermore, reliable information is needed for flow cases not considered typical. Especially the process of jet liftoff under turbine-like high density ratios evoked by a continuous increase of the coolant mass flow must be understood for the film cooling design. Also data on nonoptimal configurations, such as steep ejection angles and large hole spacings, are required, since blade geometry and manufacturing constraints can necessitate their use.

The film cooling of a flat plate is investigated using a row of holes. Special attention is given to correct representation of the temperature phenomena close to the ejection holes. The material of the present study represents an important extension of surface effectiveness results already in the literature (e.g., [13,19,14,20]) because: (*i*) new spatially recorded data are given with high local resolution as blowing rate, density ratio, blowing angle, hole spacing, and turbulence intensity are each varied independently, (*ii*) the spatially resolved effectiveness data at all geometric conditions are given for density ratios as high as 1.8, which corresponds to values used in operating gas turbine engines, and (*iii*) all data are locally corrected for conduction effects along and within the solid material using a specially adapted three-dimensional Finite Element method. These data are valuable in providing infor-

Contributed by the International Gas Turbine Institute and presented at the 44th International Gas Turbine and Aeroengine Congress and Exhibition, Indianapolis, Indiana, June 7–10, 1999. Manuscript received by the International Gas Turbine Institute February 1999. Paper No. 99-GT-46. Review Chair: D. C. Wisler.

mation on optimal flow conditions for best film cooling protection, and as a data base for CFD code validation and development of refined numerical models.

Experimental Facilities

The experimental method used in this study is the application of realistic temperature ratios to obtain engine relevant density ratios of cooling air and hot gas. This imposes the realistic heat flux direction and temperature gradients from the hot gas toward the surface. To guarantee maximum accuracy, steady-state experiments were executed in a scaled-up geometry, conceiving a similar flowfield as in real applications. The use of foreign gas or mass transfer analogy methods [21] were not considered to avoid effects on the flow properties spoiling the flow similarity [22].

The experiments were conducted in an open circuit hot wind tunnel of the Institute for Thermal Turbomachinery at the University of Karlsruhe. A schematic of the experimental plant is shown in Fig. 1. Air is delivered by a radial compressor and split into main and secondary flow, where the secondary flow rate ranges from about 0.2 to 2.5 percent of the total flux. The mass flux of both flows is controlled independently by valves and measured by orifices. The main flow passes a 270 kW electric heater, enabling hot gas temperatures of 550 K at mass flow rates of 1.3 kg/s. The hot gas temperature is equalized in a static mixer and the hot gas flow subsequently settled by a series of grids and a flow straightener before entering the test section through a high contraction ratio nozzle. Two different sets of grids and flow straightener produce levels of the turbulence intensity in the entrance of the test section of 1.5 and 4 percent, respectively. The cooling air is cooled down from compressor exit conditions to ambient temperature level in a cooler. The cooling air is delivered into a coolant plenum before it enters the test section through the ejection holes. The ejection hole diameter is $D=5$ mm and the cross-sectional area of the test section (Fig. 2) is 21×44 hole diameters. The different ejection geometries are realized as modules that fit into the coolant plenum duct. Since the main interest of this study was the influence of the hole spacing and blowing angle, hole length was kept constant. The hole entrance is perpendicular to the hole axis for all blowing angles. The inlet edge is rounded with a radius of $1D$ to reduce effects of streamline curvature on secondary flows within the hole, to keep the hole exiting flow independent from the inlet conditions.

The instrumental test plate is connected directly to the ejection module and extends $82D$ downstream of the ejection location. The test plate and ejection module have a thickness of $6D$ and are made from the same semi-crystalline thermoplast (TECAPEK). The material was chosen because of its combination of a low thermal conductivity of 0.3 W/mK and good machinability with thermoresistance to temperatures up to 550 K. With the addition of a further $6D$ thick insulation on the back of the test plate, a good approximation of an adiabatic surface is attained. The cooling air temperature was measured by a thermocouple in the plenum. By probe measurements of the coolant temperature at the hole exit, T_C was correlated with the plenum temperature. For the range of blowing rates and hot gas temperatures examined, the coolant temperatures at the hole exits were found to vary less than 1 percent of the coolant to hot gas temperature difference for different holes.

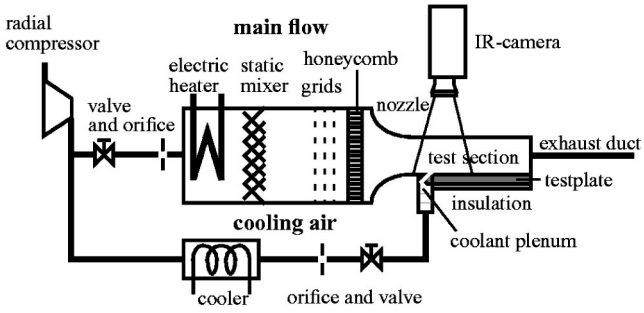

Fig. 1 Hot wind tunnel scheme

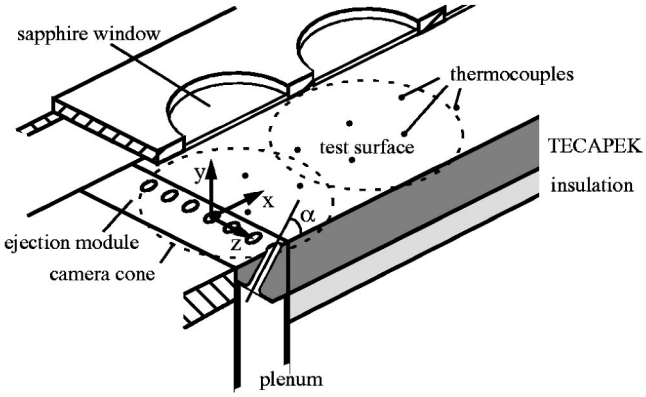

Fig. 2 Test section

The measuring technique to acquire the surface temperature field of the test plate is the infrared thermography. Thus, the top wall of the test section is equipped with infrared transparent sapphire windows. The arrangement of the windows and the IR camera position allow the overlapping of the camera cones on the test surface to obtain thermo-optical access over its entire length. The ejection module and test surface are coated with a constant emissivity dye to assure a uniform radiation situation. The measured radiation intensity is influenced by a number of uncertain boundary conditions as a reflection of the inner test section walls from the observed test surface as well as transmission and emission of the hot sapphire window. A set of 16 0.25 mm thermocouples with varying lateral position of $3.6D$ to $10.6D$ from the channel centerline is mounted flush with the test surface. For an *in situ* calibration [23], five to eight thermocouple measurements points were used to fit the temperature processing parameters of the IR camera images. This calibration procedure accounts for all effects of reflection of the surrounding channel walls from the test surface as well as transmission and emission from the sapphire windows. An additional set of thermocouples is installed on the back of the test plate to control temperature conditions and heat leakage. For every test run operating point, IR images, and thermocouple temperatures were recorded simultaneously. The accuracy of the thermocouple measurement was within ±0.2 K; surface temperatures on the calibrated IR images were captured within 1 percent of the actual coolant to hot gas temperature difference.

The operating conditions and the range of parameters are given in Table 1. Hot gas velocity was held constant at $u=60$ m/s for all runs, resulting in a constant boundary layer thickness at the ejection location. Velocity profiles showed a typical turbulent boundary layer pattern and could be well described with a 1/6 power law. Coolant temperature was about $T_C=300$ K for all runs, so that the density ratio was adjusted by the hot gas temperature. The flow cases of the present study are specified by the dimensionless geometry and flow parameters. Special interest was given to the variation of the flow parameters blowing rate

$$M=\frac{(\rho u)_C}{(\rho u)_G} \tag{2}$$

and density ratio

$$P=\frac{\rho_C}{\rho_G} \tag{3}$$

Table 1 Operating parameters

Geometry:	$\alpha = 30, 60, 90$ deg
	$s/D = 2, 3, 5$
	$L/D = 6$
Hot gas flow:	$\mathrm{Re}_D = 6800–14000$
	$\delta_1/D = 0.1$
	$Tu = 1.5, 4$ percent
Coolant flow:	$M = 0.2–2.5$
	$P = 1.2, 1.5, 1.8$

These parameters can be combined to form the momentum ratio:

$$I = \frac{(\rho u^2)_C}{(\rho u^2)_G} \tag{4}$$

Density ratio was varied from close to unity up to engine relevant conditions to bridge the gap to the mass of film cooling investigations conducted at low temperature levels. The turbulence in the test section was a background channel flow turbulence with a typical large length scale. Most runs took place at low turbulence level. However, additional runs with elevated turbulence conditions were made for particular configurations.

Data Processing

IR camera data were acquired for a range of several hole pitches close to the middle of the test surface, dependent on the hole spacing. The IR camera signal was averaged over several seconds. A resolution of 1.45 pixels per millimeter, i.e., better than 7 pixels per hole diameter, was achieved, resulting in a total resolution of 22 data points across a typical hole pitch of 3 diameters. The full information of a periodically uniform row of holes is contained in a stripe of 1/2 hole pitch, extending between *z*-normal symmetry planes in the hole centerline and in the midspan. For an even number of complete half pitches in the IR image, the temperatures from the surface points, with the same streamwise coordinate and identical distance from the according centerline, were arithmetically averaged. In this way the IR information over several hole pitches was condensed to one-half pitch stripe, equalizing stochastic local perturbations.

To obtain local values of the adiabatic surface effectiveness, corrections to the locally measured surface temperatures are required, which are described in the following. As indicated earlier, the test plate material has a finite thermal conductivity. Despite almost perfect insulation of the test plate, remnant heat fluxes in the lateral and longitudinal directions within the test plate from hot to cold regions of the surface are present. They cause a flattening of the temperature patterns at the test surface with respect to adiabatic conditions. Within the local regions of hot and cold surface temperatures, these heat fluxes are transferred to and from the surface by radiation and convection, as indicated in Fig. 4. In fact, no technical surface offers ideal adiabatic conditions in a real temperature ratio experiment. Thus, a correction method was developed, where the internal heat fluxes of the test plate computed by an FE analysis are used to compensate the deviations from the adiabatic state at the test surface.

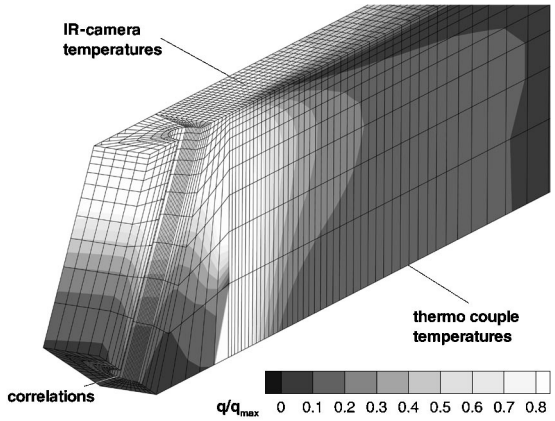

Fig. 3 FE analysis of the heat flux, $\alpha = 60$ deg, $s/D = 3$

Figure 3 shows a typical computational model and result of the heat flux analysis. It extends over a half pitch slice of the ejection module and the test plate. The reduced half pitch data of the IR image were applied as temperature boundary condition on the test surface of the model. The streamwise interpolation of the thermocouple measurement on the back of the test plate provided the laterally constant bottom surface temperature of the model.

Heat transfer coefficients from correlations for tube inlet flow and developing flow over a flat plate [24] were used as boundary conditions on the inner hole surface and on the plenum side walls of the ejection module, respectively. The complex heat transfer problem in the plenum and ejection hole was approximated by applying the averaged heat transfer coefficients based on the mean flow velocities as a constant on the regarded surfaces, with the coolant temperature as a reference. All other surfaces of the model were considered adiabatic. The result of the heat flux computation was the three-dimensional internal heat flux within the plate and, as an excerpt, the heat flux at the test surface. Figure 4 shows the local heat flux situation at the actual test surface. The temperature an adiabatic wall would attain is the temperature of the cooling film near the wall. In the presence of radiative and conductive heat flux, the surface will generally adopt a different temperature from the flow above. At a given surface location the heat flux into the wall q_W is balanced by convective and radiative heat flux at the surface

$$q_W = q_{\mathrm{conv}} + q_{\mathrm{rad}} \tag{5}$$

Radiative heat transfer from the surrounding channel walls can be approximated by a simple enclosed body approach

$$q_{\mathrm{rad}} = \sigma \varepsilon_W (T_a^4 - T_W^4) \tag{6}$$

With a given convective heat transfer coefficient h, the local adiabatic wall temperature can be calculated as

$$T_{AW} = T_W + \frac{q_W - q_{\mathrm{rad}}}{h} \tag{7}$$

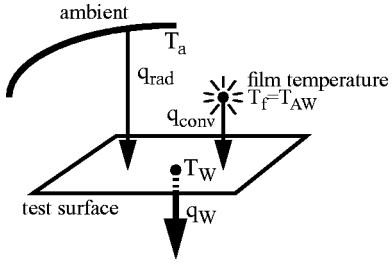

Fig. 4 Local heat flux balance at the test surface

The actual local heat transfer coefficient is the heat transfer coefficient h_f describing the convective heat flux in the presence of film cooling

$$q_{\text{conv}} = h_f (T_{AW} - T_W) \tag{8}$$

As long as precise local h_f data are not available, it was considered to be sufficient to use the heat transfer coefficient without film cooling h_0 within Eq. (7), which can be correlated for flat plate conditions [25] with

$$h_0 = (\rho u c_P)^{0.03} \text{Re}^{-0.2} \text{Pr}^{-0.67} \tag{9}$$

Note that the heat transfer coefficients h_0 were used only to correct the almost adiabatic wall conditions of the experiment to yield a precise result of the local adiabatic effectiveness. The experimental setup was designed to minimize all heat flux effects on the test surface. The actual local T_a reference within Eq. (6) was correlated to the measured channel wall temperature. It was found in experiments without blowing, where T_a was adjusted to result in the presumed zero effectiveness value after the correction procedure.

Deriving from the known error of the surface temperature data, an error of the FE-computed local heat flux into the wall q_W of 1 percent was achieved. The local ambient temperature T_a was determined with an error of 2 percent. Since effects of the coolant ejection on the heat transfer coefficient were not taken into account, an error band of 10 percent for h_0 was assumed, covering the majority of the examined ejection cases. In unfavorable situations this 10 percent error of h_0 produces an error of up to 20 percent of the correction term in Eq. (7). Deviations of the heat transfer coefficient h_f from h_0 even larger than 10 percent occur in situations of high blowing rates, when simultaneously the wall temperature gradients and resulting wall internal heat fluxes diminish [10]. The correction term in Eq. (7) then is very inexact, but its absolute value becomes very small compared to the adiabatic wall temperature. Therefore, its contribution to the error of the adiabatic wall temperature remains low. Even in cases of heat transfer coefficients up to $h_f = 1.6 h_0$ the resulting error of the local adiabatic film cooling effectiveness h stayed well below 5 percent for the examined combinations of the wall heat flux and the belonging temperature correction.

Results

The results of the effectiveness measurements are displayed as surface contour plots of the corrected local adiabatic effectiveness. For reasons of clarity, the actual results available for one half pitch are mirrored at the hole centerline to result in a full pitch picture. Position and height of the effectiveness peak in the centerline are quoted and the peak is indicated as a triangle symbol in the plots. The results are presented with respect to the blowing rate as the important design parameter; values of the momentum ratio are stated additionally.

Figure 5 shows a set of measurements for a shallow ejection angle, a typical hole spacing, and high density ratio at low turbulence level. The joint of the ejection module and the test surface is visible at $x/D = 2$ by slight perturbations of the effectiveness contours. At high blowing rates uncertain back and hole internal boundary conditions on the ejection module cause slightly too high values of the local effectiveness from the FE-heat transfer analysis.

Typical variations of the effectiveness footprint with the blowing rate are shown in Fig. 5. At low blowing rate ($M = 0.4$, $I = 0.09$) the jet is fully attached to the surface and a high peak effectiveness within a rather short region of intense cooling is present near the ejection. Downstream a fast decay of the effectiveness takes place. Increasing the blowing rate ($M = 0.6$, $I = 0.2$) yields higher coolant mass flux and, therefore, thermal capacity of the coolant jet. The intense cooled region extends downstream and the effectiveness decay is not that pronounced. Merging of adjacent jets starts at about $x/D = 5$ for low blowing rates.

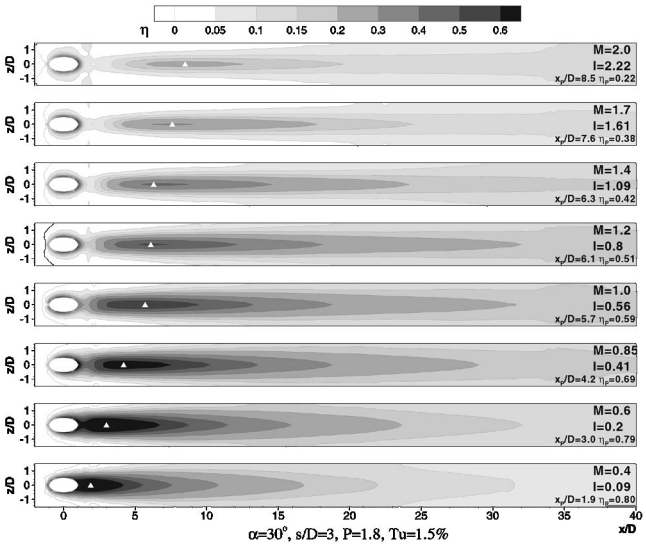

Fig. 5 Local adiabatic effectiveness distributions for typical application conditions

After raising the blowing rate to $M = 1.0$ ($I = 0.56$) the overall effectiveness reaches an optimum. While the intensely cooled region is still extending downstream, a significant decrease of the peak effectiveness can be observed. The intensely cooled region is moving away from the ejection hole. Beginning separation of the coolant jet at the hole rim by the increased coolant surface normal momentum drives the coolant away from the wall. Merging of adjacent jets shifts slightly downstream, and up to $45D$ it is necessary to achieve invariant temperatures in the lateral direction.

Increasing the blowing rate to $M = 0.2$ ($I = 2.22$), the intense cooled area narrows to the centerline and is shortened. The effectiveness peak decreases further. Merging of adjacent jets moves downstream to $x/D = 20$ and spanwise uniform temperatures are not found upstream of $x/D = 50$ at $M = 1.7$ ($I = 1.61$). Overall effectiveness decreases, showing a minimum at $M = 1.7$. Jet interaction seems to be intensified above $M = 1.7$, causing earlier merging and equalization at $x/D = 35$. At very high blowing rates an increase of the effectiveness far downstream is visible. The effectiveness peak moves continuously downstream while the blowing rates increase from very low to very high values.

Coolant jet separation at the hole exit takes place earlier for steep angle ejection than for shallow angle ejection, because the high surface normal momentum drives the coolant away from the wall (Fig. 6(*a*)). The effectiveness peaks occur closer to the ejection location and are significantly lower, while overall effectiveness is not decreased too much. Merging of adjacent jets and laterally uniform temperature profiles can be observed at somewhat lower downstream distances than at shallow angle ejection, indicating a more intense spreading of coolant in the hot gas flow. The lateral temperature profiles are even within $28D$ for low and high blowing rates and within $40D$ for moderate blowing rates, respectively. Maximum overall effectiveness and downstream extension of the intense cooling region, marking an optimum with respect to the blowing rate or the momentum ratio, is found earlier than for shallow angles at $M = 0.85$ ($I = 0.41$). At high blowing rates of $M = 1.7$ ($I = 1.61$) and above, the effectiveness far downstream is higher than for the shallow ejection angle. Therefore, the optimum condition is less pronounced at steep angle ejection.

For normal ejection, merging and establishment of laterally uniform temperature profiles take place at considerably lower downstream distances than for inclined angle injection because of very intense interaction of coolant and hot gas flows (Fig. 6(*b*)). Equable lateral temperatures are found downstream of $x/D = 24$ for all blowing rates. The effectiveness peak is located very close to

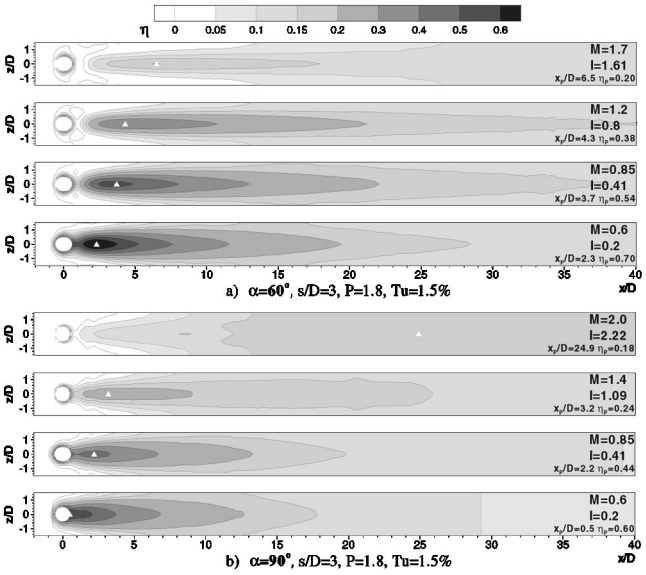

Fig. 6 Effect of the blowing angle on the local adiabatic effectiveness distributions

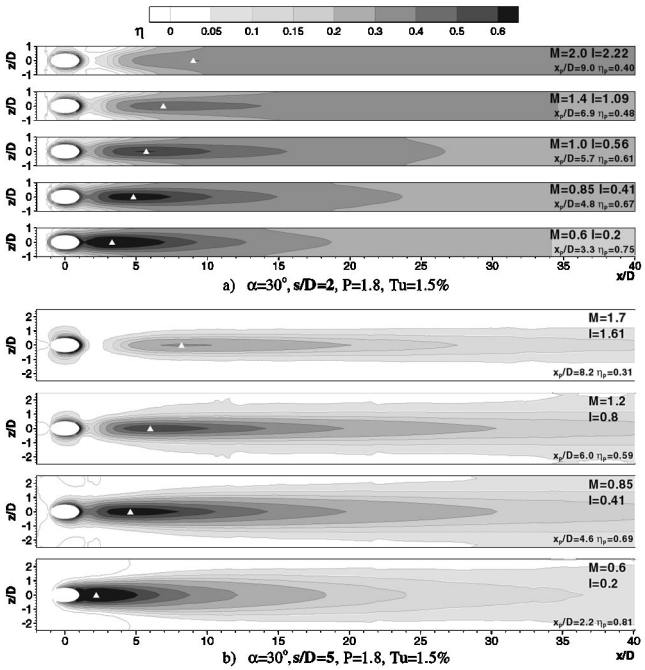

Fig. 7 Effect of the hole spacing on the local adiabatic effectiveness distributions

the ejection location except for high blowing rates. There, a pronounced local peak of the single jet on the surface is missing. The local effectiveness peaks are descending sooner with the increase of the blowing rate than for inclined ejection. While near the ejection location, the effectiveness decreases with an increase of coolant mass flux and momentum, it increases continuously downstream of about $x/D=13$. At high blowing rates, downstream effectiveness is higher than for the inclined ejection. Due to this development of the local effectiveness with blowing rate and momentum ratio, no optimum of the overall effectiveness can be spotted.

At lower blowing rates ($M=0.6$, 0.85; $I=0.2$, 0.41), the size of the intense cooled area and effectiveness peak are only affected by a variation of the hole spacing (Fig. 7). Peak effectiveness increases gradually with the hole spacing, while the peak location is slightly shifting downstream. Interaction of adjacent jets is much more intense for small pitch ejection, causing early merging at the ejection location (Fig. 7(*a*)). Lateral effectiveness variations are leveled upstream $x/D=24$. Likely to the normal ejection, downstream effectiveness increases continuously with the blowing rate without exhibiting an optimum overall effectiveness on the whole surface. No pronounced local peak of an attached jet can be found at high blowing rates, but the high overall effectiveness level of $\eta=0.4$ shows that no typical liftoff situation is present.

At large pitch ejection (Fig. 7(*b*)), merging of adjacent jets on the surface is completely suspended for low and high blowing rates; at moderate blowing rates it does not occur before $x/D=28$. Establishment of laterally uniform temperature profiles needs up to 78*D* at high blowing rates. For the typical hole spacing, a pronounced overall effectiveness optimum with respect to the blowing rate is present at $s/D=5$. The optimum is situated around $M=0.85$ ($I=0.41$), that is at somewhat lower values than for $s/D=3$. The effectiveness contours are also very similar to those of $s/D=3$ at high blowing rates, showing somewhat lower effectiveness peaks. At very high blowing rates no increase of the downstream effectiveness, as found for $s/D=3$, takes place within 40*D* downstream of the ejection.

Figure 8 displays the effect of low and medium density ratio levels on the effectiveness patterns. Optimal surface effectiveness conditions shift to significantly lower blowing rates with decreasing density ratio, being situated around $M=0.85$ for medium density ratios and well below $M=0.85$ for low density ratios. This is due to the increasing coolant velocity and momentum at constant blowing rate. From high to medium density ratio a significant downstream drift and decrease of the local effectiveness peak can be observed, as the optimum situation is shifted from above to below the blowing rate of $M=0.85$. Within the range of moderate blowing rates from $M=0.6$ to $M=1.2$ overall and peak effectiveness decrease significantly with a decrease of the density ratio, since the liftoff effects are more pronounced as the momentum ratio increases.

Elevated turbulence obviously enhances jet and hot gas interaction, causing less streamwise extension of the surface contours and, therefore, significantly earlier spanwise uniform temperatures (Fig. 9). The overall and peak effectiveness at conditions close to the optimum ($M=0.6$, 0.85; $I=0.24$, 0.48) are merely affected.

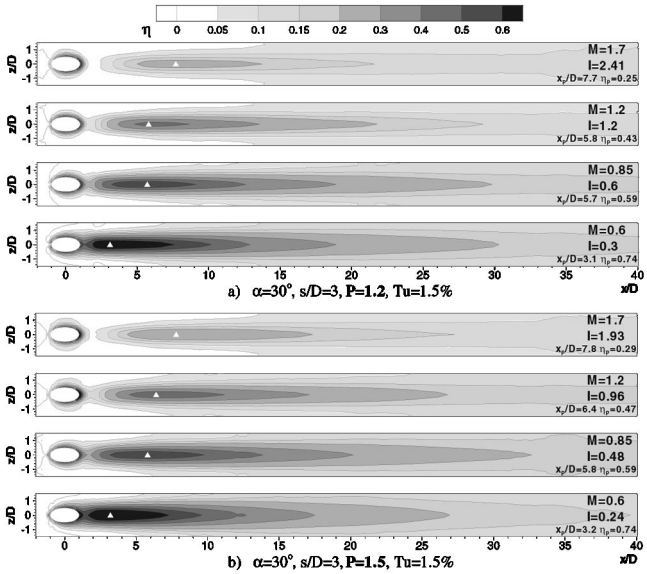

Fig. 8 Effect of the density ratio on the local adiabatic effectiveness distributions

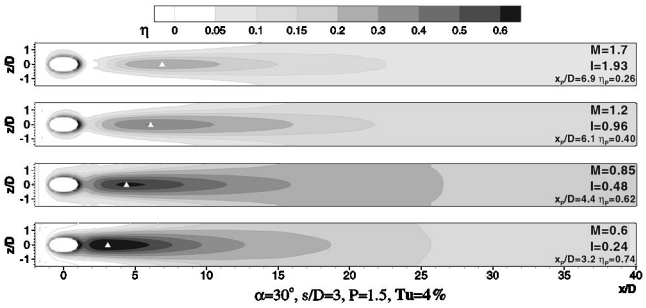

Fig. 9 Effect of augmented turbulence intensity on the local adiabatic effectiveness distributions

At higher blowing rates, the overall and peak effectiveness decrease with increased turbulence intensity. The peaks then are shifted upstream as the effectiveness deteriorates downstream because of the enhanced coolant mixing into the hot gas crossflow.

Discussion

Generally, the surface effectiveness is far from an even distribution over the cooled surface. The effectiveness patterns are dominated by a characteristic region of intense cooling in the hole centerline, being restricted approximately to the width of the ejection hole and showing a pronounced local effectiveness peak. Maximum effectiveness is not situated at the ejection location, but at some distance downstream of the ejection. Authors such as Metzger and Fletcher [26], Jabbari and Goldstein [27], Kruse [28], and Forth and Jones [29] suggested correlations for discrete hole film cooling adiabatic effectiveness, featuring a maximum starting value at the ejection location followed by an exponential decay downstream. Such models result in a significant overestimation of the film cooling potential close to the ejection location, and misleading predictions if used as boundary conditions in thermal analyses of cooled components. The surface patterns indicate that the typical situation is a zero effectiveness in the midspan between the ejection holes. An effectiveness augmentation can be found directly at the hole rim where near jet vortex phenomena, i.e., horseshoe vortices, transport coolant from the heat shear layer onto the surface, as shown by Sgarzi and Leboeuf [8] and Lee et al. [30]. Film cooling effectiveness develops downstream by spreading and merging of the coolant jets.

For the typical shallow angle ejection as presented in Fig. 5, an optimum of the achieved surface effectiveness with respect to the blowing rate or the momentum ratio is obvious. For a very low ejected coolant mass flux, the effectiveness diminishes very soon with increasing downstream distance. At high momentum ratios, only a faint temperature impact of the coolant is present on the surface as soon as the coolant jets have lifted off. For the typical configuration shown in Fig. 5, favorable effects of higher coolant mass flux and adverse effects of coolant liftoff balance each other around blowing rates of $M=1.0$ ($I=0.56$) to result in the optimum overall effectiveness. The lowest surface effectiveness and, therefore, the most extensive coolant loss can be found around $M=1.7$ ($I=1.61$) for this typical configuration. Here, the surface foot prints display least intense jet merging, giving the greatest potential for compact jets to lift off and rise high into the hot gas cross flow. At very high blowing rates the intensified coolant spreading, shown by earlier merging of adjacent jets, implies a more intense jet interaction, yielding an increase of the effectiveness far downstream.

As expected from a momentum or velocity ratio influence, the optimum conditions shift to higher blowing rates with an increase of the density ratio. The optimum momentum ratio indicating the beginning liftoff of the jets is about $I=0.5$ for typical applications. The mixing mechanisms at the borders of the exiting coolant jet that are coupled to the velocity gradient driven shear also have to be considered in their influence on jet liftoff. The characteristic coolant to hot gas velocity ratio at optimum conditions is about 0.56.

At larger blowing angles, the coolant is driven away from the wall because of higher surface normal momentum. Jet trajectory is higher and coolant to hot gas interaction is intensified, both having adverse influence on the effectiveness. At typical moderate blowing rates a decrease of the ejection angle from normal to steep angle ejection yields a significant increase of the effectiveness. The decrease to shallow angle ejection only yields a gradual increase of the effectiveness. Elevated turbulence levels also tend to reduce overall effectiveness by intensified coolant to hot gas interaction, especially at moderate blowing rates. Coupled to the coolant mass flux per surface unit, overall effectiveness is decreasing with increasing pitch. Compact and stable single jets are established at a hole spacing of $s/D=5$. The examination of larger pitches seems, therefore, not useful.

Despite significant differences in the resulting effectiveness, the optimum flow parameters of the configurations are very close for the investigated alterations of ejection angle, hole spacing, and turbulence. They are found at blowing rates around $M=0.85$ to $M=1.0$ and momentum ratios of $I=0.4$ to 0.5, respectively, indicating flow conditions of efficient coolant use. However, there are important exceptions to these general findings. These exceptions were correlated to specific flow situations, where the intense turbulence coolant mixing of distinct configurations led to deviations from the typical optimum of the overall effectiveness.

Such a flow situation occurs at normal ejection, where the coolant tends to rise from the surface even at low blowing rates. By immediate spreading in the hot gas flow and, subsequently, merging of adjacent jets, early coolant jet interaction is initiated. This mechanism seems to prevent the formerly expected extreme loss of effectiveness. At high blowing rates of 90 deg ejection, the intense merging and mixing of the normal jets in the hot gas crossflow produce higher downstream effectiveness than the ejection at shallow angles, while different surface patterns without local effectiveness show up. Another specific flow situation of intense coolant mixing is the ejection at low pitch. The intense interaction of the close coolant jets forces the constitution of a compact and stable film very close to the ejection. Here also surface patterns without local effectiveness peak occur at high blowing rates.

The resulting cooling film development of both the very steep angled and the low pitch ejection differs significantly from the usual models and has to be taken into consideration for the prediction of the adiabatic effectiveness. Both situations obviously restrict the amount of hot gas entrained into the cooling film near the ejection and prevent an optimum of the overall effectiveness. In these cases, high downstream effectiveness levels can be achieved by excessive coolant use.

Only limited interpretation of the coolant mixing mechanisms can be derived from the effectiveness distributions. The character and effects of the jet in crossflow mixing and the adjacent jet interaction become much clearer in the discussion of the local heat transfer coefficient patterns, presented in the companion paper of Baldauf et al. [10].

Conclusions

The surface effects of the film cooling flow from a row of cylindrical holes were investigated by means of the local adiabatic film cooling effectiveness emphasizing typical high density ratio conditions. The use of a high-resolution thermography system provided detailed two-dimensional surface temperature data. Careful correction of the test plate conductivity and radiation by a Finite Element analysis ensure accurate adiabatic effectiveness data, including the close vicinity of the ejection holes. The systematic study of the effectiveness footprints based on the known elementary flow structures revealed characteristic mixing

schemes. It enables better understanding and an approach to optimized design of discrete hole film cooling configurations.

The present investigation indicates optimum flow conditions for efficient cooling for a substantial range of configurations. The optimum conditions are confined to a small band of blowing rates around $M=0.85$ to 1.0 and momentum ratios of $I=0.4$ to 0.5, respectively. They describe the specific situation of coolant ejection very close to the beginning of coolant jet liftoff. The presented data document that significant and systematic changes in the mixing behavior can be observed with the change from a shallow ejection angle to normal ejection, as well as at low pitch ejection. In these cases, intense jet interaction prevents excessive coolant loss into the hot gas flow. These observations are very useful for the interpretation of the dependence of the flow situation on geometric parameters and will be necessary for the formulation of refined correlations.

The surface effectiveness data, together with local heat transfer data, are used to determine the temperature independent surface heat transfer coefficients, presented in a companion paper. Both local effectiveness and heat transfer data will be used to derive local and quantitative net heat flux reduction data to identify optimum overall cooling conditions. The high-resolution surface data are suited to be compared with computational results of adiabatic wall film cooling. They can be used for the validation of CFD codes for the prediction of film cooling effectiveness and for the development of refined numerical and turbulence models.

Acknowledgments

This study was partly funded by the Ministry of Research and Technology of the Federal Republic of Germany through the German joint research program AG Turbo and Siemens AG/KWU, Mülheim a. d. Ruhr, Germany. Very special thanks are due to Professor P. M. Ligrani of the University of Utah for his discussions and advice on the high density ratio ejection effectiveness and heat transfer.

Nomenclature

D = ejection hole diameter, m
h = heat transfer coefficient, W/m^2K
I = momentum ratio, Eq. (4)
L = ejection hole length, m
M = blowing rate, Eq. (2)
q = heat flux, W/m^2
P = coolant to hot gas density ratio, Eq. (3)
Re = Reynolds number
s = ejection hole spacing, m
T = temperature, K
Tu = turbulence intensity
u = velocity, m/s
x = streamwise coordinate, m
y = wall normal coordinate, m
z = lateral coordinate, m
α = blowing angle
δ_1 = displacement thickness of the boundary layer, m
ε = radiatiave emissivity
η = film cooling effectiveness, Eq. (1)
ρ = density, kg/m^3
σ = Stefan–Boltzmann constant $=5.67\times10^{-8}$ W/m^2K^4

Subscripts

0 = without ejection
AW = adiabatic wall
a = ambient
C = coolant
conv = convective transferred
D = hole diameter based
f = cooling film
G = hot gas
max = maximum
p = peak
rad = radiative transferred
W = wall

References

[1] Lee, S. W., Lee, J. S., and Ro, S. T., 1994, ''Experimental Study on the Flow Characteristics of Streamwise Inclined Jets in Crossflow on Flat Plate,'' ASME J. Turbomach., **116**, pp. 97–116.
[2] Pietrzyk, J. R., Bogard, D. G., and Crawford, M. E., 1989, ''Hydrodynamic Measurements of Jet in Crossflow for Gas Turbine Film Cooling Applications,'' ASME J. Turbomach., **111**, pp. 139–145.
[3] Pietrzyk, J. R., Bogard, D. G., and Crawford, M. E., 1990, ''Effect of Density Ratio on the Hydrodynamics of Film Cooling,'' ASME J. Turbomach., **112**, pp. 437–443.
[4] Burd, S. W., Kaszeta, R. W., and Simon, T. W., 1996, ''Measurements in Film Cooling Flows: Hole *L/D* and Turbulence Intensity Effects,'' ASME Paper No. 96-WA/HT-7.
[5] Thole, K., Gritsch, M., Schulz, A., and Wittig, S., 1998, ''Flow Field Measurements for Film-Cooling Holes With Expanded Exits,'' ASME J. Turbomach., **120**, pp. 327–336.
[6] Ryndholm, H. A., 1996, ''An Experimental Investigation of the Velocity and Temperature Fields of Cold Jets Injected Into a Hot Crossflow,'' ASME J. Turbomach., **120**, pp. 320–326.
[7] Kohli, A., and Bogard, D. G., 1997, ''Adiabatic Effectiveness, Thermal Fields, and Velocity Fields for Film Cooling With Large Angle Ejection,'' ASME J. Turbomach., **119**, pp. 352–358.
[8] Sgarzi, O., and Leboeuf, F., 1997, ''Analysis of Vortices in Three-Dimensional Jets Introduced in a Cross-Flow Boundary Layer,'' ASME Paper No. 97-GT-517.
[9] Walters, D. K., and Leylek, J. H., 1997, ''A Detailed Analysis of Film Cooling Physics—Part I: Streamwise Ejection With Cylindrical Holes,'' ASME J. Turbomach., **122**, pp. 102–112.
[10] Baldauf, S., Schulz, A., and Wittig, S., 1999, ''High Resolution Measurements of Local Heat Transfer Coefficients by Discrete Hole Film Cooling,'' ASME Paper No. 99-GT-43.
[11] Sen, B., Schmidt, D. L., and Bogard, D. G., 1996, ''Film Cooling With Compound Angle Holes: Heat Transfer,'' ASME J. Turbomach., **118**, pp. 800–806.
[12] Schmidt, D. L., Sen, B., and Bogard, D. G., 1996, ''Film Cooling With Compound Angle Holes: Adiabatic Effectiveness,'' ASME J. Turbomach., **118**, pp. 807–813.
[13] Ekkad, S. V., Zapata, D., and Han, J. C., 1997, ''Film Effectiveness Over a Flat Surface With Air and CO_2 Injection Through Compound Angle Holes Using a Transient Liquid Crystal Image Method,'' ASME J. Turbomach., **119**, pp. 587–593.
[14] Goldstein, R. J., Jin, P., and Olson, R. L., 1998, ''Film Cooling Effectiveness and Mass/Heat Transfer Downstream of One Row of Discrete Holes,'' ASME J. Turbomach., **121**, pp. 225–232.
[15] Lutum, E., and Johnson, B. V., 1998, ''Influence of the Hole Length to Diameter Ratio on Film Cooling With Cylindrical Holes,'' ASME J. Turbomach., **121**, pp. 209–216.
[16] Drost, U., and Bölcs, A., 1998, ''Investigation of Detailed Film Cooling Effectiveness and Heat Transfer Distributions on a Gas Turbine Airfoil,'' ASME J. Turbomach., **121**, pp. 233–242.
[17] Bell, C. M., Hamakawa, H., and Ligrani, P. M., 2000, ''Film Cooling From Shaped Holes,'' ASME J. Heat Transfer, **122**, pp. 224–232.
[18] Gritsch, M., Schulz, A., and Wittig, S., 1997, ''Adiabatic Wall Effectiveness Measurements of Film-Cooling Holes With Expanded Exits,'' ASME J. Turbomach., **120**, pp. 549–556.
[19] Haslinger, W., and Hennecke, D. K., 1996, ''The Ammonia and Diazo Technique With CO_2 Calibration for Highly Resolving and Accurate Measurement of Adiabatic Film Cooling Effectiveness With Application to a Row of Holes,'' ASME Paper No. 96-GT-438.
[20] Jung, I. S., and Lee, J. S., 1999, ''Effect of Orientation Angles on Film Cooling Over a Flat Plate: Boundary Layer Temperature Distributions and Adiabatic Film Cooling Effectiveness,'' ASME J. Turbomach., **122**, pp. 154–161.
[21] Pedersen, D. R., Eckert, E. R. G., and Goldstein, R. J., 1977, ''Film Cooling With Large Density Differences Between the Mainstream and the Secondary Fluid Measured by the Heat–Mass Transfer Analogy,'' ASME J. Heat Transfer, **99**, pp. 620–627.
[22] Baldauf, S., and Scheurlen, M., 1996, ''CFD Based Sensitivity Study of Flow Parameters for Engine Like Film Cooling Conditions,'' ASME Paper No. 96-GT-310.
[23] Martiny, M., Schiele, R., Gritsch, M., Schulz, A., and Wittig, S., 1996, ''In Situ Calibration for Quantitative Infrared Thermography,'' Quirt '96 Eurotherm Seminar No. 50, Stuttgart, Germany, Sept. 2–5.
[24] Gnielinski, V., 1975, Forschung im Ingenieurwesen 41, No. 1.
[25] Kays, W. M., and Crawford, M. E., 1980, *Convective Heat and Mass Transfer*, McGraw-Hill, New York.
[26] Metzger, D. E., and Fletcher, D. D., 1971, ''Evaluation of Heat Transfer for

Film-Cooled Turbine Components,'' J. Aircr., **8**, pp. 33–38.
[27] Jabbari, M. Y., and Goldstein, R. J., 1978, ''Adiabatic Wall Temperature and Heat Transfer Downstream of Injection Through Two Rows of Holes,'' ASME J. Eng. Power, **100**, pp. 303–307.
[28] Kruse, H., 1985, ''Effects of Hole Geometry, Wall Curvature and Pressure Gradient on Film Cooling Downstream of a Single Row,'' *Heat Transfer and Cooling in Gas Turbines*, AGARD CP-390, Paper 8.
[29] Forth, C. J. P., and Jones, T. V., 1986, ''Scaling Parameters in Film Cooling,'' *Proc. 8th Int. Heat Transfer Conference*, Vol. 3, pp. 1271–1276.
[30] Lee, J. S., Ro, S. T., and Seo, H. J., 1994, ''Mass Transfer Effects of Free Stream Turbulence and Horseshoe Vortex Formed at the Upstream Edge of Film Cooling Jets About a Cylindrical Surface,'' ASME Paper No. 94-GT-18.

An Experimental Study of Impingement on Roughened Airfoil Leading-Edge Walls With Film Holes

M. E. Taslim

Y. Pan

Mechanical, Industrial, and Manufacturing Engineering,
Northeastern University,
Boston, MA 02115

S. D. Spring
GE Aircraft Engines,
Lynn, MA 02010

Airfoil leading-edge surfaces in state-of-the-art gas turbines, being exposed to very high gas temperatures, are often life-limiting locations and require complex cooling schemes for robust designs. A combination of convection and film cooling is used in conventional designs to maintain leading-edge metal temperatures at levels consistent with airfoil life requirements. Compatible with the external contour of the airfoil at the leading edge, the leading-edge cooling cavities often have complex cross-sectional shapes. Furthermore, to enhance the heat transfer coefficient in these cavities, they are often roughened on three walls with ribs of different geometries. The cooling flow for these geometries usually enters the cavity from the airfoil root and flows radially to the airfoil tip or, in the more advanced designs, enters the leading edge cavity from the adjacent cavity through a series of crossover holes in the wall separating the two cavities. In the latter case, the crossover jets impinge on a smooth leading-edge wall and exit through the showerhead film holes, gill film holes on the pressure and suction sides, and, in some cases, form a crossflow in the leading-edge cavity, which is ejected through the airfoil tip hole. The main objective of this investigation was to study the effects that film holes on the target surface have on the impingement heat transfer coefficient. Available data in the open literature are mostly for impingement on a flat smooth surface with no representation of the film holes. This investigation involved two new features used in airfoil leading-edge cooling, those being a curved and roughened target surface in conjunction with leading-edge row of film holes. Results of the crossover jets impinging on these leading-edge surface geometries with no film holes were reported by these authors previously. This paper reports experimental results of crossover jets impinging on those same geometries in the presence of film holes. The investigated surface geometries were smooth, roughened with large and small conical bumps as well as tapered radial ribs. A range of flow arrangements and jet Reynolds numbers were investigated, and the results were compared to those of the previous study where no film holes were present. It was concluded that the presence of leading-edge film holes along the leading edge enhances the internal impingement heat transfer coefficients significantly. The smaller conical bump geometry in this investigation produced impingement heat transfer coefficients up to 35 percent higher than those of the smooth target surface. When the contribution of the increased area in the overall heat transfer is taken into consideration, this same geometry for all flow cases as well as jet impingement distances (Z/d_{jet}) provides an increase in the heat removal from the target surface by as much as 95 percent when compared with the smooth target surface.
[DOI: 10.1115/1.1401035]

Introduction

Various methods have been developed over the years to keep the airfoil temperatures below critical levels. A main objective in turbine blade cooling design is to achieve maximum heat transfer coefficients while minimizing the coolant flow rate. One such method is to route coolant air through serpentine passages within the airfoil and convectively remove heat from the blade. The coolant is then ejected either at the tip of the blade, through cooling slots along the trailing edge or film holes on the airfoil surface. To enhance the heat transfer further, the cavity walls are often roughened with ribs. Extensive research has been conducted on various aspects of the rib-roughened channels and it is concluded that geometric parameters such as passage aspect ratio (AR), rib height-to-passage hydraulic diameter or blockage ratio (e/D_h), rib angle of attack (α), the manner in which the ribs are positioned relative to one another (in-line, staggered, criss-cross, etc.), rib pitch-to-height ratio (S/e) and rib shape (round versus sharp corners, fillets, rib aspect ratio (AR_t), and skewness toward the flow direction) have pronounced effects on both local and overall heat transfer coefficients. The interested reader is referred to the work of investigators such as Burggraf [1], Chandra and Han [2], El-Husayni et al. [3], Han [4], Han et al. [5–7], Metzger et al. [8–10], Taslim and Spring [11–13], Taslim et al. [14–16], Webb et al. [17] and Zhang et al. [18].

This study, however, focuses on leading-edge jet impingement and the effects that roughening of the leading-edge surface has on the impingement heat transfer coefficient. In this flow arrangement, the coolant enters the leading edge cooling cavity as jets from the adjacent cavity through a series of cross-over holes on the partition wall between the two cavities. The cross-over jets impinge on the leading-edge wall and exit through the film holes on the airfoil leading edge (also called showerhead film holes), or through the film holes on the pressure and suction sides of the

Contributed by the International Gas Turbine Institute and presented at the 46th International Gas Turbine and Aeroengine Congress and Exhibition, New Orleans, Louisiana, June 4–7, 2001. Manuscript received by the International Gas Turbine institute February 2001. Paper No. 2001-GT-152. Review Chair: R. Natole.

airfoil, or form a crossflow in the leading-edge cavity and move toward the airfoil tip. A survey of many existing gas turbine airfoil geometries shows that, for analytical as well as experimental analyses, such cavities can be simplified by simulating the shape as a four-sided polygon with one curved side that simulates the leading edge curvature, a rectangle with one curved side (often the smaller side) or a trapezoid, the smaller base of which is replaced with a curved wall. The available data in open literature are mostly for the jet impingement on flat surfaces that are smooth or rib-roughened and a few cases of impingement on concave but smooth surfaces. These studies include the work of Chupp et al. [19], Metzger et al. [20], Kercher and Tabakoff [21], Florschuetz et al. [22–24], Bunker and Metzger [25], Metzger and Bunker [26], Van Treuren et al. [27], Chang et al. [28], Huang et al. [29], and Akella and Han [30]. However, as dictated by the external shape of an airfoil leading edge, the test section in this investigation was a symmetric channel with a circular nose, two tapered side walls, and a flat fourth wall on which the cross-over jets were positioned. Experimental results for this setup without the leading-edge film holes have already been reported by Taslim et al. [16]. In this investigation, however, depending on the flow arrangement, the impingement air was ejected entirely through a row of holes on the target surface along the leading edge simulating the airfoil showerhead film holes, or split through the showerhead holes and two rows of holes on the side walls representing the pressure and suction side ''gill'' film holes, or partially (70 percent) through the showerhead holes and the balance (30 percent) through one end of the channel representing an airfoil tip. Data points were obtained for jet Reynolds numbers as high as 40,000, which is well beyond any existing impingement data for gas turbine applications, and results were compared with those without the showerhead film holes.

Test Sections

Figures 1 and 2 show schematically the layout, cross-sectional area, and the target surface geometries for the four test sections investigated in this project. A conventional constant-heat-flux technique of heated walls in conjunction with thermocouples was used to measure the heat transfer coefficient. The test wall, where all measurements were taken, consisted of three removable cast brass pieces, which were heated by foil heaters attached on the back of the pieces. By proper adjustment of the ohmic power to the foil heater immediately underneath the brass piece, the desirable surface temperature was obtained. All test sections were 85.5 cm long. The circular wall simulating the leading-edge nose with an inner radius of 1.1 cm and an arc angle of 137 deg was made of fiberglass with a 9.9 cm long recess in the middle to house the three brass pieces. Eighteen 0.38-cm-diameter holes at a center-to-center distance of 1.63 cm were drilled along the leading edge nose at a 30 deg angle with the channel longitudinal axis. Six of these holes passed through the brass pieces while the rest were drilled symmetrically on both sides of the brass pieces on the fiberglass nose. This single row of holes, with properly scaled flow area, simulated an airfoil showerhead hole design that is typically configured as two rows. This test rig, however, was limited to one row of holes, because the brass pieces were covered with etched-foil heaters through which could not be drilled. A flange on each side of the leading-edge piece facilitated the connection of the side walls to this piece. A circular recess along the inner radius with a depth of 3.2 mm and a length of 9.9 cm allowed the brass pieces to be fitted into the fiberglass shell. The two identical side channels with cross-sectional areas of 38.86 cm^2 (5.1 cm×7.62 cm) and the same length as the leading-edge piece were also made of fiberglass. The side channels' main function was to maintain the dump pressure to consequently control the amount of flow through the gill holes on the airfoil suction and pressure sides. Eight angled cylindrical holes with a diameter of 4.88 mm and a center-to-center distance of 3.25 cm were drilled on each side channel wall at an angle of 30 deg with the side wall

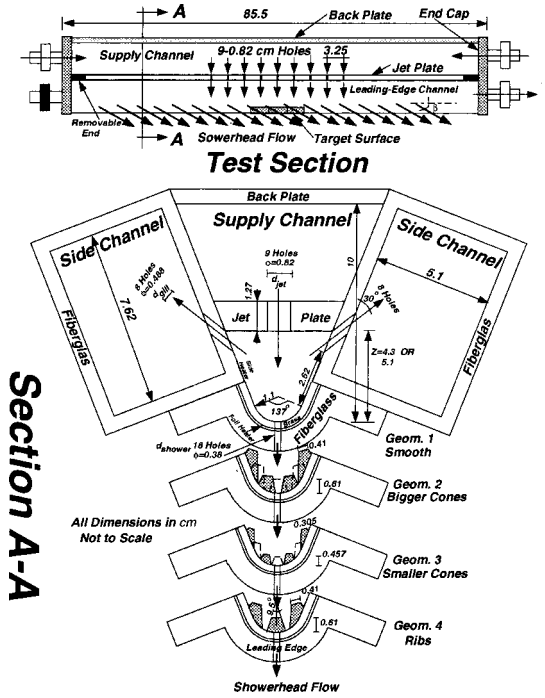

Fig. 1 Schematic of test apparatus

to simulate gill holes on the suction and pressure sides of an airfoil. These holes were staggered along the length of the test section with respect to the crossover jet holes on the jet plate.

Two removable 1.27 cm thick jet plates, used to produce impinging jets corresponding to two values of Z/d_{jet} (5.2 and 6.2), were made of acrylic. On each jet plane, nine cylindrical holes with a diameter of 0.82 cm were drilled at a distance of 3.25 cm (center to center) from each other corresponding to a span-to-diameter of 3.96. For each Z/d_{jet} test, the corresponding jet plate was attached and sealed to the side channel walls to simulate the partition wall between the leading-edge and its adjacent cavities. The cylindrical holes were centered along both the length and width of the jet plate. When the jet plate was in its nominal position, a jet impinged at the center of each brass piece. To move the impinging jets to an off-center position, two removable 0.82 cm thick pieces were attached to each end of the jet plates, allowing three different impingement locations. The removable brass pieces, installed in the fiberglass outer shell, provided interchangeability of the impingement surface geometries in the test rig. Four different geometries were manufactured and tested (Fig. 3): (1) a smooth wall that served as a baseline, (2) a roughened

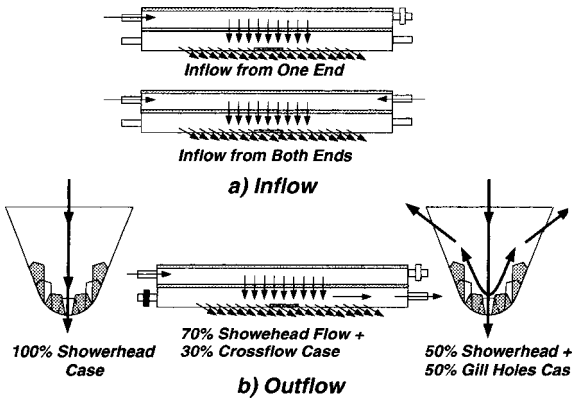

Fig. 2 Inflow and outflow arrangements

wall with seven conical bumps on each brass piece, (3) a roughened wall with fourteen smaller conical bumps on each brass piece, (4) a roughened wall with tapered radial ribs.

For each geometry, a Unigraphics® model was created and transmitted to the manufacturer electronically, and a LOM (Laminated Object Model) was made. This LOM model was used to mold and eventually create a cast brass test piece for each of the four geometries. Two 3 cm by 3.1 cm custom-made thin etched-foil heaters with a thickness of about 0.2 mm were glued around the outer surface of each brass piece to provide the necessary heat flux. For each geometry, three identical brass pieces, separated by a 1 mm thick rubber insulator, were mounted next to each other. Heat transfer coefficients were measured on the middle piece while the other two pieces acted as guard heaters to minimize the heat losses to the adjacent walls. In addition, two custom-made thin etched-foil heaters were also mounted on the test section side channel walls next to the middle brass piece free edges, again acting as guard heaters. The test section wall temperature was adjusted to a desirable level by varying the ohmic power to these heaters. Six thermocouples embedded in the middle brass piece and three thermocouples embedded in each guard brass piece measured the wall temperature. The average of the six thermocouple readings in the middle brass piece, which, if different, only differed by a fraction of a degree, was used as the surface temperature in the data reduction software for the average heat transfer coefficient. A nominal surface temperature of 45°C was selected so that with a jet temperature of about 20°C, a reasonable 25°C temperature difference existed between the wall surface and air. Two thermocouples embedded in the wall behind the guard heaters were used to measure the wall temperature adjacent to the middle brass piece. By proper adjustment of the power to the side heaters, the wall temperature under the side heaters was set to be around 45°C. AC power was supplied to individual heaters through an existing power panel with individual Variacs for each heater. Typical amperage and voltage levels for each heater varied from 0.23–0.4 Amps and 20–45 Volts, respectively. Air properties were evaluated at jet temperature.

The trapezoidal supply channel was formed by the exterior walls of the side channels, the jet plate and a 1.27 cm thick aluminum back plate as shown in Fig. 1. The end caps were fixed such that it was possible to control the flow and pressure in each channel, thus simulating many variations that may occur in actual airfoil environments. Static pressure taps and thermocouples in each channel measured the pressure and temperature at different locations. The test sections were covered on all sides, by 5 cm thick glasswool sheets to minimize heat losses to the environment. Radiational heat loss from the heated wall to the unheated walls, heat losses from the brass piece in the entrance region of the showerhead holes, and losses to ambient air were taken into consideration when heat transfer coefficients were calculated. A contact micromanometer with an accuracy of 0.025 mm of water column as well as a series of oil and mercury manometers measured the pressures and pressure differences between the static pressure taps mounted on both sides of the roughened section for each geometry. For all cases, a critical venturimeter was used to measure the total air mass flow rate entering the supply channel.

Results and Discussion

A total of 40 tests were run in this investigation. All tests had several common features. There were always nine impinging jets issuing from the jet plate. The middle jet (fifth) always impinged on the brass test piece in the middle of the test section and the reported heat transfer results are always for that middle brass test piece. The fourth and sixth jets impinged on the side brass pieces that acted as guard heaters. The remaining six jets impinged on the fiberglass leading-edge wall to simulate the flow field in a typical leading-edge cavity. The jet Reynolds number is based on the total measured mass flow rate and the total area of the nine impingement holes. Two inflow arrangements to the supply channel, as shown in Fig. 2(*a*), where air either entered from one end or both ends, were tested. Static pressure taps, installed in the middle and at each end of the supply channel, measured no significant difference between locations (about 1 cm of water column for a supply pressure ranging from 110 to 172 kPa). Three outflow arrangements for the exiting cooling air, shown in Fig. 2(*b*), were tested. The ''100 percent showerhead flow'' case was the case in which all cooling air, after impinging on the leading-edge wall, was ejected through a row of holes on the target surface. The ''50 percent showerhead flow'' case was the case in which 50 percent of the cooling air, after impinging on the leading-edge wall, was ejected through the leading-edge holes and the remaining 50 percent through the side holes simulating the gill holes on the pressure and suction sides of an airfoil. The ''70 percent shower +crossflow'' case was the case in which 70 percent of the cooling air, after impinging on the leading-edge wall, was ejected through the leading-edge holes while the remaining 30 percent was ejected from one end of the leading-edge channel simulating the airfoil tip flow. In this flow arrangement, portion of the four jets upstream of the middle jet that was not ejected through the leading-edge holes (spent air) formed a crossflow that affected the impingement heat transfer coefficient. Two jet plate positions corresponding to Z/d_{jet} values of 5.2 and 6.2 were tested for all geometries. The 70 percent shower+crossflow case consistently produced higher heat transfer coefficients compared to the other two outflow cases. The tested target geometries, for most cases, remained insensitive to both Z/d_{jet} ratios and inflow conditions (one end or both ends). Specific characteristics of each geometry are discussed next. Experimental uncertainty in heat transfer coefficient, following the method of Kline and McClintock [31] was determined to be 6 percent.

Geometry 1. Impingement on a smooth leading-edge wall, shown in Fig. 3(*a*), was tested in this geometry which served as a baseline geometry. Figure 4 shows the variation of Nusselt number versus jet Reynolds number for this geometry. To show the effects of showerhead film holes on the impingement heat transfer coefficient, the previously reported results [16] of the same geometry without the presence of showerhead film holes for the two Z/d_{jet} values are shown on the same figure. It is observed that the mere presence of the showerhead holes along the leading edge has increased the impingement heat transfer coefficient by as much as 22 percent for the entire range of the jet Reynolds number. This behavior continues to be the case for all four target surface geometries. The increase in heat transfer coefficient is explained by the increased contact with the surface of the flow after impinging on the surface and then flowing out of showerhead holes immediately adjacent to the impingement surface. For the twelve flow arrange-

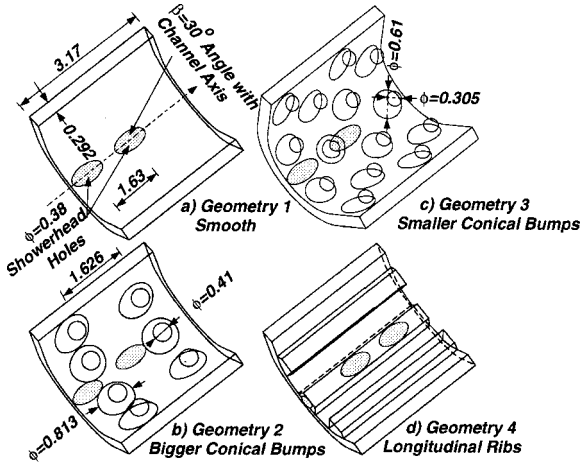

Fig. 3 Target surface geometries

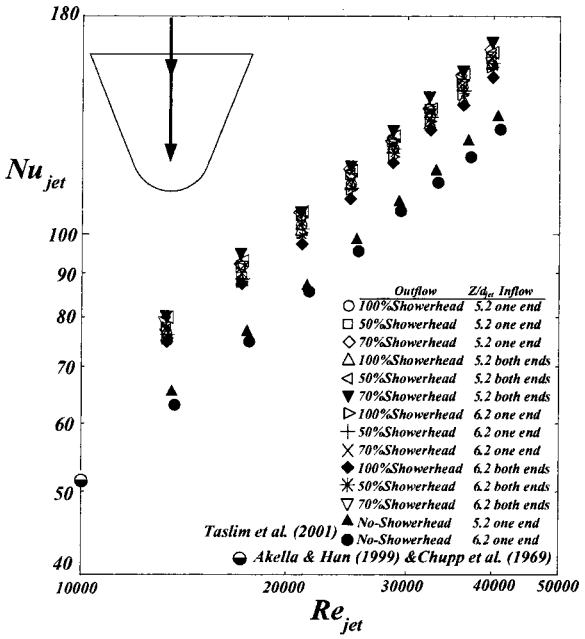

Fig. 4 Nusselt number variation with Reynolds number for geometry 1 (smooth wall) and all flow arrangements

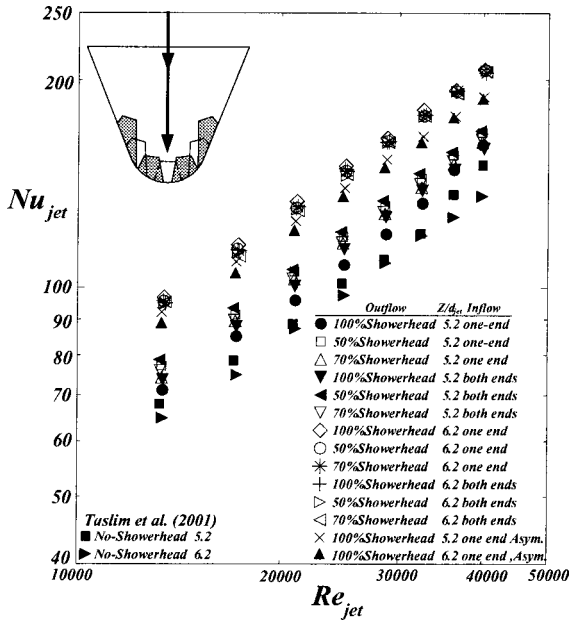

Fig. 5 Nusselt number variation with Reynolds number for geometry 2 (bigger cones) and all flow arrangements

ments tested with this geometry, all impingement heat transfer coefficients were of similar value. The case of combined showerhead and crossflow did produce a heat transfer coefficient that was about 9 percent higher than that of total showerhead flow. One data point, corresponding to a jet Reynolds number of 10,000 from Akella and Han [30] is also shown in Fig. 4. Their investigation dealt with impingement on a smooth flat surface of a channel in stationary as well as orthogonally rotating modes. The value shown was the highest jet Reynolds tested in their study and the no-showerhead data seem to extrapolate well to that data point. A data point from Chupp et al. [19], who measured impingement heat transfer on a smooth semicircular surface (no showerhead holes), again for their highest jet Reynolds number of 10,000, falls right on the data point of Akella and Han.

The lack of sensitivity of the heat transfer results to the change of Z/d_{jet} from 5.2 to 6.2 and to the inflow arrangements (one end or both ends of the supply channel) shows the dominant effect of showerhead hole presence on the target surface. The earlier report on the same geometries with no showerhead holes [16] showed considerable change in heat transfer results with variations in Z/d_{jet} and inflow arrangement.

Geometry 2. The target wall for this geometry was roughened with the bigger conical bumps (Fig. 3(*b*)). This configuration consisted of a total of seven conical bumps arranged in two staggered rows of four and three cones each. Compared to the baseline geometry, the total heat transfer area on the middle brass piece was increased by about 35 percent. Heat transfer results for this geometry are shown in Fig. 5 along with the results of the same geometry with no showerhead holes. Two additional tests for this geometry were run to investigate the symmetric and asymmetric impingement on the middle brass piece. In other tests, the middle jet impinged at the geometric center of the middle brass piece in-between the two rows of cones while the "Asymmetric" tests represent the impingement on the row of four cones (Fig. 2(*b*)). Testing of latter position was accomplished by offsetting the jet plate to the right. The two asymmetric tests were run for flow entering from one end of the supply channel and for both Z/d_{jet} values (5.2 and 6.2). The outflow arrangement was 100 percent showerhead flow. Similar to the baseline geometry, the heat transfer results with showerhead flow are higher than those with no showerhead flow by as much as 50 percent, depending on the flow arrangement. The cases of 70 percent showerhead flow and 30 percent crossflow produced the highest heat transfer coefficients while the symmetric impingement cases of 100 percent showerhead flow produced the lowest heat transfer coefficients. The 50 percent showerhead and side hole flows fell in-between the other two outflow arrangements. Asymmetric impingement (on the cones) produced heat transfer coefficients that were about 18 to 24 percent (higher Re_{jet} and lower Re_{jet} sides, respectively) higher than those of symmetric impingement. This rather large difference is attributed to a better interaction between the impinging jet and the cones in the asymmetric case since the jet is forced to impinge on the cone tip and travel down to exit from the showerhead holes abutting the cone base. Comparisons between the results of different geometries are done in upcoming figures and discussion.

Geometry 3. In an effort to create a more uniform roughness, the target wall for this geometry was roughened with a larger number of smaller conical bumps than was used for geometry 2 (Fig. 3(*c*)). This configuration consisted of a total of fourteen conical bumps made up in four staggered rows of four and three cones each. Compared to the baseline geometry, the total heat transfer area on the middle brass piece was again increased by about 35 percent. A total of fourteen tests were run for this geometry, the results of which are shown in Figs. 6 and 7 along with the results of the same geometry with no showerhead holes. The results show that compared to geometry 2, this target surface geometry produces higher impingement heat transfer coefficients. This comparison suggests that there may exist an optimum geometry with more conical bumps in number and smaller in size. In selecting the optimum geometry, the overall heat transfer area, another dominant parameter that will be discussed later has to be taken into consideration and because of this geometry 3 was chosen to have the same increased heat transfer area as that of geometry 2. This geometry showed much less sensitivity to the inflow arrangement or jet distance to the target surface than the other tested geometries. Again, the presence of showerhead holes significantly increased the impingement heat transfer coefficient over the geometries without the showerhead holes by as much as 65 percent.

Figure 7 shows the results of a series of tests performed on geometry 3 for a range of showerhead flow to total flow ratios from 50 to 100 percent with the balance of cooling air ejected

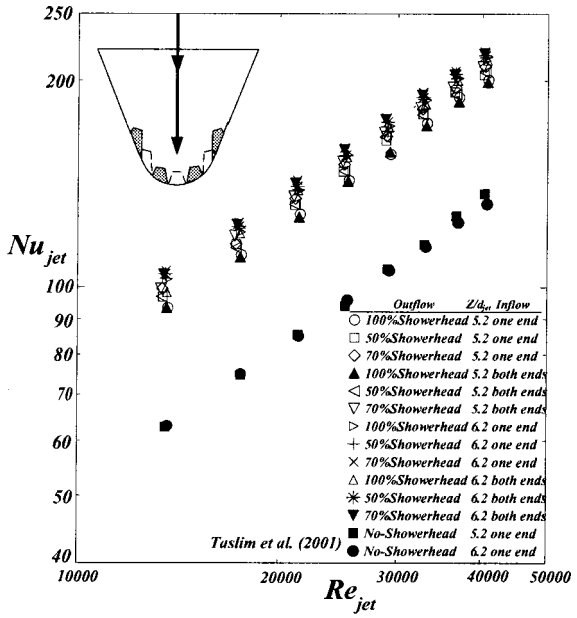

Fig. 6 Nusselt number variation with Reynolds number for geometry 3 (smaller cones) and all flow arrangements

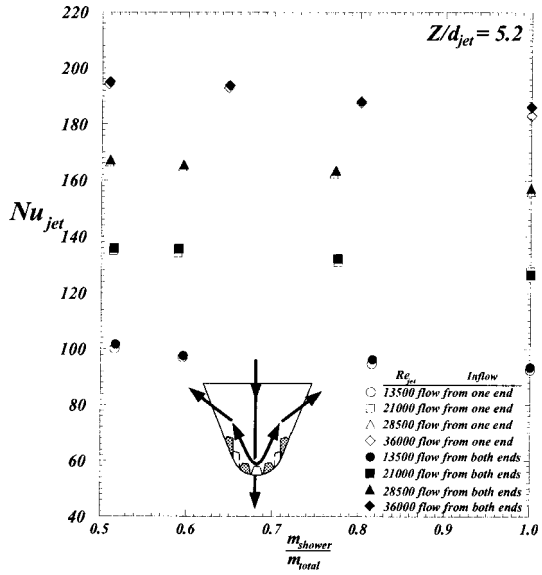

Fig. 7 Nusselt number variation with the percentage of showerhead flow for geometry 3 (smaller cones) at different Reynolds numbers

from the side (gill) holes in each case. For each jet Reynolds number, two inflow conditions are used. As discussed earlier, the inflow condition does not show any significant effect on the impingement heat transfer for this geometry. Results also indicate that, although the presence of showerhead film holes enhance the impingement heat transfer coefficient, their share of cooling air beyond 50 percent does not change the impingement heat transfer coefficient significantly. Showerhead mass flow ratios below the tested 50 percent required drilling of a new target surface, which was beyond the scope of this investigation.

Geometry 4. The target wall for this geometry was roughened with longitudinal ribs (Fig. 3(*d*)). There were three ribs along each brass piece: one on the leading-edge nose and one on each side, parallel to the middle one. The total heat transfer area on the middle brass piece was measured to be 47.3 percent higher than

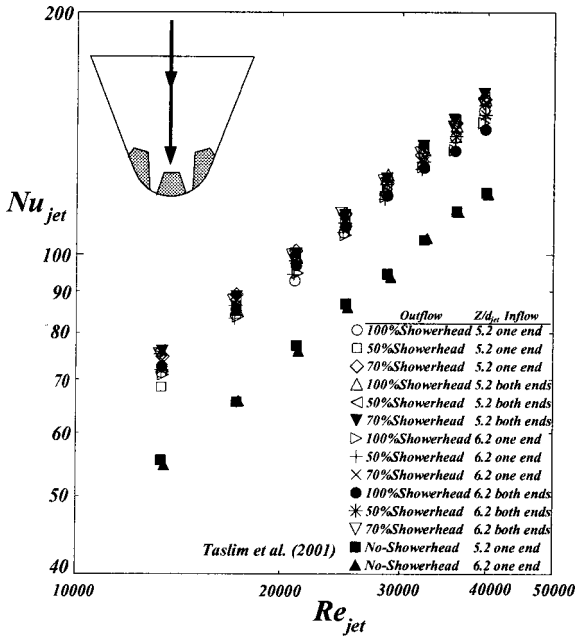

Fig. 8 Nusselt number variation with Reynolds number for geometry 4 (ribs) and all flow arrangements

that of the baseline geometry. A total of twelve tests were run for this geometry covering the three outflow cases (50, 70, and 100 percent showerhead flows), two Z/d_{jet} values (5.2 and 6.2), and two inflow arrangements. Test results of geometry 4 are shown in Fig. 8 along with the results of the same geometry with no showerhead flow. Although, consistent with the other three geometries, the showerhead film holes enhanced the impingement heat transfer coefficient, the overall performance of this geometry was inferior to that of geometries 2 and 3. It appears that the coolant air did not maintain contact with all available heat transfer areas around the ribs particularly the outer most surfaces. Similar to geometry 3, this geometry did not show much sensitivity to the

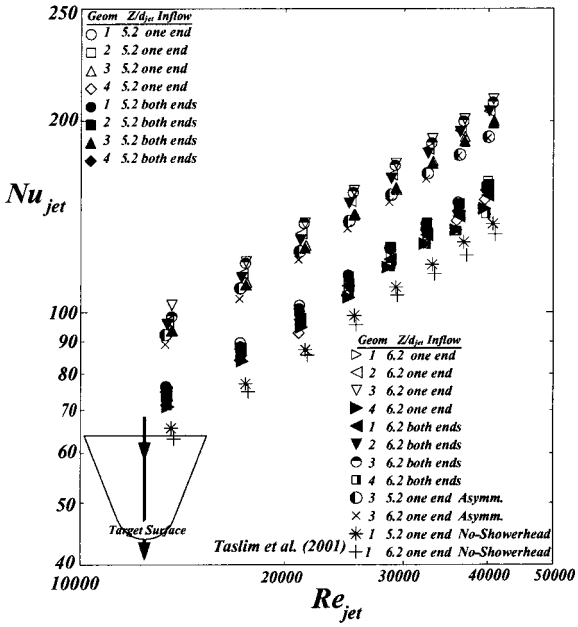

Fig. 9 Comparison between heat transfer results of all target surface geometries with 100 percent showerhead flow

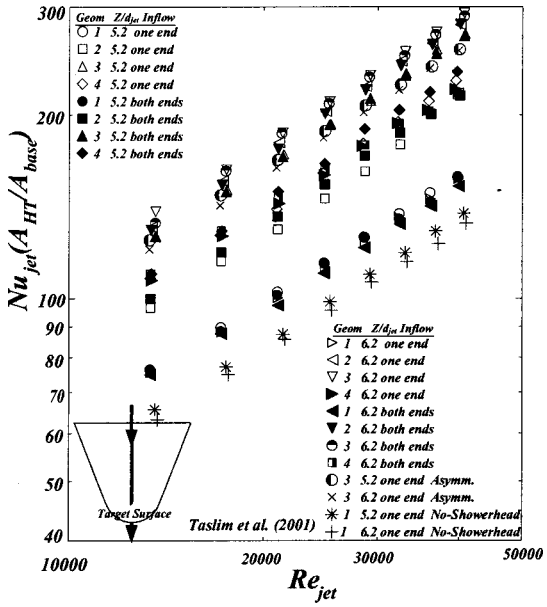

Fig. 10 Comparison between the area-augmented heat transfer results of all target surface geometries with 100 percent showerhead flow

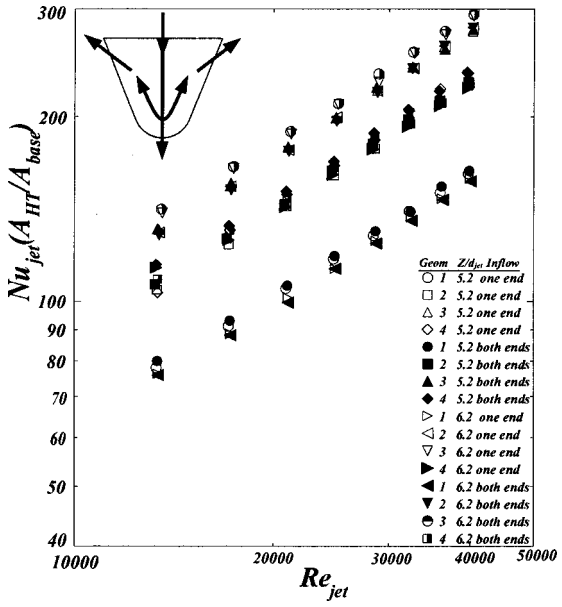

Fig. 12 Comparison between the area-augmented heat transfer results of all target surface geometries with 50 percent showerhead flow

manner in which the supply channel was fed. The larger Z/d_{jet} (6.2) produced slightly higher heat transfer coefficients than the smaller Z/d_{jet}(5.2) for all cases. It appears that a jet issued from a longer distance from the target surface diffuses more before reaching the target surface and, as a result, a portion of cooling jet will come in contact with the ribs outermost surfaces before being drawn into the showerhead holes.

Comparisons. Figures 9–14 compare the heat transfer results of all four target geometries. The 100 percent showerhead flow cases are shown in Fig. 9 along with the no-showerhead flow cases for the baseline geometry. The highest heat transfer coefficient is produced by the target geometry 3 (smaller cones), followed by geometry 2 (bigger cones), the baseline geometry (smooth wall) and finally geometry 4 (ribs) with a considerable difference (as much as 40 percent) between the cone-roughened target surface and the other two surfaces. Figure 10 includes the contribution of the increased area in the overall heat transfer from the target surface $[\text{Nu}_{\text{jet}}(A_{HT}/A_{\text{base}})]$ in the data reported in Fig. 9. When the area enhancement for geometries 2, 3, and 4 are included in these comparisons and results are compared with the baseline surface, the heat rate from geometries 2, 3, and 4 increases by as much as 80, 95, and 40 percent respectively. Figures 11 and 12 make the same comparisons for the case of 50 percent showerhead+50 percent gill flow. The general behavior of impingement heat transfer coefficient is the same as that of 100 percent showerhead flow, i.e., geometry 3 (smaller cones) is su-

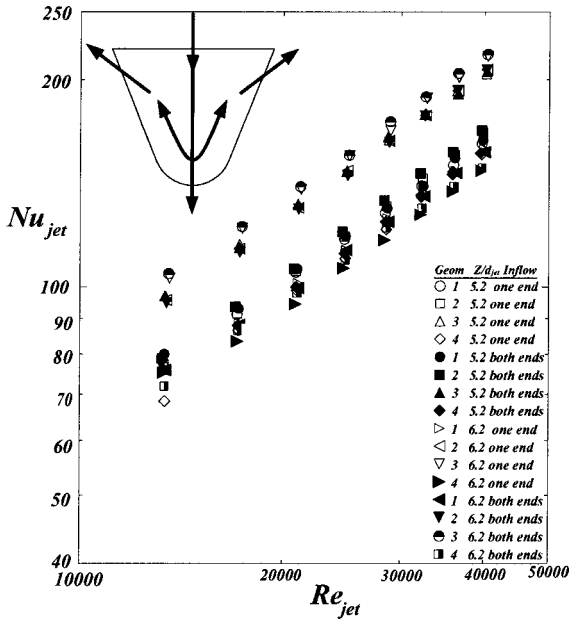

Fig. 11 Comparison between heat transfer results of all target surface geometries with 50 percent showerhead flow

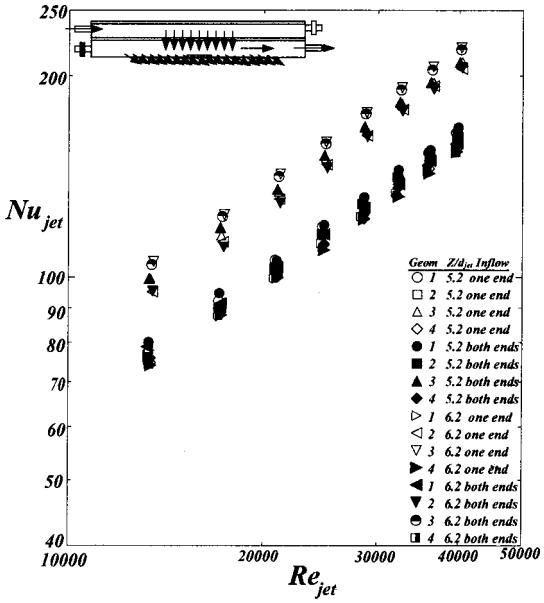

Fig. 13 Comparison between the heat transfer results of all target surface geometries with 70 percent showerhead and 30 percent crossflow

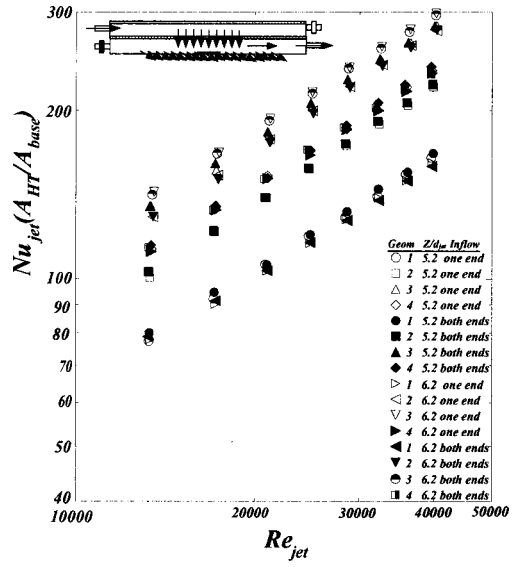

Fig. 14 Comparison between the area-augmented heat transfer results of all target surface geometries with 70 percent showerhead and 30 percent crossflow

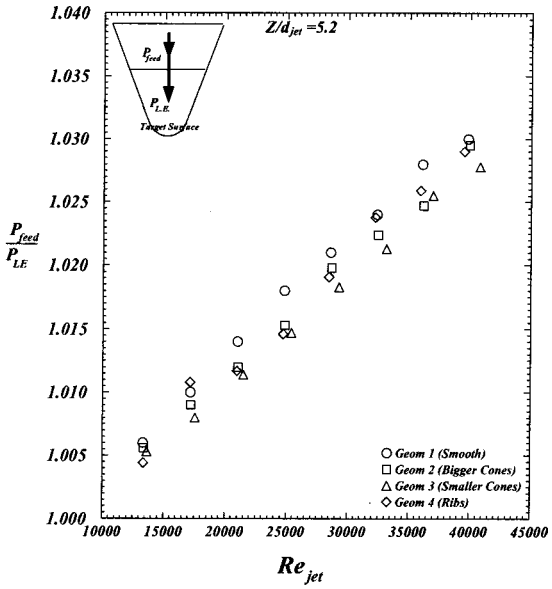

Fig. 16 Pressure ratio across the jet plate versus Reynolds number for all geometries and 100 percent showerhead flow

perior to other three geometries. Figures 13 and 14 make the same comparisons for the case of 70 percent showerhead flow and 30 percent crossflow. Again, for this outflow arrangement, geometry 3 (smaller cones) produces the highest impingement heat transfer coefficients.

Static pressure ratios across the jet plate for the baseline geometry 1 is shown in Fig. 15 for all twelve flow arrangements. The results show that at lower Reynolds number range, different flow arrangements have almost the same pressure ratio across the jet plate. At higher Reynolds numbers, however, the case of 50 percent Showerhead flow produces the highest pressure ratio, followed by the 70 percent showerhead+30 percent crossflow case and the 100 percent showerhead flow case. Across the geometries, the pressure ratio variation with the jet Reynolds number was very similar. The 100 percent showerhead flow cases of the four geometries are compared in Fig. 16. The maximum difference between the pressure ratios of the four geometries was less than 0.5 percent for all flow cases tested.

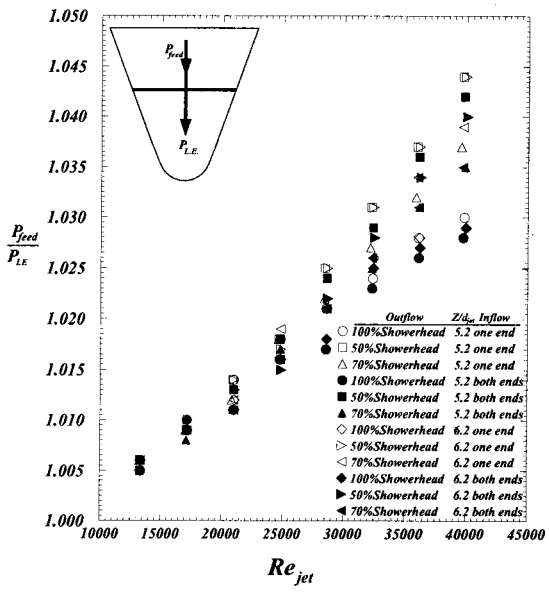

Fig. 15 Pressure ratio across the jet plate versus Reynolds number for geometry 1 (smooth wall) and all flow arrangements

Conclusion

Major conclusions of this study are:

1 The presence of showerhead film holes along the leading edge enhances the internal impingement heat transfer coefficients significantly. The enhancement for the tested target surface geometries in this study was as much as 65 percent.

2 Without the inclusion of the heat transfer area increase, the smaller conical bumps produced impingement heat transfer coefficients up to 35 percent higher than those of smooth target surface. When the contribution of the increased area in the overall heat transfer is taken into consideration, geometry 3 for all inflow and outflow cases as well as the two Z/d_{jet} values provides an increase in the heat removal from the target surface by as much as 95 percent when compared with the smooth target surface.

3 Effects of showerhead holes on altering the impingement flow field and the area enhancement due to roughening of the target surface are the two dominant parameters in leading edge cooling enhancement. Effects of inflow and outflow arrangements as well as the jet distance to the target surface, for the tested range, were of secondary importance.

Nomenclature

A_{base} = leading-edge base area for the smooth case
A_{hole} = total area of all nine cross-over holes
A_{HT} = total heat transfer area including the surface roughness
AR = cooling channel aspect ratio
AR_t = rib aspect ratio
d_{jet} = jet diameter=0.82 cm
D_h = cooling channel hydraulic diameter
e = roughness height
h = average heat transfer coefficient on the leading-edge wall=$[(vi/A_{HT})-q_{\text{loss}}]/(T_s-T_{\text{jet}})$
i = current through the foil heater on the middle brass piece
k = air thermal conductivity
m = air total mass flow rate through all nine crossover holes

Nu_{jet} = average Nusselt number based on the jet diameter $= hd_{jet}/k$
P = channel perimeter without ribs
q_{loss} = heat losses from the middle brass piece to the ambient by conduction and convection as well as the heat losses by radiation to the unheated walls
R_{nose} = channel radius at the leading edge=1.1 cm
Re_{jet} = Reynolds number based on the jet diameter $= \rho U_{jet} d_{jet}/\mu$)
S = rib pitch
T_{jet} = air jet temperature
T_s = surface temperature
U_{jet} = jet mean velocity=$m/\rho A_{hole}$
Z = distance from jet exit to the target surface (Fig. 1)
α = rib angle of attack
β = leading-edge hole angle with channel axis (30 deg, Fig. 2(a))
μ = air dynamic viscosity at jet temperature
ν = voltage drop across the foil heater on the middle brass piece
ρ = air density at jet temperature and pressure

References

[1] Burggraf, F., 1970, "Experimental Heat Transfer and Pressure Drop With Two Dimensional Turbulence Promoters Applied to Two Opposite Walls of a Square Tube," *Augmentation of Convective Heat and Mass Transfer*, A. E. Bergles and R. L. Webb, eds., ASME pp. 70–79.

[2] Chandra, P. R., and Han, J. C., 1989, "Pressure Drop and Mass Transfer in Two-Pass Ribbed Channels," J. Thermophys., **3**, No. 3, pp. 315–319.

[3] El-Husayni, H. A., Taslim, M. E., and Kercher, D. M., 1994, "An Experimental Investigation of Heat Transfer Coefficients in a Spanwise Rotating Channel With Two Opposite Rib-Roughened Walls," ASME J. Turbomach., **113**, pp. 75–82.

[4] Han, J. C., 1984, "Heat Transfer and Friction in Channels With Two Opposite Rib-Roughened Walls," ASME J. Heat Transfer, **106**, No. 4, pp. 774–781.

[5] Han, J. C., Glicksman, L. R., and Rohsenow, W. M., 1978, "An Investigation of Heat Transfer and Friction for Rib Roughened Surfaces," Int. J. Heat Mass Transf., **21**, pp. 1143–1156.

[6] Han, J. C., Park, J. S., and Lei, C. K., 1985, "Heat Transfer Enhancement in Channels With Turbulence Promoters," ASME J. Eng. Gas Turbines Power, **107**, No. 1, pp. 628–635.

[7] Han, J. C., Zhang, Y. M., and Lee, C. P., 1992, "Influence of Surface Heat Flux Ratio on Heat Transfer Augmentation in Square Channels With Parallel, Crossed, and V-Shaped Angled Ribs," ASME J. Turbomach., **114**, pp. 872–880.

[8] Metzger, D. E., Vedula, R. P., and Breen, D. D., 1987, "The Effect of Rib Angle and Length on Convection Heat Transfer in Rib-Roughened Triangular Ducts," *Proc. ASME–JSME Thermal Engineering Joint Conference*, Vol. 3, pp. 327–333.

[9] Metzger, D. E., Chyu, M. K., and Bunker, R. S., 1988, "The Contribution of On-Rib Heat Transfer Coefficients to Total Heat Transfer From Rib-Roughened Surfaces," *Transport Phenomena in Rotating Machinery*, J. H. Kim, ed., Hemisphere Publishing Co.

[10] Metzger, D. E., Fan, C. S., and Yu, Y., 1990, "Effects of Rib Angle and Orientation on Local Heat Transfer in Square Channels With Angled Roughness Ribs," *Compact Heat Exchangers: A Festschrift for A. L. London*, Hemisphere Publishing Co., pp. 151–167.

[11] Taslim, M. E., and Spring, S. D., 1988, "An Experimental Investigation of Heat Transfer Coefficients and Friction Factors in Passages of Different Aspect Ratios Roughened With 45 deg Turbulators," *Proc. ASME National Heat Conference*, Houston, TX.

[12] Taslim, M. E., and Spring, S. D., 1988, "Experimental Heat Transfer and Friction Factors in Turbulated Cooling Passages of Different Aspect Ratios, Where Turbulators Are Staggered," Paper No. AIAA-88-3014.

[13] Taslim, M. E., and Spring, S. D., 1991, "An Experimental Investigation Into the Effects Turbulator Profile and Spacing Have on Heat Transfer Coefficients and Friction Factors in Small Cooled Turbine Airfoils," Paper No. AIAA-91-2033.

[14] Taslim, M. E., Bondi, L. A., and Kercher, D. M., 1991, "An Experimental Investigation of Heat Transfer in an Orthogonally Rotating Channel Roughened 45 Deg Criss-Cross Ribs on Two Opposite Walls," ASME J. Turbomach., **113**, pp. 346–353.

[15] Taslim, M. E., Rahman, A., and Spring, S. D., 1991, "An Experimental Evaluation of Heat Transfer Coefficients in a Spanwise Rotating Channel With Two Opposite Rib-Roughened Walls," ASME J. Turbomach., **113**, pp. 75–82.

[16] Taslim, M. E., Setayeshgar, L., and Spring, S. D., 2001, "An Experimental Investigation of Advanced Leading Edge Impingement Cooling Concepts," ASME J. Turbomach., **123**, pp. 1–7.

[17] Webb, R. L., Eckert, E. R. G., and Goldstein, R. J., 1971, "Heat Transfer and Friction in Tubes With Repeated-Rib-Roughness," Int. J. Heat Mass Transf., **14**, pp. 601–617.

[18] Zhang, Y. M., Gu, W. Z., and Han, J. C., 1994, "Heat Transfer and Friction in Rectangular Channels With Ribbed or Ribbed-Grooved Walls," ASME J. Heat Transfer, **116**, No. 1, pp. 58–65.

[19] Chupp, R. E., Helms, H. E., McFadden, P. W., and Brown, T. R., 1969, "Evaluation of Internal Heat Transfer Coefficients for Impingement Cooled Turbine Blades," J. Aircraft, **6**, No. 1, pp. 203–208.

[20] Metzger, D. E., Yamashita, T., and Jenkins, C. W., 1969, "Impingement Cooling of Concave Surfaces With Lines of Circular Air Jets," ASME J. Eng. Power, **93**, No. 3, pp. 149–155.

[21] Kercher, D. M., and Tabakoff, W., 1970, "Heat Transfer by a Square Array of Round Air Jets Impinging Perpendicular to a Flat Surface Including the Effect of Spent Air," ASME J. Eng. Power, **92**, No. 1, pp. 73–82.

[22] Florschuetz, L. W., Berry, R. A., and Metzger, D. E., 1980, "Periodic Streamwise Variation of Heat Transfer Coefficients for Inline and Staggered Circular Jets With Crossflow of Spent Air," ASME J. Heat Transfer, **102**, No. 1. pp. 132–137.

[23] Florschuetz, L. W., Truman, C. R., and Metzger, D. E., 1981, "Streamwise Flow and Heat Transfer Distribution for Jet Impingement With Crossflow," ASME J. Heat Transfer, **103**, No. 2, pp. 337–342.

[24] Florschuetz, L. W., Metzger, D. E., Su, C. C., Isoda, Y., and Tseng, H. H., 1984, "Heat Transfer Characteristics for Jet Arrays Impingement With Initial Crossflow," ASME J. Heat Transfer, **106**, No. 1, pp. 34–41.

[25] Bunker, R. S., and Metzger, D. E., 1990, "Local Heat Transfer in Internally Cooled Turbine Airfoil Leading Edge Regions: Part II—Impingement Cooling With Film Coolant Extraction," ASME J. Turbomach., **112**, No. 3, pp. 459–466.

[26] Metzger, D. E., and Bunker, R. S., 1990, "Local Heat Transfer in Internally Cooled Turbine Airfoil Leading Edge Regions: Part I—Impingement Cooling Without Film Coolant Extraction," ASME J. Turbomach., **112**, No. 3, pp. 451–458.

[27] Van Treuren, K. W., Wang, Z., Ireland, P. T., and Jones, T. V., 1994, "Detailed Measurements of Local Heat Transfer Coefficient and Adiabatic Wall Temperature Beneath an Array of Impinging Jets," ASME J. Turbomach., **116**, No. 2, pp. 269–374.

[28] Chang, H., Zhang, D., and Huang, T., 1997, "Impingement Heat Transfer From Rib Roughened Surface Within Arrays of Circular Jet: The Effect of the Relative Position of the jet Hole to the Ribs," ASME Paper No. 97-GT-331.

[29] Huang, Y., Ekkad, S. V., and Han, J. C., 1998, "Detailed Heat Transfer Distributions Under an Array of Orthogonal Impinging Jets," J. Thermophys. Heat Transfer, **12**, No. 1, pp. 73–79.

[30] Akella, K. V., and Han, J. C., 1999, "Impingement Cooling in Rotating Two-Pass Rectangular Channels With Ribbed Walls," J. Thermophys. Heat Transfer, **13**, No. 3, pp. 364–371.

[31] Kline, S. J., and McClintock, F. A., 1953, "Describing Uncertainty in Single-Sample Experiments," Mech. Eng., **75**, Jan., pp. 3–8.

Film Cooling Discharge Coefficient Measurements in a Turbulated Passage With Internal Crossflow

Ronald S. Bunker

Jeremy C. Bailey

General Electric Company,
Research & Development Center,
Niskayuna, NY 12309

Gas turbine blades utilize internal geometry such as turbulator ribs for improved cooling. In some designs it may be desirable to benefit from the internal cooling enhancement of ribs as well as external film cooling. An experimental study has been performed to investigate the effect of turbulator rib placement on film hole discharge coefficient. In the study, a square passage having a hydraulic diameter of 1.27 cm is used to feed a single angled film jet. The film hole angle to the surface is 30 deg and the hole length-to-diameter ratio is 4. Turbulators were placed in one of three positions: upstream of film hole inlet, downstream of film hole inlet, and with the film hole inlet centered between turbulators. For each case 90 deg turbulators with a passage blockage of 15 percent and a pitch to height ratio of 10 were used. Tests were run varying film hole-to-crossflow orientation as 30, 90, and 180 deg, pressure ratio from 1.02 to 1.8, and channel crossflow velocity from Mach 0 to 0.3. Film hole flow is captured in a static plenum with no external crossflow. Experimental results of film discharge coefficients for the turbulated cases and for a baseline smooth passage are presented. Alignment of the film hole entry with respect to the turbulator is shown to have a substantial effect on the resulting discharge coefficients. Depending on the relative alignment and flow direction discharge coefficients can be increased or decreased 5–20 percent from the nonturbulated case, and in the worst instance experience a decrease of as much as 50 percent. [DOI: 10.1115/1.1397307]

Introduction

Film cooling has made its place as a fundamental and widely used cooling technology for virtually all gas turbines. In the highest temperature applications, hot section components now routinely utilize dozens of film hole rows comprising several hundreds of individual holes. Film holes can be located at nearly any location on a cooled turbine component as long as manufacturing access to the internal cooling supply is reasonably convenient by either casting or machining processes (e.g., electro-discharge or laser). Due to the many internal cooling methods used in today's turbine components, film holes may originate from coolant supply chambers, which use impingement jets, rib roughened surfaces, pin-fins, and various other arrangements with a wide variety of parameter space. Film holes are discharged at the hot flow path surface of the components with possible exit orientations, relative to the local surface normal direction, which span the full range of axial and radial angle combinations, including in some cases negative axial angles (i.e., injection against the mainstream flow). The possible extent of external mainstream flow conditions is equally large, from stagnation conditions to supersonic flows, and includes all of the boundary layer and freestream characteristics. As recent research has also shown, the possible shapes of film cooling holes is only limited by the imagination, though generally only a few types are used in practice for reasons of manufacturing and cost (e.g., round, diffusion shaped, or slots). Of course, the very manufacturing method affects the film hole internal geometry, and so also affects the film hole flow. In actual application then, the performance of film cooling holes is determined by a daunting number of geometric and flow parameters, which in the as-manufactured and as-operated form are each represented by a distribution about some nominal mean value.

Film cooling performance for the design and operation of cooled components is generally characterized by three measures: the film hole discharge coefficient, the adiabatic film effectiveness curve, and the local heat transfer coefficient enhancement. The latter two measures dealing with the thermal boundary conditions must in reality be complete surface distributions, but are usually cast in terms of simpler relations for the purpose of preliminary design and trade-off studies. The discharge coefficient is conceptually a much simpler measure of the film hole performance, dealing only with the mass flow capability under the given internal flow, external flow, and geometric conditions. The discharge coefficient is a single-valued quantity for any given set of conditions, with no information concerning the distribution of mass flow at any location in the film hole. In this respect, the discharge coefficient is a necessary and convenient design variable, which allows the designer to distribute and balance the cooling flow needs within a component. The discharge coefficient has a deterministic effect on the thermal performance of the film hole, as well as the aerodynamic mixing losses of a component, and as such is at the root of the design calculations for all film cooled parts.

A significant experimental database exists concerning measured film hole and orifice discharge coefficients with a wide variety of parameters. Hay and Lampard [1] provide a summary of the available data sources up to 1996. Focusing just on the most common airfoil film hole angle, that of approximately 30 to 35 deg from the surface tangent, several studies have been performed that detail various factors affecting the discharge coefficients. The studies of Hay and Lampard [2] and Hay et al. [3–6] have measured discharge coefficients for sharp-edged long holes, including the effects of radiusing, internal and external crossflow, angle relative to the mainstream direction, and exit flare. Burd and Simon [7]

Contributed by the International Gas Turbine Institute and presented at the 46th International Gas Turbine and Aeroengine Congress and Exhibition, New Orleans, Louisiana, June 4–7, 2001. Manuscript received by the International Gas Turbine Institute February 2001. Paper No. 2001-GT-135. Review Chair: R. Natole.

measured discharge coefficients with variations of hole length-to-diameter ratio, including effects of crossflow and internal fluid supply direction. Thole et al. [8] presented discharge coefficients for a round hole with varied internal crossflow Mach number and a single external Mach number. Gritsch et al. [9] presented data for round holes and two types of flared hole exits with variations in both the external crossflow and internal channel Mach numbers. Gritsch et al. [10] continued this work by including the effect of orientation of the internal crossflow direction relative to the film hole inlet. All of these research efforts have been concentrated on film holes that emanate from plenums or smooth channels, and inject into quiescent space or a crossflow on a smooth surface.

Research into the effects of discrete internal channel features on discharge coefficients, such as turbulators, has not been reported in the literature until now. Studies of Ekkad et al. [11] and Shen et al. [12] have looked at the effect of film holes within a ribbed duct upon the subsequent internal surface heat transfer coefficients. These studies each placed the film holes midway between turbulators and showed enhanced heat transfer around the hole entry regions. While discharge coefficients were not measured in these studies, no effect would be expected for film holes placed well away from the turbulators. Thurman and Poinsatte [13] also measured turbulated channel internal heat transfer coefficient distributions, but with film bleed holes located at either the midway location between turbulators, or just downstream of each turbulator. Their results showed a substantially increased surface heat transfer in the latter case, indicating that the film hole bleed significantly altered the local flow field by suctioning off the separation zone aft of each turbulator, or at least moving the reattachment location forward. Again, this study did not measure hole discharge coefficients, but the implication is that these could be greatly altered as well. Wilfert and Wolff [14] investigated the effect of internal flow deflectors, or rounded turbulators, on the resulting external film effectiveness. The focus of their study was on the preparation of flow prior to entering a film hole as a means for improving the external thermal conditions. Here again, no discharge coefficients were measured, though they would certainly be affected by such geometry alterations. In an early fundamental work, Seban [15] studied the detailed flow and heat transfer in the separated region following a downward step in a channel flow, and included the effect of either blowing or suction from a slot at the base of the step. In the case of fairly strong suction from the slot, i.e., film bleed, there was a pronounced change to the surface pressures, indicating a movement of the reattachment location forward. The heat transfer in this region was increased by as much as 50 percent. Discharge coefficients were not measured in this study.

The flow field in the region of a typical channel turbulator is also of interest to the present research. Seban et al. [16], Seban [15], and Orlov et al. [17] have all studied the flow and heat transfer characteristics for surfaces in the turbulent flow after a backward facing step. Luzhanskiy and Solntsev [18] investigated the flow and heat transfer in the turbulent separation zone ahead of a forward facing step. Seban [19] and Yamamoto et al. [20] looked at the flow and heat transfer for shallow rectangular cavities (i.e., like the cavity defined between two consecutive turbulators), the former at length-to-depth ratios up to 5, and the latter at ratios up to 25. The well-known conclusions of such studies are that the flow field depends greatly on the geometry and the strength of the flow. The general characteristics noted by all researchers include the primary separation zones at each step and the reattached flow on the cavity floor surface. Yamamoto et al. [20] included flow visualization in their study, which clearly shows typical recirculation patterns within such cavities. While these studies were all performed on isolated features or cavities rather than on repeating turbulators, the recent research of Rau et al. [21] has obtained detailed pressure and LDV measurements within a straight turbulated channel. The conclusions in the case of a turbulated channel remain the same. The simplistic view of the flow field is that shown in Fig. 1.

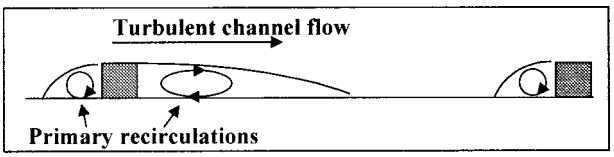

Fig. 1 Schematic of idealized flows near transverse turbulators

While internal heat transfer coefficients and external film cooling effectiveness are required for design, so too are the variations in discharge coefficients due to the presence of internal or external surface features. In fact, the latter may greatly influence the former. One of the most common internal features in cooled turbine components is the turbulator or rib roughener element. Typical investment casting tolerances, when combined with film hole machining accuracies, lead to the very real probability that film hole inlets may be located in close proximity to the turbulators. In some cases, the film hole size and density may dictate a variety of relative locations, e.g., turbulator pitch-to-height spacing of 8 with a film hole pitch-to-diameter spacing of 2. The relative location can have a substantial effect on the local flow field that the film hole entry experiences. The design of film cooled components should be such that the relative locations either do not affect the discharge coefficients, or that the discharge coefficients are measured to support a known or probable designed/manufactured geometry. The purpose of the present study is to measure film hole discharge coefficients as a function of hole pressure ratio for several cases of hole-to-turbulator placement, as well as direction and strength of internal channel Mach number.

Experimental Apparatus

The test apparatus for the present study is a simple turbulated channel containing a single film hole at the midway location as shown in Fig. 2. Venturi flow metering stations are located upstream and downstream of the main flow channel, and also downstream of the film hole discharge. The film hole flow rate is measured by its dedicated venturi meter. The flow channel is square in cross section with a hydraulic diameter of 1.27 cm. The channel wall containing the film hole is either smooth or turbulated; the other three walls of the channel remain smooth for all tests. The upstream and downstream channel inlet/exit are fed by tubes of 1.588 cm ID. There is therefore a slight step at the entry to the channel, which is about the same as a turbulator height. The venturi stations are located at least 15 cm away from the transition to the channel, and also away from the film hole discharge. The total channel length is 24.13 cm. The turbulators are of square cross section as shown in Fig. 3, with $P/e=10$ and $e/D=0.15$. The turbulators are placed at a 90-deg angle to the main flow direction. There are a total of 10 turbulator strips machined with sharp edges within the channel wall. This test section has been fabricated such that the flow direction is reversible and the film hole test plate is

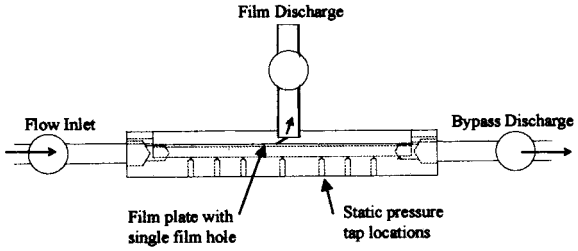

Fig. 2 Test section layout

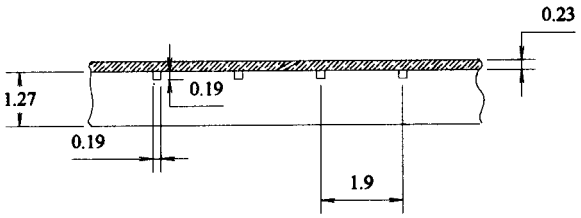

Fig. 3 Turbulated channel geometry (dimensions in centimeters)

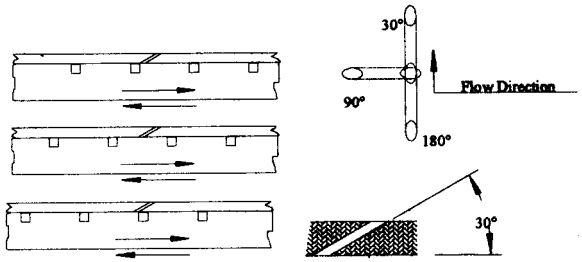

Fig. 4 Orientation and relative location of film hole to turbulators (arrows indicate reversible flow direction)

removable. In all cases then, the film hole location is after five turbulator strips, which is sufficient to develop a basic periodic flow pattern prior to the film hole. The tests are all performed at room temperature. The internal channel turbulence intensity level was not measured.

The film hole orientation is shown in Fig. 4, along with the variation in relative location to the turbulators. In all tests, the film hole has a 30-deg angle relative to the wall tangent line at discharge. The film hole was formed in the stainless steel plate by electro-discharge machining. The interior surface of the film hole is typical of electro-discharge machining, with a roughness of about 1 μm. Because the turbulators are attached after machining of the film hole, the hole entry is precisely placed as shown in Fig. 4. The nominal throat diameter of the parallel/counterflow film hole was 1.143 mm, while that of the separately machined perpendicular hole was 1.227 mm. The film hole throat was actually slightly elliptic in cross section for each case, with a minor diameter 11 percent less than nominal and a major diameter 18 percent greater than nominal, due to tool drift. The hole L/D was then about 4 and 3.75, respectively. The physical throat area used for determination of the discharge coefficient was 1.026 and 1.182 mm^2, respectively. The film hole discharges into a 2.54-cm-diam pipe section, which is large enough to act as a plenum. Three cases of hole orientation relative to the flow direction are tested, namely parallel flow (30 deg), counterflow (180 deg), and perpendicular flow (90 deg). Three cases of hole location relative to the turbulators are also tested for all orientations, these being central between two turbulators, just upstream of a turbulator, and just downstream of a turbulator.

In addition to the hole orientation and relative location, the main channel flow Mach number was also varied in these tests. The internal crossflow Mach number took on values of 0, 0.09, 0.17, and 0.25 by appropriate adjustment of the regulating valves and pressures. The Mach=0 case represents a plenum condition, but in reality has a very low Mach number flow of 0.003 or less. The discharge coefficient for these tests is calculated as

$$C_d = \frac{\text{Actual film hole mass flow rate}}{\text{Ideal film hole mass flow rate}}.$$

The actual mass flow rate of the film hole is measured and the ideal mass flow rate is based upon the isentropic expansion of the flow from the channel total pressure to the discharge plenum static pressure

$$\text{Ideal flow rate} = AP_T(P_S/P_T)^{(k+1)/2k} \times \sqrt{(2k/(k-1)RT)*((P_T/P_S)^{(k-1)/k}-1)}.$$

where A is the physical hole throat area. As shown in Fig. 2, the channel contained seven static pressure taps on the smooth opposite wall from the turbulated wall. The channel total pressure was calculated as the central static pressure opposite the film hole location plus the dynamic head determined from the channel flow rate. The discharge static pressure was measured in the exit plenum. The film hole pressure ratio reported here is the ratio of the total channel pressure at the film hole to the discharge exit plenum static pressure. To gain a clear picture of the relative flow rates and strengths involved in these tests, the following summarizes the channel Reynolds numbers, film hole Reynolds numbers for the range of pressure ratios, and ratio of mass flow rates. The film hole Reynolds numbers are representative of a large range of typical conditions found in land-based power turbines. The high channel Reynolds numbers is a consequence of the high channel internal pressure of 5 atm required to maintain appropriate conditions of Mach number and single film hole pressure ratio, while also allowing a measurable film hole flow rate. While such turbulated channel Reynolds numbers are higher than the general literature database (up to 10^5), the extended effects upon the measured discharge coefficients are not felt to be significant.

Channel Mach Number	~0, 0.09, 0.17, 0.25
Channel Re	4×10^3, 13×10^4, 25×10^4, 37×10^4
Pressure Ratio	1.02 . . . 1.8
Film Hole Re	1×10^4 . . . 6.4×10^4
M_F/M_C	0.002 . . . 0.04

The experimental uncertainty for the discharge coefficient was determined by the methods of Kline and McClintock [22]. For the range of conditions of tests reported in this study, the uncertainty in discharge coefficient varies from 4.5 to 8.75 percent, with the higher value corresponding to the very lowest magnitude conditions of hole flow rate and pressure ratio. The dominant factors in this uncertainty are the film hole diameter and the film hole flow rate. The film hole diameter was measured to within ±0.0254 mm, and the calibrated flow venturi has an accuracy of ±2 percent.

Results and Discussion

Smooth Channel Discharge Coefficients. The film hole discharge coefficients reported in the literature to date have all been for holes emanating from smooth plenums or channels. For a nominally round film hole with a length-to-diameter ratio well above unity, where the film hole has no internal roughness or blockage features and there is no crossflow internal or external to the hole, the rule-of-thumb is a discharge coefficient of about 0.8. Figure 5 shows the present results for each hole orientation case tested with the channel walls smooth. First, the two cases with zero internal crossflow condition show discharge coefficients from 0.78 to 0.8 over the entire range of pressure ratio, which agrees well with expectation. With parallel flow of varying magnitude velocity, the discharge coefficients rise to between 0.85 and 0.9. As recent CFD predictions for film hole flow and heat transfer have pointed out, a parallel hole alignment tends to ''scoop'' out the channel flow, effectively reducing the resistance to flow through the hole. In the opposite sense, counterflow alignment is seen to consistently reduce the discharge coefficients over the entire range of pressure ratios as the internal flow velocity is increased. This has been seen in CFD predictions as the separation of the hole inlet flow from the sharp corner which the flow is attempting to navigate as it reverses direction into the hole. Examples of such flow behavior predictions can be found in Lin and Shih [23] and also Kohli and Thole [24]. These effects can also be discerned in the resulting external surface flow field and thermal

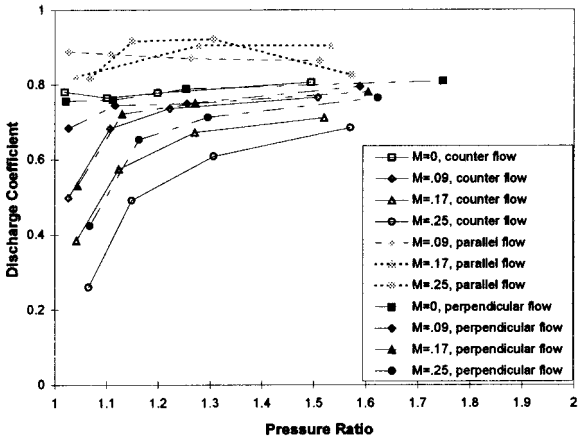

Fig. 5 Nonturbulated (smooth) channel film hole discharge coefficients

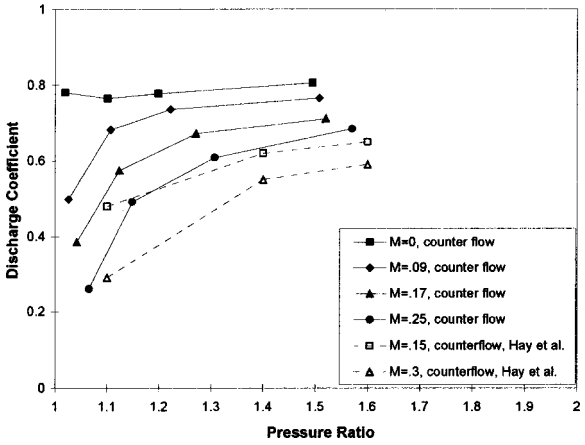

Fig. 8 Counterflow (smooth) discharge coefficient: comparison with Hay et al. [5]

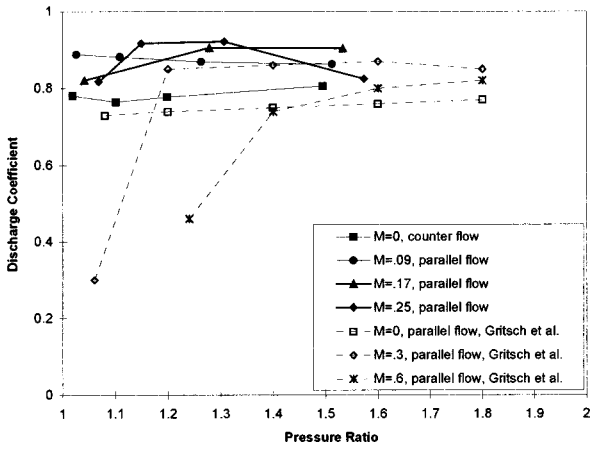

Fig. 6 Parallel flow (smooth) discharge coefficient: comparison with Gritsch et al. [10]

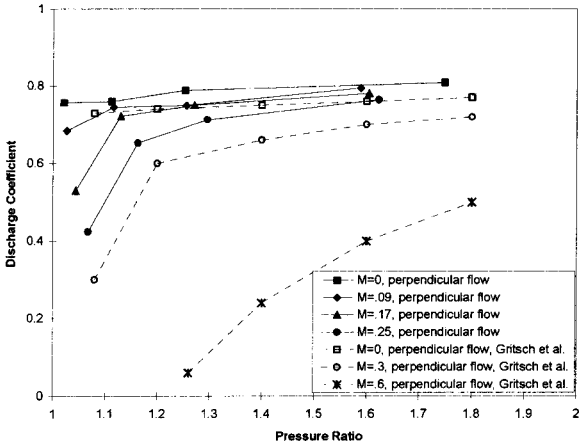

Fig. 7 Perpendicular flow (smooth) discharge coefficient: comparison with Gritsch et al. [10]

conditions on flat plates, such as those of Burd and Simon [25]. The resulting discharge coefficients for the case of perpendicular hole alignment predictably fall between parallel and counterflow for the range of pressure ratios, but tending to behave more strongly like the counterflow condition.

While the existing literature data concerning the effect of film hole orientation to internal crossflow direction is limited, the present data for both parallel and perpendicular cases can be compared with that reported by Gritsch et al. [10] for round film holes. Figure 6 shows the comparison for parallel flow with a plenum external discharge condition. The data of Gritsch et al. are for a hole L/D of 6. The supply channel geometry of Gritsch et al. is of about the same relative width with respect to the film hole diameter, but about half the relative height of the present channel. For the condition of no internal flow velocity, the comparison is quite good, with both results showing discharge coefficients of 0.75 to 0.8. The counterflow data of the present tests has been used in the absence of parallel flow data, since all such cases give the same result. In the current tests, an increase in the internal flow velocity causes the discharge coefficient to rise above 0.8, only declining again for the $M=0.25$ case as the pressure ratio becomes very high. At $M=0.3$, the data of Gritsch et al. also rise above 0.8, but only for pressure ratios greater than 1.2. This downturn at low pressure ratio is observed in the present data, but with far less magnitude. This difference is consistent with the change in hole L/D between the two sets of data.

Figure 7 shows the comparison of perpendicular film hole alignment with the data of Gritsch et al. [10]. It is quite clear that excellent agreement is achieved in both magnitudes and trends. The present internal crossflow cases of $M \leqslant 0.25$ fall short of the $M=0.3$ case of Gritsch et al., providing a nice filling of the complete discharge coefficient map. The smooth wall, parallel flow test data is the only instance in the current study of discharge coefficients greater than 0.8. This may suggest some additional sensitivities are involved in this geometry. No clear explanation for the decrease in discharge coefficient for M of 0.25 is apparent at this time.

Figure 8 shows the present counter flow film hole alignment results with the data of Hay et al. [5]. Hay et al. used a test arrangement very similar to the present study, but with a hole L/D ratio of 6. Again here, as with the comparison to Gritsch et al., the agreement is very good, with the present discharge coefficients slightly higher due to the smaller L/D.

Turbulated Channel Discharge Coefficients. With the addition of turbulators on the film hole discharge wall, the flow field supplying the region near a film hole entry can be drastically altered. As depicted in Fig. 1, for turbulator spacings that lie in the optimal performance range of P/e between 6 and 10, it is desirable to locate the film hole entry midway between the turbulators. This optimal spacing depends of course on many factors, but for the present purposes it is the spacing that allows reattachment of the flow between turbulators, and provides good performance for internal channel heat transfer coefficients. The current channel

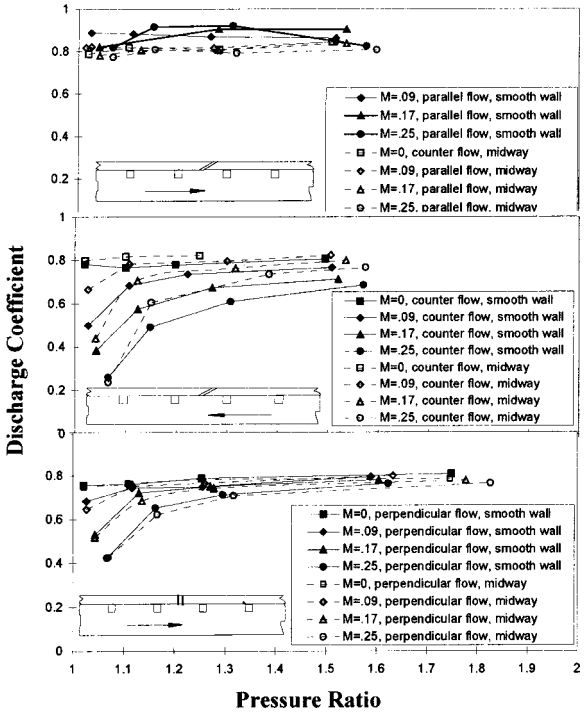

Fig. 9 Effect of turbulated wall with film hole placed midway between turbulators

utilizes a spacing of $p/e=10$. By allowing for reattachment near the film hole entry, the film hole is located outside the more highly variable regions of separations near the turbulators, which then provides a more consistent and predictable film hole performance. Figure 9 shows the present discharge coefficient data for all three cases of film hole orientation, comparing the smooth wall results to those obtained with the film hole located midway between two turbulators.

For parallel flow, there is a decrease in the discharge coefficient to a constant value of 0.8 for all internal channel velocities, indicating that the location in the reattachment region of flow has leveled the performance as desired. For counter flow, only the $M=0$ case is unchanged by the addition of turbulators. As the internal crossflow velocity increases in counterflow, the resulting discharge coefficient for the turbulated wall increases slightly but consistently above that for a smooth wall, from 5 to 20 percent. This indicates the more sensitive nature of the counterflow geometry to changes in local flow behavior. One might speculate that the local relative flow angle to the hole entry near reattachment is less than that for the smooth wall, producing less separation of flow at the hole inlet corner. Finally, perpendicular alignment results in essentially no change in discharge coefficients for the turbulated wall compared to the smooth wall.

Effect of Film Hole Entry Just Aft of Turbulator. In the case where a film hole is located just aft of a turbulator (downstream), the entry to the film hole finds itself in the separated recirculation region behind a backward facing step. Flow strength, geometry, and relative flow rate will all play a role in determining the effect on the discharge coefficient. In the present test, the turbulator height is about 1.5 times the film hole nominal diameter. This means that for turbulent channel flow over the turbulators, the separation region will more than cover the entire film hole entry footprint for all orientations of the film hole. The film hole entry will actually see the reverse flow of the recirculation zone. Moreover, since the present tests achieve a maximum relative film hole flow rate equal to 4 percent of the channel flow, it is not expected that the film hole will divert the main channel flow pattern by suction of the flow. Such geometry and flow conditions are representative of the conditions to be found in actual turbine airfoil cooling passages.

Figure 10 shows the measured discharge coefficients for each film hole orientation with the entry placed just aft of the turbulator. The smooth wall discharge coefficients are plotted in each case for direct comparison. As expected, the $M=0$ condition for internal flow provides the same nearly constant discharge coefficient as the smooth wall. The most striking result obtained is that of parallel flow in which the discharge coefficient is drastically reduced at pressure ratios of less than 1.4. As shown in Rau et al. [21] for a turbulated channel flow, the region just aft of a turbulator contains the lowest static pressure near the wall due to the high flow acceleration and also high total pressure loss coming off the turbulator. For a similar P/e ratio and average channel Re number, Rau et al. measured a pressure coefficient C_p in this region of about -0.17. In parallel orientation then, the film hole entry experiences a lower local pressure ratio than that measured with smooth wall. Another feature of this flow field is that the hole entry is within the reverse flow of the recirculation, and hence the very local flow is more like counter flow.

The effect of placing the film hole entry just aft of the turbulator has also brought the parallel flow results to be nearly the same as those for counter flow in this same situation. The counterflow, discharge coefficients are actually modestly improved (5 to 20 percent) from the smooth wall condition for all conditions of $M>0$. The counterflow hole orientation must also experience the lower local pressure ratio due to the turbulator, but this has been compensated by the fact that the film hole entry within the recirculation region now sees the reverse flow, i.e., local parallel flow. In the perpendicular orientation, there is again little difference to the smooth wall results, only a small decrease at the higher M conditions. This orientation is in the neutral position with respect to the flow reversal behind the turbulator. Undoubtedly, the presence of the film hole suction does alter the recirculation region behind the turbulator to some degree, just as Seban [15] demonstrated, but the combined effects of pressure field, location, and

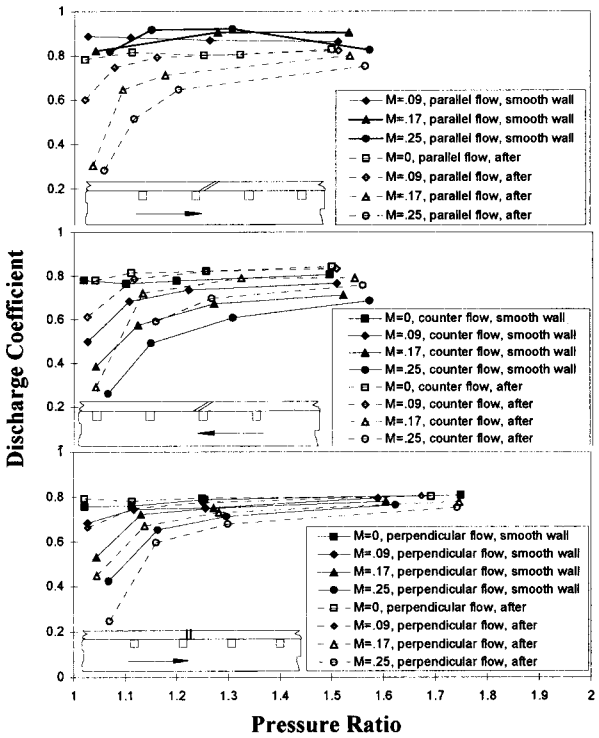

Fig. 10 Discharge coefficients for film holes located just aft of turbulator

orientation have resulted in all film holes having essentially the same discharge coefficient behavior in this location.

Effect of Film Hole Entry Just Prior to Turbulator. A film hole entry located just before a turbulator also experiences a recirculation region, but one of a different nature to the aft separation. The recirculation zone just before a turbulator is a region of high pressure due to the impingement on, and blockage of the turbulator. Again from the study of Rau et al. [21], the pressure coefficient in this location was measured to be about +0.19. The velocity field measurements of the same study also show this region to be of relatively small extent by comparison with the aft separation, covering about one turbulator height in front of the blockage.

Figure 11 shows the measured discharge coefficients for each film hole orientation with the entry placed just prior to the turbulator. In this case, because the recirculation region is small to begin with, the film hole entry footprint is likely to be just barely covered by this reverse flow area. Parallel orientation of the film hole with the mainstream direction results in a constant but lower discharge coefficient than that of the smooth wall. The discharge coefficient is now reduced slightly to 0.8. The combined effects of blockage and reverse flow have made it more difficult for the flow to enter the film hole in this orientation, despite the higher local pressure. The discharge coefficient is however, remarkably constant over the entire pressure ratio range, reflecting the unwaivering nature of the small recirculation region here.

The counterflow discharge coefficients are greatly improved over those of the smooth wall. The presence of the turbulator blockage and the reverse flow has directed the flow into the film hole entry.

There is still a substantial effect of internal mainstream velocity. For the perpendicular film hole orientation, the discharge coefficients are only slightly improved over the smooth wall results. As with the smooth wall, the perpendicular orientation results lie between those of the parallel and counter flow cases.

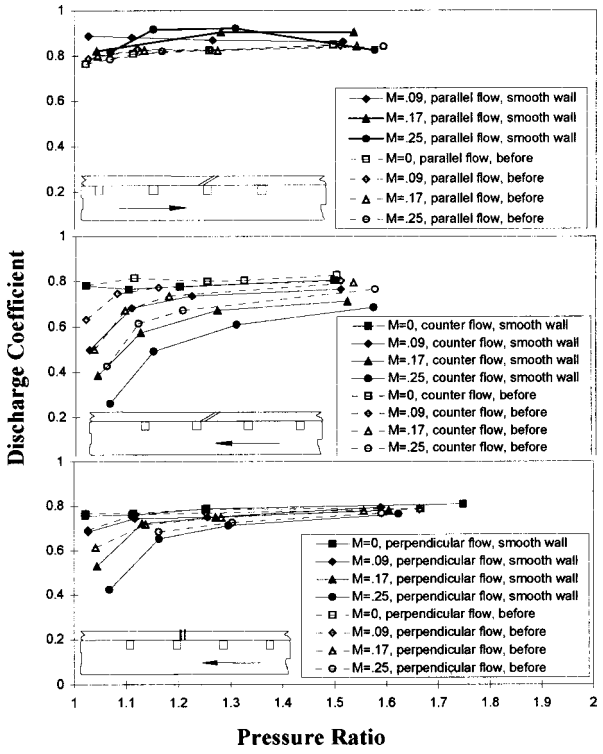

Fig. 11 Discharge coefficients for film holes located just before turbulator

Conclusions

The present study has investigated the effect of film hole entry placement near a channel turbulator on the resulting film hole discharge coefficient. This is the first such study to measure discharge coefficients as influenced by turbulators. The turbulated channel flow is representative of a typical turbine airfoil cooling passage. Discharge coefficients have been presented as a function of film hole pressure ratio with variation of the film hole orientation, location, and internal channel flow Mach number. The major conclusions from this study are:

- Alignment of the film hole relative to the channel flow direction for the nonturbulated channel has a great effect on discharge coefficients. The present results agree with previous studies, finding that discharge coefficients decrease as the film hole is rotated from parallel to perpendicular to cross flow orientation.
- Alignment of the film hole entry with respect to the turbulator can have an equally substantial effect on the resulting discharge coefficients.
- Placement of the film hole midway between two turbulators has relatively small effect, showing some modest increase in the counterflow condition, and a small decrease in the parallel flow condition. For typical ''optimal'' turbulator P/e geometries, this is the preferred location of film holes within the channel to obtain low sensitivity relative to the smooth wall discharge coefficients that form the bulk of the available design database.
- Placement of the film hole just aft of the turbulator results in a severe decrease in discharge coefficients for parallel flow orientation compared to a smooth wall, and smaller changes for perpendicular and counter flow orientations. All cases of orientation are essentially equalized in this location, showing very similar magnitudes over all pressure ratios and channel Mach numbers.
- Placement of the film hole just prior to the turbulator results in improved discharge coefficients for the counter flow orientation, but a small decrease for parallel flow, due to the blockage effect of the turbulator.
- In most cases the typical behavior of decreasing discharge coefficients is the channel flow Mach number increases is observed.
- The most robust film hole orientation is that of perpendicular flow, which displays the least changes over the entire range of locations relative to the turbulator, as well as between smooth and turbulated walls.

Acknowledgments

This study was prepared with the support of the U.S. Department of Energy, under Cooperative Agreement No. DE-FC21-95MC31176. However, any opinions, findings, conclusions, or recommendations expressed herein are those of the author and do not necessarily reflect the views of the DOE. The authors also wish to acknowledge the contributions of Dr. Nesim Abuaf and Mr. Alan Richter of GE R&D for their assistance in the planning and execution of this study.

Nomenclature

A = physical film hole throat area, cm^2
C_d = film hole discharge coefficient
C_p = pressure coefficients= $(p_s - p_{ref})/(0.5\rho U^2)$
D = film hole throat diameter, mm
D_h = channel hydraulic diameter, cm
e = height of turbulator, cm
k = ratio of specific heats
L = film hole length, mm
M = channel Mach number
M_C = channel flow rate, kg/s
M_F = film hole flow rate, kg/s
P = pitch between turbulators
P_S = exit plenum static pressure
P_T = channel total pressure at film hole location

R = gas constant
Re_C = channel Reynolds number based on smooth hydraulic diameter
Re_F = film hole Reynolds number based on nominal diameter
T = total temperature
ρ = density of film hole air

References

[1] Hay, N., and Lampard, D., 1998, ''Discharge Coefficient of Turbine Cooling Holes: A Review,'' ASME J. Turbomach., **120**, pp. 314–319.
[2] Hay, N., and Lampard, D., 1995, ''The Discharge Coefficient of Flared Film Cooling Holes,'' ASME Paper No. 95-GT-15, *IGTI Turbo Expo. Houston*.
[3] Hay, N., Lampard, D., and Benmansour, S., 1983, ''Effect of Crossflows on the Discharge Coefficient of Film Cooling Holes,'' ASME J. Eng. Power, **105**, pp. 243–248.
[4] Hay, N., Khaldi, A., and Lampard, D., 1987, ''Effect of Crossflows on the Coefficient of Discharge of Film Cooling Holes with Rounded Entries or Exits,'' presented at the 2nd ASME/JSME Thermal Engineering Conference, HI.
[5] Hay, N., Henshall, S. E., and Manning, A., 1994, ''Discharge Coefficients of Holes Angled to the Flow Direction,'' ASME J. Turbomach., **116**, pp. 92–96.
[6] Hay, N., Lampard, D., and Khaldi, A., 1994, ''The Coefficient of Discharge of 30° Inclined Film Cooling Holes With Rounded Entries or Exits,'' ASME Paper No. 94-GT-180.
[7] Burd, S. W., and Simon, T. W., 1999, ''Measurements of Discharge Coefficients in Film Cooling,'' ASME J. Turbomach., **121**, pp. 243–248.
[8] Thole, K. A., Gritsch, M., Schulz, A., and Wittig, S., 1997, ''Effect of a Crossflow at the Entrance to a Film-Cooling Hole,'' ASME J. Fluids Eng., **119**, pp. 533–540.
[9] Gritsch, M., Schulz, A., and Wittig, S., 1998, ''Discharge Coefficient Measurements of Film-Cooling Holes With Expanded Exits,'' ASME J. Turbomach., **120**, pp. 557–563.
[10] Gritsch, M., Saumweber, C., Schulz, A., Wittig, S., and Sharp, E., 2000, ''Effect of Internal Coolant Crossflow Orientation on the Discharge Coefficient of Shaped Film-Cooling Holes,'' ASME J. Turbomach., **122**, pp. 146–152.
[11] Ekkad, S. V., Huang, Y., and Han, J. C., 1998, ''Detailed Heat Transfer Distributions in Two-Pass Square Channels With Rib Turbulators and Bleed Holes,'' Int. J. Heat Mass Transf., **41**, pp. 3781–3791.
[12] Shen, J. R., Wang, Z., Ireland, P. T., Jones, T. V., and Byerley, A. R., 1996, ''Heat Transfer Enhancement Within a Turbine Blade Cooling Passage Using Ribs and Combinations of Ribs With Film Cooling Holes,'' ASME J. Turbomach., **118**, pp. 428–434.
[13] Thurman, D., and Poinsatte, P., 2001, ''Experimental Heat Transfer and Bulk Air Temperature Measurements for a Multipass Internal Cooling Model With Ribs and Bleed,'' ASME J. Turbomach., **123**, pp. 90–97.
[14] Wilfert, G., and Wolff, S., 2000, ''Influence of Internal Flow on Film Cooling Effectiveness,'' ASME J. Turbomach., **122**, pp. 327–333.
[15] Seban, R. A., 1964, ''Heat Transfer to the Turbulent Separated Flow of Air Downstream of a Step in the Surface of a Plate,'' ASME J. Heat Transfer, **86**, pp. 259–264.
[16] Seban, R. A., Emery, A., and Levy, A., 1959, ''Heat Transfer to Separated and Reattached Subsonic Turbulent Flows Obtained Downstream of a Surface Step,'' J. Aerosp. Sci., pp. 809–814.
[17] Orlov, V. V., Ovchinnikov, V. V., Mukhina, N. N., and Karsten, V. M., 1984, ''Investigation of Turbulence and Heat Transfer in a Separating Flow Behind a Step,'' Heat Transfer-Sov. Res., **16**, No. 2, pp. 58–68.
[18] Luzhanskiy, B. Ye., and Solntsev, V. P., 1971, ''Experimental Study of Heat Transfer in the Zone of Turbulent Boundary Layer Separation Ahead of a Step,'' Heat Transfer-Sov. Res., **3**, No. 6, pp. 200–206.
[19] Seban, R. A., 1965, ''Heat Transfer and Flow in a Shallow Rectangular Cavity With Subsonic Turbulent Air Flow,'' Int. J. Heat Mass Transf., **8**, pp. 1353–1368.
[20] Yamamoto, H., Seki, N., and Fukusako, S., 1979, ''Forced Convection Heat Transfer on Heated Bottom Surface of a Cavity,'' ASME J. Heat Transfer, **101**, pp. 475–479.
[21] Rau, G., Cakan, M., Moeller, D., and Arts, T., 1998, ''The Effect of Periodic Ribs on the Local Aerodynamic and Heat Transfer Performance of a Straight Cooling Channel,'' ASME J. Turbomach., **120**, pp. 368–375.
[22] Kline, S. J., and McClintock, F. A., 1953, ''Describing Uncertainties in Single Sample Experiments,'' Mech. Eng. (Am. Soc. Mech. Eng.), **75**, Jan., pp. 3–8.
[23] Lin, Y.-L., and Shih, T. I.-P., 1998, ''Computations of Discrete-Hole Film Cooling Over Flat and Convex Surfaces,'' ASME Paper No. 98-GT-436.
[24] Kohli, A., and Thole, K. A., 1998, ''Entrance Effects on Diffused Film-Cooling Holes,'' ASME Paper No. 98-GT-402.
[25] Burd, S. W., and Simon, T. W., 1997, ''The Influence of Coolant Supply Geometry on Film Coolant Exit Flow and Surface Adiabatic Effectiveness,'' ASME Paper No. 97-GT-25.

Effect of Crossflows on the Discharge Coefficient of Film Cooling Holes With Varying Angles of Inclination and Orientation

Michael Gritsch
ALSTOM Power,
Gas Turbine Base Development,
5405 Baden-Dättwil, Switzerland

Achmed Schulz

Sigmar Wittig

Institut für Thermische Strömungsmaschinen,
Universität Karlsruhe (TH),
76128 Karlsruhe, Germany

Measurements of discharge coefficients for five configurations of cylindrical film cooling hole geometries are presented. These comprise holes of varying angles of inclination (α =30, 45, and 90 deg) and orientation (γ=0, 45, and 90 deg), which are tested over a wide range of engine-like conditions in terms of internal and external crossflow Mach numbers (Ma_m=0 . . . 1.2, Ma_c=0 . . . 0.6) as well as pressure ratios (p_{tc}/p_m =1 . . . 2.25). Results show that discharge coefficients do not depend solely on hole geometry, but are also profoundly affected by the internal and external crossflow conditions. The effect of increasing the orientation angle on the discharge behavior is very similar to the effect of increasing the inclination angle. Both result in higher losses, particularly at the cooling hole inlet while the losses at the hole exit are only slightly affected. [DOI: 10.1115/1.1397306]

Introduction

A viable option for keeping turbine blade temperatures at acceptable levels is film cooling, which comprises ejection of relatively cold compressor bleed air through discrete cooling holes on the blade's surface. The knowledge of discharge coefficients of these film cooling holes is vital for an accurate and reliable design of turbine blade cooling systems. The discharge behavior of the holes is known to depend on both hole geometry as well as flow conditions upstream and downstream of the hole.

Recently, Hay and Lampard [1] gave a comprehensive review of published data on discharge coefficients for film cooling applications. In the absence of design features like turbulators, pin-fins, etc., the main geometric parameters affecting the discharge coefficient comprise the hole length [2], hole inclination angle [3], hole orientation angle [4], hole entry and exit radiusing [5,6] as well as hole shape [7–9].

Contributed by the International Gas Turbine Institute and presented at the 46th International Gas Turbine and Aeroengine Congress and Exhibition, New Orleans, Louisiana, June 4–7, 2001. Manuscript received by the International Gas Turbine Institute February 2001. Paper No. 2001-GT-134. Review Chair: R. Natole.

The effect of engine-like crossflows on the internal as well as on the external side of the film cooling hole has received much less attention, particularly for the case when crossflows are present simultanously on both sides of the hole. The study of Hay et al. [3] was the only presenting discharge coefficients with crossflows being present on both sides of the hole, albeit for a limited range of flow conditions and hole geometries.

However, there is no study present where the effect of internal and external crossflow on the discharge coefficient of cylindrical film cooling holes with different angles of inclination and orientation is systematically studied for a wide range of flow conditions, i.e., Mach numbers and pressure ratios. Therefore, the intention of the present study is to provide an extensive data base of discharge coefficients focusing on the effect of internal and external crossflows for cylindrical film cooling holes with different angles of inclination and orientation.

Experimental Apparatus

Test-Rig Design. The study was carried out in a continous flow wind tunnel at Karlsruhe University. The wind tunnel con-

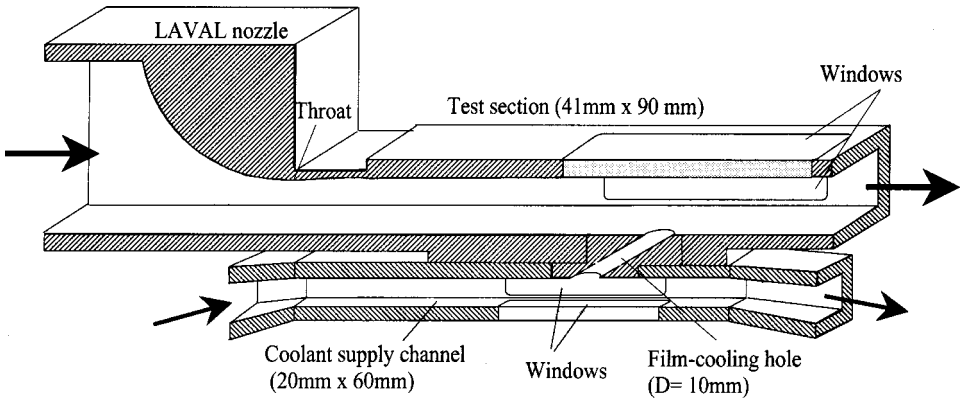

Fig. 1 Film-cooling test section

Table 1 Film-cooling hole geometries tested in present study

Hole	inclination α	orientation γ	t/D	L/D
1	30deg	0deg	3	6
2	45deg	0deg	3	4.24
3	90deg	0deg	3	3
4	30deg	45deg	3	6
5	30deg	90deg	3	6

Table 2 Operating conditions of the discharge coefficient study

Pressure ratio	p_{tc}/p_m	1 . . . 2.25
Temperature ratio	T_{tc}/T_{tm}	1.0
Internal Mach number	Ma_c	0. . . 0.6
External Mach number	Ma_m	0. . . 1.2
Internal Reynolds number	$Re_{D,c}$	up to $2.5 \cdot 10^5$
External Reynolds number	$Re_{D,m}$	up to $2.1 \cdot 10^5$
Film hole Reynolds number	$Re_{D,hole}$	up to $1.5 \cdot 10^5$
Boundary layer thickness	δ_{99}/D	0.5
External turbulence level	Tu_m	<2 %
Internal turbulence level	Tu_c	1 %

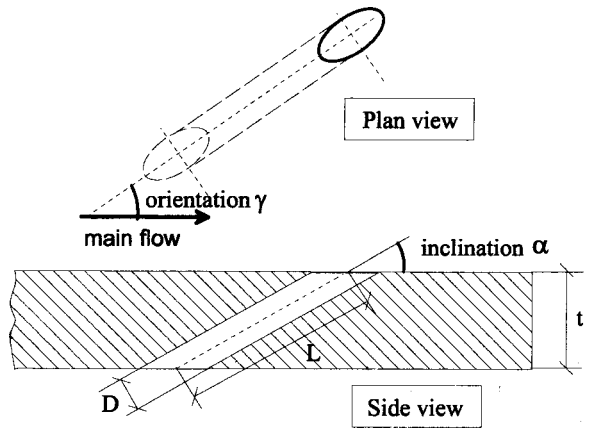

Fig. 2 Definition of inclination and orientation angles

sists of two loops representing the external and internal crossflow of a film cooled airfoil. Both loops were controlled independently and linked by a single, scaled-up film cooling hole (Fig. 1). For all tests presented in this paper, both loops were oriented parallel to each other, representing a flow condition usually found, for instance, in the mid portion of nozzle guide vanes.

The main challenge for the test rig design was to measure the

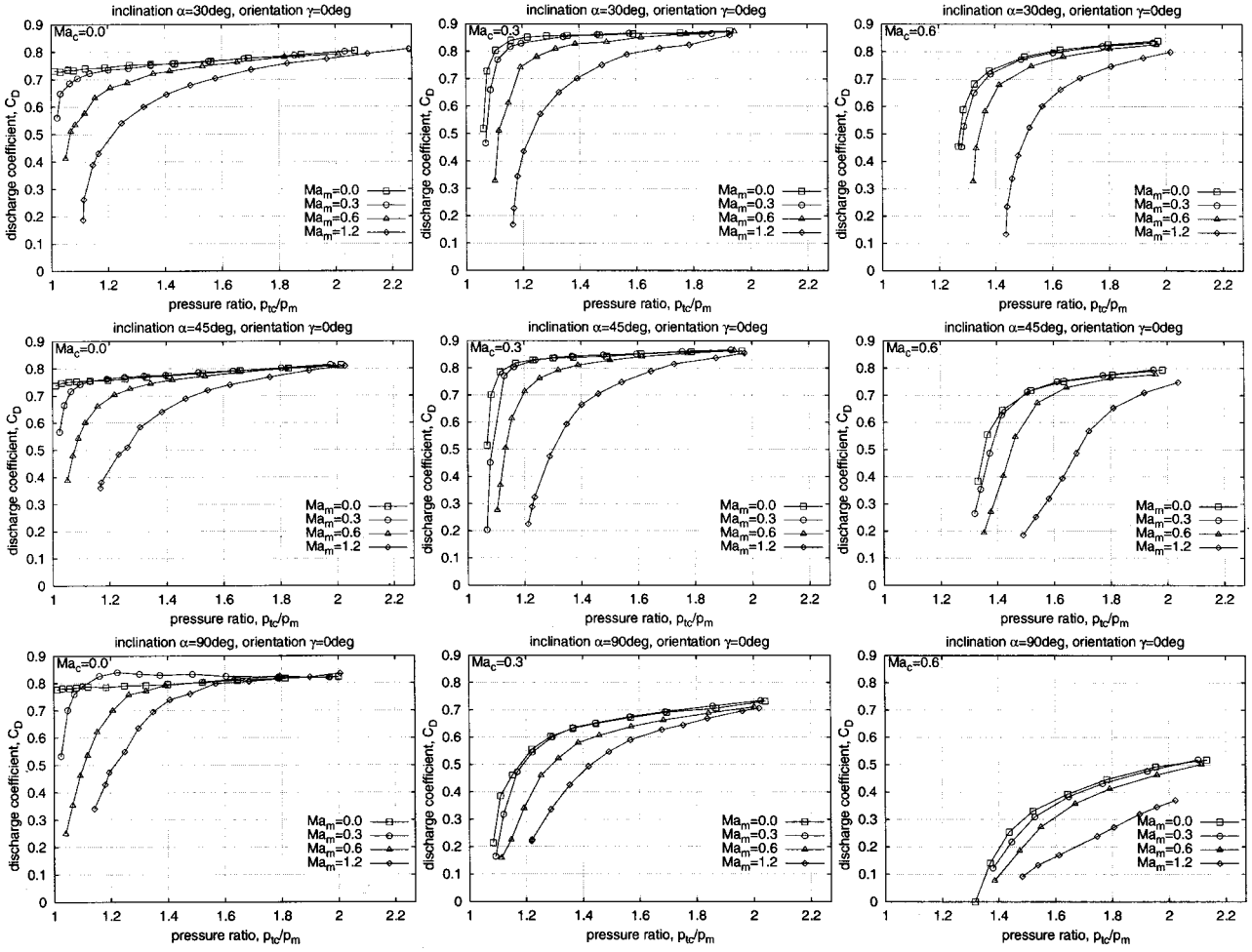

Fig. 3 Discharge coefficients of holes with varying inclination angles (α=30, 45, and 90 deg) and fixed orientation angle (γ=0 deg)

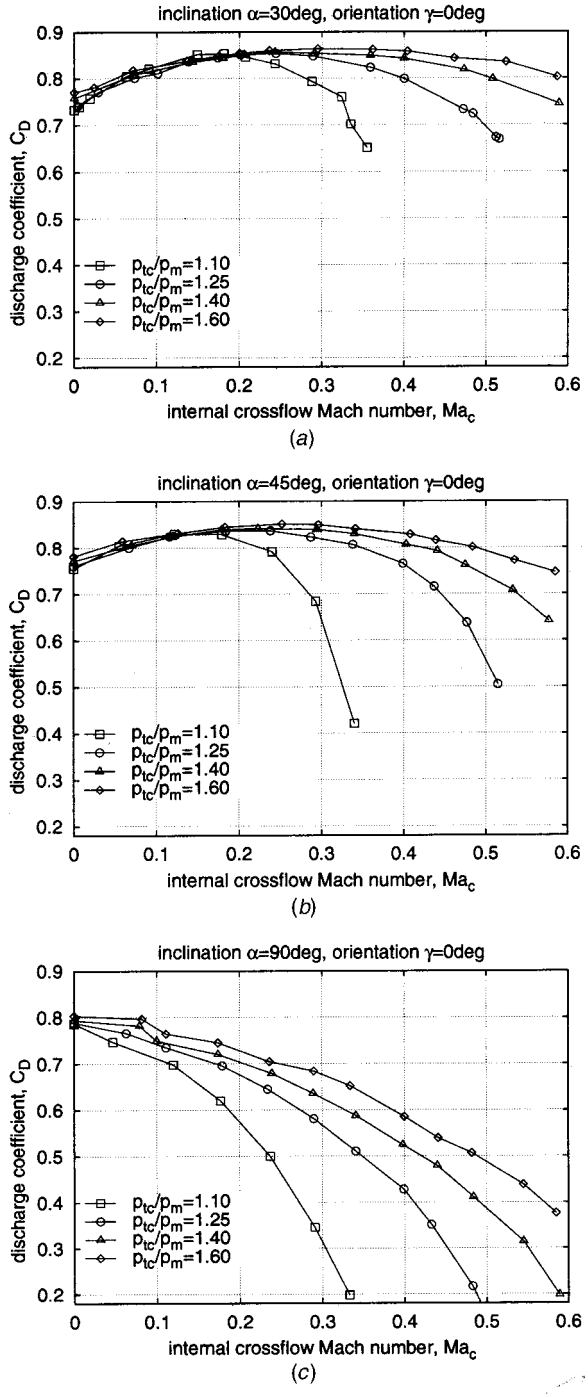

Fig. 4 Effect of internal crossflow for holes with different inclination angles: (*a*) $\alpha=30$ deg, (*b*) $\alpha=45$ deg, (*c*) $\alpha=90$ deg

flow rate accurately through the film cooling hole with crossflows being present on both sides of the hole. Since the flow rate through the hole is only a few percent of the crossflow rates, the standard configuration, i.e., measuring the flowrate up- and downstream of the hole location and calculating the hole flow rate from the difference of these two flow rates, would lead to undesirably high uncertainties for the discharge coefficient.

Therefore, the secondary loop representing the internal coolant flow was designed as a ''closed loop,'' which allows to easily control and accurately measure the flow rate entering the loop as ''substitute'' for the film cooling hole bleed. The hole flow rate is obtained directly for all flow cases, independently of the crossflow rates. A more detailed description of the test facility was given by Wittig et al. [10].

In total, five hole geometries were tested (Table 1). A cylindical hole with an inclination angle of $\alpha=30$ deg ejecting in mainflow direction (orientation angle $\gamma=0$ deg) serves as a baseline geometry. For a given blade design (fixed wall thickness t) the designer of the cooling system has only two possibilities of varying the geometry of a cylindrical film cooling hole: the inclination and the orientation angle. This was taken into account for the present study by altering the inclination as well as the orientation angle of the film cooling hole. Starting from the baseline geometry ($\alpha=30$ deg and $\gamma=0$ deg), two additional inclination angles ($\alpha=45$ and 90 deg) as well as two additional orientation angles ($\gamma=45$ and 90 deg) were studied covering the range of typical cylindrical film cooling hole geometries; see Fig. 2. The diameter D of all holes was 10 mm. The wall thickness t was kept constant at 30 mm. Entry and exit of the holes were sharp-edged and the interior surfaces of the holes were aerodynamically smooth.

Definition of the Discharge Coefficient. The discharge coefficient C_D is the ratio of actual mass flow rate and ideal mass flow rate through the film-cooling hole. The ideal mass flow rate is calculated assuming an isentropic one-dimensional expansion from the total pressure in the coolant supply p_{tc} to the static pressure in the mainflow p_m. This leads to

$$C_D=\frac{\dot{m}}{p_{tc}\left(\frac{p_m}{p_{tc}}\right)^{\kappa+1/2\kappa}\sqrt{\frac{2\kappa}{(\kappa-1)RT_{tc}}\left(\left(\frac{p_{tc}}{p_m}\right)^{\kappa-1/\kappa}-1\right)}\frac{\pi}{4}D^2}$$

The total pressure and temperature in the coolant supply were measured $1D$ upstream of the cooling hole inlet with a probe located $2D$ off channel centerline. The static pressure in the mainflow was measured at the top wall opposite of the hole.

Test Program. When deciding on the test program, the intention was to study each hole geometry over a wide range of engine-like flow conditions. A matrix of three internal (coolant) Mach numbers ($Ma_c=0$, 0.3, and 0.6) and four external (mainflow) Mach numbers ($Ma_m=0$, 0.3, 0.6, and 1.2) was considered to be studied over a range of pressure ratios $p_{tc}/p_m=1\ldots2.25$. Additionally, in order to focus on the effect in internal crossflow, each hole was tested at four fixed pressure ratios $p_{tc}/p_m=1.1$, 1.25, 1.4, and 1.6 over a range of internal crossflow Mach numbers ($Ma_c=0\ldots0.6$) without a crossflow at the hole exit side ($Ma_m=0$). Mainflow and coolant were at equal total temperatures of 290 K. Table 2 provides the detailed set of operating conditions.

Estimates of Accuracy. Uncertanties were estimated following the procedure given by Kline and McClintock [11]. The uncertainty in the values of C_D resulted from the uncertainty in measuring the actual flow rate through the film-cooling hole and the uncertainty in determining the ideal flow rate.

Due to the fact that the coolant supply was designed as a closed loop [10], the actual flow rate could be measured for all flow cases directly using a standard orifice leading to an uncertainty of 2 percent except for very low mass flow rates. The uncertainty in determining the ideal flow rate was calculated to be much less than 2 percent except for very low pressure ratios. Overall, the uncertainty (95 percent confidence level) of the C_D values was found to be less than 2 percent in most of the cases considered, increasing for low pressure ratios and mass flow rates up to 4 percent.

Results and Discussion

Holes With Varying Inclination Angles. Figure 3 shows the discharge coefficients plotted versus pressure ratio for the holes with varying inclination angles α of 30, 45, and 90 deg and a fixed orientation angle $\gamma=0$ deg. Within each plot, the internal cross-

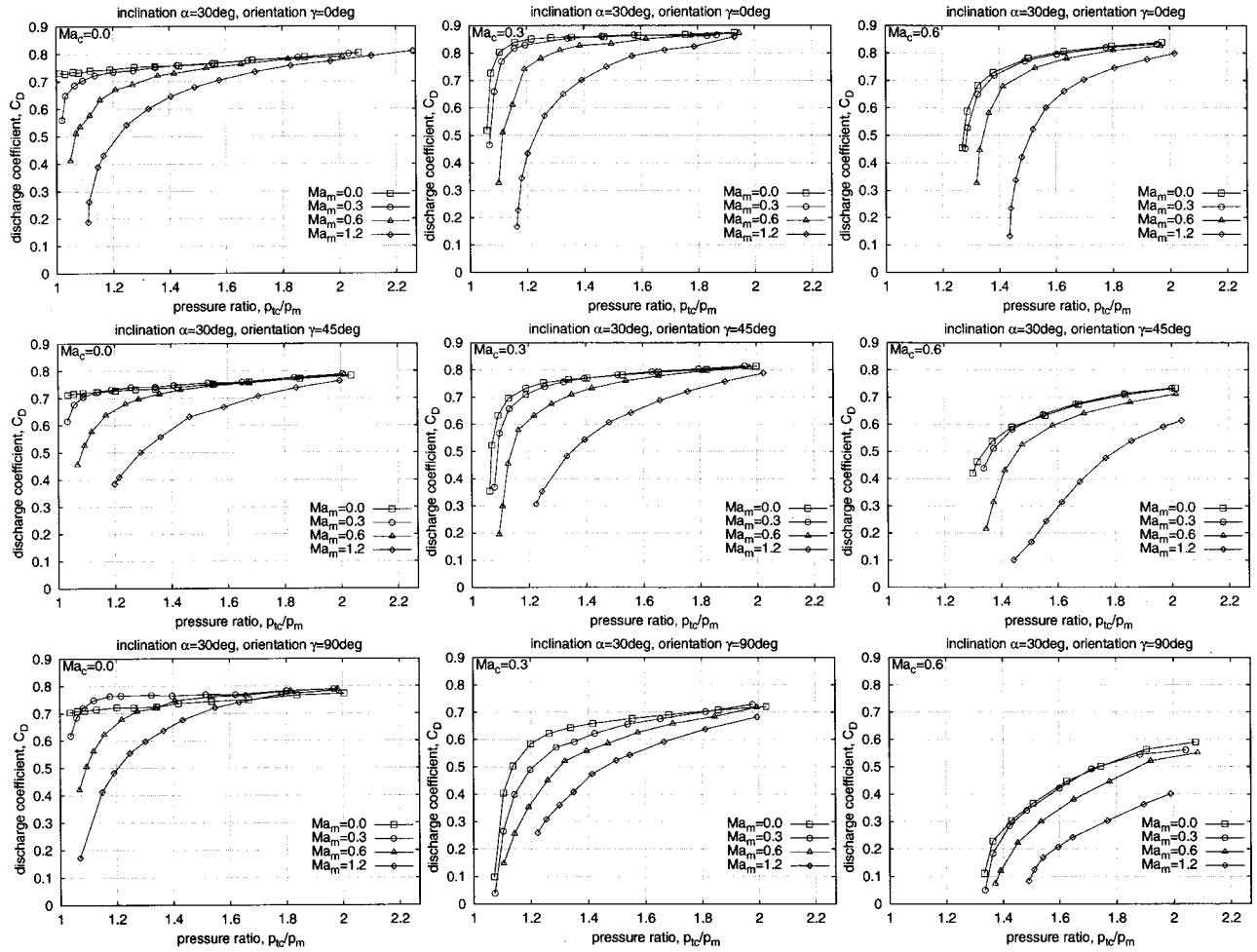

Fig. 5 Discharge coefficients of holes with varying orientation angles ($\gamma=0$, 45, and 90 deg) and fixed inclination angle ($\alpha=30$ deg)

flow Mach number Ma_c was kept constant while the external Mach number was varied from $Ma_m=0$ to 1.2. Two general trends were found:

1 For all flow cases investigated, increasing the pressure ratio results in higher discharge coefficients, particularly at high external crossflow Mach numbers
2 Keeping the pressure ratio constant and increasing the external Mach number leads to decreasing discharge coefficients. The only exception is the $\alpha=90$ deg hole without internal crossflow ($Ma_c=0$). This case will be discussed later.

The effect of the internal Mach number, on the other hand, does not become sufficiently clear from the plotted data. It seems that increasing the internal Mach number results in lower discharge coefficients. However, this issue needed further investigation to get a more detailed view. Therefore, additional experiments without external crossflow ($Ma_m=0$) were conducted where the pressure ratio was kept constant and the internal Mach number was varied from $Ma_c=0$ to 0.6 (Fig. 4).

It becomes evident that for each pressure ratio an appropriate internal Mach number occurs where the discharge coefficient peaks out. This Mach number shifts to lower values when the pressure ratio is decreased. The level of this maximum discharge coefficient, however, is only very slightly affected by the pressure ratio. For each pressure ratio, increasing the inclination angle α moves the Mach number for which the maximum discharge coefficient occurs to lower values. Consequently, maximum discharge coefficients for the $\alpha=90$ deg hole occur at plenum condition, $Ma_c=0$ (Fig. 4(*c*)). This behavior reflects the findings of Thole et al. [12]. Their LDV measurements showed that flow separation at the hole entry is responsible for the losses when the flow enters the hole. The size of the separation region, which is primarily dependant on the crossflow conditions and the hole angles, determines the amount of the losses and, therefore, the discharge coefficient.

Holes With Varying Orientation Angles. Figure 5 shows the discharge coefficients plotted versus pressure ratio for the holes with varying orientation angles γ of 0, 45, and 90 deg and a fixed inclination angle $\alpha=30$ deg. For each plot, the internal crossflow Mach number Ma_c was kept constant while the external Mach number was varied from $Ma_m=0$ to 1.2. At a first glance, the results show a remarkable similarity to those of Fig. 3. Obviously, increasing the orientation angle has the same effect on discharge coefficients as increasing the inclination angle. The general features discussed for the holes with varying inclination angle in terms of effect of pressure ratio and external Mach number can be found for the holes with varying orientation angles as well. This also holds true for the detailed view on the effect of internal Mach number given in Fig. 6.

Effect of Internal and External Crossflows. It becomes obvious from the data presented that the effect of internal and external crossflow on the discharge coefficient is rather complex and cannot be easily deduced from the plots presented. Comparison from one hole geometry to another is difficult. In order to over-

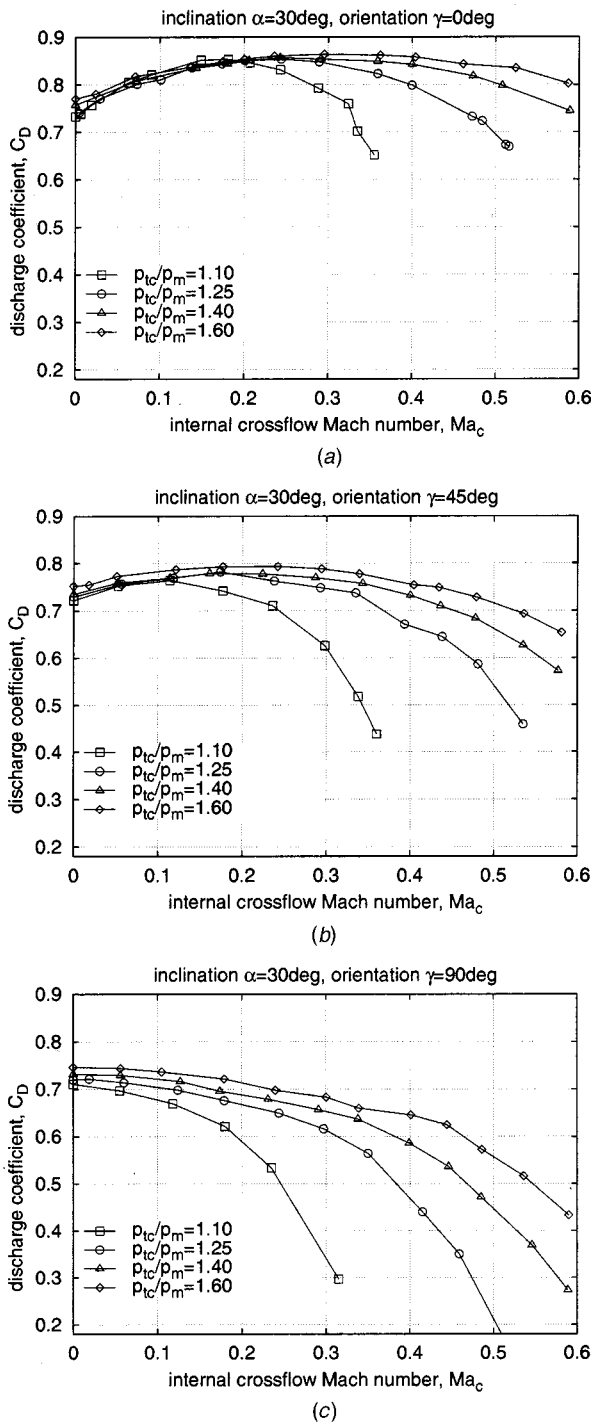

Fig. 6 Effect of internal crossflow for holes with different orientation angles: (*a*) $\gamma=0$ deg, (*b*) $\gamma=45$ deg, (*c*) $\gamma=90$ deg

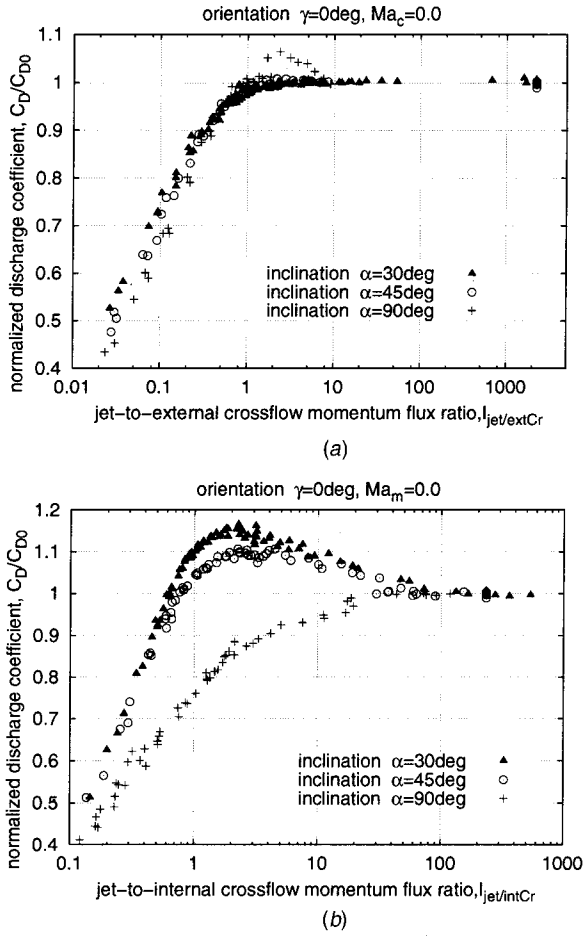

Fig. 7 Normalized discharge coefficient for holes with different inclination angles: (*a*) effect of external crossflow, (*b*) effect of internal crossflow

come this problem, it was decided to use the method proposed by Gritsch et al. [13] to separate the crossflow effects. They introduced a prediction scheme for discharge coefficients that is based on the assumption that the losses occurring at the inlet, inside, and at the outlet of the hole can be treated separately of each other. This scheme was first developed for predicting the discharge coefficient of a cylindrical hole with an inclination angle $\alpha=30$ deg and later successfully applied to holes with a diffuser shaped exit portion, i.e., "fan shaped" holes [9]. This scheme is now used to analyze in-depth the effect of internal as well as external crossflow for cylindrical holes with varying inclination and orientation angles.

First, the holes with varying inclination angles will be examined (Fig. 7(*a*)). In order to separate the effect of external crossflow, all data collected with zero internal crossflow are used. For these flow cases, the discharge coefficients are normalized by the discharge coefficient for the plenum-to-plenum case ($Ma_c=0$, $Ma_m=0$) at the same nominal pressure ratio in order to eliminate the contribution of the baseline losses inside the hole. This ratio is then plotted versus the jet to external crossflow momentum flux ratio

$$I_{\mathrm{jet}/extCr}=\frac{(\rho u^2)_{\mathrm{jet}}}{(\rho u^2)_m}$$

For each hole geometry, all data were found to nearly collapse on a single curve.

At low momentum flux ratios the discharge coefficient is lower than for the plenum-to-plenum case, indicating additional losses due to the external crossflow. For momentum flux ratios exceeding about 2, the discharge coefficient is not affected by the external crossflow for $\alpha=30$ and 45 deg. For the $\alpha=90$ deg hole discharge coefficients appear to be increased as compared to the plenum-to-plenum case in the range of $I=0.8\ldots50$. This "crossover" effect was noted before by other researchers (e.g., [14,15]). Also Hay et al. [5] found that for a $\alpha=90$ deg hole normalized discharge coefficients exceed unity in the range of $I=1$ to about 30, which is in good agreement with the results of the present

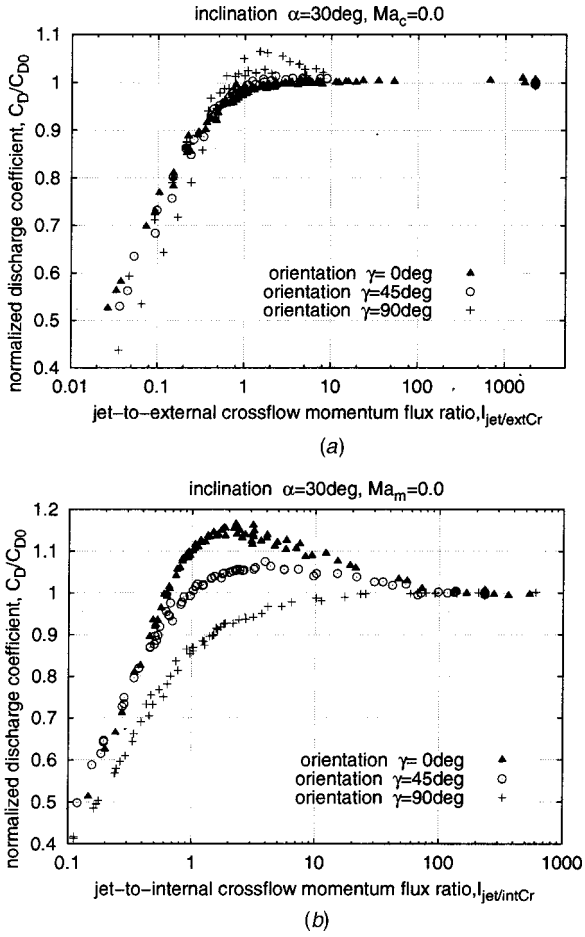

Fig. 8 Normalized discharge coefficient for holes with different orientation angles: (*a*) effect of external crossflow, (*b*) effect of internal crossflow

study. This effect is believed to be due to fact that the pressure field in the vicinity of the hole is altered by the crossflow in such a way that the crossflow sucks the flow emerging from the hole. In general, the differences between the hole geometries investigated are rather small, less than 10 percent for most of the range of momentum flux ratios considered.

The same scheme is also used to analyze the effect of internal crossflow (Fig. 7(*b*)). The discharge coefficients collected with zero external crossflow are normalized by the plenum-to-plenum discharge coefficient at the same nominal pressure ratio and then plotted versus the jet to internal crossflow momentum flux ratio

$$I_{\mathrm{jet}/intCr}=\frac{(\rho u^2)_{\mathrm{jet}}}{(\rho u^2)_c}$$

As compared to external crossflow, the internal crossflow has a bigger effect on the normalized discharge coefficient. Additionally, the hole inclination angle plays a more important role.

Three regimes can be found describing the effect of internal crossflow. At low momentum flux ratios, i.e., rather high internal crossflow Mach numbers, resulting low static pressures in the supply channel provide only insufficient pressure drop across the hole to overcome the hole losses, which leads to low discharge coefficients. At high momentum flux ratios, i.e., rather low internal crossflow Mach numbers, the additional affect of crossflow disappears and the normalized discharge coefficients approachs unity. In between, however, for the $\alpha=30$ deg and the $\alpha=45$ deg holes, there is a range of momentum flux ratios for which discharge coefficients exceed those of the plenum-to-plenum case. Obviously, the internal crossflow makes it easier for the flow to enter the hole. It was shown by Thole et al. [12] that this effect is directly linked to the formation of flow separation regions at the hole inlet. At low momentum flux ratios a separation zone forms on the leeward side of the hole inlet. At high momentum flux ratios the separation zone was found on the windward side. In between these two extremes, there is a range of momentum flux ratios where the flow can enter the hole without forming a separation zone, or if there is one it is only small. This causes much lower losses when entering the hole and leads to high discharge coefficients. For the $\alpha=90$ deg hole with its hole axis perpendicular to the supply flow, however, an internal crossflow will always cause additional losses at the hole inlet. Consequently, the normalized discharge coefficient is always lower than unity.

The same procedure is then applied to look at the holes with varying orientation angles (Fig. 8). As pointed out before, the effect of increasing the orientation angle has a very similar effect on the discharge behavior as increasing the inclination angle. This is now fortified by the amazing analogy of the plots in Figs. 7 and 8. Basically, all major findings can be transferred to the holes with varying orientation angles. As a main result of the present study it can be stated that the overall flow losses are predominantly governed by the degree of turning of the flow when entering the hole. Whether the degree of turning is prescribed by an inclination or orientation angle does not play a significant role.

With respect to the effect of the external crossflow the data presented in Fig. 8(*a*) are also very consistent with those of Burd and Simon [2] who found negative additive outlet losses (i.e., normalized discharge coefficients exceeding unity) for laterally injecting holes ($L/D=2.3$, $\alpha=35$ deg, $\gamma=90$ deg) at momentum flux ratios $I>0.7$.

Conclusions

Discharge coefficients for cylindrical film cooling holes with varying angles of inclination and orientation were presented over a wide range of engine like conditions in terms of crossflow Mach numbers and pressure ratios across the hole. Special attention was turned to the effect of internal as well as external crossflow. The main findings can be summarized as follows:

1 Discharge coefficients of all holes investigated depend strongly on the flow conditions applied (pressure ratio, internal and external crossflow Mach number). Increasing the pressure ratio leads to higher discharge coefficients. The effect of internal and external crossflow is rather complex but can be conveniently analyzed by plotting a normalized discharge coefficient versus jet-to-crossflow momentum ratio.

2 Altering the inclination or orientation angle has a much more profound effect on the losses at the hole entry than at the hole exit. Increasing the angles of inclination or orientation results in increased losses at the hole entry and, thus, decreased discharge coefficients.

3 On the hole exit side, increasing the angles of inclination or orientation only slightly affects the flow losses.

4 Large angles of inclination or orientation promote the crossover effect occuring within a certain range of jet-to-external crossflow momentum flux ratios, which is due to a suction effect at the hole discharge.

Acknowledgments

This study was performed at the Institut für Thermische Strömungsmachinen (ITS), University of Karlsruhe, Germany and was partly funded by the European Union within the Brite Euram program ''Investigation of the Aerodynamics and Cooling of Advanced Engine Turbine Components'' under Contract AER2-CT92-0044.

Nomenclature

C_D = discharge coefficient
D = film-cooling hole diameter
I = let-to-crossflow momentum flux ratio
L = film-cooling hole length
Ma = Mach number
$\dot{m}$ = mass flow rate through the film-cooling hole
p = static pressure
p_t = total pressure
R = gas constant
Re_D = Reynolds number based on hole diameter
t = wall thickness
T_t = total temperature
Tu = turbulence intensity
u = flow velocity
α = angle of hole inclination
γ = angle of hole orientation
κ = ratio of specific heats
ρ = flow density

Subscripts

c = internal flow conditions (''coolant'')
jet = film hole flow conditions, area-averaged
m = external flow conditions (''mainflow'')
0 = plenum to plenum condition ($\mathrm{Ma}_c = 0$, $\mathrm{Ma}_m = 0$)

References

[1] Hay, N., and Lampard, D., 1998, ''Discharge Coefficient of Turbine Cooling Holes: A Review,'' ASME J. Turbomach., **120**, pp. 314–319.
[2] Burd, S. W., and Simon, T. W., 1999, ''Measurements of Discharge Coefficients in Film Cooling,'' ASME J. Turbomach., **121**, pp. 243–248.
[3] Hay, N., Lampard, D., and Benmansour, S., 1983, ''Effect of Crossflows on the Discharge Coefficient of Film Cooling Holes,'' ASME J. Eng. Power, **105**, pp. 243–248.
[4] Hay, N., Henshall, S. E., and Manning, A., 1994, ''Discharge Coefficients of Holes Angled to the Flow Direction,'' ASME J. Turbomach., **116**, pp. 92–96.
[5] Hay, N., Lampard, D., and Khaldi, A., 1994, ''The Coefficient of Discharge of 30° Inclined Film Cooling Holes With Rounded Entries or Exits,'' ASME Paper No. 94-GT-180.
[6] Hay, N., and Spencer, A., 1992, ''Discharge Coefficients of Cooling Holes With Radiused and Chamfered Inlets,'' ASME J. Turbomach., **114**, pp. 701–706.
[7] Hay, N., and Lampard, D., 1995, ''The Discharge Coefficient of Flared Film Cooling Holes,'' ASME Paper No. 95-GT-15.
[8] Gritsch, M., Schulz, A., and Wittig, S., 1998, ''Discharge Coefficient Measurements of Film-Cooling Holes With Expanded Exits,'' ASME J. Turbomach., **120**, pp. 557–563.
[9] Gritsch, M., Saumweber, C., Schulz, A., Wittig, S., and Sharp, E., 2000, ''Effect of Internal Coolant Crossflow Orientation on the Discharge Coefficient of Shaped Film Cooling Holes,'' ASME J. Turbomach., **122**, pp. 146–153.
[10] Wittig, S., Schulz, A., Gritsch, M., and Thole, K. A., 1996, ''Transonic Film-Cooling Investigations: Effects of Hole Shapes and Orientations,'' ASME Paper No. 96-GT-222.
[11] Kline, S. J., and McClintock, F. A., 1953, ''Describing Uncertainties in Single-Sample Experiments,'' Mech. Eng. (Am. Soc. Mech. Eng.), **75**, Jan., pp. 3–8.
[12] Thole, K. A., Gritsch, M., Schulz, A., and Wittig, S., 1997, ''Effect of a Crossflow at the Entrance to a Film-Cooling Hole,'' ASME J. Fluids Eng., **119**, pp. 533–541.
[13] Gritsch, M., Schulz, A., and Wittig, S., 1998, ''Method of Correlating Discharge Coefficients of Film-Cooling Holes,'' AIAA J., **36**, pp. 976–980.
[14] Rowbury, D. A., Oldfield, M. L. G., and Lock, G. D., 1997, ''Engine Representative Discharge Coefficients Measured in an Annular Nozzle Guide Vane Cascade,'' ASME Paper No. 97-GT-99.
[15] Rowbury, D. A., Oldfield, M. L. G., and Lock, G. D., 2001, ''A Method for Correlating the Influence of External Crossflow on the Discharge Coefficients of Film Cooling Holes,'' ASME J. Turbomach., **123**, pp. 258–265.

Shock Wave–Film Cooling Interactions in Transonic Flows

P. M. Ligrani
Professor
Convective Heat Transfer Laboratory,
Department of Mechanical Engineering,
University of Utah,
Salt Lake City, UT 84112
Fellow ASME

C. Saumweber

A. Schulz

S. Wittig

Lehrstuhl und Institute für Thermische
Stroemungsmaschinen,
Universitaet Karlsruhe (T.H.),
Kaiserstrasse 12,
D-76128 Karlsruhe, Germany

Interactions between shock waves and film cooling are described as they affect magnitudes of local and spanwise-averaged adiabatic film cooling effectiveness distributions. A row of three cylindrical holes is employed. Spanwise spacing of holes is 4 diameters, and inclination angle is 30 deg. Free-stream Mach numbers of 0.8 and 1.10–1.12 are used, with coolant to free-stream density ratios of 1.5–1.6. Shadowgraph images show different shock structures as the blowing ratio is changed, and as the condition employed for injection of film into the cooling holes is altered. Investigated are film plenum conditions, as well as perpendicular film injection crossflow Mach numbers of 0.15, 0.3, and 0.6. Dramatic changes to local and spanwise-averaged adiabatic film effectiveness distributions are then observed as different shock wave structures develop in the immediate vicinity of the film-cooling holes. Variations are especially evident as the data obtained with a supersonic Mach number are compared to the data obtained with a free-stream Mach number of 0.8. Local and spanwise-averaged effectiveness magnitudes are generally higher when shock waves are present when a film plenum condition (with zero crossflow Mach number) is utilized. Effectiveness values measured with a supersonic approaching free-stream and shock waves then decrease as the injection crossflow Mach number increases. Such changes are due to altered flow separation regions in film holes, different injection velocity distributions at hole exits, and alterations of static pressures at film hole exits produced by different types of shock wave events.
[DOI: 10.1115/1.1397305]

Introduction

The trend of modern aeroengine development is toward increasing power-to-weight ratios. This requires engine designs with higher compressor pressure ratios, higher gas temperatures, higher air flow rates, and smaller engine cross sections. The last three of these tend to restrict flow passage areas and increase local Mach numbers. Because of the high gas temperatures required to produce the required power levels, film cooling is often employed in the first turbine stages. However, our knowledge of the detailed effects and interactions of these high Mach number flows with film cooling is limited, even though a number of recent studies consider global film cooling performance in transonic turbine cascades [1–8]. Such interactions are important to aeroengine development because the behavior and performance of transonic film cooling with supersonic freestream flow is, in most cases, significantly different from film cooling behavior when all flow components are either subsonic and compressible, or subsonic and incompressible. In other words, this is a situation where low-speed, subsonic, constant property tests cannot be used to simulate the key characteristics of flow behavior.

Two general types of shock wave are present in turbine stages of transonic turbines. The *first type* are generally initially induced at the trailing edges of transonic stator vanes in the first turbine stage. As each pair of shock waves emanates from a trailing edge, it repeatedly encounters different rotor blades in the rotating row of airfoils just downstream. As each of these shocks approaches rotor airfoil surfaces, the shock waves may be chopped up, reflected, or absorbed. As a result, families of as many as six shock waves may advect through different portions of rotor passages at any one moment, where some move upstream, some move downstream, some strengthen, and some attenuate [9]. These shock waves produce significant variations of static pressure along rotor blade surfaces, including at the exits of film cooling holes, which changes instantaneous film cooling flow rates from these holes [3,10–12].

The *second type* of shock wave may interact with the first type, and are produced when supersonic mainstream flow approaches the film from a row of holes. Thus, the origin of the second type of shock wave is different from the first type. Wittig et al. [13] examine these phenomena and present experimental data with a free-stream Mach number of 1.2, which shows that the blockage effect of the coolant results in the formation of a bow shock wave just upstream of the injection location. This may then lead to additional shock waves, and local boundary layer separations. Three hole types are considered by Wittig et al., each with a simple angle orientation: round (or cylindrical), laterally diffused (or fan shaped), and forward-laterally diffused (or laid-back-fan shaped). According to the authors, the positions and shapes of the shock waves depend strongly on both the hole shape and blowing ratio.

Gritsch et al. [14] present spatially resolved and spatially averaged surface film effectiveness data downstream of single holes having the same hole shapes. These investigators indicate that bow shock waves and related events can induce larger concentrations of film to be present near a test surface (than if these events are not present). This increases local protection compared to a situation where all flow components are subsonic. Mainstream Mach numbers of 0.3, 0.6, and 1.2, and coolant passage Mach numbers of 0 and 0.6 are utilized. The dramatic changes to transonic flow fields in the vicinity of cooling holes is further illustrated by the study of Liess [15]. His results show no measurable changes to film cooling effectiveness distributions when the free-stream Mach number varies since his free-stream Mach numbers are only as high as 0.9, and the mainstream flow always remains subsonic.

Most other studies examine effects of the *first type* of shock waves. Of these investigations, Nix et al. [5], Popp et al. [6,7], and Smith et al. [8] examine the effects of propagating shock waves on heat transfer and film cooling performance using a stationary transonic turbine cascade with inlet and exit Mach numbers of 0.3 and 1.2, respectively. According to these authors, un-

Contributed by the International Gas Turbine Institute and presented at the 46th International Gas Turbine and Aeroengine Congress and Exhibition, New Orleans, Louisiana, June 4–7, 2001. Manuscript received by the International Gas Turbine Institute February 2001. Paper No. 2001-GT-133. Review Chair: R. Natole.

steady heat transfer from passing shock waves is driven, in large part, by induced temperature fluctuations, with little effects from shock waves on time-averaged heat transfer levels.

Norton et al. [1] present results from experiments using flat plates, a two-dimensional cascade with blades having a variety of film hole arrangements, and a rotating three-dimensional turbine rig. Although results for each part are somewhat limited in scope, some information is provided on the influences of Mach number, and the passage of shock waves and wakes from the motion of upstream blades. Rigby et al. [2] provide additional insight into the Norton et al. [1] results. The same steady-state cascade results are presented in both sources. Rigby et al. [2] indicate different influences of wakes and shocks depending on the location of the film holes on the blade surface and on the blowing ratio of the film. Injectant lift-off is found to be particularly important. According to Rigby et al., the passage of simulated nozzle guide vane wakes and shocks produces significant changes to film cooling on blade suction surfaces. On the pressure surface of the blade tested, little influences of the shocks and wakes are evident because of film lift-off at low blowing rates.

Abhari and Epstein [3] show that flow pulsations from the passage of wakes, shocks, and potential flow interactions can have a dramatic effect on the performance of film cooling. The authors examine film cooling in a rotating transonic turbine within a test facility which simulates full engine nondimensional conditions. The Mach number at the exit of the nozzle guide vanes is 1.18. The unsteadiness from the relative motion of two adjacent blade rows results in a 12 percent decrease in time-averaged heat transfer on the suction surface and a 5 percent increase in time-averaged heat transfer rates on the pressure surface. Abhari [4] provides additional evidence in investigations of flow and heat transfer in a transonic, high pressure ratio, single stage turbine. His predictions of time-resolved film cooled flow behavior near a turbine rotor show large fluctuations of the coolant injection flow out of the holes. Heat transfer predictions from the pressure surface show time-averaged magnitudes of the unsteady surface heat flux to be as much as 230 percent greater than the steady prediction. This is due to reductions of the adiabatic film effectiveness by as much as 64 percent relative to steady values. Ligrani et al. [10–12] show that the unsteady pulsations from such phenomena produce important changes to the flow structure, especially because the film instantaneously changes its momentum and position in the boundary layer over each pulsation period. These investigators also show that film concentrations move to and from the wall with each imposed bulk flow pulsation which often gives a different mean injectant trajectory, and acts to spread the same amount of injectant over a larger volume. As a result, important changes to *time-averaged* injectant distributions occur, which result in alterations to film cooling protection [16].

A number of other investigations [17–28] consider shock wave interactions with secondary injection and film cooling as applied to engine inlets, scramjet combustors, and exhaust nozzles. In some cases, results presented in these studies are inconsistent with each other. In addition, experimental conditions and geometric configurations are considerably different from those in turbines.

The present study focuses on the *second type* of shock wave encountered in transonic turbines, and their effects on film cooling from a single row of cylindrical, simple angle holes. New understanding of these phenomena is provided by surface film cooling effectiveness distributions and shadowgraph flow visualization images. A wider range of flow conditions are examined than are considered by the other known investigations of this type of shock wave as applied to turbine components in gas turbine engines [1,13,14]. The present data are obtained with a density ratios of 1.5–1.6, blowing ratios of 0.5, 1.0, and 1.5, and injection cross-flow Mach numbers ranging from 0 (which gives a plenum condition) to 0.6. Two free-stream Mach numbers of 0.8 and about 1.12 are employed to produce flow over the test plate with and without shock waves. The comparisons made with these data illustrate the unique effects and interactions of the second type of shock waves with film cooling.

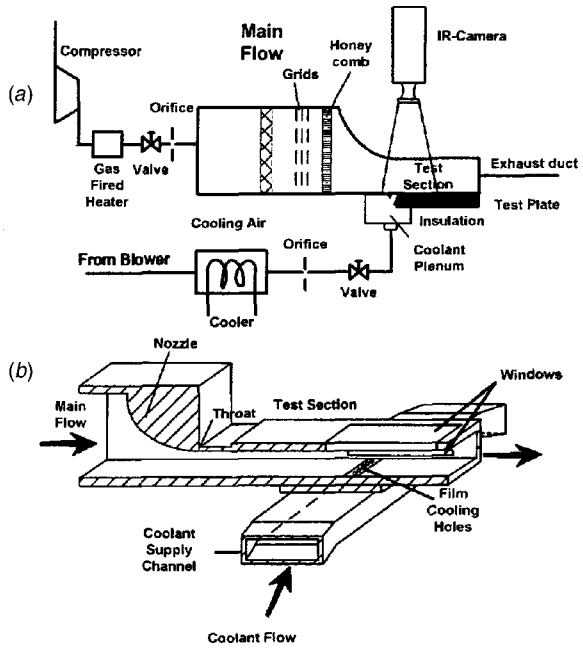

Fig. 1 Schematic diagram showing: (*a*) overall arrangement of the experimental facility, and (*b*) a cut-away view of the test section

Experimental Apparatus and Procedures

HPHT Test Facility and Test Section. The high-pressure, high-temperature (HPHT) test facility, located in the Institute for Thermal Turbomachinery (Lehrstuhl und Institute für Thermische Stroemungamaschinen) at the University of Karlsruhe, is employed for the study. The facility is shown in Fig. 1(*a*) and operates in a steady-state mode. It contains a primary flow loop for the external flow, a secondary flow loop for the film coolant supply, and is described by Wittig et al. [13].

A schematic diagram showing a cut-away view of the test section is presented in Fig. 1(*b*). The test section is 90 mm wide and about 300 mm long. The test section height at its entrance is set at either 30 mm or 25.2 mm to achieve mainflow Mach numbers of 0.8 and 1.12, respectively. The instrumented test plate is located just downstream of an ejection module, which contains the film cooling holes.

The mainflow air is delivered to the test section by a screw-type compressor (operating with a pressure ratio of 11). A blower supplies secondary air at a rate ranging from about 0.2 to 2.5 percent of the main air flow rate. Mass fluxes of both flows are controlled independently by valves, and determined from measured pressure drops across venturi nozzles and orifice plates. The pressure levels of supply vessels are also used to adjust and control injectant and mainstream mass flow rates. Mainstream mass flow rates as high as 1.0 kg/s are achieved with the arrangement. The main flow is heated using one of four available burners. The temperature is adjusted by altering the ratio of air to combustion gas. With the one heater employed, a hot gas stagnation temperature as high as 562 K is produced. The spatial uniformity of the main flow is improved using a series of grids, a honeycomb flow straightener, and a high contraction ratio, converging–diverging nozzle located just upstream of the test section. Because this nozzle is contoured only on one side, its height can be varied so that the flow area at the downstream and can be adjusted.

A heat exchanger, with water as the coolant, is employed to control the temperature of the injectant air after it exits the supply blower. This air is delivered into a secondary flow passage before it enters the test section through the film cooling ejection holes. With this apparatus, the film air can pass by film hole entrances with crossflow Mach numbers as high as 0.6. Alternatively, the cooling air can enter this passage from two sides to produce a plenum condition, with near-zero injectant Mach number, at the entrance to the film holes.

Both the test plate and ejection module have a thickness of 30 mm and are made from a semi-crystalline thermoplast material called TECAPEK. This material is employed because of its machinability, ability to maintain its shape at temperatures up to 550 K, and low thermal conductivity of 0.3 W/mK. With this arrangement, the test plate approximates an adiabatic surface.

Film Cooling Hole Geometry. A single row of three film cooling holes is employed. The diameter d of each round, cylindrical hole is 5 mm. Spanwise hole spacing is $4d$, length of each hole is $6d$, and inclination angle from the test surface is 30 degrees.

Pressure and Temperature Measurements. Air temperatures are measured in the injectant supply ducting, injectant plenum, and mainflow at the inlet of the test section using calibrated type K (nickel/chromium–nickel) thermocouples. When employed in a moving gas stream, each thermocouple junction is placed inside of a small venturi shield so that stagnation temperature is measured directly. Stagnation coolant temperatures are determined from measurements made in the coolant supply channel. Mainstream recovery temperatures are deduced from measured stagnation temperatures, and several other quantities including the mainflow Mach number, which is determined from measurements of stagnation pressure and static pressure at the test section inlet. Setra variable capacitance type 239 and type 204 differential pressure transducers are employed for such pressure measurements, as well as to measure pressures in the injectant supply ducting, injectant plenum, and at two locations along the test surface.

Temperature and pressure data are acquired as tests are underway using a Scanivalve 48-channel rotary pressure scanner, a Prema 5017 digital multimeter/analog-to-digital converter, and an 80-channel in-house-built multiplexer. Labview software from National Instruments Corp. is used with an Intel type 486Dx 66 MHz processor to capture and process signals from the thermocouples, pressure probes, and pressure transducers employed throughout the test section.

Local Adiabatic Film Cooling Effectiveness Measurement. Because the present measurements are made in transonic environment, the local adiabatic film cooling effectiveness is determined using an equation of the form

$$\eta=(T_{aw}-T_{r\infty})/(T_{oc}-T_{r\infty}) \tag{1}$$

where T_{aw} is the local adiabatic surface temperature, $T_{r\infty}$ is the free-stream recovery temperature at the location of the film cooling holes, and T_{oc} is the coolant stagnation temperature.

Spatially resolved temperature distributions along the test surface are determined using infrared imaging in conjunction with thermocouples, and *in situ* calibration procedures. To accomplish this, the infrared radiation emitted by the TECAPEK test surface is captured using an Agema Thermovision 900 Infrared Imaging Camera. This single-sensor camera operates with a scanning system and produces images with an array of 272 by 136 pixels. This amounts to about 1.5 pixels per millimeter. Temperatures, measured using calibrated 0.50-mm-diam, type K (nickel/chromium–nickel) thermocouples distributed along the test surface adjacent to the flow, are used to perform the *in situ* calibrations as the radiation contours from surface temperature variations are recorded. To do this, surface thermocouple readings and infrared images are recorded simultaneously as each test is conducted.

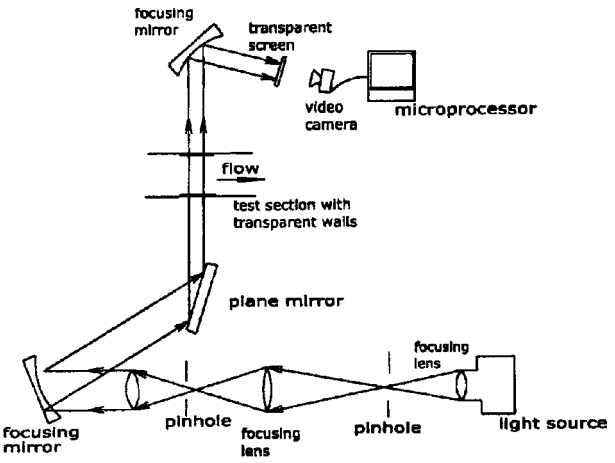

Fig. 2 Schematic diagram of shadowgraph flow visualization apparatus

This is accomplished as the camera views the test surface through a custom-made, planar sapphire window. This is installed just above the test surface in the top wall of the test section. The ejection module and test surface are coated with a constant-emissivity dye to produce uniform radiation emission from these surfaces. Seven thermocouple junction locations are present in the field viewed by the camera. With these thermocouple data, thermal radiation contours, measured with the infrared camera, are readily converted to temperatures. This *in situ* calibration approach accounts for less-than-perfect transmission and emission through the sapphire window, and variable boundary conditions produced by reflection from test section walls. Images from the infrared camera are captured and recorded as an ASCII data array, and then digitized and processed using a Motorola model 68020 16 MHz microprocessor. The software converts radiation levels to temperature at each pixel location using calibration data. Each final image is a time-average of 32 instantaneous images obtained over a 4 to 5 second time interval. Schulz [29] provides additional details of infrared imaging procedures.

Because of the finite conductivity of the test surface material, corrections are made for conduction in the streamwise and spanwise directions. Without this correction, temperature variations are smeared, and are not representative of true local and global adiabatic conditions. Procedures described by Bauldauf et al. [30], in which internal heat fluxes are computed using a finite-element analysis, are employed to make these corrections. Temperatures, measured using the thermocouples placed along the backside of the model, as well as just upstream and downstream of the model, provide boundary condition information and other data needed to estimate conduction loss magnitudes. With this approach, deviations from an adiabatic state along the test surface are taken into account. Corrections for radiation to and from the test model surface are also included in the analysis [30].

Shadowgraph Flow Visualization System. A schematic diagram of the shadowgraph flow visualization system is shown in Fig. 2. The system consists of a point light source, several lenses, focusing mirrors, a number of additional pin holes, and a screen. A Sony model XC-003P 3CCD analog video camera with 75 mm lens is used to record images, which are then captured, recorded, and digitized using a Matrox Metnor II frame grabber card, and an Intel Pentium III 350 MHz microprocessor. Each shadowgraph image is obtained at the same time as the surface effectiveness distributions are measured. Density variations through the test section are apparent in shadowgraph images as a result of oblique shock waves and Mach waves.

Table 1 Experimental conditions

Run	M_∞	M_C	m	ρ_c/ρ_∞	u_c/u_∞	I	P_{OC}/P_∞
1	.80	.00	.51	1.59	.31	.15	1.26
2	.80	.00	1.00	1.59	.63	.63	1.48
3	.80	.00	1.50	1.54	.97	1.46	1.88
4	1.12	.00	.53	1.47	.36	.19	1.48
5	1.12	.00	.98	1.49	.66	.64	1.86
6	1.12	.00	1.48	1.49	.99	1.47	2.50
7	.80	.30	.49	1.61	.30	.15	1.25
8	.80	.30	1.00	1.56	.64	.64	1.75
9	.80	.31	1.51	1.59	.95	1.43	2.41
10	1.10	.30	.32	1.56	.21	.07	1.30
11	1.10	.30	.54	1.56	.35	.19	1.56
12	1.10	.15	.51	1.54	.33	.17	1.45
13	1.10	.59	.47	1.61	.29	.14	1.68

Flow Conditions

Table 1 gives the experimental conditions of the results obtained in this study.

With a free-stream Mach number M_∞ of 0.8, mainstream stagnation temperature $T_{0\infty}$ is usually about 530.4 K, and mainstream static temperature T_∞ is about 470.1 K. With a free-stream Mach number of 1.10 to 1.12, these temperatures are then about 562.3 K, and about 452.9 K. The top wall of the test section is arranged so that free-stream Mach numbers are approximately constant with streamwise distance over the test model. Corresponding mainstream Reynolds numbers at $x/d=25$ (and based on streamwise distance along the test surface) are 1.06×10^6 and 1.49×10^6 for free-stream Mach numbers of 0.8 and 1.12, respectively. The ratio of external boundary layer thickness to hole diameter at the location of the film cooling holes is estimated to be about 0.5. Free-stream turbulence has an intensity of less than 2 percent, and large length scales (with sizes on the order of the honeycomb passage width which is about 4 mm) [14].

Note that the coolant Mach numbers M_C listed in Table 1 are given for the injectant flow passage located just in front of the film hole entrances. The turbulence level in this internal secondary loop is typically about 1 percent [14]. Coolant static and stagnation temperatures (T_C and T_{OC}) at the exit planes of the holes are typically 298.0 K and 291.3 K, respectively. The ratio of coolant static temperature to mainstream static temperature is 0.62 to 0.67, giving film-to-mainstream static density ratios from 1.49 to 1.61. Coolant Reynolds number (based on hole diameter) is then as high as 0.9×10^5.

Experimental Uncertainties

Uncertainty estimates are based on 95 percent confidence levels, and determined using procedures described by Kline and McClintock [31] and Moffat [32]. Uncertainty of temperatures is ±0.2°C. Uncertainty of the Mach number M is ±3 percent. Uncertainty of the density ratio ρ_c/ρ_∞ is ±1.5 percent. Blowing ratio m uncertainty is ±2.0 percent. Discharge coefficient C_D uncertainty is $\pm.035$, for a typical nominal value of $C_D=0.80$. Surface temperatures are measured using infrared thermography within 1 percent of the difference between the coolant temperature and mainstream temperature. Spatial resolution achieved with the infrared imaging is 0.6 mm. Adiabatic film effectiveness uncertainty is then typically about ±4.0 percent.

Experimental Results

Discharge Coefficients. Discharge coefficients are presented in Fig. 3 as dependent upon the ratio of coolant stagnation pressure to freestream static pressure. For this ratio, free-stream static pressures are measured at the inlet of the test section.

The overall procedures employed to measure discharge coefficients are described by Gritsch et al. [33]. Here, discharge coefficients are based on ideal mass flow rates determined using coolant stagnation pressures, coolant stagnation temperatures, and free-stream static pressures. Coolant stagnation pressures and temperatures are measured in the injectant supply channel using a probe located 84d upstream of hole entrances. Free-stream static pressures are measured on one side wall of the test section 18d upstream of the film cooling holes. With this approach, values presented in Fig. 3 are in agreement with values extrapolated from Gritsch et al. [33] for $M_\infty=0.8$ and $M_C=0$. C_D values in Fig. 3 for $M_\infty=1.10-1.12$ are then generally lower than values measured with $M_\infty=0.8$. This is due to shock waves in the vicinity of the film hole exits at the higher free-stream Mach number, which cause the static pressure at these locations to be different from values measured 18d upstream of the film cooling holes.

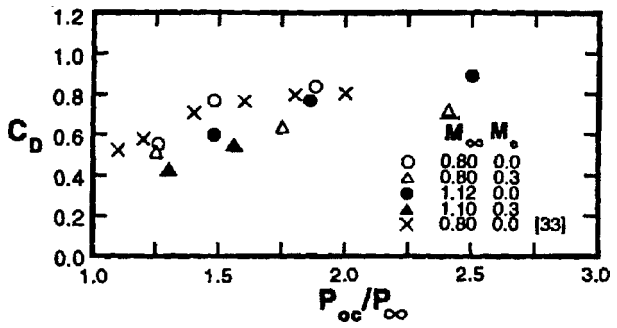

Fig. 3 Discharge coefficients as dependent upon ratio of coolant to mainstream pressure, mainstream Mach number, and coolant passage Mach number.

Study	Inclination angle	m	l/d	ρ_c/ρ_∞	M_∞	M_c	Spanwise hole spacing
—●— Present study	30°	0.49	6	1.59	0.8	0	4d
—△— Gritsch et al. [14]	30°	0.62	6	1.85	0.6	0	—
—○— Schmidt et al. [34]	35°	0.63	4	1.60	<0.1	0	3d
—◇— Bell et al. [35]	35°	0.70	3	1.39	<0.1	0	3d

Effectiveness Comparisons With Other Studies. Results from the present study are compared to data from other investigations in Fig. 4. Note that only a reasonable match of experimental conditions and film hole geometries is obtained, as a perfect match is not possible. In spite of this, centerline local effectiveness data agree well with results from Gritsch et al. [14] and Schmidt et al. [34] in Fig. 4(a). Spanwise-averaged effectiveness data are lower than results from Schmidt et al. [34] and Bell et al. [35] in Fig. 4(b) (when compared at the same x/d). This is mostly because of larger spanwise spacing between holes in the present study. Such behavior validates the measurement procedures and apparatus employed. Note that the present *spanwise-averaged* data are not compared with similar data from Gritach et al. [14]. This is because their results are obtained downstream of one hole, with significantly different spanwise-averaged behavior compared to a row of holes with interactions of injectant concentrations from neighboring holes.

Local Adiabatic Film Cooling Effectiveness Distributions. Figures 5–10 present distributions of local film cooling effectiveness along the surface downstream of the central film cooling hole for Runs 1, 4, 6, and 11 listed in Table 1. Shock waves are present in the vicinity of the injection hole exits whenever $M_\infty=1.12$. The nature and characteristics of these shock waves are described in sections of the paper which follow.

The contour plots in Fig. 5 are given for a subsonic free-stream with $M_\infty=0.80$, and hence, no shock waves are present. Blowing ratio m is 0.49, and a plenum condition is used in the chamber just upstream of the film hole entrances such that $M_C=0$. The effectiveness distribution shows very high values within a short distance just downstream of the holes, which indicates that substan-

tial concentrations of the film are next to the surface. Such behavior is partially a result of interactions between film concentrations from adjacent holes, which seems to begin at x/d just greater than zero. Local adiabatic film effectiveness magnitudes then decrease rapidly at $x/d>4$ as the film advects farther downstream.

Figure 6 shows how such a distribution (obtained for $M_\infty = 1.12$, $M_C = 0$, and $m = 0.53$) is altered by the presence of shock waves. Here, the action of the shock waves in forcing larger amounts of injectant closer to the surface is apparent. Local film cooling effectiveness magnitudes are higher over a much larger portion of the test surface. For example, the line corresponding to $\eta = 0.3$ extends to $x/d = 18$ (when shock waves are present) in Fig. 6, but only to $x/d = 13$ (when no shock waves are present) in Fig. 5. In spite of these differences, both distributions are consistent with the attached coolant jet regime of behavior described by L'Ecuyer and Soechting [36]. With this type of behavior, a vortex is present on each side of the film as it advects downstream. Each of these vortices is located between a region of low effectiveness, along the midspan between holes, and a region of relatively higher effectiveness in the wake region along a hole centerline.

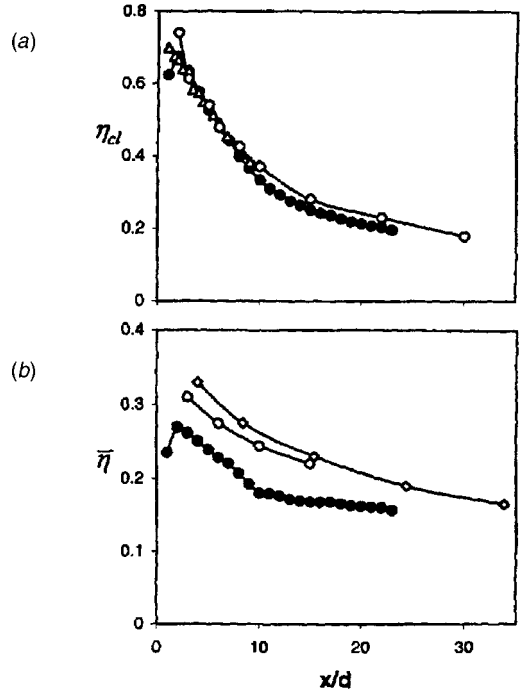

Fig. 4 Comparisons of adiabatic film cooling effectiveness data from the present study to results from other investigations: (*a*) Comparison of centerline data with results from Gritsch et al. [14] and Schmidt et al. [34]. (*b*) Comparison of spanwise-averaged data with results from Schmidt et al. [34] and Bell et al. [35].

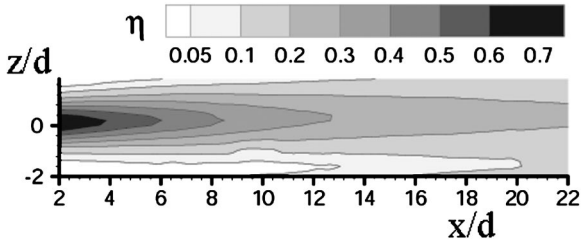

Fig. 5 Local surface adiabatic film cooling effectiveness distribution for $m = 0.49$, $M_\infty = 0.80$, and an injectant plenum condition giving $M_C = 0.0$

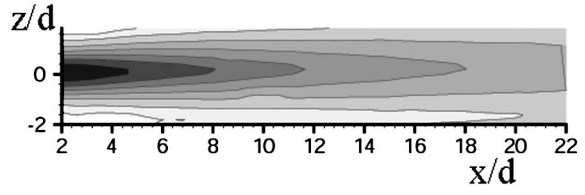

Fig. 6 Local surface adiabatic film cooling effectiveness distribution for $m = 0.53$, $M_\infty = 1.12$, and an injectant plenum condition giving $M_c = 0.0$. Scale for contour map is given in Fig. 5.

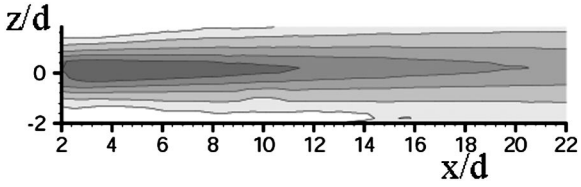

Fig. 7 Local surface adiabatic film cooling effectiveness distribution for $m = 1.48$, $M_\infty = 1.12$, and an injectant plenum condition giving $M_C = 0.0$. Scale for contour map is given in Fig. 5.

As the blowing ratio then increases, Fig. 7 (obtained using the same M_∞ and M_C, but with $m = 1.48$) shows effectiveness distributions near the holes which are even lower than the ones presented in Fig. 5. This, of course, is due to partial lift-off of the largest film concentrations away from the surface, which occurs regardless of whether shock waves are present. This penetrating coolant jet regime is characterized by penetration of the coolant jet into the hot freestream gas. In addition, much interaction occurs between jets from neighboring holes, and a turbulent wake is located downstream of the trailing edge of the ejection hole and beneath the jet [36].

Local effectiveness values diminish even further in Fig. 8 for $M_\infty = 1.10$, $m = 0.54$, and $M_C = 0.3$ when crossflow of the injectant is present at the entrances to the film cooling holes. This is due to alteration of the flow separation region near hole entrances. With the perpendicular cross flow employed here, this separation region forms on the side of the hole entrance closest to the oncoming direction of the cross flow. With an injectant plenum condition, the separation region forms on the leeward (or downstream) side of the hole entrance. These differences result in changes to the distributions of injectant velocity and turbulence intensity at the exit planes of the holes. Different interactions between the injectant and external shock waves then occur, which causes larger amounts of injectant to be lifted off of the surface with $M_C = 0.3$ (Fig. 8) than when $M_C = 0.0$ (Fig. 6).

Additional quantitative comparison of local effectiveness distributions is provided by the results in Figs. 9 and 10, which give local centerline ($z/d = 0$) and local midspan ($z/d = 2$) effectiveness data, respectively. Experimental conditions are the same as for the results presented in Figs. 5–8. Comparing the $M_\infty = 0.8$

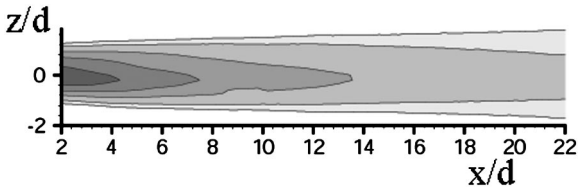

Fig. 8 Local surface adiabatic film cooling effectiveness distribution for $m = 0.54$, $M_\infty = 1.10$, and perpendicular injectant crossflow with $M_C = 0.30$. Scale for contour map is given in Fig. 5.

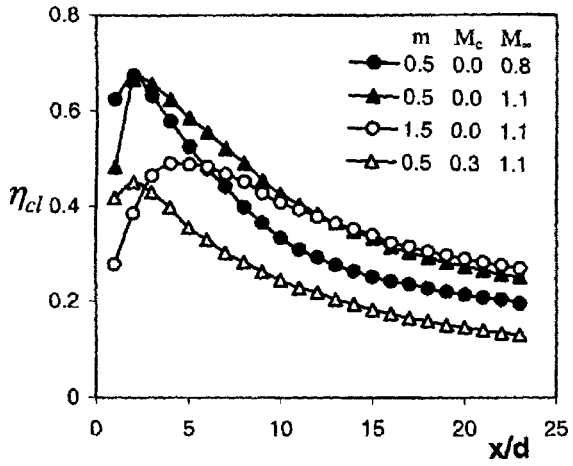

Fig. 9 Local centerline surface adiabatic film cooling effectiveness values for the same experimental conditions as for the results in Figs. 5–8

and $M_\infty = 1.12$ data in Figs. 9 and 10 (for $m = 0.5$ and $M_C = 0$) shows that the shock waves force larger amounts of film closer to the test surface along the centerline for all x/d greater than 2. Local effectiveness values along the midspan for $M_\infty = 1.12$ are then about the same as values measured with $M_\infty = 0.8$ at each x/d location.

Interactions Between Shock Waves and Film Cooling With a Plenum Injectant Condition and $M_C = 0$. In each shadowgraph image, shown in Figs. 12, 14, and 16, the flow moves from right to left. The location of the film cooling holes is identified along the bottom of each image. Darker, shaded lines then denote density changes in the test section associated with shock waves and Mach waves. The shadowgraph image in Fig. 12(*a*) shows the family of shock waves and Mach waves which forms around the exits of the film cooling holes when $M_\infty = 1.12$, $M_C = 0$, and blowing ratio m is 0.53. As the mainstream flow approaches the front edges of the film cooling holes, it is deflected upward into itself, and an oblique shock wave forms. The film and mainstream then deflect again near the downstream edge of the holes, where another oblique shock wave forms. Because of the angles of these two shock waves with respect to the surface, they intersect near the middle of the channel. The angles of these shock waves with respect to the surface, their relative positions, and the events around them indicate that they are weak rather than strong oblique shock waves. The shock wave leg located above the point of intersection is then stronger than each of these two legs located in the bottom half of the channel. Note also that several Mach waves extend from the top wall to intersect on the upstream part of the stronger shock wave also in the top half of the channel.

Another interesting feature of Fig. 12(*a*) is the reflection off the bottom surface by the shock wave leg connected to the downstream edges of the film cooling holes. This reflected shock wave is then reflected again off of the top channel surface. Considering the entire progression of events near the bottom wall, the strongest oblique shock wave is the one farthest upstream, and thus, the oblique shock waves become weaker as they are located farther downstream. This is a natural consequence of the intersections and reflections that occur [37], and the relatively low blowing

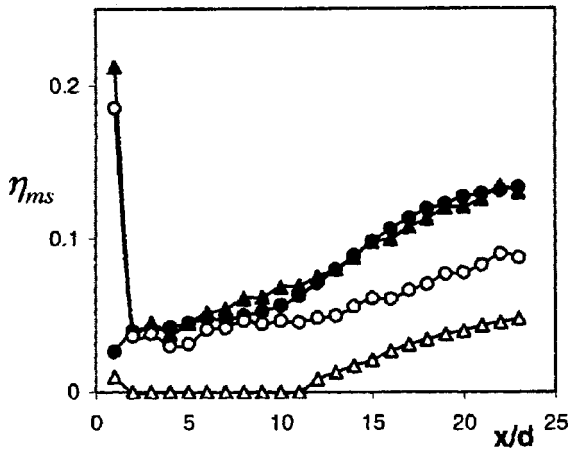

Fig. 10 Local midspan surface adiabatic film cooling effectiveness values for the same experimental conditions as for the results in Figs. 5–8. Symbol lables are given in Fig. 9.

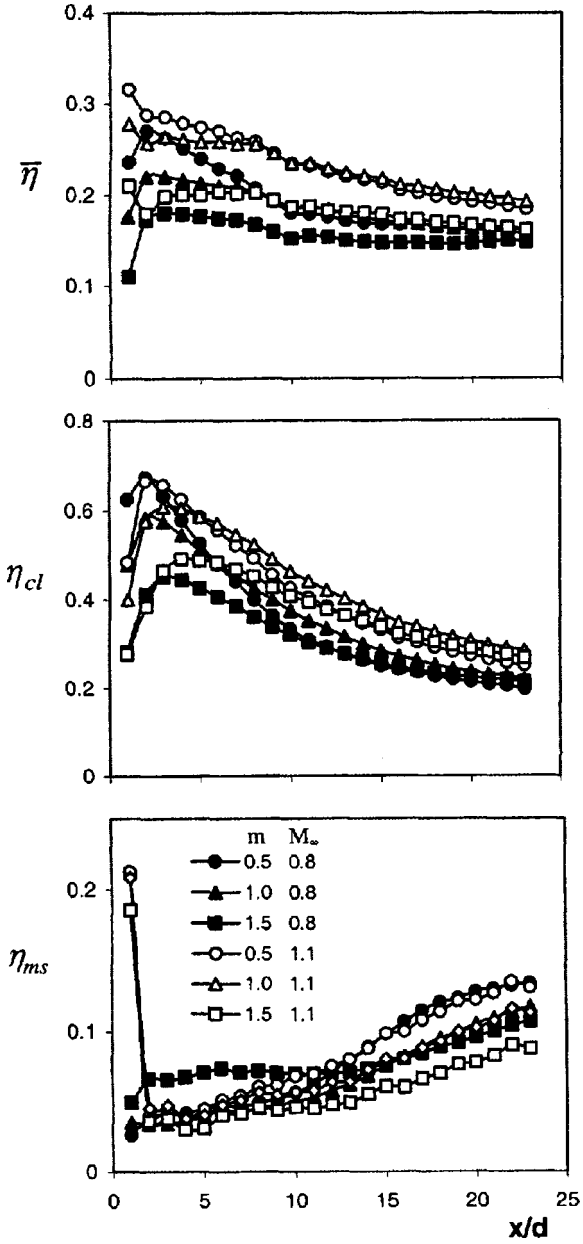

Fig. 11 Adiabatic film cooling effectiveness distributions for different M_∞ and m, with a plenum injectant condition with $M_c = 0$: (*a*) spanwise-averaged values; (*b*) centerline values; (*c*) midspan values

ratio of the cooling film. This gives subsonic film flow in the film holes just *upstream* of the hole exits, even if some local jetting occurs. Thus, in this case, the film does not, by itself, induce the shock structures seen in Fig. 12(*a*). As it merges with the main flow, the film fluid then accelerates, becomes supersonic, and then deflects. Note that most of the mainstream flow remains supersonic throughout the entire sequence of events.

Also notice that static pressure rises as flow proceeds across each oblique shock wave. This continual and sequential increase in static pressure occurs along the bottom wall of the channel, along with deflections to the directions of the flow streamlines. This combination of events forces larger concentrations of injectant near the bottom test surface than if $M_\infty = 0.8$ and no shock waves are present. The result on adiabatic effectiveness is illustrated by the spanwise-averaged, centerline, and midspan data shown in Figs. 11(*a–c*). For $m = 0.5$, the first two of these quantities are higher when $M_\infty = 1.12$, than when $M_\infty = 0.8$ for most all x/d values examined.

Figure 12(*b*) shows shock wave structure when the blowing ratio m is 0.98. As the main flow approaches the hole, it deflects because of significant film blockage. Weak oblique shock waves are then formed, which emanate from channel top and bottom walls. These are followed by a second flow deflection, and a strong shock wave just downstream (which is also located *upstream* of the film holes). Note that all of these shock waves intersect near the middle of the channel. The flow then becomes and remains subsonic as it advects over the holes and locations farther downstream. As the film emerges from the holes, it is entrained by the free stream and also remains subsonic. The Mach number of the film at the hole exits is thus not believed to be high enough to induce additional shock wave events.

Because of the presence of the strong shock wave, the static pressure can increase by as much as 50 percent relative to the value upstream at the test section inlet. This may provide a reduction to the effective blowing ratio. These events, as well as the mainstream flow deflections, force larger quantities of cooling film near the surface compared to a situation in which no shock waves are present. As a result, corresponding spanwise-averaged and centerline effectiveness values in Figs. 11(*a–c*) (at most x/d locations) are substantially higher when $M_\infty = 1.12$ and $m = 0.98$, than when $M_\infty = 0.8$ and $m = 1.0$.

A similar conclusion is reached if the $M_\infty = 1.12$, $m = 1.48$ data are compared to the $M_\infty = 0.8$, $m = 1.50$ data in Figs. 11(*a–c*). In this case, Fig. 12(*c*) shows a single strong oblique shock wave located in front of the holes. Immediately downstream, the mainstream flow is subsonic. A weaker oblique shock wave then forms downstream of the holes due to deflection of the supersonic film emerging from the holes. This weak oblique shock wave is then seen to reflect off of the top wall. The static pressure in the main flow must then rise dramatically across the strong shock wave. It then drops as the film merges with the freestream, and then rises in a sequential fashion as successive, weak oblique shock waves are traversed.

Interactions Between Shock Waves and Film Cooling with Perpendicular Injectant Crossflow and $M_C = 0.3$. In contrast to the results just discussed, Figs. 13(*a–c*) show that local and spanwise-averaged magnitudes of adiabatic effectiveness *decrease*

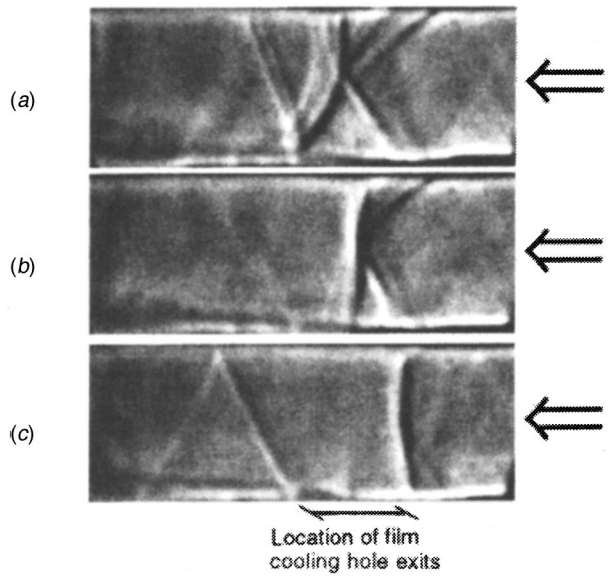

Fig. 12 Shadowgraph flow visualization images for $M_\infty = 1.12$ and $M_C = 0$: (*a*) $m = 0.53$; (*b*) $m = 0.98$; (*c*) $m = 1.48$. Arrows denote mainflow direction.

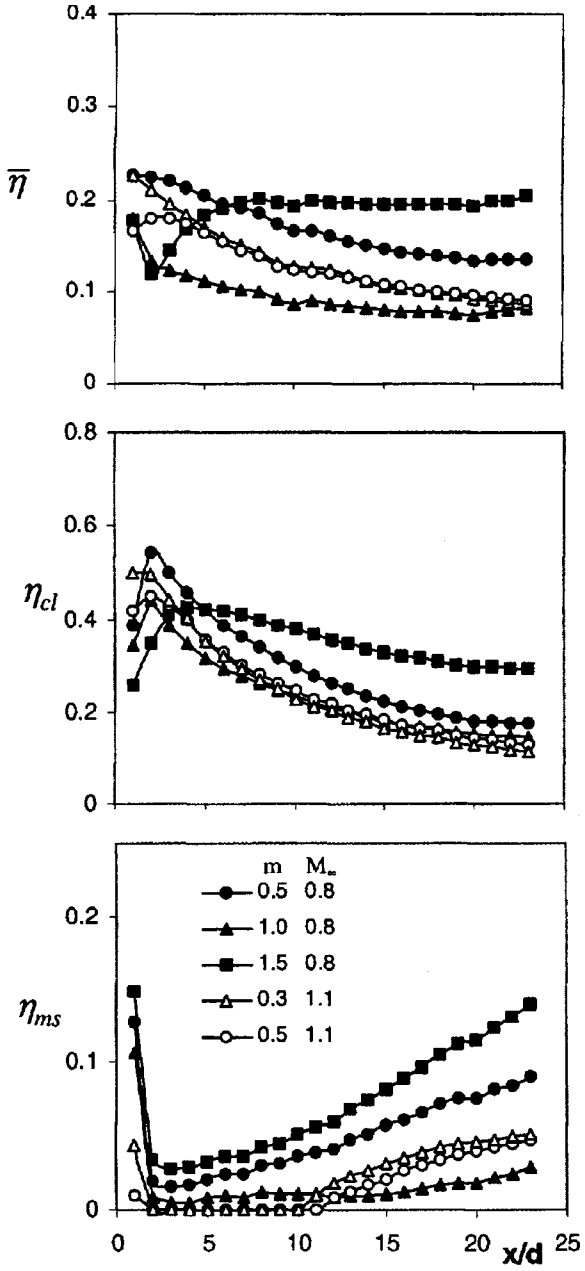

Fig. 13 Adiabatic film cooling effectiveness distributions for different M_∞ and m, with perpendicular injectant crossflow with $M_C = 0.3$: (*a*) Spanwise-averaged values; (*b*) centerline values; (*c*) midspan values

when shock waves are present near film hole exits, and perpendicular injectant crossflow with $M_C = 0.3$ is employed. This is evident if the $M_\infty = 0.8$, $m = 0.49$, data are compared to the $M_\infty = 1.10$, $m = 0.54$ data in Figs. 13(*a–c*). Because of the limited number of blowing ratios studied when $M_\infty = 1.1$ and $M_C = 0.3$, this comparison is made only for $m = 0.5$.

Corresponding shadowgraph images in Figs. 14(*a*, *b*) show that the effect of using $M_C = 0.3$ is increased blockage by the film. As a result, the $m = 0.32$, $M_C = 0.3$, $M_\infty = 1.10$ film seems to behave somewhat like a film produced using $m = 1.0$, $M_C = 0$, and $M_\infty = 1.12$. This is indicated by comparing the shadowgraph image in Fig. 14(*a*) with the one in Fig. 12(*b*). A similar comparison results if the $m = 0.54$ image in Fig. 14(*b*) is compared to the $m = 1.48$ image in Fig. 12(*c*).

Other noteworthy characteristics of the data in Figs. 13(*a–c*) are the high effectiveness values present when $m = 1.5$, $M_C = 0.3$, and $M_\infty = 0.8$. Here, $\overline{\eta}$, η_{cl}, and η_{ms} values are even higher than data measured with $m = 0.5$ at each x/d. This further illustrates the significant effects of perpendicular crossflow injection on film cooling behavior. This is especially evident when effectiveness data for $M_C = 0$ in Figs. 11(*a–c*) are also considered, since they generally decrease continually with increasing blowing ratio at each value of x/d.

Effects of Injectant Chamber Crossflow Mach Number on Shock Waves and Film Effectiveness. The influences of injectant crossflow on transonic film cooling behavior with shock waves is further illustrated by the results given in Figs. 15 and 16 for $m = 0.5$. The first of these figures shows that $\overline{\eta}$, η_{cl}, and η_{ms} magnitudes generally increase when shock waves are added to the flow and an injection plenum condition with $M_C = 0$ is utilized. This is evidenced by a comparison of the $M_\infty = 1.10$ data with $M_\infty = 0.3$ data.

When $M_\infty = 1.10$ in Figs. 15(*a–c*), $\overline{\eta}$, η_{cl}, and η_{ms} magnitudes then decrease as M_C increases from 0 to 0.3. Values then increase by small amounts as M_C increases further from 0.3 to 0.6 (except η_{cl} values which decrease slightly as M_C increases from 0.3 to 0.6). Such behavior is different from the results presented by Gritsch et al. [14]. In that study, film effectiveness magnitudes generally increase when $M_C = 0.6$ injectant crossflow is employed parallel to, and in the same direction as, the external free-stream flow (compared to results obtained with injection from a plenum with $M_C = 0$). The present study is different because: (*i*) perpendicular injectant crossflow is used, and (*ii*) shock wave events are present near the hole exits.

Shadowgraphs in Figs. 16(*a–d*) show that the associated shock wave structures are more advanced than ones produced using an injection plenum condition with $M_C = 0$. This means that $M_C = 0.3$ injectant produces more blockage than when the same blowing ratio is used with $M_C = 0$. This also means that low blowing ratio shadowgraph data in Figs. 16(*a–d*) (for $M_c = 0.3$) look like high blowing ratio shadowgraph data in Figs. 12(*a–c*) (for $M_C = 0$).

Summary and Conclusions

Interactions between shock waves and film cooling are described as they affect magnitudes of local and spanwise-averaged adiabatic film cooling effectiveness distributions. A row of three cylindrical holes is employed. Spanwise spacing of holes is 4 diameters, and inclination angle is 30 deg. Free-stream Mach numbers of 0.8 and 1.10–1.12 are used, with coolant to free-

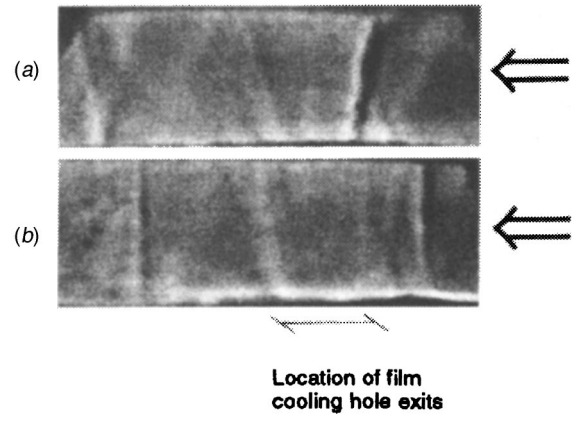

Fig. 14 Shadowgraph flow visualization images for $M_\infty = 1.10$ and $M_C = 0.30$: (*a*) $m = 0.32$; (*b*) $m = 0.54$. Arrows denote main-flow direction.

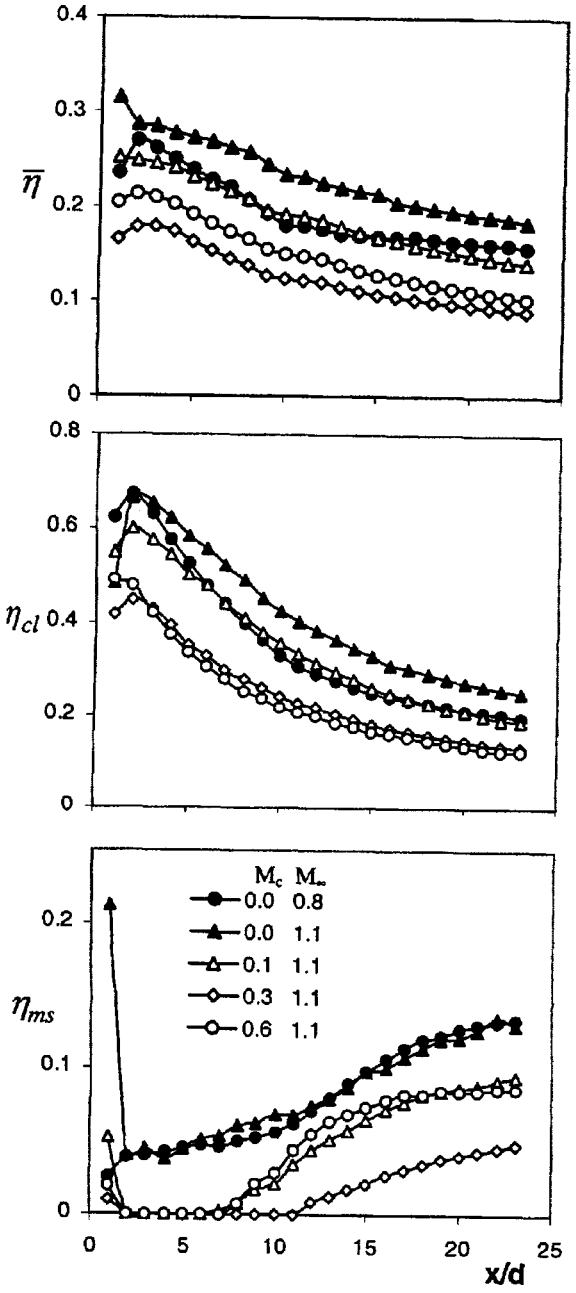

Fig. 15 Adiabatic film cooling effectiveness distributions for different M_∞ and M_C, for $m = 0.5$: (*a*) spanwise-averaged values; (*b*) centerline values; (*c*) midspan values

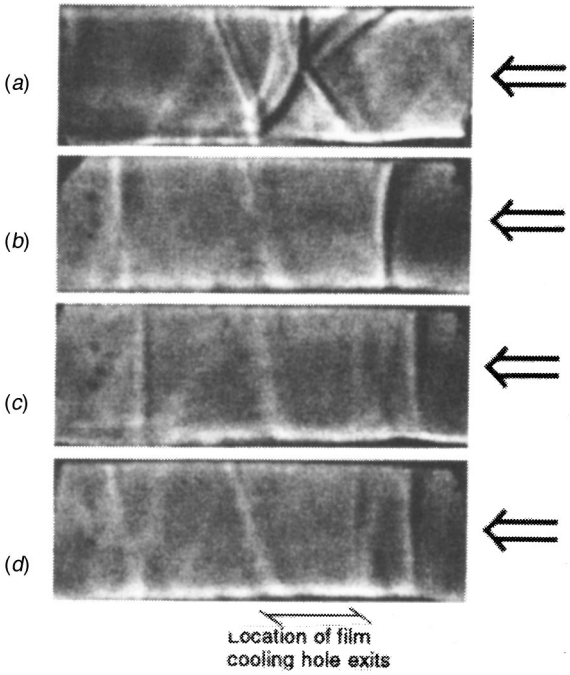

Fig. 16 Shadowgraph flow visualization images for $M_\infty = 1.10–1.12$ and $m = 0.5$: (*a*) $M_c = 0$; (*b*) $M_C = 0.15$; (*c*) $M_C = 0.30$; (*d*) $M_c = 0.59$. Arrows denote mainflow direction.

stream density ratios of 1.5–1.6. Also investigated are film plenum conditions, as well as perpendicular film injection crossflow Mach numbers of 0.15, 0.3, and 0.6.

When $M_\infty = 1.12$, and a film plenum condition is employed with $M_C = 0$, shadowgraph flow visualization images show shock wave structures, which develop in the immediate vicinity of the film hole exits. The number, locations, shapes, and character of these oblique shock waves vary significantly as the blowing ratio is changed. For example, the shock waves can be weak or strong. In addition, they sometimes interact with each other, and/or reflect off of channel surfaces. Static pressure rises as the flow proceeds across each oblique shock wave, and by large percentages of upstream pressure levels when these shocks are strong. This, along with the flow deflections which that occur across shocks, can reduce the effective blowing ratio, as well as force larger concentrations of the injectant film near the test surface (compared to situations when no shock waves are present). As a result, local and spanwise-averaged effectiveness magnitudes are generally higher when shock waves are present when a film plenum condition (with zero cross-flow Mach number) is utilized.

Different behavior is observed when injectant crossflow is utilized at the film hole entrances, which is oriented perpendicular to the mainstream flow direction with a Mach number M_C of 0.3. In this case, the films seem to produce more blockage at lower blowing ratios compared to situations when $M_C = 0$. This increased blockage results in stronger, more well-developed oblique shock waves. These are evidenced by shadowgraph images, which show oblique shock structures at low blowing ratios with $M_C = 0.3$, which look like shock structures that exist at high blowing ratios when $M_C = 0$. Local and spanwise-averaged effectiveness distributions for a blowing ratio of 0.5 and $M_C = 0.3$ are then lower at each streamwise location when shock waves are present (compared to situations with no shock waves).

As the injection crossflow Mach number increases from 0 to 0.3 (and the blowing ratio is held constant at 0.5), effectiveness values generally decrease significantly at each streamwise location when the approaching free-stream is supersonic and shock waves are present. Relatively small increases are then generally observed as the injection crossflow Mach number increases further from 0.3 to 0.6. Such changes are due to altered flow separation regions in film holes, different injection velocity distributions at hole exits, and alterations of static pressures at film hole exits produced by different types of shock wave events.

Acknowledgments

This work was sponsored by the Lehrstuhl und Institute für Thermische Stroemungsmaschinen, Universitaet Karlsruhe. The first author gratefully acknowledges this support.

Nomenclature

C_D = discharge coefficient
d = diameter of the film cooling holes
I = momentum flux ratio $= \rho_c u_c^2 / \rho_\infty u_\infty^2$
l = length of film cooling holes
M = Mach number
m = blowing ratio $= \rho_c u_c / \rho_\infty u_\infty$
P = static pressure
T = static temperature
u = velocity
x = streamwise coordinate from downstream edge of film cooling holes
z = spanwise coordinate measured from test surface spanwise centerline
η = local adiabatic film cooling effectiveness
$\overline{\eta}$ = spanwise-averaged adiabatic film cooling effectiveness
ρ = density

Subscripts

aw = adiabatic wall value
c = film coolant value at exit planes of film cooling holes or within film injectant passage
cl = value along film cooling hole spanwise centerline
ms = value along spanwise midspan location between two adjacent film cooling holes
o = total or stagnation value
r = recovery value
w = local surface value
∞ = local free-stream value

References

[1] Norton, R. J. G., Forest, A. E., White, A. J., Henshaw, D. G., Epstein, A. H., Schultz, D. L., and Oldfield, M. L. G., 1990, "Turbine Cooling System Design, Vol. **1**—Technical Report," Report WRDC-TR-89-2109, Aero Propulsion and Power Laboratory, Wright Research Development Center, Air Force System Command, Wright-Patterson Air Force Base, OH.
[2] Rigby, M. J., Johnson, A. B., and Oldfield, M. L. G., 1990, "Gas Turbine Rotor Blade Film Cooling With and Without Simulated NGV Shock Waves and Wakes," ASME Paper No. 90-GT-78.
[3] Abhari, R. S., and Epstein, A. H., 1994, "An Experimental Study of Film Cooling in a Rotating Transonic Turbine," ASME J. Turbomach., **116**, pp. 63–70.
[4] Abhari, R. S., 1996, "Impact of Rotor–Stator Interaction on Turbine Film Cooling," ASME J. Turbomach., **118**, pp. 123–133.
[5] Nix, A. C., Reid, T., Peabody, H., Ng, W. F., Diller, T. E., and Schetz, J. A., 1997, "Effects of Shock Wave Passing on Turbine Blade Heat Transfer in a Transonic Cascade," AIAA Paper No. 07-0160.
[6] Popp, O., Smith, D. E., Bubb, J. V., Grabowski, H., III, Diller, T. E., Schetz, J. A., and Ng, W. F., 1999, "Steady and Unsteady Heat Transfer in a Transonic Film Cooled Turbine Cascade," ASME Paper No. 99-GT-259.
[7] Popp, O., Smith, D. E., Bubb, J. V., Grabowski, H., III, Diller, T. E., Schetz, J. A., and Ng, W. F., 2000, "Investigation of Heat Transfer in a Film Cooled Transonic Turbine Cascade, Part II: Unsteady Heat Transfer," ASME Paper No. 2000-GT-203.
[8] Smith, D. E., Bubb, J. V., Popp, O., Grabowski, H., III, Diller, T. E., Schetz, J. A., and Ng, W. F., 2000, "An Investigation of Heat Transfer in a Film Cooled Transonic Turbine Cascade, Part I: Steady Heat Transfer," ASME Paper No. 2000-GT-202.
[9] Abhari, R. S., Guenette, G. R., Epstein, A. H., and Giles, M. B., 1992, "Comparison of Time-Resolved Turbine Rotor Blade Heat Transfer Measurements and Numerical Calculations," ASME J. Turbomach., **114**, pp. 818–827.
[10] Ligrani, P. M., Gong, R., Cuthrell, J. M., and Lee, J. S., 1996, "Bulk Flow

Pulsations and Film Cooling: Part I, Injectant Behavior,'' Int. J. Heat Mass Transf., **39**, No. 11, pp. 2271–2282.
[11] Ligrani, P. M., Gong, R., and Cuthrell, J. M., 1997, ''Bulk Flow Pulsations and Film Cooling: Flow Structure Just Downstream of the Holes,'' ASME J. Turbomach., **119**, pp. 568–573.
[12] Ligrani, P. M., Gong, R., Cuthrell, J. M., and Lee, J. S., 1997, ''Effects of Bulk Flow Pulsations on Film-Cooled Boundary Layer Structure,'' ASME J. Fluids Eng., **119**, pp. 56–66.
[13] Wittig, S., Schulz, A., Gritsch, M., and Thole, K. A., 1996, ''Transonic Film Cooling Investigations: Effects of Hole Shapes and Orientations,'' ASME Paper No. 96-GT-222.
[14] Gritsch, M., Schulz, A., and Wittig, S., 1998, ''Adiabatic Wall Effectiveness Measurements of Film-Cooling Holes with Expanded Exits,'' ASME J. Turbomach., **120**, pp. 549–556.
[15] Liess, C., 1975, ''Experimental Investigation of Film Cooling With Injection from a Row of Holes for the Application to Gas Turbine Blades,'' ASME J. Eng. Power, **97**, pp. 21–27.
[16] Seo, H. J., Lee, J. S., and Ligrani, P. M., 1998, ''The Effect of Injection Hole Length on Film Cooling With Bulk Flow Pulsations,'' Int. J. Heat Mass Transf., **41**, No. 22, pp. 3515–3528.
[17] Goldstein, R. J., Eckert, E. R. G., Tsou, F. K., and Haji-Sheikh, A., 1966, ''Film Cooling With Air and Helium Injection Through a Rearward-Facing Slot into a Supersonic Air Flow,'' AIAA J., **4**, No. 6, pp. 981–985.
[18] Parthasarathy, K., and Zakkay, V., 1970, ''An Experimental Investigation of Turbulent Slot Injection at Mach 6,'' AIAA J., **8**, No. 7, pp. 1302–1307.
[19] Cary, A. M., and Hefner, J. N., 1970, ''Film Cooling Effectiveness in Hypersonic Turbulent Flow,'' AIAA J., **8**, No. 11, pp. 2090–2091.
[20] Alzner, E., and Zakkay, V., 1971, ''Turbulent Boundary-Layer Shock Interaction With and Without Injection,'' AIAA J., **9**, No. 9, pp. 1769–1776.
[21] Baryshev, Y. V., Leont'yev, A. I., and Rozdestvenskiy, V. I., 1975, ''Heat Transfer in the Zone of Interaction Between a Shock Wave and the Boundary Layer,'' Heat Transfer—Soviet Research, **7**, No. 6, pp. 19–24.
[22] Cary, A. M., Bushnell, D. M., and Hefner, J. N., 1979, ''Predicted Effects of Tangential Slot Injection on Turbulent Boundary Layer Flow Over a Wide Speed Range,'' ASME J. Heat Transfer, **101**, pp. 699–704.
[23] Straight, D. M., 1979, ''Effect of Shocks on Film Cooling in a Full Scale Turbojet Exhaust Nozzle Having an External Expansion Surface,'' AIAA Paper No. 79-1170.
[24] Inger, G. R., 1985, ''Transonic Shock Interaction With a Tangential Injected Turbulent Boundary Layer,'' J. Aircr., **22**, No. 6, pp. 498–502.
[25] Holden, M. S., Nowak, R. J., Olsen, G. C., and Rodrigues, K. M., 1990, ''Experimental Studies of Shock Wave/Wall Jet Interaction in Hypersonic Flow,'' AIAA Paper No. 90-0607.
[26] Kamath, P. S., Holden, M. S., and McClinton, C. R., 1990, ''Experimental and Computational Study of the Effect of Shocks on Film Cooling Effectiveness in Scramjet Combustors,'' AIAA Paper No. 90-1713.
[27] Olsen, G. C., Nowak, R. J., Holden, M. S., and Bakner, N. R., 1990, ''Experimental Results for Film Cooling in 2-D Supersonic Flow Including Coolant Delivery Pressure, Geometry, and Incident Shock Effects,'' AIAA Paper No. 90-0605.
[28] Juhany, K. A., and Hunt, M. L., 1992, ''Flow-Field Measurements in Supersonic Film Cooling Including the Effect of Shock Wave Interaction,'' AIAA J., **32**, No. 3, pp. 578–585.
[29] Schulz, A., 2000, ''Infrared Thermography as Applied to Film Cooling of Gas Turbine Components,'' Meas. Sci. Technol., **11**, No. 7, pp. 948–956.
[30] Baldauf, S., Schulz, A., and Wittig, S., 2001, ''High-Resolution Measurements of Local Effectiveness From Discrete Hole Film Cooling,'' ASME J. Turbomach., **123**, this issue pp. 758–765.
[31] Kline, S. J., and McClintock, F. A., 1953, ''Describing Uncertainties in Single Sample Experiments,'' Mech. Eng. (Am. Soc. Mech. Eng.), **75**, pp. 3–8.
[32] Moffat, R. J., 1988, ''Describing the Uncertainties in Experimental Results,'' Exp. Therm. Fluid Sci., **1**, No. 1, pp. 3–17.
[33] Gritsch, M., Saumweber, C., Schulz, A., Wittig, S., and Sharp, E., 2000, ''Effect of Internal Coolant Crossflow Orientation on the Discharge Coefficient of Shaped Film Cooling Holes,'' ASME J. Turbomach., **122**, pp. 146–152.
[34] Schmidt, D., Sen, B., and Bogard, D., 1996, ''Film Cooling with Compound Angle Holes: Adiabatic Effectiveness,'' ASME J. Turbomach., **118**, pp. 807–813.
[35] Bell, C. M., Hamakawa, H., and Ligrani, P. M., 2000, ''Film Cooling From Shaped Holes,'' ASME J. Heat Transfer, **122**, pp. 224–232.
[36] L'Ecuyer, M. R., and Soechting, F. O., 1985, ''A Model for Correlating Flat Plate Film Cooling Effectiveness for Rows of Round Holes,'' Paper 19, AGARD-CP-390, Heat Transfer and Cooling in Gas Turbines.
[37] Anderson, J. D., 1990, *Modern Compressible Flow*, McGraw-Hill, New York.

Mark K. Harrington[1]
e-mail: Mark.Harrington@ae.ge.com

Marcus A. McWaters[2]
e-mail: mmcwater@ford.com

David G. Bogard
e-mail: dbogard@mail.utexas.edu

Mechanical Engineering Department,
University of Texas at Austin,
Austin, TX 78712

Christopher A. Lemmon[3]
Mechanical Engineering Department,
University of Wisconsin-Madison,
Madison, WI 53706
e-mail: calemmon@bme.jhu.edu

Karen A. Thole
Mechanical Engineering Department,
Virginia Polytechnic Institute and State
University,
Blacksburg, VA 24061
e-mail: thole@vt.edu

Full-Coverage Film Cooling With Short Normal Injection Holes

An experimental and computational investigation was conducted on the film cooling adiabatic effectiveness of a flat plate with full coverage film cooling. The full coverage film cooling array was comprised of ten rows of coolant holes, arranged in a staggered pattern, with short $L/D=1$, normal coolant holes. A single row of cooland holes was also examined to determine the accuracy of a superposition prediction of the full coverage adiabatic effectiveness performance. Large density coolant jets and high mainstream turbulence conditions were utilized to simulate realistic engine conditions. High-resolution adiabatic effectiveness measurements were obtained using infrared imaging techniques and a large-scale flat plate model. Optimum adiabatic effectiveness was found to occur for a blowing ratio of $M=0.65$. At this blowing ratio separation of the coolant jet immediately downstream of the hole was observed. For $M=0.65$, the high mainstream turbulence decreased the spatially averaged effectiveness level by 12 percent. The high mainstream turbulence produced a larger effect for lower blowing ratios. The superposition model based on single row effectiveness results over-predicted the full coverage effectiveness levels. [DOI: 10.1115/1.1400111]

Introduction

Film cooling is used in the turbine section of modern jet engines as a means of protecting the surface of the turbine airfoils from the hot gases entering the turbine section from the combustion chamber. Most film cooling studies have focused on single row configurations, but recently there has been renewed interest in the performance of full coverage film cooling. Full coverage cooling incorporates rows of coolant holes located over the entire area that is to be cooled. Previously there have been relatively few studies of adiabatic effectiveness performance for full coverage film cooling as indicated in Table 1.

Listed in Table 1 are summaries of the geometries and operating conditions for these previous studies. Because of the differences in geometric configurations among these studies, it is difficult to determine a consensus of the expected performance for full coverage cooling. For normal hole injection, Cho and Goldstein [1] found a maximum average adiabatic effectiveness of $\bar{\bar{\eta}}\approx 0.4$ ($\bar{\bar{\eta}}$ is spatially averaged adiabatic effectiveness) at a blowing ratio of $M=0.22$, with decreased adiabatic effectiveness for $M=0.36$. However, with larger spacing between holes. Metzger et al. [2] found a maximum adiabatic effectiveness of $\bar{\bar{\eta}}\approx 0.3$ for $M=0.2$.

It is important to recognize that none of these previous studies investigated short holes, large density ratios, or high mainstream turbulence. Large density ratio and high mainstream turbulence represent the conditions present within an actual gas turbine engine.

Objectives

The primary objective of this study was to evaluate the film cooling performance of a full coverage configuration of film cooling holes. The film cooling holes were short, $L/D=1.0$, and had a normal injection angle. Experiments were conducted using low and high mainstream turbulence conditions. CFD predictions were also made for a single row of holes.

The film cooling performance was evaluated using spatial variations of adiabatic effectiveness, including determining the optimum blowing ratio. Sellers' [6] superposition model was used to determine if full coverage film cooling effectiveness is predictable using single row experimental measurements or single row CFD predictions. Detailing the spatial variation in the adiabatic effectiveness is useful for understanding the complexities of the

Table 1 Previous full coverage film cooling studies with adiabatic effectiveness measurements

Authors	Cho & Goldstein [1]	Mayle & Camarata [3]	Metzger et al. [2]	Metzger et al. [4]	Sasaki et al. [5]
Hole Arrangement	in-line	staggered	in-line & staggered	in-line & staggered	staggered
Row Spacing (S/*D*)	3	8, 10, & 14	4.8	4.8	5 & 10
Hole Spacing (P/*D*)	=S/*D*	=0.866× S/*D*	=S/*D*	=S/*D*	3
Hole Length (*L*/*D*)	long	long	>10	>10	4.12
Injection Angle	90	compound angle	90	90	45
Density Ratio (*DR*)	1.0	1.0	1.0	1.0	0.94
Blowing Ratio (*M*)	0.22, 0.36	0.5-1.5	0.1, 0.2	0.1-0.5	0.15-0.5
Mainstream Turbulence	low	low	low	low	low

[1]Currently at General Electric Aircraft Engines.
[2]Currently at Ford Motor Co.
[3]Currently at Johns Hopkins University.

Contributed by the International Gas Turbine Institute and presented at the 46th International Gas Turbine and Aeroengine Congress and Exhibition, New Orleans, Louisiana, June 4–7, 2001. Manuscript received by the International Gas Turbine Institute February 2001. Paper No. 2001-GT-130. Review Chair: R. Natole.

interaction between the mainstream and coolant jets, as well as providing a benchmarking database for CFD validation.

Several aspects of the present study were unique. The present study was the first full coverage film cooling study that incorporated a large density ratio and high mainstream turbulence effects. It is also one of only two studies (including experimental and computational efforts) that examined short, normal holes; the only other being Hale et al. [7] who used unit density ratio and low mainstream turbulence.

Experimental Facilities and Techniques

Details of the facility and techniques are presented in Harrington [8]. The following is an overview of essential components. Adiabatic effectiveness tests were performed in a closed-loop wind tunnel. The mainstream flow was accelerated through a 9:1 contraction into the test section. Figure 1 shows a schematic representation of the test section and the secondary flow loop. The secondary loop provided the coolant flow for the adiabatic effectiveness tests. A density ratio of $DR=1.7$ was achieved by cooling the secondary flow, using liquid nitrogen in the heat exchanger, to about $T_j=-90°C$. Downstream of the heat exchanger before entering an insulated plenum, the total flow rate of the coolant was measured with an orifice flow meter.

A jets-in-cross-flow turbulence generator produced the high mainstream turbulence required for the present study. Figure 2 presents a schematic of the turbulence generator and shows its relative position to the test plate. The basic configuration of this turbulence generator was developed by Thole et al. [9] and later modified to obtain more uniform flow as described by Johnston et al. [10].

The turbulence generator produced a mainstream turbulence intensity $Tu=0.18$ and an integral length scale $\Lambda_f=3.5D$ at the first row of coolant holes in the test plates used in the present study. By the ninth row of coolant holes of the full coverage test plate, the turbulence intensity decayed to $Tu=0.11$ and the integral length scale increased to $\Lambda_f=4.5D$. Vertical uniformity of the turbulence field was checked and the turbulence intensity was found to be uniform within ± 6 percent of the average turbulence intensity.

Figure 3 gives a schematic representation of the primary test plate. The coordinate system used throughout the study is also presented in this figure. The primary test plate had coolant holes of diameter $D=6$ mm. The 55 cm long$\times$61 cm wide test plate had ten rows of coolant holes with nine holes in each row. The rows were arranged in a staggered pattern. The row-to-row spacing was $S/D=7.14$. The hole-to-hole pitch within each row was $P/D=7.14$. The hole injection angle was normal to the surface. The plate thickness matched the hole diameter in order to obtain a

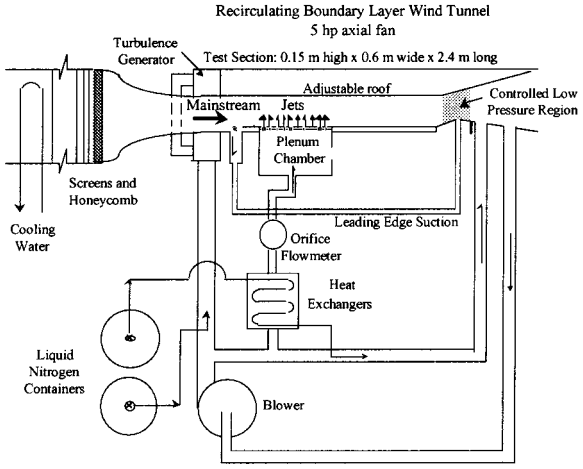

Fig. 1 Test facility including turbulence generator and coolant flow loop

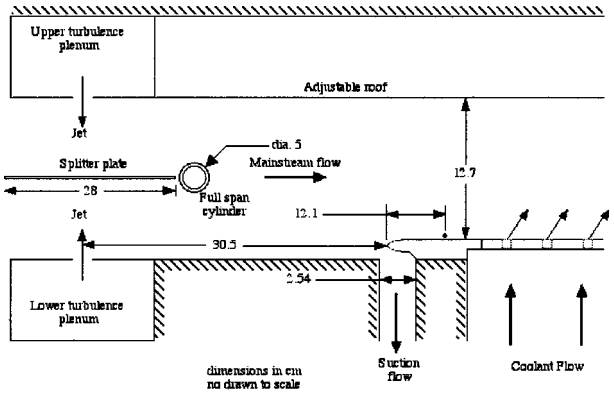

Fig. 2 Schematic of jets-in-crossflow turbulence generator

hole length to diameter ratio $L/D=1.0$. This test plate was constructed of low conductivity polyurethane foam, with a thermal conductivity $k=0.048$ W/m·K.

A second coolant hole test plate was constructed specifically to evaluate conduction effects on measured adiabatic wall temperatures. This test plate was scaled 2.6 larger than the primary test plate, and was constructed of polystyrene with a thermal conductivity $k=0.024$ W/m·K. This test plate had the same row and hole spacing ratios and the same injection angle, but the array of coolant holes only contained four rows with three or four holes in the rows. Consequently, the coolant hole diameter of the scaled-up test plate was $D=15.8$ mm.

The plenum for the coolant flow was located directly below the test plate and contained two flow conditioning screens that redistributed the in-flow to the plenum resulting in a uniform supply of air to all the film cooling holes. Velocity measurements at the hole exits verified that coolant flow from the holes was uniform. Furthermore, the lateral distribution adiabatic effectiveness with film cooling for $7.14 \leqslant z/D \leqslant 57.2$ (i.e., 7 holes in the center of a row) was also examined, and verified to have a regular periodic distribution.

Test plate surface temperatures were measured with an Inframetrics Model 600L infrared (IR) camera. A sodium chloride window was located on the adjustable roof of the test section. A thin cellophane window was located on the outer roof of the test section. The IR camera resolution was a function of the distance between the camera and the test plate surface. The minimum resolution of the camera in the present study was 4.5 mm$\times$4.5 mm ($0.75D\times 0.75D$). This value represents the area over which the IR camera averages to produce a temperature value for a single pixel, although the pixel resolution was finer than this.

Since the IR camera was not designed to operate at the very low temperatures encountered in these experiments, $-20°C$ to $-90°C$, the internal camera calibration could not be used. Consequently the IR camera grayscale video output was calibrated externally. These grayscale-temperature calibrations were nonlinear at low temperatures, and separate calibrations were performed for each experiment to maximize accuracy.

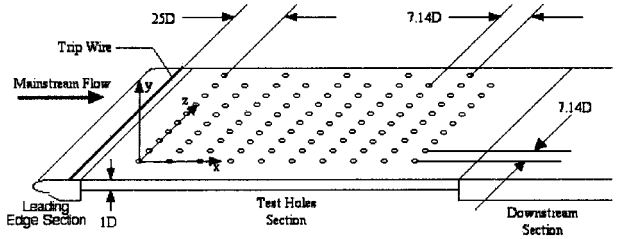

Fig. 3 Schematic of test plate with $D=6$ mm holes

The mainstream temperature was monitored with thermocouples located upstream of the test plate. Several thermocouples were used in the coolant plenum to verify the uniformity of the coolant temperature throughout the plenum. Measurements through the coolant hole showed that the measured plenum temperature was an accurate measure of the coolant temperature at the hole entrance. Temperature profile measurements were made with a miniature thermocouple probe. The thermocouple sensor used in this probe was approximately 0.5 mm in diameter.

Test Conditions

Full coverage adiabatic effectiveness tests were performed for both low mainstream turbulence intensity, $Tu<0.005$, and high mainstream turbulence intensity, $Tu=0.18$. The mainstream velocity was $U=10$ m/s, giving a Reynolds number based on coolant hole diameter of $\mathrm{Re}_D=4{,}000$. A two-dimensional, 1.6 mm diameter boundary layer trip was located 12 cm downstream of the leading edge, which was 14.5 cm upstream of the first row of coolant holes. The trip induced a turbulent boundary layer over the coolant hole section of the test plate with a momentum thickness of $\theta/D=0.075$ and Reynolds number of $\mathrm{Re}_\theta=300$ at the first row of coolant holes.

A density ratio of $DR=1.7$ was used with the blowing ratio ranging from $M=0.25$ to $M=1.0$. The corresponding momentum flux range was $I=0.04$ to $I=0.59$.

The test plate with $D=15.8$ mm holes was mainly used to evaluate the conduction correction used for the measured adiabatic wall temperatures for the test plate with $D=6$ mm holes. The thermal resistance of the test plate with $D=15.8$ mm holes was five times that of the test plate with $D=6$ mm holes, significantly reducing the conduction error for this plate compared to the primary test plate. One-dimensional conduction corrections were applied to the measurements from the primary test plate. A measure of the conduction error was obtained from measurements between the holes in the first row where actual adiabatic effectiveness should have been zero. Comparison of these corrected results with results from the high-thermal-resistance test plate (which had negligible conduction errors) confirmed the reliability of the conduction corrections.

The mainstream velocity for the $D=15.8$ mm test plate was also $U_\infty=10$ m/s. The resulting Reynolds number was $\mathrm{Re}_D=10{,}500$. Computation predictions were done for the film cooling performance for a range of Re_D. Little effect of Re_D on the film cooling performance was found (see Lemmon [11]).

Spanwise Uniformity, Repeatability, and Uncertainty

The overall precision uncertainty in the effectiveness measurements was determined with repeatability tests, where the same test conditions were investigated on separate days. Based on the repeatability tests, precision uncertainty for local adiabatic effectiveness was $\delta\eta=\pm0.025$, for a 95 percent confidence interval. Results from repeated laterally averaged effectiveness tests indicated a precision uncertainty of $\delta\overline{\eta}=\pm0.01$. For the primary test plate, conduction corrections of $\Delta\overline{\eta}=0.06$ to 0.10 were applied, depending on the blowing ratio. The uncertainty of this correction was estimated to be $\delta\overline{\eta}=\pm0.015$. Consequently, overall uncertainty for the laterally averaged adiabatic effectiveness measurements on the primary test plate was $\delta\overline{\eta}=\pm0.02$.

The uncertainty of the superposition prediction examined in the present study was determined using the sequential perturbation technique [12] incorporating the uncertainty for the single row. The uncertainty in the superposition prediction was $\delta\overline{\eta}=\pm0.07$ by the ninth row of holes. The uncertainty in the superposition prediction for $M=0.25$ was the same magnitude as the $M=0.65$ prediction. The increase in uncertainty with row number was caused by the propagation of the uncertainty inherent with the superposition model.

Computational Methodology

Two test cases were computationally simulated for this study, which included the blowing ratios of $M=0.25$ and $M=0.65$ at low mainstream turbulence conditions. For the simulations, the computational domain included the supply chamber, a single half film-cooling hole, and the external flat plate were modeled. Appropriate symmetry boundary conditions for the film-cooling hole were applied at the hole centerline and mid-pitch locations. The inlet boundary condition for the external flow was set at 20 hole diameters upstream of injection while an outflow boundary condition was placed at 30 hole diameters downstream of injection.

The Reynolds-Averaged Navier–Stokes (RANS) equations and energy equations were discretized using a second-order upwind scheme and solved using *Fluent*, V5. The mesh consisted of quadrilateral cells near the wall and tetrahedral cells throughout the remainder of the domain. The turbulence model used was the RNG $k-\epsilon$ model with a two-layer zonal method for the near-wall treatment. The two-layer zonal model resolves the near-wall region whereby the average location of the first cell was at a $y^+=1.8$ for the studies reported in this paper. Note that all of the turbulence modeling coefficients remained as the model-specified values.

A number of computational studies were conducted to determine grid sensitivity with the final mesh requiring 1.2×10^6 cells. Nominally 2100 iterations were required for convergence, which was determined based on a decrease of the energy equation residuals by three orders of magnitude. Performing 500 iterations beyond the 2100 iterations resulted in changes of the centerline effectiveness levels by $\delta\eta=0.001$.

Results

In the following results, experimental and computationally predicted single row performance are presented first. These data were the baseline for superpositions predictions. Following this, experimental results for full coverage film cooling are presented for low and high mainstream turbulence levels. Finally, superposition predictions are compared with actual full coverage film cooling performance.

Single Row, Low Mainstream Turbulence. Single row adiabatic effectiveness tests were performed on the $D=15.8$ mm test plate to minimize the conduction correction (essentially negligible) and thereby increase accuracy. Adiabatic effectiveness measurements were made for $x/D\leqslant44$. These single row measurements were made primarily to provide a baseline for use with superposition predictions, and for comparison with computational predictions. Laterally averaged adiabatic effectiveness, $\overline{\eta}$, results are presented in Fig. 4 for blowing ratios of $M=0.25$ and $M=0.65$. Preliminary tests had shown that the blowing ratio of $M=0.65$ provided the maximum adiabatic effectiveness. The low laterally averaged adiabatic effectiveness, $\overline{\eta}$, levels downstream of the row of coolant holes can be attributed to the large hole-to-hole spacing within the row, $P/D=7.14$. For distances greater than $20D$ downstream, $\overline{\eta}$ levels were less than 0.08 which required extreme precision for accurate measurement. Although these levels might be considered low enough to be inconsequential, the cumulative effects when using superposition for full coverage film cooling predictions requires that these low levels be accurately determined.

For both blowing ratios, $M=0.25$ and $M=0.65$, the computational results under-predicted the effectiveness levels for $x/D<20$. But the computationally predicted $\overline{\eta}$ levels decayed at a slower rate than the experimentally measured levels so that $\overline{\eta}$ level for experiments and computations were comparable in the range $20<x/D<40$.

Differences between the experimental measurements and computational predictions were clarified by the spatial distribution of adiabatic effectiveness downstream of the holes. Figure 5 presents the measured and predicted two-dimensional adiabatic effective-

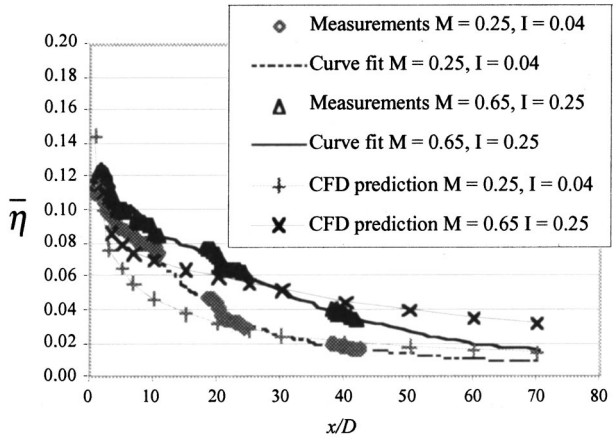

Fig. 4 Single row laterally averaged adiabatic effectiveness; experimental measurements and CFD predictions

ness contours for the blowing ratios $M=0.25$ and $M=0.65$. At both blowing ratios the computationally predicted distribution of η was distinctly narrower than the measured distribution. Also, centerline values of η for the computational predictions were larger than experimental measurements. Both these differences suggest that the lateral dispersion of the coolant for the computational prediction was less than actually occurred.

For both blowing ratios, experiments showed the maximum local η level immediately downstream of the hole was $\eta \approx 0.5$. This relatively low level suggested the possibility of jet separation. The computational results also indicate a distinct double peak in the near hole region for the M=0.65 case indicating a jet lift-off in this region. To investigate this possibility, thermal field measurements were made above the surface.

The measured and predicted thermal profiles of the coolant jet above the surface of the test plate and along the centerline of the jet are shown in Fig. 6 for blowing ratios of $M=0.25$ and $M=0.65$, respectively. The thermal profiles shown are in terms of non-dimensional temperature, Θ. These coolant jet profiles show that the computational predictions of the jet lift-off were in good agreement with experimental measurements. For $M=0.25$, experiments and computations showed the coolant jet positioned very close to the wall, indicating negligible separation. However, for $M=0.65$ the core of the coolant jet, identified by maximum Θ values, is distinctly above the surface, indicating a significant separation. Although the Θ levels predicted by the computations were larger than the experimentally measured Θ levels, the predicted penetration height of the separated coolant jet was very similar to the measured height.

The coolant jet separation is most clearly evident from the computational velocity field predictions. Figure 7 shows a large reverse flow region which occurs for the $M=0.65$ blowing ratio. For $M=0.25$ the computationally predicted velocity field showed a very slight separation region close to the wall (not shown).

Although the low η levels downstream from the hole can be attributed to jet separation for $M=0.65$, for $M=0.25$ the experimental measurements indicate the decreased η levels are due to smaller Θ levels at the exit of the hole. The maximum non-dimensional temperature measured at the hole exit was $\Theta=0.8$, and the coolant appears to exit from the downstream part of the hole. These measurements suggest ingestion of mainstream fluid into the hole (there is insignificant heating of the coolant as it passes through the hole due to the very low conductivity polystyrene material). The computational results give a maximum value of $\Theta>0.9$ indicating less ingestion into the hole as compared with the experiments.

Full Coverage, Low Mainstream Turbulence. Figure 8 shows the build-up of laterally averaged adiabatic effectiveness

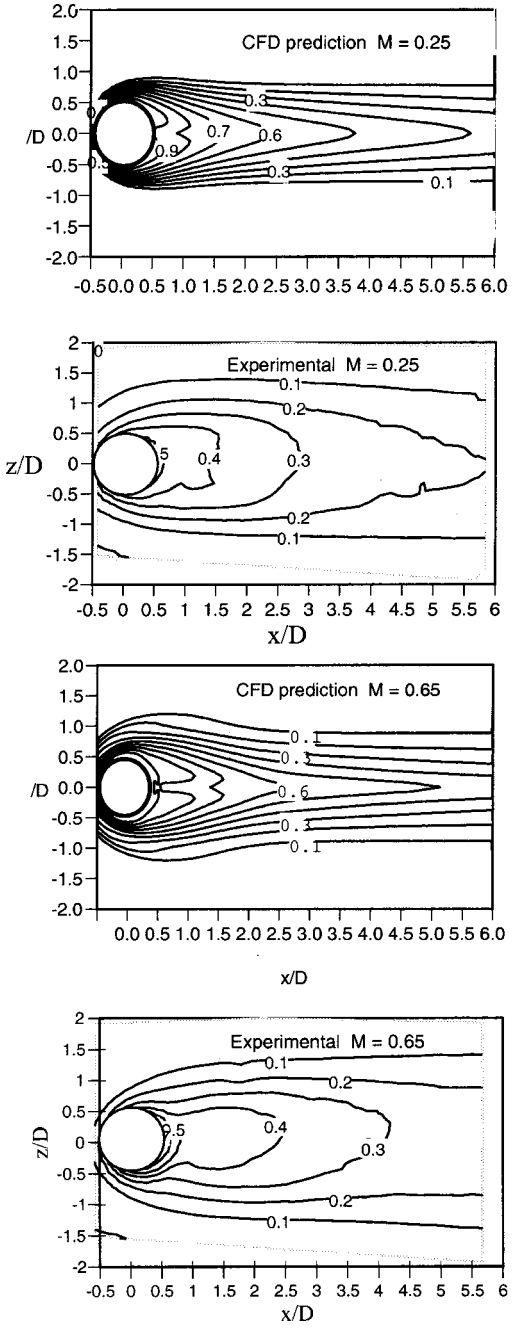

Fig. 5 Single row adiabatic effectiveness contours; experimental measurements and CFD predictions

for the full coverage operation with blowing ratios of $M=0.25$ and $M=0.65$. The data shown in the figure were taken at multiple IR camera positions, which include rows 1, 2, 3, 4, 5, 8, and 9. The average adiabatic effectiveness was just slightly less for $M=0.25$ compared to $M=0.65$ for the first several rows of holes. However, downstream of the fourth row of holes the performance gap between the two blowing ratios widened, and by the eighth row the difference in laterally averaged effectiveness for the blowing ratios of $M=0.25$ and $M=0.65$ was $\Delta\bar{\eta}\approx 0.10$.

Adiabatic effectiveness for $M=0.25$ injection appeared to reach an asymptotic fully developed level by the fourth row of holes. For $M=0.65$, the fully developed level was reached by the eighth row of holes (no images were made for the sixth and seventh rows of holes).

Figure 9 shows the effect of blowing ratio for rows eight and

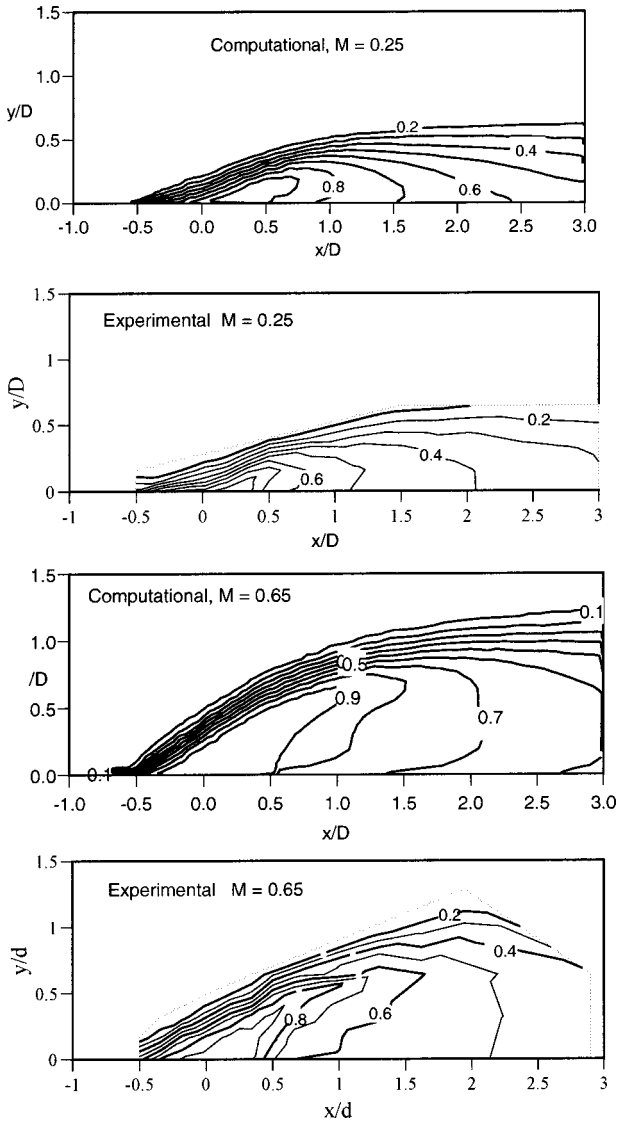

Fig. 6 Thermal profiles along the centerline of the coolant jet for $M=0.25$ and 0.65

nine, which may be regarded as the fully developed effectiveness region for the full coverage operation. All three blowing ratios, $M=0.25$, $M=0.65$, and $M=1.0$, exhibited no variation in laterally averaged effectiveness levels between the eighth and ninth row of holes. The intermediate blowing ratio, $M=0.65$, and the high blowing ratio, $M=1.0$, produce nominally the same laterally averaged effectiveness levels, so operation at $M=1.0$ would be of little benefit.

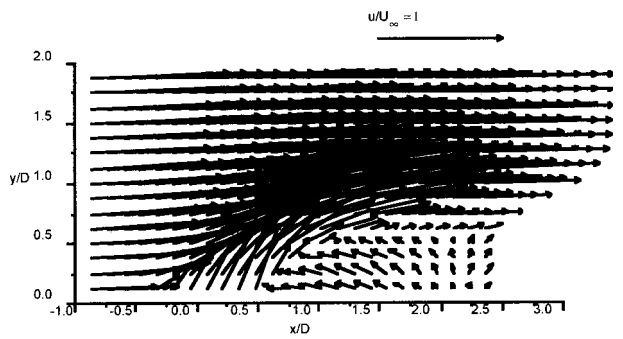

Fig. 7 CFD prediction of velocity field for $M=0.65$ coolant jet injection

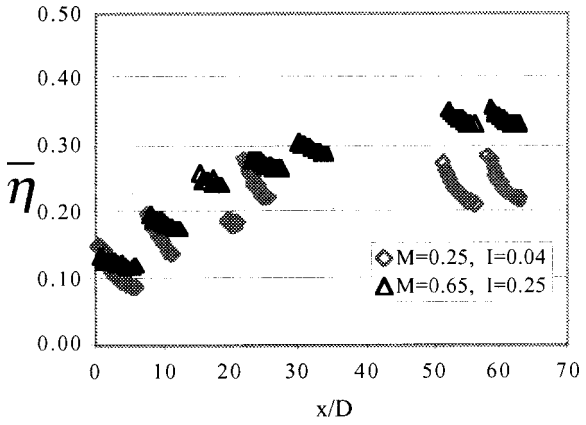

Fig. 8 Full coverage adiabatic effectiveness with low mainstream turbulence, $Tu=0.005$

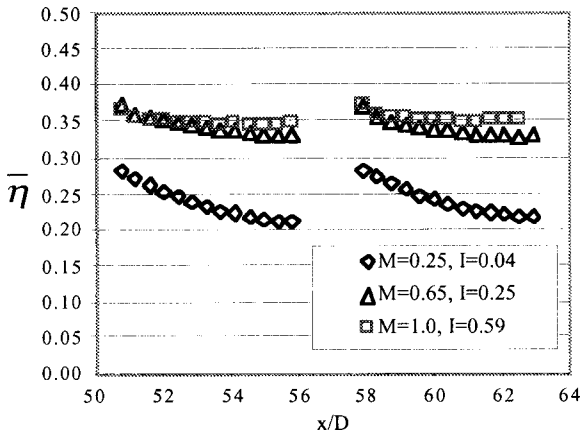

Fig. 9 Effect of blowing ratio on full coverage performance for the fully developed region (rows 8 and 9) with low mainstream turbulence, $Tu=0.005$

Full Coverage, High Mainstream Turbulence. Figure 10 shows the effect of mainstream turbulence on laterally averaged

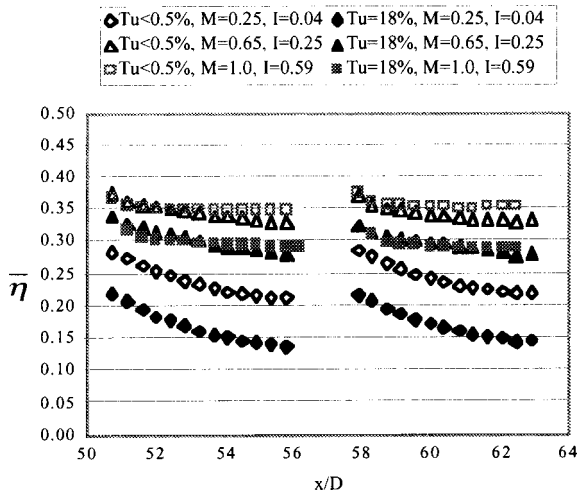

Fig. 10 Comparison of full coverage adiabatic effectiveness with low and high mainstream turbulence, $Tu=0.005$ and 0.18

Table 2 Spatially averaged adiabatic effectiveness levels, $\bar{\bar{\eta}}$, for the fully developed region with full coverage film cooling

M	$Tu=0.5$	$Tu=18$	Percent change
0.25	0.23	0.16	30
0.65	0.34	0.30	12
1.0	0.35	0.30	14

adiabatic effectiveness for the eighth and ninth rows of the full array. These results are summarized in Table 2 in terms of the spatially averaged effectiveness, $\bar{\bar{\eta}}$, which is an overall area average of the adiabatic effectiveness (excluding the coolant holes). For low blowing ratio, $M=0.25$, there was a 30 percent decrease in the spatially averaged effectiveness with high mainstream turbulence. The intermediate blowing ratio, $M=0.65$, showed a 12 percent decrease and the high blowing ratio, $M=1.0$, showed a 14 percent decrease.

Spatial distributions of adiabatic effectiveness in the fully developed region are presented in Figs. 11 and 12 for low and intermediate blowing ratios, respectively. In each case the general pattern of the effectiveness distribution downstream of the holes was similar for low and high mainstream turbulence. However, the high mainstream turbulence caused a relatively uniform decrease of $\Delta\eta=0.05$ in local effectiveness levels. The much narrower distribution of effectiveness, and sharper decrease in effectiveness

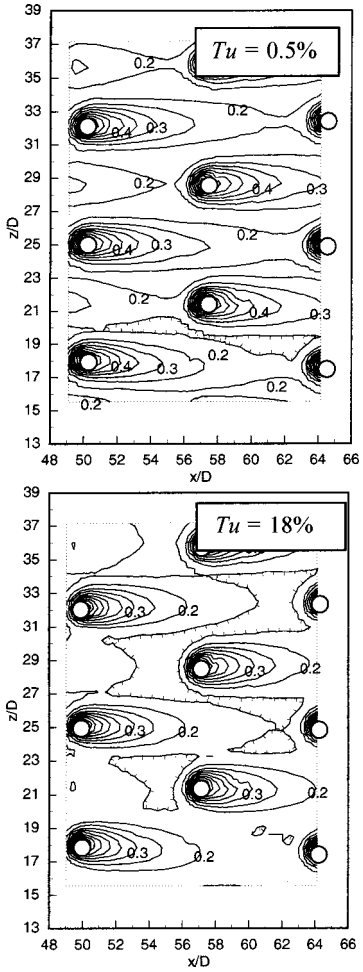

Fig. 11 Effect of high mainstream turbulence on full coverage adiabatic effectiveness distribution for $M=0.25$

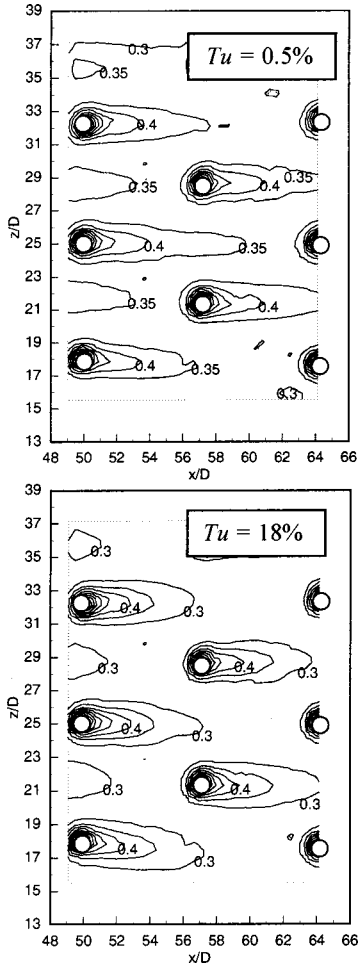

Fig. 12 Effect of high mainstream turbulence on full coverage adiabatic effectiveness distribution for $M=0.65$

for the $M=0.65$ case compared to the $M=0.25$ case is another indication of the significant separation which occurs for $M=0.65$.

Superposition Predictions. The superposition model developed by Sellers [6] was used to predict the performance of the multiple rows of holes for full coverage performance. These predictions require the use of a baseline database for a single row of holes. Consequently, predictions were made using the experimental measurements for single row operation (as presented in Fig. 4), and the computational prediction for a single row of holes.

As part of the computational study, full coverage with seven rows was simulated using a coolant with density ratio $DR=1.1$ and a blowing ratio of $M=0.25$. The results of this study indicated good agreement between the CFD single row simulations using superposition and the CFD multiple row simulations.

Superposition predictions, experimental and computational, are compared with the measured $\bar{\eta}$ values for full coverage film cooling with a blowing ratio of $M=0.25$. The superposition prediction based on the experimental single row data showed good agreement with measurements over the first four rows of holes, but over-predicted the effectiveness level at the eighth and ninth rows. The superposition based on the computational results underpredicted the effectiveness level over the first several rows of the array, but showed good agreement with measured levels at the eighth and ninth rows.

For the full coverage measurements, the $\bar{\eta}$ level downstream of the fourth row of holes was essentially the same level as that downstream of the eighth and ninth rows. This suggests that for

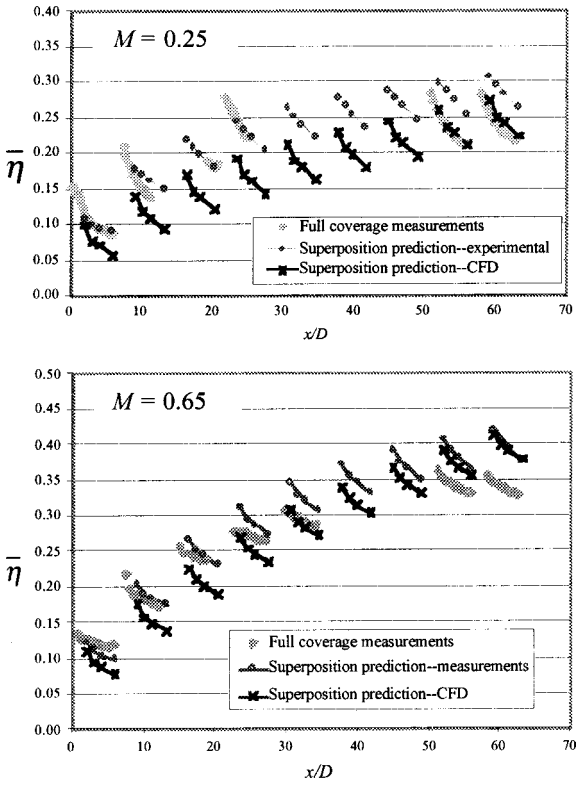

Fig. 13 Superposition predictions using experimental and CFD single row baselines. Low mainstream turbulence, *Tu* = 0.005

$M = 0.25$ a fully developed condition was achieved by the fourth row of holes. Furthermore, this indicates that the coolant from the first rows of holes must interact with the coolant jets of the second through fourth rows of holes in such a way as to eliminate any cooling effect from the first row of holes by the fifth row.

Figure 13 shows a comparison of the predicted and measured full coverage $\overline{\eta}$ values for a blowing ratio of $M = 0.65$. The experimental superposition prediction showed good agreement with the measured effectiveness levels for the first three rows of holes. After the fourth row, the experimental superposition prediction over-predicted the effectiveness levels and the discrepancy increased with increasing streamwise position. The computational superposition prediction was similar to the experimental superposition prediction, with the exception of poorer agreement with the measured effectiveness levels over the first three rows of holes.

Since there was no difference in the measured $\overline{\eta}$ levels evident between the eighth and ninth rows of holes, it was apparent that a fully developed condition had been achieved by the eighth row. This indicates that the effect of the coolant from the first row of holes was eliminated by the interaction of the jets from the second to eighth rows of holes.

When the superposition predictions were extended beyond the nine rows of holes as shown in Fig. 13 (see Harrington [8]), a continuing increase in laterally averaged adiabatic effectiveness was predicted up to 20 rows. These predictions were clearly contrary to the experimental measurements of the full coverage film cooling showing that fully developed levels were established within four and eight rows of holes for $M = 0.25$ and $M = 0.65$, respectively.

The main deficiency of the superposition model proposed by Sellers [6] was an inability to account for the degradation of the coolant jet caused by the interaction with coolant from downstream rows of holes. The prediction for $M = 0.25$ produced good agreement with the measurement over the first four rows of holes in the full array. For the $M = 0.65$, the prediction only produced good agreement over the first three rows of holes.

Conclusions

There were several unique aspects of this full coverage film cooling study compared to previous studies. Large density coolant was used, the effects of very high mainstream turbulence were investigated, and relatively short, normal holes were used. For the full coverage configuration studied, as many as eight rows of holes were required to reach an asymptotic "fully developed" adiabatic effectiveness level. Maximum spatially averaged adiabatic effectiveness of 0.35 was found to occur for a blowing ratio of $M = 0.65$. Increasing the blowing ratio to $M = 1.0$ resulted in essentially the same average adiabatic effectiveness.

Particular attention was placed on jet separation. The coolant jet remained attached to the surface of the test plate for $M = 0.25$. Significant separation of the coolant jet from the surface, both measured and predicted, was evident for $M \geq 0.65$.

The high mainstream turbulence reduced the spatially averaged effectiveness by 30 percent for the blowing ratio of $M = 0.25$. The reduction in spatially averaged effectiveness for the blowing ratios of $M = 0.65$ and $M = 1.0$ was not as severe, only about a 14 percent reduction. The smaller reduction in adiabatic effectiveness at higher blowing ratios might be attributed to the coolant jet being separated from the surface at higher blowing ratios. For separated coolant jets, the increased dispersion caused by a highly turbulent mainstream can have a beneficial effect of returning coolant to the surface of the test plate.

The superposition prediction of the full coverage laterally averaged effectiveness levels based on the single row effectiveness measurements tended to overpredict adiabatic effectiveness. Superposition predicted increasing adiabatic effectiveness performance beyond nine rows of holes, whereas the experiments showed maximum adiabatic effectiveness was reached within four to eight rows, depending on blowing ratio. These results indicate that there are row-to-row interactions, which limit the maximum adiabatic effectiveness, and these interaction are not accounted for by the superposition model.

Acknowledgments

Our sincere thanks to Pratt and Whitney, the sponsors of this research, for their continued support. In particular, we appreciate the support and guidance of William Kvasnak, Fred Soechting, and Joel Wagner.

Nomenclature

D = film cooling hole diameter
DR = density ratio of coolant to mainstream $= \rho_j / \rho_\infty$
I = momentum flux ratio of coolant to mainstream $= \rho_j U_j^2 / \rho_\infty U_\infty^2$
k = thermal conductivity
L = hole length
M = mass flux ratio of coolant to mainstream $= \rho_j U_j / \rho_\infty U_\infty$
P = lateral hole pitch
Re = Reynolds number
S = streamwise row spacing
T = temperature
Tu = turbulence intensity $= u_{\text{rms}} / U \times 100$ percent
U = mean velocity
x = streamwise coordinate originating at centerline of cooling hole in the first row
y = vertical coordinate originating at test surface
z = spanwise coordinate originating at centerline of central hole
η = adiabatic effectiveness $= (T_{aw} - T_\infty)/(T_j - T_\infty)$
Λ_f = turbulence integral length scale
ρ = density

θ = momentum thickness
Θ = nondimensional temperature $=(T-T_\infty)/(T_j-T_\infty)$

Subscripts

aw = adiabatic wall
j = coolant jet
∞ = mainstream

Superscripts

$\bar{}$ = lateral average
$\bar{\bar{}}$ = spatial average

References

[1] Cho, H. H.,and Goldstein, R. J., 1995,"Heat (Mass) Transfer and Film Cooling Effectiveness With Injection Through Discrete Holes: Part II—On the Exposed Surface," ASME J. Turbomach., **117**, pp. 451–460.

[2] Metzger, D. E., Takeuchi, D. I., and Kuenstler, P. A., 1973,"Effectiveness and Heat Transfer With Full-Coverage Film Cooling," ASME J. Eng. Power, **95**, pp. 180–184.

[3] Mayle, R. E., and Camarata, F. J., 1975,"Multihole Cooling Film Effectiveness and Heat Transfer," ASME J. Heat Transfer, **97**, pp. 534–538.

[4] Metzger, D. E., Kuenstler, P. A., and Takeuchi, D. I., 1976, "Heat Transfer With Film Cooling Within and Downstream of One to Four Rows of Normal Injection Holes," ASME Paper No. 76-GT-83.

[5] Sasaki, M., Takahara, K., Kumagai, T., and Hamano, M., 1979,"Film Cooling Effectiveness for Injection From Multirow Holes," ASME J. Eng. Gas Turbines Power, **101**, pp. 101–108.

[6] Sellers, J. P., 1963,"Gaseous Film Cooling With Multiple Injection Stations," AIAA J., **1**, pp. 2154–2156.

[7] Hale, C. A., Plesniak, M. W., and Ramadhyani, S., 2000, "Film Cooling for Short Film Cooling Holes Fed by a Narrow Plenum," ASME J. Turbomach., **122**, pp. 553–557.

[8] Harrington, M. K., 2000, "Adiabatic Effectiveness for Full Coverage Film Cooling With Normal Holes on a Flat Plate," M. S. Thesis, University of Texas at Austin.

[9] Thole, K. A., Bogard, D. G., and Whan-Tong, J. L., 1994,"Generating High Freestream Turbulence Levels," Exp. Fluids, **17**, pp. 375–380.

[10] Johnston, C. A., Bogard, D. G., and McWaters, M. A., 1999, "Highly Turbulent Mainstream Effects on Film Cooling of a Simulated Airfoil Leading Edge," ASME Paper No. 99-GT-261.

[11] Lemmon, C., 2000, "Simulation of Film Cooling for Gas Turbine Applications," M. S. Thesis, University of Wisconsin—Madison.

[12] Moffat, R. J., 1988, "Describing the Uncertainties in Experimental Results," Exp. Therm. Fluid Sci., **1**, pp. 3–17.

Heat/Mass Transfer Measurement Within a Film Cooling Hole of Square and Rectangular Cross Section

Hyung Hee Cho
e-mail: hhcho@yonsei.ac.kr

Seung Goo Kang

Dong Ho Rhee

Department of Mechanical Engineering,
Yonsei University,
134, Shinchon-dong, Seodaemoon-gu,
Seoul 120-749, Korea

An experimental study has been conducted to investigate the heat/mass transfer characteristics within film cooling holes of square and rectangular cross section. The experiments for this study have been performed using a naphthalene sublimation method, and the flow field has been analyzed by numerical calculation using a commercial code (FLUENT). The rectangular cross section has the aspect ratio of 2 and the same hydraulic diameter as the square cross section. A duct flow enters into a film cooling hole in a cross direction. For the film cooling hole with square cross section, it is observed that the reattachment of separated flow and the vortices within the hole enhance considerably the heat/mass transfer around the hole entrance region. The heat/mass transfer on the leading edge side of hole exit region increases as the blowing rates decrease because the mainflow induces a secondary vortex. Heat/mass transfer patterns within the film cooling hole are changed slightly with the various Reynolds numbers. For the film cooling hole with rectangular cross section, overall heat/mass transfer characteristics are similar with those for the square cross section. However, heat/mass transfer on the leading edge side of hole entrance region has two peak regions due to split flow reattachment, and heat/mass transfer on the leading edge side of hole exit region is less sensitive to the blowing ratios than the square cross-sectional case. [DOI: 10.1115/1.1400109]

Introduction

The thermal efficiency and specific power of gas turbine engines depend strongly on the turbine inlet temperature. However, inlet temperature is limited by the potential structural failure of engine components mainly attributable to high thermal stresses and reductions in material strength due to high wall temperature. Thus, the inlet temperature has in past decades been raised to the values which make intensive cooling of the hot components imperative. Therefore, many cooling methods have been developed, and film cooling, especially of the turbine blades and combustion chamber walls, has become a standard method.

The two-dimensional slot film cooling shows the best performance. However, in general, rows of discrete circular film cooling holes are used for the cooling of combustors and turbine blades. Film cooling with discrete holes has some problems such as the nonuniformity in lateral direction and the penetration of cooling jet into the hot gases. To reduce these problems, rows of rectangular or expanded-shape film cooling holes are used in recent years. Much research on film cooling performances has been performed with the expanded-shape and circular cross-sectional film cooling hole [1–6].

However, only limited research has been conducted for square/rectangular film cooling holes. Muldoon and Acharya [7] and Licu et al. [8] investigated flow characteristics and film cooling performance downstream of the rectangular hole with numerical and experimental methods, respectively. Watanabe et al. [9] and Takahashi et al. [10] measured the temperature field and film cooling performance for a row of holes with various hole shapes including square and rectangular holes, and they reported that the rectangular/oval-shape film cooling holes show better cooling performance than the circular hole and the film cooling performance increases with aspect ratios.

A complete analysis of heat transfer with film cooling requires heat transfer coefficient distributions on internal walls and inside the hole surfaces as well as adiabatic wall temperatures (film cooling effectiveness) and heat transfer coefficient distributions on the exposed surfaces [11].

Metzger and Cordaro [12] investigated the average heat transfer rate in a short branch tube with crossflow entering. They showed that the heat transfer is enhanced with increasing crossflow-to-tube velocity ratio. Byerley et al. [13] studied the heat transfer near and within the entrance of a branch hole with a crossflow stream using a liquid crystal technique, and found that local heat transfer coefficients on the duct wall downstream of the branch hole are up to six times those of fully developed flow. Cho et al. [14] and Cho and Goldstein [15,16] studied heat/mass transfer characteristics on the internal wall and inside a circular film cooling hole, and reported that a complex heat/mass transfer pattern was observed inside the film cooling hole due to separation and reattachment of coolant flows. Lee et al. [17] studied the flow characteristics inside a circular film cooling hole.

In the present study, local heat/mass transfer characteristics inside square/rectangular film cooling holes are investigated with the variations of blowing rates and Reynolds numbers. To prevent hot spots and obtain better cooling performance, not only information of overall heat transfer coefficients but also its local variations are required [16]. Therefore, a naphthalene sublimation method is used to measure the local heat/mass transfer coefficients inside the film cooling holes. The boundary conditions of isothermal and adiabatic wall can be easily imposed and errors analogous to conductive losses in a wall can be excluded in this method. Mass transfer data obtained by this method can be converted to heat transfer data through heat and mass transfer analogy.

The information about the flow characteristics inside the hole is needed to analyze the heat/mass transfer characteristics more pre-

Contributed by the International Gas Turbine Institute and presented at the 46th International Gas Turbine and Aeroengine Congress and Exhibition, New Orleans, Louisiana, June 4–7, 2001. Manuscript received by the International Gas Turbine Institute February 2001. Paper No. 2001-GT-128. Review Chair: R. Natole.

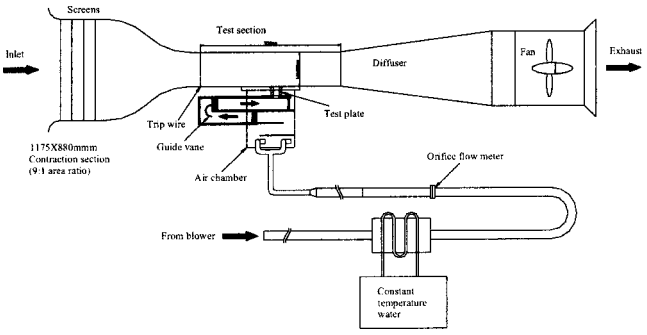

Fig. 1 Schematic view of wind tunnel and test section for square and rectangular film cooling holes

cisely. Therefore, the numerical simulation using a commercial code (FLUENT) is accomplished to obtain the flow patterns inside the square film cooling hole.

Experimental Apparatus and Procedure

1 Experimental Apparatus *Wind Tunnel and Secondary Flow Injection System.* Figure 1 shows the schematic diagram of the-experimental apparatus. The wind tunnel used for this experiment is an open circuit and suction type. The test section is 400 mm wide by 300 mm high by 1200 mm long and the area ratio of the contraction section is 9:1. A trip wire of diameter 3.5 mm is attached at the beginning of the test section to ensure fully developed turbulent boundary layer in the test section. The mainstream velocity is operated at 10~26 m/s during the experimental tests. Average turbulence intensity of the mainstream without injection is measured 0.5 percent. The boundary layer thickness based on 99 percent mainstream velocity is 16 mm at the location of the hole.

The secondary flow injection system consists of a blower, a heat exchanger, an orifice flow meter, and a plenum duct. The plenum duct is designed to generate secondary flow parallel to the mainstream and baffles and honeycombs are installed in the plenum duct to reduce fluctuations in secondary flow. The secondary flow enters the film cooling hole in cross direction, and is ejected into the mainstream in the normal direction as shown in Fig. 2.

The cross section of the plenum duct is 150 mm wide by 100 mm high. The sidewalls of the plenum duct are $3D_h$ apart from the center of the film cooling hole, and the closed endwall is $2D_h$ apart from the center of the film cooling hole.

Temperature of the secondary flow is controlled by the heat exchanger, and the temperature difference between mainstream and secondary air is maintained within 0.2°C using a constant temperature reservoir system. To measure the temperature of mainstream and secondary flow, J-type thermocouples are installed at the test section.

Square/Rectangular Film Cooling Hole. A schematic view of the square/rectangular film cooling hole installed in the test section is shown in Fig. 2. The square hole and the rectangular hole with the aspect ratio of 2.0 are used in the present study.

The size of the film cooling hole is 50 mm×50 mm for the square hole, and 75 mm×37.5 mm for the rectangular hole. Each hole configuration has the same hydraulic diameter of 50 mm. The scale presented in this study is normalized by hydraulic diameter, D_h. The length of film cooling hole (L) is designed to be $2D_h$ so that the separated flow at hole inlet region reattaches to the wall before injected into the mainstream [18].

Naphthalene is coated on all the surfaces inside the film cooling hole to measure local heat/mass transfer coefficients. A J-type thermocouple is positioned inside the coated naphthalene layer near the surface. The vapor pressure and density of naphthalene on the surface are calculated from the measured temperature.

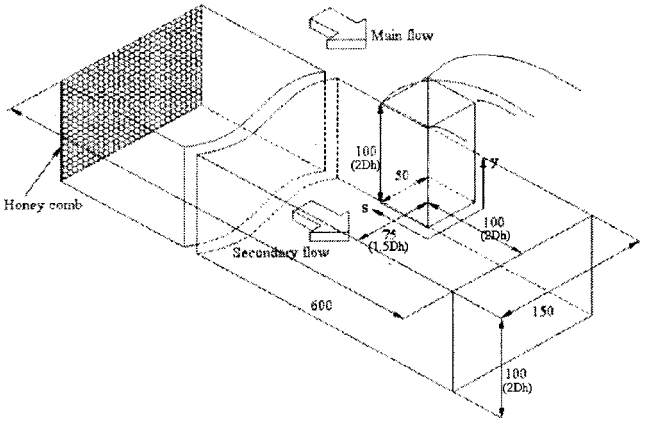

(*a*) **Square injection hole**

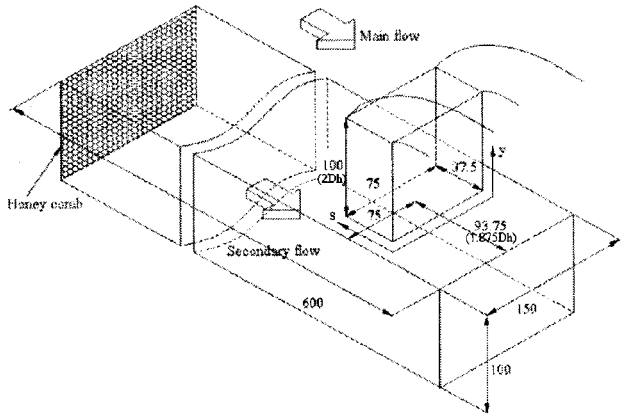

(*b*) **Rectangular injection hole**

Fig. 2 Schematic views of injection holes and crossflow ducts

2 Data Acquisition. In order to obtain local mass transfer coefficients, the profile of the naphthalene surface coated on the test plate is scanned by an automated surface measuring system before and after exposure to air flow. Sublimation depth during the run is calculated from the difference of the surface profiles. The measuring system consists of a depth gauge, a linear signal conditioner (LUCAS ATA-101), a digital multimeter (Keithley model 2001), two stepping-motor driven positioners, a motor controller, and a personal computer with GPIB (IEEE-488) board. The depth gauge is a Linear Variable Differential Transformer (LVDT) made by Schaevitz Engineering (LBB-375TA-020), which has a resolution of 0.025 μm. Error of the LVDT measurements on a flat plate is within 1 percent of averaged sublimation depth of 40 μm during the run. The automated system typically obtains more than two thousand data points in an hour.

3 Heat/Mass Transfer Coefficient. The local mass transfer coefficient is defined as:

$$h_m = \frac{\dot{m}}{\rho_{v,w} - \rho_{v,\infty}} = \frac{\rho_s (dy/d\tau)}{\rho_{v,w}} \tag{1}$$

since incoming flow contains no naphthalene, $\rho_{v,\infty} = 0$ in the present study. Therefore, the mass transfer coefficient is calculated from the local sublimation depth of naphthalene (dy), run time ($d\tau$), density of solid naphthalene (ρ_s), and naphthalene vapor density ($\rho_{v,w}$). The naphthalene vapor pressure is obtained from a

Table 1 Test parameters for square/rectangular film cooling hole

Hydraulic diameter, D_h	Secondary flow		Mainstream	Blowing rate, M
	U_2 (m/s)	Re_{Dh}	U_∞	
50 mm	4.8	15,000	12.3	0.39
	7.8	25,000	0	Free jet
			10	0.78
			12.6	0.62
			20	0.39
	10.2	32,000	26	0.39

correlation of Ambrose et al. [19]. Then the naphthalene vapor density, $\rho_{v,w}$, is calculated from the perfect gas law.

The Sherwood number can be expressed as:

$$\mathrm{Sh}=\frac{h_m D_h}{D_{naph}} \tag{2}$$

D_{naph} is based on the discussion of naphthalene properties given by Goldstein and Cho [20].

The mass transfer coefficients can be converted to the heat transfer coefficients using the heat and mass transfer analogy [21]. Prandtl number is 0.71 for air and Schmidt number is 2.28 for naphthalene vapor in air at 25°C. The experiments are conducted at room temperature, and Lewis number (Pr/Sc) for this study is about 0.307.

$$\frac{\mathrm{Nu}}{\mathrm{Sh}}=\left(\frac{\mathrm{Pr}}{\mathrm{Sc}}\right)^{0.4}, \quad \mathrm{Nu}=0.624\ \mathrm{Sh} \tag{3}$$

Uncertainty of the Sherwood numbers using Kline and McClintock's [22] method for single sample experiments, considering the measured temperature, depth, position and correlation equations, is within 7.1 percent in the entire operating range of the measurement, based on a 95 percent confidence interval. This uncertainty is attributed mainly to the uncertainty of properties of naphthalene, such as the naphthalene saturated vapor pressure (3.8 percent), and diffusion coefficient of naphthalene vapor in the air (5.1 percent). However, uncertainty due to the sublimation depth measurement is only 0.7 percent. The other uncertainties are 0.2 percent, 1.1 percent and 4.9 percent for T_w, ρ_s and h_m, respectively.

4 Numerical Analysis. The numerical simulations using a commercial code (FLUENT) are accomplished to understand the flow patterns within a film cooling hole. The computation domain is modeled by the geometry used in the experimental study (Fig. 2(*a*)). The grids are created using the GAMBIT solid modeling, and the number of grids is about $40\times40\times80$. Various grids are used to verify the grid independence of the solution. The steady solutions for turbulent flow field within a square film cooling hole are calculated using a RNG $k-\varepsilon$ model with a standard wall function for the near wall region.

The velocity and turbulence intensity of mainstream is 20 m/s and 0.5 percent, respectively. Average velocity and turbulence intensity of secondary flow at the inlet of the secondary duct is set to 1.3 m/s and 2.0 percent, and mean velocity inside the film cooling hole is 7.8 m/s, which corresponds to $M=0.39$.

Results and Discussion

In this study, flow and heat/mass transfer characteristics within a square/rectangular film cooling hole are investigated with the variations of blowing rates and Reynolds numbers. Test geometry and operating conditions are shown in Table 1.

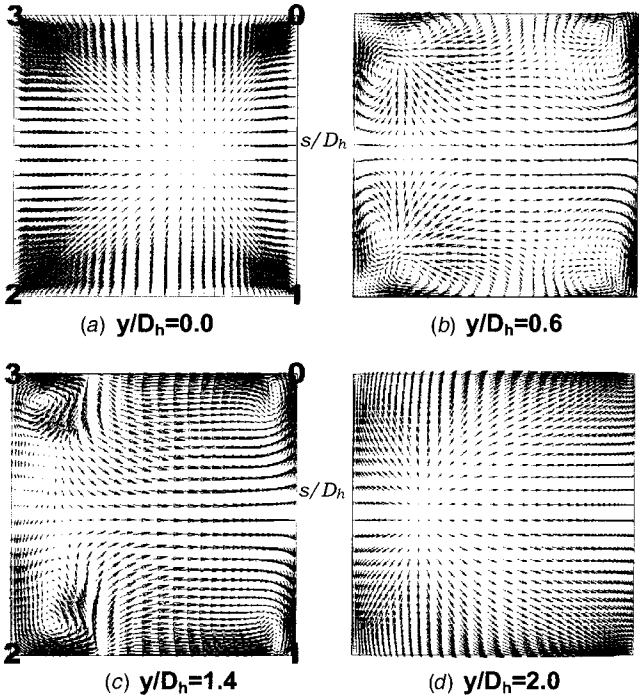

Fig. 3 Velocity vector plots in square film cooling hole: 0-1: trailing edge side; 1-2, 3-0: sidewalls: 2-3: leading edge side

1 Flow Characteristics Within a Square Film Cooling Hole. When the secondary flow enters the hole, the flow turning effects significantly change the hole flow pattern at the inlet region. The hole flow includes the separation at the hole inlet, reattachment on the hole surface, and secondary flows. In the present study, a numerical simulation is performed to investigate the flow characteristics inside a square film cooling hole.

Figure 3 shows the internal flow pattern for the square film cooling hole and the numbers at each corner represent s/D_h. At $y/D_h=0.0$, the flow separation occurs at each corner as shown in Fig. 3(*a*). A large separation region is formed at $2\leqslant s/D_h\leqslant 3$ surface (leading edge side), and the center of flow is shifted to the trailing edge side due to the turning effect of the cross-entering flow. As the fluid flows downstream, as shown in Fig. 3(*b*), a pair of vortices is generated at each corner, and this vortex pattern is similar to a duct flow having secondary vortices at each corner. However, the size of vortices at the leading edge side is larger than that at the trailing edge side and the flow at the center of the hole moves toward the trailing edge side. At $y/D_h=1.4$ (Fig. 3(*c*)), only one vortex is observed at each corner of the leading edge side, and the vortex at the trailing edge side is shrunk because the mainstream starts to affect the flow pattern inside the hole at this position.

At the hole exit ($y/D_h=2.0$, Fig. 3(*d*)), the mainstream pushes the cooling jet toward the trailing edge of the hole and the coolant is detached from the leading edge side. Therefore, the reverse flow pattern is observed near the leading edge side. The secondary flow, which counter-rotates with the horseshoe vortex in the mainstream, is generated and interacts with the cooling jet near the leading edge side. The existence of secondary flow (i.e., corner vortex) at this region will be shown in the side view of the hole flow (Figs. 4 and 5).

Figures 4 and 5 show the flow pattern at center-plane and near the surfaces inside the film cooling hole. The symbols at the top of the vector plots in Fig. 5, such as ⊙, →, ⊗ denote the leading edge side, the sidewalls, and the trailing edge side, respectively.

The overall flow pattern at the center-plane is similar to that for a circular hole. However, some different patterns are observed

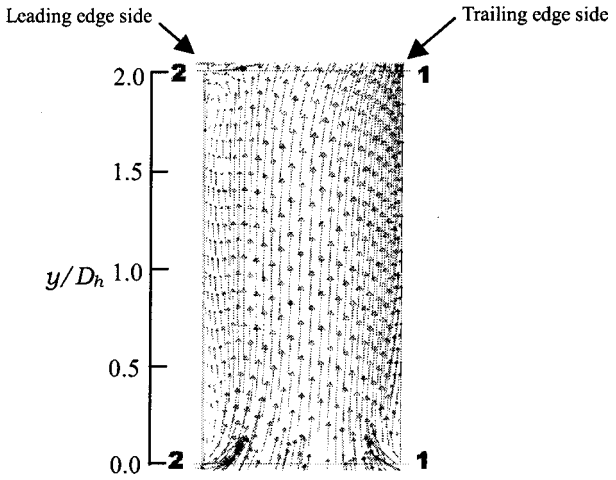

Fig. 4 Velocity vector plot at center-plane

near each surface. The reattachment point is $y/D_h \approx 0.4$ on the leading edge side ($2 \leqslant s/D_h \leqslant 3$, Fig. 5(*a*)) because a large separation bubble is generated with the cross-entering flow condition. As flow approaches the hole exit, the cooling jet is shifted toward the trailing edge of the hole and detached from the leading edge side. Therefore, a low momentum region is formed on the leading edge side. Then, the corner vortex induced by the horseshoe vortex of the mainstream is generated at the hole exit, which is shown clearly in Fig. 4.

A complex flow pattern having several vortices is observed at the sidewall ($1 \leqslant s/D_h \leqslant 2$, Fig. 5(*b*)). A large separation region having strong downward flow is observed around $s/D_h = 2$. The injected jet is shifted toward the trailing edge side near the hole exit, and the downward flow induced by the vortex is observed near the leading edge side. At $0 \leqslant x/D_h \leqslant 1$ (the trailing edge side, Fig. 5(*c*)), the separated flow at the hole inlet region reattaches at $y/D_h = 0.2$, and then spreads out toward the corner ($s/D_h = 0,1$).

2 Hest/Mass Transfer Characteristics Within a Square Film Cooling Hole. Figure 6 shows the distributions of experimentally measured heat/mass transfer coefficients inside circular and square holes without mainstream.

For the circular film cooling hole, studied by Goldstein et al. [11], the value of Sh shows the peak at the trailing edge (180 deg) and decreases circumferentially to the leading edge side (0 deg) as shown in Fig. 6(*a*). The peak value at the trailing edge side is due to the impingement effect of the inlet crossflow. Also, a high pressure field is formed at the trailing edge side due to the impingement effect, and a secondary flow is generated inside the hole. Downstream hole flow ($y/d > 0.9$) shows that Sh is distributed fairly uniformly along the perimeter of the hole due to this secondary flow. However, somewhat different heat/mass transfer characteristics are observed inside the square film cooling hole of the present study. The contour plot of Sh for the square film cooling hole is shown in Fig. 6(*b*), and the regions of high transfer are divided into two subregions, Region I and Region II. Different heat/mass transfer patterns are formed on each surface because different separation flow fields are generated near each surface and these separation bubbles are not easily amalgamated into one bubble. Region I is formed due to the reattachment of the separated flow at the hole inlet, and observed clearly at different locations on the trailing edge side and leading edge side. Region II is formed on the sidewalls due to the corner vortices near the inlet region. Thus, heat/mass transfer coefficients are very nonuniformly distributed along the perimeter of the square hole near the inlet region due to the reattachment and corner vortex effects, which are not observed in a circular hole. The nonuniform distributions of Sh inside the square film cooling hole are shown clearly in local distribution (Fig. 9).

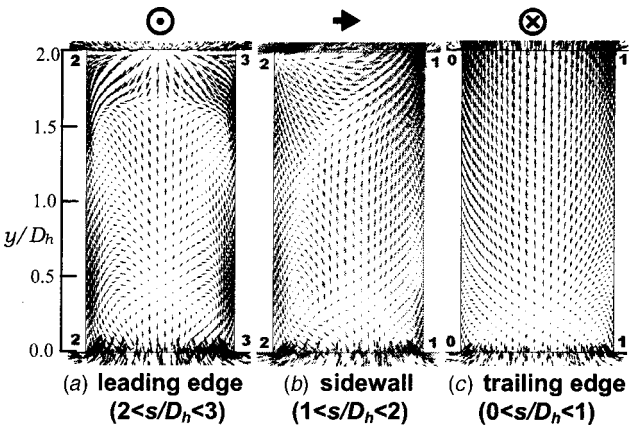

Fig. 5 Velocity vector plots in square film cooling hole

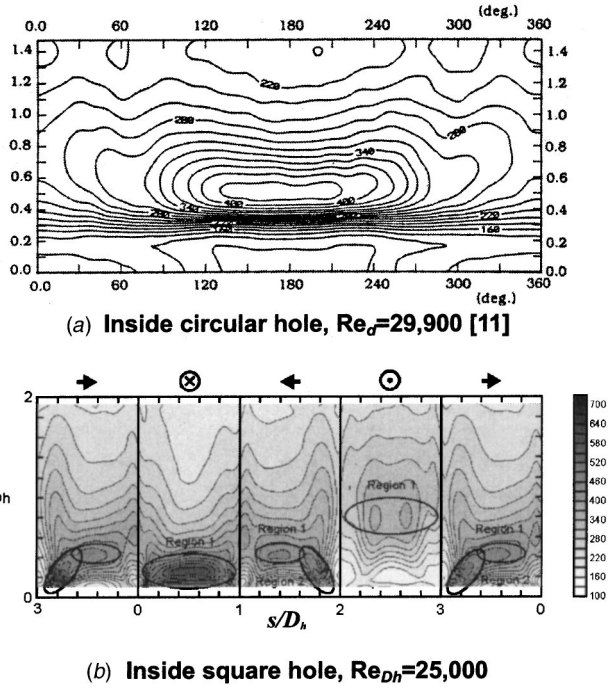

Fig. 6 Contour plots of Sh for the inside hole surface without mainstream

As shown in the numerical results, the entering flow reattaches at $y/D_h \approx 0.2$ on the trailing edge side ($0 \leqslant s/D_h \leqslant 1$). The peak value on this region is higher than that on the leading edge side due to the impingement effect of secondary flow as mentioned above. Then, the boundary layer develops and the flow spreads out toward the corners ($s/D_h = 0,1$). Therefore, relatively high heat/mass transfer coefficients are observed near the corners ($s/D_h = 0,1$).

At the leading edge side ($2 \leqslant s/D_h \leqslant 3$), the region of low Sh is formed near the inlet of the hole due to the flow separation. The heat/mass transfer enhanced region due to the flow reattachment is formed at $y/D_h \approx 0.8$, but the peak value on this region is lower than that for the trailing edge side because the larger separation bubble is formed with weak momentum of the flow on this side.

At the sidewalls, the high transfer regions (Region II) are formed at the corner near the leading edge side due to the flow turning into the hole, which is not observed for a circular film

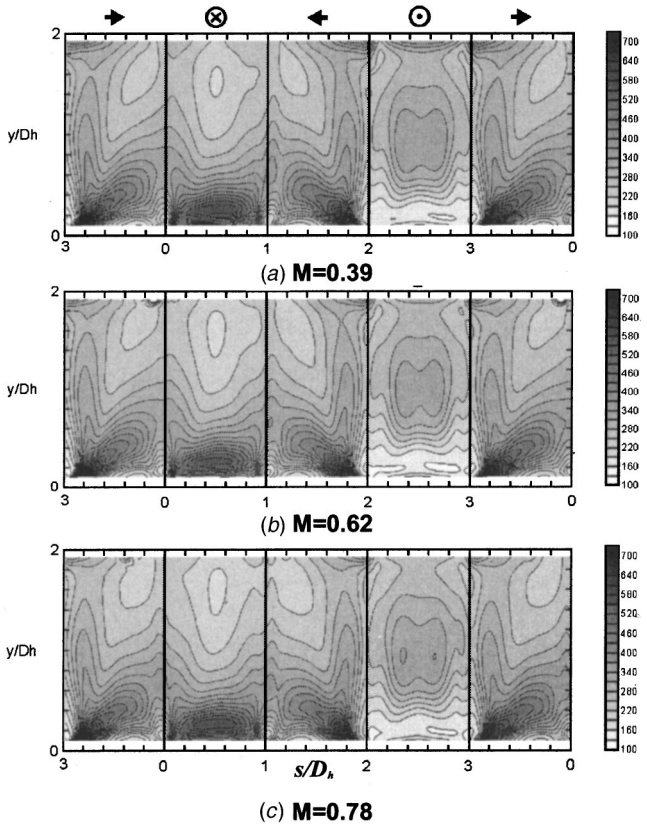

Fig. 7 Contour plots of Sh for square film cooling hole at Re_{Dh}=25,000

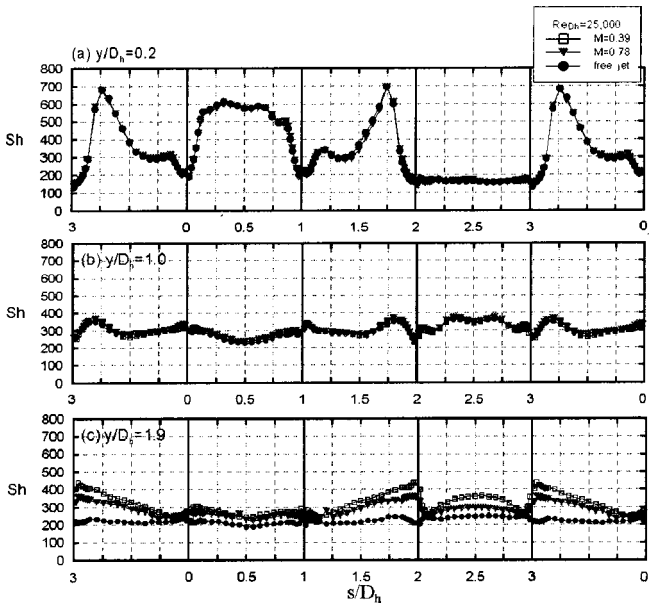

Fig. 9 Local distributions of Sh for square film cooling hole at Re_{Dh}=25,000

cooling hole. The hole flow near the sidewalls approaches the corner at the leading edge, and a relatively high heat/mass transfer region is formed at this corner.

The Effect of Blowing Rate. Figure 7 shows the contour plots of Sh at Re_{Dh}=25,000 for various blowing rates. The heat/mass transfer pattern inside the hole is affected little by the mainstream for the inlet region of $0.0 \leqslant y/D_h < 1.4$. However, the heat/mass transfer pattern at the exit region of $y/D_h \geqslant 1.4$ is changed with the mainstream, and the effect of the mainstream is increased as the blowing rate decreases because the hole flow has less momentum with the low blowing rate. At the exit region, the heat/mass transfer increases on the leading edge side and sidewalls, but not on the trailing edge side because the secondary vortex induced by the mainstream is formed on those regions as numerically shown in Figs. 4 and 5.

The contour plot of calculated heat transfer coefficients is shown in Fig. 8, and the overall pattern is similar to that for the experimental results (Fig. 7). However, the enhanced region due to the flow reattachment is smaller than that for the experimental results, and the enhancement at each corner near the inlet region is not observed clearly. In addition, the region affected by the mainstream near the hole exit is somewhat overpredicted in the numerical calculation.

Figure 9 shows the local distributions of Sh for various blowing rates at Re_{Dh}=25,000. As mentioned before, the local distributions are similar for all blowing rates except near the hole exit region. Near the hole inlet region (Fig. 9(*a*)), high heat/mass transfer coefficients are observed at the trailing edge side ($0 < s/D_h < 1$) due to the reattachment and impingement effects of the inlet entering flow.

At the sidewalls, Region II (heat/mass transfer enhanced region by the corner vortex) is shown clearly. Uniform distributions of Sh are observed at the middle region (y/D_h=1.0) as flow develops. However, the local distributions are changed with blowing rates at the hole exit region (Fig. 9(*c*)). The injected flow is deflected towards the trailing edge side by the mainstream, and the heat/mass transfer coefficients are increased slightly by the mainstream because of the hole flow acceleration at the trailing edge surface. The heat/mass transfer rate is increased largely at the leading edge side and sidewalls due to the secondary vortex induced by the mainstream, and the magnitude of the values is increased as the blowing rate decreases.

The affected zones at the hole exit are plotted schematically for the circular film cooling hole in Fig. 10 (Cho and Goldstein [15]). The dotted area represents the region affected by the mainstream. The region affected by the mainstream increases and spreads

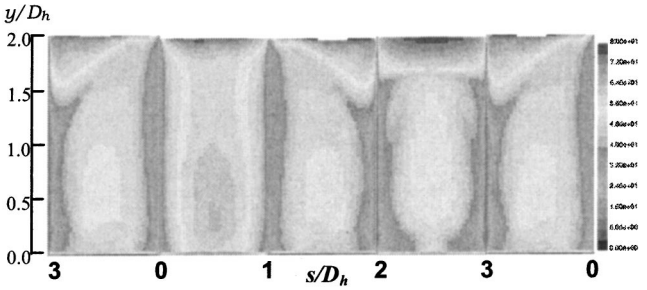

Fig. 8 Calculated heat transfer coefficients on the inside hole surface at M=0.39

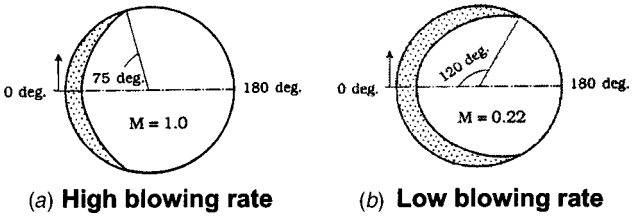

Fig. 10 Affected area of the inside circular hole surface by mainflow [15]

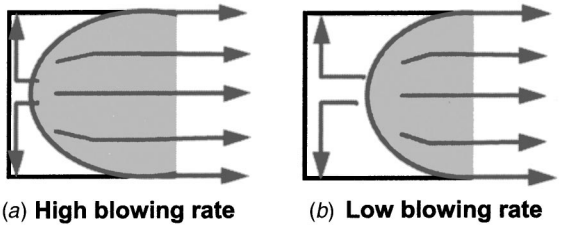

Fig. 11 Affected area of the inside square hole surface by mainflow

along the periphery of the hole as blowing rate decreases. For a square film cooling hole, the overall pattern is similar to that for a circular hole as presented in Fig. 11. The portion of the injected jet in the hole exit is decreased as blowing rate decreases, and the region affected by mainstream is also increased. However, the pattern of the affected region is different from the circular hole. A large portion of the sidewalls on the leading edge side is affected by mainstream regardless of blowing rates.

Figure 12 presents the distribution of averaged heat/mass transfer coefficients for various blowing rates at $Re_{Dh}=25{,}000$. The average heat/mass transfer coefficients show low values at the inlet region due to the flow separation, and then increase rapidly due to the flow reattachment. The reattachment positions are different for each surface, but Sh shows the maximum value at $y/D_h \cong 0.3$ on the trailing edge side and sidewalls due to the flow reattachment and the corner vortex. Therefore, the peak value of average heat/mass transfer coefficient is located at $y/D_h=0.3$ regardless of the blowing rates. The deviation of average values due to the mainstream appears at $y/D_h \cong 1.4$, and the average value near the hole exit increases as the blowing rate decreases because the effect of mainstream increases.

The open circle symbol represents the results of a circular film cooling hole without mainstream at Re=30,000 [14]. Note that the experimental conditions are not the same for both cases. For the circular hole, the reattachment point is formed at $y/D_h \cong 0.5$ (Fig. 6(*a*)), and the region of low transfer rates is larger than that for the square hole. In addition, the overall level of $\overline{Sh}$ is lower than that for the square hole, because the circular hole has a large separation bubble with the shared flow/pressure field, and the corner vortices are not generated inside the circular hole.

The Effect of Reynolds Number. Figures 13 and 14 show the contour plots of Sh and average values for various Reynolds numbers at $M=0.39$, respectively.

The overall values increase with the Reynolds number, but heat transfer patterns are the same for all Reynolds numbers in local and average values. Therefore, the distributions of heat/mass transfer coefficients can be correlated inside the hole for different Reynolds numbers.

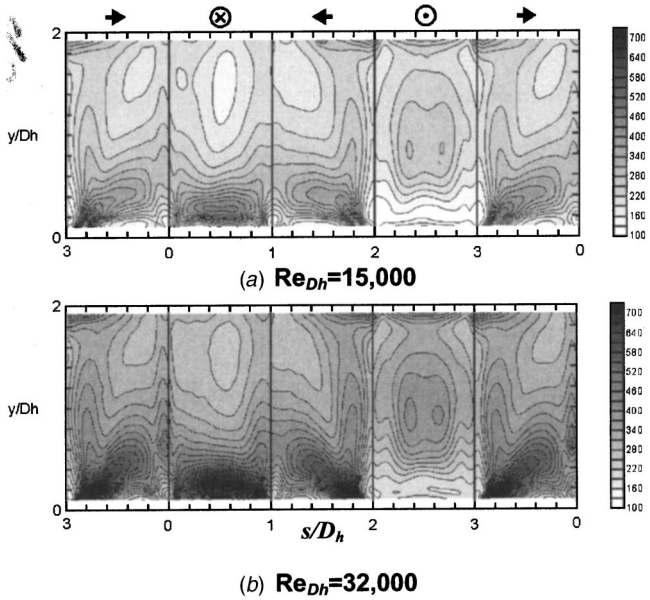

Fig. 13 Contour plots of Sh for square film cooling hole at $M=0.39$

3 Heat/Mass Transfer Characteristics Within a Rectangular Film Cooling Hole.

The Effect of Blowing Rate. The contour plots of Sh inside the rectangular hole are presented for various blowing rates at $Re_{Dh}=25{,}000$, in Fig. 15. Figure 15(*a*) shows the results without mainstream. The heat/mass transfer pattern for this case is similar to that for the square hole (Fig. 6(*b*)) in overall view. At the leading edge and trailing edge surfaces, heat/mass transfer is dominated by flow reattachments, and heat/mass transfer is enhanced due to the flow turning and corner vortex at the sidewalls. However, somewhat different heat/mass transfer patterns are observed at the trailing edge side. Region I is divided into two regions near the hole inlet due to the large aspect ratio.

Contour plots of Sh inside the rectangular hole with the mainstream are shown in Figs. 15(*b*) and 15(*c*). As mentioned above, heat/mass transfer coefficients are similar for all the cases except the hole exit region. The region affected by the mainstream is observed at $y/D_h \cong 1.8$ on the leading edge side and sidewalls. However, the effect of the mainstream is not strong at the leading

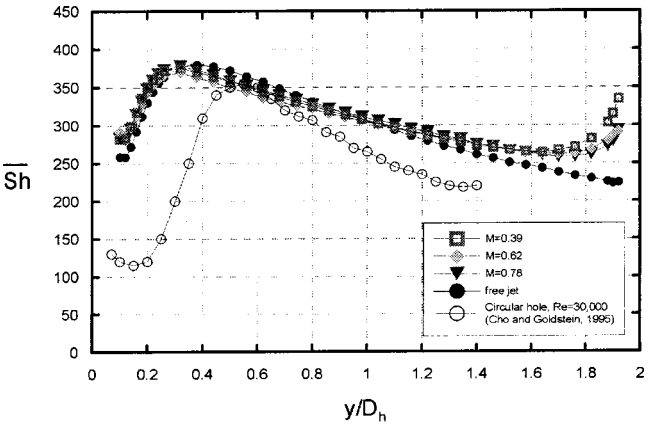

Fig. 12 Streamwise distribution of $\overline{Sh}$ in square film cooling hole with various blowing ratios at $Re_{Dh}=25{,}000$

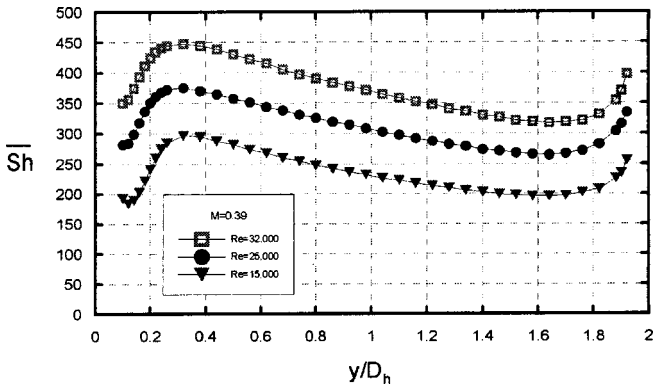

Fig. 14 Streamwise distribution of $\overline{Sh}$ in square injection hole with various Reynolds numbers at $M=0.39$

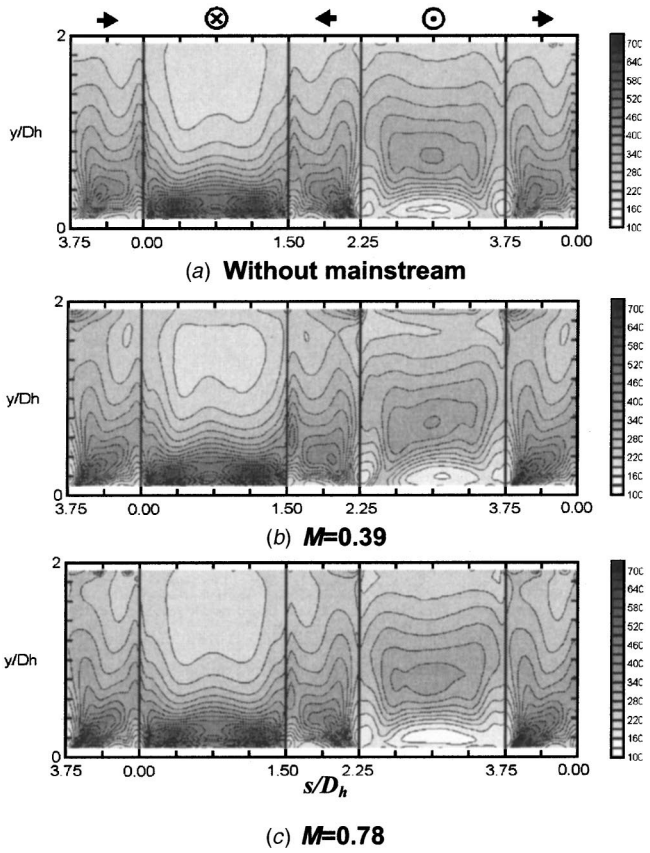

Fig. 15 Contour plots of Sh for rectangular film cooling hole at Re_{Dh}=25,000

edge side, while the heat/mass transfer pattern is similar to that for the square hole at the sidewalls. The enhanced region due to the secondary vortex induced by the horseshoe vortex is reduced to the edges of sidewalls.

Figure 16 shows the distributions of average heat/mass transfer coefficients for various blowing rates at Re_{Dh}=25,000. At the region of $y/D_h \leqslant 1.4$, heat/mass transfer patterns and levels are similar to those for the square hole. However, the effect on the heat/mass transfer by the mainstream at the region of $y/D_h > 1.6$ is less than that of the square hole. The reason is that the strength of the secondary vortex induced by the mainstream is weakened and the affected region is confined to the corners with the increase of aspect ratio.

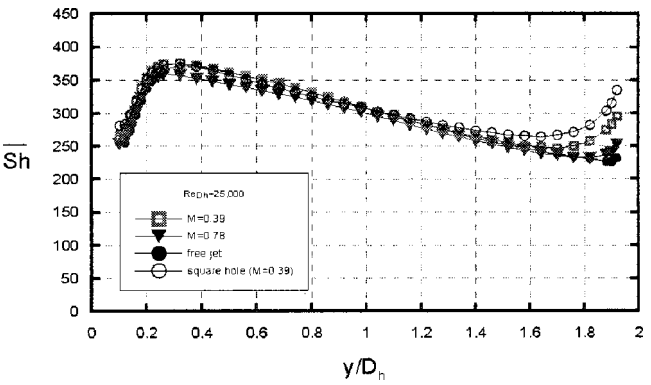

Fig. 16 Streamwise distribution of $\overline{Sh}$ in rectangular film cooling hole for various blowing rates at Re_{Dh}=25,000

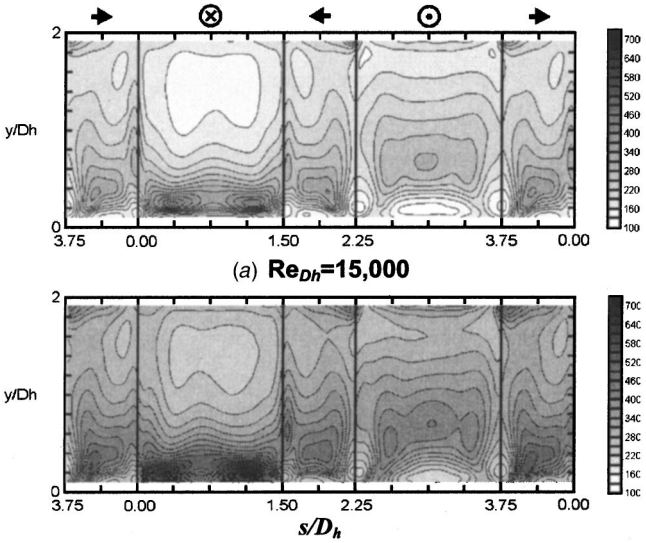

Fig. 17 Contour plots of Sh for rectangular film cooling hole at M=0.39

The Effect of Reynolds Number. Figure 17 shows the contour plots of Sh inside the rectangular film cooling hole at $M=0.39$ for various Reynolds numbers. As one can expect from the results for the square hole, heat/mass transfer coefficients are enhanced as the Reynolds numbers increase. However, the heat/mass transfer patterns are similar for all the cases.

4 The Effect of Asymmetric Flow Entrance. The geometry of the secondary flow duct has a large influence on the heat/mass transfer characteristics inside the film cooling hole. The secondary flow entering film cooling holes is usually asymmetric in actual situations. Therefore, the effect of asymmetric inlet flow condition is investigated in this study. Figure 18 shows a schematic view of the experimental apparatus with the asymmetric inlet condition of secondary flow. One sidewall (adjacent to $1 < s/D_h < 2$ surface) is $1.5D_h$ (75 mm) apart from the center of the film cooling hole, while the other sidewall is $2D_h$ (100 mm) apart from the center of the film cooling hole. Other experimental conditions and test parameters are the same as those for the symmetric cases.

Figure 19 presents the calculated flow patterns inside the film cooling hole with the asymmetric flow condition. Asymmetric

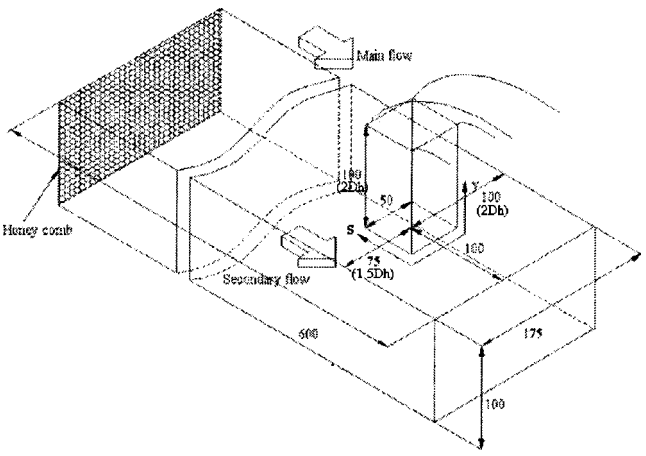

Fig. 18 Schematic view of asymmetric crossflow duct

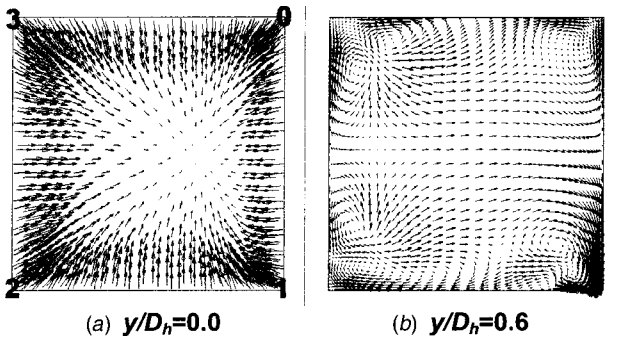

Fig. 19 Velocity vector plots in square injection hole with asymmetric crossflow duct

flow patterns in the hole are obtained with the shifted inlet duct condition. At the inlet plane ($y/D_h=0.0$), the core of flow is shifted slightly to the sidewall (3~0 sidewall) and swirl flow is generated. Asymmetric vortices are observed at the corners for the middle region ($y/D_h=0.6$).

The contour plot of Sh for $M=0.39$ and $\mathrm{Re}_{Dh}=25{,}000$ is presented with the shifted inlet duct condition in Fig. 20. Overall heat/mass transfer patterns are similar to those with the symmetric inlet duct condition; Region I and Region II are observed at each surface. However, as expected from the numerical results, heat/mass transfer with the asymmetric inlet condition is significantly changed from that with the symmetric case (Fig. 9(*a*)). The asymmetric patterns are formed on each surface and high heat/mass transfer regions appear locally due to vortices induced by the swirl flow effect. At the exit region, the effect of the mainstream is weaker than in the case of the symmetric inlet condition.

Figure 21 shows streamwise distributions of $\overline{\mathrm{Sh}}$ with the asymmetric entrance flow for various Reynolds numbers at $M=0.39$.

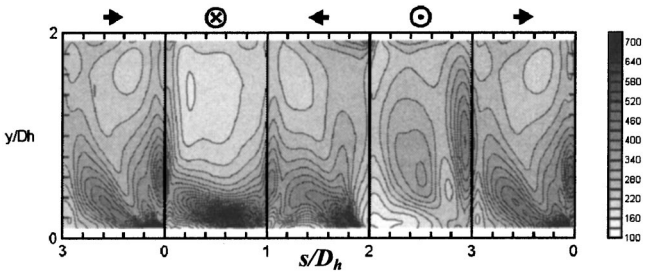

Fig. 20 Contour plot of Sh for square injection hole with asymmetric crossflow duct for $M=0.39$ and $\mathrm{Re}_{Dh}=25{,}000$

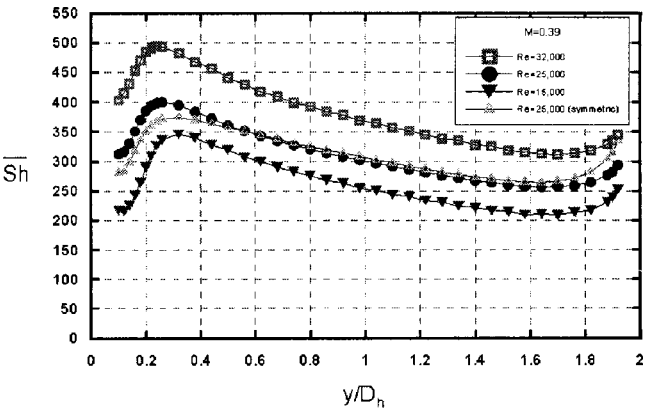

Fig. 21 Streamwise distributions of $\overline{\mathrm{Sh}}$ with asymmetric crossflow duct for various Reynolds numbers at $M=0.39$

The overall values increase with Reynolds numbers and the patterns are similar for all the tested Reynolds numbers. For the same Reynolds number ($\mathrm{Re}_{Dh}=25{,}000$), the average heat/mass transfer coefficient is higher than that with the symmetric inlet condition due to the swirl flow effect at the inlet region. However, the heat/mass transfer coefficients near the exit region are less affected by the mainstream with the asymmetric inlet condition. Based on these results, it has been concluded that it is not essential to consider the departure from symmetry of the conditions for the film cooling hole design to determine the cooling performance inside the hole.

Conclusions

Flow and heat/mass transfer characteristics inside the square/rectangular film cooling holes are investigated with various blowing rates and Reynolds numbers. The results are summarized as follows:

1 When the secondary flow enters the hole inlet, the flow turning effects significantly change the hole flow. Complex flow patterns are observed having flow separations and reattachments with several corner vortices. As the hole flow moves toward the exit region, flow patterns inside the hole are affected by the mainstream, with the result that the injected jet is deflected and the secondary vortex is generated due to the mainstream at the leading edge.

2 For a square film cooling hole, the region of high transfer can be divided into two subregions, such as Region I and Region II, having different heat/mass transfer patterns on each surface at the inlet region. Region I is formed by the flow reattachments of the inlet flow. Region II is formed on the sidewalls due to the corner vortices near the inlet region.

3 The effects of blowing rates are not significant for the overall heat/mass transfer. However, the region affected by the mainstream increases as the blowing rate decreases, because the strength of the secondary vortex induced by the mainstream is enhanced.

4 The overall level of Sh increases linearly with Reynolds number, and heat/mass transfer patterns are similar for all the tested Reynolds numbers.

5 The overall heat/mass transfer for the rectangular hole is similar to that for the square hole. However, the heat/mass transfer at the exit region is less affected by the mainstream.

6 For the shifted inlet duct conditions, heat/mass transfer patterns are quite different from those with the symmetric crossflow duct involving strong asymmetric corner vortices due to the inlet swirl flows.

Acknowledgments

The authors wish to acknowledge support for this study by Ministry of Science and Technology through National Research Laboratory program.

Nomenclature

D_h = hydraulic hole diameter
dy = local sublimation depth of naphthalene
$d\tau$ = test duration
D_{naph} = mass diffusion coefficient of naphthalene vapor in air
h_m = local mass transfer coefficient
$\dot{m}$ = local naphthalene mass transfer per unit area and time
Nu = Nusselt number based on the hydraulic hole diameter$=hD_h/k$
Pr = Prandtl number
Re_{Dh} = Reynolds number based on the hydraulic hole diameter and the average velocity in the hole
Sc = Schmidt number

Sh = Sherwood number based on the hydraulic hole diameter$=h_m D_h/D_{naph}$
$\overline{\text{Sh}}$ = average Sherwood number
s,y = coordinate system, Fig. 2
ρ_2 = density of secondary flow
ρ_s = density of solid naphthalene
$\rho_{v,w}$ = naphthalene vapor density on the surface
$\rho_{v,\infty}$ = naphthalene vapor density of the mainflow
ρ_∞ = density of mainflow

References

[1] Goldstein, R. J., Eckert, E. R. G., and Burggraf, F., 1974, "Effects of Hole Geometry and Density on Three-Dimensional Film Cooling," Int. J. Heat Mass Transf., **17**, pp. 595–607.

[2] Gritsch, M., Schulz, A., and Wittig, S., 1988, "Adiabatic Wall Effectiveness Measurements of Film-Cooling Holes With Expanded Exits," ASME J. Turbomach., **120**, pp. 549–556.

[3] Kohli, A., and Bogard, D. G., 1999, "Effects of Hole Shape on Film Cooling With Large Angle Injection," ASME Paper No. 99-GT-165.

[4] Chen, P. H., Ding, P. P., Hung, M. S., and Shih, P. C., 1999, "Film Cooling Over a Concave Surface Through a Row of Expanded Holes," ASME Paper No. 99-GT-33.

[5] Cho, H. H., Rhee, D. H., and Kim, B. G., 1999, "Film Cooling Effectiveness and Heat/Mass Transfer Measurement Around a Conical-Shaped Hole With Compound Angle Injection," ASME Paper No. 99-GT-38.

[6] Bell, C. M., Hamakawa, H., and Ligrani, P. M., 2000, "Film Cooling From Shaped Holes," ASME J. Heat Transfer, **122**, pp. 224–232.

[7] Muldoon, F., and Acharya, S., 1999, "Numerical Investigation of the Dynamical Behavior of a Row of Square Jets in Crossflow Over a Surface," ASME Paper No. 99-GT-127.

[8] Licu, D. N., Findlay, M. J., Gartshore, I. S., and Salcudean, M., 2000, "Measurements of Heat Transfer Characteristics for Film Cooling Applications," ASME J. Turbomach., **122**, pp. 546–552.

[9] Watanabe, K., Matsuura, M. Suenaga, K., and Takeishi, K., 1999, "An Experimental Study on the Film Cooling Effectiveness With Expanded Hole Geometry," *Proc. of 7th IGTC*, **2**, pp. 615–622.

[10] Takahashi, H., Nuntadusit, C., Kimoto, H., Ishida, H., Ukai, T., and Takeishi, K., 2000, "Characteristics of Various Film Cooling Jets Injected in a Conduit," *Turbine 2000 Intemational Symposium on Heat Transfer in Gas Turbine Systems*, Izmir, Turkey, pp. 76–78.

[11] Goldstein, R. J., Cho, H. H., and Jabbari, M. Y., 1997, "Effect of Plenum Crossflow on Heat (Mass) Transfer Near and Within the Entrance of Film Cooling Holes," ASME J. Turbomach., **119**, pp. 761–769.

[12] Metzger, D. E., and Cordaro, J. V., 1979, "Heat Transfer in Short Tubes Supplies From a Cross-Flowing Stream," ASME Paper No. 79-WA/HT-16.

[13] Byerley, A. R., Ireland, P. T., Jones, T. V., and Ashton, S. A., 1988, "Detailed Heat Transfer Measurements Near and Within the Entrance of a Film Cooling Hole," ASME Paper No. 88-GT-155.

[14] Cho, H. H., Jabbari, M. Y., and Goldstein, R. J., 1997, "Experimental Mass(Heat) Transfer in and Near a Circular Hole in a Flat Plate," Int. J. Heat Mass Transf., **40**(10), pp. 2431–2443.

[15] Cho, H. H., and Goldstein, R. J., 1995, "Heat(Mass) Transfer and Film Cooling Effectiveness With Injection Through Discrete Holes—Part I: Within Holes and on the Back Surface," ASME J. Turbomach., **117**, pp. 440–450.

[16] Cho, H. H., and Goldstein, R. J., 1997, "Total Coverage Discrete Hole Wall Cooling," ASME J. Turbomach., **119**, pp. 320–329.

[17] Lee, S. W., Park, S. W., and Lee, J. S., 2001, "Flow Characteristics Inside Circular Injection Holes Normally Oriented to a Crossflow: Part I—Flow Visualizations and Flow Data in the Symmetry Plane," ASME J. Turbomach., **123**, pp. 266–273.

[18] Hay, N., and Lampard, D., 1995, "The Discharge Coefficient of Flared Film Cooling Holes," ASME Paper No. 95-GT-15.

[19] Ambrose, D., Lawrenson, I. J., and Sparke, C. H. S., 1975, "The Vapor Pressure of Naphthalene," J. Chem. Thermodyn., **7**, pp. 1173–1176.

[20] Goldstein, R. J., and Cho, H. H., 1995, "A Review of Mass Transfer Measurement Using Naphthalene Sublimation," Exp. Therm. Fluid Sci., **10**, pp. 416–434.

[21] Eckert, E. R. G., 1976, "Analogies to Heat Transfer Processes," in: *Measurements in Heat Transfer*, E. R. G. Eckert, and R. J. Goldstein, eds., pp. 397–423, Hemisphere Pub., New York.

[22] Kline, S. J., and McClintock, F., 1953, "Describing Uncertainty in Single Sample Experiments," Mech. Eng. (Am. Soc. Mech. Eng.), **75**, Jan., pp. 3–8.

Effects of Reynolds Number and Pressure Ratio on Leakage Loss and Heat Transfer in a Stepped Labyrinth Seal

K. Willenborg
e-mail: klaus.willenborg@its.uni-karlsruhe.de

S. Kim

S. Wittig

Lehrstuhl und Institut für Thermische Strömungsmaschinen,
Universität Karlsruhe,
76128 Karlsruhe, Germany

The influence of Reynolds number and pressure ratio on the operating characteristics of a stepped labyrinth seal was experimentally determined. The geometries investigated represent designs of a stepped labyrinth seal typical for modern jet engines. Heat transfer and discharge measurements were obtained for two plane models with various seal clearances. The experiments covered a range of Reynolds numbers and pressure ratios. Independent variation of Reynolds number and pressure ratio was obtained by adjusting the back pressure at the seal exit for a given pressure ratio. Dimensionless discharge coefficients, describing the sealing performance, were derived from the measured leakage rates. Pressure ratio, Reynolds number, tip geometry, and seal clearance all affected the sealing performance. Finite element calculations were employed to calculate the local heat transfer coefficients from the measured wall and gas temperatures. Averaging of the local values yielded mean heat transfer coefficients and mean Nusselt numbers. The heat transfer was mainly determined by the Reynolds number. Compressibility effects on the heat transfer were observed to be very small. [DOI: 10.1115/1.1397304]

Introduction

Labyrinth seals represent an important flow element in the secondary air system of aero engines. They are used as sealing devices to reduce leakage from high to low-pressure regions through gaps between rotating and stationary engine parts. Due to the wide flight envelope of jet engines including varying altitude and speed conditions, a wide Reynolds number range is encountered. At high altitudes, low mass-flow rates pass the labyrinth seal and result in relatively low Reynolds numbers. For low-level, high-speed missions, typical for military engines, high Reynolds numbers occur. Typical values of the Reynolds number ranging from 100 to 20,000 are given by Zimmermann et al. [1,2].

In the complex cooling system of jet engines, labyrinth seals control to a large extent the distribution of coolant for components with high thermal loads. The simple and compact design, as well as the high reliability and applicability at high temperatures and high circumferential speeds, have kept labyrinth seals competitive with new seal designs like brush or carbon seals.

The air mass flow discharged through labyrinth seals can amount to several percent of the compressor flow and represents a direct penalty for the overall efficiency of the engine. Hence, for a reduction of the specific fuel consumption, the leakage rates are to be minimized. With respect to the integrity of the single engine components and the engine itself, it has to be ensured that a sufficient amount of cooling air is provided to thermally highly loaded components under all operating conditions.

The heat balance of the whole engine is affected by the amount of heat transferred in the seal. For structural and thermal analysis of the seal and the adjacent components, information on the local heat transfer rates in the seal is required.

As described above, the design of the labyrinth seal configuration in a new aeroengine represents an optimization process. Leakage rates have to be minimized in order to reduce losses in the secondary air system. At the same time, the integrity of all parts has to be ensured by distributing a sufficient amount of cooling gas to the respective components at any time. Hence, for an efficient and safe engine design, the discharge behavior and heat transfer characteristics of labyrinth seals have to be accurately known.

The design of labyrinth seals depends to a large extent on experimental data. These data have been usually obtained from measurements on large-scale models. The enlarged geometry offers the advantage of reduced uncertainties in the measurement of the air flow rates discharged through the seal. In addition, the machining tolerances for the larger scale can be kept significantly below those for the real size model. This is of particular importance for labyrinth seal flow, which responds to changes in the geometry, especially of the fin tip. However, a change of the scale results in a change of the Reynolds number and the question of validity for the real size application arises.

The sealing performance, including discharge coefficients, of labyrinth seals is the subject of a large number of publications. Fundamental descriptions of the flow through labyrinth seals have been established by Martin [3], Stodola [4], Egli [5], Kearton et al. [6], Komotory [7], and others. A comprehensive summary of these publications has been given by Trutnovsky et al. [8]. In more recent studies, advanced experimental techniques together with numerical methods have been applied to obtain detailed information of the complex flow field in labyrinth seals and to identify the relevant parameters influencing the labyrinth flow (e.g., Stocker [9], Wittig et al. [10], Morrison et al. [11], Prasad et al. [12], Rhode et al. [13], Schramm et al. [14]). A list of correlations for calculating the seal leakage of different types of labyrinth seals is presented by Zimmermann et al. [15]. In all references cited above, discharge coefficients are given as a function of either the pressure ratio across the seal or the Reynolds number.

Wittig et al. [16] investigated the effects of pressure ratio and Reynolds number on straight-through labyrinth seals by measuring leakage rates of geometrically similar, two-dimensional plane models at different scales. Plotting the nondimensional discharge coefficients against the overall pressure ratio for different scales allowed the identification of both effects on the discharge behavior. This influence was most evident for small clearances.

Cntributed by the International Gas Turbine Institute and presented at the 46th International Gas Turbine and Aeroengine Congress and Exhibition, New Orleans, Louisiana, June 4–7, 2001. Manuscript received by the International Gas Turbine Institute February 2001. Paper No. 2001-GT-123. Review Chair: R. Natole.

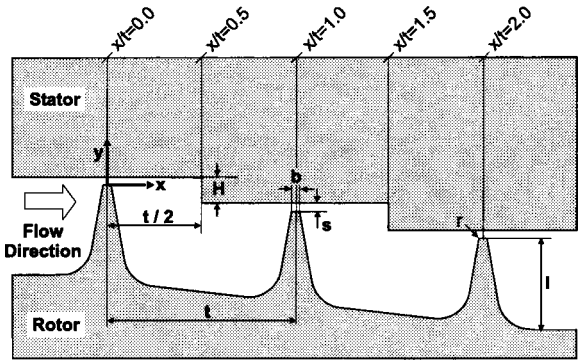

Fig. 1 Labyrinth seal geometry: $l/t=0.46$, $H/t=0.14$, $b/t=0.047$, $s/t=0.043\ldots0.114$, $t(1\times)=7$ mm, $t(4\times)=28$ mm

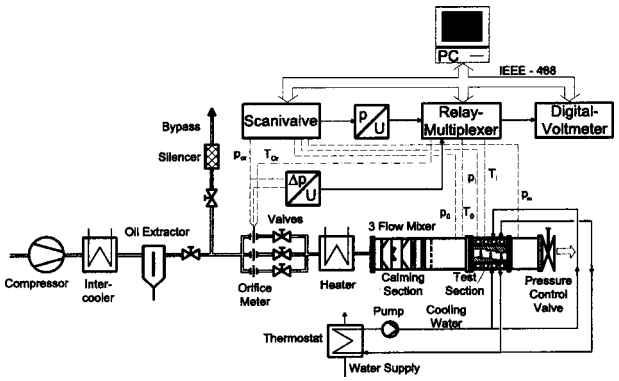

Fig. 2 Labyrinth seal test facility

Fewer publications dealing with the heat transfer in labyrinth seals are available in the literature. Averaged heat transfer coefficients have been obtained by Sheinin [17], Shvets et al. [18], and Kapinos et al. [19]. More detailed investigations of the distribution of the local heat transfer coefficients have been conducted by Metzger et al. [20], Wittig et al. [21], and Willenborg et al. [22]. These studies consider different types of labyrinth seals and several geometric parameters like seal clearance, step height, or stator configuration. The effects of rotation on the heat transfer have been investigated by Kapinos et al. [23] and more in detail by Waschka et al. [24,25]. The Nusselt numbers obtained in these heat transfer studies have been correlated with the Reynolds number. To the authors' knowledge, no attempt has been made to identify effects of compressibility on the heat transfer in labyrinth seals.

The main objective of the present study is to analyze the influence of Reynolds number, pressure ratio, and labyrinth tooth geometry on the discharge behavior and the heat transfer of a nonrotating stepped labyrinth seal. Data obtained in nonrotating models can be corrected for rotational effects by applying the results of Waschka et al. [24,25] when the circumferential velocity exceeds the axial velocity and rotational effects can no longer be neglected.

Experimental Approach

Models. The geometry of the stepped labyrinth seal with three fins investigated in the present study is shown in Fig. 1. As indicated, flow direction was always from the left to the right. The basic geometry of this study is identical with that investigated in a previous study (Schramm et al. [14], Willenborg et al. [22]). Two models of this geometry at different scales ($1\times$ and $4\times$) have been manufactured. Optical inspection of the fin tips revealed deviations between the corner radii of the two models at this position. Whereas the relative fin tip radius of the $4\times$ model is relatively small ($r/b=0.06$), the fins of the $1\times$ model are well rounded ($r/b=0.5$). Therefore, the two models of the labyrinth seal have distinctive different geometries. As mentioned earlier, changes in the geometry at this position affect the flow in the seal considerably.

Test Facility and Rig Instrumentation. The labyrinth seal test facility at the Institut für Thermische Strömungsmaschinen, used in several previous studies (Wittig et al. [10,21], Waschka et al. [24,25], Willenborg et al. [22]), was modified for the present experiments. An additional throttling valve was mounted downstream of the test section in order to enable the setting of the back pressure at the exit of the seal (Fig. 2).

Air is provided to the test facility by a compressor with a maximum absolute pressure of 4 bars. The pressure at the orifice meters was kept at a constant value by adjusting the bypass flow rate. The valves upstream of the heater in combination with the pressure control valve downstream of the test section allow independent adjustment of the pressure ratio across the seal and the pressure level in the seal. Three high-precision orifice meters were used for the accurate measurement of the air mass flow passing the test section. The back pressure of the seal was varied from 1 to 3 bars while pressure ratios between 1.07 and 1.6 were adjusted. This yielded air flow rates from 5 to 300 g/s. The maximum output pressure of the compressor represented the limiting factor for the maximum pressure ratio across the seal at the respective pressure level.

Smooth temperature and velocity distributions were achieved by the calming section positioned upstream of the test section and equipped with several screens and meshes. The temperature of the air entering the seal geometry was adjusted by means of the intercooler and the electrical heater.

The test sections as shown in Fig. 3 were mounted directly to the calming section. The seal geometry is formed by a stator and a rotor part. Three different gap widths were adjusted by assembling the two parts with spacers. Due to a large ratio of channel width to seal clearance, sidewall effects can be neglected. The water-cooled plates above and below the test section generated a temperature gradient across the upper and the lower part for the heat transfer measurements.

Both stator and rotor model walls are equipped with thermocouples to resolve the temperature distribution on the stator and rotor walls. Type *K* thermocouples positioned halfway of the width of the test section and mounted flush with the surface were used for the measurement of these surface temperatures. The distribution of the air temperature was obtained from additional thermocouple probes. These sensors were inserted from the side into the seal and were aligned horizontally in order to avoid errors in the temperature readings as a result of heat conduction in the

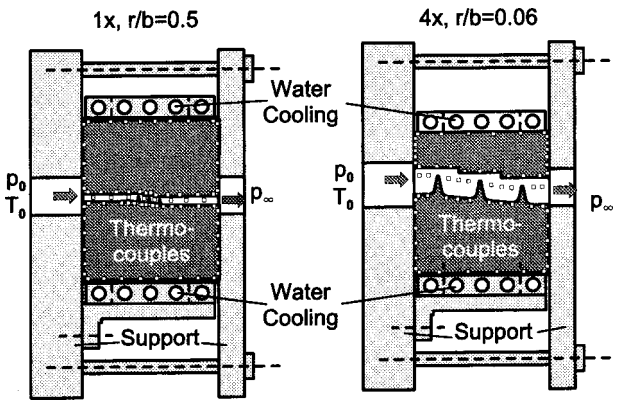

Fig. 3 Test sections with instrumentation

probe support. A computer-based data acquisition system performed the processing of the temperature and pressure signals (Fig. 2).

A steady-state technique was chosen for measuring the heat transfer in the labyrinth seal geometry. By discharging hot air through the test section and simultaneously cooling the outside of the labyrinth seal by means of the cooling plates a temperature gradient was imposed on the seal parts. With an air inlet temperature of 250°C and a cooling water temperature of 15°C, the surfaces facing the flow were at temperatures in the range from 40 to 180°C in the heat transfer experiments. Note that the discharge coefficient measurements were conducted for cold, i.e., unheated, air flow in order to avoid heat transfer effects influencing the discharge behavior.

Data Reduction. The hydraulic diameter of the labyrinth gap $(2 \cdot s)$ represents the characteristic length scale for the Reynolds number:

$$\mathrm{Re} = \frac{\rho c 2s}{\mu} = \frac{2\dot{m}}{B\mu} \tag{1}$$

Several definitions of flow parameters describing the discharge behavior of labyrinth seals can be found in the literature. For the present study the dimensionless discharge coefficient C_D as introduced by Wittig et al. [16] has been chosen to characterize the sealing performance. The coefficient C_D represents the ratio of the measured leakage rate to a reference mass flow for isentropic nozzle flow:

$$C_D = \frac{\dot{m}}{\dot{m}_{\mathrm{ideal}}} \tag{2}$$

$$\dot{m}_{\mathrm{ideal}} = \frac{A p_0}{\sqrt{T_0}} \sqrt{\frac{2\kappa}{R(\kappa-1)} \left[\left(\frac{1}{\pi}\right)^{2/\kappa} - \left(\frac{1}{\pi}\right)^{(\kappa+1)/\kappa} \right]} \tag{3}$$

In Eq. (3), for the subsonic conditions of the present study, the overall pressure ratio π represents the ratio of inlet to outlet pressure $(\pi = p_0 / p_\infty)$. The area available for the flow to pass the seal gap is calculated as $A = B \cdot s$.

The local heat transfer coefficient can be calculated:

$$h = \frac{-\lambda_W \left. \frac{\partial T_w}{\partial n} \right|_W}{T_G - T_W} \tag{4}$$

The two-dimensional temperature distribution in the stator and the rotor part was obtained from finite element calculations. The surface temperatures measured in the experiment served as boundary conditions for this task. Temperature values were interpolated from the experimental data for each boundary node of the finite element mesh. Note that the fins of the labyrinth stator have not been resolved in the finite element mesh, since they were not equipped with thermocouples. The heat flux from the fins is considered in the finite element calculations by positioning thermocouples on both sides of the fin base. An in-house Fortran code was applied for the finite element calculations. Grid independence was tested successfully. Furthermore, a direct comparison of the in-house code with a commercial code (ABAQUS) showed identical results.

Mean heat transfer coefficients were computed with the total heat flux normalized to the surface area exposed to the flow and with the mean values of gas and wall temperature:

$$\overline{h} = \frac{\dot{Q}_{W,\mathrm{total}}}{A(\overline{T}_G - \overline{T}_W)} \tag{5}$$

The mean gas and wall temperatures were calculated by averaging the local values along the surface. In accordance with the finite element calculations, this reference area for the rotor does not contain the fin surface. For both models, the heat transfer rates in the range $-0.5 \leqslant x/t \leqslant 2.5$ (Fig. 1) were considered.

Analogous to the Reynolds number, local and mean Nusselt numbers are defined with the hydraulic diameter of the seal gap:

$$\mathrm{Nu} = \frac{h 2s}{\lambda_G}, \quad \overline{\mathrm{Nu}} = \frac{\overline{h} 2s}{\lambda_G} \tag{6}$$

A detailed error analysis yielded values of the uncertainty in the dimensionless discharge coefficients of 3 percent for the 4× seal geometry and 5 percent for the 1× model (Kline et al. [26]). Note that the uncertainty in the measurement of the gas mass flow was below these values. Results deviated less than 2 percent from different sets of data which were acquired over a period of several months.

In order to minimize uncertainties in the heat transfer measurements, the geometric dimensions of the stator and the rotor part were optimized and the most suitable material was chosen (Willenborg et al. [22]). Based on a one-dimensional error analysis, the maximum uncertainty of the local Nusselt numbers was computed to be in the range from 12–25 percent. Due to the averaging process, the uncertainty in the mean values is distinctly reduced. For the mean Nusselt numbers, based on the same one-dimensional error analysis with the mean values of gas and wall temperature, an uncertainty of 5 percent was computed. The reproducibility of the mean Nusselt numbers was within the range of the uncertainty.

Results and Discussions

The results of the discharge and heat transfer measurements are presented in the following paragraphs. Following the discussion of the discharge behavior the heat transfer is characterized by means of local and mean Nusselt numbers.

Discharge Coefficients. In the following the results of the discharge measurements are presented. The dimensionless discharge coefficient C_D as defined in Eqs. (2) and (3) is used to describe the sealing performance. The measurements of the leakage rates were conducted for unheated flow with ambient inlet temperature.

In Figs. 4–6 the discharge coefficients obtained in this study are presented for the three gap widths investigated. The plots show the development of the discharge coefficients with the Reynolds number. Each curve represents a distribution of C_D values for a constant pressure ratio. Because of the smaller cross-sectional area, relatively low Reynolds numbers have been obtained for the seal model in 1× scale with $r/b = 0.5$. Due to the limited maximum output pressure of the compressor providing air to the test section, the highest pressure ratio was only investigated for lower back pressures.

Figure 4 shows the distributions of the discharge coefficients for the smallest gap width $s/b = 0.909$. The discharge coefficients of the 1× model with $r/b = 0.5$ show a significant increase with increasing Reynolds number. As the Reynolds number increases from 2500 to 8050, the discharge coefficients for the pressure ratio $\pi = 1.07$ increase by 9 percent. The Reynolds numbers obtained with the 4× model with $r/b = 0.06$ are shifted to higher values as a result of the higher leakage rates with enlarged absolute seal clearance. Here, the discharge coefficient are more a function of pressure ratio than Reynolds number. The influence of the Reynolds number is distinctly less pronounced and a fairly uniform distribution of the discharge coefficients was measured for each pressure ratio. For the two lowest pressure ratios ($\pi = 1.07$, $\pi = 1.1$), a slight increase of the discharge coefficients was measured. For a given Reynolds number, both models show a continuous increase of the C_D values with increasing pressure ratio across the seal. This trend is in agreement with the results of a previous study by Schramm et al. [14] who investigated the same seal geometry.

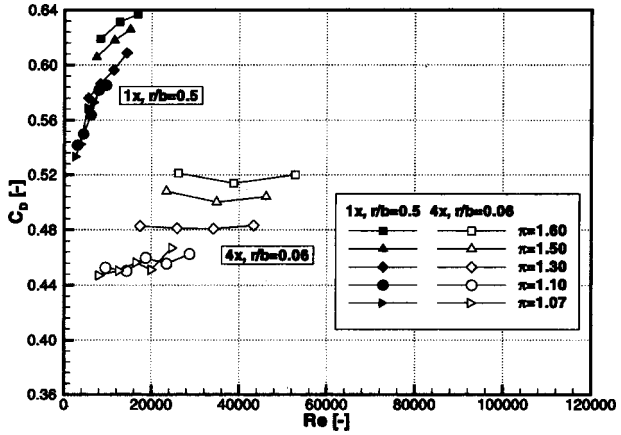

Fig. 4 Discharge coefficients, $s/b=0.909$

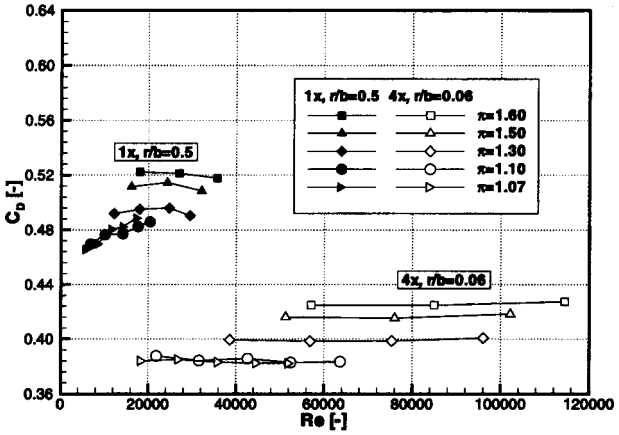

Fig. 6 Discharge coefficients, $s/b=2.424$

The absolute levels of the C_D values of the two seal models differ significantly. Due to the larger relative corner radius, the sealing performance of the model with $r/b=0.5$ in $1\times$ scale is distinctly below that of the model with $r/b=0.06$ in $4\times$ scale. For identical Reynolds number and pressure ratio of 9500 and 1.1, respectively, the discharge coefficients of the two geometries in Fig. 4 differ by approximately 30 percent. This magnitude corresponds to values given by Zimmermann et al. [15] in his list of correlations.

Discharge coefficients for the gap width $s/b=1.515$ are presented in Fig. 5. Again, a distinct increase of the C_D values with increasing Reynolds number is visible for the $1\times$ model with $r/b=0.5$ for low Reynolds numbers. For higher pressure ratios and hence higher values of the Reynolds number, the gradient of the curves is reduced. For the $4\times$ scale model with $r/b=0.06$, the variation of the discharge coefficients with the Reynolds number is almost negligible. The distributions of the discharge coefficients exhibit a slight local maximum before a constant value is reached only for the two smallest pressure ratios. As shown in Fig. 5, the C_D values increase continuously with the pressure ratio for a given Reynolds number. In accordance with the distributions of the gap width $s/b=0.909$, the seal geometry with $r/b=0.06$ shows better sealing performance due to the smaller corner radii of the fin tips.

The highest Reynolds numbers have been obtained for the largest gap width $s/b=2.424$ (Fig. 6). For the $1\times$ model with $r/b=0.5$, an increase of the C_D values occurs only for the two lowest pressure ratios ($\pi=1.07$, $\pi=1.1$). A fairly uniform distribution develops for the higher pressure ratios of $\pi=1.3-1.6$. The discharge coefficients obtained with the $4\times$ seal with $r/b=0.06$ are independent of Reynolds number and depend only on the pressure ratio.

The discharge coefficients presented in Figs. 4–6 decrease with increasing seal clearance. These results are in accordance with the previous study by Schramm et al. [14] where the same development of the relative leakage rate with increasing seal clearance was observed.

A general trend in the distributions of the discharge coefficients for constant pressure ratio can be identified from Figs. 4–6. In the range of low Reynolds numbers, the discharge coefficients show a significant increase with increasing Reynolds numbers. This effect is most pronounced for the smallest gap width of the $1\times$ model (Fig. 4). Further increasing the Reynolds number yields a slight decrease of the C_D values before the sealing performance becomes independent of the Reynolds number. For sufficiently high Reynolds numbers, the discharge coefficient of the respective seal configuration depends only on the overall pressure ratio across the seal.

For the flow through pipe orifices, a similar distribution of the discharge coefficient was measured by Johansen [27]. The same characteristic development of the flow coefficient α, for a single sharp-edged orifice, with a critical value of the Reynolds number of $Re_C=1000$ is given by Egli [5]. The flow coefficient, α, in Fig. 7 was defined identically to the discharge coefficient, C_D, of the present study. Compared to the present results, the Egli value of the critical Reynolds number is relatively low. Results from the present study (Figs. 4–6) put the critical Reynolds number in the 30,000 to 40,000 range.

For corresponding relative gap geometries, similar results have been obtained by Bell et al. [28] for the flow of water and oil

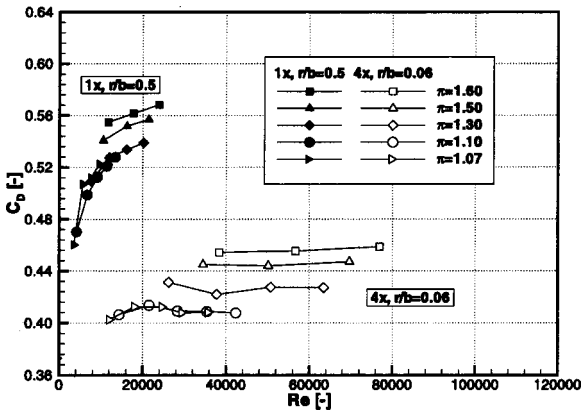

Fig. 5 Discharge coefficients, $s/b=1.515$

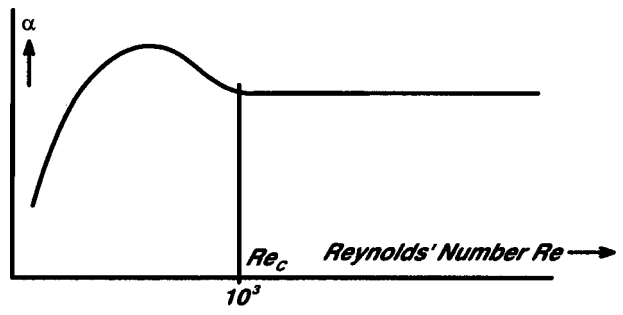

Fig. 7 Flow coefficient α of a sharp-edged orifice as a function of Reynolds number (Egli [5])

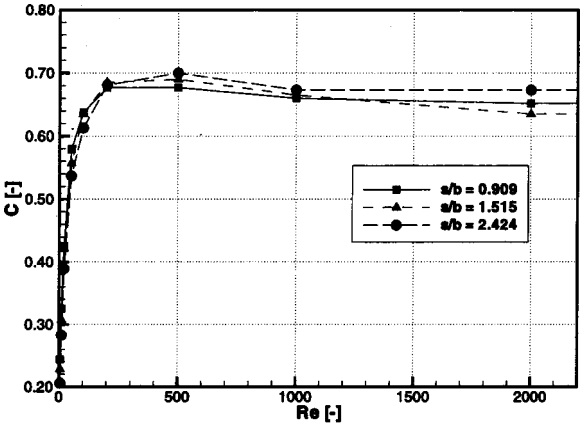

Fig. 8 Coefficients of discharge for annular orifices (Bell et al. [28])

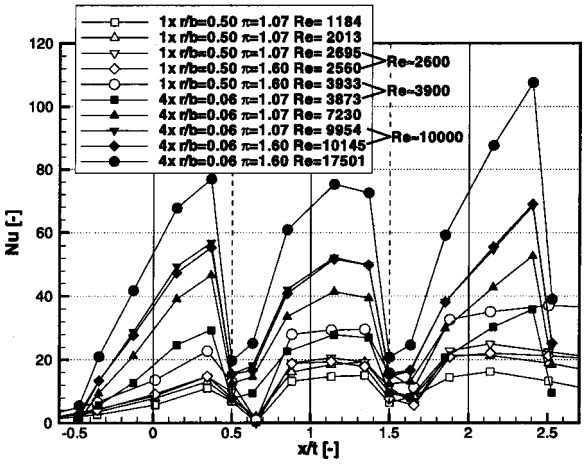

Fig. 9 Local Nusselt numbers at the stator, $s/b=0.909$

through annular orifices (Fig. 8). The orifice coefficient C represents the ratio of measured leakage rate to the flow rate for frictionless flow of an incompressible fluid.

For some of the geometries investigated in their study, Wittig et al. [16] also found a relative maximum in the distributions of the discharge coefficients.

Contraction and friction effects may serve as an explanation for the discharge behavior observed in the present study. For high Reynolds numbers, the leakage rate is determined by the cross-sectional area of the contraction forming at the exit of the seal gap. At sufficiently high Reynolds numbers, the shape of the contraction is independent of the Reynolds number and the discharge coefficient is constant. Below a certain value the vena contracta widens with decreasing Reynolds number and the area available for the through flow increases. Finally, at relatively low Reynolds numbers with relatively high friction, reducing the Reynolds number causes the discharge coefficient to rapidly decrease.

Local Heat Transfer. The local Nusselt numbers are presented in Figs. 9–12 for the stator and rotor sides of the two seal models. Each curve represents a distribution of the local Nusselt number for a given Reynolds number. As indicated in the figures, similar Reynolds numbers were obtained for different pressure ratios. The respective pressure ratio is included in the legend. Due to the time consuming experimental procedure, heat transfer experiments were conducted for the largest and smallest gap width for two different pressure ratios at different back pressures.

The shape of the distributions of the local Nusselt numbers for the 4× seal model with $r/b=0.06$ in Figs. 9–12 agrees well with the distributions obtained with the same geometry in a previous study. A detailed discussion of the flow field and the distribution of the local heat transfer coefficients is given by Willenborg et al. [22] and shall not be repeated here. The effects of Reynolds number and pressure ratio on the Nusselt number profiles are focused on in the present paper.

For the gap width $s/b=0.909$, at the stator wall (Fig. 9) the local Nusselt numbers increase with increasing Reynolds number. The curves for Reynolds numbers of Re≈2,600 and Re≈10,000, of which each has been obtained for two different pressure ratios, show very good agreement. At the forward facing step of the stator ($x/t=0.5$, $x/t=1.5$), slight deviations between the qualitative distribution of the local Nusselt numbers of the two seal models are shown. One reason for this difference can be attributed to the different instrumentation of the two models. Due to the smaller dimensions, fewer thermocouples were available for resolving the surface temperature distribution of the 1× model. It was found that slight changes in the temperature boundary condition for the finite element calculations in this region can result in considerable changes of the local heat transfer coefficients at this point. However, the change of the mean values and thus the mean Nusselt numbers was negligible. Therefore, the agreement of the distributions of the local Nusselt number for Re≈3,900 in Fig. 9 is considered as good.

Similar results have been obtained for the rotor with the gap width $s/b=0.909$ (Fig. 10). Again, the values of the local Nusselt numbers increase with increasing Reynolds number. The profiles for Re≈2,600 and Re≈10,000 show excellent agreement. Also for the rotor, differences in the qualitative distributions of the local Nusselt numbers for the two seal models are visible. Due to the lower resolution of the surface temperature distribution in the 1× model the position of the impingement of the flow on the rotor as observed by Willenborg et al. [22] is not reflected as precisely as for the 4× model. Compared to the stator, larger differences in the distribution of the local Nusselt number from the two models occur for Re≈3,900. However, the absolute level of the local values is comparable.

The qualitative distribution of the local Nusselt numbers at the stator exhibits no definite dependence on the gap width (Figs. 9 and 11), which is in accordance with the results obtained by Willenborg et al. [22]. Also for the larger gap width $s/b=2.424$ the profiles of the local Nusselt numbers of the two seal models differ in the vicinity of the step at the stator (Fig. 11). Whereas the two Nusselt number distributions for Re≈6,200 agree very well, the distributions of the larger scale for Re≈22,000 show significant deviations. Here, the local values for the pressure ratio $\pi=1.6$ are shifted to a higher level and also exceed the values obtained for

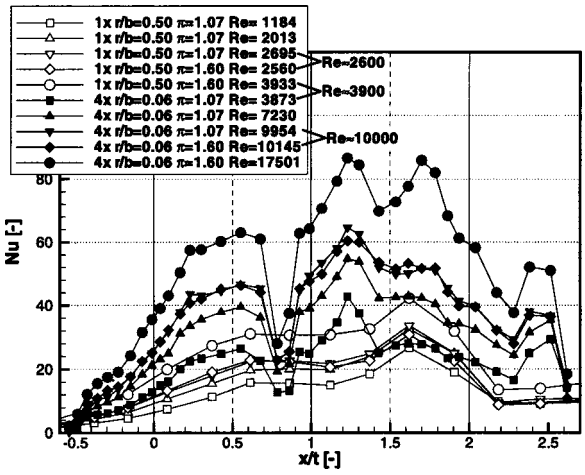

Fig. 10 Local Nusselt numbers at the rotor, $s/b=0.909$

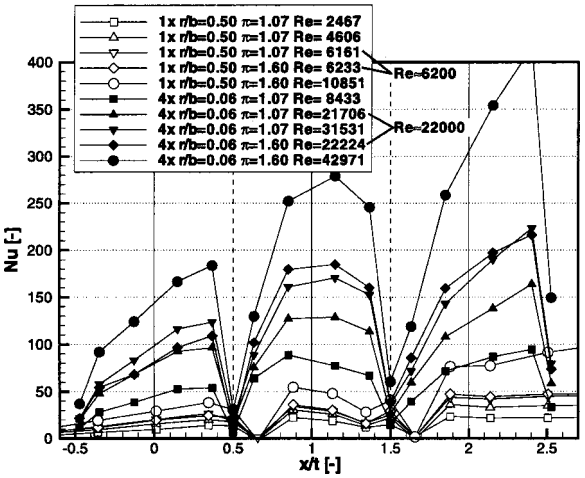

Fig. 11 Local Nusselt numbers at the stator, $s/b=2.424$

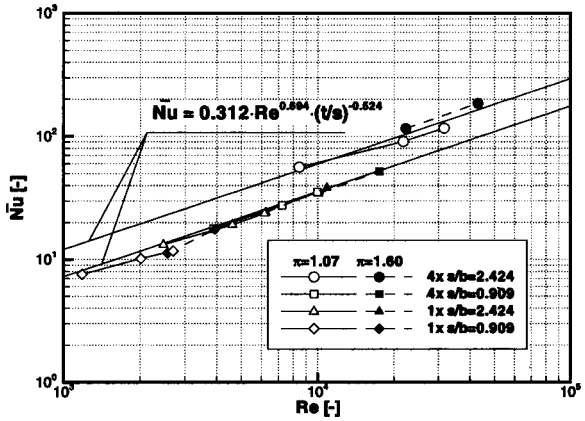

Fig. 13 Mean Nusselt numbers for the stator

Re=31,531. Furthermore, the local Nusselt numbers for Re =10851 (1×) are below the values for Re=8433 (4×). However, the characteristic shape of the curves of local Nusselt numbers is identical for all Reynolds numbers.

In Fig. 12, local Nusselt numbers for the rotor with the largest gap width $s/b=2.424$ are presented. For the 4× model, the downstream shift of the point of impingement of the flow on the rotor (Willenborg et al. [22]) with the larger gap width is reflected in the distribution of the local Nusselt numbers, compared to the results for $s/b=0.909$ (Fig. 10). The maxima of the Nusselt number distribution in the labyrinth chamber are shifted to higher x/t values. In contrast to the 4× model, the same qualitative distribution of the local Nusselt number can be observed for the 1× model for the two gap widths (Fig. 10 and Fig. 12). As mentioned above, this can be attributed to the lower spatial resolution of the temperature measurement in the seal model in 1× scale.

Similar to the results of the stator, no definite dependence of the values of the local Nusselt number on the Reynolds number occurs. For the 1× model the two distributions of Nu for Re ≈6,200 show good agreement (Fig. 12). However, for the 4× model the curves for Re≈22,000 show significant disagreement. While the qualitative shape of the curves coincide, the absolute level for $\pi=1.6$ is distinctly above the values for $\pi=1.07$. Analogous to the stator, also the values of the distribution with the next higher Reynolds number (Re=31,531) are exceeded.

Mean Heat Transfer. Mean Nusselt numbers computed from the local values as described by Eqs. (5) and (6) are plotted against the Reynolds number in a log–log scale in Figs. 13 and 14. The correlations of the Nusselt number with Reynolds number and relative gap width presented by Willenborg et al. [22] for the 4× model with $r/b=0.06$ are included in the plots. A comparison of these correlations with results obtained in an earlier study by Wittig et al. [21] for a geometrically related labyrinth geometry has been given by Willenborg et al. [22] and showed good agreement between the different sets of data.

At the stator (Fig. 13), the mean Nusselt numbers of the 4× model show an excellent agreement with the correlation curve and confirm the strong gap size dependence. For a given gap width, the Reynolds number is the relevant parameter determining the heat transfer. A slight influence of the pressure ratio on the mean Nusselt numbers is shown for the larger gap width $s/b=2.424$. Compared to the change of the Nusselt numbers with the Reynolds number, this influence is relatively small.

In contrast to the 4× model with $r/b=0.06$, no distinct gap size dependence of the Nusselt numbers is evident for the 1× model with $r/b=0.5$. As indicated by the distributions of the local values, the influence of the pressure ratio on the mean Nusselt numbers for a given Reynolds number is negligible. All heat transfer data of the 1× model correspond to the correlation curve obtained for the smaller gap width of the 4× geometry.

For the rotor wall (Fig. 14), the distribution of the mean Nusselt numbers from the 4× model with $r/b=0.06$ agrees with the correlation developed in the previous study (Willenborg et al. [22]). Again, the Reynolds number governs the heat transfer character-

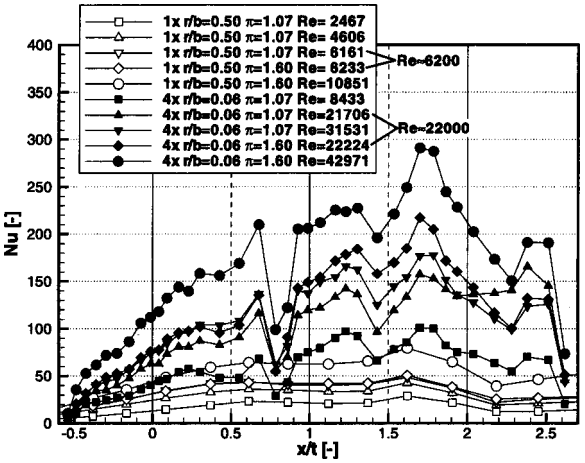

Fig. 12 Local Nusselt numbers at the rotor, $s/b=2.424$

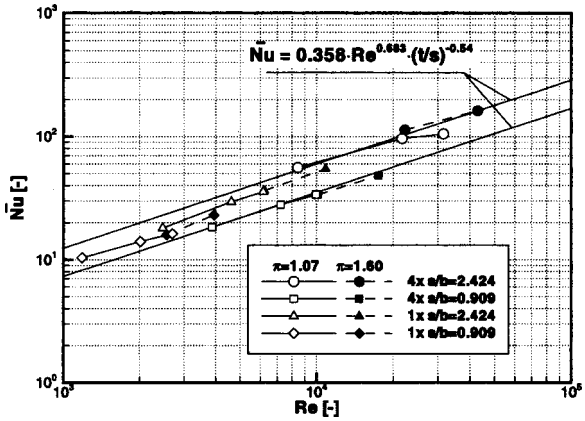

Fig. 14 Mean Nusselt numbers for the rotor

istics. Slight deviations of the mean Nusselt numbers with varying pressure ratio occur only for the larger gap width, $s/b=2.424$, with the 4× model.

Similar to the situation at the stator, the gap size dependence of the Nusselt numbers for the 1× model is very weak. The gradient of the linear relationship between Nusselt and Reynolds number, in the log–log scale of Fig. 14, is comparable to that of the 4× model. However, the absolute level of the mean Nusselt numbers for the 1× model is in between the two correlation curves obtained from the 4× model. For the 1× model, no distinct influence of the pressure ratio on the heat transfer can be identified.

Conclusions

An experimental study was conducted to determine effects of Reynolds number and pressure ratio on the discharge behavior and the heat transfer of a stepped labyrinth seal. Measurements of the leakage rate and the heat transfer were performed for two plane models of different geometries at different scales. In the experiments, independent variation of Reynolds number and pressure ratio was achieved by adjusting the back pressure at the seal exit. Dimensionless discharge coefficients and Nusselt numbers describing the sealing performance and the heat transfer have been derived from the experimental data.

The two seal geometries showed a significantly different sealing performance which was attributed to the different fin tip corner radii. The discharge coefficients obtained from the 1× model with the larger corner radius exceed the values of the 4× model with the smaller corner radii by as much as 30 percent. The difference in the C_D values as a result of the different relative fin tip geometry corresponds to data available in the literature.

As a result of the combined influence of contraction and friction effects, a general dependence of the discharge coefficients on the Reynolds number was identified. In the region of low Reynolds numbers, the discharge coefficient increases considerably with the Reynolds number. The largest increase of 9 percent was observed for the smallest gap width for the seal geometry in 1× scale, i.e., for the lowest Reynolds numbers. For sufficiently high Reynolds numbers, the discharge coefficients of a given seal configuration depend only on the pressure ratio.

No effects of the pressure ratio on the distributions of the local Nusselt numbers were identified for the gap width $s/b=0.909$. The local Nusselt numbers continuously increase with increasing Reynolds number with identical qualitative distribution for all Reynolds numbers. A certain influence of the pressure ratio on the absolute level of the local Nusselt numbers was observed for the 4× model for the larger gap width $s/b=2.424$. Again, a consistent shape of the curves of the local Nusselt numbers was obtained for all Reynolds numbers.

The gradient of the linear relationship between Nusselt number and Reynolds number in a log–log scale is in agreement for the two geometries. In contrast to the results from the 4× model, no distinct gap size dependence of the mean Nusselt numbers was obtained from the 1× model.

Compared to the influence of the Reynolds number on the mean Nusselt numbers, the effect of the pressure ratio on the heat transfer is very small and the Reynolds number represents the governing parameter.

Acknowledgments

The authors greatly acknowledge support for this work by the German BMWi. The work presented here was part of the German Luftfahrtforschungsprogramme 1995–98. Special thanks are due to Bruce Johnson for intensive technical discussions.

Nomenclature

$A=B\cdot s$ = area, m^2
B = width of the test section, m
b = fin tip thickness, m
C = annular orifice discharge coefficient
$C_D=\dot{m}/\dot{m}_{ideal}$ = discharge coefficient
$c=\dot{m}/\rho A$ = mean throughflow velocity, m/s
H = step height, m
h = heat transfer coefficient, $W/(m^2K)$
l = fin height, m
$\dot{m}$ = mass flow rate, kg/s
n = vector normal to the wall
$Nu=h2s/\lambda$ = Nusselt number
p = pressure, N/m^2
$\dot{Q}$ = heat load, W
R = specific gas constant, J/kg K
r = fin tip radius, m
$Re=2\dot{m}/B\mu$ = Reynolds number
s = gap width, seal clearance, m
t = pitch, m
T = temperature, K
x, y, z = Cartesian coordinates, m
α = orifice flow coefficient
κ = ratio of specific heats
λ = thermal conductivity, W/mK
μ = dynamic viscosity, kg/ms
$\pi=p_0/p_\infty$ = pressure ratio
ρ = density, kg/m^3

Subscripts

C = critical
G = gas
ideal = ideal
total = total
W = wall
0 = inlet
∞ = outlet

Superscripts

$\bar{}$ = mean value

References

[1] Zimmermann, H., 1990, ''Some Aerodynamic Aspects of Engine Secondary Air Systems,'' ASME J. Eng. Gas Turbines Power, **112**, pp. 223–228.
[2] Zimmermann, H., Kammerer, A., and Wolff, K. H., 1994, ''Performance of Worn Labyrinth Seals,'' ASME Paper No. 94-GT-131.
[3] Martin, H. M., 1908, ''Labyrinth Packings,'' Engineering, **85**, pp. 33–36.
[4] Stodola, A., 1922, *Dampf- und Gasturbinen*, 5. Auflage, Springer-Verlag, Berlin.
[5] Egli, A., 1935, ''The Leakage of Steam Through Labyrinth Seals,'' Trans. ASME, **57**, pp. 115–122.
[6] Kearton, W. J., and Keh, T. H., 1952, ''Leakage of Air Through Labyrinth Glands of Staggered Type,'' Proc. Inst. Mech. Eng., **166**, pp. 180–188.
[7] Komotori, K., 1961, ''Probleme bei Labyrinth-Stopfbüchsen,'' Proc. Fujihara Memorial Faculty of Eng., Keio Univ., **14**, No. 54.
[8] Trutnovsky, K., and Komotori, K., 1981, *Berührungsfreie Dichtungen*, VDI-Verlag, Düsseldorf.
[9] Stocker, H. L., 1978, ''Determining and Improving Labyrinth Seal Performance in Current and Advanced High Performance Gas Turbines,'' AGARD-CP-237 Conf. Proc., pp. 13/1–13/22.
[10] Wittig, S., Schelling U., Jacobsen, K., and Kim, S., 1987, ''Numerical Predictions and Measurements of Discharge Coefficients in Labyrinth Seals,'' ASME Paper No. 87-GT-188.
[11] Morrison, G. L., Johnson, M. C., and Tatterson, G. B., 1991, ''3-D Laser Anemometer Measurements in a Labyrinth Seal,'' ASME J. Eng. Gas Turbines Power, **113**, pp. 119–125.
[12] Prasad, B. V. S. S. S., Sethu Manavalan, V., Nanjunda Rao, N., 1997, ''Computational and Experimental Investigations of Straight-Through Labyrinth Seals,'' ASME Paper No. 97-GT-326.
[13] Rhode, D. L., Adams, R. G., 2000, ''Computed Effect of Rub-Groove Size on Stepped Labyrinth Seal Performance,'' ASME Paper No. 2000-GT-0292.
[14] Schramm, V., Willenborg, K., Kim, S., and Wittig, S., 2000, ''Influence of a Honeycomb Facing on the Flow Field and Discharge Behavior of a Stepped Labyrinth Seal,'' ASME J. Eng. Gas Turbines Power, in press.
[15] Zimmermann, H., and Wolff, K. H., 1998, ''Air System Correlations, Part 1: Labyrinth Seals,'' ASME Paper No. 98-GT-206.
[16] Wittig, S., Dörr, L., and Kim, S., 1983, ''Scaling Effects on Leakage Losses in Labyrinth Seals,'' ASME J. Eng. Power, **105**, pp. 305–309.
[17] Sheinin, E. I., 1961, ''Experimentelle Untersuchung des Wärmübergangs in der Zone der Endabdichtungen von Gasturbinen (Russian),'' Energomashinostroenie, **1**, pp. 25–27.
[18] Shvets, I. T., Khavin, V. Y., and Dyban, E. P., 1963, ''Heat Exchange in Laby-

rinth Seals of Turbine Rotor (Russian),'' Energomashinostroenie, **12**, pp. 8–12.
[19] Kapinos, V. M., and Gura, L. A., 1970, ''Investigation of Heat Transfer in Labyrinth Glands on Static Models,'' Thermal Eng., **17**, No. 11, pp. 54–56.
[20] Metzger, D. E., and Bunker, R. S., 1985, ''Heat Transfer for Flow Through Simulated Labyrinth Seals,'' presented at the Symposium on Transport Phenomena in Rotating Machinery, Honolulu, USA.
[21] Wittig, S., Jacobsen, K., Schelling, U., and Kim, S., 1988, ''Heat Transfer in Stepped Labyrinth Seals,'' ASME J. Eng. Gas Turbines Power, **110**, pp. 63–69.
[22] Willenborg, K., Schramm, V., Kim, S., and Wittig, S., 2000, ''Influence of a Honeycomb Facing on the Heat Transfer in a Stepped Labyrinth Seal,'' ASME J. Eng. Gas Turbines Power, in press.
[23] Kapinos, V. M., and Gura, L. A., 1973, ''Heat Transfer of a Stepped Labyrinth Seal,'' Thermal Eng., **20**, No. 6, pp. 28–32.
[24] Waschka, W., Wittig, S., and Kim, S., 1992, ''Influence of High Rotational Speeds on the Heat Transfer and Discharge Coefficients in Labyrinth Seals,'' ASME J. Turbomach., **114**, pp. 462–468.
[25] Waschka, W., Scherer, T., Kim, S., and Wittig, S. 1992, ''Study of Heat Transfer and Leakage in High Rotating Stepped Labyrinth Seals,'' ISROMAC-4, pp. 326–334.
[26] Kline, S. J., and McClintock, F. A., 1953, ''Describing Uncertainties in Single-Sample Experiments,'' Mech. Eng. (Am. Soc. Mech. Eng.), **75**, pp. 3–8.
[27] Johansen, F. C., 1930, ''Flow Through Pipe Orifices at Low Reynolds Numbers,'' Proc. R. Soc. London, Ser. A, **126**, pp. 231–245.
[28] Bell, K. J., and Bergelin, O. P., 1959, ''Flow Through Annular Orifices,'' Trans. ASME, **79**, pp. 593–601.

Kelly R. Navarra

Douglas C. Rabe

Air Force Research Laboratory,
Wright-Patterson AFB, OH 45433-7251

Sergey D. Fonov

Larry P. Goss

Innovative Scientific Solutions, Inc.,
Dayton, OH 45440-3638

Chunill Hah

NASA Glenn Research Center,
Cleveland, OH 44135

The Application of Pressure- and Temperature-Sensitive Paints to an Advanced Compressor

An innovative pressure-measurement technique that employs the tools of molecular spectroscopy has been widely investigated by the aerospace community. Measurements are made via oxygen-sensitive molecules attached to the surface of interest as a coating, or paint. The pressure-sensitive-paint (PSP) technique is now commonly used in stationary wind-tunnel tests; this paper presents the use of this technique in advanced turbomachinery applications. New pressure- and temperature-sensitive paints (P/TSPs) have been developed for application to a state-of-the-art transonic compressor where pressures up to 1.4 atm and surface temperatures to 90°C are expected for the suction surface of the first-stage rotor. PSP and TSP data images have been acquired from the suction surface of the first-stage rotor at 85 percent of the corrected design speed for the compressor near-stall condition. A comparison of experimental results with CFD calculations is discussed.
[DOI: 10.1115/1.1400116]

Introduction

The turbomachinery community is continually striving to improve the performance of gas turbine engines. Engine performance depends upon the work input per stage and the efficiency. The aerodynamic turning of the flow that creates work results in the pressure profile over the suction and pressure surfaces of the blade. These opposing profiles create blade loading. Measuring the time-averaged blade loading and measuring the changes in the blade loading have only been possible for sections of the blade. This has been accomplished by mounting miniature pressure transducers in the surface of the blade.

Sexton, O'Brien, and Moses made early surface-pressure measurements of a subsonic rotor in 1973 using blade-mounted pressure transducers [1]. A multi-channel radio telemetry system was employed to transmit the rotating measurement signals to the stationary laboratory reference frame. Blade-mounted pressure transducers remain today as the primary means of measuring the blade surface pressure. Telemetry as well as high-performance slip rings are used to transmit the rotating electronic signal to the stationary reference frame. Unfortunately this technique has many limitations; the mounting of the transducers and its leads results in a compromise to the structural integrity of the blade and tends to disturb the actual airflow. The transducers have limited reliability in full-scale transonic turbomachinery environments while being very costly to obtain and install in full-scale compressor hardware. Typically the installation of these transducers significantly lengthens the assembly time required. Most importantly, this approach does not provide a full understanding of the blade loading, since a practical application of pressure transducers covers less than 5 percent of the blade surface. In particular, this technique provides limited information on shock position. For these reasons, improved blade-surface pressure-measurement techniques are needed to aid in the understanding of the flow behavior and the structural integrity of advanced turbomachinery components.

The relatively new technique that employs pressure-sensitive paints is the subject of this paper. Recent papers reported the first application of PSP to a large-scale commercial-engine inlet [2] and continuing progress toward rotational applications [3,4]. The objective of this research effort was to demonstrate the state of the art of optical pressure and temperature measurements in advanced rotating machinery. References [5] and [6] report parallel work being conducted by colleagues at NASA Glenn and Purdue University.

Contributed by the International Gas Turbine Institute and presented at the 45th International Gas Turbine and Aeroengine Congress and Exhibition, Munich, Germany, May 8–11, 2000. Manuscript received by the International Gas Turbine Institute February 2000. Paper No. 2000-GT-614. Review Chair: D. Ballal.

Measurement Concept

The ability to make an accurate determination of pressure and temperature distributions over an aerodynamic surface based on the emitted luminescence signal from a coating has attracted much attention in the aerospace community [7–12]. PSP measurements exploit the oxygen (O_2) sensitivity of luminescent probe molecules dispersed within gas-permeable binder materials. The mechanism for temperature-sensitive-paint (TSP) sensitivity is based on thermal-deactivation processes inherent in the probe species and temperature-dependent viscosity changes of the binder [13]. This effect also occurs in PSP and must be taken into account whenever the temperature changes enough to influence the pressure measurement. This is clearly the case when PSP is used to measure surface conditions within transonic compressors.

If the test surface under study is surrounded by an atmosphere containing O_2 (e.g., air), the experimental intensity (I) and lifetime (τ) can be described as a function of O_2 partial pressure (P_{O2}) on the test surface within a Stern–Volmer framework [13].

$$\frac{\tau_0}{\tau} = \frac{I_0}{I} = 1 + K_{SV} P_{O2} = 1 + k_q \tau_0 P_{O2} \tag{1}$$

In this expression I and τ represent the luminescence intensity and the excited-state lifetime at a given P_{O2}, respectively. The subscript 0 denotes measurements in the absence of O_2 (vacuum). K_{SV} is the Stern–Volmer quenching constant that provides a measure of the sensitivity of the luminescent species to O_2. The bimolecular quenching constant (k_q) reflects the quenching-process efficiency.

For intensity-based pressure measurements, it is often convenient to use a modified form of the Stern–Volmer expression that replaced the vacuum calibration (i.e., 0) with a reference standard

$$I_{\text{ref}} = A(T) + B(T)\frac{P}{P_{\text{ref}}} \tag{2}$$

In this approach, the measured reference intensity (I_{ref}) at a known reference pressure (P_{ref}) is divided by the measured intensity (I) at some test condition (P) over the region of interest. The calibration coefficients A and B are determined experimentally for

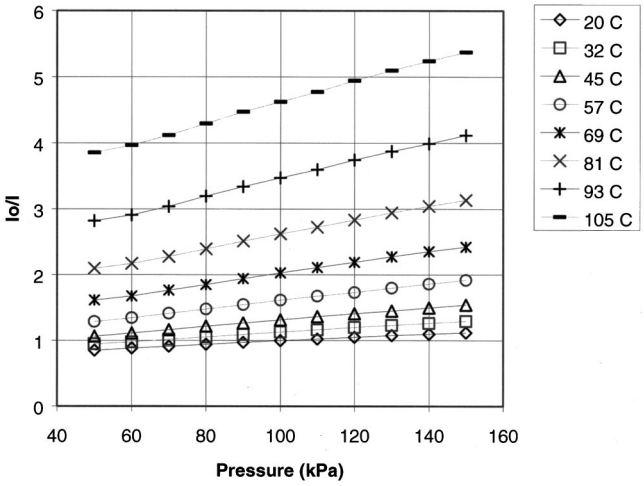

Fig. 1 Calibration of Ru-sol-gel PSP as a function of pressure and temperature

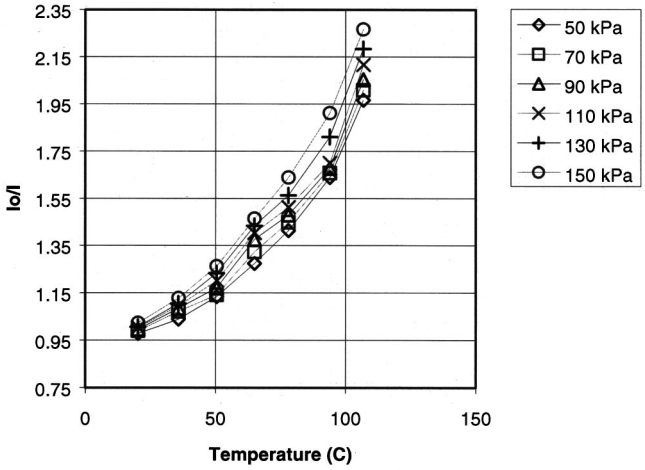

Fig. 2 Calibration of bis-pyrenal propane-bostic TSP as a function of temperature and pressure

a given paint formulation and are a function of temperature (T). In practice, the intensities are generally measured over an entire surface by a detector array such as a charge-coupled-device (CCD) camera. The unknown pressure can then be backed out by dividing the measured intensities at the two conditions and applying the calibration coefficients. With today's CCD cameras having a million or more pixels, this technique provides unequaled spatial resolution of the surface-pressure measurement.

Paint Development

The application of PSP to turbomachinery was demonstrated in previous work [3,4]. However, this work identified that significant improvements were required to reduce the measurement uncertainties, which were on the order of 7 percent [3,4]. While significant improvements can be obtained using a back-lit slow-scan CCD camera and a higher power laser, the toughest obstacle was optimizing the signal output of the paints for the desired pressure and temperature range.

To improve the system signal-to-background ratio (S/B), the binding matrix supporting the luminophores was re-engineered. Through the use of sol-gel technology (described in detail in [14]) it was possible to develop paints exhibiting both higher intensity output and greater pressure sensitivity.

Paint Performance. Characteristics of T/PSP thin-film coating materials suitable for deployment in the high-pressure/high-temperature environment of the turbine engine include high-temperature stability, optical transparency, ease of application and removal, and tunable porosity to affect changes in the pressure and temperature sensitivity. The salient criteria governing the temperature capability of PSPs include the probe and binder thermal stability, the temperature dependence of the binder viscosity, and the robustness to temperature cycling. The low viscosity versus temperature dependence of sol-gel-based composites coupled with their high-temperature stability (can be sintered at $>1000°C$) makes these materials attractive candidates for extreme-temperature applications. Figure 1 shows the pressure sensitivity data at various temperatures for a sol-gel-based PSP that incorporates ruthenium bathophenanthroline [$Ru(dpp)_3$] pressure probe.

These data illustrate the utility of sol-gel based PSPs for probing surface-pressure distributions to at least 130°C. This paint displayed a pressure sensitivity range of 1.84 percent/psi at 20°C to 3.1 percent/psi at 100°C. The increased pressure sensitivity at elevated temperatures is due to an increased rate of oxygen diffusion into the binder. However, these data also show the major limitation of current PSP technology; the temperature dependence of the pressure paint. The Ru-based pressure paint utilized in this study displays a temperature sensitivity of 1.0 percent/°C at 20°C, which increases to 2.7 percent/°C at 100°C. These data show that some form of compensation must be used to account for the temperature dependence of the pressure paint. Such compensation is necessary in general for all pressure paint systems when the surface temperature varies between the wind-off and wind-on measurements.

Temperature-Sensitive Paint. The most widely used method of temperature correction is *in situ* calibration. This technique requires the use of a pressure tap to calculate a linear shift for the PSP data. Since the reported test did not have blade mounted transducers, this technique could not be used. Another popular method of correcting for the temperature dependence of PSPs is to use a temperature-sensitive paint (TSP). A common strategy for the development of TSPs is to incorporate luminescent probes within polymeric matrices that are impermeable to oxygen. In this approach, the interplay of nonradiative decay processes of the probe and temperature-dependent viscosity changes of the binder imparts intensity-based temperature sensitivity. The TSP used during this test was bis-pyrenal propane (BPP) immobilized in a marine grade sealant Bostic™ [3]. The performance of this TSP paint is shown in Fig. 2. The temperature sensitivity of this paint is 0.8 percent/°C at 20°C and 1.0 percent/°C at 100°C.

It should be noted that this temperature paint displays some pressure sensitivity ranging from 0.4 percent/psi at 20°C to 1.1 percent/psi at 100°C. Overall, the PSP is three times more sensitive to pressure than the TSP at elevated temperatures. However, the pressure sensitivity of the TSP must be taken into account if accurate temperature corrected pressure measurements are to be made.

Test-Article Description

The selected PSPs and TSPs were applied to a full-scale state-of-the-art two-stage transonic compressor to obtain quantitative pressure measurements from the suction surface of this first-stage rotor. The first stage of this two-stage compressor is an integrally bladed rotor (IBR) of 16 blades.

To accommodate the testing schedule, the painting of the rotor blade was performed in place and an *a priori* calibration was used. An *a priori* calibration uses a test coupon painted along with the test article. This coupon is then calibrated separately in a calibration chamber and the calibration is applied to the data obtained from the rotor. The ideal calibration method would be to take the calibration directly from the test surface. However, because the test surface is over 70 cm in diameter mounted in the test facility, this method was not practical. In general the aerodynamic perfor-

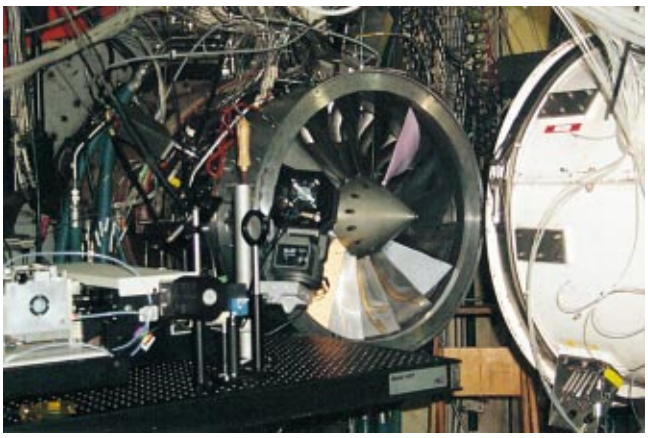

Fig. 3 PSP test setup (TSP: white, PSP: yellow, Reference: pink)

mance of this rotor is similar to the one presented in [15]. At the aerodynamic design point, the relative Mach number is supersonic over the majority of the blade span. At 85 percent design speed, the blade tip is supersonic. The following paragraphs describe the test setup and data-acquisition procedure.

Test Setup. Figure 3 shows a photograph of the test setup. Here the upstream ducting on the right was pulled away to allow viewing of the rotor. The colored blades of the rotor are blades painted with TSP (white) and PSP (yellow). A fused-silica window (305×25 mm) was placed ~260 mm upstream of the rotor leading edge. A back-lit slow-scan charge-coupled device (CCD) camera (16 bit, 512×512 pixel), viewed the blades across the flow path. The tripled output (355 nm) of a pulsed (10 ns pulse @30 Hz) Nd:YAG laser system was used to illuminate the blades. The CCD camera was mounted on a pan/tilt stage, coupled with a filter wheel (for different PSP formulation comparisons), and a fixed optical breadboard. The output of the Nd:YAG laser was expanded using a diffuser and directed to the PSP-coated blade surface through the window. For these experiments the camera shutter was open for a maximum of 20 ms, but the exposure time was mitigated by the luminescence lifetime of the probe molecules dispersed in the paint binder. Probe lifetimes did not exceed 2 μs.

Prior to PSP application, the engine-inlet surface was first cleaned with alcohol and a lint-free cloth. The surrounding area was masked to prevent overspray. A white basecoat was applied and allowed to dry for ~1 h prior to sol-gel deposition. The sol-gel layers of the TSP and PSP utilized in this study were typically 5–10 μm. Finally, registration (fiduciary) marks were drawn on the painted surface in a grid formation and the precise locations were determined using a coordinate mapping system (CMS). Standard ''rub-on'' fiduciary marks could not be used on the compressor. Previous tests have shown that these fiduciary marks do not adhere to the paint when the compressor is at a high-speed condition. To overcome this problem, fiduciary marks were placed on the painted blades using permanent ink from a Sharpie™ marker. The ink could be used on both the sol-gel and the Bostic™. The blade leading-edge tip was used as the reference coordinate. The fiduciary marks allow reference images to be registered and accurately ratioed with the spatially distorted images acquired at a test condition.

Data-Acquisition Procedure. Fifty images were recorded and averaged for each measurement point: a wind-off reference image for both the PSP and the TSP, a wind-on test image for the PSP and TSP, a dark image, and a white image. For defining the thermal noise of the CCD array and ambient light contamination, the dark images were taken without the laser firing. A white image was taken of a uniformly illuminated surface of arbitrary intensity. This image was used for flat-field correction. Both the dark and flat-field images were strictly camera-dependent and could be taken either before or after the test. Thus, during a scheduled testing period, only the wind-off and wind-on images were acquired. The necessity for acquiring the described images will be further discussed in the Image Processing Section.

For acquiring the wind-off images, the rotor was rotated at 150 rpm (1.1 percent of the design speed), where the pressure gradient was assumed to be negligible. This approach provided valid reference images while allowing the timing circuitry to be used for accurate positioning of the blade. The *A/D* count at this condition was roughly 33,000 units. Sequential images were acquired using various timing delays until the desired painted blade was in the view of the CCD. Care was taken to determine the delays required to place the TSP and PSP blades in the same location. The image pixel coordinates of the blade leading edge were used as a reference. The delay and coordinates of each blade were recorded. Fifty wind-off images were acquired for each paint for steady-state averaging.

Once the wind-off images were acquired, the compressor was set at the desired test speed and condition. At high speeds, where the surface temperature of the blade tip is over 90°C, the *A/D* counts drop to roughly 7000 units due to the increased temperature. Because of the lower signal level at this condition, it was essential to take multiple shots (50) for averaging. To provide a constant background noise from image to image, the shutter value remained constant for all of the wind-on images, regardless of the rotational speed. From the coordinates previously recorded during the acquisition of the wind-off images, the delays required to superimpose the TSP and PSP blades were determined, and the corresponding wind-on images were acquired.

Image Processing

Image registration is an area of active research in the PSP community. Current PSP systems require that wind-on images be ratioed at an isobaric condition (wind-off). The surface deflections between the wind-on and wind-off conditions result in systematic errors in the calculated intensity ratio. Identical image locations on the model rather than identical CCD camera pixel locations must be ratioed.

In practice, image processing for paint-sensor systems falls into two categories—image registration and image resection. Image registration is concerned with the effects of model movement and deformation on the calculation of the $I_{\text{wind-off}}/I_{\text{wind-on}}$ ratio; image resection involves the accurate placement of the resulting two-dimensional image of pressure values on a three-dimensional grid for spatial quantitative visualization. Algorithms for image registration and image resection in the area of PSP appear in the published literature [16,17].

A new algorithm for image registration incorporating automated techniques has been developed. This algorithm, called Quantum Pixel Energy Distribution (QPED), is based on the discrete pixel-based architecture of the CCD camera and is intended to augment the linear-interpolation algorithm used for fractional-pixel image shifting.

The QPED process is used as the foundation for an optimizing search algorithm [18]. In this algorithm, the QPED matrix values for each pixel in a wind-off image are adjusted on a pixel-by-pixel basis. The result in QPED image is ratioed with the wind-on image, and the quality of the resulting intensity-ratio image is assessed. The QPED matrix values are adjusted until the optimal condition is found. The results from the QPED algorithm have been compared with those obtained using the direct linear transformation (DLT) functions included in commercially available PSP data-reduction software [2].

The data processing procedure utilized in this study for the pressure and temperature images consists of four steps including: (1) image averaging, (2) alignment and ratio of wind-off and wind-on images, (3) image resection, and (4) conversion to tem-

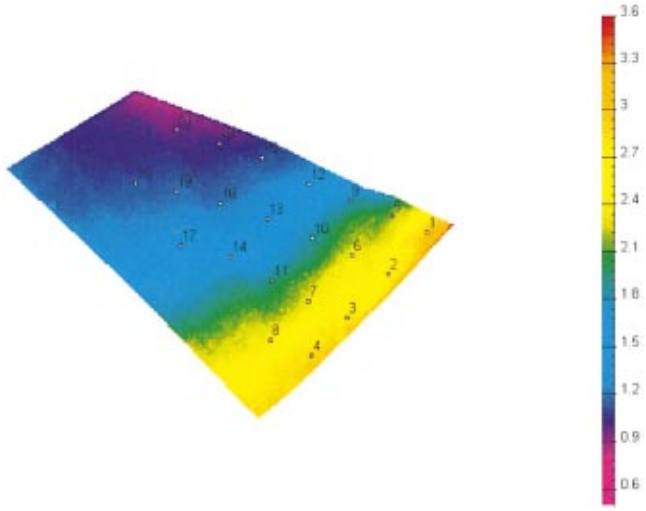

Fig. 4 Relative intensity in the pressure sensitive data with fiduciary marks identified

perature and pressure. The results of this process are experimental temperatures and pressures, which can be directly compared to CFD results.

Step 1. Image Averaging: To increase the signal-to-noise of the experimental data, 50 images were averaged for each experimental configuration (wind-on and wind-off). Because of the increased time jitter associated with the min-speed (150 rpm) condition that was utilized for wind-off measurements, each image had to be registered (aligned) before averaging could be accomplished. Image alignment was accomplished using displacement information obtained by the QPED process between the first image in the series and each subsequent image. Once aligned, the intensity distribution from each image was normalized by the recorded laser intensity to account for the shot-to-shot instability of the excitation laser.

Step 2. Alignment and Ratio of Wind-off and Wind-on Images: This step was performed using the Field Program from the Optical Measurement System (OMS) analysis package developed by Fonov et al. [19]. Alignment was performed using the fiduciary points painted on the blade's surface. The relative intensity distribution resulting from the ratioed wind-off to wind-on images were filtered and the fiduciary points removed using a bi-linear interpolation scheme (Fig. 4).

Step 3. Image Resection: Image resection was performed using a mesh corresponding to the suction side of the blade consisting of 43 sections and 89 nodes. This mesh (Fig. 5) provided by the compressor manufacturer was modified to increase node density using the Edgraph program [19].

Fig. 5 (*a*) Source mesh: 43 sections with 89 nodes; (*b*) mesh used for resection: 172 sections with 89 nodes

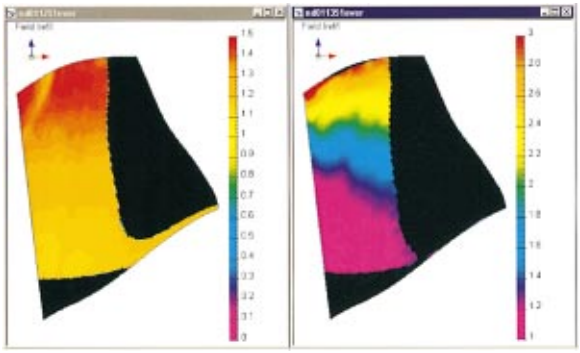

Fig. 6 Relative intensity distributions for temperature (left) and pressure-sensitive data (right) after resectioning

The resection procedure was performed in the interactive mode, where it was necessary to align the image of the mesh relative to the image of the blade. The same set of angular and scale resection parameters was used for both the pressure sensitive and temperature sensitive images. The relative intensity distributions corresponding to the pressure and temperature sensitive data after the resection procedure are presented in Fig. 6.

Step 4. Conversion to Temperature and Pressure Fields: The conversion of the relative intensity distributions to temperature and pressure was accomplished using fitted coefficients obtained from experimental calibration data sets. The calibration data sets were obtained in an environmental chamber capable of precise control of temperature and pressure. The calibration data for the temperature paint was fitted with the following equation:

$$T = \sum_{i=0}^{3} \chi_i I_r^{\,i}, \tag{3}$$

where I_r is the relative intensity in the temperature sensitive data and χ_i is the calibration coefficient. The calibration data for the pressure paint were fitted with an equation that took into account its temperature dependence:

$$P = \sum_{i,j=0}^{3} \vartheta_{ij} I_r^{\,i} T^j, \tag{4}$$

where I_r is the relative intensity in the pressure sensitive data, T is the temperature in the pressure-sensitive data, and ϑ_{ij} is the pressure calibration coefficient. Ideally, the temperature information obtained from the temperature data is used with the relative intensity of the pressure data to obtain the pressure field. As will be discussed in the Results Section, this proved to be difficult. An alternative approach was found to be necessary to correct the temperature sensitivity of the pressure paint.

Because the derived pressure and temperature fields are on a three-dimensional mesh, the results can be easily compared to CFD calculations.

Error Analysis

The error in the pressure measurement can have contributions from several factors including signal photon statistics, detector thermal noise, temperature measurement uncertainty, system contamination (fog or lubricating oil), and many other effects that can influence intensity based measurements. These error sources can be categorized into two separate error contributions, namely, intensity measurement error and temperature measurement error. Both contribute to the error in the derived pressure field, but with different weighting factors. To understand these errors, an analysis of the measurement uncertainty is in order.

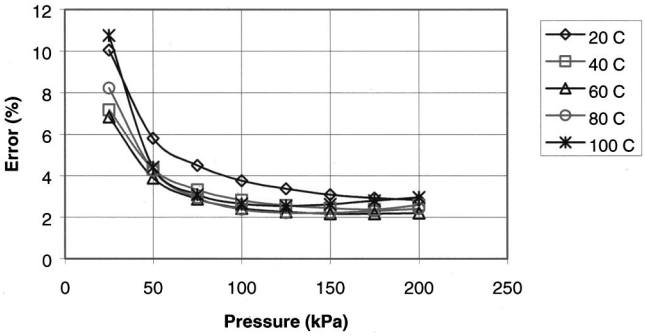

Fig. 7 Error in pressure due to 1 percent error in relative intensity measurement as a function of temperature and pressure

The pressure images are converted to absolute pressure through fitted calibration curves [see Eq. (4)]. The error in the measured pressure is given by

$$\omega_P = \left[\left(\sum_{i,j=0}^{3} \left(\frac{\partial P}{\partial a_{i,j}} \right)^2 \omega_{a_{i,j}}^2 \right) + \left(\frac{\partial P}{\partial I_R} \right)^2 \omega_{I_R}^2 + \left(\frac{\partial P}{\partial T} \right)^2 \omega_T^2 \right]^{1/2} \quad (5)$$

where the first term represents the error in the calibration coefficients, the second term represents the error in the intensity measurement, and the third term represents the error in the temperature measurement. Making the simplifying assumption that the maximum errors are due to the intensity and temperature measurements, Eq. (5) reduces to

$$\omega_P = \left[\left(\frac{\partial P}{\partial I_r} \right)^2 \omega_{I_r}^4 + \left(\frac{\partial P}{\partial T} \right)^2 \omega_T^2 \right]^{1/2} \quad (6)$$

Utilizing the calibration parameters, the measurement error predicted by Eq. (6) can be evaluated for the paints employed in this study. Figure 7 depicts the error in the pressure measurement due to a 1 percent error in the intensity measurement over a range of pressures and temperatures. Of special note is the dramatic increase in the error at low pressures. This is due to the increased sensitivity of the PSP to pressure in this region. Figure 8 depicts the error in pressure measurement due to a 1 percent error in the absolute temperature measurement over a range of pressures and temperatures. In this case the uncertainty increased dramatically with elevated temperature. Again this is due to the high sensitivity of the PSP to temperature changes at elevated temperatures. These plots indicate that highly accurate temperature measurements are needed for accurate determination of the pressure field. This is the case even in static wind tunnel tests where the change in the surface temperature is expected to be only a few degrees. As will be discussed in the Results Section, experimentally determining the surface temperature proved to be difficult in the Compressor Research Facility (CRF) environment due to fogging and surface contamination.

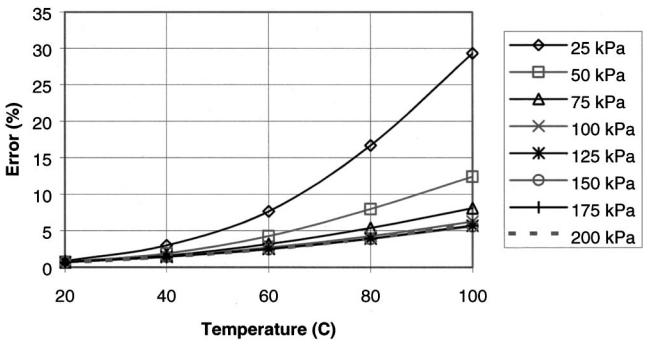

Fig. 8 Error in pressure due to 1 percent error in absolute temperature measurement as a function of temperature and pressure

CFD Calculations

A CFD code, which has been validated with a wide range of experimental data for turbomachinery flows, has been applied in the current study [20]. The current code solves the governing equations with an implicit relaxation method using a fully conservative control volume approach. A third-order accurate interpolation scheme is used for the discretization of the convection terms and central differencing is used for the diffusion terms. The method is of second-order accuracy with smoothly varying grids. Details of the current method and applications to transonic flows are given by Hah and Wennerstrom [20].

The computational grid used for the current study is shown in Fig. 9. The current computational grid was generated to give an orthogonal grid near the leading edge and near the blade surface where the most important flow phenomena (passage shock, shock-boundary layer interaction, etc.) occur. With this grid, spatial periodicity of the grid points is not enforced at the periodic boundaries; therefore, the physical periodicity of flow properties is handled inside the flow solver using an interpolation function. The grid consists of 50 nodes in the blade-to-blade direction, 46 nodes in the spanwise direction, and 150 nodes in the streamwise direction. Six grid nodes in the spanwise direction are used to describe the tip-clearance region of the compressor. In this region, the blade is collapsed to zero thickness and a periodicity condition is applied. The standard boundary conditions for transonic flow in a compressor are used [21]. A standard two-equation turbulence model, modified for low Reynolds-number-effects, is used for closure.

Approximately one CPU hour of Cray YMP time is required to obtain a fully converged solution for each operating condition.

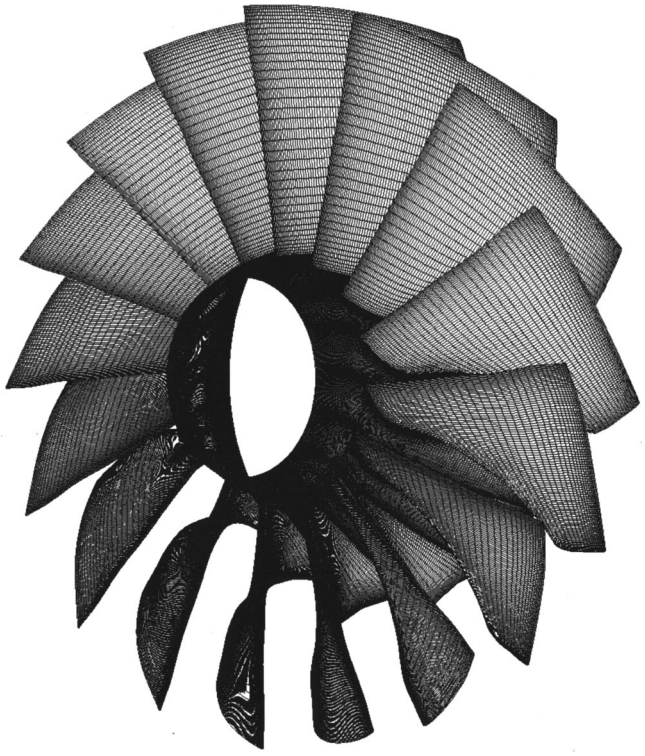

Fig. 9 Computational mesh used for CFP calculations

Results

The measurement campaign was conducted at the Air Force Research Laboratory Compressor Research Facility (CRF). The state-of-the-art facility used no preconditioning of the air prior to entering the compressor section during this test. This proved to be a problem due to the high humidity of the air experienced during the summer test, which resulted in condensation (fogging) in the test section at speeds above 68 percent design speed.

To overcome this drawback, the facility was run at reduced inlet pressure (~10 psi). This greatly reduced fogging due to humidity condensation, but caused seepage of lubricating oil into the test section. The effects of this contamination were reduced relative intensities, smearing of fiduciary marks, and stripping of the painted surface.

The main source of error in the temperature data was light scattering from the fluid particles in the flow. This resulted in a reduced relative intensity (offset) and erroneous temperature field. Two methods of determining a temperature distribution despite the contamination were investigated. Both approaches utilize the CFD results to act as an *in situ* reference. In the first method, a limited number of calculated pressure values are used in conjunction with the experimental pressure data to determine what temperatures would be necessary to give agreement. The temperature derived in this manner is then used to determine the scale factor needed to adjust the temperature data to achieve these values. This scale factor is then applied to the entire temperature data to determine the experimental temperature field distribution. The result of this method is shown in Fig. 10. The blue line represents the spanwise temperature distribution derived in this manner at 10 percent chord.

The second method is to disregard the temperature measurement and utilize only the measured pressure data along with the CFD results to determine the temperature distribution. For example, along the 10 percent chord, the CFD analysis predicts that the pressure field is relatively constant (0.3 reduced pressure units). From this knowledge, the temperature distribution along the chord can be calculated from the pressure data. This is represented in Fig. 10 as the dashed line. The agreement between the two methods is quite good considering the contamination experienced in the test.

Both approaches can also be utilized to produce the full temperature field as shown in Fig. 11. Here vertical and horizontal slices, inserts *A-A* and *B-B*, respectively, are plotted for quantitative comparison. While the temperature fields do not completely agree, the similarities give weight to using these approaches to determine temperature. It should be noted, however, that the T/PSP coatings yield information about the surface temperature and pressure where the CFD code predicts the near wall temperature and pressure. In some areas on the blade surface there could be real differences between these two parameters.

Once determined, the temperature field can be used to correct the experimental pressure measurement allowing the pressure field to be determined. Utilizing the scaled temperature field for this purpose, the experimental pressure field is plotted against the CFD pressure in Fig. 12. Both approaches display the location and magnitude of the shock at the 85 percent near stall condition (see inserts *A-A* and *B-B*). The major differences occur at the leading edge and blade tip. Based upon examination of the blade surfaces after testing, these locations are the most susceptible to lubricating oil build up that would adversely effect the experimental pressure results. The more subtle differences (post shock region shown in insert *A-A*) are likely due to temperature field inaccuracy or due to differences in the parameters being predicted by the CFD versus those being measured by the paints, as previously mentioned. Thus, heat transfer and other physical effects may also contribute to the differences between the two results. Finally, even though past validation studies have indicated that the present CFD code calculates the pressure field very well, some discrepancies near the tip could be due to the shortcomings of the applied turbulence model. Considering the simplified approach to determining the temperature in this case and the high sensitivity of the pressure paint to temperature, the agreement is reasonable.

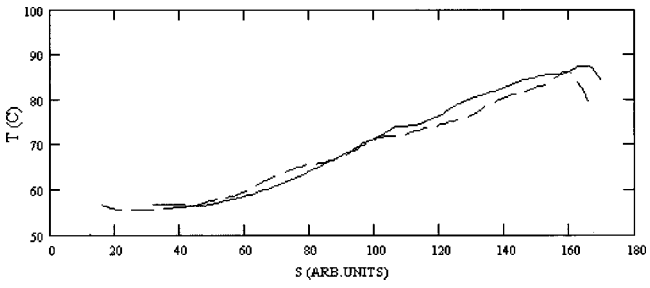

Fig. 10 Spanwise temperature distribution at 10 percent blade chord. Solid: using scaled temperature data. Dashed: using CFD temperature distribution and experimental pressure data

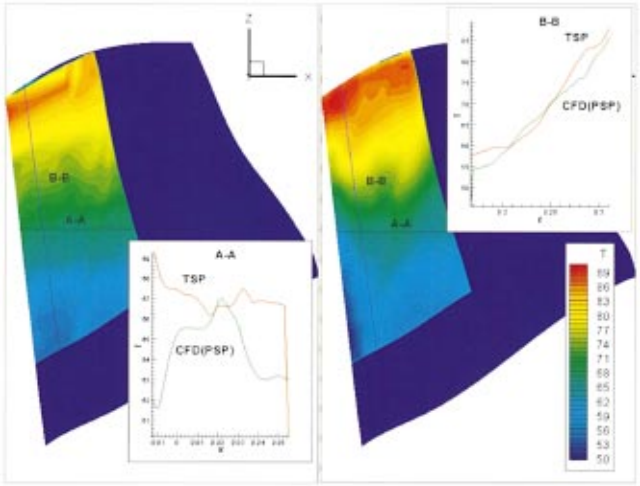

Fig. 11 Temperature fields obtained from scaled TSP data and temperature fitting of the CFD pressure and PSP relative intensity distributions

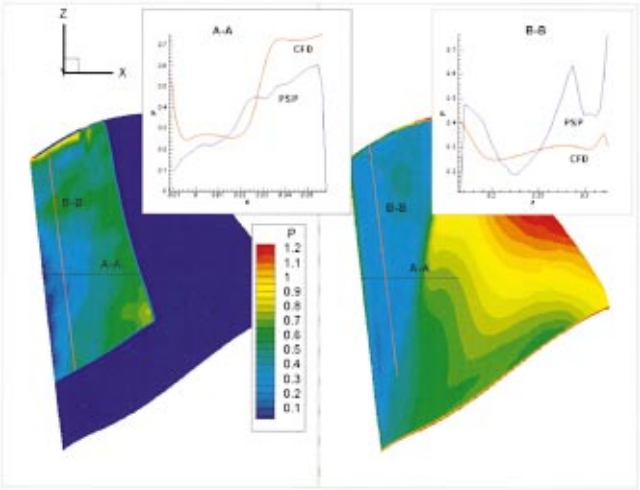

Fig. 12 Pressure fields obtained from PSP (left) and CFD (right)

Conclusion

Overall, this research has demonstrated the potential of using T/PSP techniques to obtain static temperature and pressure measurements on the surface of advanced turbomachinery rotor blades. Through this work the steady-state data acquisition system has been optimized. This success was achieved despite contamination problems encountered with operating the facility at a reduced inlet pressure. The sol-gel-derived T/PSPs developed have been shown to exhibit higher output signal and improved pressure sensitivity as compared to the silicone-based systems demonstrated in the initial tests [3,4]. More importantly, this work has demonstrated the ability to optimize the T/PSP for the desired need. An error analysis of the measurement approach indicates that a highly accurate temperature measurement is required to correct the pressure measurement. In particular at elevated temperatures above 80°C, the temperature measurement uncertainty must be better than 1°C to ensure a 1 percent error in the pressure measurement due to temperature. This proved to be a formidable requirement in this study due to the humidity and lubricating oil contamination encountered during the tests. *In situ* calibration utilizing the CFD temperatures proved to be an adequate approach to correcting the experimental temperature data for interferences. The overall three-dimensional shock location and the shock structure calculated by the CFD agree fairly well with the T/PSP results. This good agreement indicates that the viscous blockage in the rotor passage is correctly modeled in the CFD simulation.

Ideally, this new measurement technique must be independent of the predictive codes we wish to verify or further develop. In this test many problems prevented the measurement of surface temperature and we were forced to rely on predicted surface temperatures to determine pressure. As previously described, the condition predicted by the CFD (near-wall) is not the same condition measured by the paint (surface). The near-wall predictions of the CFD model can be expected to be different from the surface measurement results of the T/PSP coatings due to heat transfer and other physical effects. An independent pressure measurement will not be achieved using pressure-sensitive paints until we are able to accurately measure surface temperature and understand the fundamental differences (e.g., heat transfer effects) between the measured surface conditions and predicted near wall conditions. To this end, future efforts will be directed toward more accurate temperature measurements and towards the development of a heat transfer measurement technique for turbomachinery applications. These improvements will provide valuable data to aid in the understanding of heat transfer and other effects in the flow field that will be of use to both CFD development and the advancement of the subject measurement technique.

Acknowledgments

The authors would like to thank the employees of Compressor Research Facility (CRF), Air Force Research Laboratory and General Electric Aircraft Engines, for their support during the compressor test, Darryl Trump of Innovative Scientific Solutions, Inc. (ISSI) for his electronics expertise, which allowed us to image the rotor, Dr. William Weaver of ISSI for the development of the image processing software, and John Davis of ISSI for his skillful paint applications. Special thanks are owed to Drs. Jeff Jordan of NASA Langley and Neil Watkins of Science and Technology Corporation for their contributions to this effort.

References

[1] Sexton, M. R., O'Brien, W. F., and Mosts, H. L., 1973, "An On-Rotor Investigation of Rotating Stall in an Axial Compressor," Defense Technical Information Center (DTIC) Technical Report, Cameron Station, Alexandria, VA, pp. 33.1–10.

[2] Jordan, J. D., Watkins, A. N., Davis, J. C. P. N., Weaver, W. L., Dale, G. A., Navarra, K. R., Urban, J., Devoid, W., and Strange, R., 1999, "Pressure-Sensitive-Paint Measurements in a Large-Scale Commercial-Engine Test Stand," *Proc. 18th Int. Congress on Instrumentation in Aerospace Simulation Facilities*, Paper No. 21, Toulouse, France.

[3] Navarra, K. R., Goss, L., Jordan, J., Rabe, D., Gord, J., and Car, D., 1997, "Optical Measurements of Surface Pressure and Temperature in Turbomachinery," *Proc. Research and Technology Organization 90th Meeting and Symposium of the Propulsion and Energetics Panel on Advanced Non-Intrusive Instrumentation for Propulsion Engines*, Paper No. 18, Brussels, Belgium.

[4] Sabroske, K. R., Rabe, D. C., and Williams, C., 1995, "Pressure-Sensitive Paint Investigation for Application in Turbomachinery," ASME Paper No. 95-GT-92.

[5] Liu, T., Johnston, R., Torgerson, S., Fleeter, S., and Sullivan, J., 1997, "Rotor Blade Pressure Measurement in a High Speed Axial Compressor Using Pressure and Temperature Sensitive Paints," AIAA Paper No. 97-0162.

[6] Bencic, Tim, 1998, "Rotating Pressure and Temperature Measurements on Scale-Model Fans Using Luminescent Paints," AIAA Paper No. 98-3452.

[7] Kavandi, J., Callis, J., Gouterman, M., Khalil, G., Wright, D., Green, E., Burns, D., and McLachlan, B., 1990, "Luminescence Barometry in Wind Tunnels," Rev. Sci. Instrum., **61**, No. 11, pp. 3340–3349.

[8] Morris, M., Donovan, J., Kegelman, J., Schwab, S., Levy, R., and Crites, R., 1995, "Aerodynamic Applications of Pressure Sensitive Paint," AIAA Paper No. 92-0264.

[9] McLachlan, B., and Bell, J., 1995, "Pressure-Sensitive Paint in Aerodynamic Testing," Exp. Therm. Fluid Sci., **10**, pp. 470–485.

[10] Liu, T., Campbell, B., Burns, S., and Sullivan, J., 1997, "Temperature- and Pressure-Sensitive Luminescent Paints in Aerodynamics," Appl. Mech. Rev., **50**, No. 4, pp. 227–246.

[11] Gruber, M. R., Nejad, A. S., and Goss, L. P., 1997, "Surface Pressure Measurements in Supersonic Transverse Injection Flowfields," AIAA Paper No. 97-3254.

[12] Navarra, K. R., 1997, "Development of the Pressure-Sensitive-Paint Technique for Turbomachinery Applications, Master's Thesis, Virginia Polytechnic Institute and State University, Blacksburg, VA.

[13] Lakowicz, J., 1983, *Principles of Fluorescence Spectroscopy*, Plenum Press, New York.

[14] Jordan, J. D., Watkins, A. N., Weaver, W. L., Dale, G. A., and Navarra, K. R., 1999, "Sol-Gel-Based Pressure-Sensitive Paint Development," AIAA Paper No. 99-0566.

[15] Russler, P., Rabe, D., Cybyk, B., and Hah, C., 1995, "Tip Flow Fields in a Low Aspect Ratio Transonic Compressor," ASME Paper No. 95-GT-089.

[16] Donovan, J., Morris, M., Pal, A., Benne, M., and Crites, R., 1993, "Data Analysis Techniques for Pressure- and Temperature-Sensitive Paint," AIAA Paper No. 93-0178.

[17] Bell, J., and McLachlan, B. 1993, "Image Registration for Luminescent Paint Sensors," AIAA Paper No. 93-0178.

[18] Weaver, W., Jordan, J., Dale, G., and Navarra, K., 1999, "Data-Analysis Methods for the Development and Deployment of Pressure-Sensitive Paints," AIAA Paper No. 99-0565.

[19] Fonov, S., 2000, Edgewood Technologies Corporation, 809B Cuesta Drive, #192, Mountain View, CA 94040; private communication.

[20] Hah, C., Rabe, D. C., Sullivan, T. J., and Wadia, A. R., 1998, "Effects of Inlet Distortion on the Flow Field in a Transonic Compressor Rotor," ASME J. Turbomach., **120**, pp. 233–246.

[21] Hah, C., and Wennerstrom, A. J., 1990, "Three-Dimensional Flowfields Inside a Transonic Compressor With Swept Blades," ASME Paper No. 90-GT-359.